

Departamento de Química-Física

Facultad de Ciencias Químicas



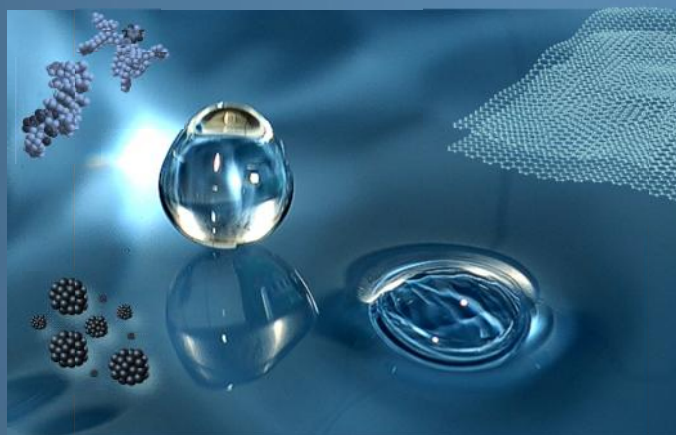
VNiVERSiDAD  
D SALAMANCA

CAMPUS DE EXCELENCIA INTERNACIONAL

# SELF-ASSEMBLED SYSTEMS OF NANOMATERIALS ON LANGMUIR-BLODGETT FILMS

---

*Sistemas Auto-ensamblados de Nanomateriales en  
Películas Langmuir-Blodgett*



Beatriz Martín García

Salamanca 2013



**VNiVERSiDAD  
D SALAMANCA**

CAMPUS DE EXCELENCIA INTERNACIONAL

**FACULTAD DE CIENCIAS QUÍMICAS**

**Departamento de Química-Física**

**SELF-ASSEMBLED SYSTEMS OF NANOMATERIALS ON  
LANGMUIR-BLODGETT FILMS**

*SISTEMAS AUTOENSAMBLADOS DE NANOMATERIALES EN  
PELÍCULAS LANGMUIR-BLODGETT*

**BEATRIZ MARTÍN GARCÍA**

**Salamanca, 2013**





**VNiVERSiDAD  
DSALAMANCA**

CAMPUS DE EXCELENCIA INTERNACIONAL

**FACULTAD DE CIENCIAS QUÍMICAS**

**Departamento de Química-Física**

**SELF-ASSEMBLED SYSTEMS OF NANOMATERIALS ON  
LANGMUIR-BLODGETT FILMS**

*SISTEMAS AUTOENSAMBLADOS DE NANOMATERIALES EN  
PELÍCULAS LANGMUIR-BLODGETT*

**Memoria que para optar al grado de Doctor por la Universidad de  
Salamanca presenta la licenciada Beatriz Martín García**

**Salamanca, 15 de Abril de 2013**

A handwritten signature in blue ink, reading "Beatriz Martín García".

**Fdo. Beatriz Martín García**



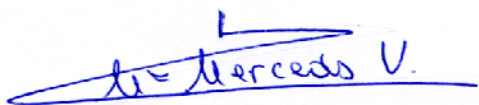
D<sup>a</sup>. M<sup>a</sup> Mercedes Velázquez Salicio, Catedrática de Universidad en el Departamento de Química-Física de la Universidad de Salamanca,

**INFORMA:**

Que el trabajo presentado como Tesis Doctoral por la licenciada en Ingeniería Química Beatriz Martín García para optar al grado de Doctor por la Universidad de Salamanca, titulado **"Self-assembled Systems of Nanomaterials on Langmuir-Blodgett Films / Sistemas Auto-ensamblados de Nanomateriales en Películas Langmuir-Blodgett"** ha sido realizado en el laboratorio del G.I.R de Coloides e Interfases en el Dpto. Química-Física de la Facultad de Ciencias Químicas de la Universidad de Salamanca (España) y en las instalaciones del Grupo de Fotoquímica Molecular del Instituto Superior Técnico de Lisboa (Portugal).

Como directora del trabajo, autoriza la presentación del mismo, al considerar que se han alcanzado los objetivos marcados.

Y para que conste, firmo el presente en Salamanca a 15 de Abril de 2013.



Fdo. M<sup>a</sup> Mercedes Velázquez Salicio



El trabajo que engloba la presente Memoria se ha realizado durante el periodo de disfrute de una Beca de Colaboración (curso 2006/2007) en el Departamento de Química-Física del Ministerio de Educación y Ciencia y una ayuda a la contratación de Personal Investigador de Reciente Titulación Universitaria (2008/2012) de la Junta de Castilla y León concedida al amparo de la Orden EDU/330/2008 de 3 de marzo.

El trabajo desarrollado dentro del G.I.R. de Coloides e Interfases del Departamento de Química-Física ha sido financiado por los proyectos: MAT 2004-04180, MAT 2007-62666 y MAT 2010-19727 del Ministerio de Educación y Ciencia; y SA038A05 y SA038A08 de la Junta de Castilla y León.





*"I am among those who think that science has great beauty.  
A scientist in his laboratory is not only a mere technician:  
he is also a child confronting natural phenomena  
which impress him like a fairy tale"*  
**by Marie Skłodowska Curie**



## ***Acknowledgments***

*En estas líneas quiero expresar mi agradecimiento a todas aquellas personas que de una manera u otra han intervenido en el desarrollo del presente trabajo y por tanto, lo han hecho posible. Espero no olvidarme de nadie, pero por si acaso, pido disculpas por anticipado. Agradecerles su compañía en esta difícil tarea y su ayuda a crecer como persona tanto humana y como científicamente.*

*En primer lugar quisiera agradecer a mi Directora, Prof. Dra. D<sup>a</sup>. Mercedes Velázquez Salicio, por brindarme la oportunidad de introducirme en el mundo de la investigación dentro del Grupo de Coloides e Interfases de la Universidad de Salamanca y transmitirme cada día su ilusión por este trabajo. Así como su inestimable ayuda en el trabajo de cada día y en la elaboración de esta memoria.*

*Dentro del Departamento de Química-Física, quisiera agradecer también a la Prof. Dra. D<sup>a</sup>. M<sup>a</sup> Dolores Merchán Moreno el apoyo y los consejos recibidos durante este tiempo. También hacer un especial agradecimiento a los Prof. Drs. José Luis Usero, M<sup>a</sup> Ángeles del Arco, Carmen Izquierdo, Julio Casado y Emilio Calle, por su colaboración en determinados momentos.*

*Al Dpto. de Química Orgánica, en especial a los Prof. Drs. D. Francisco Bermejo y D<sup>a</sup>. Josefa Anaya por su asesoramiento en síntesis; y al Prof. Dr. Joaquín R. Morán por compartir su sabiduría a la hora resolver cuestiones puntuales sobre productos y disolventes. Al Dpto. de Química Inorgánica, concretamente a Prof. Drs. D. Vicente Rives y D<sup>a</sup>. Raquel Trujillano por su disponibilidad y facilidades para utilizar varios equipos. Al Dpto. de Bioquímica y Biología Molecular, en especial a la Prof. Dra. D<sup>a</sup>. Nieves Pérez por su amabilidad y accesibilidad para el uso de las centrifugas. Al Servicio de Microscopía, con mención a sus técnicos Juan y en los últimos tiempos, a Marta por su fantástica predisposición. Al Dpto. de Química Analítica, por las pruebas en las centrifugas, algunos compuestos químicos y el agua cuando fallaba el MilliQ, y sobre todo como ellos dicen por salvarme la "vida". Al*

*CLPU y todo su equipo por facilitar la realización de las medidas de AFM, pero con especial hincapié en José y Juan, por su paciencia y dedicación.*

*Y continuando con la Física, al Prof. Dr. D. Enrique Diez y su doctorando, Cayetano S. Cobaleda, del Laboratorio de Bajas Temperaturas (Universidad de Salamanca) por adentrarme en el mundo del grafeno. In questa linea, vorrei anche ringraziare il Prof. Dr. Vittorio Bellani ed il Dr. Francesco Rosella (Università di Pavia, Italia) per la loro inestimabile collaborazione ed il loro appoggio. Aquí, también me gustaría dedicar unas palabras de agradecimiento a la gente del ISOM-UPM, en especial a M<sup>a</sup> Mar, David, Maika, Alicia y José Antonio. Al Grupo de Dispositivos Semiconductores (Universidad de Salamanca), en especial al Prof. Drs. D. Tomás González y al D. Ignacio Íñiguez de la Torre, por hacer posibles las medidas de conductividad y su dedicación.*

*Al Grupo de Sistemas Complejos de la Universidad Complutense de Madrid (UCM), en especial a los Prof. Drs. Francisco Ortega y Ramón G. Rubio por darme la oportunidad de realizar una estancia en el grupo y permitir el acceso al uso del elipsómetro, y al Dr. José E.F. Rubio por las medidas. Destacar la fantástica acogida y las charlas con Eduardo, Armando, Hernán, Marta y Mónica. También al Prof. Dr. D. Valentín García Baonza de la UCM, por algunas pruebas de Espectroscopía Raman.*

*Asimismo, agradecer a la Prof. Dra. D<sup>a</sup>. Margarita González Prolongo y a su equipo del Departamento de Materiales y Producción Aeroespacial de la Escuela Técnica Superior de Ingenieros Aeronáuticos de la Universidad Politécnica de Madrid (UPM) por permitirnos utilizar el equipo de Calorimetría Diferencial de Barrido (DSC).*

*Al Prof. Dr. José Luis G. Fierro del Instituto de Catálisis y Petroquímica (CSIC), por su colaboración y discusiones de las medidas de XPS. Al Prof. Dr. Albert Cicera y a Sergi Claramunt del Departamento de Electrónica de la Universitat de Barcelona, por facilitar la realización de las medidas de FE-SEM.*

*À Professora Silvia M.B. Costa, do Instituto Superior Tecnico da Lisboa, pela oportunidade de fazer uma estadia no seu grupo de investigação, a sua implicação no desenvolvimento do trabalho, preocupação e atenções. Também por deixa-me participar nas reuniões do grupo, como um membro mais, e poder apresentar e discutir o nosso trabalho. Ao*

*Dr. Pedro M.R. Paulo pela sua dedicação, ajuda, ensinamentos e longas discussões dos resultados durante e depois da minha estadia. Com licença e humildade, gostaria de poder lhes dedicar o capítulo da tese da fotofísica dos quantum dots, onde agradeço a ajuda na elaboração da redação ao Dr. Pedro M.R. Paulo. Muito obrigada também a todos os membros do Grupo de Fotoquímica Molecular pelo trato recebido durante a minha estadia.*

*Para el final querría hacer un punto de inflexión, para agradecer los momentos divertidos y de apoyo de los que considero mis compañeros y mis amigos. Primeramente, a Teresa, con la que empecé mi andadura en el doctorado y con la que he tenido la oportunidad de trabajar y compartir buenos y malos momentos, estancias y congresos, un gran apoyo y amiga, simplemente gracias. A mis "asesores"... por el apoyo y los sabios consejos. A mis amigos, por las velas, las oraciones y la confianza en mí. Por lo importante que ha sido el entorno de trabajo, a mis compañeros de laboratorio, David, Rubén y Sofía. A los compañeros de Departamento, tanto a los que están como a los que afortunadamente han encontrado un post-doc o trabajo, por hacer más ameno el día a día, el paintball, las discusiones científicas y conseguir artículos, Pablo, Jesús, Susana, Marina, Jorge, Mario, Rafa, Fabián, Manso, Teresa, Jessica, Nico y Ruth. Sin poderme olvidar tampoco de los orgánicos de Villarriba en especial de Ángel, gracias por todo, aquí incluiré también a Sole y a Juan, por las cenas, el argón y los disolventes; ni de las analíticas, Sara, un poco culpable de que me dedique a esto de la investigación, y Ana. A Cayetano, por su ayuda durante mi estancia en la sala blanca y sus mal-logrados intentos en Bilbao junto a Mario de convertirme al QHE. Gostaria também de agradecer à gente da Lisboa: as minhas Raqueis, o Pedro, com licença, a Vanda, o Vipin, a Sofía, a Marta, o André, o Sergio, o Quaresma,...., Jose Antonio e Elisa, a todos por fazer que estivera como na minha casa durante a estadia, imensamente obrigada sempre.*



## **Contents**





## Contents

<b>Aims and Scope of the Thesis</b>	<b>1</b>
<b>I. State of the Art</b>	<b>7</b>
I.1. Self-assembly of Polymers at the Air-Water Interface	11
I.2. Self-assembly of Nanoparticles at the Air-Water Interface	12
I.3. Self-assembly of Carbon Allotropes at the Air-Water Interface	14
<b>II. A General Overview</b>	<b>15</b>
II.1. Langmuir Monolayers	15
II.2. Mixed Langmuir Monolayers	21
II.3. Langmuir-Blodgett Films	22
II.4. Polymer Langmuir Monolayers	26
II.5. Langmuir Monolayers of Nanoparticles	32
II.6. Langmuir Monolayers of Graphene Derivatives	37
<b>III. Experimental Section</b>	<b>41</b>
III.1. Materials and Reagents	41
III.2. Langmuir Monolayers: Preparation Procedure	45
III.3. Experimental Techniques	47
III.3.1. Langmuir Trough	47
III.3.2. Surface Potential: Kelvin Probe	54
III.3.3. Brewster Angle Microscopy	58
III.3.4. Langmuir-Blodgett Trough	62
III.3.5. Atomic Force Microscopy	63
III.3.6. Electronic Microscopy	67
III.3.7. Ellipsometry	70
III.3.8. Micro-Raman Spectroscopy	75

---

III.3.9. UV-vis Spectrofotometry	78
III.3.10. Fourier Transform Infrared Spectroscopy	79
III.3.11. X-Ray Photoelectron Spectroscopy	80
III.3.12. Differential Scanning Calorimetry	83
III.3.13. Four-point Probe Conductivity Measurements	84
III.3.14. Dual Focused Ion Beam/Scanning Electron Microscopy	87
III.3.15. Fluorescence Lifetime Imaging Microscopy	90
III.3.16. Electron Beam Lithography	97
<b>IV. Polymer Monolayers</b>	<b>103</b>
IV.1. PS-MA-BEE Monolayers	105
IV.2. PS-b-MA Monolayers	123
<b>V. Preparation and Properties of QDs Films</b>	<b>133</b>
V.1. Experimental Section	136
V.2. Preparation of QDs Films	139
V.2.1. Langmuir and Langmuir-Blodgett Films of QDs and PS-MA-BEE	139
V.2.2. LB Films of QDs transferred onto a LB Film of Polymer	154
V.2.3. Surface Ligand Exchange: PSMABEE-capped QDs	161
V.2.3.1. Surface Ligand Exchange Process	161
V.2.3.2. Langmuir and Langmuir-Blodgett Films of PSMABEE-capped QDs	165
V.3. Dynamic Properties of QD/PS-MA-BEE Mixed Systems	172
V.3.1. Effect of Shearing on Film Morphology and Monolayer Reorganization	174
V.4. Photoluminescence of QDs in Langmuir-Blodgett Films	191
V.4.1. Experimental Details	193

---

V.4.2. Selection of the Experimental Conditions by Steady-State Measurements	195
V.4.3. Photoluminescence Dynamics of QDs	197
V.4.3.1. Photoluminescence Dynamics of QDs in Solution	198
V.4.3.2. Effect of the Excitation Energy on QDs LB Films	201
V.4.3.3. Effect of the Exposure Time on QDs LB films	204
V.4.4. Photoluminescence Dynamics of QD/PS-MA-BEE LB Films	209
V.4.4.1. Interpretation of the QDs Photoluminescence Dynamics	215
V.4.4.2. Effect of Capping Exchange on the QDs Photoluminescence Dynamics: PSMABEE-capped QDs LB Films	229
V.4.5. Imaging Characterization of Mixed QD/PS-MA-BEE Films	233
V.4.5.1. QD <sub>TOPO</sub> /PS-MA-BEE Langmuir-Blodgett Films	234
V.4.5.2. QD <sub>p</sub> /PS-MA-BEE Langmuir-Blodgett Films	240
<b>VI. Chemically derived Graphene</b>	<b>243</b>
VI.1. Oxidation and Reduction Procedures of Graphitic Material	247
VI.1.1. Graphite Oxide Production	247
VI.1.2. Reduction of Graphite Oxide	252
VI.1.2.1. Chemical Reduction of GO with Hydrazine	257
VI.1.2.2. Chemical Reduction of GO with Vitamin C	258
VI.1.2.3. Chemical Reduction of GO assisted by the Surfactant DDPS	258
VI.2. RGO samples: Characterization and Langmuir-Blodgett Deposition	259
VI.2.1. Characterization of RGO samples	259

---

VI.2.2. Langmuir-Blodgett Films of Graphite Oxide	265
VI.2.3. Langmuir-Blodgett Films of RGO samples	267
VI.2.4. Langmuir-Blodgett deposited Sheets of RGO functionalized with the Surfactant DDPS	273
VI.2.5. Electric Conductivity Measurements	276
VI.2.6. Electron Beam Lithography: RGO sheets Au-contacted	279
<b>VII. Conclusions</b>	<b>283</b>
<b>VIII. References</b>	<b>289</b>
<b>Articles / Manuscripts</b>	<b>335</b>
<b>Appendix</b>	
Nomenclature	<i>i-vii</i>
<b>Resumen (<i>Summary</i>)</b>	<b>I-XLV</b>

## **Aims and Scope of the Thesis**



## **Aims and Scope of the Thesis**

In recent years, the development and study of the nanomaterials have focused the attention of the scientists to use them as building blocks looking for novel properties inside technological and biological applications. The small size of the materials leads to unique properties that allow the construction of small devices ranging from nanometers to a few micrometers. Within this field one of the most important issue is the control of the size and shape of these structures in order to use them. In this sense, two of the challenges are the knowledge and understanding of the structures' formation to tune the architecture of the nanomaterial system looking for the modulation of the properties.

In some applications, as the construction of optoelectronic devices such as sensors, LEDs or photovoltaic cells, nanomaterials are deposited onto solids. In these cases it becomes necessary to develop the proper methodology to achieve a good coverage, avoid nanomaterials 3D agglomeration and allow the variation of the density of nanomaterials, spacing and even arrangement. An effective and convenient method to pattern a surface on an nm- $\mu$ m scale without the use of lithographic processes, is the self-assembly approach. It is a low-cost, large-area scalable and solution-processing technique that does not require sophisticated equipments. In the self-assembly the behaviour of the nanomaterial at the interface, in which it is placed, plays a decisive role. Thus, to obtain a good quality or optimize the assembly formation, it is important to understand the mechanism or forces involved in the self-assembly process. Therefore, the study of the behaviour of nanomaterials at the interfaces, by means of the equilibrium and dynamic properties, is the starting point to achieve the assembly modulation. In this sense, the overall objective of this thesis is to study the self-assembly process of three different nanomaterials at the air-water interface and onto solids. The systems proposed were polymers, CdSe quantum dots (QDs) and chemically derived graphene. The common aspect between them is the use of the Langmuir



and Langmuir-Blodgett (LB) techniques to evaluate the effect of the equilibrium and dynamic properties on their self-assembly process. These techniques render the self-assembly process of different nanomaterials at the air-water interface under well controlled and reproducible conditions. The LB technique was chosen because it has proved to be a versatile and interesting method to obtain thin films that allows a control of the surface concentration, which can be readily modified by compressing or expanding the film using barriers. Moreover, some dewetting processes have been observed in the preparation of the LB films that could be used to pattern at the nanoscale.<sup>[1-3]</sup>

From this picture, the thesis has been organized in three different part according to the nanomaterials studied.

The first part is focused on polymer thin films. Research on thin polymer films has revealed that various physical properties, such as unexpected instabilities, chain conformations, dewetting processes or glass-transition temperature variations, exhibit characteristics strongly deviating from their bulk behaviour, with major implications for most technological applications based on such nanoscopic films.<sup>[4]</sup> Despite the extensive research work a clear understanding of thin polymer film properties has not yet been reached. Therefore, in order to prepare good quality films for the construction of devices it is necessary previously to understand the equilibrium and dynamic properties of the monolayers precursors of the LB films. In this setting, we decided to study styrene-maleic anhydride copolymers' films because these polymers have shown potential application in optical waveguides, electron beam resists and photodiodes.<sup>[5, 6]</sup> The polymers selected were the block copolymer poly (styrene-co-maleic anhydride) partial 2-butoxy ethyl ester cumene terminated, PS-MA-BEE, and poly (styrene-co-maleic anhydride) cumene terminated, PS-b-MA. Consequently, they could be used as a pattern for the fabrication of layered molecular electronic devices. Moreover, the interfacial rheology is interesting due

to the polymer films are exposed to external disturbances. Thus, the stability properties of the films are important in applications such as coating or adhesion processes. In this sense, the aim was to study the effect of the addition of electrolytes in the aqueous subphase and temperature on the equilibrium and dynamic properties of Langmuir monolayers of the two polymers selected. Moreover, Langmuir-Blodgett films prepared from polymer monolayers onto different substrates have been characterized by different techniques to analyze the influence of different factors such as subphase composition, temperature and polymer nature on the film formation.

The second system studied was hydrophobic CdSe QDs films. These nanoparticles present attractive optical applications in the fabrication of solar cells or LEDs due to their band-gap tunability. QDs show size-dependent optoelectronic properties that allow modulating the match with the solar spectrum in photovoltaic devices or improving the emission efficiency producing white (or coloured) light in LEDs. The most important optical advantages are a broad and continuous absorbance spectrum (from the UV to the far-IR), a narrow emission spectrum whose maximum position depends on the QD size, ligand-affected physico-chemical properties and high light stability. However, optoelectronic device applications based on QDs may either involve a very large number of dots in an ensemble with controllable architecture to avoid the deterioration of film quantum efficiency. Therefore, the thickness and uniformity of the assembled QD films are crucial factors in the emission properties of the films.<sup>[7-11]</sup> Some theoretical arguments suggest that the interactions between particles and a self assembled material can produce ordered structures.<sup>[12]</sup> Thus, diblock copolymers are known to self-assemble spontaneously into structures in the order of tens of nanometers in length, and these structures can be transferred onto substrates by LB or dip-coating methods.<sup>[13]</sup> Some research revealed that the organization of nanoparticles is governed by molecular interactions between the diblock copolymers and nanoparticles that constitute the mixed monolayers at the

air-water interface.<sup>[14, 15]</sup> Despite some successful results, more research must be carried out to develop nanometric structures that may provide new properties associated with the reduction of the materials size.<sup>[16]</sup> Thus, the objective in this part was to use the copolymers ability of self-assembly at the air-water interface to modulate the QDs organization forming hybrid systems by the LB technique. The objective of this work is focused on the self-assembly process of CdSe QDs onto solids assisted by the polymer PS-MA-BEE. Different approaches using the LB methodology as the deposition technique and the polymer PS-MA-BEE to assist the self-assembly of the QDs on the solid were explored. On the one hand, polymer LB film is employed to modify the surface properties of the substrate and on the other hand, the polymer assist the QD Langmuir monolayer formation. Furthermore, in the last one, to understand the film patterning the equilibrium and dynamic properties of the mixed Langmuir monolayers of QDs and polymer were studied. In this way, the influence of the polymer concentration and nature of the nanoparticle ligand on the morphology of the films was also analyzed. The role of the QDs ligand was studied by exchanging the synthesis organic ligand of the QDs, trioctylphosphine oxide (TOPO), by the polymer PS-MA-BEE.

To ensure a good processability and reliability of the mixed QD/polymer films to device construction and functioning, the study of their dynamic properties is important.<sup>[17]</sup> Moreover, in general the monolayers prepared by compression lead to metastable states. A way to avoid these states and promote the formation of more ordered and homogeneous films is the application of successive compression-expansion cycles.<sup>[18]</sup> Moreover, the air-water interface (Langmuir trough) has been also proposed as a good platform to carry out the study of the dynamics of thin films. In this field, there is little work with nanoparticle monolayers due to the time-consuming and complexity of the experimental data performing and interpretation. The available studies are mainly focused on the study of nanoparticles.<sup>[18-20]</sup> Moreover, to the best of our

knowledge for mixed systems only studies performed with surfactants and nanoparticles exists.<sup>[21]</sup> For nanoparticle/polymer systems only theoretical studies are available with regard to the reorganization and dynamics of these systems.<sup>[22-24]</sup> In this sense, the aim is to study the influence of shearing on the QD/PS-MA-BEE film morphology and the dynamic processes involved in the reorganization of these monolayers after shearing.

Moreover, as the optical properties of the QDs are relevant for their application the photophysical properties of the QD/polymer LB films onto solid substrates were analyzed by means of Fluorescence Lifetime Imaging Microscopy (FLIM). Thus, the aim of this study is to evaluate the effect of the QDs arrangement in the films and the ligand role on their photoluminescence properties. The FLIM technique was selected because it presents a high sensitivity to surface and environmental changes.<sup>[25]</sup>

In the third part the system studied was chemically derived graphene. Graphene has received enormous attention due to its extraordinary mechanical and electrical properties.<sup>[26]</sup> These remarkable properties make graphene and its derivatives promising candidates for fabrication of electronic devices and as reinforcing fillers in composites with applications in medicine<sup>[27]</sup>. The success of graphene in technological applications is related to the availability of production methods for the synthesis of large amounts of material at low cost. Several physical methods such as epitaxial growth, micromechanical exfoliation and chemical vapour deposition with a high-cost, have been proposed leading to the best material properties, but nowadays the expectation is focused on chemical-solution processing approaches that provides low-cost material. This method is based on the exfoliation of graphite by chemical oxidation and the subsequent reduction process to restore the graphite  $C_{sp^2}$  structure. Besides, it is necessary to deposit the material obtained on solids. Therefore, several efforts are being made in the development of chemical and deposition processes to achieve good quality

sheets (high reduction degree and low structural defects) and controllable adhesion onto solid substrates. However, chemical oxidation disrupts the electronic structure of graphene by introducing O-containing groups in the network, which cannot be completely removed by chemical reduction. Besides, the tendency of the reduced graphite oxide (RGO) to agglomerate makes further processing quite difficult. In order to avoid this, the functionalization of graphite oxide with different stabilizers such as ionic surfactants has been proposed.<sup>[28]</sup> Moreover, as the most remarkable properties are associated with few-layer graphene ( $\leq 5$  layers), a control in the film thickness is also important. In this picture, we propose a colloidal-chemistry route where the chemical reduction is assisted by a zwitterionic surfactant, N-dodecyl- N,N-dimethyl-3-ammonio-1-propanesulfonate (DDPS), in order to improve the reduction degree and defect repair achieved by the reducer agents and, furthermore, to functionalized the RGO obtained. This approach is based on the better adsorption that these surfactants present on graphite surfaces than on ionic ones. Furthermore, the functionalization can allow the attachment of metal cations or polymers to construct nanocomposites with potential applications.<sup>[29, 30]</sup> Moreover, the surfactant can also modulate the self-assembly of the sheets at the air-water interface, which has been proposed as a good platform to study the graphene derivatives due to they present a high specific surface area. Thus, the aims in this work are to develop and check the new synthetic route and the analysis of the quality of the produced material. By means of different techniques, such as X-Ray photoelectron or Raman spectroscopies, and conductivity measurements the effect of the surfactant on the reduction degree and defect repair was evaluated for two different reduction agents: hydrazine and vitamin C. Moreover, as the transference of the material onto solids in a controllable way is also important for the material characterization and application, in this work the LB technique has been proposed to deposit the graphitic material onto the substrate. Thus, the influence of the material properties on the sheets' assembly deposited onto silicon by the LB method was also studied.

## **I. State of the Art**



## I. State of the Art

In this chapter some of the most relevant concepts in the different research areas involved in the nanostructured materials are summarized: from the nanomaterials to the self-assembly process focusing on the role of the Langmuir-Blodgett technique.

Nanomaterials are a broad and assorted kind of materials, which have structured components with at least one dimension less than 100 nm. Nanostructures constitute a bridge between molecules and infinite bulk systems and include organic molecules, polymers, clusters, nanoparticles (quantum dots), carbon-based nanostructures (carbon allotropes, nanotubes, graphene sheets) or biomacromolecules (proteins, DNA, RNA). The nanostructures can organize into arrays, assemblies (surface and thin films) or superlattices of the individual nanostructures.<sup>[31]</sup>

The physical and chemical properties of nanostructures are distinctly different from those of either a single atom (molecule) or of the bulk matter with the same chemical composition. These differences between nanomaterials and their molecular and bulk counterparts are related to the spatial structures and shapes, phase changes, electronic structure and chemical reactivity of large, finite systems and their assemblies. Therefore, it is possible to process materials which can be tuned via size control to achieve specific functionality, i.e. the size-dependent properties. In this sense, a suitable control of the properties and response of nanostructures can lead to new devices and technologies, with especially potential applications in optoelectronic and magnetic devices.

Nowadays, there are two approaches for the building up of nanostructures: the top-down and the bottom-up methods. In the top-down methods, the features are written directly onto a substrate, for example, by electron beams, and then by applying appropriate etching and deposition



processes (lithography, patterning), the nanoscopic features are engraved. In the bottom-up approach, nano-components are made from precursors employing either chemical or physical deposition processes that are integrated into building blocks within the final material structure. In this approach, the self-assembly and the self-organization methods are used in structuring nanomaterials. The organization during self-assembly processes is driven mainly by competing molecular interactions between the components, while in the self-organization methods the collective interaction between the system components is driven by an external force, which drive the system far from equilibrium resulting in the self-organization of its constituents.<sup>[32]</sup>

Self-assembled systems are interesting from both the fundamental point of view<sup>[33]</sup> and the technological applications<sup>[34, 35]</sup>. Several approaches using self-assembly for nanofabrication are already under investigation. They range from molecular manipulation through the use of self-assembled monolayers and supramolecular chemistry, to much larger systems made by the controlled self-assembly of colloids or directly hierarchical architectures. The self-assembly could be an efficient method for manufacturing nanoscale devices and systems, but it is still necessary a lot of work in order to a functional device is built in a commercial way.

Self-assembly is considered as a powerful tool in modern molecular science. The ability of carefully designed building blocks to spontaneously assemble into complex nanostructures without human intervention underpins developments in a wide range of technologies ranging from materials science through to molecular biology.<sup>[36, 37]</sup> Thus, the self-assembly is defined as a process in which components, either separately or linked, spontaneously form aggregates.<sup>[38, 39]</sup> The interactions involved are usually non-covalent and connect the molecular building blocks in a reversible, manipulable and specific way. Furthermore, the key is to generate nanoscale complexity from the new behaviour

that offers the assembled structures<sup>[40]</sup> by understanding that structural control via self-assembly is dependent on the design at the molecular level since a combination of environmental and molecular factors dictate kinetic and thermodynamic aspects of self-assembly<sup>[41]</sup>. This approach is theoretical and technologically interesting<sup>[39]</sup> in several fields: Chemistry, Physics, Biology, Materials Science, Nanoscience and Manufacturing. However, much effort has been directed to understand the mechanisms or the role of the interactions or forces involved in the self-assembly processes.

The interactions are generally weak and non-covalent in the self-assembled systems. However, not only the interaction between the compounds define the final state of the systems, but also the interactions can often be influenced or selected by physical processes and geometrical constraints, such as gravitational effects, Marangoni convection, spinodal decomposition and entropic interactions, or by external forces such as external electromagnetic fields, which can modify the outcome of a self-assembly process, and sometimes provide flexibility to the process.<sup>[42-45]</sup> Some of them belong to the self-organization process, that occurs as natural responses of complex systems to strong external stimulations.<sup>[32]</sup> However, in the self-assembly process the components either equilibrate between aggregated and non-aggregated states, or adjust their positions relative to one another once in the aggregate.

The self-assembly of nanomaterials is normally carried out in solution or at a smooth interface, such as solid-liquid, liquid-liquid and vapour-liquid boundaries, since these media allow the required motion of the components.<sup>[46]</sup> At the interfaces, reduction in the interfacial energy causes the spontaneous assembly.<sup>[37]</sup> Likewise, the interaction of the components with their environment can strongly influence the result of the process. Moreover, sometimes templates or surface-modified substrates are used to reduce defects and control structures.<sup>[32]</sup> Directed self-assembly can provide not only the ability to tune the interaction

between individual assembling components but also the ability to position the final assembly at a desired location.

Within the different media, the air-water interface can be considered as a platform for the self-assembly, which can illustrate important physical, chemical and biological phenomena and provide simple robust routes for the fabrication of two-dimensional (2D) and three-dimensional (3D) functional nanostructures.<sup>[47-48]</sup> Besides, this interface can provide a medium to exploit the adsorption properties of the monolayer in order to incorporate molecules from the subphase<sup>[49]</sup> or allows spontaneous growth of thin films from the subphase by precursors reaction<sup>[50]</sup>.

In this sense, nanostructuring macromolecules and nanomaterials at the air-water interface through Langmuir monolayers, following by transfer onto solid substrates forming Langmuir–Blodgett (LB) films that have been effectively used to investigate surface chemical and physical properties and achieve well-controlled surface morphologies.<sup>[3]</sup>

The LB technique was introduced in the 1990s as a powerful method for the assembly and orientation control of molecular monolayers for applications such as organic electronics and non-linear optics, in the so called molecular electronics.<sup>[51]</sup> The LB approach offers several advantages in the preparation of thin films comparing with other techniques such as spin coating or layer-by-layer. Within the advantages stand out, the relative simplicity of preparing films; the possibility to deposit single layers, thus, allowing a high degree of control over layer thickness and phase state; to make multiple and alternating layer films deposition; to enable structures with varying layer composition and/or orientation; and to allow to modulate the interparticle distance.<sup>[1, 52]</sup> Besides, the subphase present in the LB environment provides enormous opportunity to add value and functionality to the deposited films.<sup>[2, 51]</sup> Furthermore, the method can extend its employment in the field of sensors and nanotechnology based on the

use of both amphiphilic and non-amphiphilic nanoscale materials at the air-water interface.<sup>[3]</sup> However, it is necessary an understanding of the LB process and the ability to control it in order to lead to an increase in the reproducibility and optimization of the whole process.<sup>[2]</sup>

Within the self-assembly of nanomaterials at the air-water interface, the thesis is focused on the study of three different systems: polymers, nanoparticles and chemical graphene derivatives.

### **I.1. Self-assembly of Polymers at the Air-Water Interface**

Within polymers, amphiphilic block copolymers are an interesting and important class of molecules for device fabrication <sup>[53]</sup> that have been shown to self-assemble into well-defined nanoscale and mesoscale structures in both two <sup>[54-57]</sup> and three dimensions <sup>[58]</sup>. The 2D self-assembly of amphiphilic block copolymers at the air-water interface is a proven route to understand interfacial structures and properties such as wettability, chemical functionality and structural stability in amphiphilic polymer systems.<sup>[3]</sup> The lateral dimensions of the aggregates obtained at the air-water interface can be orders of magnitude larger than the polymer chain dimensions, suggesting that a large number of blocks can overlap to form the surface features with block junctions localized underneath the aggregates.<sup>[14, 55, 56]</sup>

The formation of various 2D polymer surface features in Langmuir monolayers is the result of spontaneous block copolymer aggregation balance at the air-water interface, which arises from an interplay of attractive interactions between the hydrophilic block and the water surface and repulsive interactions between hydrophobic block and water and between the different blocks as the spreading solvent evaporates; kinetic factors such as chain entanglements and the ultimate “freezing” of the glassy polymer can also influence the final morphologies.<sup>[3, 56]</sup>

Various block copolymer has been extensively studied, mainly the self-assembly at the air-water interface of block copolymers based on a hydrophobic polystyrene-based (PS) block. The hydrophilic block can be poly(ethylene oxide) (PEO) <sup>[54-57]</sup>, polylactide (PLA) <sup>[59]</sup>; poly methyl methacrylate (PMMA) <sup>[60]</sup>; polyvinyl pyridine (PVP)<sup>[61]</sup>; or poly N-isopropyl acrylamide (NIPAM) <sup>[62]</sup>. Thus, the surface-active nature of hydrophilic block promotes its spontaneous adsorption at the air-water interface, although above a critical two-dimensional (2D) overlap density, the solubility of this block causes it to become easily detached from the interface and dissolved in the aqueous subphase. In order to combat this effect, the hydrophobic block is required together the hydrophilic blocks to the surface above the critical surface density.<sup>[41]</sup>

In addition, monolayers of polymeric surface features obtained by self-assembly at the air-water interface can be easily transferred by the Langmuir-Blodgett (LB) method to various solid substrates for potential applications. The surface features obtained from LB films depend on factors such as the nature (amphiphility, solubility, molecular weight, block ratio) of the blocks, surface pressure, pH, temperature and concentration of the spreading solution.<sup>[63]</sup> For example, the ionization of repeating units in block copolymers by changing the pH or adding electrolytes in subphase, produces changes in the interfacial behaviour and morphologies of Langmuir monolayers, precursors of the LB films.

## **I.2. Self-assembly of Nanoparticles at the Air-Water Interface**

Self-assembly of nanoparticles is becoming a leading methodology in fabrication of functional materials with unique optical, electronic, chemical, and biological properties.<sup>[51, 64]</sup> In nanoparticle self-assembled structures, each individual nanoparticle is the fundamental building-block that serves for constructing the ordered structure. The understanding of the size- and shape-dependent properties of individual nanoparticles, and the collective properties of assemblies is interesting for their applications.<sup>[7]</sup>

Focusing on the semiconductor nanoparticles, the most important factor on their self-assembly is the organic ligands that are attached to its inorganic core surface. Various organic ligands are used, such as phosphine oxides, phosphanes, alkyl thiols, amines and carboxylic acids, and they drive the self-assembly of the nanoparticles at the air-water interface. The controlled assembly of semiconducting NPs into two-dimensional (2D) structures is a critical step toward their use as functional elements in new materials because collective properties and function are governed by nanoparticle organization on a combination of length scales.<sup>[8, 65, 66]</sup> The air-water interface, and concretely the Langmuir monolayers, provide a system that allows the manipulation of the nanoparticles and their transfer to LB films.<sup>[67-69]</sup>

Moreover, the self-assembly of nanoparticles at the air-water interface can be controlled by adding free excess of surfactant or amphiphilic block copolymer molecules. The interfacial self-assembly of the mixed components leads to different aggregates from which obtained from either pure components. Thus, it is proposed as a technique that prevents the 3D aggregate formation and could help to drive the 2D self-assembly process of the nanoparticles.<sup>[67, 70]</sup> The formation of these new features is directed by the balance of interactions between the molecules added and the nanoparticles' ligands.<sup>[3, 14]</sup> This synergistic self-assembly strategy results in highly stable hybrid surface features.<sup>[3]</sup> Moreover, the better understanding of the interactions' role is a key to build these systems.

In addition, in the case of block copolymers, self-assembly strategies offer additional possibilities for tuning the mechanical, optical, electronic, magnetic and catalytic properties of new nanostructured composites.<sup>[14, 71]</sup> In this case, the different nature of the hydrophobic interaction between blocks of the copolymer and the nanoparticle ligands directs the self-assembly of each component.<sup>[3, 14]</sup>

### I.3. Self-assembly of Carbon Allotropes at the Air-Water Interface

From fullerenes to carbon nanotubes, the ability of the air-water interface has been demonstrated to build thin films of carbon derivatives. In the case of the fullerenes,  $C_{60}$  not only form stable monolayers but also tend to 3D aggregates. Therefore, two strategies were proposed: to use functionalized  $C_{60}$ , that presents amphiphilic character; and to mix  $C_{60}$  with a film-forming agent as surfactants or polymers.<sup>[72, 73]</sup> On the other hand, for the single-wall carbon nanotubes (SWNTs) the air-water interface is presented as a means that allows tube orientation and thickness control.<sup>[74]</sup>

At present, it is the moment of the graphene-sheet derivatives.<sup>[75]</sup> Oxide and partially reduced oxide few-layer thick graphene are viewed as unconventional soft-materials, concretely, as 2D membrane-like colloids. Moreover, from a scientific and technological point of view it is important to know how these thin sheets assemble and how they behave when interacting with each other.<sup>[76]</sup> In this type of colloid there are two kind of interactions: face-to-face ( $\pi$ -stacking) and edge-to-edge. The last one controls the 2D self-assembly due to the electrostatic repulsion promoted by the residual oxidation groups at the edges, mainly carboxylic acid groups. Therefore, the air-water interface is suggested as an ideal platform to investigate these interactions.<sup>[76]</sup>

## **II. A General Overview**





## II. A General Overview

In this chapter some of the most important properties of the Langmuir monolayers and Langmuir-Blodgett films formed by surfactants, polymers or other soft materials are summarized. Langmuir monolayers are defined as films formed by spreading of surface active molecules, such as surfactant, polymer or other materials, on the clean aqueous interface without exchange of material between the monolayer and the subphase.

### II.1. Langmuir Monolayers

Langmuir monolayers are known since the Babylonians, 18<sup>th</sup> century B.C., who used them as form of divination based on pouring oil on water (or water on oil) and observing the subsequent spreading. A thousand years later, this practice was adopted by the Greeks.<sup>[77]</sup> However, the first recognized technical application of the monolayers was in the ancient art of Japanese marbling, known as suminagashi. This art has its origin in China over 2000 years ago, although the Japanese began to practise it in the 12<sup>th</sup> century, converting a divinatory purpose in an art. The technique consists of the application, on an aqueous surface, of an ink-drop and so on other drop that disperses the other. They are blown across to form delicate swirls, after which the image (network) was picked up by laying a sheet of paper or silk on the ink-covered water surface.<sup>[78, 79]</sup>

The first scientific investigation was made by Benjamin Franklin, in 1774, who observed that when a small amount of oil is deposited on a water pond, the oil spreads on the all surface.<sup>[80]</sup> However, was Lord Rayleigh, in the 19<sup>th</sup> century, the first to carry out measurements of surface tension in olive oil monolayers spread on water, and on from the area-density measurements, he estimated the thickness of the oil film to be 16 Å.<sup>[81]</sup> During the following year, Agnes Pockels made a systematic compression studies of oil monolayers on an aqueous subphase by compressing layers with "barriers", in a "primitive" Langmuir trough, thus

observing that the surface tension fell rapidly when the monolayer was compressed below a certain "area".<sup>[82]</sup> Later, Lord Rayleigh explained this phenomenon by supposing that the oil molecules form a monomolecular film, and that at this area the oil molecules were closely packed.<sup>[83]</sup> In 1917, Irving Langmuir began to study interfaces of chemically pure substances and put forward evidence for the monomolecular nature of the film as well as the orientation of the molecules at the air-water interface.<sup>[84]</sup> A few years later, Katharine Blodgett, working joined to Langmuir, showed that these monolayers could be transferred onto solid substrates<sup>[85]</sup>, and also carried out the sequential transfer of monolayers onto the solid substrate to form multilayer films<sup>[86]</sup>, which are now referred to as Langmuir-Blodgett films.

Langmuir monolayers are formed from insoluble or a little soluble amphiphilic molecules, as surfactants or polymers, by material deposition on the interface, in which, there is not material exchange between the interface and the liquid that supports the monolayer (subphase), that is usually water. Because of it, it is possible to establish a relation between the surface concentration,  $\Gamma$ , and the occupied area,  $A$ , according to the following expression:

$$A = \frac{1}{\Gamma} \quad \text{[II. 1]}$$

Thus, from the expression, a reduction of the available area produces an increase in the surface concentration. Therefore, by compression experiences (area reduction), the material density deposited on the monolayer can be increased finding a great variety of aggregation bi-dimensional states similar to the states that exist in three-dimensions (3D).

In a monolayer the surface pressure,  $\pi$ , is related to the 3D pressure,  $P$ . The surface pressure is a pressure distributed over the film thickness of the spread material in the monolayer,  $\Delta\ell$ , that is usually around several nanometres.

$$\frac{\pi(N/m)}{\Delta l(m)} = P(N/m^2) \quad [\text{II.2}]$$

The surface pressure,  $\pi$ , is defined as the difference between the surface tension of the pure liquid subphase,  $\gamma_0$ , and the surface tension when the surface is covered by a monolayer of adsorbed material,  $\gamma$ :  $\pi = \gamma_0 - \gamma$ .

The basic technique used in the study of the insoluble monolayers is the Langmuir trough, that allows the measurement of the surface pressure as a function of the available area at constant temperature. In this way, the Langmuir isotherms can be obtained by compression, and in which the different states or even surface aggregates have been reported.<sup>[1, 87]</sup>

In the case of materials of low molecular weight, the isotherm  $\pi$ - $A$  can present different quasi-bidimensional states when the available area decreases. Some regions of phase coexistence can be observed in the Langmuir isotherms. However, not all the isotherms present these regions. The position and the width of them depend on the material and temperature.<sup>[87]</sup> Not all the phase transitions are presented in all the isotherms. Figure II.1. shows an ideal isotherm in which are represented the majority of the possible surface states and some coexistence regions.

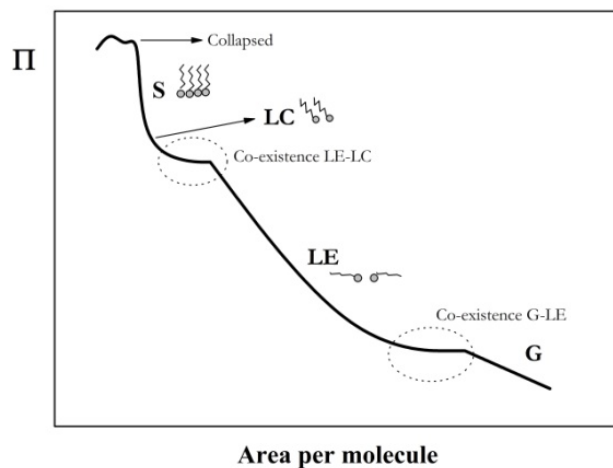


**Figure II.1.** Langmuir isotherm of an insoluble surfactant, where are showed de different states of aggregation (phase transition) that it is possible to find in a monolayer.

At large areas the monolayer behaves similarly to a two-dimensional (2D) gas (G), where the molecules are far apart and are believed to weakly interact with each other and the surface pressure remains unchanged. This region obeys to state equations similar to 3D gases. When the area of the monolayer is reduced by film compression, the molecules become closer and start to interact appearing the two-dimensional liquid state regions: liquid-expanded (LE) and liquid-condensed (LC) phases. When the temperature is below the critical temperature, a phase co-existence region appears. This first-order phase transition is due to attractive interactions between molecules. Not all the molecules that form 2D monolayers present the two liquid states. However, in the cases that it occurs, the expanded phase appears at low surface pressures and great areas.

Under further compression, film molecules are closely packed and assumed to be vertically oriented, i.e., the solid region (S). The structure of these phases depends on the molecule structure. On further compression monolayer

collapse occurs, and multilayers and non-homogeneous three-dimensional (3D) structures are formed.<sup>[88]</sup>

The morphology of the isotherm,  $\pi$ -A, is influenced by many factors including the experimental conditions and the chemical structure of the molecule. Only the molecules that possess at least 12 carbon atoms can form an insoluble Langmuir monolayer. The increasing of the number of carbon atoms leads to the appearance of a great variety of liquid<sup>[89]</sup> and solid<sup>[90]</sup> phases. The polarity of the molecule's head group also modifies its interaction with the aqueous subphase, influencing the arrangements and the shape of the isotherm.<sup>[91]</sup>

The main properties that produce great changes in the structure of the monolayers are: pH, the presence of ions in the aqueous subphase and the temperature. The subphase pH mainly affects when the monolayer corresponds to molecules with ionizable head groups, such as -COOH or -NH<sub>2</sub>.<sup>[87]</sup> In some cases, when the head groups are completely ionized, the molecules at the interface are dissolved in water subphase and the monolayer becomes instable. The effect of the monolayer solubilisation in the subphase is the shift toward lower molecular areas in comparison to the isotherm recorded for uncharged molecules, i.e., obtaining more expanded isotherms. Therefore, in these cases it is necessary to work at the subphase pH in which the ionisable groups are in its non-ionized form.<sup>[92]</sup>

The addition of electrolytes in the subphase plays a critical role in the stability of the monolayers. This effect is more accentuated in the case of multivalent ions. The complexation of metal ions with the acid group of amphiphiles generally causes isotherms more condensed.<sup>[93]</sup> Divalent metal ions interact with the acid group (-COOH) in different ways, depending on their electronegativity: the ions with high electronegativity interact covalently while those with lower electronegativity interact electrostatically. The origin of the interaction affects the alkyl chains packing.<sup>[94]</sup>

On the other hand, phase transitions are strongly influenced by the subphase temperature, thus, when the temperature increases the co-existence phase regions are shifted to higher pressures and they can disappear at sufficiently high temperatures.<sup>[95]</sup>

One of the most important factor that affects the morphology of the compression isotherm is the stability of the monolayer. To check the stability of the monolayer, the surface pressure is registered during a period of time at constant area after a barrier-compression.<sup>[96]</sup> In some cases, the monolayer does not reach the equilibrium during the compression process, because it requires some time after to reach the equilibrium state. In these cases after the compression with the barriers stops the surface pressure evolves to the equilibrium value, and when this value is reached, it remains constant. An alternative method to check the monolayer stability is to prepare the monolayer by addition, deposition method. Using this methodology the surface the density of adsorbed molecules is modified by successive addition of the surfactant spreading solution. After waiting time to solvent evaporation, the surface tension is measured until it reaches a constant value. By comparing the surface pressure values reached by two methods one may be able to infer on the stability of the monolayer. Poor monolayer stability can be associated with slow material dissolution into the subphase. However, aggregation or dynamic processes can be responsible for differences between the surface pressure values obtained by both methodologies.

Another way of checking monolayer stability is by performing hysteresis experiments, where the monolayer is compressed to a fixed surface pressure or area and subsequently expanded to the original state. Even for stable monolayers, some hysteresis is normally observed, which is attributed either to differences between the organization and disorganization processes or to the formation of irreversible domains during compression process. For poorly stable monolayers,

by applying consecutive compression-expansion cycles, usually a continuous shift is observed in consecutive isotherms towards lower mean molecular areas.<sup>[97]</sup> When aggregates are formed the domain size often depends on the initial surface pressure of the monolayer.<sup>[98]</sup>

To gain insight into the states of the monolayers, the values of the equilibrium elasticity modulus, which is the reciprocal of compressibility ( $C_s$ ), are widely used:

$$C_s^{-1} = -A \left( \frac{d\pi}{dA} \right) \quad [\text{II. 3}]$$

A useful method for classification of the monolayer phase is to examine the values of equilibrium elasticity modulus, such dependencies are also of help in detecting the phase transition, which appears as a characteristic minimum in the compression modulus vs. surface pressure plots.<sup>[99]</sup>

## II.2. Mixed Langmuir Monolayers

Mixed monolayers formed by co-spreading two different compounds have important application in the formation of functional LB films. Thus, mixed monolayers are an option adopted in many cases to improve monolayer stability<sup>[100, 101]</sup> and the film properties<sup>[102]</sup>. Mixed monolayers have also been useful for constructing LB films with interlocking structures<sup>[103]</sup> and improving the orientational order of molecules in films<sup>[104]</sup>. One of the most important aspect to use accurately mixed monolayers is to study both the miscibility and the interactions between the components. The methodology widely used to study the interactions between components is to analyse the composition dependence of the mean area per molecule ( $A_{12}$ ) expressed as<sup>[99]</sup>:

$$A_{12} = A_1X_1 + A_2X_2 \quad [\text{II. 4}]$$



Where  $A_1$ ,  $A_2$  are the molecular areas of single component at the same surface pressure and  $X_1$ ,  $X_2$  are the mole fractions of components 1 and 2 in mixed films.

The way mean molecular areas depend on the composition of the mixture can be used to infer possible interactions in the mixed monolayer. Thus, if two components are ideally miscible or immiscible,  $A_{12}$  linearly depends on the monolayer composition.<sup>[105-107]</sup> Deviations of this behaviour indicate attractive or repulsive interactions between components.<sup>[108]</sup> In order to analyse the nature of interactions between the components, the excess area of mixing ( $A^{exc}$ ) defined as:

$$A^{exc} = A_{12} - (A_1X_1 + A_2X_2) \quad [\text{II. 5}]$$

is usually employed. Accordingly, positive  $A^{exc}$  values, positive deviation from the ideal mixing, indicate repulsive interaction between components. While negative values are signature of attractive interactions between them.<sup>[99, 109]</sup> However, it is often difficult to obtain homogeneous and ordered mixed LB films, because phase separation of the components is often observed. The mixed monolayers and transferred multilayers generally give heterogeneous structures with small domains of each component.<sup>[87]</sup>

### II.3. Langmuir-Blodgett Films

As it has been mentioned above, Katherine Blodgett joined to Irving Langmuir, was the first person able to transfer fatty acid monolayers from the air-water interface onto solid substrates, forming as-called Langmuir-Blodgett (LB) films.<sup>[85]</sup> The objective was to transfer, assemble and manipulate simple films, previously prepared at the air-water interface. Since then, the possibilities that offer this technique have increased due to the necessity of organized systems construction by controlling the assembly of monolayers looking for the development of molecular machines.<sup>[110]</sup> Nowadays, the LB technique is an useful tool to build self-assembled systems with applications in several areas of the Nanotechnology and in the development of new electronic and optoelectronic devices.<sup>[1, 111]</sup>

The LB method consists in placing a solid substrate on a support perpendicularly to the air-water interface covered by the monolayer that will be transferred by immersion or emersion of the solid. During the transfer process the surface pressure is kept constant by barrier compression in order to compensate the loss of molecules transferred onto the solid.

One variant of this methodology is the horizontal deposition technique, named as Langmuir-Schaefer (LS) technique.<sup>[112]</sup> In this method, the solid substrate, placed parallel to the air-water interface, is made to contact with the surface of the monolayer. In other words, the deposition is done by dipping the substrate horizontally through a floating monolayer from the gas phase (air) toward the liquid phase (monolayer). In this way, the monolayer is transferred with the hydrophobic part on the solid and the polar head in contact with the air. Another possibility is the Kossi-Leblanc technique, where the substrate is placed inclined with regard to the air-water interface, usually with an angle of 40°, and then is submerged on the subphase. The transfer occurs by dipping up the support as in the LB deposition.<sup>[113]</sup>

The understanding of the physicochemical phenomena (mechanisms) that control the LB transfer are still understudy.<sup>[114, 115]</sup> The molecular interactions involved in the air-water interface can be different than the interactions at the air-solid interface. When the monolayer is transferred from the air-water interface onto the solid the interface changes, and therefore, in the majority of the cases the monolayer structure is not kept. Because of it, the construction of high quality LB films requires a high degree of skill joined to a careful control of all the experimental parameters, such as: stability and homogeneity of the monolayer; subphase properties (composition, pH, presence of electrolytes and temperature); substrate nature (structure and hydrophilic or hydrophobic character); solid speed of immersion/emersion; angle of the substrate with the interface; surface pressure during the deposition process; and number of transferred monolayers.<sup>[111]</sup>

The effect of the substrate nature in the transfer process is reflected in the distinct types of arrangement of the molecules in the deposited layer: X, Y and Z (Figure II.2). For example, when a hydrophilic substrate is used, firstly, the substrate is submerged before the formation of the monolayer. In this way, the monolayer is transferred by emerging the solid from the subphase. This type of deposition is called Y-type, and the arrangement of the film is centre-symmetric, with a configuration head-to-head and tail-to-tail in successive transfers. In the case of X-type structure, the substrate is immersed during the transfer (down direction); and for Z-type the substrate is only emerged (up direction). In both cases, the films are centre-asymmetric.<sup>[111]</sup>

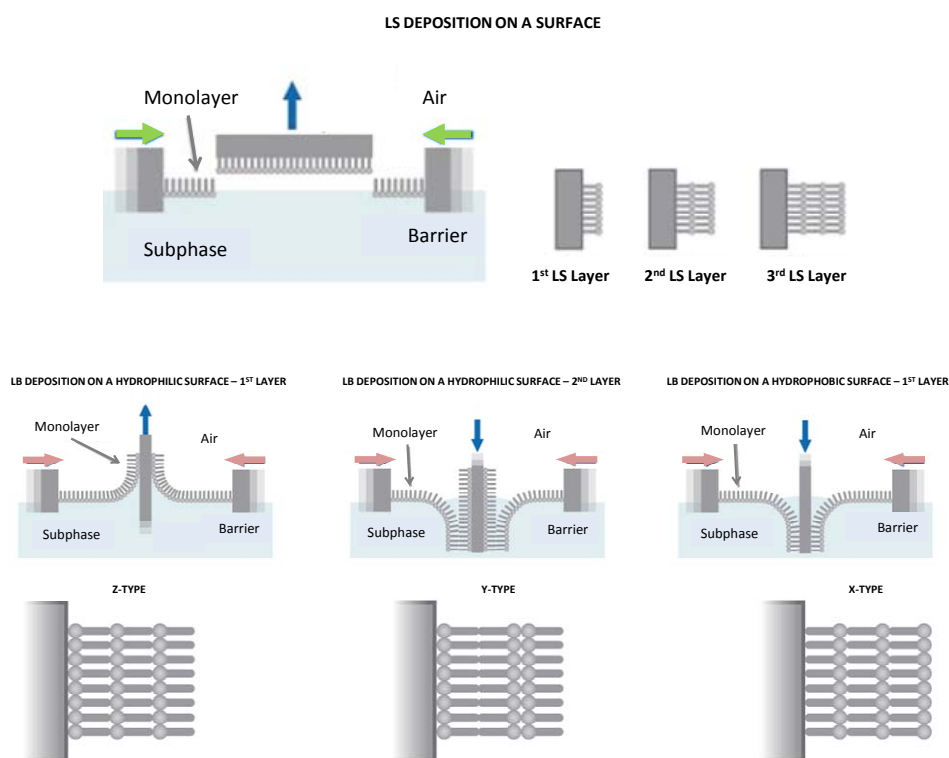


**Figure II.2.** Langmuir-Schaefer (LS) deposition scheme (top). Langmuir-Blodgett (LB) deposition on a solid surface and type of arrangement for multilayers obtained after repeated deposition (bottom).

In the LB films, the molecular arrangement is not as perfect as in the theoretical schemes. As it has been well established in a number of experiments, the properties of transferred LB films may differ from those of the corresponding Langmuir films, even for simple model amphiphilic molecules. This is not unexpected, since the factors governing the equilibrium packing arrangement of the molecules in Langmuir and LB films are presumably different. The molecules can reorganize during or immediately after transfer to a more stable arrangement on a solid support. A typical example is the observation of transition from a X-type to a Y-type LB film during monolayer transfer, usually explained in terms of an over-turning mechanism (detach-turnover-reattach) when the film is inside the subphase water.<sup>[116]</sup> Moreover, several forces act during the dewetting promoting the drying-mediated self-assemblies.<sup>[69]</sup>

A comparison between Langmuir and Langmuir-Blodgett films is still possible, nevertheless, particularly if one accounts for the change of interface and possibility of molecular over-turning due to processes such as dewetting<sup>[44, 45]</sup> that occurs at the air-solid interface. However, there are some parameters such as level of mixing between components in a mixed monolayer and the composition of the monolayer and the degree of ionization of head groups, which can conveniently be assumed as unchanged during the transfer process if there is no specific interaction between the monolayer material and the substrate.<sup>[79]</sup>

After the construction of the LB films it is important to study the architecture and organization of the molecules in order to establish the theoretical molecular models in films: molecular orientation or interactions. For this purpose, complementary techniques such as atomic force microscopy, transmission and scanning electronic microscopy, ellipsometry and UV-vis, IR or Raman spectroscopy, give information about the density of the adsorbed molecules, structure, morphology and composition of the film<sup>[117]</sup>, respectively.

## II.4. Polymer Langmuir Monolayers

The study of insoluble monolayers constituted by polymers is important in the basic material science and in several technological applications such as adhesion, colloids stabilization and coatings. Polymers spread at the air-water interface can be viewed as pseudo-two-dimensional systems of fundamental interest for studying the effects of one-dimensional confinement on the structure and dynamics of polymer molecules. On the other hand, polymer thin films are relevant in the development of electronic devices or different kind of sensors whose characteristics depend on the surface properties. It is necessary to emphasize that despite the amount of studies in this matter, several questions in the polymer systems spread at interfaces are not yet well understood.<sup>[118]</sup>

As in the case of polymers in solution, in the structure of adsorbed polymers influence not only the concentration but also their interaction with the subphase. For polymers in solution it is possible to establish several concentration regimes, Figure II.3. Dilute solutions, where the polymer concentration is low enough that the chains do not interact. If the polymer concentration increases and the overlap concentration,  $c^*$ , is reached the polymer chains began to interact forming a network where solvent molecules are present, i.e., in semi-dilute solutions. Thus, according with the interactions polymer-solvent, it is possible to differentiate three behaviours: good-solvent,  $\theta$ -solvent and poor-solvent. For good-solvent conditions the polymer chains do not interpenetrate and are mixed with the solvent. There is a repulsive potential between the chains due to the volume excluded effect. At poor-solvent conditions there is a repulsive interaction polymer-solvent, so the polymer conformation is closed in order to expulse the solvent molecules. In the  $\theta$ -solvent conditions, there are not interactions polymer-solvent and the polymer chains are in a non-perturbed situation.

In these systems the scaling-laws are applied <sup>[119]</sup> to predict the polymer-interface behaviour. The overlap concentration,  $c^*$ , is a parameter that allows us to determine the polymeric chain radius of gyration ( $R_g$ , or Flory's radius) and the solvent quality by:

$$c^* \sim \frac{N}{R_g^d} \quad [\text{II. 6}]$$

Where,  $N$  is the number of monomers in the chain, and  $d$ , the spatial dimensionality (in two-dimension  $d = 2$ ). Besides, the radius of gyration <sup>[120, 121]</sup> is related to the number of monomers in the chain by the following expression:

$$R_g \sim N^{\nu} \quad [\text{II. 7}]$$

Where  $\nu$ , is the Flory's scaling exponent, that is a measurement of the polymer-solvent interactions and whose value depends on the dimensionality,  $d$ :

$$\nu = \frac{3}{d + 2} \quad [\text{II. 8}]$$

Finally, when the polymer concentration reaches the double-overlap concentration, i.e, in concentrated solutions, the chains are very closed and consequently, there is low solvent content between the chains, lead to a semi-crystalline, glassy or melt state.

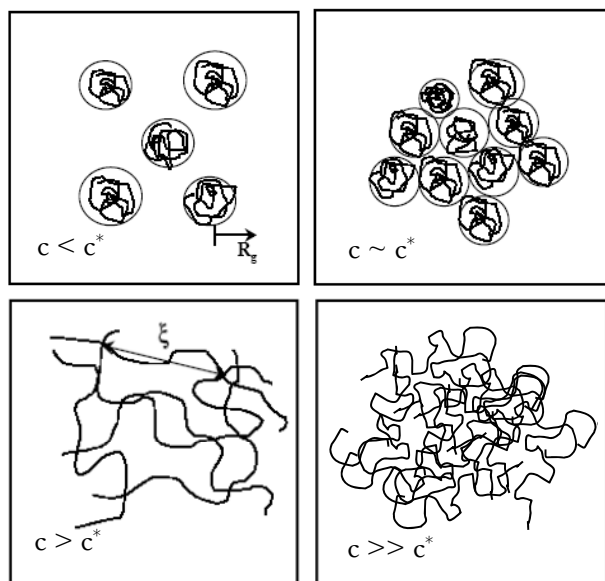


**Figure II.3.** Proposed structures for the different concentration regimes in polymer solutions.

The equilibrium properties of solutions in the semi-diluted regime can be expressed with the scaling laws proposed by de Gennes and are based on the existence of a correlation length,  $\xi$ , that corresponds to the mean value of the distance between two intercrossing points.<sup>[119]</sup> According to this model, the length varies with the polymer concentration with a power-law and is independent of the number of monomers in the chain,  $N$ , by:

$$\xi(c) \approx R_g \left( \frac{c}{c^*} \right)^m \quad [\text{II. 9}]$$

In the equation  $m$  represents the scaling exponent. This equation can be reorganized by including the overlap concentration according to the Flory's law (Equation II.6), given:

$$\xi(c) \approx c^{-v/(vd-1)} \quad [\text{II. 10}]$$

Finally, as the number of intercrossing points between the different chains is proportional to the osmotic pressure,  $\Pi$ , and inversely proportional to the

intercrossing distance,  $\xi$ , the scaling law can be expressed for the osmotic pressure as below:

$$\frac{\Pi}{RT} \sim \xi(c)^{-d} \sim c^{vd/(vd-1)} \quad [\text{II. 11}]$$

In order to establish the different states of the polymer molecules at the monolayer, it is usual to apply the polymer in solution concentration regimes by analogy with 3D polymer solution. Accordingly, it is possible to differentiate three regimes in the polymer isotherms. The diluted regime where the surface pressure slowly increases with the surface concentration. The semi-diluted region, that begins at the overlap concentration ( $\Gamma^*$ ), in which the pressure increases quickly, and the concentrated region. This region corresponds to the monolayer collapse leading to 3D structures.

Spread polymer films do not show the variety isotherm behaviour as that for compounds of low relative molecular weight. Depending on the isotherm morphology, generally, two types are observed: liquid expanded and condensed films.<sup>[88]</sup> In the expanded monolayers the increasing of surface pressure with the concentration is less than in the condensed monolayers, Figure II.4. The surface pressure isotherms for polymers are usually represented in terms of the surface concentration ( $\Gamma$ ), because the relative molecular weight of polymers is generally not an unique value.



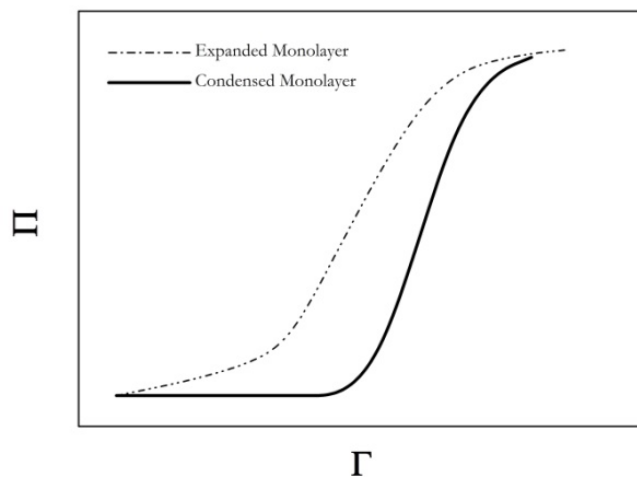


**Figure II.4.** Schematic surface pressure isotherms of the two major types encountered in spread polymer films.

As it was mentioned, the surface property widely used to characterize the polymer monolayers state at the interface, is the equilibrium elasticity,  $\varepsilon_0$ , obtained from the surface pressure isotherm <sup>[122]</sup>:

$$\varepsilon_0 = \left( \frac{\partial \pi}{\partial \ln A} \right) = \Gamma \left( \frac{\partial \pi}{\partial \Gamma} \right)_T \quad [\text{II. 12}]$$

The equilibrium elasticity is related to the response of the monolayer to a deformation and gives information about its conformational state. Thus, values below  $20 \text{ mN m}^{-1}$  correspond to high disorder conformations that lead to high flexibility states, while values above this value correspond to very rigid conformations as in the case of condensed polymer random-coils.<sup>[88]</sup> In this sense, the different states of the monolayer are characterized by the equilibrium elasticity values as follows: liquid expanded states show values between  $12.5$  and  $50 \text{ mN m}^{-1}$ ; liquid condensed films varying between  $100$  and  $250 \text{ mN m}^{-1}$ ; and solid condensed states present values from  $1000$  to  $2000 \text{ mN m}^{-1}$ .<sup>[123, 124]</sup>

Generally, the equilibrium properties of adsorbed polymers in the semi-dilute regime were interpreted by the scaling laws adapted to two-dimensional systems.<sup>[125]</sup> However, it is not clear the validity of Flory scaling exponent in 2D, because the theory of polymer solutions is based upon the existence of entanglements between polymer chains and the existence of entanglements in polymer quasi-2D systems is still a matter of controversy.<sup>[126-128]</sup>

The models for polymer in solution were later adapted to two-dimensional systems,  $d=2$ . In this case the polymer concentration represents the polymer surface concentration,  $\Gamma$ . Accordingly, the scaling law for polymeric monolayers can be expressed as follows<sup>[129]</sup>:

$$\xi(\Gamma) \sim \Gamma^{\frac{\nu}{1-2\nu}} \quad [\text{II. 13}]$$

And for the surface pressure,  $\pi$ :

$$\pi \sim \Gamma^{\frac{2\nu}{2\nu-1}} \quad [\text{II. 14}]$$

The rheological properties of monolayers play an important role to predict the behaviour of thin layers in technological processes, such as the transference of polymer monolayers onto solid substrates, or natural processes, as the rheological behaviour of lung surfactant responsible for facilitating breathing. Even though the rheological properties of monolayers have received great attention, the physical mechanism involved in the dynamics of polymer chains at interfaces is still a challenge.<sup>[130, 131]</sup>

The monolayers are subjected to external perturbations that originate different kinds of movement or reorganization processes, therefore it is necessary to know the dynamic properties. In order to study these phenomena, the interfacial rheology is used. The basic methodology consists in producing a deformation and studying the system response, i.e., the monolayer response.

From the relation between the amplitudes of the response and deformation is used to obtain information about the processes involved in the deformation. In the case of Langmuir monolayers, one resorts to mechanical deformations in the Langmuir trough. The mechanical deformation can be carried out by two ways: sudden step-compression/expansion or sinusoidal oscillatory experiments. These experiments are in the frequency range of 1mHz-1 Hz. This low frequency causes slow collective movements in the monolayer, accordingly, the information obtained is related to these movements.<sup>[130]</sup>

The results available for polymer monolayers show that they present a complex dynamics and the results can be interpreted from the models for polymers in solution in the semi-dilute regime.<sup>[125, 132, 133]</sup>

## II.5. Langmuir Monolayers of Nanoparticles

In recent years, nanoparticles have received much attention due to their great potential to be used in biological and technological applications. This possibility is related to their size dependent optical, electric and/or magnetic properties.

The studies on nanoparticle materials at the air-water interface are relied on traditional amphiphilic molecules. The nanoparticles (NPs) have a polar core with a hydrophilic or hydrophobic surface. Consequently, the hydrophobic NPs serve as the surface-active molecules to build a Langmuir monolayer, while the hydrophilic ones can be dispersed in the aqueous subphase and incorporated to the monolayer by attractive interactions with amphiphilic molecules adsorbed on the air-water interface. Thus, the hydrophobic NPs form themselves the Langmuir monolayer while the hydrophilic ones need additives. An alternative method to obtain hydrophobic NPs from the hydrophilic ones is by capping alkyl chains on the particle surfaces, either by via chemical grafting<sup>[134-136]</sup> or by physical adsorption<sup>[137-139]</sup>.

Focus the attention on hydrophobic NPs, the surface pressure-area isotherms of their monolayers present a characteristic behaviour. Thus, they display a first transition plateau at negligible surface pressure. In this region, the NPs are probably clustered as small islands floating on the subphase. A steep rise in surface pressure follows as the islands begin to touch. The islands merge to form a monolayer which can withstand surface pressures up to  $65 \text{ mN m}^{-1}$  before collapsing.<sup>[140]</sup> Moreover, on hydrophobic NPs, ligand-ligand interactions play a decisive role in the monolayers assembly and dynamics behaviour. For example, shorter ligands lead to a more densely packed monolayers. In this sense, other important factors that influence the NPs monolayer properties are: particle size<sup>[140, 141]</sup>, material composition, nature of surface stabilizing molecules, and surrounding environment<sup>[67]</sup>. In fact, the monolayer behaviour and quality have been reported to be strongly dependent on the degree of surface hydrophobic character, as well as the capping method used. Therefore, when such particles are spread at the air-water interface, the weak particle-water interaction results in the formation of void defects or 3D aggregates in the monolayer.<sup>[139, 142, 143]</sup> A possible solution is to modulate the hydrophobic character by using mixed systems.

Besides, the  $\pi$ -A isotherms other measurements that are carried out in these systems at the air-water interface to gain insight about the changes in the film during compression, are the surface potential and the rheological properties. Concerning to surface potential measurements, they allow to obtain information about film morphology. At larger areas, the NPs are randomly distributed at the air-water interface and as result, the total surface potential contribution is zero. The film can be compressed with minimum particle-particle interactions. When the monolayer is further compressed, the hydrophobic part of the NPs began to stretch out of the water and the change of the dipole moment resulted in a rapid increase of surface potential corresponding to the lifting point of the surface pressure. The monolayer is in a state similar to a liquid condensed phase where the NPs started to interact among them. From this point, a slight increase of the

surface potential was observed although the change of surface pressure was still significant. This may be due to the reorientation of the NPs in order to maximize the exposure of hydrophobic ligand moiety to the air. The maximum of the surface potential corresponds to the solid phase region of the isotherm. At this solid phase region of the isotherm, the surface potential curve changed its slope.<sup>[139]</sup>

Moreover, mixed systems have been proposed with NPs, concretely, two approach have been developed in mixed monolayers with NPs. One methodology widely used is based on the mixture of different kind or size NPs to form complex architectures <sup>[69]</sup> called superlattices. Multicomponent NPs superlattices are proposed to create multifunctional materials by combining independently tailored functional components.<sup>[9]</sup> Another option is the addition of a surfactant <sup>[67, 144-149]</sup> or polymer <sup>[14, 15, 148, 150]</sup> excess or even co-mixtures <sup>[151]</sup> in order to control the NPs assemblage and can be also used to develop hybrid materials <sup>[9]</sup>. The thermodynamic treatment of these mixed monolayers is similar to amphiphilic molecules mixtures. The study of the mixed monolayers is based on the average area and collapse pressure values behaviour. Thus, a non-linear area trend suggests that the self-assembly of the two components is synergistic in nature, thus, the presence of one component influences the surface conformation of the other.<sup>[150]</sup> As in the case of amphiphilic mixed monolayers, the collapse pressure variation with composition is other parameter to highlight the two-component miscibility. Thus, if the NPs collapse pressure is maintained almost constant, the two components of the mixed monolayer are immiscible and there is minimum interdigitation among the NPs ligand and the co-spread molecules. However, a change in the collapse surface pressure can be a result of miscibility and interdigitation of the two components at the interface.<sup>[145]</sup>

The field of the dynamic properties of NPs monolayers at the air-water interface is largely unexplored although is very remarkable for their

applications.<sup>[152]</sup> In spite of their relevance, there is little detailed work in the literature<sup>[19-21]</sup> and mainly focused on NP films without co-additives due to only the understanding of the dynamical NPs behaviour requires a very complex study.

The first observation in the dynamic properties of NPs monolayers is the hysteresis that their isotherms presents<sup>[70, 143, 145]</sup>, indicating that the films are rigid and interparticle interactions at the air-water interface are attractive<sup>[140, 143, 153]</sup>. The hysteresis behaviour is also explained in terms of a low re-spreading ability of NPs or a slow expansion rate of the NPs.<sup>[145]</sup> The overcompression cycles annealing the NP monolayer structures so that the monolayer defects disappear. This is due to the increase of the long and short-range order induced by the ligands converging towards a homogeneous interdigitation fraction and compensating for NP core size inhomogeneities.<sup>[18]</sup> Accordingly, there is a lot of interest to study the dynamic properties in the case of NPs layer at the air-water interface, because is a good methodology to self-assembly NPs in an ordered and homogeneous way. However, one of the difficulties encountered with measurements on particle monolayers is that they are solid-like, non-zero shear modulus, and the standard data analysis is no longer valid. To illustrate this picture, in the rheological studies, relaxation measurements and continuous or oscillatory deformations are carried out by means of barrier movements in a Langmuir trough. In these experiments, one observation is the surface pressure anisotropy effect. The effect consists in measuring the different increase with compression of the surface pressure in the perpendicular and parallel compression (push) direction for NP monolayers. This anisotropy occurs when the water surface is fully covered by particles and becomes more prominent with the increase of surface concentration. This effect reflects the non-homogeneous distribution of particles at the interface, so that the particle distance decrease in the parallel direction is much more prominent than that in the perpendicular direction, leading to the non-homogeneous states of particles distribution (Figure II.5).

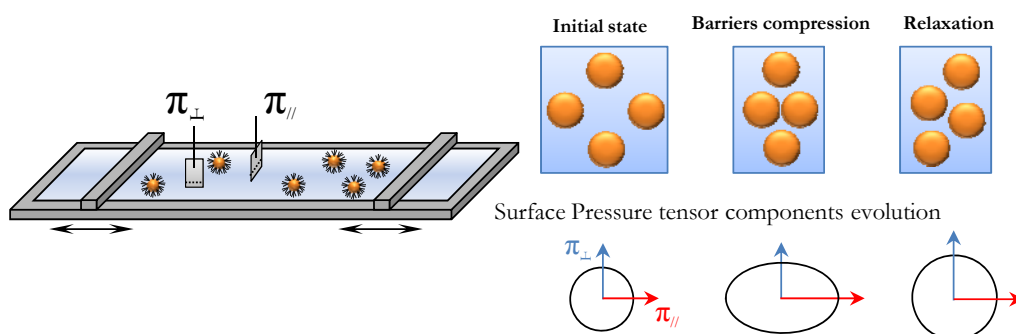


**Figure II.5.** Dynamic mechanism of the nanoparticle monolayer. The scheme shows the evolution of the surface pressure tensor. At the initial state (equilibrium) the surface pressure is a symmetrical tensor. Under barrier unidirectional compression, particles are more condensed in this push-direction and the surface pressure becomes unsymmetrical. After relaxation, the particles rearrange reaching a new equilibrium state, then the surface pressure becomes symmetrical again. (Adapted from Zang, 2010<sup>[154]</sup>).

On the other hand, the NPs films present a complex relaxation of surface pressure that involves three timescales which are related to the damping of surface fluctuation, rearrangement of particle rafts and particle motion inside each raft. Therefore, the particle layer possesses a long relaxation time and a fast compression brings the particle layer to a non-equilibrium state. While under oscillation, additional energy is provided to the layer. This accelerates the decay dynamics remarkably and the suppression of surface pressure decay. With the increase of oscillation time, surface pressure response amplitude decays exponentially and eventually reaches the equilibrium value. Upon long term barrier oscillation, the particle aggregates organize parallel to the barrier and respond collectively to compression.<sup>[20, 154]</sup>

Finally, recent dynamic studies have been carried out with NP/surfactant mixed monolayers to evaluate the effect of NPs on the surfactant monolayer properties. These investigations have important implications on technological applications or biological studies such as modeling respiratory cycles in the presence of particle pollutants with lung surfactants.<sup>[21, 155]</sup> The results point out

that the presence of NPs induces significant changes in both the phase behaviour and the dynamic response of surfactant monolayers due to the reduction of the available area to the surfactant molecules at the interface and to the disruption of the interfacial structure of the monolayer caused by the incorporation of the NPs. Significant differences in the interfacial properties of these mixed systems have been evidenced depending on the NP surface nature and concentration.<sup>[21, 155]</sup>

## II.6. Langmuir Monolayers of Graphene Derivatives

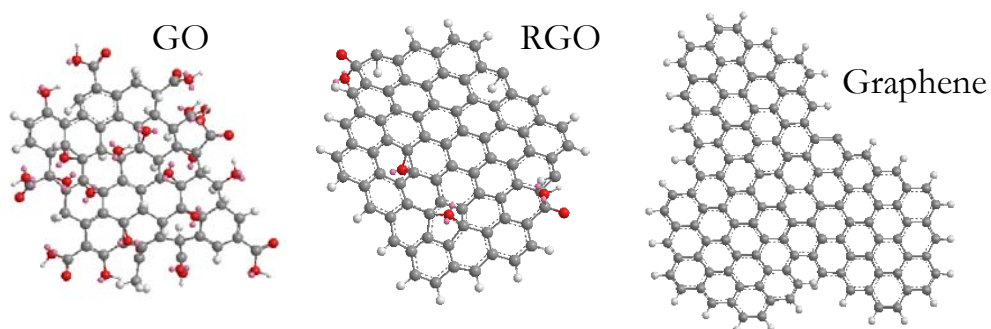
From the graphene work performed by K. Novoselov and A. Geim in 2004, the graphene and its derivatives have extraordinary re-emerged and become very important from a fundamental and applied point. Their excellent mechanical and electrical properties favour their use in technologic and biological applications such as the construction of solar cells, batteries and biosensors.<sup>[156]</sup> However, the challenge is the graphene large scale production. In this way, the chemical routes are one of the most promising approaches due to are cheap, processable and scalable methods, although the graphene material obtained presents slightly inferior properties than pristine graphene.<sup>[157]</sup> These approaches are based on the oxidation of carbon materials obtaining graphene oxide and its subsequent reduction to reduced graphene oxide. By continuing with this way, different liquid phase exfoliation methods have been developed to produce dispersions of graphene or graphene oxide sheets.<sup>[158]</sup> However, the next challenge to implement the graphene is how to transfer the sheets formed from the dispersion onto a substrate in a controlled manner at variable coverage on an arbitrary surface.<sup>[159]</sup> Moreover, for practical application or simply for fundamental research purposes, a good adhesion and an uniform and reproducible deposition of graphene to the substrate is of great importance. Thus, recently Langmuir-Blodgett (LB)<sup>[75, 160]</sup> and Langmuir-Schaefer (LS) deposition<sup>[159, 161]</sup> have shown promising results in preparing graphene layers with high degree of control and under ambient



conditions in contrast to other techniques such as spin-coating<sup>[162]</sup> or drop casting<sup>[163]</sup>.

Therefore, we focus our attention on graphene oxide (GO) and reduced GO (RGO) and their deposition onto a solid by using the Langmuir-Blodgett technique.

The GO sheets contains carboxylic acid, hydroxyl and epoxide groups that render this material water-processable but insulating. However, conductivity may be partially restored through reduction by chemical<sup>[164, 165]</sup>, thermal<sup>[163, 166]</sup>, photothermal<sup>[167, 168]</sup>, and photochemical<sup>[169]</sup> treatments, producing chemically modified graphene sheets, i.e., RGO. Although the resulting graphene product is more defective (residual oxygen functionality or broken into smaller flakes) and therefore less conductive than pristine graphene, but due to the ease of synthesizing GO or RGO, its solution processability and its functionalization it is a very attractive precursor to fabricate graphene-based materials and devices.<sup>[156-158]</sup> In order to use, these materials are usually processed as films. The properties of the resulting film depend not only on the quality of the individual sheets but also on how they are assembled. This generates thin film microstructures that ultimately determine the film properties. For that reason, the interparticle control that provide the air-water interface and the LB technique is promising. Thus, the LB films can be used as a model system to investigate such microstructure–property relationships of solution-processed graphene-based thin films and to the films construction.



**Scheme II.1.** Chemical structures of the different graphene materials: graphene oxide (GO), reduced graphene oxide (RGO) and pure graphene. The structures were calculated by molecular mechanics, MM2, with the Chem 3D Ultra 9.0. software.

GO sheets can be considered amphiphilic with an edge-to-center distribution of hydrophilic and hydrophobic domains. The edges of GO are hydrophilic due to the ionizable  $\text{-COOH}$  groups, while its basal plane contains many poly-aromatic islands of unoxidized graphene nanodomains that provides hydrophobic character. Thus, GO can adhere to interfaces and lower interfacial energy, acting as a surfactant. Due to its surface activity, it is possible to employ molecular assembly methods as the Langmuir-Blodgett technique to create monolayers in order to process the GO with a precise control over film thickness.

To spread GO at the air-water interface it is necessary to use a solvent. Though typical spreading solvents are volatile and water-immiscible (e.g., chloroform, toluene), these solvents do not disperse GO well.<sup>[170]</sup> Since GO is amphiphilic, it can be spread from alcohols that are even miscible with water, such as methanol.<sup>[76]</sup> When methanol droplets are gently dropped on water surface, it can first spread rapidly on the surface before mixing with water. In this way, the GO surfactant sheets can be effectively trapped at the air-water interface. The density of sheets can then be continuously tuned by moving the barriers and the packing is controlled by the surface pressure. At zero surface pressure, the film consists of dilute, well-isolated flat sheets. As compression continues, a gradual increase in surface pressure begins to occur and the sheets start to close pack. If

the compression continues, the soft sheets are forced to fold and wrinkle at their edges. This behaviour at the collapse region is different than the 3D aggregation observed for surfactants or polymers. A technique used to observe the GO assembly at the air-water interface is the Brewster angle microscopy (BAM). The GO sheets are visible due to their large lateral dimension and optical contrast. However, BAM imaging of a freshly prepared GO dispersion revealed little material on the surface. This can be attributed to the different GO sheets solubility on water. In this way, the large sheets are less hydrophilic and can float on the water surface while small, more oxidized are more hydrophilic sheets and therefore, sink into the subphase. Therefore, as the GO dispersion is usually polydisperse, the water surface itself, without any features, can be used as a size-separation method for GO sheets.<sup>[171]</sup> A way to minimize the GO sheets sinking is to bubble a gas in the subphase. Thus, the process can be controlled by bubbling air or nitrogen where the surface active sheets adhere to rising gas bubbles and become trapped upon reaching the water surface.<sup>[160]</sup> When these monolayers are transferred onto a solid, the LB assembly produces flat GO thin films with uniform and continuously tunable coverage, thus avoiding the uncontrollable wrinkles, overlaps, and voids in films fabricated by other techniques such as dip-coating, spin coating, drop casting, etc.<sup>[156, 158]</sup>

In opposite of GO, the RGO has a more hydrophobic character due to after the reduction step some oxygen groups are reduced. Accordingly, the RGO sheets can be firstly dispersed and then spread at the air-water interface using organic solvents such as 1,2-dichloroethane<sup>[75]</sup> or dimethylformamide<sup>[161]</sup> and can float more easily. With respect to the RGO sheets, their packing behaviour response to barrier compression and LB deposition process are similar to the GO.

### **III. Experimental Section**



### III. Experimental Section

In this chapter are detailed the characteristics of the materials and reagents together with the methodology, experimental conditions and the instrumentation (equipments and techniques) that have been used to carry out this work.

#### III.1. Materials and Reagents

The **polymer** mainly used is the block copolymer poly (styrene-co-maleic anhydride) partial 2 butoxy ethyl ester cumene terminated, PS-MA-BEE, and was supplied by Sigma Aldrich<sup>®</sup>. Its structure is shown in the Figure III.1.

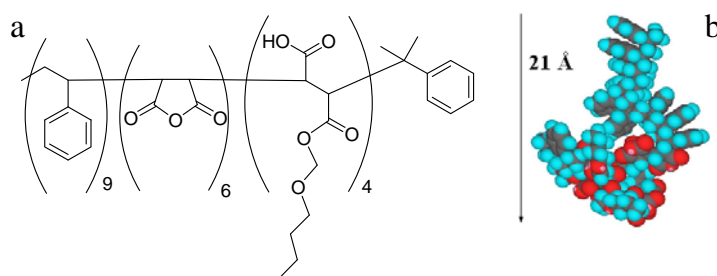


**Figure III.1.** Polymer structure PS-MA-BEE (a); Polymer structure PS-MA-BEE calculated by molecular mechanics, MM2, with the Chem 3D Ultra 9.0. software (b).

According to the data provided by the manufacturer, the polymer molecular weight is  $M_n=2.5$  kDa, and an ester:acid ratio of 1:1. The polymer was used as received without further purification, but it was necessary to dry under vacuum and conserved in a dessicator with calcium chloride ( $\text{CaCl}_2$ ) closed by vacuum.

This polymer was chosen following a researching line of work with maleic anhydride derivative polymers. Another polymer, previously studied by López-Díaz and collaborators<sup>[172]</sup> were used. This polymer was the poly (styrene-co-maleic anhydride) cumene-terminated, PS-b-MA, and was supplied by Sigma Aldrich<sup>®</sup>. The manufacturer data indicate that the PS-b-MA has a molecular

weight,  $M_r$ : 1.9 kDa, and a styrene weight composition of 75%. Its structure is shown in the Figure III.2.

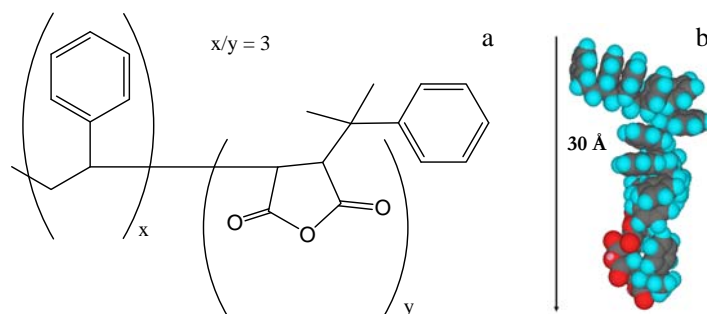


**Figure III.2.** Structure of PS-b-MA (a). Polymer structure calculated by molecular mechanics, MM2, with the Chem 3D Ultra 9.0. software (b).

The water used as **subphase** in the monolayers, or in the different procedures, was ultra purified by using a combination of RiOs and Milli-Q systems from Millipore<sup>®</sup> and has a resistivity less than  $18.2 \mu\Omega \text{ cm}^{-1}$ .

In the case of the ionic subphases, the compound used is hexahydrate magnesium nitrate ( $\text{Mg}(\text{NO}_3)_2 \cdot 6 \text{H}_2\text{O}$ ) (99%) supplied by Sigma Aldrich<sup>®</sup>.

The quantum dots (QDs) and graphene oxide derivatives used in this work were synthesized in our laboratory. The characteristics of the reactives that were necessary in each case are detailed below.

**Materials to TOPO-capped CdSe QDs synthesis.** Trioctylphosphine (TOP, technical grade, 90%), cadmium oxide powder (CdO, 99.99%), selenium powder (Se, 99.99%), oleic acid (technical grade, 90%) and 1-octadecene were purchased from Sigma-Aldrich<sup>®</sup>.

Apart from these materials, in the QDs study, the trioctylphosphine oxide (99%,  $M_m = 386.63 \text{ g mol}^{-1}$ ) was also used and supplied by Sigma-Aldrich<sup>®</sup>, Figure III.3.

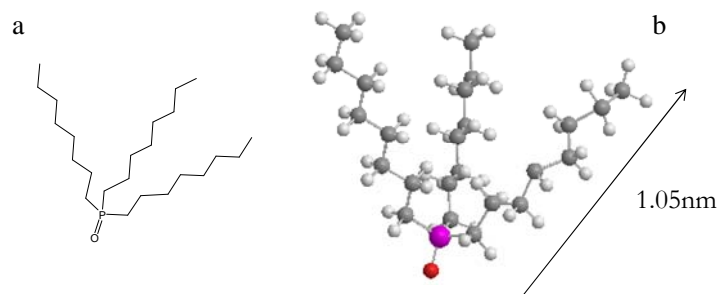


**Figure III.3.** Molecular Structure of trioctylphosphine oxide molecule, TOPO, and the optimum conformation calculated within the MM2 approximation.

**Materials to graphene oxide derivatives.** The batch material (carbon source) was natural graphite flakes, 99.02 fixed C, from Qingdao super graphite Co., LTD (China). Other materials were:  $\text{NaNO}_3$  (99%),  $\text{H}_2\text{SO}_4$  (98%w),  $\text{KMnO}_4$  (>99%),  $\text{H}_2\text{O}_2$  (30%w), hydrazine hydrate (80%w) and Vitamin C (ascorbic acid, puriss.) were purchased from Sigma-Aldrich<sup>®</sup> and used as received without further purification.

The zwitterionic **surfactant**, dodecyl dimethyl ammoniopropyl sulfonate (DDPS,  $\text{cmc } 25.3 \cdot 10^{-4} \text{ M}$ ,  $\text{Mm} = 335.55 \text{ g mol}^{-1}$ ), Figure III.4, was purified by recrystallization in isopropanol until obtain constancy in the surface tension value of a surfactant solution of concentration close to the cmc, critical micelle concentration, as previously reported.<sup>[173, 174]</sup>



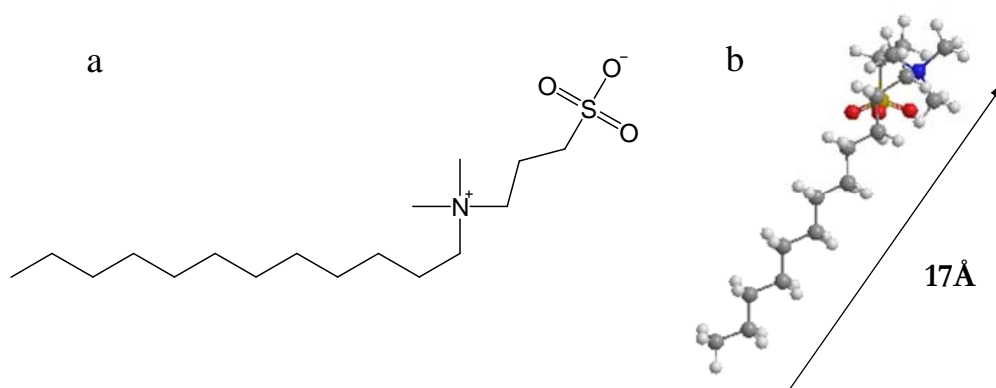


**Figure III.4.** Zwitterionic surfactant structure DDPS (a); Surfactant structure DDPS calculated by molecular mechanics, MM2, with the Chem 3D Ultra 9.0. software (b).

For the Langmuir-Blodgett deposition, several **substrates** were used. The substrates were generally chosen taking into account the requirements of the experimental techniques. These substrates are: muscovite, mono and polycrystalline silicon wafers, quartz discs and copper grids.

Muscovite (mica) quality V-1 was supplied by EMS (USA). The mica surface was freshly cleaved before use.

Silicon monocrystalline wafers, Si(100), supplied by Siltronix (France), are single side polished and were used without pretreatment.

Silicon polycrystalline wafer were supplied by Graphene Industries (U.K.). These As-doped wafers has a dry thermal 280-310 nm silicon oxide (SiO<sub>2</sub>) layer, a resistivity of 0.001-0.050 Ω cm<sup>-1</sup>, a single side polished and gold-alignment laser marks (spacing 200 μm). This substrate was used in the study of graphene derivatives. Thus, we use a silicon wafer with thickness of around 300 nm of SiO<sub>2</sub> in order to enhance the optical contrast of the graphene flakes under white-light illumination for Raman measurements.<sup>[175]</sup> The cleaning procedure<sup>[176]</sup> for these wafers was by mild sonication with acetone (PAI quality, Panreac<sup>®</sup>) (30 s), methanol (PAI quality, Panreac<sup>®</sup>) (30 s) and MilliQ water (30 s) and finally dried in an oven at 90°C.

Quartz discs (diameter 1 inch; thickness  $1/8$  inch, polished) were cleaned by the RCA procedure.<sup>[176]</sup> Firstly, the discs were cleaned with acetone (PAI quality, Panreac<sup>®</sup>), ethanol (PAI quality, Panreac<sup>®</sup>) and MilliQ water. In a glass beaker MilliQ water and ammonia (25% vol, Sigma Aldrich<sup>®</sup>) (5:1 v/v) are mixed up to 60 mL and heated until 70°C, and then 10 mL of hydrogen peroxide (30% w, Panreac<sup>®</sup>) are added. Then discs are submerged and maintained during 15 min at 70°C. After, the discs are rinsed with abundant MilliQ water and dried. These substrates were supplied by TedPella (USA).

Formvar<sup>®</sup>-carbon coated copper grids were supplied by the Servicio de Microscopía Electrónica (Universidad de Salamanca). The carbon copper grids were from TedPella (USA).

### III.2. Langmuir Monolayers: Preparation Procedure

Chloroform was used to prepare the spreading solutions of the different materials (polymer, nanoparticles and graphene derivatives) in order to form the Langmuir monolayers on the subphase. The solvent is PAI quality, filtered and supplied by Sigma Aldrich<sup>®</sup>. The selection of this solvent is due to present good spreading characteristics on the air-water interface<sup>[87]</sup> and also is a good solvent for the different materials.

Cleaning procedure for the different components of the Langmuir trough is the following. The trough is washed with water and abundantly rinsed with lukewarm MilliQ water. Next, it is cleaned with acetone (PAI quality, Panreac<sup>®</sup>) in order to eliminate the rest of water; chloroform (PAI quality, Panreac<sup>®</sup>) and again with acetone to eliminate the rest of chloroform. Finally, the acetone, which remains, is swept out with abundantly MilliQ water. Also, a Derquim<sup>®</sup> (Panreac) cleaning is used once a month.

Pt-Wilhelmy plate is burned with methanol to eliminate the remains of material adsorbed. Once a week, it is cleaned by using a 1 M solution of hydrochloric acid (HCl, Panreac<sup>®</sup>).

In order to guarantee the correct cleaning of the subphase, the surface tension is measured at several areas, thus, if it differs of the value for the subphase at the working temperature, the barriers are compressed (closed) and the interface is sucked up with a glass Pasteur pipette connected to a water pump (Oakton WP-15-1 model) until to achieve the right surface tension. When the surface of subphase was compressed, it is checked that the surface pressure did not exceed  $0.3 \text{ mN m}^{-1}$  during the compression, also ensuring the cleaning.

Deposition of materials on the interface is carried out by the addition of small volumes (10-50  $\mu\text{L}$ ) of the prepared solution using a Hamilton microsyringe (precision  $\pm 1\mu\text{L}$ ), on different zones of the interface. After the addition, the wait time to ensure the solvent evaporation and the right formation of the monolayer is 20-30 min.

The experimental conditions for the Langmuir films preparation of the different materials are detailed below.

For the polymer films the concentrations of the spreading solution in chloroform were *ca.*  $0.06 \text{ mg mL}^{-1}$  for PS-MA-BEE and  $0.70 \text{ mg mL}^{-1}$  for PS-b-MA and were prepared by weight using an analytical balance precise to  $\pm 0.01 \text{ mg}$ . The polymer monolayer was transferred to solid substrates by compression at a barriers speed of  $5 \text{ mm min}^{-1}$ , with the substrate into the trough by vertically dipping it up at  $5 \text{ mm min}^{-1}$ .

In the case of QDs and QD/polymer mixed films the concentrations range for the components in the spreading solutions prepared in chloroform were from  $2 \cdot 10^{-7}$  to  $1 \cdot 10^{-6} \text{ M}$  and  $0.060$  to  $0.0002 \text{ mg mL}^{-1}$  for QDs and PS-MA-BEE, respectively, depending on the mixture mole ratio. Monolayers were transferred to

solid substrates by compression at a barriers speed of  $5 \text{ mm min}^{-1}$ , with the substrate into the trough by vertically dipping it up at  $5 \text{ mm min}^{-1}$ , except for the copper grids. In the case of copper grids for TEM measurements, the rate of dipping up was reduced to  $2 \text{ mm min}^{-1}$ . The subphase temperature was maintained in all the experiments at  $23.0 \pm 0.1^\circ\text{C}$  (296K).

Finally, the GO Langmuir films were prepared by spreading a dispersion ( $\sim 0.5 \text{ mg mL}^{-1}$ ) in MeOH:H<sub>2</sub>O (5:1 v/v, sonication 30 min) on the air-water interface. The GO sheets were transferred onto silicon by symmetric barrier compression ( $50 \text{ mm min}^{-1}$ ) with the substrate into the trough by vertically dipping it up at  $2 \text{ mm min}^{-1}$  by LB method. On the other hand, the RGO sheets were deposited onto the water subphase using a dispersion ( $\sim 0.1 \text{ mg mL}^{-1}$ ) in chloroform. The RGO sheets were transferred from the air-water interface onto silicon by symmetric barrier compression ( $50 \text{ mm min}^{-1}$ ) with the substrate into the trough by vertically dipping it up at  $5 \text{ mm min}^{-1}$ . The water subphase temperature was maintained in all the experiments at  $20.0 \pm 0.1^\circ\text{C}$  (293K).

### III.3. Experimental Techniques

In this section are briefly described the equipments and techniques employed in the research together with the work conditions used to carry out the measurements.

#### III.3.1. Langmuir Trough

The equipment, which was used to prepare the surface pressure isotherms and the rheological study of the insoluble monolayers, is a teflon trough (KSV Instruments LTD Mini model, Finland) controlled by computer. A photograph of it is showed in the Figure III.5. The main components of the equipment are: the trough, the movable barriers and the electrobalance.



**Figure III.5.** Photograph of the Mini model trough (KSV Instrument LTD).

The trough, built in teflon, with dimensions of 32.4 x 7.5 cm, has an area of 243 cm<sup>2</sup> and contains the subphase, water or an aqueous solution of different electrolytes. As teflon is a hydrophobic material the subphase adopts the form of the trough edges and with the water forms a contact angle next to  $\pi/2$  avoiding the wetting phenomena. The subphase temperature is maintained with through jackets at the bottom of the trough by flowing thermostated water from a thermostat/cryostat Lauda Ecoline RE-106. The temperature near the surface was controlled/measured with a calibrated sensor from KSV Instrument LTD.

Movable barriers are built with a hydrophilic material called Delrin<sup>®</sup> (polyoxymethylene), thus they form a concave curvature with the subphase avoiding the material loose of the monolayer under the barriers. In order to ensure that the area changes are produced in the perpendicular plane to the liquid surface, the barriers are placed on stainless steel pieces and connected to an electromechanic device that automatically controls their movement, allowing to programme different kinds of experiments. The speed range for the barriers movement goes from 1 to 120.5 mm min<sup>-1</sup>.

### Equilibrium Measurements

The surface pressure was measured with a Pt-Wilhelmy plate connected to an electrobalance. The plate is placed at the air-water interface, thus, the surface pressure is directly determined without correction of the obtained values. The porous Pt-plate forms a nulling contact angle with the subphase, so the surface wetting was right. As the plate is hung from an electrobalance, when the plate makes contact with the interface, an increasing of weight,  $\Delta W$ , is produced, that is related to the surface tension following the expression:

$$\gamma = \frac{\Delta W}{p \cos\theta} \quad [\text{III. 1}]$$

Where,  $p$ , is the perimeter of the plate (10x19.62 mm), and  $\theta$ , the contact angle between the subphase and the plate that comes from:

$$\left[\frac{h}{a}\right]^2 = 1 - \text{sen}\theta \quad [\text{III. 2}]$$

In this expression  $a$  and  $h$  represent the capilar length and the height of the top part of the meniscus formed over the liquid surface level, respectively.

The electrobalance is able to measure surface pressures of  $0.01 \text{ mN m}^{-1}$ , but the data precision in the experimental conditions is not more than  $0.1 \text{ mN m}^{-1}$ , due to the influence of external factors as the temperature and mechanical stability. In order to minimize the mechanical vibrations, the trough is placed on an anti-vibration table.

The equipment allows to characterize the Langmuir monolayer measuring different physical properties as surface pressure and potential while the available area is being modified with a movable barriers mechanical system by symmetric compression or expansion.

## Dynamic Measurements

In the dynamic studies of insoluble monolayers, the system in equilibrium is disturbed. An option to perturb the monolayer are the relaxation experiments, that consist of apply a distortion (deformation) to the system and analyze the response of this with the study of the relaxation of the tensions that act on the system by recording the temporal variation of the surface pressure. Depending on the type of deformation applied, there are two kinds of experiments: sudden-step method and dynamic oscillation method (sinusoidal deformation).

The **sudden-step experiments**, i.e., step-compression or step-expansion are quickly carried out by moving the barriers ( $120.5 \text{ mm min}^{-1}$ ) in order to modify the available area in the monolayer controlled with the software. The time necessary to make the compression was slightly less than 2 s. The system response is measured by recording the surface pressure with the time. When the trough area is modified then the surface concentration is also modified, i.e., during the compression the system losses the equilibrium and an increase in the surface pressure is produced. When the compression stops, the relaxation of tensions in the monolayer begins decreasing the surface pressure until a constant value is reached, that corresponds to the pressure value of the new equilibrium. A scheme of the process, for a step-compression, is showed in Figure III.6.

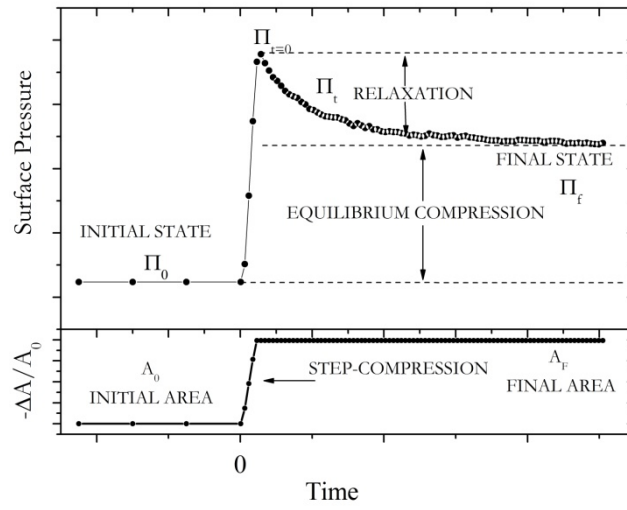


**Figure III.6.** Representative scheme of a step-compression experiment.

In small and independent molecules, i.e., without interaction with the environment molecules, the response of the surface pressure can be interpreted as a Debye exponential relaxation <sup>[133]</sup>:

$$\pi(t) = \pi_f + \sigma_0 \exp\left[\frac{-t}{\tau}\right] \quad \text{[III. 3]}$$

In this equation  $\tau$  and  $\sigma_0$  represent the relaxation time and the relaxation amplitude, respectively.

From the values of the area increment (strain),  $-\Delta A/A_0$ , and the relaxation amplitude,  $\sigma_0$ , are determined the dynamic elasticity,  $\epsilon$ , and the dilatational viscosity,  $\kappa$ , <sup>[177]</sup> by using the following expressions:

$$\epsilon = \frac{\sigma_0}{-\Delta A/A_0} \quad \text{[III. 4]}$$

$$\kappa = \frac{\sigma_0}{-\Delta A/A_0} \tau = \epsilon \tau \quad \text{[III. 5]}$$



The dynamic elasticity represents the instantaneous elastic response of the monolayer, while the dilatational viscosity represents the friction losses that are produced.

The **dynamic oscillation experiments** consist of the sinusoidal deformation as a time function of the available area in the monolayer. In order to carry out oscillatory barrier movements are programmed maintaining the frequency constant. Thus, by the analysis of the surface pressure response with different changes of area (strain), it is possible to determine the strain range in which the system response is linear.

The variation function of the area with the time is expressed by the following equation:

$$U(t) = \frac{U_0}{2} [1 + \text{sen}(\omega t + \varphi_u)] \quad \text{[III. 6]}$$

Where,  $U(t) = \Delta A/A_0$ . The parameters  $U_0$ ,  $\omega$  and  $\varphi_u$ , are respectively the deformation amplitude (strain), the angular velocity and the phase lag angle with regard to the equilibrium position of the wave. Figure III.7. shows the experimental results for a PS-MA-BEE monolayer deposited on an aqueous subphase.

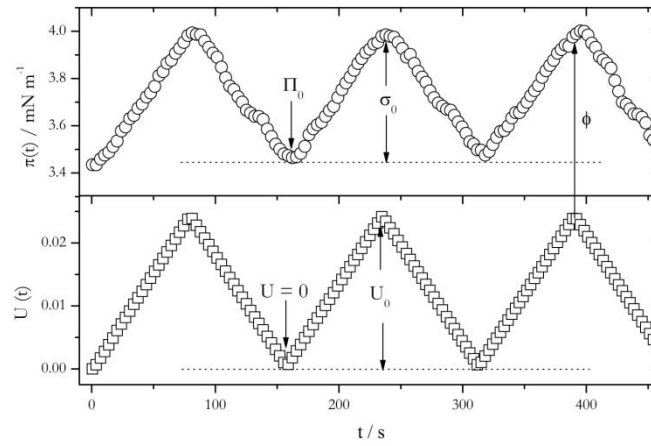


**Figure III.7.** Graph of a PS-MA-BEE monolayer response due to a sinusoidal area change,  $U(t)$  at 296 K.

The strain promotes the modification of the surface concentration and as result, a change in the surface pressure that depends on the time according to the expression:

$$\pi(t) = \pi_0 + \frac{\sigma_0}{2} [1 + \text{sen}(\omega t + \varphi_\sigma)] \quad [\text{III. 7}]$$

Where  $\pi_0$ , is the equilibrium surface pressure,  $\sigma_0$ , the amplitude of the stress (system response) and  $\varphi_\sigma$ , the phase lag angle with regard to the equilibrium position of the surface pressure wave.

In this work, several measurements were carried out by the step-compression method. However, to use this technique, it is necessary to work in the linear regime, i.e., the range where the amplitude of the stress is proportional to the strain, according to Hooke's Law. To check the strain range, oscillatory barrier measurements were carried out in the monolayers.

### III.3.2. Surface Potential: Kelvin Probe

Surface potential is a magnitude that gives information not only about the structure of the double dielectric layer of the adsorbed molecules at the interface, but also about the orientation of the molecules at the interface. When an adsorbed monolayer exists at a fluid interface, a sensible increase of the existent Volta potential between this surface and a metal electrode placed on a certain distance is produced. In a Langmuir monolayer the surface potential measures as the presence of the monolayer affects the potential of the clean subphase, thus the surface potential is termed as the difference in potential between a monolayer-covered subphase and a clean subphase.<sup>[79]</sup>

$$\Delta V = V - V_{subphase} \quad \text{[III. 8]}$$

This magnitude is measured with the ionizing probe technique or the vibrating capacitor technique. The first method, actually in disuse, implies the use of a fix electrode of polonium or another emitter of particles  $\alpha$ , that cause the ionization of the air gap between the fluid surface and the electrode, making it sufficiently conductor to determine the impedance between this electrode and one of reference introduced in the subphase. A method more precise, and that not use radioactive material, is the method used in this work. It is the noncontact vibrating electrode (plate) capacitor or Kelvin probe method. It consists of a metal electrode (plate) located at approximately 2 mm above the aqueous surface and other as reference submerged in the subphase. If the plate is made to vibrate, the distance between the plate and the interface changes, and therefore, the capacity of the formed condenser changes, appearing an alternating current over to the applied potential. This current is proportional to the surface potential. The equipment cancels this current by applying an external bias till the potential difference between the plates is zero. The Kelvin probe used in this work is the SPOT2 model from KSV Instrument LTD and allows us to obtain values of

surface potential with a precision of  $\pm 20$  mV. The surface potential of monolayers was determined relative to the surface potential of the supporting electrolyte and of water if no salt was added to the subphase. Each reported value is an average over five measurements and the standard deviation of these measurements was considered the experimental error. In Figure III.8, a photograph of the equipment is showed.



**Figure III.8.** Photograph of the Kelvin probe SPOT 2 model (KSV Instrument LTD) placed on the Langmuir trough.

Theoretical models have been developed in the course of the years to interpret the surface potential measurements and to relate quantitatively the measured potentials to the group dipole moment of the film-forming molecules. Such models are based on the Helmholtz model <sup>[178]</sup>, in which the interface structure is considered as a parallel plate condenser, with plates spaced a distance,  $d$ , equal to the interface thickness, and charged with opposite signs and a surface density of charge,  $\sigma$ . Therefore, comprising a sheet of uniformly distributed dipoles, leading to an increase of surface potential described by:

$$\Delta V = \frac{4 \pi \sigma d}{\epsilon \epsilon_0} = \frac{\mu_n}{\epsilon \epsilon_0 A} \quad [\text{III. 9}]$$

Where  $\varepsilon$  and  $\varepsilon_0$ , are the electric permittivity of the monolayer and the permittivity of free space, respectively;  $d$ , represents the monolayer thickness; and  $\mu_n$ , is the normal component of the dipole moment per adsorbed molecule.

Improvements of the Helmholtz equation have been made in order to take into account the dipole moment contributions from distinct molecular groups. Davies and Rideal <sup>[179]</sup> proposed the decomposition of the dipolar moment,  $\mu_n$ , in three components:  $\mu_1$ , is the contribution from reorientation of water molecules from the subphase due to the presence of the monolayer;  $\mu_2$ , is the contribution from head groups; and  $\mu_3$ , arises from the hydrophobic moiety. Since it is impossible to measure  $\mu_1$  independently, it is customary to combine with  $\mu_2$  as the former anyway depends on the type of the head group. This was the approach adopted by Vogel and Möbius <sup>[180]</sup>, in which the monolayer is modelled as a two-layer capacitor. Thus the effective dipole moments are divided into two contributions, from the air-film interface,  $\mu^\alpha$ , and film-water interface,  $\mu^\beta$ , and the surface potential can thus be expressed as follows:

$$\Delta V = \frac{\mu^\alpha + \mu^\beta}{A \varepsilon_0} \quad [\text{III. 10}]$$

When the film is compressed, the surface potential changes due to alteration of either the head or the tail group orientation.

Demchak and Fort <sup>[181]</sup>, introduced the concept of effective relative permittivities for different regions which allows to take into account the induced polarization due to neighbouring molecules, in this way, proposed the three-layer capacitor, in which the monolayer surface potential is expressed as:

$$\Delta V = \frac{1}{A \varepsilon_0} \left( \frac{\mu_1}{\varepsilon_1} + \frac{\mu_2}{\varepsilon_2} + \frac{\mu_3}{\varepsilon_3} \right) \quad [\text{III. 11}]$$

The contribution  $\mu_1/\epsilon_1$  is due to reorientation of water molecules, while  $\mu_2/\epsilon_2$  and  $\mu_3/\epsilon_3$  correspond to hydrophilic and hydrophobic group regions, respectively.

In the Figure III.9. is showed a scheme of the three explained models.

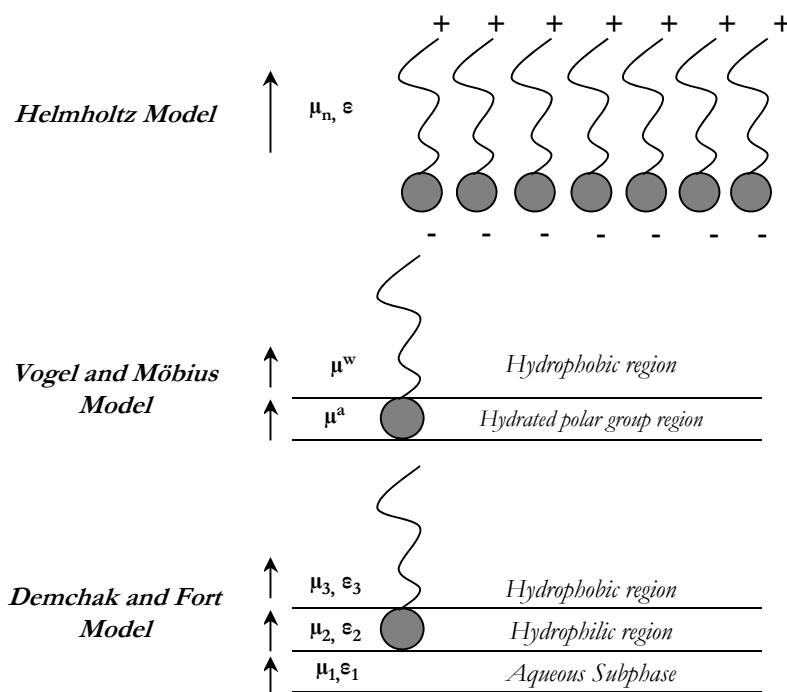


**Figure III.9.** Models to explain the non-ionic monolayer surface potential.

The surface potential has a value close to zero in gaseous monolayers very expanded. The apparition of a value of surface potential different to zero, at high areas per molecule of the isotherm, is attributed to impurities in the subphase.<sup>[182]</sup> When the density of adsorbed molecules increasing, even at surface pressure values close to zero, the potential begins to increase. The area at which the potential begins to significantly increase is denoted as critical area and is usually located around two times the area at the beginning of the surface pressure increase. The existence of the critical area has been related to the formation of structures by hydrogen-bonding between the water molecules and polar groups of

the molecules that forms the monolayer. The observation of the intermolecular interaction is consistent with the results obtained by Brewster angle microscopy (BAM) or fluorescence.

In ionic monolayers is formed a double-layer electric below the interface that contributes to the surface potential in a quantity,  $\Psi_0$ , that is included in the Helmholtz equation to calculate the monolayer potential. The value of  $\Psi_0$  can be obtained solving the Gouy-Chapman model for the electric double-layer.<sup>[183]</sup>

$$\Delta V = \frac{\mu_n}{A \varepsilon \varepsilon_0} + \Psi_0 \quad [III. 12]$$

### III.3.3. Brewster Angle Microscopy (BAM)

Brewster Angle Microscopy was independently introduced by two groups<sup>[184, 185]</sup> to the characterization of the molecular monolayers at the air-water interface, due to probe information about the two-dimensional organization of adsorbed material, including size and shape of co-existence phase domains and also the heterogeneity that appears in Langmuir films. The main advantage of this technique is that it does not contact with the monolayer, therefore it does not modify the formed structures, not contaminate, as it can occur in the case of the epifluorescence microscopy.<sup>[186]</sup>

This technique is based on the behaviour that the polarized light presents when is reflected on a dielectric thin surface. When this occurs, the incident light beam on the surface is transformed in a partial polarized light beam. It means that the reflected electric vector vibrates in the parallel plane to the material surface. The intensity of the reflected light depends on the incident angle. For a polarized light beam parallel to the incident plane exists an angle in which there is not reflection. This angle is called Brewster angle, and for the case of the air-water interface has a value of 53.1°.<sup>[79]</sup>

Sir David Brewster discovered, at the beginning of S.XIX, that exist incident angles in which the reflected light is totally polarized in the parallel direction to the surface plane. It is the Brewster angle, characteristic of the material that forms the surface and of the propagation medium and is related to the refractive index of the two phases that origin the interface following the equation:

$$\frac{n_2}{n_1} = \frac{\text{sen}\theta_i}{\text{sen}\theta_r} = \frac{\text{sen}\theta_i}{\text{sen}\theta_{90^\circ-i}} = \tan\theta_i \quad [\text{III.13}]$$

Where  $\theta_i$  and  $\theta_r$  represent the incident and refracted angle, respectively,  $n_1$  the refractive index of the medium where the light is propagated; and  $n_2$  the refractive index of the medium where the light is reflected. A scheme of the Brewster angle principle is showed in the Figure III.10.

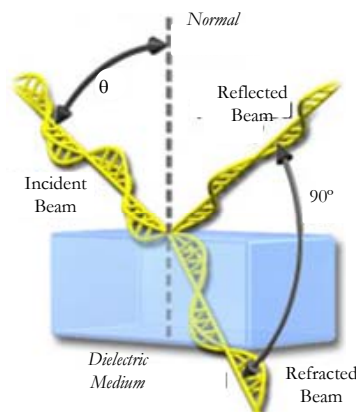


**Figure III.10.** Scheme of the reflection and refraction phenomena of the light in dielectric media, where  $\theta$  is the Brewster angle.

When a light beam impinges in a surface of a transparent medium that has a refractive index greater than the air, for example water, forming an angle equal to the Brewster angle, the polarization degree of the reflected beam is 100% with an orientation of the electric vectors perpendicular to the plane of incidence and parallel to the surface that reflect them. In this way, the operation principle of the Brewster angle microscope is based on the change in the refractive index,



therefore, in the change in the Brewster angle originated when a material is deposited at the air-water interface in order to form the monolayer and that produces the reflection of the light. A scheme of this phenomenon is showed in Figure III.11.

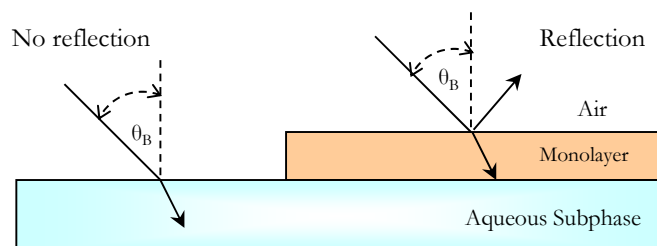


**Figure III.11.** Scheme of the reflection phenomenon due to the presence of a monolayer at the air-water interface, where the incident angle  $\theta_B$  is the Brewster angle.

The Brewster angle microscopy used in this work is from KSV Instrument LTD (Finland), Optrel BAM 3000 model. In general, a microscopy of these characteristics has the following components: Goniometer, Light source and Analysis module. A photograph of BAM is shown in Figure III.12.

### Goniometer

Goniometer (1) is composed by two movable pieces that allow modifying the height with regard to the interface and the angle that forms these pieces. In each piece there are placed the light source and the analysis module.

### Light Source

Light source is a He-Ne laser (2) that emits light in a wavelength of 632.8 nm with a power of 10 mW. It is joined to a polarizer (3) that polarizes the light emitted by the laser.

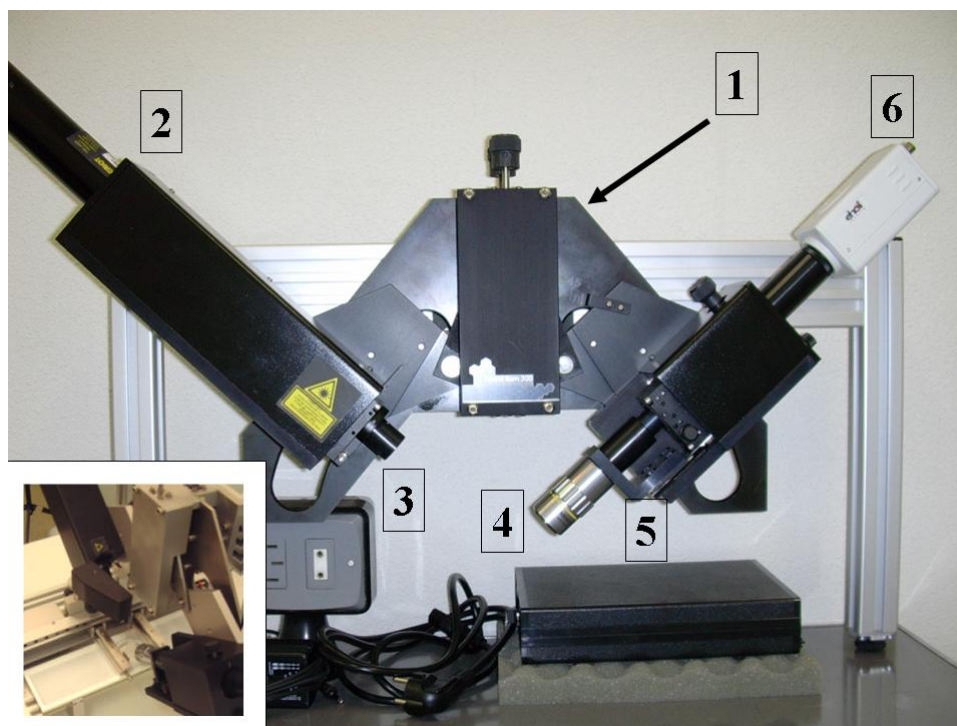


**Figure III.12.** Brewster Angle Microscopy Optrel BAM 3000 (KSV Instrument LTD).

### Analysis Module

Analysis module consists of objective, polarizer and camera. The optical objective (4), with a capacity of 5 magnifications (5X), is from Mitutoyo (USA). Joined to this, there is a polarizer (5), which fit the direction of polarization that comes from the surface. Finally, the light arrives to a digital high resolution monochromatic camera (6) from EHD (Kam Pro-02 model) that has a resolution of 768 X 494 pixels.

This technique allows us to study of the interface morphology due to taking into account that as the light in the Brewster angle is polarized in the direction of the surface, i.e., the air-water interface, if a polarizer is perpendicularly placed on the reflected beam, the image collected by the camera will be null, because no light arrives. However, when a material is deposited to form an insoluble monolayer, the refractive index changes and therefore the Brewster

angle changes, arriving light to the camera and allowing to see an image. If the monolayer has phases with different refractive index, the images show bright and dark domains (areas) depending on the difference of the phase angle with regard to the Brewster angle of the interface.

BAM images are digitalized and filtered in order to reduce diffraction fringes caused by the coherent nature of the laser beam and finally processed to improve quality. In this way, the images provided by BAM are zones of different tonality that are related to either different phases of the monolayer.<sup>[79]</sup>

### III.3.4. Langmuir-Blodgett Trough

The equipment for the deposition of LB films was a teflon trough (KSV2000 Standard model, Finland) controlled by computer (Figure III.13). This trough is similar to the Langmuir trough before explained. In this case the trough has an area of 780 cm<sup>2</sup> (dimensions 52 x 15 cm).



**Figure III.13.** Langmuir-Blodgett Standard trough (KSV Instruments). The inset shows the dipping arm which holds the substrates for the LB deposition.

The transfer of the Langmuir monolayers from the air-water interface to solid substrates is carried out by using a dipper (dipping arm which holds the substrate) connected to the trough and the computer interface. The dipper is

controlled by computer and moves perpendicular to the interface. For the transfer is important the control and optimization of several parameters depending on the type of monolayer and substrate: the transfer ratio, the compression rate of the monolayer and the dipping speed (immersion or emersion) during the deposition. Other factors that affects to the process are: surface pressure, type of molecules that forms the monolayer and composition, temperature and pH of the subphase. The LB film deposition was carried out by dipping up, i.e., firstly the substrate is submerged, then the monolayer is formed and finally, the monolayer is transferred by move up the substrate. In general, for dipping starting from below the air-liquid interface, the substrate is hydrophilic, and for dipping starting above the air-liquid interface the substrate is hydrophobic. Multilayers can be achieved by successive dipping through alternating monolayers.<sup>[86, 187]</sup> During the transfer, surface pressure is maintained constant by symmetric compression of the barriers. The used substrates were quartz, muscovite (mica), silicon and copper grids (for TEM).

### III.3.5. Atomic Force Microscopy (AFM)

The AFM technique was used to characterize the morphology and thickness of the different studied Langmuir-Blodgett films deposited onto several substrates. The measurements was carried out under laboratory conditions at constant repulsive force mode by using an AFM (Nanotec Cervantes-Dulcinea, Spain) with a rectangular microfabricated silicon nitride ( $\text{Si}_3\text{N}_4$ ) cantilever (Olympus OMCL-RC800PSA) with a length of 100  $\mu\text{m}$ , with a silicon pyramidal tip and a spring constant of 0.73  $\text{mN m}^{-1}$ . The scanning frequencies rate were usually in the range 0.5-1.2 Hz per line. The equipment is located in an antivibration table, and in several times, it was necessary to minimize the environment acoustic and electronic noise. The acquisition and analysis were carried out with the WSxM 5.0 software free supplied by Nanotec.<sup>[188]</sup> The

measurements were done in the Ultrashort Ultraintense Pulsed Lasers Centre (CLPU) of the Universidad de Salamanca.

Although the resolution depends on the type of sample, generally, the technique has a resolution around 0.01 nm for heights ( $z$ ) and a lateral resolution ( $x, y$ ) of 0.7-5nm for soft materials. The running of this technique is based on the interaction/repulsion forces between the tip, which scans the surface of the sample keeping up to a distance, and the material of the sample that is studied. The tip is anchored to a cantilever, because of it, according to the interactions between the tip and the surface of the sample, the distance between both is modified. This distance is optically controlled by the system, during the scan of the sample, by a laser beam focus on the back of the cantilever for monitoring its shift (deflection), Figure III.14. The reflected beam is collected by a photodiode that multiplies the cantilever shift (deflection), improving the sensibility of the equipment, and through a feedback circuit controls the distance tip-sample that the software converts into the topographic map of the surface sample. During the scan of the sample surface, the movement (3D position) of the tip is controlled by a scanner built onto a piezoelectric system.

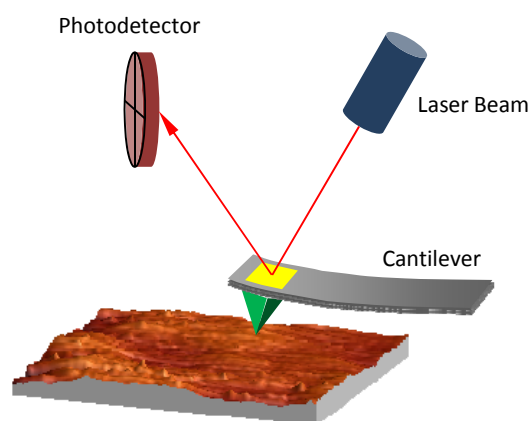


**Figure III.14.** Schematic picture of the main components of the AFM.

The main interaction force between the tip and the sample is the Van der Waals force, which depends on their distance (Figure III.15). In the contact regime, the probe (tip-cantilever) is held less than a few angstroms from the sample surface, and the interatomic force between the probe and the sample is repulsive. In the non-contact regime, the probe is held on the order of tens to hundreds of angstroms from the sample surface, and the interatomic force between the cantilever and sample is attractive (largely a result of the long-range Van der Waals interactions).

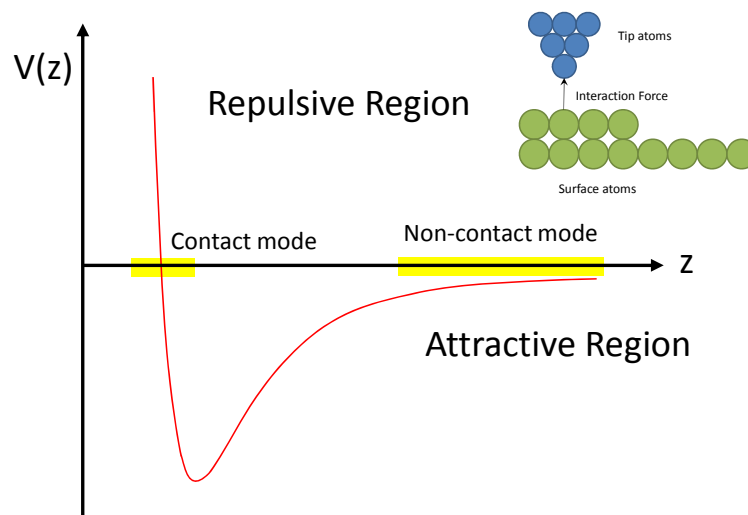


**Figure III.15.** Potential energy ( $V(z)$ ) vs distance ( $z$ ) diagram between a probe and a sample.

The usual operation modes for this equipment are:

- **Contact Mode.** In this case, the tip slightly contacts with the surface of the sample. It is possible to work by two ways, fixing the distance between tip-surface or establishing the force applied by the tip onto the sample, due to the deflection of the cantilever is proportional to the force acting on the tip, according to a Hooke's Law, where  $k$  is the spring constant of the cantilever. By this mode, it is possible to manipulate or damage the sample and contaminate the tip.

- Non Contact Mode. In this mode, the probe (tip-cantilever) operates in the attractive force region with tip-sample distances of 10-100 Å, minimizing the tip-sample interaction. The use of this mode allows scanning without influencing the shape of the analyzed sample.
- Tapping Mode (intermittent contact mode). It is the main used mode in our samples, due to allow to obtain high resolution and reproducible images of the sample surface, avoiding problems as the friction or adhesion of the tip, but the scanning rate is lower than the contact mode. In this mode, the cantilever is oscillating close to its resonance frequency by using a piezoelectric crystal controlled by an electronic feedback loop. This loop ensures that the interaction tip-sample remains constant during scanning. Forces that act between the sample and the tip do not cause a change in the oscillation amplitude, but also change the resonant frequency and phase of the cantilever. The selection of the optimum oscillating frequency and the force on the sample are assisted by the software, maintaining the force in the low possible level in order to avoid the damage of the surface during the vertical intermittent contacts that occur.<sup>[189]</sup>

### **AFM image artefacts**

Taking into account that the AFM images are always a convolution of the probe geometry and the shape of the features being imaged, some image artefacts can be often observed, Figure III.16.<sup>[190]</sup> For example, features can be appear too large or small, however, the height of the feature measured by the line profile is correct. Moreover, the images are also affected by the distance between features. If the features are close enough it is not possible to discern between them and results in a larger measured feature size and a smaller feature density. In these situations, the electronic microscopic measurements are recommended to obtain information about the real lateral dimensions and density of domains while AFM must be used to determine its roughness.<sup>[191]</sup>

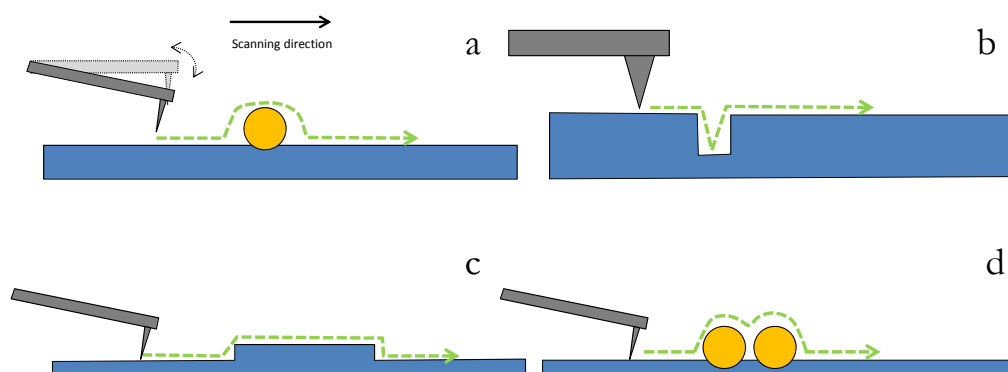


**Figure III.16.** Schematic diagram of the AFM tip scanning on different situations: (a) tip over a sphere: the side of the probe will cause a broadening of the features in the image; (b) tip over a hole: due to the width of the probe, it does not reach the bottom of the hole; (c) tip over a sharper feature: due to the extreme probe sample angle, the line profile will show an artefact at the left edge of the feature; and (d) two dots closely spaced features: due to the probe size, it will not touch the substrate region between the features.

To minimize some effects on the AFM images, each sample was recorded several times at the same and different locations on the substrate, and in several cases a statistical analysis of feature dimensions was carried out. Furthermore, electron microscopic measurements were also carried out when it was possible.

### III.3.6. Electronic Microscopy

The fundamental basis of this technique is supported on the wave-particle duality of the electrons, i.e., the electrons in movement present a wave associated to a wavelength several magnitude orders less than the visible light, therefore, allows to achieve smaller resolution limits; and on the other hand, as they are particles with electric charge, they can be deflected by electrostatic or magnetic lens. The electrons are accelerated, up to achieve the desired rate, by the application of an adequate electrostatic potential difference. The trajectory, that cover the electrons, is modified in the presence of electric and magnetic fields



conveniently placed in order to achieve that the divergent electron beam from the objective can focus on a point forming an enlarged image of the sample. In this way, the electrostatic lens are used in the illumination system of the microscopy to extract and accelerate the electrons; and the magnetic lens to control the current density of the beam, its displacement and projection.

When the electron beam comes into contact with a sample, a series of interactions, which are responsible for the observed images contrast, are produced and give rise to different secondary radiations that can be used to obtain complementary information. This allows to combine observation and analysis giving rise to different types of microscopes. If the sample is thin enough, a great part of the incident electrons will achieve to pass through it, without changes in their trajectory and energy, producing the transmitted beam, Figure III.17. Part of the incident electrons can be scattered forward or backward, giving rise to the scattered beam and the backscattered beam, respectively, with energies that vary from the initial to several eV.<sup>[192]</sup>

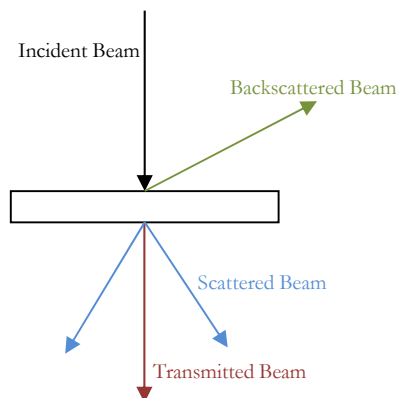


**Figure III.17.** Scheme of the resulting interaction of the electron beam with the sample.

In the Transmission Electron Microscopy (TEM), a sample thin enough ( $\leq 200$  nm), in order to be transparent for the electrons, is irradiated with a parallel electron beam of uniform current density that goes through the sample forming an image of the crossed section. In this work, the samples were deposited onto Formvar<sup>®</sup>-carbon coated copper grids by the Langmuir-Blodgett technique.

Mainly, it was used to study the size and distribution of the nanoparticles in the LB films. The TEM images were acquired with the following equipments: TEM (ZEISS EM 902, Germany) at a accelerating voltage of 80kV, that belongs to the Servicio de Microscopía of the Universidad de Salamanca; and a TEM JEOL JEM 4000 EX (100kV) of the Centro de Microscopía Electrónica Luis Brú (Universidad Complutense de Madrid).

In the Scanning Electron Microscopy (SEM), the electrons are focused on the surface of a thick sample, opaque to the electrons. The incident electron beam scans the surface of the sample, and as a result of the interaction with the sample, a secondary electron emission is produced: the surface reflects and/or backscatters electrons, that give rise to a signal. This signal is driven to a cathode ray tube. The emission intensity depends on the incident angle of the electron beam onto the material surface and therefore, on the sample topography. In this tube, the signal scans the display synchronized with the electron beam movement over the sample, forming an image of the surface.<sup>[192]</sup>

This technique, and concretely, a Field Emission Scanning Electron Microscopy (FE-SEM) (Nova<sup>TM</sup> NanoSEM 230, FEI, USA) has allowed the characterization of the oxidized and reduced graphene flakes deposited onto polycrystalline silicon, with a 300 nm SiO<sub>2</sub> layer, by Langmuir-Blodgett. The access to this equipment was possible thanks to the collaboration with the Dpto. Electrónica of the University of Barcelona (Spain). FE-SEM images were acquired using the high resolution detector in high vacuum (HV) mode, usually applying an accelerating voltage of 10 kV. The instrument can be operated in two types of image modes: secondary electron image (SEI) and backscattered electron image (BEI).

### III.3.7. Ellipsometry

It is a sensitive optical technique for determining properties of surfaces and thin films, based on the use of elliptically polarized light generated by the interaction between the linearly polarized light and a surface. The shape and orientation of the ellipse depend on the angle of incidence, the direction of the polarization of the incident light, and the reflection properties of the surface. In this way, it is possible to measure the polarization of the reflected light with a quarter-wave plate (QWP) followed by an analyzer; the orientations of the quarter-wave plate and the analyzer are varied until no light passes through the analyzer. From these orientations and the direction of polarization of the incident light, it is possible to calculate the relative phase change,  $\Delta$ , and the relative amplitude change,  $\Psi$ , introduced by reflection from the surface.

An ellipsometer measures the changes in the polarization state of light when it is reflected from a sample, thus, when the thickness of the sample varies, change the reflection properties of the light. Measuring these changes in the reflection properties can allow to deduce the actual change in the film thickness. As this technique is based on the reflection, some general basics of this phenomenon are indicated. In the reflection, the plane of incidence contains the beam light before and after the reflection, and it is perpendicular to the surface. As the used radiation is plane-polarized, there are two kinds of polarizations: polarization p, when it is polarized in the plane of incidence and s, when the polarization is perpendicular to the plane of incidence.

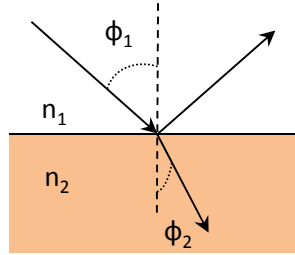


**Figure III.18.** Reflection and transmission of the light in an interface.

For the reflection of radiation in an interface that divides two media, Figure III.18, where part of the light is reflected and other part transmitted, it is defined the Fresnel's reflection coefficient,  $r$ , as the ratio between the amplitude of the waves reflected and incidental in the interface. For the two polarization states, p or s, of the incident light, the Fresnel's coefficients are defined as:

$$r_{12}^p = \frac{n_2 \cdot \cos\phi_1 - n_1 \cdot \cos\phi_2}{n_2 \cdot \cos\phi_1 + n_1 \cdot \cos\phi_2} \quad r_{12}^s = \frac{n_1 \cdot \cos\phi_1 - n_2 \cdot \cos\phi_2}{n_1 \cdot \cos\phi_1 + n_2 \cdot \cos\phi_2} \quad [\text{III. 14}]$$

Where the superscripts represent the polarization state of the waves (p or s), the subscripts 1 and 2 the media that divide the interface, and  $n$  is the complex index of refraction. The reflectance,  $\mathfrak{R}$ , is defined as the ratio between the incident and reflected intensities, and is related to  $r$  by the expression:

$$\mathfrak{R}^p = |r^p|^2 \quad \mathfrak{R}^s = |r^s|^2 \quad [\text{III. 15}]$$

In the analyzed samples, there are multiple interfaces (several layers or media), because of it, the total reflection is the sum of the reflection in the outer surface, with all the components of the reflection in each intermediate interface where the light is transmitted, Figure III.19.

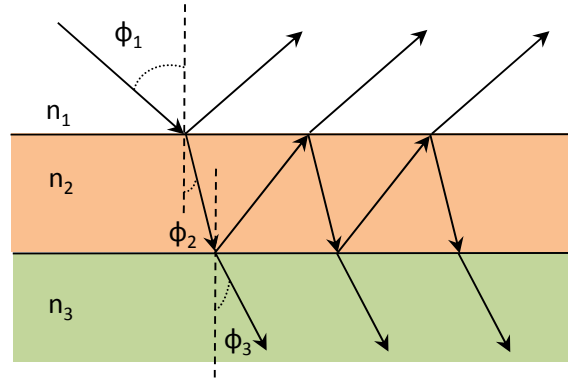


Figure III.19. Reflection and transmission with multiple interfaces.

For these cases, the Azzam's and Heavens' expressions are used. They deduced the relation between the amplitude of the resultant wave with regard to the incident wave, i.e., the total reflection coefficients,  $R$ .<sup>[193, 194]</sup>

$$R^p = \frac{r_{12}^p + r_{23}^p \cdot e^{-2\beta j}}{1 + r_{12}^p \cdot r_{23}^p \cdot e^{-2\beta j}} \quad R^s = \frac{r_{12}^s + r_{23}^s \cdot e^{-2\beta j}}{1 + r_{12}^s \cdot r_{23}^s \cdot e^{-2\beta j}} \quad [III. 16]$$

In this expression the subscript  $ij$  ( $i = 1, 2, 3$  y  $j = i+1$ ) is referred to the reflection coefficient between the media  $i$  and  $j$ .  $\beta$  is the phase thickness of the film:

$$\beta = 2\pi \left( \frac{h_{op}}{\lambda} \right) n_2 \cos \phi_2 \quad [III. 17]$$

where  $h_{op}$  is the film's thickness. When  $h_{op} \rightarrow 0$ , the total reflection coefficient is equal to the Fresnel's coefficient.

As was previously exposed, between the incident and reflected radiation over the sample, there is a difference or change of phase between the parallel and perpendicular components,  $\delta$ . The difference in the phase, between the incident beam (1) and the reflected beam (2) defines the first ellipsometric angle,  $\Delta$ , that varies between 0 and 360°.

$$\Delta = \delta_1 - \delta_2 \quad [\text{III. 18}]$$

Also the amplitude of the light components is modified, and is related to the psi angle,  $\Psi$ , that can vary between 0 and 90°.

$$\tan\Psi = \left| \frac{R^p}{R^s} \right| \quad [\text{III. 19}]$$

These two angles are experimentally determined in the ellipsometric measurements, and are related to the total reflection coefficients,  $\rho$ , following the fundamental equation of the ellipsometry.<sup>[195]</sup>

$$\rho = \frac{R^p}{R^s} = e^{\Delta j} \cdot \tan\Psi \quad [\text{III. 20}]$$

### Equipment and Data Analysis

The measurements were carried out in the CAI of Spectroscopy of the Universidad Complutense de Madrid, with a nulling ellipsometer EP<sup>3</sup> model (Nanofilm, Germany). Radiation source of the ellipsometer is a Nd-YAG laser with a wavelength of 532 nm (green) and maximum power of 50 mW, but in the experiments a power of ~2% was used. The ellipsometric measurements were carried out by varying the incident angle in the range 50° to 86° and also the ellipsometer was used as a Brewster angle microscopy to observe the surface of the sample and choose several points for measurement. The laser beam was focused on the LB films on silicon substrates positioned on the goniometer plate.

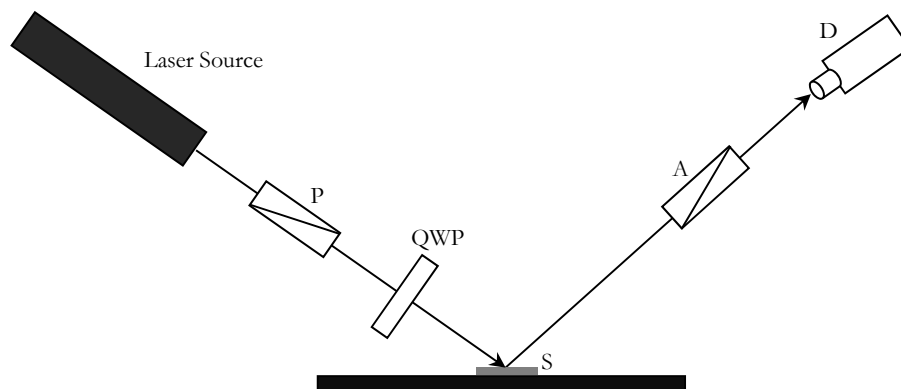


**Figure III.20.** A schematic diagram of a nulling ellipsometer with the quarter-wave plate placed before the light is reflected from the sample. P: the polarizing prism; QWP: the quarter-wave plate compensator; S: the sample under study; A: the analyzer prism; D: the light detector.

The main optical elements of the ellipsometer are: the polarizer (P), the analyzer (A), the quarter-wave plate (QWP) and the detector (D), Figure III.20. The polarizer and analyzer are used to convert the non polarized light in polarized light, and to determinate the polarization state of a beam, respectively. The quarter-wave plate allows to elliptically polarize the components of the wave that goes out from the polarizer. The ellipticity produced by the plate compensates the ellipticity produced by the reflection in the surface, thus the light that arrives into the analyzer was linearly polarized. As detector a CCD camera is used.

For the data analysis <sup>[194]</sup> a specific model of interface (two layers) is proposed. It is characterized by the thickness and refractive index of each layer, in which the ellipsometric angles,  $\Delta$  and  $\Psi$ , obtained from the experimental measurements, are fitted. The precision on these ellipsometric angles is ca. 0.0006. The computational analysis of the data is carried out with a numerical minimization routine such as a Simplex method <sup>[196, 197]</sup> by fitting the ellipticity from the Fresnel's equations following the formalism set out by Drude <sup>[198]</sup>. The iterative program, developed in Excel<sup>®</sup> by the Solver<sup>®</sup> tool, solves these equations

by minimizing the differences between the values of the ellipsometric experimental and calculated angles, extracting the values that better fit for the thickness and the refractive index. In the two layer model proposed, the first layer corresponds to the substrate material, silicon with a native oxide layer of  $\sim 2$  nm, and a refractive index,  $n = 4.1264 - 0.2300i$ ; the second layer is the LB film deposited onto the substrate. The thickness of the first layer was determined by using a clean silicon wafer.

### III.3.8. Micro-Raman Spectroscopy

The Raman spectroscopy was used to characterize the graphene oxide and graphene reduced oxide flakes deposited by the Langmuir-Blodgett technique onto polycrystalline silicon with a silicon oxide ( $\text{SiO}_2$ ) layer of 300 nm that allows their display by optical microscopy.<sup>[175]</sup> These measurements were done in the Dipartimento de Física Alessandro Volta of the University of Pavia (Italy). The Raman dispersion measurements were carried out at room temperature with a micro-Raman spectrometer (Horiba Jobin-Yvon LabRAM HR, U.S.A.) with a 100x objective (confocal microscopy) and a laser focus of  $\sim 1\mu\text{m}^2$ , Figure III.21. The spectral resolution of the instrument is approximately  $2\text{ cm}^{-1}$ , the spatial resolution is  $0.5\ \mu\text{m}$  and the laser excitation wavelength is 632.81 nm. The equipment has a notch filter before the CCD detector to cut the laser beam. Before the measurements, an accurate calibration was carried out by checking the Rayleigh band and Si band at 0 and  $520.7\text{ cm}^{-1}$ , respectively. The sample area was scanned with a spatial resolution of approximately  $0.5\ \mu\text{m}$ . The acquisition time was around a few minutes at each point, while the laser excitation power was kept below 1 mW to avoid heating and preserve the samples.<sup>[199]</sup>





**Figure III.21.** Photograph of the micro-Raman LabRAM HR model (Horiba Jobin Yvon).

Raman spectroscopy is based on inelastic scattering of monochromatic light, like from a laser source. Inelastic scattering means that the frequency of photons in monochromatic changes upon interaction with a sample, the photons of the laser light are absorbed by the sample and then reemitted. Frequency of the reemitted photons is shifted up or down in comparison with original monochromatic frequency, which is called the Raman effect. This shift provides information about vibrational, rotational and other low frequency transitions in molecules.

In the case of derivative graphite thin films, the Raman spectrum show characteristic peaks or bands highlighting the electronic structure of graphite (graphene, if the film is only a honeycomb carbon layer), mainly dominated by the  $sp^2$  nature of the C-C covalent bonds that form the ring-structure, where the excitation resonates with  $\pi$  states. Mainly, the study is centred on the D, G and 2D bands. The G band,  $\sim 1580\text{ cm}^{-1}$ , is due to the bond stretching of all pairs of  $sp^2$  atoms in both rings ( $C(sp^2)-C(sp^2)$ ), while the D band,  $\sim 1350\text{ cm}^{-1}$ , is due to

the breathing modes of  $sp^2$  atoms in rings. The shift of the G band and the ratio between the D and G bands intensity indicate the disorder degree in the  $sp^2$  structure of the sample. In this way, the average G band position moves from  $1581\text{ cm}^{-1}$  to  $1600\text{ cm}^{-1}$  within an ordered graphite layer, which corresponds to the reduction of the in-plane correlation length ( $L_a$ ). The D band appears and increases in relative intensity following the Tuinstra & Koenig relation,  $I_D/I_G \propto L_a^{-1}$ , that indicates the degree of defects and disorder in general of the sample is proportional to the number of aromatic rings, i.e., the structural quality of the sample. In fact, this D band appears in the borders of defect-free graphene. The G band full width at half maximum (FWHM) is a measure of disorder too and increases continuously as the disorder increases.<sup>[200]</sup>

On the other hand, the existence of a sufficient concentration of defects in the aromatic ring network, produces the appearance of a D' band, located at  $\sim 1620\text{ cm}^{-1}$ , which can partially merge with the G band. The defects would cause the phonon confinement allowing the Raman activation of the band. Between these defects could found isolated double bonds C=C that resonant in higher frequencies than the G band. Likewise, the presence of functional groups as carbonyl, epoxy or hydroxyl groups, come from a residual oxidation, or amides, resulting in an increase of the D and G band width.<sup>[201]</sup>

The 2D band,  $\sim 2700\text{ cm}^{-1}$ , is correlated to the second order (overtone) of the D band, and allows to know the number of layers of the sample up to a limit of five, above it, it is not possible to discern with the bulk graphite 2D band. For example, if the sample is a bilayer graphene, due to the interaction between the graphite layers, the  $\pi$  and  $\pi^*$  bands splits in four components, with a different gap for electrons and holes (phonons), giving rise to four possible optical transitions. This is observed in the appearance of a 2D band which deconvolutes in four components.<sup>[202]</sup>

### III.3.9. UV-vis Spectrophotometry

The UV-vis spectrophotometry was used to characterize the nanoparticles and to analyze the reduction degree of the reduced graphene oxide dispersions. The equipment was a spectrophotometer Shimadzu UV-2401PC and the spectra were acquired in the wavelength range from 700 to 200 nm. As it is a usual technique, a brief description of the fundamental theory is explained. In this technique, the monochromatic light goes through the sample and it is compared, the intensity of the transmitted light with the incident light intensity, i.e., the radiation absorption or transmission of the sample in the UV-vis region (spectrum).

The absorption of light by a molecule in this region produces the migration of electrons to high energy orbitals. The absorbance is important because it is related to the concentration of the specie absorbs light, at a wavelength, in the sample by the Lambert-Beer's Law.<sup>[203]</sup> In the special case of the quantum dots, the quantum confinement plays a key role for the determination of the size-dependent properties of nanoparticles. In fact, the transmission and emission colours depend on the nanoparticles size and are a result of the size-dependent band gaps. Also, the extinction coefficient of the first excitonic absorption peak depends on the nanoparticle size. This extinction coefficient is independent of ligand nature, solvent refractive index, fluorescence quantum yield and the synthesis method, therefore, allows to determinate the nanoparticle concentration in a solution from its absorbance. Moreover, the absorption spectrum allows us to know the nanoparticles size by empiric expressions<sup>[204]</sup> which relate the nanoparticle diameter and the extinction coefficient to the first absorption peak position (wavelength).

### III.3.10. Fourier Transform Infrared Spectroscopy (FTIR)

The FTIR spectroscopy was used, in collaboration with the Departamento de Química Inorgánica (Universidad de Salamanca), to characterize solid samples prepared as pellets. In order to prepare the pellets, we grind a small quantity of sample with KBr, that acts as inert matrix (ratio 1:200). This powder mixture is then pressed, 8 ton  $\text{cm}^{-2}$ , in a mechanical press to form a translucent pellet through which the beam of the spectrometer can pass. The equipment is an Fourier Transform Infrared (FTIR) spectrometer 1600 (Perkin-Elmer, USA) controlled by a data unit model 3700. The spectrum was acquired in the frequency range from 4000 to 400  $\text{cm}^{-1}$ . Due to it is a usual technique, a brief description about the theoretical fundament of the technique is exposed. In this technique, the light is passed through the sample. Some of the light is absorbed by the sample and some of it is passed through (transmitted). When it is compared the intensity of the transmitted light with the incident light, i.e., it is analyzed the absorption or transmission (I) of the sample radiation in the infrared region. The resulting spectrum represents the molecular absorption and transmission, creating a molecular "fingerprint" of the sample (intensity vs frequency).

The absorption comes from excitation by bond deformation of tension or flexion. The tension excitation involves changes in the vibrational frequency of the atoms bonded throughout the axis bond, while the flexion deformation involves movements of the atoms outside of the axis bond. Within the possible deformations in a molecule, only are active to the IR that in which the excitation exists a change in the bond dipolar moment with respect to the ground state. Besides, the infrared region contains significant absorption bands, not only due to fundamental modes of tension and flexion, but also overtones, combination bands, couplings and Fermi's resonant bands. This technique is used as a qualitative analysis tool, because of the wavenumber position of the absorption bands is characteristic of each functional group found in a molecule. Moreover,

the bands can shift slightly its position due to changes in the molecular environment.

In the FTIR spectroscopy a key in the equipment is the interferometer, in which, an incident beam of light strikes a tilted semitransparent surface (beamsplitter) and divides the source radiation into a reflected and transmitted wave, generating a retard between the two generated waves. In this way, as the sample is placed between the outlet of the interferometer and the detector, the obtained spectrum, called interferogram, is the subtraction between the source spectrum and the spectrum of the sample, which subsequently is divided by the reference interferogram in order to obtain the infrared transmission spectrum. The main advantage of this system is that offers a better relation signal/noise for a given resolution.<sup>[203, 205]</sup>

### III.3.11. X-Ray Photoelectron Spectroscopy (XPS)

The X-ray photoelectron spectroscopy was used to characterize the different graphitic materials obtained by oxidation and later reduction of natural graphite flakes. Powder samples were prepared by filtration of the different dispersions. Measurements were carried out in the Instituto de Catálisis y Petroleoquímica (CSIC, Madrid). Samples were analyzed with a VG Escalab 200 R spectrometer (Fisons Instruments, USA) equipped with an excitation source of MgK $\alpha$  ( $h\nu = 1253.6$  eV) radiation and a hemispherical electron analyzer, Figure III.22. The working conditions for the high resolution spectra acquisition were 20 eV analyzer pass energy, and the residual pressure in the analysis chamber was maintained under  $2 \cdot 10^{-7}$  Pa.<sup>[206]</sup>

Based on the photoelectric effect, this technique consists of the excitation of a surface with X-Ray photons, which pull out electrons of the atoms of the studied sample. The measurement of the binding energy of the extracted electrons of the atom inner (core) levels (localized in the superficial region of a few atomic

layers) and of the photoemission peak intensity allows to carry out an elemental chemical analysis of the surface (identify atoms and their relative concentration) and to establish the oxidation and coordination state (chemical shift). Also, it is possible to carry out measurements by varying the incident angle, obtaining information at different depths from the surface. This technique has a relative high detection limit.

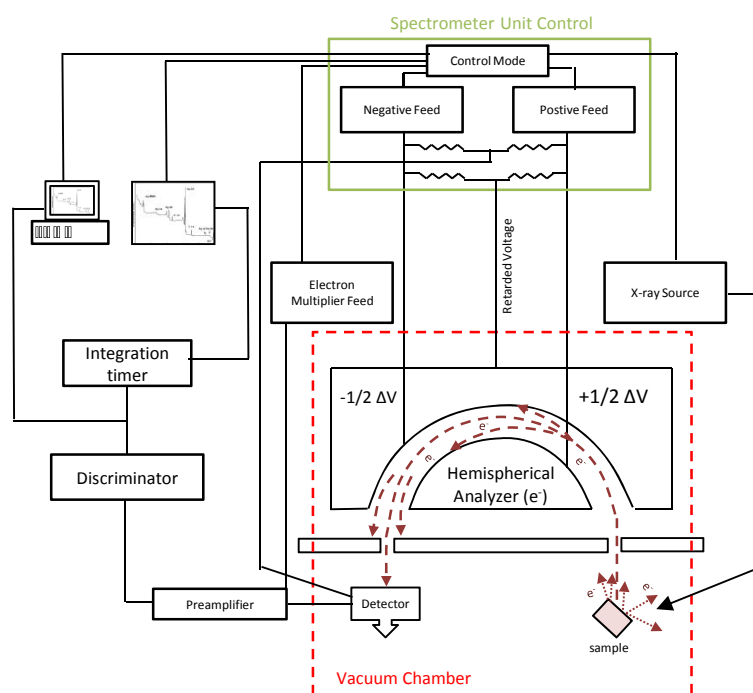


Figure III.22. A XPS spectrometer schematic diagram.

The interaction of X-ray photons with the atoms of a surface produce the emission of photoelectrons belonging to the inner levels of the atom, thus the holes formed are filled with electrons of upper energetic levels producing fluorescence X-rays emission and Auger emission processes. The kinetic energy ( $E_k$ ) of the emitted photoelectron is related to the binding energy ( $E_B$ , difference between the energy of the initial and final state, respectively) corresponding to the electronic level from which it was emitted, and with the incident photon energy ( $h\nu$ ) by the equation III.20, where  $\phi$  is the material work-function.

$$E_k = h\nu - E_B - \phi \quad [\text{III. 20}]$$

From the expression is deduced that the measurement of the photoelectron kinetic energy allows to determine its binding energy, characteristic of each chemical element. This allows to identify elements by the fingerprint procedure. Also, due to the binding energy is, in some ways, a measurement of the intensity of the interaction between the electron and the nuclear charge, it is possible to state that it follows the energy of the electronic levels and that increases with the atomic number.

The binding energy for an atom is affected by changes in the oxidation state, the ligands electronegativity, the type and number of atom bonds in a compound, that influence on the charge state of the atom before the ionization with a X-ray photon. These factors known as initial state effects, produce a shift of the atomic peak in the photoemission spectrum called chemical shift. Moreover, the possibility of measurement of chemical shifts is one of the most important advantages of this technique.

A XPS spectrum is the representation of the number of registered electrons by the detector as a function of the kinetic or binding energy of the emitted photoelectron. It contains information about the absorption and ionization (initial state), the atom response and production of a photoelectron (final state) and the transport and leak of the electron (intrinsic and extrinsic energy losses).

Qualitative analysis by XPS is possible for the  $Z > 2$  elements (H and He have not inner electronic levels) with a sensibility around 0.5% and an analytical minimum depth of one or two atomic layers. In the usual procedure of the XPS analysis of a sample firstly it is registered a general spectrum of the sample from 0 to 1000 eV binding energy for the identification of the elements presented in the

excited sample. Then, a study of each element is carried out by acquiring its corresponding spectrum in a narrower energy range.

This technique also allows doing semiquantitative estimates, with an error between 10-20%, of the relative atomic concentration of the samples by applying different methods of quantification. The most used method of analysis is the atomic sensitivity factors method (ASF). In this way, for a sample that contains two different atoms, A and B, the relative atomic concentration is:

$$\frac{n_B}{n_A} = \frac{I_B/S_B}{I_A/S_A} \quad [\text{III. 21}]$$

In this expression, S is the sensitivity atomic factor. As reference, S=1, is used the factor S for the fluor 1s line and by an empiric way are determined the ratios  $S_{xy}/S_{F1s}$  to the relevant spectral lines (y) of the all elements (x), then the ratio  $S_B/S_{As}$  can be calculated from the database.<sup>[207]</sup>

### III.3.12. Differential Scanning Calorimetry (DSC)

The glass transition temperature of the polymer in bulk,  $T_g$ , was determined using Differential Scanning Calorimetry (DSC) measurements. This technique, no available in our laboratory, was carried out in the Departamento de Materiales y Producción Aeroespacial de la Escuela Técnica Superior de Ingenieros Aeronáuticos de la Universidad Politécnica de Madrid. The equipment was a Mettler Star<sup>e</sup> DSC instrument using 20 K min<sup>-1</sup> heating rate. The temperature scale was calibrated using 1-octane, indium and tin. The heat capacity,  $C_p$ , scale was calibrated with sapphire.

Glass transition temperature was obtained from the inflection point of the DSC thermogram curve.<sup>[208]</sup> In order to determine the position of the inflection



point, the thermogram curve is derived. In the Figure III.23. are showed the results for the PS-MA-BEE polymer and the value for glass transition temperature,  $T_g = 76^\circ\text{C}$  (349 K), determined as the maximum in the derivative thermogram.

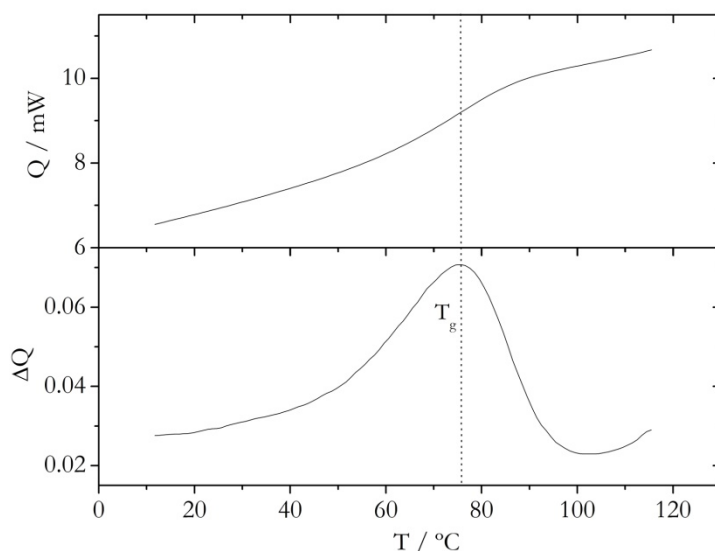


**Figure III.23.** Thermogram obtained for the PS-MA-BEE polymer by DSC measurements.

### III.3.13. Four-point Probe Conductivity Measurements

For electrical conductivity measurements in thin films, we applied a film four-point probe setup<sup>[209]</sup> with gold electrodes (1 mm x 4.25 mm x 0.1 mm) over the samples. For the case of RGO paper-like films, they were fabricated by filtration using a PVDF membrane filter (0.2  $\mu\text{m}$  pore size, Filter-lab), and washing with MilliQ<sup>®</sup> water and methanol in order to remove the excess of reducer agents and free-surfactant.<sup>[209, 210]</sup> Three measurements were performed by means of a Keithley 4200 SCS Semiconductor Parameter Analyzer for each sample to obtain an average value for the electrical conductivity value, Figure III.24. These measurements were carried out in collaboration with the Electronic Group (Department of Applied Physics, Universidad de Salamanca).

The determination of the conductivity (resistivity) is important in the semiconductor material research as a way to test the quality of a sample. The resistivity of the semiconductor is often determined using a four-point probe or Kelvin technique, in which, two of the probes are used to source current and the other two probes are used to measure voltage. Using four probes eliminates measurement errors due to the probe resistance, the spreading resistance under each probe and the contact resistance between each metal probe and the material under study.

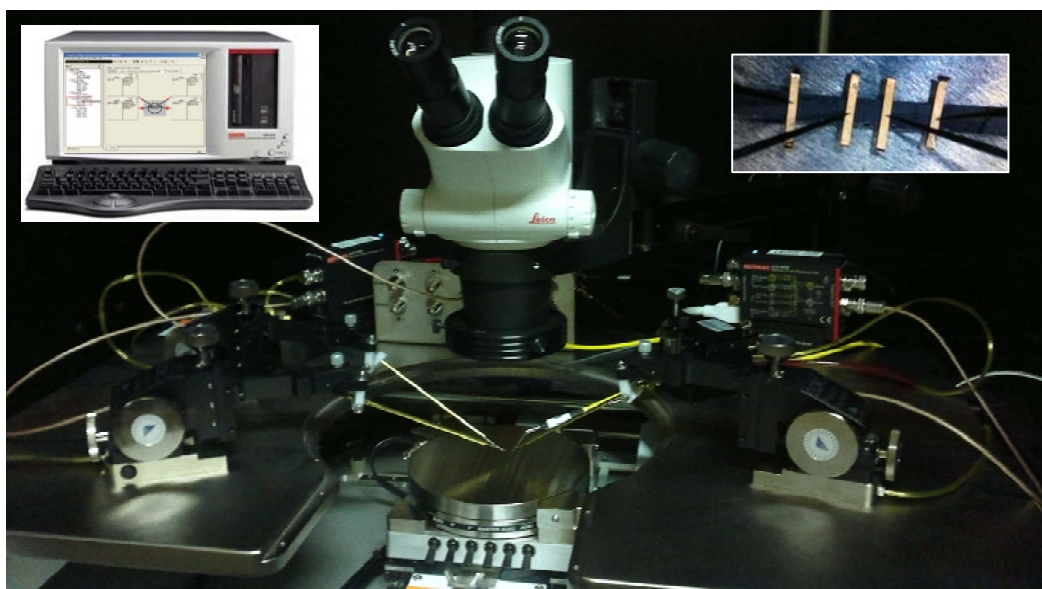


**Figure III.24.** Photograph of the manual-monitored four probe station connected to a Keithley 4200 SCS Semiconductor Parameter Analyzer (left inset). The inset of the right shows the gold electrode connections with the four-point collinear probe over a RGO paper-like thin film.

Two common Kelvin techniques for determining the resistivity of a material are the four-point collinear probe method and the Van der Pauw method. In our case, we used the first one.

The four-point collinear probe method involves bringing four equally spaced probes in contact with a material of unknown resistance, a scheme is

shown in Figure III.25. The two outer probes are used for sourcing current (source-measure units (SMU): SMU1 and ground unit) and the two inner probes (SMU2 and SMU3) are used for measuring the resulting voltage drop across the surface of the sample. This four-point probe measurement was set up in the Keithley interactive interface application (FourPtProbe<sup>®</sup>).

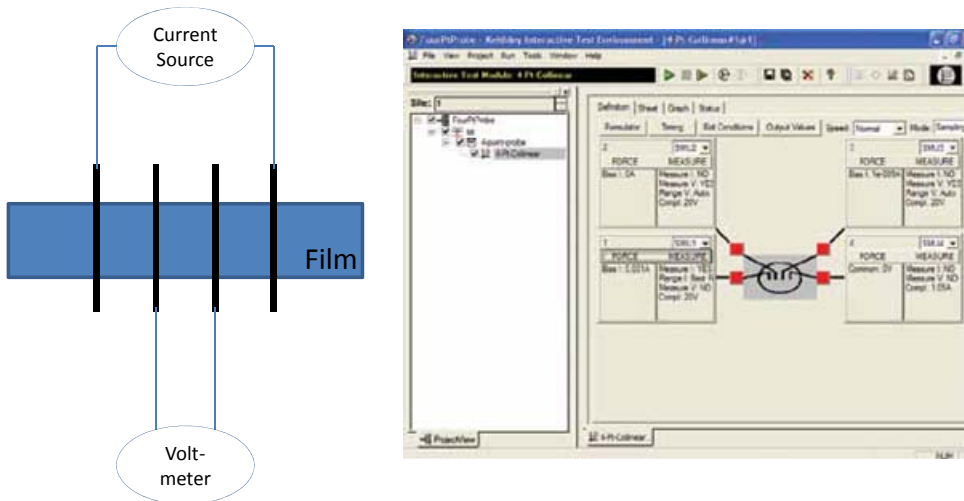


**Figure III.25.** Four-point collinear probe setup for conductivity measurements (left). Screen capture of Keithley 4200 SCS interface project (right).

The conductivity,  $\kappa$ , of the sample is calculated as follows taking into account the correction factors based on the probe dimensions and separation,  $d$ , and sample thickness,  $t$ , <sup>[209]</sup>:

$$\kappa = \frac{d \cdot I}{V \cdot w \cdot t} \quad [\text{III. 21}]$$

In this equation,  $I$ , is the current;  $V$ , the voltage difference between the inner probes and  $w$ , the film width.

### **III.3.14. Dual Focused Ion Beam/Scanning Electron Microscopy Workstation**

In order to assist the conductivity measurements, it was necessary to determine the film thickness. A workstation combining Scanning Electron Microscopy (SEM) and Focused Ion Beam (FIB) technique sample preparation was used to carry out thickness measurements.<sup>[211]</sup> These measurements were carried out in collaboration with Dr. Benito Rodríguez-González (imaging) and International Iberian Nanotechnology Laboratory (INL) in Braga (Portugal) (Dual FIB/SEM facility) using a FEI Helios 450 dual-beam FIB/SEM. This equipment simultaneously allows to achieve images with the electron beam at ultra-high resolution using a Schottky field emitter while at the same time to thin with the ion beam using a liquid Gallium ion emitter.

In order to measure the film thickness, some cross-sections of the sample in different regions of interest were made using the dual-beam FIB/SEM system. In our case, to protect the sample surface, a first thin platinum (Pt) layer deposited with electrons, followed by a thicker Pt layer deposited with ions were deposited. With the Pt the protection layer finished, we started the making of the cross section using the standard conditions included in the software of the FIB. To get nice images of the cross section, the front surface of the sections was polished using the cleaning cross section method with soft milling conditions. Finally we get the SEM images of the sections, and did the thickness measurements over the images. The film thickness was done using the cross section correction to get accurate thickness values.

#### **Focused Ion Beam System**

The FIB system consists of an ion beam generated from an ion source and focused through a chamber of optics onto a sample in vacuum conditions, Figure

III.26. The main components are the ion source, the ion column and the beam writing mechanism.

The main ion emission sources are gas field ionization sources (GFIS) and liquid metal ion sources (LMIS), of general using in FIB/SEM systems, and more concretely gallium source. For a LMIS to emit ions, firstly, a cone must be developed in an electric field with a small enough tip radius that field evaporation can occur when exposed to an electric field. When the cone is formed, the production of ions occurs by field evaporation. In this way, the LMIS uses the quantum mechanical field emission/ field evaporation mechanism, appearing at high electric field strengths for Ga metal ionization. Therefore, the high field strength at the emitter tip enables the metal atoms to evaporate and ionize. They are extracted through the extraction aperture and can be further accelerated through the column. The column focuses ions from the source onto the sample operating in a high vacuum environment. It contains the LMIS, the electrostatic lenses (optics), a set of blanking plated, beam acceptance aperture, an automatically variable aperture, and a deflector.

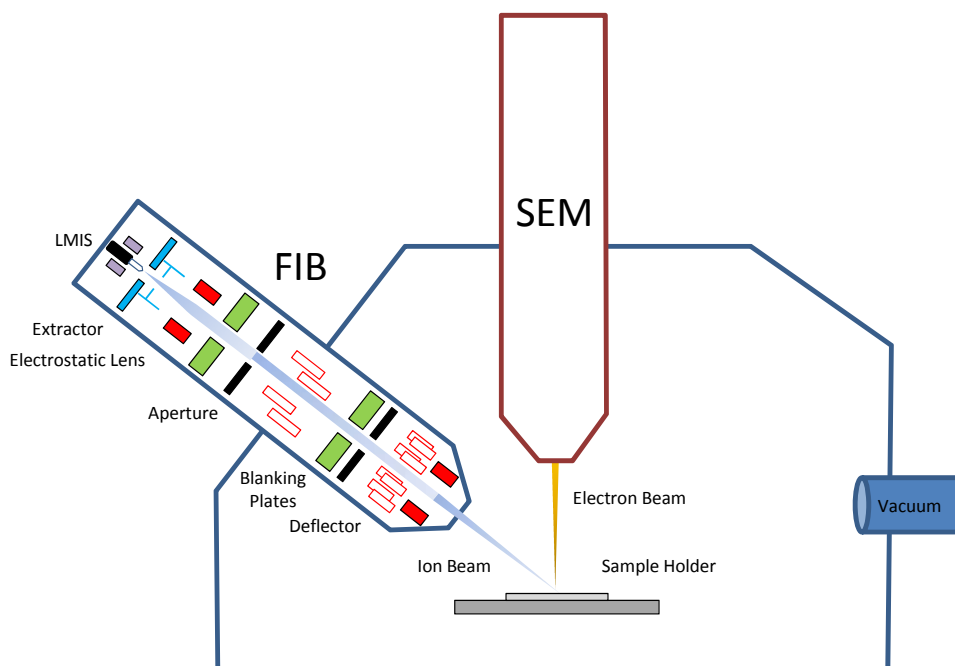


**Figure III.26.** Dual-beam Focused Ion Beam/Scanning Electron Microscopy System general scheme.

The ion beam writing mechanism is based on ion-matter interaction and the main effects can be: electron emission, sputtering, ion induced deposition and ion induced etching, which are used for the development of applications such as imaging and sample preparation. In the case of cross sectioning, the FIB technique has the ability to get down to defects less than  $0.5\ \mu\text{m}$ . Moreover, in a dual-beam FIB/SEM the sample can be viewed without ever removing the sample. The cross sectioning is carried out by applying sputtering. An example is shown in Figure III.27. Usually, the strategy is to image an area on the computer screen and then a box is drawn by processing software. The program can then scan over this area to deliver the specified ion dose.

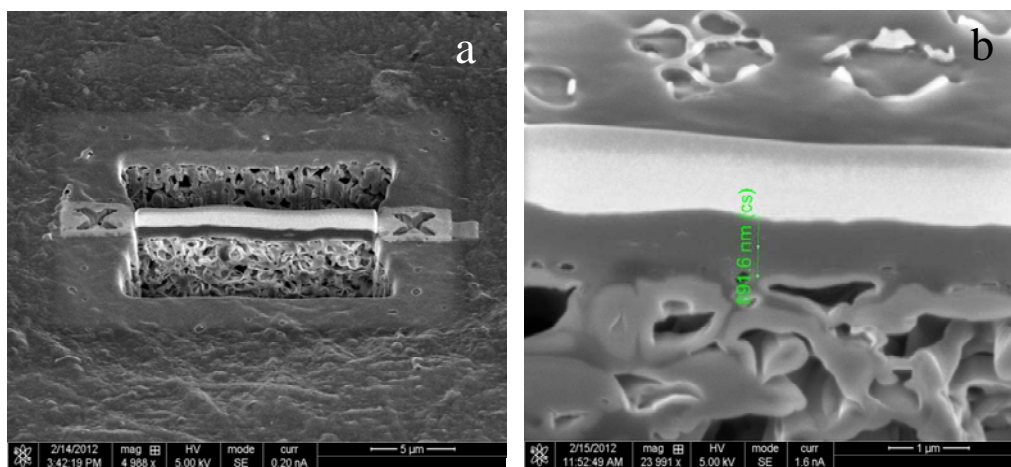


**Figure III.27.** An example of cross-sectional SEM images of a RGO paper-like film (a). The thickness values of this film are also indicated in (b).

On the other hand, with the dual-beam system it is possible to deposit a metal or insulator over smaller particles or defects without damaging the sample with the electron beam. For defects less than  $0.2 \mu\text{m}$  the ions used for depositing will damage defect during the initial exposure. Once the initial layer has been deposited with the electron beam, the remaining amount can be deposited with the ion beam.<sup>[212]</sup>

### III.3.15. Fluorescence Lifetime Imaging Microscopy

Fluorescence Lifetime Imaging Microscopy (FLIM) technique was employed to investigate the photoluminescence properties of LB films onto quartz substrates. These measurements were carried out in collaboration with the Molecular Photochemistry Group (Instituto Superior Técnico, Lisbon, Portugal) during a stay of several months. FLIM technique allows the study of the fluorescence dynamics in different systems by analyzing the decay curves and fluorescence images. In the case of the semiconductor materials, knowledge about the influence of parameters such as material density, distance and environment on fluorescence dynamics is relevant for the development of devices.<sup>[25]</sup>

The equipment used was a MicroTime200 time-resolved confocal fluorescence microscope system from PicoQuant GmbH (Berlin, Germany), Figure III.28. Excitation source is a pulsed picosecond diode laser of 480 nm excitation wavelength (2.5 MHz repetition rate, triggered by the internal oscillator) that is passed through a narrow band clean-up filter and reflected with a dichroic beam splitter into a standard inverted microscope base. In the IX 71 Olympus<sup>®</sup> microscope, a water immersion objective (x60 with N.A. 1.2) focus the laser beam into the sample and collects the emission from the sample. In order to preserve the LB film from water a glass coverslip between the water drop and the sample was used. Point and area ( $80 \times 80 \mu\text{m}^2$ ,  $400 \times 400$  pixels, integration time of 1 ms per pixel) measurements were carried out by raster scanning the sample with a piezo table.



**Figure III.28.** External photograph of the optical unit (MicroTime 200, PicoQuant) joined to the Olympus microscope. A zoom of the objective changer (nosepiece) and sample holder is shown.

To select an area or point in the sample, the microscope is connected to a computer-controlled high resolution XY-piezo scanner. Moreover, a CCD camera



is also integrated into the beam path and serves as a permanent online diagnostic tool for the focus quality by monitoring the backscattered excitation light from a glass interface, allowing to position the laser focus on the sample. Fluorescence emission was collected with the same objective, filtered by a dichroic mirror and a long-pass filter to reject any remaining scattered laser light and passed through a 30  $\mu\text{m}$  pinhole to enable confocal detection. The fluorescence emission was detected with avalanche photodiodes by using the method of time-correlated single photon counting (TCSPC) with a resolution of 152 ps/channel. Additional band pass filters may be placed before the avalanche photodiodes for further spectral selection of emission. A scheme of the optical unit is shown in Figure III.29.

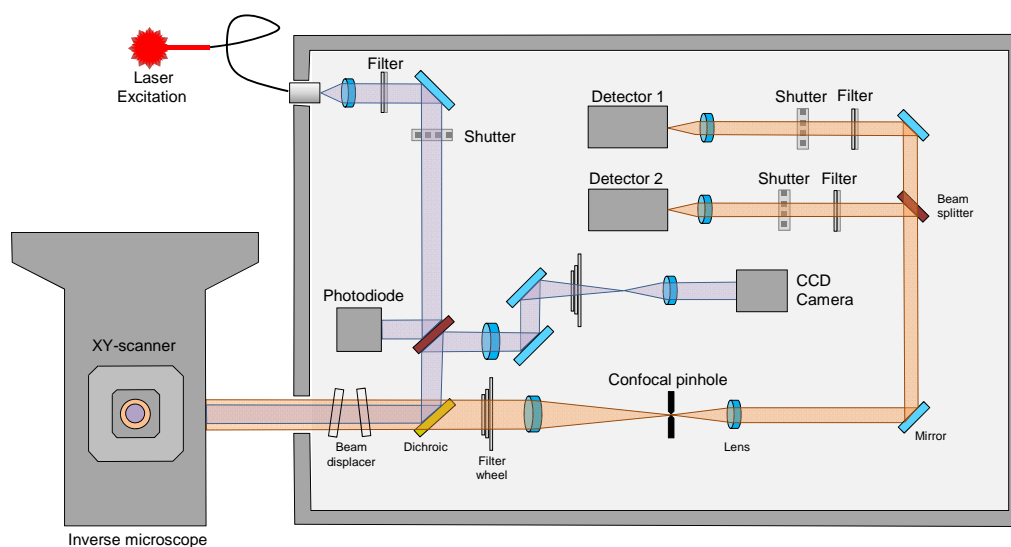


**Figure III.29.** Layout of the optical unit MicroTime 200 (PicoQuant) indicating the different components: the confocal detection setup with a pinhole and up to two detection channels with suited beam splitting optics for selection; and electro-mechanical shutters installed in the excitation beam path and in front of each detector to ensure safe operation of the system.

The data acquisition was done by the TimeHarp 200 TCSPC PC-board working in the special Time-Tagged Time-Resolved Mode (TTTR) which stores all relevant information for every detected photon for further data

analysis, i.e., the photon arrival time at the detector relative to the corresponding laser excitation pulse, the position of the sample and the number of the detection channel. SymPhoTime<sup>®</sup> software (version 4.7.) was used to control the optical unit, and the digital piezo controller or shutters and to perform any measurement.

### **Time-Correlated Single Photon Counting Basics**

In TCSPC<sup>[213]</sup>, single photon events at the detector are timed relative to a reference pulse. The method is based on the precise measurement of the time difference between the moment of excitation and the arrival of the first photon at the detector (TCSPC time). The sample is excited by a pulsed laser source and as excited electrons relax to their ground state the sample begins to photoluminescence. At the same time the TCSPC module receives a reference signal from a detector in a secondary beam path which starts an internal timer. The photoluminescence is collected and filtered down until no more than one photon per excitation pulse arrives at the detector. The detector produces a voltage pulse in response to the photon, and this photon stops the timer. The time between the excitation pulse and the emission pulse is then recorded. This is repeated for millions of photons (multiple cycles with periodic excitation) and a histogram is created showing the correlation between the number of photons, which is proportional to the photoluminescence intensity, and the time after excitation. This histogram of photon arrival times with respect to the excitation pulse can then be analyzed to extract the fluorescence lifetime and signal amplitude, and corresponds to the fluorescence decay curve.

### **Time-Tagged Time-Resolved Mode (TTTR)**

This measurement mode is based on adding a second timing information, the time tag, to each measured TCSPC time.<sup>[214]</sup> This time tag is taken from a continuous running clock and represents the arrival time of each photon relative

to the beginning of the experiment. In this way, one photon event in the TTTR data stream consist of three individual pieces of information: the TCSPC time, the time tag and the routing information, and all information about the photon dynamics is conserved. The measurement scheme of the TTTR is shown in Figure III.30.

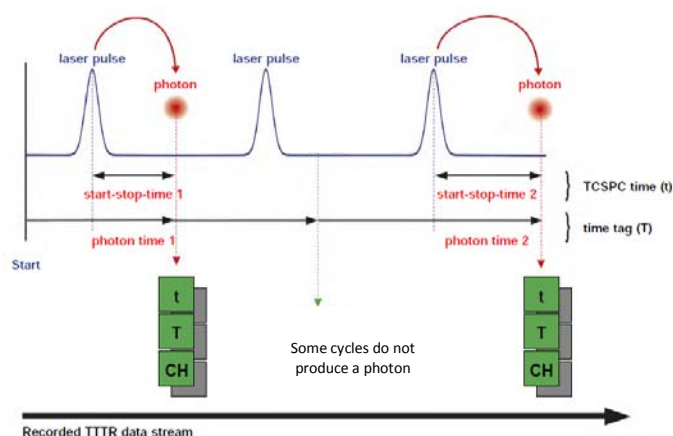


**Figure III.30.** Measurement scheme of the Time-Tagged Time Resolved (TTTR). The time difference between the moment of excitation and the arrival of the first photon at the detector is the TCSPC time ( $t$ ) and is stored into the TTTR data stream along with the time tag ( $T$ ) and an information from which detector the photon came from ( $CH$ ).

Depending on how the individual information in the data stream is combined, different analysis procedures are possible, such as intensity time trace analysis (MCS) or fluorescence lifetime imaging (FLIM). The Intensity Time Trace analysis (MCS) allows to study the lifetime fluctuations of the sample, count rate and on-off histogramming. Fluorescence Lifetime Imaging can be viewed as the time-domain multi-colour imaging, that allows to extract information about the local environment of the molecules in the sample from their time-resolved emission.

## Fluorescence Decay Fitting Procedure

The analysis of the lifetimes was performed using the Symphotime<sup>®</sup> and FluoFit<sup>®</sup> software (version 4.4) from PicoQuant.<sup>[215]</sup> The decay curves were iteratively fitted to a multi-exponential decay function (Equation III.22) taking into account the instrument response. The data must be a convolution of the instrument response with the real photoluminescence lifetime. In order to remove the instrument response, a reconvolution fit was performed. The background count was fixed as a constant parameter in each fit and was assessed from the background counts arriving before the rising edge of the instrument response function (IRF). The IRF is the response of the instrument to a short pulse, Figure III.31, and is measured as the response function (decay curve) of the excitation laser pulse. It is recorded by scattering some of the incident laser light from a clean point of the sample area (not covered by the sample) into the detector, for which the emission filter is removed.

$$I(t) = \int_{-\infty}^t IRF(t') \sum_{i=1}^n A_i e^{-\frac{t-t'}{\tau_i}} dt' \quad [\text{III. 22}]$$

The fit parameters are:  $\tau_i$  that is the lifetime of the  $i^{\text{th}}$  decay component;  $A_i$ , the amplitude of the  $i^{\text{th}}$  component, in counts, at time zero;  $\text{Bkgr}_{\text{Dec}}$  the decay background, in counts;  $\text{Bkgr}_{\text{IRF}}$  the IRF background, in counts; and  $\text{Shift}_{\text{IRF}}$ , the time shift between IRF and decay. The A-factors sum is normalized to unity.

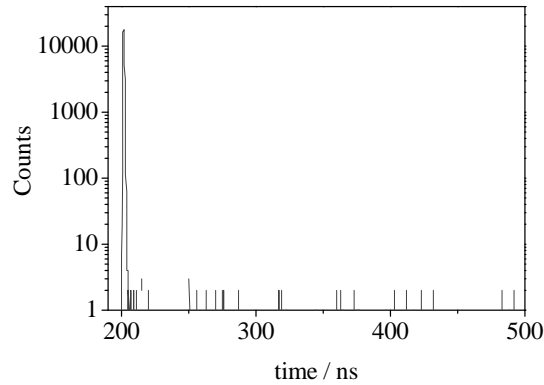


**Figure III.31.** An example of the IRF of the instrument to a short pulse.

A value for  $\tau$  is determined by minimising the weighted sum of squares of residuals between the fitted function and the experimental data. The quality of any fit is judged from the value of the reduced chi-squared function,  $\chi^2$ . A value close to unity indicates that a good fit has been achieved.

$$\chi^2 = \frac{1}{N-p} \sum_{i=1}^N W(t_i)^2 [Decay(t_i) - Fit(t_i)]^2 \quad \text{[III. 23]}$$

Where  $N$  is the number of fitted channels (i.e. data points) and  $p$  is the number of fitted parameters. The difference,  $N-p$ , is the degrees of freedom. Decay is an array of  $N$  intensity values, i.e., the experimentally measured decay curve. The  $Fit(t_i)$  values are calculated using the exponential model and the iterated values of model parameters.  $W(t_i)$  is the weighting factor.

The goodness of a decay curve fit can be illustrated by a plot of weighted residuals,  $R(t_i)$ , between the experimental and fitted points vs time. It is a useful tool because shows where the misfit occurs.

$$R(t_i) = W(t_i)[Decay(t_i) - Fit(t_i)] \quad \text{[III. 24]}$$

The residuals' autocorrelation function is a tool for assessing the fit quality. It is a measure of correlation between the weighted residuals in distinct channel

separated by various correlation times. Small and randomly distributed values of the autocorrelation function indicates a good fit due to the random distribution of weighted residuals.

To sum up, the time-resolved fluorescence decay curves were reconvoluted with the instrument signal and fitted to multi-exponential functions by a Levenberg–Marquard algorithm for non-linear least-squares error minimization. The quality of fittings was judged by the reduced chi-squared value,  $\chi^2$ , the weighted residuals and the autocorrelation functions. Moreover, for comparative purposes between different samples, it is possible to determinate the average lifetime ( $\tau_{AV}$ ) by using the following equation <sup>[216]</sup>:

$$\tau_{AV} = \frac{\sum a_i \tau_i^2}{\sum a_i \tau_i} \quad [\text{III. 25}]$$

where  $a_i$  is the pre-exponential lifetime and  $\tau_i$  is the lifetime obtained in the multi-exponential fitting of the decay curves. The intensity fraction of each component,  $f_i$ , which provides information about the relative contribution of the component  $i$ , is calculated from:

$$f_i = \frac{a_i \tau_i}{\sum_j a_j \tau_j} \quad [\text{III. 26}]$$

### FLIM images procedure

The fast FLIM mode from SymPhoTime<sup>®</sup> was used for the FLIM images treatment, which calculates the lifetime of each pixel from the TCSPC histogram as a weight average of the channel components.

### III.3.16. Electron Beam Lithography

The Electron Beam Lithography (EBL) technique is used to make devices at nanometer scale due to its very short wavelength, which provides higher

resolution, and reasonable energy density characteristics. This technique offers some advantages as higher resolution and versatile pattern formation over photolithograph techniques. In the semiconductor industry, EBL is used for projection printing and direct writing. In projection printing, a relatively large-sized electron-beam pattern is projected in parallel through a mask onto a resist-coated substrate by using a high-precision lens system; while in direct writing, a small spot of the electron beam is written directly onto a resist-coated substrate, eliminating the expensive and time-consuming production of masks. Because of it, the direct writing EBL has been the most flexible system used to fabricate a variety of nanodevices with critical dimensions below 10 nm.<sup>[217]</sup>

Normally, the direct write systems use a finely focused Gaussian round beam that moves with the wafer to expose the wafer one pixel at a time (as raster scans or vector scans), with either fixed or variable beam geometry. Basically, a direct writing system consists of a source of electrons, a focusing optics set, a blanker to turn the beam on and off, a deflection system for moving the beam, and a stage for holding the substrate. However, as direct writing transfers the pattern by exposing one pixel or one image element at a time, this imposes a limitation on the exposure speed or the rate of the pattern to be transferred onto the wafer depending on the sample and the use of resist coatings (lift-off process).

### **Lift-Off Process**

The Lift-Off process is the most popular process used in direct writing EBL. It is an additive process that adds material to the substrate and consists of several steps: e-beam resist coating, exposure, and development. Firstly, a positive or negative resist coating is deposited onto the sample, then the resist coating is exposed by e-beam direct writing using a vector or raster scan, and finally the exposed resist (the nanostructure pattern) is developed and removed in a solvent appearing the pattern for metal deposition. The metal layer (the nanostructure material) can be deposited by an e-gun or an evaporation process onto the

substrate. The final step of the lift-off process is accomplished by soaking the substrate in a solvent bath (e.g., acetone for PMMA resist) to wash away the remaining resist and unwanted material.

Frequently, the lift-off process prefers a thick resist layer for forming undercut profiles and good adhesion with the substrate for the subsequent additive or subtractive processes. These electron beam resists are normally coated on the substrate to record the image of the pattern to be transferred. The final pattern made by the EBL is a relief structure in the coated resist layer representing the pattern being exposed.

The e-beam resists are high molecular-weight polymers dissolved in a solvent. The use of them is based on the structural polymer changes when is exposed to radiation, including electron radiation. Electron beam resists can be either positive or negative. After exposure to electrons, the positive resists are weakened by the scission of main- and side-chains and the exposed resists become more soluble in the developing solution. A solvent developer selectively washes away the weakened or lower molecular-weight resist; thus, a positive tone pattern is formed in the resist film. On the other hand, the negative resists are strengthened during exposure by a radiation-initiated cross-linking reaction and become less soluble in the developer. After the resists are developed, the pattern is transferred to the substrate through the lift-off process mentioned earlier.

In the case of graphene, usually positive resists are used, concretely we employed polymethyl methacrylate (PMMA). Besides, PMMA is the most commonly used positive resist and has a moderate glass transition temperature of 114 °C. For its use, the PMMA powder is dissolved in a solvent, such as anisole or chlorobenzene, in a desired concentration. The resist liquid is dropped onto the substrate and then spun at high speed to form a thin coating by spin coating. This step is followed by soft bake processing at temperatures ranging from 130 °C to 170 °C with a hot plate to bake out the casting solvent. The final resist thickness is



determined by the PMMA concentration and by the spin speed. For instance, 950 K PMMA (2% in anisole) resist spun at 3000 rpm would result in a thickness of about 200 nm. The dose values of the electron beam used for exposure range from 100 to 500  $\mu\text{C cm}^{-2}$ . The typical developers used are 1:3 methyl isobutyl ketone: isopropyl alcohol (MIBK:IPA) for the highest contrast and 1:1 MIBK:IPA for the highest sensitivity.<sup>[218]</sup> The developed region is then removed by rinsing in pure IPA for 30 s. PMMA has extremely high resolution, and its ultimate resolution has been demonstrated to be less than 10 nm; its major problems are its relatively poor sensitivity, poor dry etch resistance, and moderate thermal stability.<sup>[217]</sup>

In this way, the step-by-step process carried out with our samples in the Nanofabrication clean room at Central de Tecnología del Instituto de Sistemas Optoelectrónicos y Microtecnología (CT-ISOM, Universidad Politécnica de Madrid, Spain) is briefly detailed below.<sup>[219]</sup> Firstly the chemically reduced graphene samples were deposited onto highly (degenerately) doped silicon wafers with a thermally grown  $\text{SiO}_2$  layer (300 nm thickness) and Au alignment network marks (200  $\mu\text{m}$  separation). These alignment marks are a guide for the pattern design and to construct the EBL coordinates.

In order to create the master pattern electrodes, a computer-aided design (CAD) file was done for each sample in the EBL equipment using the CABL<sup>®</sup> software. The electrodes were designed with a 300-1000 nm separation in Van der Pauw and Hall-bar geometry. The samples were coated with a PMMA (PMMA/MA 33% in 1-methoxy-2-propanol, AR-P 617 from ALLRESIST<sup>®</sup>) resist layer by spin coating (4500 rpm during 1 minute to reach 0.5  $\mu\text{m}$  thickness) followed by a hot plate drying step (160 °C during 2 minutes). The EBL direct writing was carried out using a Crestec CABL-9500C High Resolution Electron Beam Lithography System, Figure III.32, securing previously the samples to the sample stage with conductive tape to ground the samples. The beam voltage was

kept constant at 50 keV with a current of 1 nA and a dose of  $0.20 \mu\text{s}$  which makes a total charge of  $200 \mu\text{C cm}^{-2}$ . The beam current was checked before and after lithographic processing using a Faraday cup. Beam diameter was kept constant at 10 nm, (2 nm beam spot; 10 nm line width).



**Figure III.32.** Photographs of Nanolithography System for Electron Beam Lithography (CRESTEC CABL-9500C) on the left and e-beam evaporator equipment (Varian VT 118), on the right, at the Nanofabrication Clean Room in the CT-ISOM (Madrid).

The pattern was developed by a MIPK:IPA solution (AR-600-50 from ALLRESIST<sup>®</sup> during 2 min 30 s) following by a stopper bath in propanol (AR-600-60 from ALLRESIST<sup>®</sup> during 30 s) leaving visible the "holes" for metal deposition (Figure III.33a) in the e-beam evaporator. To remove the developer residues, the sample is cleaned with isopropyl alcohol. The deposition process was performed by e-beam evaporation of Ti/Au (50/500 Å) electrodes using a Varian VT 118 equipment. In the metal deposition, first a titanium layer is deposited to allow the gold adhesion followed by a gold layer. After this step, the samples were cleaned by soaking with acetone (50-60°C during 15 minutes) followed by ethanol to lift off PMMA and metal residues, Figure III.33b. Then the samples are prepared to carry out the electrical measurements.

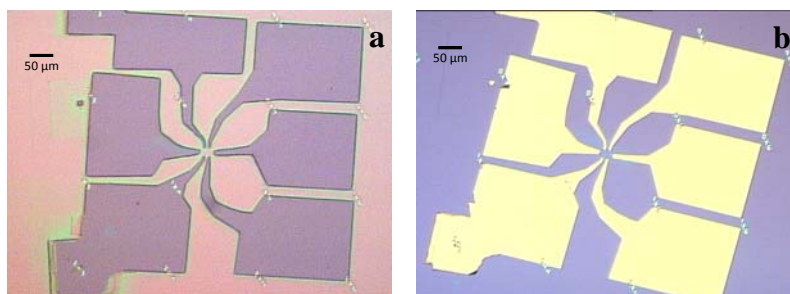
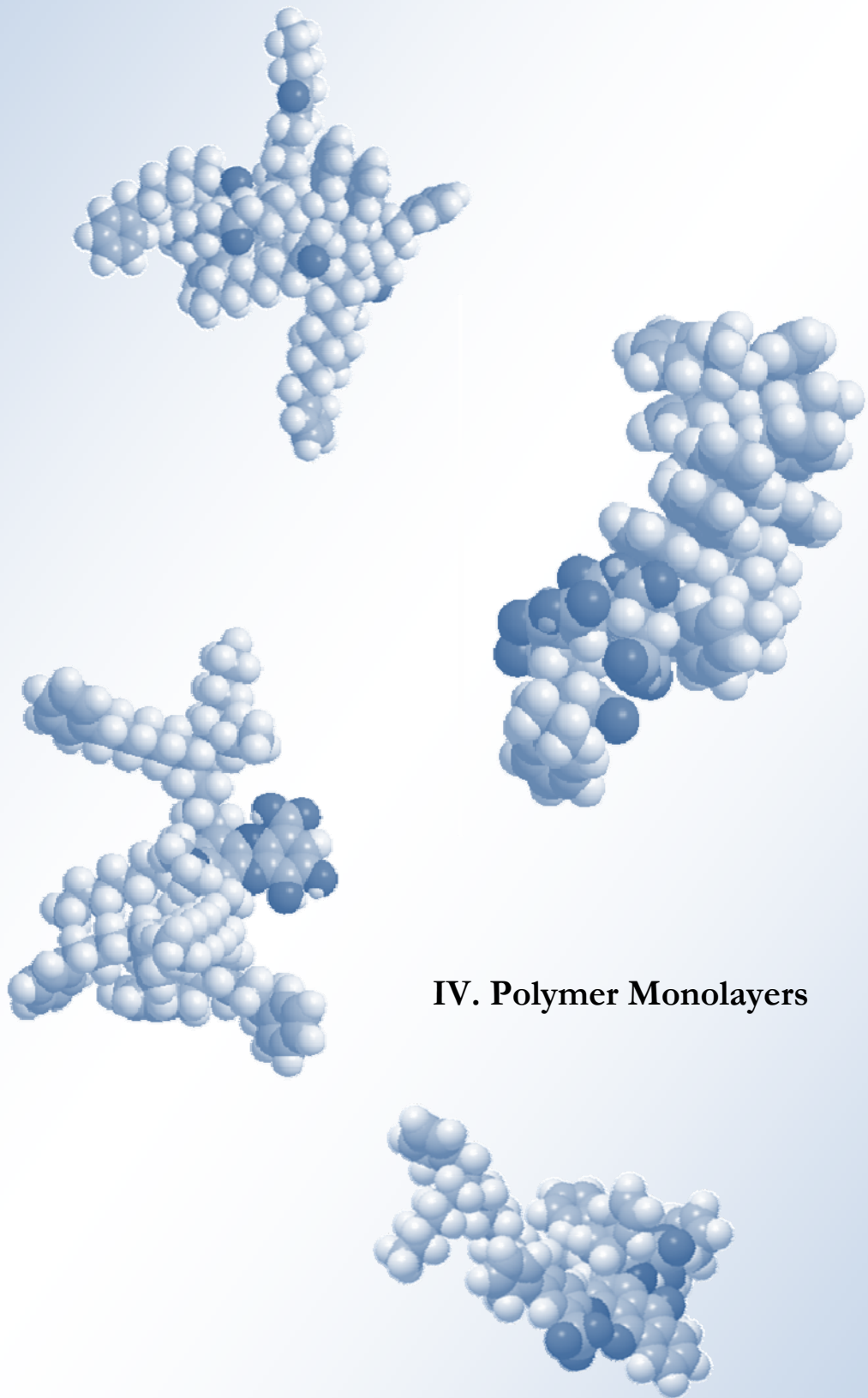


**Figure III.33.** Optical microscope photographs of the PMMA resist covered sample after develop step (a) and Ti/Au contacts in the sample after metal deposition step (b) results in a chemical reduced graphene sample.

This work was carried out by a stay inside the Ministerio de Ciencia e Innovación fellowships for the use of singular Scientific-Technological Facilities Program at the CT-ISOM with the collaboration of the Drs. D. López-Romero, M.C. Sabido Siller and A. Fraile Chamizo.



#### **IV. Polymer Monolayers**



## IV. Polymer Monolayers

Polymers adsorbed to interfaces play an important role for basic materials science as well as for the design and development of technological applications such as adhesives, optical or protective coatings, and biosensors.<sup>[88, 220]</sup> Therefore, polymers are applied in large quantities such as thin films or coatings where the stability, appearance or durability substantially depends on the surface properties. Monolayers of water insoluble polymers, Langmuir monolayers, can be used to build ultrathin solid films by means of Langmuir-Blodgett (LB) methodology. These extremely thin films with high degree of structural order are used in a wide range of technologies such as electronic devices, UV and electron beam resists, or biosensors.<sup>[1]</sup> In addition, polymer films with thickness of nanometers provide ideal sample geometry for studying the effects of one dimensional confinement on the structure and dynamics of polymer molecules.

To construct LB films efficiently is necessary to know the equilibrium and rheological properties of Langmuir monolayers used for LB preparation. It is well established that the rheological properties are linked to the monolayer properties and play an important role in the transfer process of polymers from the air-liquid interface to solid supports.<sup>[221]</sup> Studies carried out with synthetic and natural polymers adsorbed at the interfaces showed that small changes on temperature<sup>[222-224]</sup>, on polymer concentration<sup>[133, 224-226]</sup> or structure<sup>[128, 227]</sup> lead to significant changes on the Langmuir monolayers and consequently, on the LB films generated from ordered monolayers deposition from the air-water interface onto solid substrates<sup>[228]</sup>.

On the other hand, the interactions between insoluble monolayers of surfactants and multivalent ions dissolved in the subphases have received a great interest because they are of major importance in the manufacture of high-quality Langmuir-Blodgett films with potential applications in thin film technology.<sup>[111]</sup>

When ions are present in the subphase, the surfactant monolayer usually becomes more ordered<sup>[229]</sup> and transfers more easily to a solid substrate (LB films)<sup>[230]</sup>. Moreover, the presence of some divalent ions in the subphase results in the appearance of surface structures<sup>[231]</sup> interesting from the fundamental point of view<sup>[33]</sup> and the technological applications<sup>[34,35]</sup>.

For many applications, nanomaterials must be embedded in a polymer matrix. These matrices provide chemical and mechanical stability and prevent the aggregation of nanomaterials.<sup>[8, 53]</sup> In these cases polymers used as patterns often self-assemble at nanometer scale providing well-organized structures which play an important role in practical applications. The self-assembly structures have to be transferred onto solids to build nanodevices by using different techniques such as spin-coating, layer-by-layer assembly or Langmuir-Blodgett methodology. The Langmuir-Blodgett (LB) technique offers the possibility of preparing homogeneous thin films with well-defined layered structures and a very precise control of the thickness and composition.<sup>[1]</sup> On the other hand, small changes on composition, temperature, addition of salt in the subphases of the Langmuir films which serve as precursor of the LB films can improve the properties of the solid-supported polymer films. Therefore, to construct LB films efficiently the characterization of the Langmuir films is required.

As was mentioned above, polymer thin films are an ideal system to study the changes on the structure and dynamics of polymer molecules from the bulk (3D system) to the interface (2D system). Therefore, as Langmuir polymer monolayers have a thickness of the order of the gyration radius, they allow to study the glass-transition temperature,  $T_g$ , decreasing with the dimensionality reduction. In fact, some authors<sup>[172, 222, 232-234]</sup> showed that the  $T_g$  of polymer films decreases when their thickness is lower than 100 nm. In this way, it is possible to analyze the glass-transition by the equilibrium and dynamic properties of polymer monolayers.

In this chapter, we report the study of the equilibrium and dynamic properties of Langmuir monolayers of two maleic anhydride copolymer derivatives, PS-MA-BEE and PS-b-MA, and the effect of the electrolyte addition in the water subphase on the film properties. We also analyze the effect of Langmuir monolayer properties on the structure of polymer LB films. We have chosen this type of polymers because some styrene/anhydride polymer derivatives have shown potential as electron beam resists.<sup>[5]</sup> Consequently, they could be used as pattern for the fabrication of layered molecular electronic devices. Finally, to study the effect of the addition of salts on both, the Langmuir and LB films, we have chosen a salt of divalent cation, magnesium nitrate ( $\text{Mg}(\text{NO}_3)_2$ ), because divalent cations interact stronger than the monovalent ones with acid groups.<sup>[11]</sup> Besides the magnesium cation is used in the genome formation at drug delivery, for which it is important to know the stability and interaction between the divalent cation and polymer.<sup>[235]</sup> On the other hand, we continue a previous study in our group in order to observe the polymer structure influence on the 2D glass-transition temperature.

## IV.1. PS-MA-BEE Monolayers

**Equilibrium Properties of Polymer Monolayers.** Firstly it is also necessary to check the stability of the monolayers prepared by addition. With this purpose the following test was done: after addition of a given volume of the spreading solution, the surface pressure was monitored at least 4 h. In all monolayers the surface pressure was found constant within the experimental uncertainty, indicating stable monolayers. Figure IV.1 shows the surface pressure vs. the surface concentration isotherms for PS-MA-BEE monolayers at 23°C prepared in water and magnesium saline subphases. The isotherms were obtained by equilibration after each addition. For the sake of comparison isotherms obtained by continuous compression are represented in Figure IV.1 by lines.



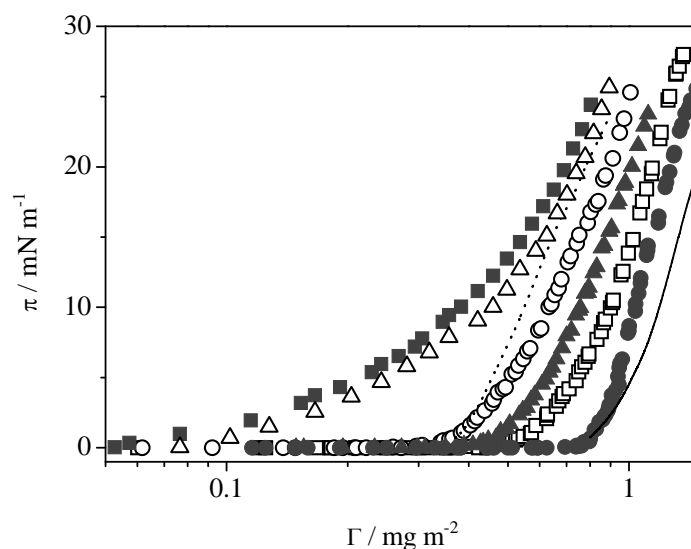


**Figure IV.1.** Surface pressure isotherms of PS-MA-BEE monolayers prepared in different subphases: (solid circles) water; (open squares) 0.12 M  $\text{Mg}(\text{NO}_3)_2$ ; (triangles) 0.18 M  $\text{Mg}(\text{NO}_3)_2$ ; (open circles) 0.24 M  $\text{Mg}(\text{NO}_3)_2$ ; (open triangles) 0.40 M  $\text{Mg}(\text{NO}_3)_2$ ; (solid squares) 0.50 M  $\text{Mg}(\text{NO}_3)_2$ . Surface isotherms were obtained by addition (symbols) and by symmetric compression (dot and solid lines).

Results in Figure IV.1 show that monolayers in saline solutions are more expanded than monolayers in unsalted subphase. This effect increases as the electrolyte concentration in the subphase increases until it reaches the value of 0.4 M. The further addition of  $\text{Mg}(\text{NO}_3)_2$  in the aqueous subphases does not modify the isotherm.

Figure IV.1 also shows that the isotherms obtained for addition and for continuous compression agree with each other until a given surface pressure. Above this pressure the monolayer obtained by compression is far from the equilibrium state and two opposite trends are observed as a function of the subphase composition. Thus, in water subphase, the surface pressure values for monolayers prepared by compression are lower than the values corresponding to the monolayers obtained by addition, while for monolayers prepared in saline

subphases, the surface pressure obtained by compression is higher than the addition one. In the later if the barriers stop, the surface pressure decreases until the value corresponding to the equilibrium. These facts can be due to the existence of dynamic processes on the polymer monolayer.<sup>[172, 236, 237]</sup> In order to gain some insights into this dynamic process, the step-compression method combined with oscillatory barriers experiments were carried out in the Langmuir trough. These experiments allow us to obtain information of slow relaxation processes in monolayers.

Figure IV.2 show the electric surface potential isotherms of PS-MA-BEE monolayers in water and in saline subphases.

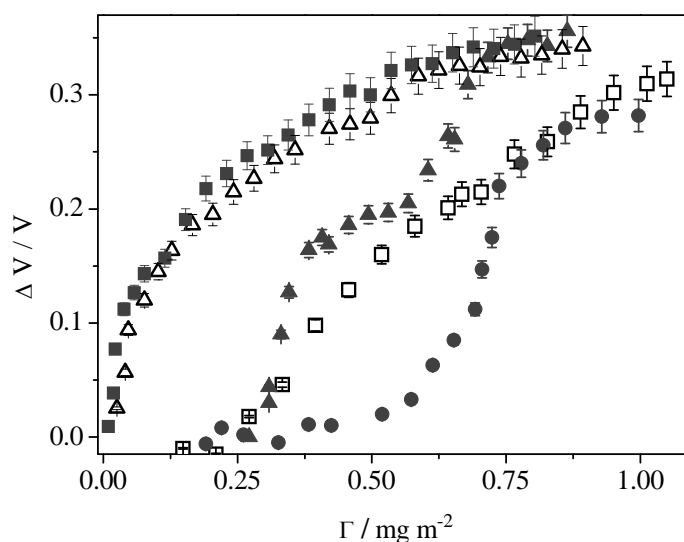


**Figure IV.2.** Surface potential isotherms at 296 K of PS-MA-BEE monolayers prepared in different subphases: (solid circles) water; (open squares) 0.12 M  $\text{Mg}(\text{NO}_3)_2$ ; (solid triangles) 0.24 M  $\text{Mg}(\text{NO}_3)_2$ ; (open triangles) 0.40 M  $\text{Mg}(\text{NO}_3)_2$  and (squares) 0.50 M  $\text{Mg}(\text{NO}_3)_2$

The surface potential values are always positive and for a given surface concentration they increase as the electrolyte concentration in the subphase increase. The effect is more marked in the dilute surface concentration regime.

As can be observed the surface potential curves have similar trend to the

surface pressure ones; thus, the surface potential isotherms are shifted to lower surface concentration when the electrolyte concentration in the subphase increases. The isotherm in 0.24 M  $\text{Mg}(\text{NO}_3)_2$  shows a pseudo-plateau while it is marked by a kink in the isotherms at lower electrolyte concentration in the subphase. The plateau almost disappears when the monolayer is built in saline subphases containing electrolyte concentrations above 0.4 M.

It is also interesting to notice that the surface potential at high surface coverage does not increase with the electrolyte concentration for monolayers containing high electrolyte concentration and the value remains constant in a value of 0.35 V. This fact indicates that in these monolayers all acid groups are dissociated.

Figure IV.3 presents the equilibrium elasticity modulus,  $\epsilon_0$ , for different polymer monolayers. The elasticity modulus is obtained from the pressure isotherms.

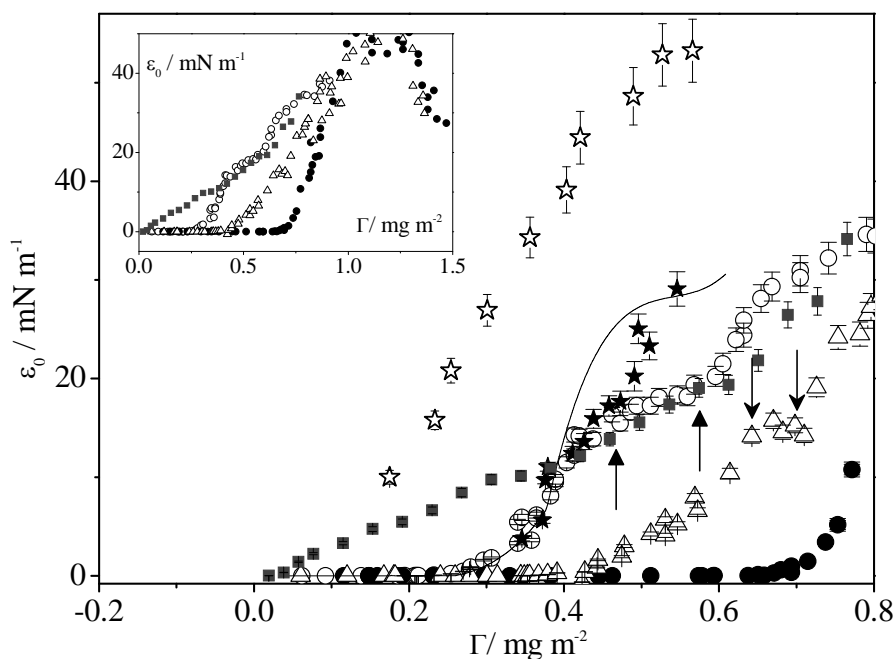


**Figure IV.3.** Variation of the equilibrium elasticity with polymer surface concentration for monolayers prepared in different subphases at 296K: (solid circles) water; (triangles) 0.12M  $\text{Mg}(\text{NO}_3)_2$ ; (open circles) 0.24 M  $\text{Mg}(\text{NO}_3)_2$ ; (solid squares) 0.50 M  $\text{Mg}(\text{NO}_3)_2$ . The arrows point polymer concentrations at which the kink in the surface potential isotherms appears. Solid and open stars represent the dilational modulus obtained from step-compression experiments for subphases containing 0.24 M  $\text{Mg}(\text{NO}_3)_2$  and (solid squares) 0.50 M  $\text{Mg}(\text{NO}_3)_2$ , respectively, see text.

Small elasticity values are observed for monolayers in water until the surface concentration reaches a value of  $0.8 \text{ mg m}^{-2}$ . A sudden increase of elasticity is observed above this surface concentration until it reaches a value of  $50 \text{ mN m}^{-1}$ . Finally, when the surface concentration is further increased a weak decrease of the elasticity is observed. This behaviour is characteristic of films formed exclusively by polymer molecules at concentrated regime. In these concentrated films the conformational degrees of freedom of the polymer coils decrease and consequently, the elasticity modulus also decreases.<sup>[172, 222]</sup> It is also

interesting to notice that the equilibrium elasticity modulus values are consistent with liquid-expanded surface states <sup>[123]</sup> in all these monolayers. On the other hand, and because the isotherms obtained by compression do not correspond to the equilibrium ones (isotherms prepared by addition), the elasticity values calculated from the isotherm obtained by compression are far from the equilibrium elasticity values, see Figure IV.3.

Differences between the elasticity modulus of monolayers in saline and in the unsalted subphases are the following: on the one hand, the equilibrium elasticity values for dilute monolayers ( $\Gamma < 1 \text{ mg m}^{-2}$ ) are higher for monolayers in saline subphase than in the subphase without salt. The effect is more marked when the salt concentration increases. On the other hand, the equilibrium elasticity curves for monolayers in saline subphases with salt concentrations below 0.4 M, present a kink or a plateau at the same surface concentration values than in the surface potential curves. For comparative purposes the arrows in Figure IV.3 point to the position of the pseudo-plateau in the surface potential isotherms, Figure IV.2.

The surface potential and pressure isotherms of PS-MA-BEE clearly show that the monolayers become more expanded when the  $\text{Mg}(\text{NO}_3)_2$  concentration in the subphase increases until it reaches a value of 0.4 M. Above this concentration the isotherm remains unaffected by the increase of electrolyte concentration. This behaviour could be attributed to the formation of a complex between the divalent cation  $\text{Mg}^{2+}$  and the acid groups of the polymer molecules. The isotherm expansion was observed by other authors when metal-surfactant complexes are formed at the interface and the surfactant contains bulky head groups.<sup>[238]</sup> This could be the scenario in our system because the hydrophilic part of the polymer is too bulky and some molecular rearrangements have to be carried out in order to form the complexes between the divalent cation and the carboxylic groups of the polymer. Results also show that the isotherm expansion

stop when the  $\text{Mg}(\text{NO}_3)_2$  concentration in the subphase reaches a value of 0.4 M. This fact indicates that at this salt concentration all the polymer molecules are bound to the divalent cation.

The coincidence between the kink and the plateau positions observed in the surface potential and the equilibrium elasticity isotherms may be indicative of phase transitions that in this system can be originated by different populations of free and bound polymer molecules. Accordingly, the plateau disappears when the cation-polymer complexes at the interface predominate,  $[\text{Mg}(\text{NO}_3)_2] \geq 0.4 \text{ M}$ .

**Dynamic Properties of Polymer Monolayers.** As was previously mentioned, the polymer isotherms obtained by continuous addition and compression agree with each other when the surface concentration is relatively low. This behaviour can be signature of dynamic processes on the monolayer. To study these processes we have used the step-compression method.<sup>[222]</sup> In this method, the monolayer is perturbed by a quick compression, and then the relaxation to the new equilibrium condition is followed by surface pressure measurements. Previously, we also use oscillatory barrier measurements to check the strain range where the amplitude of the stress,  $\sigma_0$ , is proportional to the strain,  $U_0$ , the linear regime. Examples of oscillatory experiments are presented in Figure IV.4 and performed at a frequency of 0.006 Hz. For the sake of clarity Figure IV.4 shows the results obtained for two different subphases, water and 0.24 M  $\text{Mg}(\text{NO}_3)_2$ .

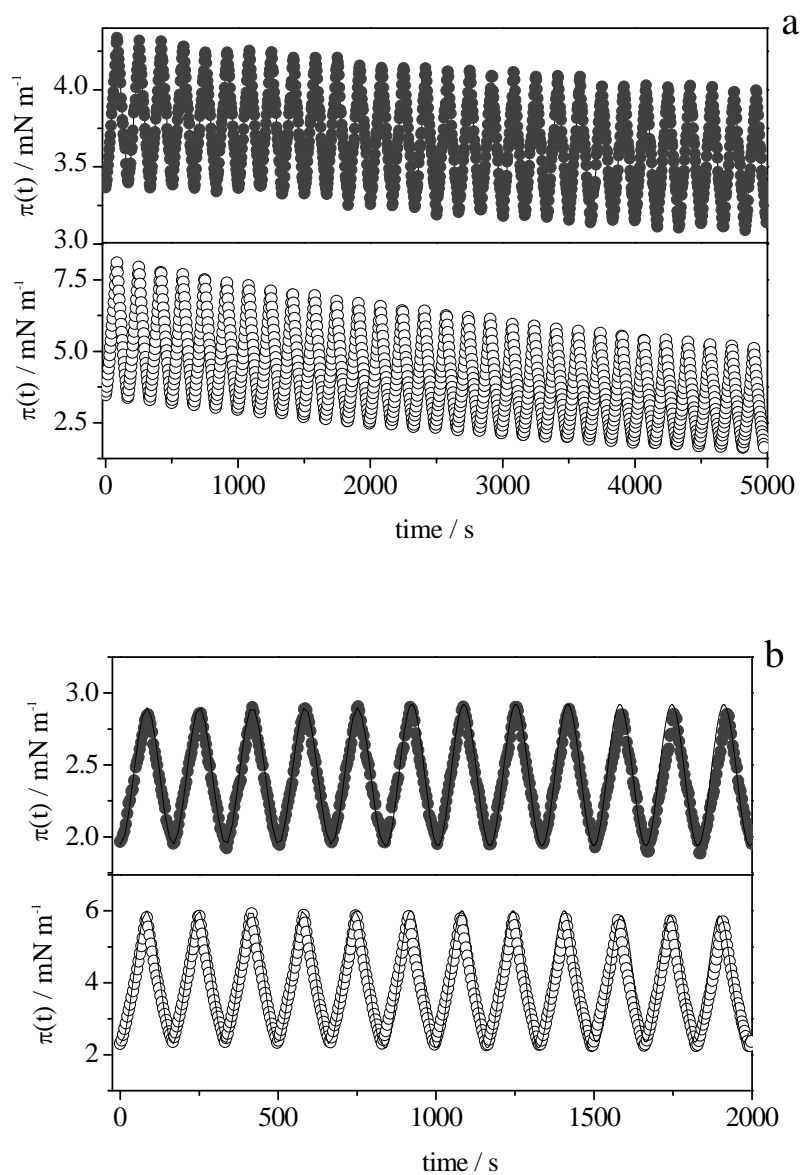


**Figure IV.4.** Oscillatory experiment results at 296 K for different monolayers: (a) pure water and polymer surface concentration around  $0.9 \text{ mg m}^{-2}$ ; (b)  $0.24 \text{ M Mg(NO}_3)_2$ , and polymer surface concentration around  $0.42 \text{ mg m}^{-2}$ . The strain amplitude was 4.3 % (solid circles) and 12 % (open circles). The experiments were carried out at the frequency of 0.006 Hz.

As can be seen in Figure IV.4a for monolayers deposited on water

subphase, after each compression-expansion cycle, the former initial state is not recovered and the pressure decreases after each cycle. The amplitude of the stress remains almost constant at low strains while it decreases at high strains. This behaviour is not observed in monolayers prepared in saline subphases and can be explained by developing of irreversible features in the film as it is strained by subsequent compression-expansion cycles. This behaviour has been observed in other polymer monolayers<sup>[130]</sup>; however, this fact could be simply due to the desorption process followed by the polymer dissolution in the subphase. To disregard this possibility we carried out the following experiment: a polymer monolayer prepared by addition was submitted to compression-expansion cycles, then the barriers were stopped and the pressure monitored with time (2 h). The surface pressure decrease was least of 1%. Similar results were obtained at different surface coverage. This observation is compatible with no polymer dissolution in the subphase when the monolayer is strained.

Moreover, we carried out several oscillation barriers experiments changing the cycle frequency from 0.003 to 0.04 Hz. For the case of polymer monolayers in water subphase the surface pressure decreasing varies with frequency. The initial state of the monolayer is not recovered, decreasing the surface pressure in a more marked way when the frequency decreases. It could confirm the formation of irreversible features in the film mainly at slow timescale. However in the case of saline subphases the response amplitude does not show relevant changes with frequency. Therefore, we decided to work at a slow suitable frequency for the times of the processes involved, 0.006 Hz, which at the same time, is not affected by the hydrodynamic limitations of the technique.

As we are interested in studying the relaxation process of polymer monomers adsorbed in the monolayer, we have only studied the dynamic processes on the monolayers prepared on saline subphases. Figure IV.5 presents the variation of the amplitude of the stress  $\sigma_0$  with the strain,  $U_0$  for monolayers in



saline subphases. As can be seen in the figure, deviations of the Hookean linear behaviour are observed for the area change above 10% of the total area. Consequently, in the step-compression experiments the area change,  $\Delta A$ , is kept below 10% in order to ensure that the system remains in the linear regime. This nonlinear behaviour has been found for other polymer monolayers.<sup>[128, 223]</sup>

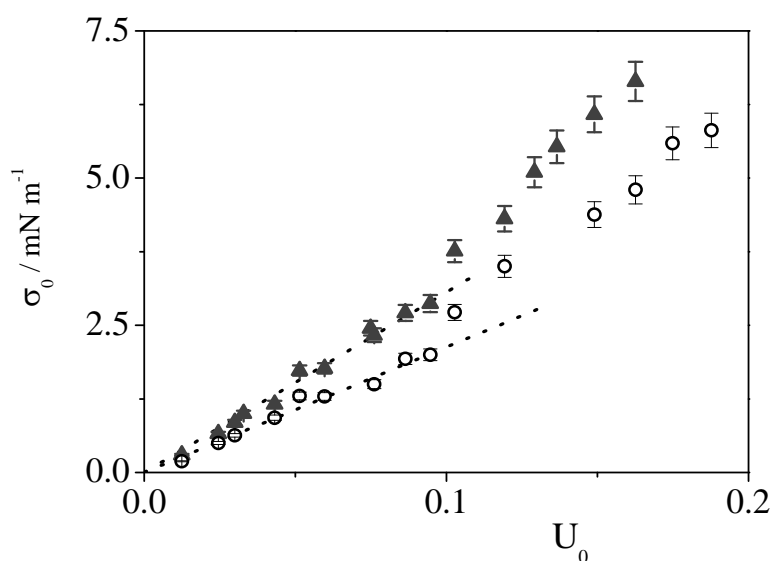


**Figure IV.5.** Variation of the amplitude of the stress,  $\sigma_0$ , with the strain,  $U_0$  for polymer monolayers prepared in 0.12 M  $\text{Mg}(\text{NO}_3)_2$  subphase (triangles) and in 0.24 M  $\text{Mg}(\text{NO}_3)_2$  (circles). The dot lines represent the Hookean's linear behavior.

Stress-relaxation experiments show that in the low-coverage region, before the end of the kink or the pseudo-plateau in the isotherms, the stress-relaxation curve can be described by a single exponential function, Figure IV.6. However, when the surface coverage is further increased no single-exponential relaxations are found, this fact is indicative of additional processes in the monolayer. In monolayers prepared in the most concentrated saline subphases,  $\text{Mg}(\text{NO}_3)_2 \geq 0.4$  M, the stress-relaxation curves are single-exponential functions for surface concentrations below  $1 \text{ mg m}^{-2}$ . Above this surface concentration no single-

exponential relaxations were found.

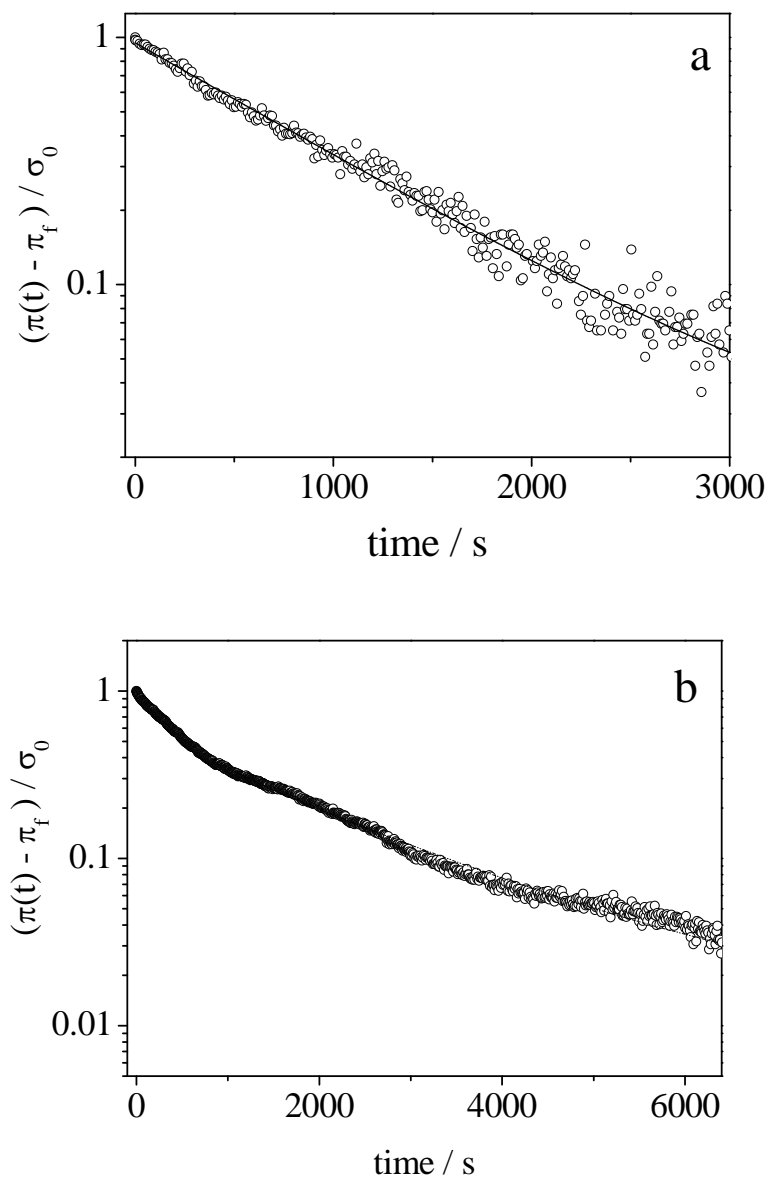


**Figure IV.6.** Stress-relaxation experiments for a polymer monolayer in 0.24M Mg(NO<sub>3</sub>)<sub>2</sub> subphase with a surface concentration of 0.38 (a) and 0.55 (b) mg m<sup>-2</sup> at 296 K. Line is the single exponential curve (a) and multi-exponential curve (b).

Figure IV.7 shows the concentration dependence of the relaxation time

obtained for different monolayers. For the sake of clarity only some results are presented in Figure IV.7. As can be seen in the figure different trends are found. For monolayers in saline subphases with salt concentrations below 0.4 M, at low-coverage, before the kink or the pseudo-plateau, the relaxation time increases with the polymer concentration, this behaviour is characteristic of slow collective motions of the polymer coils adsorbed at the interface<sup>[130, 238]</sup>. Conversely, at high-coverage the relaxation time decreases when the polymer surface concentration increases. According to the equilibrium properties, these surface concentrations correspond to regions in the isotherm in the phase transitions. Consequently, the concentration dependence of the relaxation time is a further indication of a possible phase transition between a state in which we have polymer molecules bound to the  $\text{Mg}^{2+}$  and a state with free polymer molecules.

On the other hand, when monolayers are prepared in subphases containing electrolyte concentrations above 0.4 M, the stress-relaxation experiments have led to relaxation curves described by a single exponential in the surface concentration range between 0.15 and 1  $\text{mg m}^{-2}$  and the relaxation time increases with the surface concentration. As can be seen in Figure IV.7, the relaxation time values are quite similar to those obtained for monolayers in 0.24 M of  $\text{Mg}(\text{NO}_3)_2$  at low surface coverage.

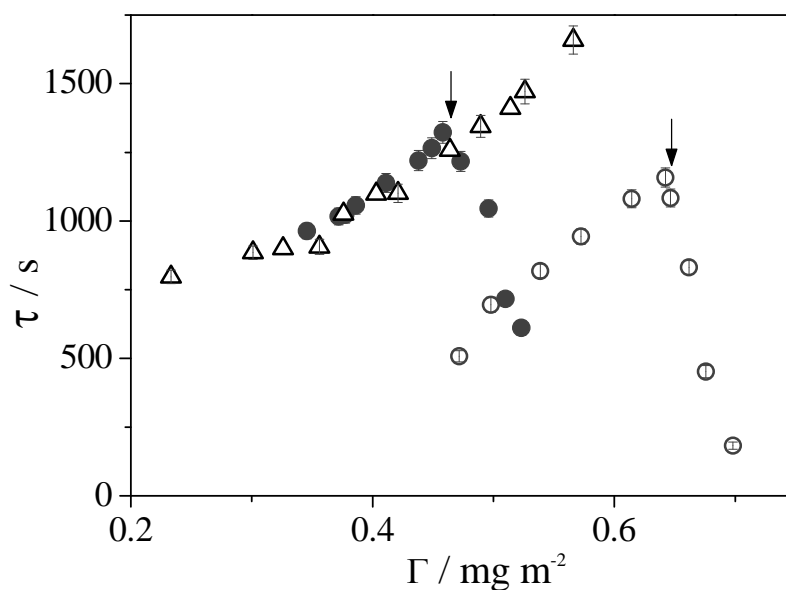


**Figure IV.7.** Variation of the relaxation time with the polymer surface concentration for monolayers prepared in the following subphases at 296K: (open circles) 0.12 M  $\text{Mg}(\text{NO}_3)_2$ ; (solid circles) 0.24 M  $\text{Mg}(\text{NO}_3)_2$  and (open triangles) 0.50 M  $\text{Mg}(\text{NO}_3)_2$ . The arrows point polymer concentrations at which the kinks in the surface potential and equilibrium elasticity isotherms appear.

We have also determined the dilatational modulus,  $|\varepsilon|$ , from the relaxation curves as  $|\varepsilon| = \frac{\sigma_0}{U_0}$ . Some of these values are represented in Figure IV.3

by stars. For the sake of clarity we only represent the values for monolayers in subphases with 0.24 M and in 0.5 M of  $\text{Mg}(\text{NO}_3)_2$ . Results in Figure IV.3 show that in the monolayers prepared in the subphase containing  $\text{Mg}(\text{NO}_3)_2$  0.24 M, there is an excellent agreement between the dilatational modulus and the equilibrium elasticity at low-coverage. However, when the coverage increases the dilatational modulus is higher than the equilibrium elasticity, this is indicative of viscoelastic behaviour. The crossover between the elastic and viscoelastic behaviour appears at the polymer surface concentration where deviations between the isotherms obtained by addition and compressions become important. This behaviour is observed for all monolayers with electrolyte concentrations below 0.4

M; however, when the electrolyte concentration in the subphase increases,  $[\text{Mg}(\text{NO}_3)_2] \geq 0.4 \text{ M}$ , the dilatational modulus values are always higher than the equilibrium elasticity ones. The differences between dilatational and equilibrium elasticity values are quite marked. This fact indicates that the formation of complexes between the polymer and the divalent cation increases the viscoelastic behaviour of the monolayer.

As was indicated above the stress-relaxation experiments in the densest monolayers have led to relaxation curves described by no single-exponential curves in the densest monolayers. This behaviour can signify additional processes such as disorder-order transitions<sup>[128]</sup> or polymer aggregation. To disregard this point we transfer polymer monolayers from the liquid interface to mica and/or Si (100) via the Langmuir-Blodgett technique (LB) because several studies showed that aggregates produced by self-assembly monolayers can survive when are transferred from the Langmuir monolayer to solid supports.<sup>[239-241]</sup> AFM results show that the morphology of the polymer LB films is similar in mica and silicon when the subphase is water, Figure IV.8. However, when the subphase contains electrolytes both, AFM and optical microscopy show the formation of magnesium salt crystals, Figure IV.9. Therefore, we decide to use silicon as substrate for the polymer films study.

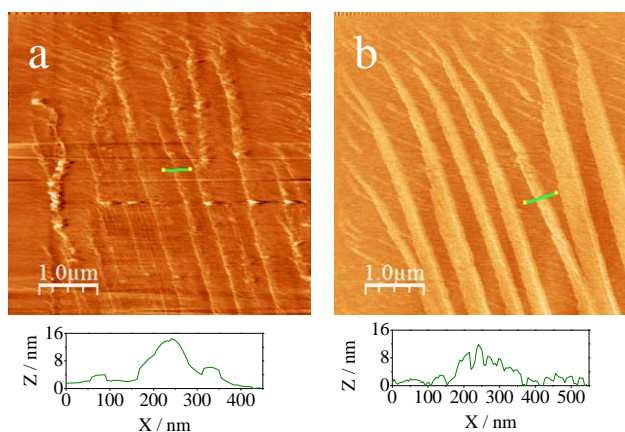


**Figure IV.8.** AFM images of the LB films on mica (a) and Si (100) (b) for PS-MA-BEE monolayers in water subphase at surface pressure  $14 \text{ mN m}^{-1}$  by compression.



**Figure IV.9.** Optical microscopy image of the  $\text{Mg}(\text{NO}_3)_2$  crystals formed on mica after the LB deposition of a polymer film prepared on saline subphase.

For comparative purposes we have also constructed LB films from Langmuir monolayers at low surface coverage, below the end of the kink (in the pseudo plateau). The AFM images show no domains in these LB films. However, the first aggregates were clearly observed at the end of the pseudo-plateau, Figure IV.10.

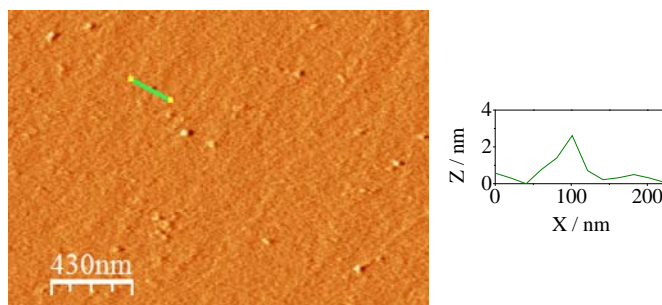


**Figure IV.10.** AFM image of the LB film on Si (100) for PS-MA-BEE monolayer in  $\text{Mg}(\text{NO}_3)_2$  0.12M at surface pressure  $4 \text{ mN m}^{-1}$  (end of pseudo-plateau) by compression.

According to the differences observed in the properties of Langmuir films prepared by addition and by compression, we build the LB films by transferring Langmuir films prepared by the two different methodologies. Different mesoscopic structures are detected as a function of the methodology used. To illustrate this fact several AFM images are collected in Figure IV.11. We have checked the reproducibility of the transfer procedure by obtaining each LB film at least three times. The results agree with each other except for LB films built by transferring the Langmuir film prepared by addition in a water subphase.

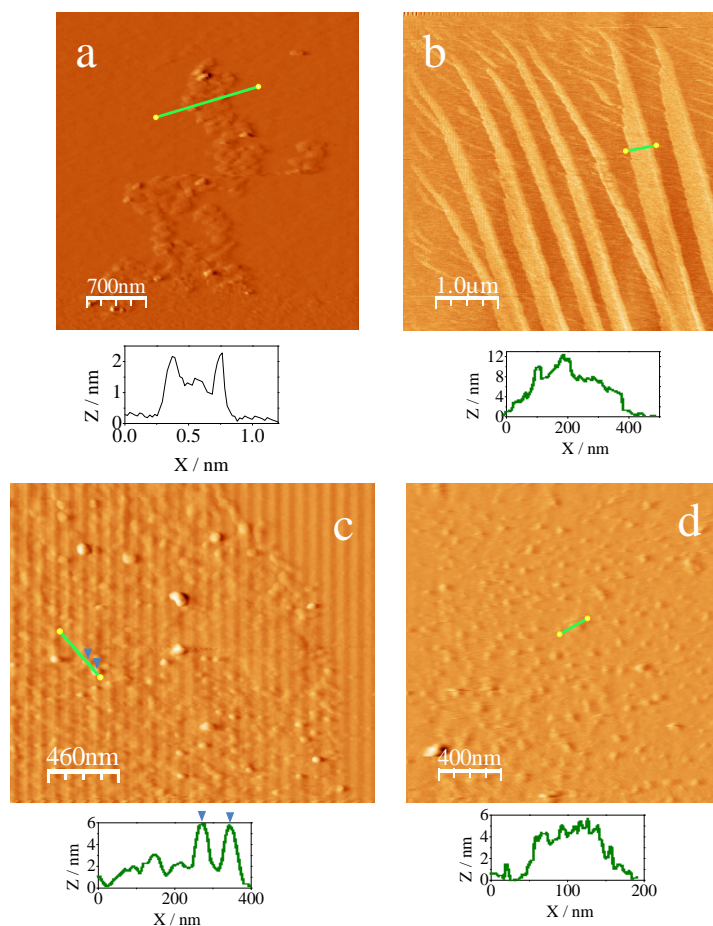


**Figure IV.11.** AFM images of the LB films on Si (100) for different PS-MA-BEE monolayers: in water subphase at surface pressure  $14 \text{ mN m}^{-1}$  and  $0.12 \text{ M Mg(NO}_3)_2$  at  $10 \text{ mN m}^{-1}$ , by subsequent additions (a, c) and by compression (b, d), respectively. Below are the corresponding cross section profiles. In addition the green angle pairs correspond to the angles pairs in the Figure 12c.

Images in Figure IV.11 clearly show different structures as a function of both, the subphase composition and the methodology employed to prepare the Langmuir monolayer which serve to build the LB films. Thus, when the Langmuir monolayer was prepared in aqueous subphase by compression, long stripes are observed, Figure IV.11b. These aggregates present a high degree of reproducibility. In contrast, aggregates with different morphologies are observed when the Langmuir monolayer is obtained by addition in water subphase, Figure



IV.11a. In this case the morphology of these aggregates also changes when the polymer concentration of the spreading solution changes. This behaviour is consistent with results obtained in previous work for diblock copolymers with immiscible blocks confined to the surface.<sup>[242]</sup> A theoretical model has been proposed to interpret this fact.<sup>[237]</sup> The model considers that the fast evaporation of the spreading solvent and the extremely low solubility of the hydrophobic blocks compared with the hydrophilic ones are the main reasons of the association in metastable aggregates.

In the case of stripes, Figure IV.11b, the formation of this type of 2D nanostructures has been previously observed and interpreted by spinodal dewetting mechanism.<sup>[243-245]</sup> A detailed discussion of this mechanism is presented in Chapter V.

Figures IV.11c and d, show images of LB films built from dense Langmuir monolayers in saline subphases 0.12M of  $\text{Mg}(\text{NO}_3)_2$  prepared by addition and by compression methodologies, respectively. Even though the morphology of aggregates acceptably agrees with each other, differences in the monodispersity degree can be observed. Thus, LB films built by transferring Langmuir films prepared by compression are almost monodisperse and the average value of the roughness is around 5 nm. In contrast, the LB prepared by addition show higher polydispersity degree and the roughness values are between 3 and 5 nm. Finally, it is interesting to notice that results in saline subphases obtained by the two methodologies are reproducible.

Although the images in Figure IV.11c and d correspond to LB films built with Langmuir films in 0.12 M  $\text{Mg}(\text{NO}_3)_2$  subphase; similar images are observed for the rest of films prepared in saline subphases. From the AFM results it is possible to conclude that aggregates transferred from the concentrated monolayers of polymer have different morphology than the ones transferred from monolayers containing polymer-cation complexes.

Finally, we have also used a laser ellipsometer to obtain the layer thickness of the different LB films. In order to obtain the film thickness, different approaches have been used to model the interfaces. We have modelled these films as three layers: the first one is the Si substrate with a refractive index of 4.1264; the second layer is the native oxide layer of a refractive index of 1.4653.<sup>[242]</sup> The thickness of this layer was obtained in an ellipsometry experiment using the clean silicon wafer. Finally, the third layer (polymer film/air) thickness and the refractive index are obtained from the fitting of the two ellipsometric angles,  $\Psi$ , and  $\Delta$ , to Fresnel equation. Results obtained are collected in Table IV.1. From data in Table IV.1 it is possible to conclude that the thickness values obtained by ellipsometry are in good agreement with the average roughness of films obtained by AFM measurements.

**Table IV.1.** Thickness and roughness values obtained from Ellipsometry and AFM measurements of different PS-MA-BEE LB films deposited onto silicon wafers, respectively.

Subphase	$\pi$ /mN m <sup>-1</sup>	LB Method	Roughness AFM (nm)	Thickness Ellipsometry (nm)
Water	14	Addition	1.5 – 2.5	2.5 ± 0.7
	14	Compression	8.0 ± 0.6	8.1 ± 2.4
Mg(NO <sub>3</sub> ) <sub>2</sub> 0.12 M	3.8	Addition	1.0 ± 0.5	1.8 ± 0.5
	10	Addition	3-5	2.9 ± 0.8
	10	Compression	5.0 ± 0.5	4.4 ± 1.3

## IV.2. PS-b-MA Monolayers

In order to check the functional group by which the PS-MA-BEE forms the complex with the Mg<sup>2+</sup>, we decide to compare this behaviour with another maleic anhydride polymer, PS-b-MA, that is also a styrene/maleic anhydride derivative. This polymer does not present a block with the carboxylic group, which could be responsible for the formation of a complex in the case of PS-MA-

BEE monolayers between the  $\text{COO}^-$  and  $\text{Mg}^{2+}$ .<sup>[79]</sup> Thus, the aim of this brief work is to confirm the effect of the polymer structure on the film properties.

**Equilibrium Properties.** Surface pressure vs surface concentration isotherms on water and  $\text{Mg}^{2+}$  (0.12 M) aqueous subphases were prepared by equilibration after each addition and by continuous compression. In this case, the behaviour observed is opposite. As it is shown in Figure IV.12a, the isotherm shifts to higher surface concentration when ions are added into subphase, i.e., the isotherm is more condensed. This behaviour is in agreement with the lack of interactions between the functional groups of PS-b-MA and the magnesium cation, reinforcing that the effect observed on PS-MA-BEE is due to a  $\text{Mg}^{2+}$ -acid group complexation.

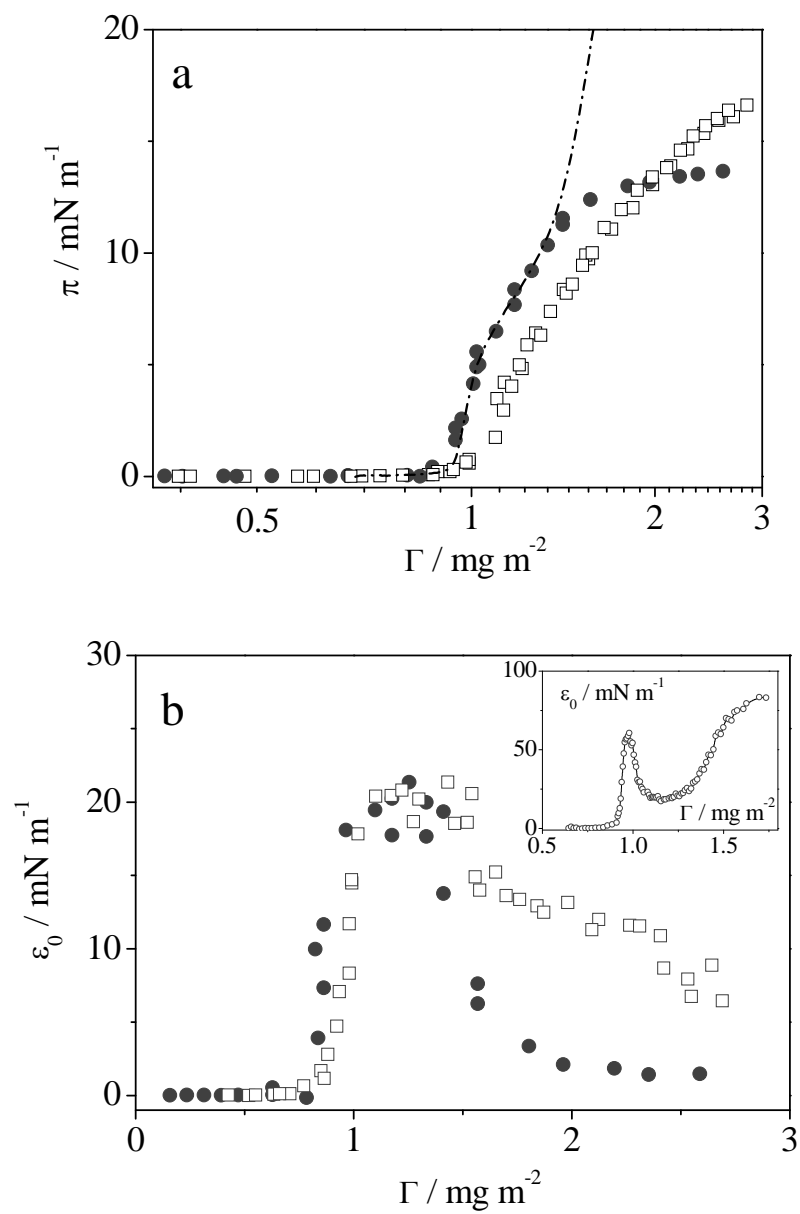


**Figure IV.12.** Surface pressure (a) and equilibrium elasticity (b) isotherms of PS-b-MA monolayers prepared in different subphases: (circles) water; and (squares) 0.12M  $\text{Mg}(\text{NO}_3)_2$ . Surface isotherms were obtained by addition (symbols) and by symmetric compression (dot-solid lines) at 293K.

On the other hand, LB depositions of the monolayers were made for the different subphases to observe the influence of polymer structure and the subphase on the aggregates obtained. The Langmuir monolayers were deposited at a surface pressure of  $10 \text{ mN m}^{-1}$  on water and  $\text{Mg}^{2+}$   $0.12\text{M}$  aqueous subphases at  $20^\circ\text{C}$  onto silicon wafers. At this surface pressure the monolayer is the state that corresponds to the maximum elasticity value, Figure IV.13b, as in the case of PS-MA-BEE at  $\pi=14 \text{ mN m}^{-1}$ . AFM images for PS-b-MA show the same type of aggregates (Figure IV.13) independently of the type of subphase. In this case, the polymer forms enough homogeneous circular aggregates of 3-4 nm height and  $\sim 100 \text{ nm}$  radius, Table IV.2, that could be attributed to plane/starfish or nanodot surface micelles observed for other authors on polystyrene derivatives at the air-water interface <sup>[246-248]</sup> and they would be promoted by polystyrene block. In fact, the surface micelle formation is based on the aggregation of hydrophobic blocks to form an isolated phase of various shapes and it is stabilized by the corona of hydrophilic blocks spread on the water surface.<sup>[246]</sup> Moreover, the observation of surface micelles is in agreement with theoretical models proposed for morphologies of the structures formed by block copolymers.<sup>[249]</sup> In this case, the ratio between PS and MA blocks (number of monomers in each block,  $N_{\text{PS}}$ ,  $N_{\text{PS}} \sim 15$  and  $N_{\text{MA}} \sim 5$ ) at low grafting density would lead to spherical interspersed micelles. Likewise, as there are not interactions between the functional groups of PS-b-MA and magnesium cation, the structure is kept.

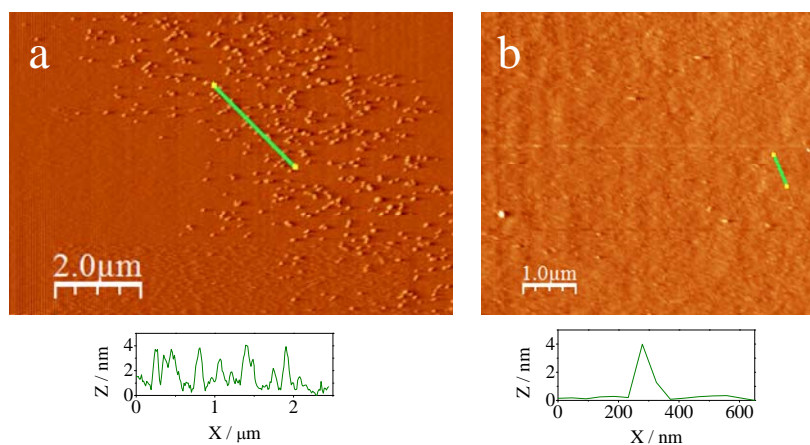


**Figure IV.13.** AFM images of a LB films on Si (100) for a PS-b-MA monolayers in water (a) and 0.12M  $\text{Mg}(\text{NO}_3)_2$  aqueous subphase (b) at surface pressure  $10 \text{ mN m}^{-1}$  by compression with its corresponding cross section profile.

**Table IV.2.** Average values of the dot-like feature dimensions formed in PS-MA-BEE and PS-b-MA LB films deposited at a surface pressure of  $10 \text{ mN m}^{-1}$  obtained from AFM measurements.

Polymer	Subphase	Diameter / nm
PS-b-MA	Water	$121 \pm 43$
	$\text{Mg}(\text{NO}_3)_2$ 0.12 M	$95 \pm 32$
PS-MA-BEE	$\text{Mg}(\text{NO}_3)_2$ 0.12 M	$55 \pm 10$

Reported values are averages and error represents the standard deviation determined from at least 40 surface features.

Besides, ellipsometric measurements, collected in Table IV.3, were carried out in order to confirm the roughness obtained by AFM profiles by applying the same interface model as in the case of PS-MA-BEE.

**Table IV.3.** Thickness and roughness values obtained from Ellipsometry and AFM measurements of different PS-b-MA LB films deposited at the surface pressure of  $10 \text{ mN m}^{-1}$  by symmetric compression onto silicon wafers, respectively.

Subphase	Roughness AFM (nm)	Thickness Ellipsometry (nm)
Water	$3.5 \pm 0.5$	$4.3 \pm 1.2$
$\text{Mg}(\text{NO}_3)_2$ 0.12 M	$4.0 \pm 0.5$	$5.0 \pm 1.4$

In previous work of the group<sup>[172]</sup>, the soft-glass transition of two maleic anhydride derivative polymers, PMAO and PS-b-MA, were observed by surface potential measurements and confirmed by rheological measurements, both at the air-water interface. From these results, the 2D glass transition temperatures were determined at 27°C (300K) for PS-b-MA and 22°C (295K) for PMAO. In order to check the effect of the electrolytes presence on the water subphase, we carry out surface potential measurements by temperature variation of PS-b-MA monolayers on  $\text{Mg}^{2+}$  (0.12 M) subphase. For comparison the measurements were carried out at the overlap surface pressure as in the case of water subphase.<sup>[172]</sup> Results in Figure IV.14 show that surface potential increases when decrease the temperature due to a restriction of the hydrophobic chains movements promoting a higher orientation in the monolayer highlighted with the potential surface increasing.<sup>[250]</sup> This fact indicates that the glass state is highly ordered due to intermolecular interactions between the molecules that forms the glass phase.

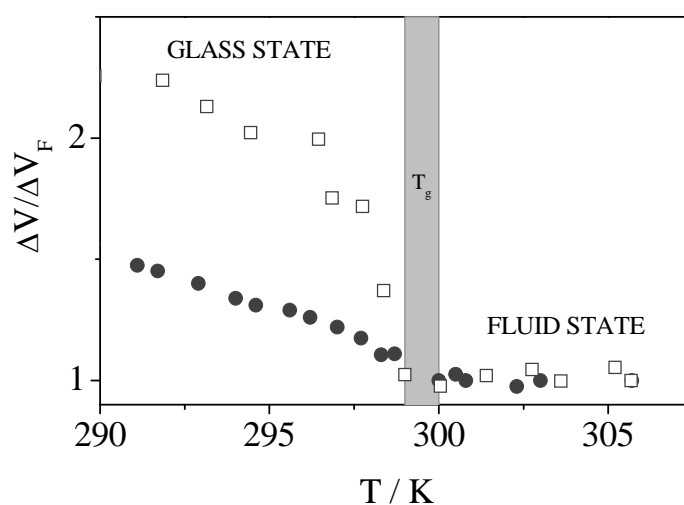


**Figure IV.14.** Surface potential variation with temperature for monolayers of PS-b-MA on water (circles) and  $\text{Mg}(\text{NO}_3)_2$  (squares) subphases. The surface potential values are normalized to the final one,  $\Delta V_F$ .

Accordingly, the surface potential measurements show a change in the orientation of the molecules at the temperature of  $299.5 \pm 0.5 \text{K}$ , the 2D glass

transition temperature. Besides, this temperature is not significantly modified with the addition of salts on the water subphase. The most significant difference is the slope of the surface potential in the glass state in the presence of  $Mg^{2+}$ . This behaviour could be ascribed to a more perpendicular orientation of the dipole induced by the ions.<sup>[79]</sup>

In the case of PS-MA-BEE the surface potential measurements did not allow to observe the 2D glass transition temperature. This picture could be due to different chain flexibility as indicate the bulk glass transition temperature: PS-MA-BEE (76°C, 349K) and PS-b-MA (122°C, 395K) measured by DSC, Figure IV.15. The chain mobility is related to the greater flexibility of the different units that form the chain, thus a greater flexibility more chain mobility and lower glass transition temperature.<sup>[251]</sup> Accordingly, it is not possible to observe the 2D glass state for the PSMABEE at the air-water interface because usually this temperature is around 100 degrees below the bulk glass transition temperature.<sup>[222]</sup> This 2D  $T_g$  reduction in adsorbed films with respect to bulk polymers can be attributed to the decrease of the intermolecular interactions due to the reduction of one dimensionality.<sup>[252]</sup> Therefore, the surface potential values point out to the chain orientation as an important factor.



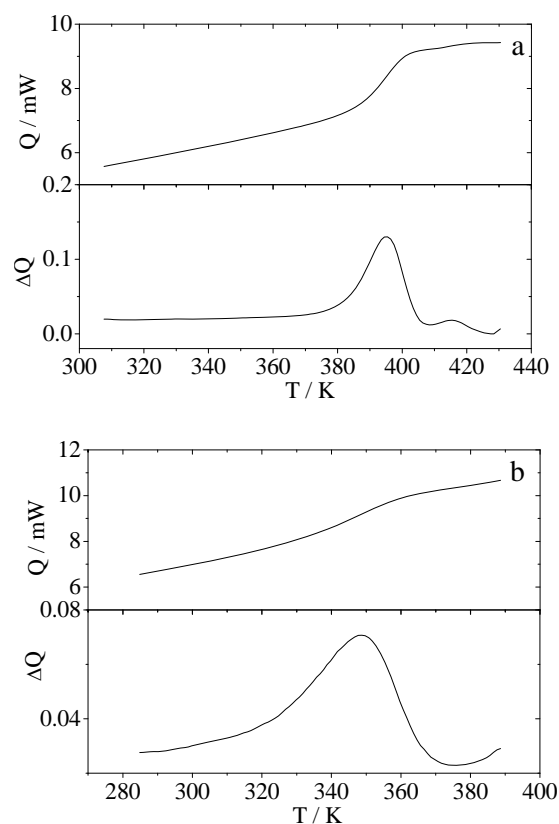


**Figure IV.15.** Thermograms for bulk polymers by DSC measurements: (a) PS-b-MA; and (b) PS-MA-BEE.

**Dynamic Properties.** We carried out oscillatory barrier measurements to check changes in the dynamic properties of the polymer monolayer below and above the soft-glass transition temperature following a previous investigation in our group<sup>[172]</sup>. The facts observed were: an increase in the elastic modulus,  $\epsilon$ , and the dilatational viscosity,  $\kappa$ , for the PS-b-MA polymer monolayer at the solid-like state in agreement with an increasing in the mechanical rigidity.<sup>[232, 253]</sup> On the other hand, an exponential behaviour of the dilatational viscosity with the oscillation frequency ( $\kappa \sim \omega^{-\alpha}$ ) in both states: glass and fluid was observed, Figure IV.16.<sup>[222]</sup>

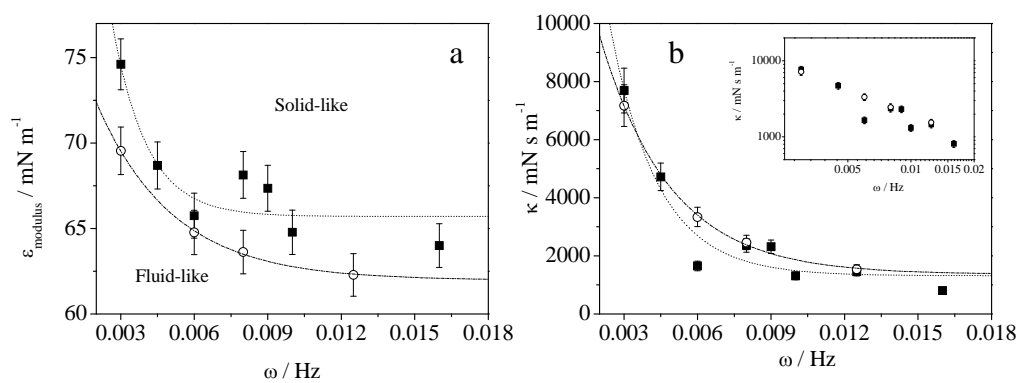
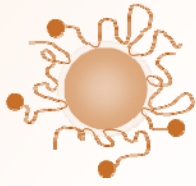
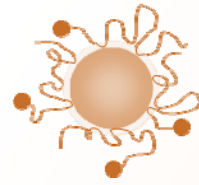
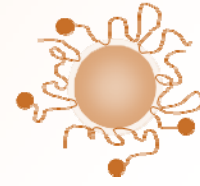
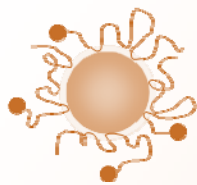


**Figure IV.16.** Elasticity modulus (a) and dilatational viscosity (b) variation with oscillatory frequency for PS-b-MA monolayers on water subphase at 293K (squares) and 307K (circles). Oscillatory barrier experiments were carried out at 10% strain and at a polymer surface concentration of  $1 \text{ mg m}^{-2}$ .





## **V. Preparation and Properties of QDs Films**





## V. Preparation and Properties of QDs Films

Semiconductor quantum dots (QDs) have attracted much attention in recent years owing to their unique chemical and physical properties<sup>[7]</sup> and their applications as building blocks for photovoltaic,<sup>[254, 255]</sup> optoelectronic<sup>[256]</sup> or magnetic devices,<sup>[257]</sup> and for selective recognition of ions<sup>[258]</sup> or biomedical applications<sup>[259]</sup>. Inside the QDs, the hydrophobic nanoparticles present higher quantum efficiency than the hydrophilic ones.<sup>[260]</sup> The current interest in the fabrication of nanodevices is focused on the incorporation of QDs in well defined layers and their immobilization onto solid substrates to obtain good quality devices.<sup>[37, 51]</sup> In this sense the interfacial self-assembly is a selective method to provide well-organized structures with controlled size and shape for the fabrication of optoelectronic devices with QDs.

Moreover, the nanoparticle-polymer blend systems have shown potential applications based on the modulation of the hybrid material properties to achieve significant enhancements.<sup>[8]</sup> However, many nanofillers used in nanocomposites tend to agglomerate by attractive interactions<sup>[153, 261]</sup> decreasing the quality of nanocomposites. Therefore, the most recent efforts involve the use of polymer or surfactant molecules to minimize filler agglomeration. Despite the great interest aroused in the last years, more work must be carried out to develop multifunctional materials with novel electric, magnetic or optical properties.<sup>[63, 262, 263]</sup>

An important issue concerning the properties of filler deposited on solids is to achieve control over the organization and assembly of nanoparticles at interfaces. Many techniques have been used to achieve good-quality nanocomposites.<sup>[264-266]</sup> For hydrophobic nanoparticles an effective method to produce well-defined QDs monolayers could be the Langmuir-Blodgett technique (LB). The LB methodology (LB) has been proposed as a platform that renders the self-assembly process of different hydrophobic nanomaterials at the air-water

interface under well controlled and reproducible conditions.<sup>[1, 2]</sup> Therefore, it offers the possibility of preparing polymer and nanoparticle reproducible films with the control of the interparticle distance necessary to exploit the nanocomposites in technological applications. In addition, the dewetting processes observed in the preparation of LB films can be employed to achieve patterning without a defined template. Despite the above mentioned advantages, when the hydrophobic nanoparticles were transferred from the air-water interface onto glass, silicon or mica substrates without treatment to become the solid surface hydrophobic, low coverage and nanoparticle agglomeration have been observed in LB films.<sup>[69, 140]</sup> To solve this problem some authors have proposed two approaches. In the first one, mixed Langmuir films of surfactants<sup>[67, 146-149]</sup> or polymers<sup>[14, 15, 148, 267]</sup> and hydrophobic nanoparticles are transferred from the air-water interface onto solid substrates by the LB method. This approach seeks to control the assemblage of hydrophobic nanoparticles on water. In the case of polymers, if the polymer is an amphiphilic block copolymer, the most hydrophilic block can favour the nanoparticles spreading and the adsorption on the solid avoiding the 3D aggregation. Moreover, because block copolymers can aggregate at the interface<sup>[59, 63]</sup>, the self-assembly of nanoparticles on these copolymers can be proposed as a way to organize hybrid materials at nanometre scale<sup>[13, 267, 268]</sup>. The second methodology proposed is the interchange of the stabilizer ligand, TOPO, by thiols<sup>[269]</sup>, alkylamines<sup>[270]</sup>, alkylphosphoramines<sup>[7]</sup> and block copolymers<sup>[14, 150, 271, 272]</sup>. Even though some improvements have been achieved with this methodology, the appropriate control of the self-assembly process remains still a challenge. Despite the successful results reported, more efforts must be carried out to develop nanometric structures that may provide new phenomena associated with the size reduction of materials.<sup>[147]</sup> Thus, major advances in the field of self-assembly must be made in order to achieve a better understanding of the process to make use of the functionality offered by nanomaterials and to improve their practical applications.

With this objective in mind, we focus our interest on the self-assembly of CdSe QDs onto solid substrates assisted by the block copolymer PS-MA-BEE. We choose this polymer because it self-assembles at the air-water interface at a given polymer surface concentration.<sup>[273]</sup> Therefore, as polymer assembly modifies the surface properties<sup>[274-277]</sup> it provides us an excellent way to study the role of the surface properties of the precursor Langmuir monolayer on the LB film architecture and photoluminescence properties. On the other hand, styrene/maleic anhydride copolymers have shown potential application in optical waveguides, electron beam resists and photodiodes.<sup>[5, 6]</sup> Therefore, it could be a good candidate to prepare hybrid materials for optoelectronic devices fabrication.<sup>[13, 267, 268]</sup>

To assist the QDs self-assembly, we use the polymer PS-MA-BEE in three different ways. In the first strategy, we use the polymer as matrix to assist the QDs self-assembly at the air-water interface. Thus, a QD/PS-MA-BEE mixed Langmuir monolayer is transferred by the LB method onto the solid. In the second one, a LB film constructed by the polymer PS-MA-BEE is used as coating for the substrate to deposit the QDs Langmuir films. Here the polymer was used in order to control the QDs adsorption on the solid. We use this polymer because it spreads well onto the substrates used. The presence of the polymer on the solid essentially modifies the surface properties of the substrate and could allow tuning the QDs film properties. In the third approach, the QD stabilizer, TOPO, is exchanged by the polymer to analyze the effect of the ligand on the modulation of self-assembly at the air-water interface. This polymer contains a free carboxylic acid group that can interact with the Cd<sup>2+</sup> localized in the surface of the QD core.<sup>[8]</sup> The assemblies obtained with these QDs are transferred by the LB methodology onto the solid wafer.

Accordingly, this chapter is organized in three parts. In the first one, we prepare the LB films by the proposed strategies and study the different film



morphologies by means of atomic force microscopy (AFM) and transmission electron microscopy (TEM). Previously, we carried out the characterization of the Langmuir monolayers which serve as precursors of the LB films by performing the surface-pressure isotherms and by obtaining images of the monolayers using the Brewster Angle Microscopy (BAM).

In the second part of the chapter, the dynamic properties of mixed Langmuir films of PS-MA-BEE and QDs were studied. This part has a double objective. On the one hand, the study of the influence of the shearing on the QD/PS-MA-BEE film morphology and on the other hand, to analyze the dynamic processes involved in the reorganization of the monolayers after shearing due to the knowledge of the dynamic properties of these nanocomposites is essential in order to guarantee the processability, reliability and stability of QD/polymer devices.<sup>[17]</sup> In this sense, the effect of the mixture composition is also investigated.

Finally, as the QDs emission can be used to fabricate LEDs, the fluorescence properties of the QD films were studied analyzing the effect of the self-assemblies morphology on the QD emission properties. This photoluminescence characterization was performed by means of Fluorescence Lifetime Imaging Microscopy (FLIM).

## V.1. Experimental Section

In this section the synthesis, extraction and size characterization of the TOPO-capped CdSe QDs used in this work is briefly presented.

The hydrophobic QDs were synthesized by the method proposed by Yu and Peng.<sup>[278]</sup> This method uses cadmium oxide and selenium powders as precursors. Firstly, a selenium precursor solution was prepared by mixing Se (0.030 g), TOP (0.4 mL) and octadecene (5 mL). The solution is stirred and

warmed as much as necessary to speed dissolution of the Se, forming a colourless solution of trioctylphosphine selenide (TOPSe) valid for five syntheses that was stored at room temperature in a sealed container.

In order to make the QDs synthesis, cadmium oxide (0.013 g), oleic acid (0.6 mL) and octadecene (10 mL) were loaded into a flask with a condenser assembly under Ar flow and agitation (Figure V.1). The mixture was heated to 210°C obtaining a clear and colourless solution and then 1 mL of the solution of TOPSe was injected. Nucleation and growth of the CdSe QDs occurred until the desired particle size was reached by controlling both the temperature and the reaction time. During this stage a change in the colour of the solution was observed from yellow to red as it is shown in the small bottles of Figure V.1 inset. QDs were collected as powder by size-selective precipitation (centrifugation at 1000 rpm) with acetone and dried under vacuum.



**Figure V.1.** Photographs of the QDs synthesis equipment set-up. The inset shows several bottles with QDs in the order that the growth of the nanocrystals occurs: from yellow (1.8 nm diameter) to red (3.4 nm diameter).

According to this synthetic route, the QDs obtained are TOPO-capped. However, in order to ensure that we had achieved a TOPO capping, we carried

out FTIR measurements with QD powder and TOPO, Figure V.2. The FTIR spectrum of nanoparticles presents peaks matching the TOPO spectrum, except for the peak at  $1144\text{ cm}^{-1}$  corresponding to the P=O stretch. It was demonstrated that this peak is shifted between 20 and  $60\text{ cm}^{-1}$  lower relative to bulk TOPO upon complexation with CdSe.<sup>[279]</sup> Therefore, the peak centred at  $1108\text{ cm}^{-1}$  in the FTIR spectrum of QDs can be ascribed to the phosphonate molecules bound to the nanoparticles surface. Thus, by comparing the QDs and TOPO FTIR spectra, namely the P=O stretch frequency<sup>[280]</sup>, we confirmed the presence of the phosphonate ligand on the nanoparticle surface. Furthermore, latter studies indicate that in similar syntheses<sup>[281]</sup> a thorough surface analysis reveals that the nanoparticles are capped by octylphosphonate derivative ligands, which remain bound to the surface ( $\text{Cd}^{2+}$  binding) after precipitation/washing steps.

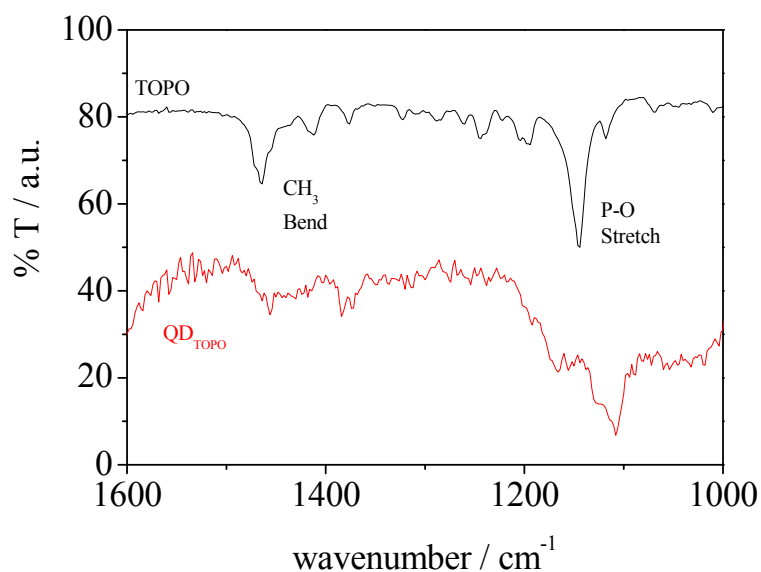


**Figure V.2.** FTIR spectra of TOPO and TOPO-capped QDs, ( $\text{QD}_{\text{TOPO}}$ ), dispersed in KBr. For clarity, the %T-scale is shifted and the  $\text{QD}_{\text{TOPO}}$  spectrum amplified.

The diameter of the QDs was determined by the position of the maximum of the visible spectrum of the QDs dispersed in chloroform<sup>[204]</sup>, Figure V.3. The

value found was  $(566 \pm 1 \text{ nm})$  that corresponds to a nanoparticle diameter of  $(3.41 \pm 0.05 \text{ nm})$ , the red solution bottle in Figure V.1 inset. The QD size selected is the most controllable size in the synthesis used as the nanocrystal growth and population is controlled by time. Therefore, by this synthesis the maximum diameter, *ca.* 4 nm, and the greatest QDs population are achieved at longer times. The concentration of nanocrystals was calculated from the UV-Vis absorption spectrum of the QDs solutions by using the extinction coefficient per mole of nanocrystals at the first excitonic absorption peak.<sup>[204]</sup> UV-Vis absorption spectra were recorded on a Shimadzu UV-2401PC spectrometer, Figure V.3.

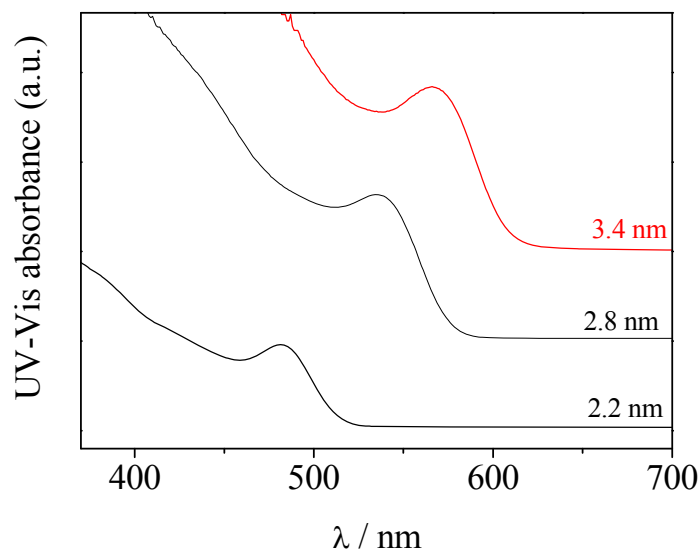


**Figure V.3.** Normalized absorption spectra of several CdSe QDs solutions in chloroform. The diameter of the nanoparticles is also indicated.

## V.2. Preparation of QDs Films

### V.2.1. Langmuir and Langmuir-Blodgett Films of QDs and PS-MA-BEE

The first strategy employed was to use the polymer as matrix to assist the QDs self-assembly. Therefore, we transfer mixed Langmuir monolayers of

TOPO-capped CdSe QDs and PS-MA-BEE from the air-water interface onto mica. As small changes on the composition of a mixed monolayer modify the structure of the film,<sup>[172, 174, 250, 282]</sup> we study the effect of the polymer concentration on the surface properties of the Langmuir films precursors of the LB films. The characterization of these mixed monolayers allows us to select monolayers with very different surface properties and to transfer them onto mica, in order to investigate the role of these properties on both, the morphology of QDs films and the self-assembly process.

The surface properties of the Langmuir monolayers were studied by recording the surface pressure-concentration isotherms of the pure components and mixtures of QDs and polymer at different composition. According to results presented in chapter IV, the LB films obtained by transferring PS-MA-BEE Langmuir monolayers prepared by addition consist of metastable states. Thus, we prepare the Langmuir monolayers by compression because this method renders the most reproducible and stable LB films in the case of the polymer. Figure V.4a shows the isotherms of different mixtures and pure components, QDs and PS-MA-BEE.

In the case of mixed monolayers it is well established that their surface properties depend on the spreading technique.<sup>[172, 283, 284]</sup> Therefore, we test the isotherm properties of monolayers obtained by spreading both components at the interface, named as co-spreading, or adding the components separately. In all cases the isotherms were very stable. A representative example for mixed monolayers of polymer mole fraction  $X_p = 0.50$  is presented in Figure V.4b. Significant differences between the isotherms can be observed. Thus, from the three spreading procedures the densest monolayer is that obtained by co-spreading. This behaviour was observed in other systems<sup>[172, 283]</sup> and ascribed to the existence of attractive interactions between polymer and QDs molecules in the spreading solution<sup>[283]</sup>. As was demonstrated in our previous work,<sup>[172, 284]</sup> the

co-spreading method proved to be the most reproducible technique and consequently, was chosen to build the mixed QD/PS-MA-BEE monolayers.

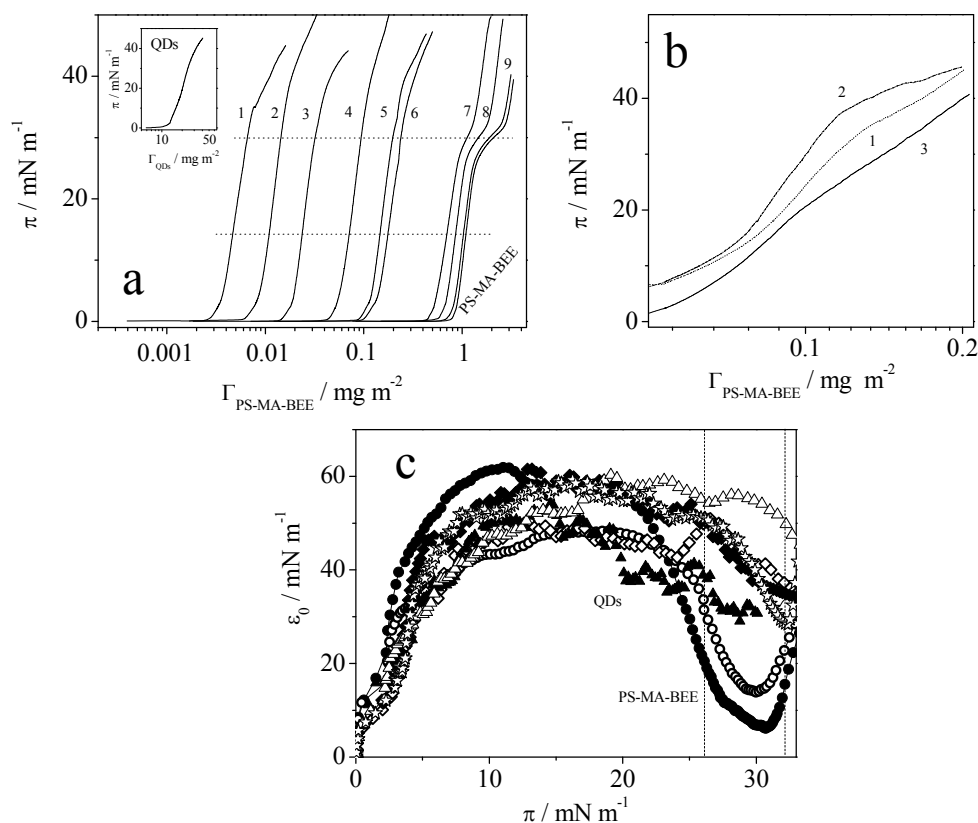


**Figure V.4.** (a) Surface pressure isotherms of mixed Langmuir monolayers of QDs and PS-MA-BEE with polymer mole fraction of: 0.07 (1); 0.15 (2); 0.35 (3); 0.55 (4); 0.65 (5); 0.80 (6); 0.93 (7); 0.96 (8); 0.98 (9); 0.99 (10) and pure PS-MA-BEE. The inset shows the QDs surface pressure isotherm. The dotted lines indicate the surface pressures for the LB deposition: 14 and 30  $\text{mN m}^{-1}$ . (b) Surface pressure isotherms for QD/PS-MA-BEE mixed monolayers at polymer mole fraction of 0.50 obtained with separate spreading of QDs and PS-MA-BEE (1) and PS-MA-BEE and QDs (2), respectively, and co-spreading (3). (c) Equilibrium surface elasticity vs. surface pressure for several mixed Langmuir monolayers of QDs and PS-MA-BEE at different polymer mole fraction: QDs (closed triangles); 0.07 (open rhombi); 0.35 (closed rhombi); 0.55 (open triangles); 0.65 (stars); 0.96 (open circles); and PS-MA-BEE (closed circles). The dashed lines delimit the surface pressures where the plateaux in the surface pressure isotherms appear. The isotherms were recorded by symmetric barrier compression at 5  $\text{mm min}^{-1}$  and 23°C.

The QDs and PS-MA-BEE isotherms agree with those reported previously.<sup>[67, 273]</sup> In mixed monolayers, at high polymer concentration,  $X_p \geq 0.95$ , the isotherms present a plateau at the surface pressure value of  $30 \text{ mN m}^{-1}$ . This plateau could be related to phase coexistence and has been previously observed in other block-copolymer isotherms.<sup>[57, 285, 286]</sup> To gain insight into the states of the monolayers we have calculated the equilibrium elasticity modulus,  $\epsilon_0$ , from the surface pressure isotherms. For the sake of comparison the elasticity values are represented against the surface pressure values in Figure V.4c. These results show that the monolayer elasticity increases with the surface pressure and reaches a maximum at a given surface pressure. The maximum position is shifted to higher surface pressures for mixed monolayers. Beyond the maximum, when the surface pressure is further increased, the elasticity decreases and for monolayers with surface compositions  $X_p \geq 0.95$  the elasticity goes through a minimum at the surface pressure value of  $30 \text{ mN m}^{-1}$ . The region around the elasticity minimum corresponds to the plateau in the surface pressure isotherm. For comparative purposes dashed lines in Figure V.4c delimit the plateau region.

Comparison between the elasticity and surface pressure isotherms of the polymer PS-MA-BEE with those reported for other Langmuir monolayers of block copolymers allowed us to obtain information about the polymer states at the interface. Results in the literature demonstrated that at low surface pressures the polymer blocks presents an almost flat conformation without tails protruding from the subphase, in this regime the elasticity increases with the surface concentration until it reaches the maximum value. In this state the monolayer can be formed by aggregates with different features.<sup>[57, 248, 286]</sup> As it is discussed next, the polymer PS-MA-BEE aggregates in stripes. At surface pressures beyond the elasticity maximum, the polymer hydrophilic blocks protrude into the water subphase and the elasticity values decrease until a minimum at which the polymer brush conformation predominates. In this region the aggregates coexist with brush structures, and it corresponds to the plateau in the surface pressure

isotherms. In our system the phase coexistence is between stripes and brushes. For surface pressures beyond the elasticity minimum, is generally admitted that interactions between the polymer blocks lead to a further increase of the surface elasticity.<sup>[285, 287]</sup>

For mixed QD/polymer monolayers, the morphology of the elasticity curves, Figure V.4c, also depends on the surface composition. From results in Figure V.4c, it is possible to notice that the minimum in the elasticity curve appears for mixed monolayers with high polymer concentration,  $X_p \geq 0.95$ . Taking into account that the elasticity minimum also appears in the polymer monolayer and it was ascribed to the polymer brush state, the behaviour observed in mixtures seems to indicate that the brush regime is only reached in mixed monolayers with high polymer concentration.

To gain insight into the morphology of QD/PS-MA-BEE monolayers, we use the Brewster Angle Microscopy (BAM). Several images corresponding to monolayers at two surface pressure values,  $14 \text{ mN m}^{-1}$  and  $30 \text{ mN m}^{-1}$  and different surface compositions are collected in Figure V.5. BAM images of monolayers at  $14 \text{ mN m}^{-1}$  and low polymer concentration, Figures V.5a and b, show QD agglomerates. However, when the polymer concentration increases, the QD agglomeration decreases, Figures V.5c and d. This behaviour can be interpreted if one considers that, in the absence or at low polymer concentration, the interactions between water subphase and the QDs stabilizer, TOPO, are too weak, and they promote the agglomeration of nanoparticles at the air-water interface<sup>[143, 153]</sup>. However, when the polymer concentration increases, attractive interactions between the polymer hydrophobic block and the alkyl chains of TOPO favour the QDs spreading on the water surface across the polymer hydrophilic blocks avoiding the QDs agglomeration.<sup>[67, 243, 244]</sup>



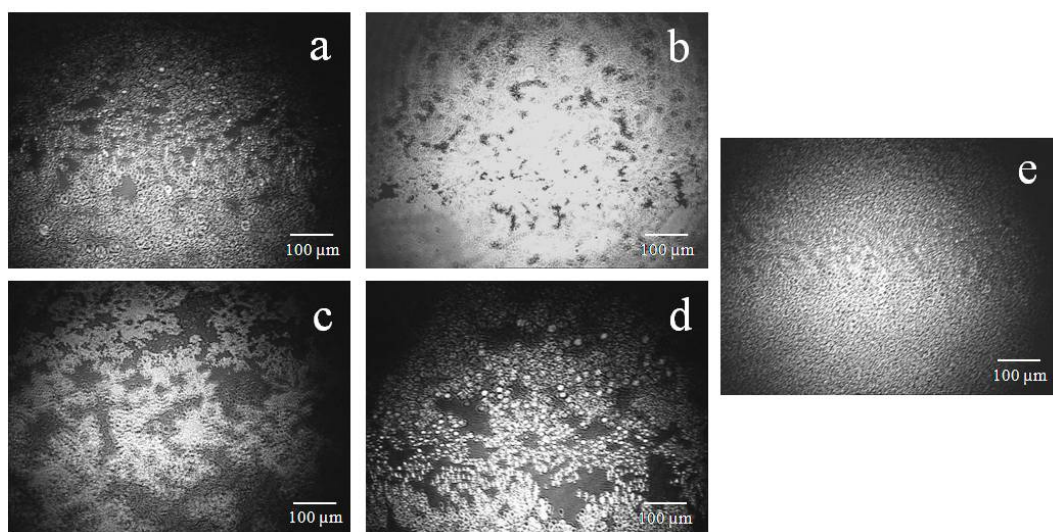


**Figure V.5.** BAM images ( $800 \times 600 \mu\text{m}$ ) at  $14 \text{ mN m}^{-1}$  for different QD/PS-MA-BEE mixed monolayers with different polymer mole fractions: (a) pure QDs; (b) 0.50; (c) 0.96 and (d) 0.98. BAM image of QD/PS-MA-BEE mixed monolayer at  $30 \text{ mN m}^{-1}$  and at polymer mole fraction of 0.96 (e).

Monolayers with high surface coverage ( $\pi = 30 \text{ mN m}^{-1}$ ) are constituted by domains so close-packed that BAM images do not allow us to visualize details of its morphology. As illustrative example, we present in Figure V.5e the BAM image of the mixed monolayer at  $30 \text{ mN m}^{-1}$  and  $X_p = 0.96$ .

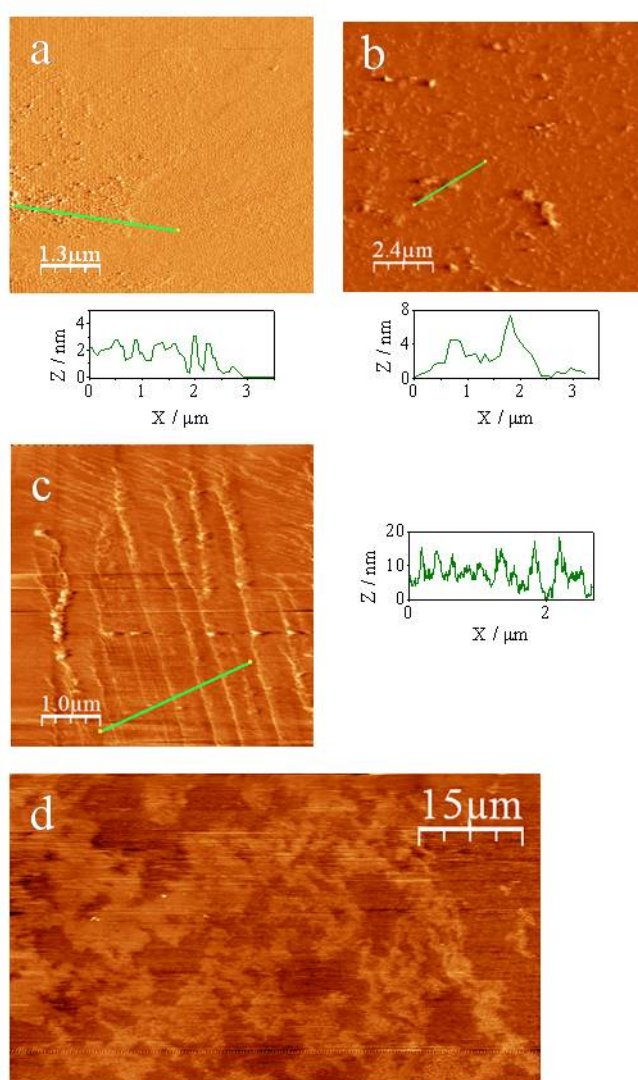
The next step was to transfer the polymer Langmuir monolayers from the air-water interface onto mica by using the Langmuir-Blodgett technique. The monolayers were transferred at the surface pressure values of 14 and  $30 \text{ mN m}^{-1}$ . We chose these monolayers because correspond to representative states of the polymer monolayer. Thus, the monolayer at the surface pressure of  $14 \text{ mN m}^{-1}$  is far from the brush regime and corresponds to the most elastic surface state, while the monolayer at  $30 \text{ mN m}^{-1}$  corresponds to the polymer brush regime, minimum in the elasticity curve. For the sake of comparison, we have also transferred QDs monolayers at the same surface pressure values,  $14$  and  $30 \text{ mN m}^{-1}$ , onto mica without polymer.

The AFM images of QDs films are collected in Figures V.6a and b. As can be seen in Figure V.6a the QDs film is mainly constituted by QDs 3D agglomerates of different sizes and when the surface concentration of the QDs transferred was further increased until a surface pressure value of  $30 \text{ mN m}^{-1}$ , the density of agglomerates increases and even more 3D aggregates are formed. This fact can be interpreted if one considers that due to the low affinity of the QDs stabilizer TOPO and the solid mica, the nanoparticles do not spread well. This favours the QD 3D agglomeration.

On the other hand, the AFM images of polymer LB films, Figures V.6c and d, revealed that the films obtained at different surface densities have different morphologies. Thus, the polymer aggregates in stripes with a height profile of  $\sim 8\text{--}10 \text{ nm}$  when the surface pressure of the Langmuir monolayer transferred on mica is  $14 \text{ mN m}^{-1}$ , Figure V.6c,<sup>[273]</sup> while films with domains separated by holes were observed when the surface coverage increases until  $30 \text{ mN m}^{-1}$ , Figure V.6d. The domain height profile found was  $\sim 2 \text{ nm}$ , which agrees with the polymer thickness calculated by means of molecular mechanic MM2 calculations ( $2.1 \text{ nm}$ ).

In polymer LB films the existence of two different features depending on the polymer concentration points to two distinct dewetting mechanisms. Thus, stripes and other 2D structures were previously observed and interpreted by spinodal dewetting mechanism.<sup>[243-245]</sup> While, domains separated by holes were observed in films in which the gravitatory effects are important.<sup>[44]</sup> In an attempt to interpret the different behaviour observed it was necessary to analyze the driving forces involved in the surface arrangement. Taking into account that the molecular weight of this polymer is too low, one expects that the gravitatory effects were neglected; however, it is necessary to compare this effect with that of the capillary waves. It is well established that the damping coefficient passes through a maximum at low elasticity values<sup>[288]</sup> and decreases when the elasticity modulus increases. Accordingly, in the case of the most elastic monolayer ( $\pi = 14$

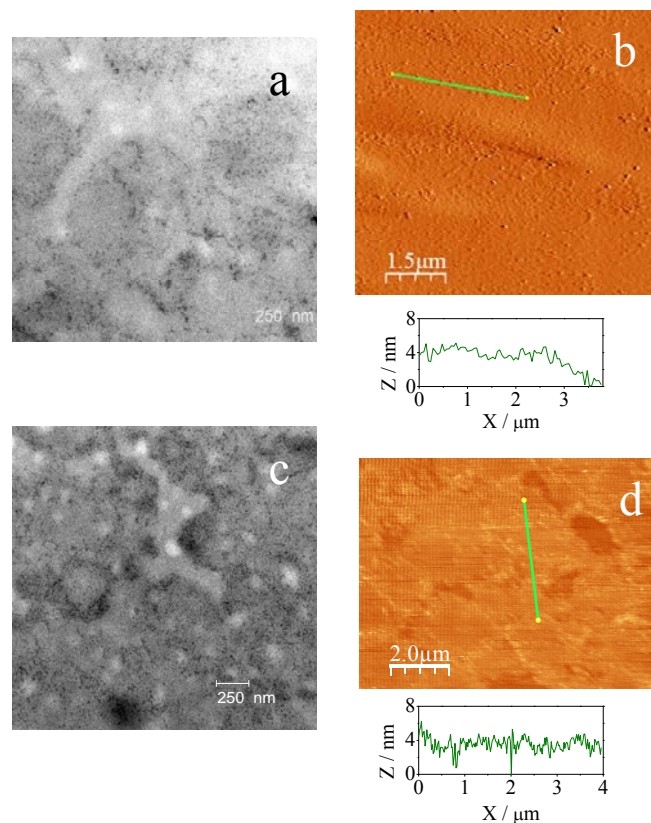
$\text{mN m}^{-1}$ ), the capillary effects could predominate against the gravitatory ones and the dewetting mechanism is driven by the capillary waves resulting in films constituted by stripes. Conversely, in less elastic monolayer ( $\pi = 30 \text{ mN m}^{-1}$ ), the capillary waves are quickly damped and the polymer film breaks in domains separated by holes due to gravitatory effects. Consequently, the growth of holes dewetting mechanism predominates against the spinodal one in this monolayer state.



**Figure V.6.** AFM images of QDs (a, b) and PS-MA-BEE (c, d) LB films deposited at the surface pressures values of (a, c)  $14 \text{ mN m}^{-1}$  and (b, d)  $30 \text{ mN m}^{-1}$ .

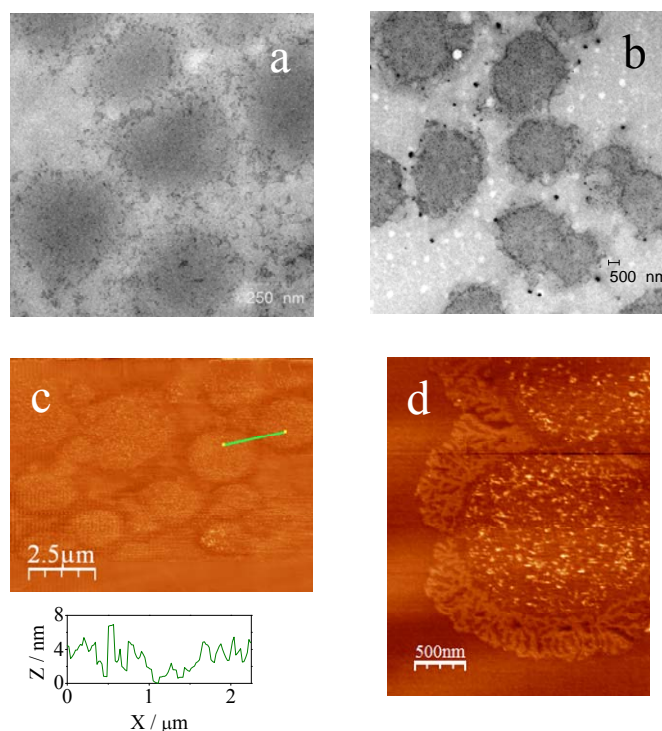
We transferred mixed monolayers of polymer PS-MA-BEE and CdSe QDs from the air-water interface onto mica by the LB methodology. In order to study the effect of the surface properties of the Langmuir monolayer precursors of the LB films on the nanoparticles self-assembly, we have transferred Langmuir monolayers at the surface pressure values of  $14 \text{ mN m}^{-1}$  and  $30 \text{ mN m}^{-1}$ . As in the case of pure components, we chose these values because correspond to representative states of the polymer monolayer: stripes and brush-stripes phase coexistence. To study the effect of surface composition on the self-assembly process, we transfer monolayers containing different polymer concentration expressed as polymer mole fraction,  $X_p$ , at the two surface pressure values selected,  $14$  and  $30 \text{ mN m}^{-1}$ .

Figure V.7 shows the AFM and TEM images of some mixed LB films prepared with Langmuir monolayers at the surface pressure value of  $14 \text{ mN m}^{-1}$  and different surface composition. Results presented in this figure indicate that, even when the polymer concentration is low, Figures V.7a and b, mixed LB films are denser than the LB films prepared by transferring exclusively QDs onto mica, Figure V.6a. This can be interpreted by considering that the QDs interact with the most hydrophobic block of the polymer, styrene block,<sup>[264]</sup> remaining adsorbed on the polymer and, the hydrophilic blocks of the polymer favour the interaction with the solid increasing the efficiency of the transfer process.



**Figure V.7.** TEM (a, c) and AFM (b, d) images of mixed QD/PS-MA-BEE LB films deposited at the surface pressure of  $14 \text{ mN m}^{-1}$ . The film composition expressed as polymer mole fraction is: 0.35 (a, b); and 0.50 (c, d).

When the polymer concentration increased the film begins to break, see Figures V.7c and d. Moreover, for polymer concentrations above  $X_p > 0.5$  the QDs films presents the formation of domains distributed in islands, Figures V.8a to c. Figure V.8d presents a high magnification AFM image of these domains, showing that the islands are surrounded by polymer molecules. It is important to note that the morphologies observed by AFM and TEM agree with each other and that the domains height determined from AFM is independent of the polymer concentration. The average height profile value of 4 nm is compatible with the diameter of the QDs ( $3.41 \pm 0.05 \text{ nm}$ ).



**Figure V.8.** TEM (a, b) and AFM (c, d) images of mixed QD/PS-MA-BEE LB films deposited at the surface pressure of  $14 \text{ mN m}^{-1}$ . The film composition expressed as polymer mole fraction is: 0.65 (a); and 0.98 (b, c, d).

Our results also demonstrated that even when the QDs composition was too small, the film morphology of QD/PS-MA-BEE mixed films is different to that corresponding to the polymer PS-MA-BEE. This fact indicates that small concentrations of QDs modify the interactions between the polymer molecules<sup>[289-291]</sup> distorting the polymer film architecture.

To analyze the effect of the polymer concentration on the QD domain size, a statistical analysis of domain dimensions was carried out. Results are collected in Table V.1 and show that the domain size decreases as the polymer mole fraction increases.

**Table V.1.** Average values of the feature dimensions of QD/PS-MA-BEE mixed LB films obtained from AFM measurements.

Domains (dots) at $\pi = 14 \text{ mN m}^{-1}$			Holes at $\pi = 30 \text{ mN m}^{-1}$		
$X_p$	X-direction / $\mu\text{m}$	Y-direction / $\mu\text{m}$	$X_p$	X-direction / $\mu\text{m}$	Y-direction / $\mu\text{m}$
0.65	$2.22 \pm 1.36$	$2.15 \pm 1.29$	0.95	$0.83 \pm 0.19$	$0.77 \pm 0.20$
0.96	$1.14 \pm 0.39$	$1.05 \pm 0.31$	0.96	$0.57 \pm 0.18$	$0.47 \pm 0.16$
0.99	$0.50 \pm 0.23$	$0.54 \pm 0.23$			

Reported values are averages and the error represents the standard deviation determined from at least 50 surface features.

We have also transferred QD/PS-MA-BEE Langmuir films at the surface pressure  $30 \text{ mN m}^{-1}$  from the air-water interface onto mica by LB technique. Representative AFM and TEM images of these LB films are collected in Figures V.9 and V.10. As was observed in mixed films at  $14 \text{ mN m}^{-1}$ , the film coverage increases with the polymer addition and the 3D agglomeration of nanoparticles is avoided even at low polymer concentration, Figures V.9a and b. When the polymer concentration increases two different behaviours can be observed depending on the surface composition according to the LB films images. In the first one, for LB films of polymer composition below  $X_p < 0.95$  shown in Figures V.9c-f, the films are constituted by large QDs domains of height profile 3 nm. The evolution of the domain size with the polymer concentration is similar to that observed for films prepared from Langmuir monolayers at the surface pressure of  $14 \text{ mN m}^{-1}$ . Thus, when the polymer concentration increases the film evolves to small domains and the distance between domains increases.

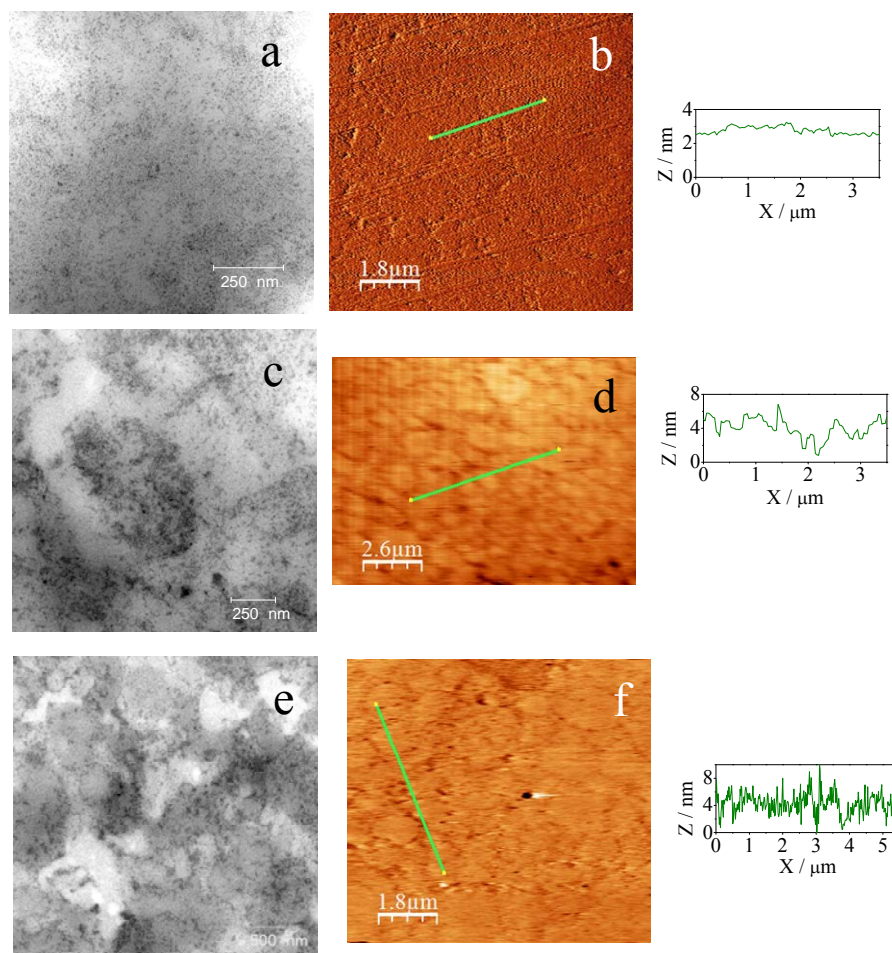


**Figure V.9.** TEM (a, c, e) and AFM (b, d, f) images of mixed QD/PS-MA-BEE LB films at the surface pressure of  $30 \text{ mN m}^{-1}$ . The film composition expressed as polymer mole fraction is: 0.35 (a, b); 0.50 (c, d); and 0.65 (e, f).

The second behaviour, Figure V.10, was observed for monolayers with high polymer concentration,  $X_p \geq 0.95$ . At this polymer concentration range the surface pressure isotherms present a plateau and the elasticity values go through a minimum. The AFM and TEM images of these films, Figures V.10a-d show well-organized hexagonal networks. It is interesting to note that the height of rims around the holes was 4 nm, which is compatible with the diameter of the CdSe QDs dissolved in chloroform (3.4 nm). This fact indicates that the nanoparticles are mainly localized in the rims<sup>[15]</sup> and do not form 3D aggregates. The hole size



of the hexagonal domains was measured from the AFM images by taking an average of at least 50 holes per sample and the statistical results are presented in Table V.1. Results show that the hole size in the network decreases with the polymer concentration. This behaviour agrees very well with results in previous work corresponding to mixed LB films of the polymer PMAO and QDs.<sup>[284]</sup> Finally, when the polymer concentration is further increased above  $X_p \geq 0.99$ , the QDs concentration is too low and the film morphology is similar to that corresponding to the polymer film, Figure V.10e, with regions of height 4 nm, which indicates the presence of QDs.

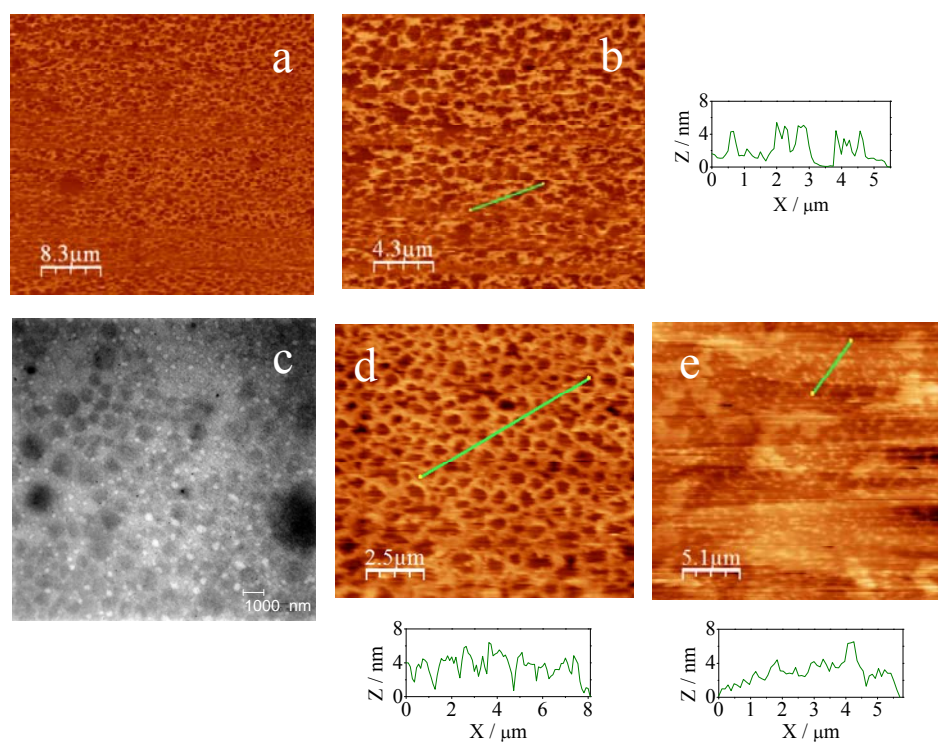


**Figure V.10.** AFM (a, b, d, e) and TEM (c) images of mixed QD/PS-MA-BEE LB films at the surface pressure of  $30 \text{ mN m}^{-1}$ . The film composition expressed as polymer mole fraction is: 0.95 (a, b); 0.96 (c, d); and 0.99 (e).

The hexagonal network structures in this system are similar to those observed for mixed QD/PMAO LB films,<sup>[284]</sup> and both are interpreted in terms of nucleation and growth of holes dewetting processes<sup>[44]</sup>. Focus the attention on the

nucleation and growth of holes, this dewetting mechanism is driven by gravitational effects, consequently, it is easy to understand that this effect predominates in films containing high molecular weight material such as the polymer PMAO (40 kDa).<sup>[284]</sup> However, it is not so evident in the QD/PS-MA-BEE films because the polymer PS-MA-BEE (2.5 kDa) is too small. To interpret this behaviour it is necessary to analyze the balance between the driving forces involved in the surface arrangement: gravitational and capillary forces, Figure V.11. As was mentioned, it is well established that the damping coefficient passes through a maximum at low elasticity values<sup>[288, 292]</sup> and decreases when the elasticity modulus increases. Thus, according to the elasticity curves, Figure V.4c, the elasticity goes through a minimum for QD/PS-MA-BEE monolayers at the surface pressure value of  $30 \text{ mN m}^{-1}$  and for polymer concentrations above 0.95. Consequently, in these monolayers the capillary waves are quickly damped and the film breaks in domains separated by holes due to gravitational effects. Conversely, the capillary waves for monolayers with higher elasticity values ( $\pi = 14 \text{ mN m}^{-1}$  or  $\pi = 30 \text{ mN m}^{-1}$  and  $X_p < 0.95$ ), do not damp so quickly and they drive the dewetting mechanism. In these situations, the spinodal dewetting mechanism predominates against the growth of holes process leading to circular QDs domains.

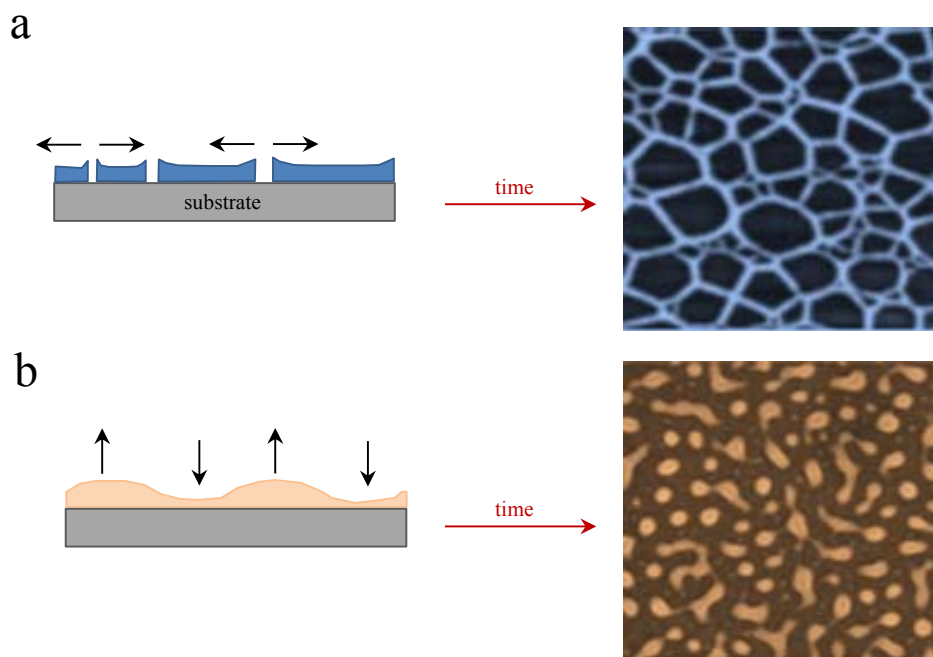


**Figure V.11.** Schematic representation of the time evolution of ruptured thin films by the two dewetting mechanism: (a) Dewetting by nucleation, growth and coalescence of holes; (b) spinodal dewetting. (*Adapted from Gentili, 2012*<sup>[44]</sup>)

### V.2.2. Langmuir-Blodgett Films of QDs transferred onto a LB Film of Polymer

An alternative approach to fabricate QDs films by using LB technique is to use polymers as coating for the substrate to deposit the nanoparticles. The methodology consists in transferring QDs from the air-water interface onto the LB film constituted by a PS-MA-BEE film. As was shown in the previous chapter, this polymer presents a good adhesion onto mica and forms different features depending on the surface concentration. Accordingly, the deposition of the polymer film onto the substrate modifies the surface properties of the solid and therefore, could allow us to modulate the QDs self-assembly.

In previous section, we have characterized the Langmuir monolayers precursors of the LB films by the surface pressure and elasticity isotherms. Thus,

we choose the polymer LB film prepared from the Langmuir monolayer at the surface pressure of  $14 \text{ mN m}^{-1}$ , corresponding to the maximum elasticity state, because it is composed by wide stripes that could favour the adsorption of the QDs. At this state, a good polymer coverage is achieved. On the other hand, the QDs elasticity isotherm obtained from the surface pressure isotherm also shows a maximum at the surface pressure of  $9 \text{ mN m}^{-1}$ . Thus, this surface pressure is chosen for the QDs LB deposition together with a higher value,  $30 \text{ mN m}^{-1}$ , in order to evaluate the effect of QDs concentration on the film morphology. To compare the effect of the polymer layer, Figure V.12 present the AFM and TEM images of the QD LB film at  $9 \text{ mN m}^{-1}$  and  $30 \text{ mN m}^{-1}$  directly deposited onto mica.

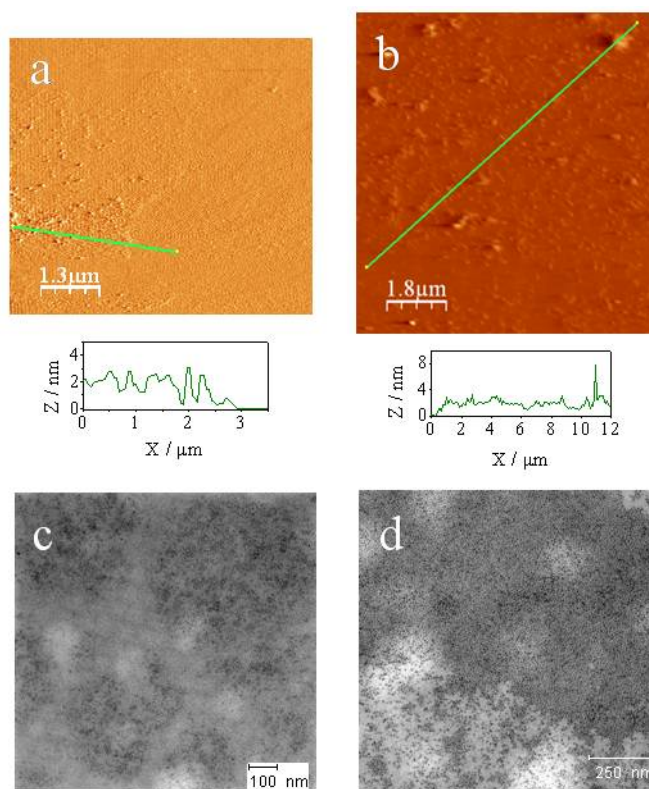


**Figure V.12.** AFM (a, b) and TEM (c, d) images of QDs LB films deposited at the surface pressures of  $9$  (a, c) and  $30$  (b, d)  $\text{mN m}^{-1}$ .

We transfer the QDs onto the polymer LB film at two different surface pressure values 9 and 30 mN m<sup>-1</sup>. Figure V.13 shows the AFM and TEM images of these LB films. The images indicate that the film is mainly constituted by QD domains with irregular architecture. The density of domains increases when the surface pressure of the QDs Langmuir monolayer increases, Figure V.13d. However, the increase of the population of domains does not modify the features of QDs and island-like QDs aggregates are also observed. It is interesting to note that the nanoparticles are randomly adsorbed on the polymer LB film. Consequently, the stripes observed in the polymer LB film cannot be used as pattern for nanoparticle deposition. Besides, the AFM height profiles in Figure V.13 indicate that no 3D aggregates are formed. Thus, by comparing with QD films directly deposited onto mica, Figure V.12, the polymer film avoids the QD agglomeration.

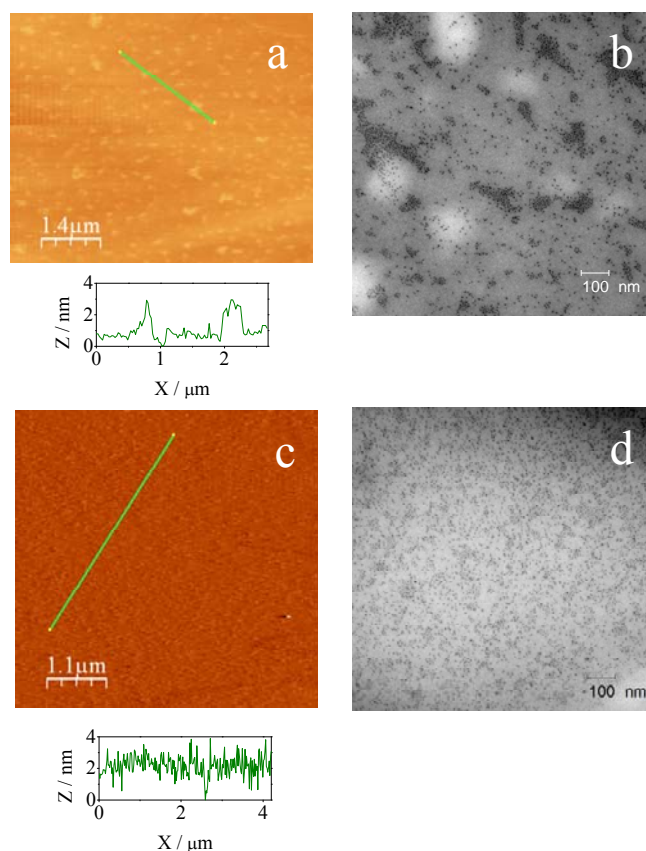


**Figure V.13.** AFM (a, c) and TEM (b, d) images of QDs LB films deposited onto a PS-MA-BEE LB film at the surface pressures of 9 (a, b) and 30 (c, d)  $\text{mN m}^{-1}$ . The polymer LB film was deposited at the surface pressure of  $14 \text{ mN m}^{-1}$ .

To understand the differences observed between the QDs assembly on the mica and on the polymer LB film, it is necessary to analyze the driving forces involved in the surface arrangement. In the case of bare mica, the QD agglomeration in the films deposited is mainly due to the preferential attractions between the nanoparticles<sup>[143]</sup> in comparison with the QD-mica attractions. This occurs in low energy substrates such as mica ( $0.38 \text{ mN m}^{-1}$ ). However, when the substrate is covered with the polymer, the surface energy is increased minimizing the dewetting processes.<sup>[293, 294]</sup> In this situation, the nanoparticles assembly process can be related to the interaction between the neighbouring layers.<sup>[295]</sup> Accordingly, we interpret our results by analyzing the ability of QDs to wet the

polymer coating by means of the spreading parameter. The spreading parameter has been used previously in LB films to evaluate their stability<sup>[296]</sup> and to interpret the nanostructures formed by nanoparticles on substrates with different natures<sup>[297]</sup>. Moreover, it is established that the ability of a thin film to wet the substrate and form smooth films is related to the interfacial energy when there is no specific interactions between the layers.<sup>[298]</sup> Therefore, we analyze the spreading parameter indicative of the balance between QD-polymer (adhesive forces) and QD-QD (cohesive forces) intermolecular forces.

The spreading parameter,  $S$ , is calculated by:

$$S = \gamma_{\text{polymer/air}} - (\gamma_{\text{QD/polymer}} + \gamma_{\text{QD/air}});$$

where  $\gamma_{\text{polymer/air}}$ ,  $\gamma_{\text{QD/polymer}}$  and  $\gamma_{\text{QD/air}}$ , represent the surface tensions at the polymer-air, QDs-polymer and QDs-air, interfaces respectively.<sup>[44]</sup> The QDs surface tension value used in these calculations was taken from the literature as  $\gamma_{\text{QD/air}} = 33 \text{ mN m}^{-1}$ .<sup>[13]</sup> To determine the  $\gamma_{\text{polymer/air}}$ , we consider the surface tension value of the hydrophobic moiety exposed to the air. In this case, taking into account that it is a Y-type LB deposition, the polystyrene (PS) block is oriented to the air, therefore  $\gamma_{\text{polymer/air}}$  can be approximated as the polystyrene/air surface tension  $39.3 \text{ mN m}^{-1}$ .<sup>[299]</sup> On the other hand, since the interface for PS-MA-BEE//QDs films is constituted by styrene groups of the polymer PS-MA-BEE and the hydrocarbon chains corresponding to the QDs stabilizer TOPO, the  $\gamma_{\text{QD/PSMABEE}}$  was taken as the interfacial tension between polystyrene and polyethylene molecules<sup>[500]</sup>,  $8.3 \text{ mN m}^{-1}$ .<sup>[299]</sup> By using these interfacial tension values the spreading parameter  $S$  estimated for the PS-MA-BEE//QDs system is negative. This means that the QDs do not spread well on the PS-MA-BEE LB film.<sup>[44]</sup> This could be consequence of weaker interaction between the nanoparticles stabilizer, TOPO, and the polymer PS-MA-BEE deposited on the solid as compared with the QD-QD interactions. Accordingly, the QD-QD attractive interaction prevails against the PS//QD interaction promoting the QDs aggregation forming islands.

In order to gain insight into the interactions of the layers, QDs and polymer, we analyze the properties of mixed Langmuir monolayers of TOPO, the stabilizer molecule of QDs, and PS-MA-BEE. The aim is to study their interaction in order to get a better understanding of the QD/PS-MA-BEE miscibility at the air-water interface.

We study the properties of mixed Langmuir monolayers of PS-MA-BEE and TOPO, containing different compositions by recording the surface-pressure isotherms. Figure V.14a shows these isotherms. The isotherm recorded for TOPO is in good agreement with that presented by other authors.<sup>[99]</sup> In order to analyze the nature of interactions between TOPO and PS-MA-BEE we calculate the dependence of the excess area,  $A^{\text{exc}}$  with the surface composition. Figure V.14b shows the composition dependence of the  $A^{\text{exc}}$  with the TOPO mole fraction at the interface,  $X_T$ , for different states. From Figure V.14b it is possible to conclude the existence of positive deviations from the ideality for mixtures with  $X_T < 0.6$ . Above this TOPO surface composition, the mixture is close to the ideal behaviour showing slight negative deviations for  $X_T = 0.8$ . Positive deviations indicate repulsive interactions between the two components, TOPO and PS-MA-BEE, while  $A^{\text{exc}}$  values close to zero correspond to ideal mixtures or immiscibility of components on the monolayer.<sup>[99, 301]</sup>



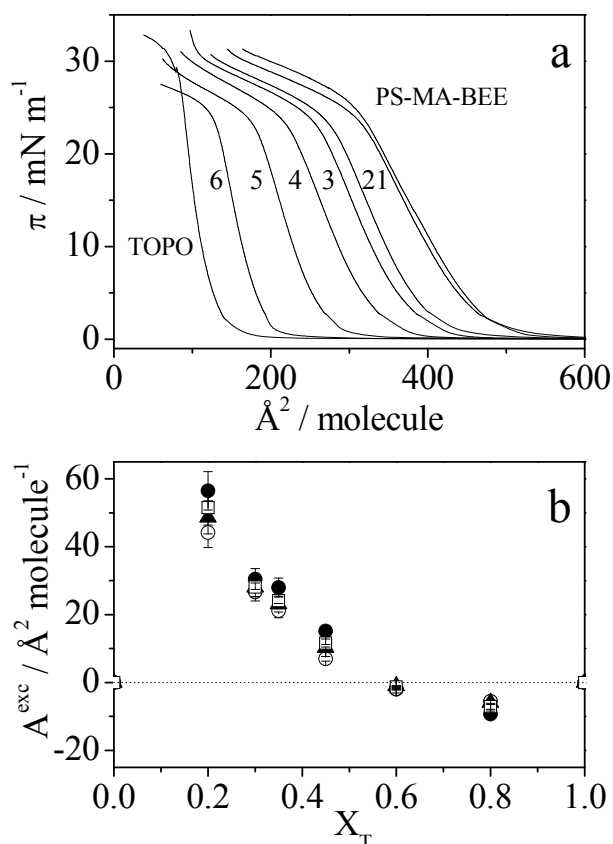


**Figure V.14.** (a) Surface pressure-area isotherms recorded for pure TOPO and PS-MA-BEE monolayers and for mixed monolayers of TOPO with PS-MA-BEE by symmetric barrier compression at  $5 \text{ mm min}^{-1}$  and  $23^\circ\text{C}$ . The TOPO mole fraction values are: 0.20 (1), 0.30 (2), 0.35 (3), 0.45 (4), 0.60 (5) and 0.80 (6). (b) Excess molecular area ( $A^{\text{exc}}$ ) vs composition for mixtures of TOPO with PS-MA-BEE at different surface pressures:  $5 \text{ mN m}^{-1}$  (solid circles),  $10 \text{ mN m}^{-1}$  (open squares),  $15 \text{ mN m}^{-1}$  (solid triangles) and  $20 \text{ mN m}^{-1}$  (open circles).

Our results demonstrate that the origin of the interactions between TOPO and PS-MA-BEE molecules depends on the surface composition at the interface. Thus, when the polymer predominates, repulsions between the polymer chains govern the structure of the monolayer. In contrast, when the TOPO concentration increases, a quasi-ideal behaviour between TOPO and PS-MA-BEE become stronger and dominate the structure of the monolayer.

Although it is not possible to establish a direct comparison, the results observed in mixed monolayers of PS-MA-BEE and TOPO point to the existence of repulsions between the QD stabilizer, TOPO, and the polymer PS-MA-BEE. This fact can be consistent with the spreading parameter value calculated above and the formation of QD islands in the bilayer system.

### V.2.3. Surface Ligand Exchange: PSMABEE-capped QDs

Previous work demonstrated that the nature of the surface cap influences the interactions between QDs and consequently, the properties of the nanoparticles.<sup>[8]</sup> Therefore, to study the effect of the capping molecule on the QDs self-assembly at the interface and to exploit the self-assembly properties of copolymers at the air-water interface for the organization of QDs,<sup>[150]</sup> we prepare QDs capped with the polymer PS-MA-BEE, QD<sub>p</sub>, hereafter. The surface modification is achieved through surface ligand exchange reaction<sup>[139]</sup>.

#### V.2.3.1. Surface Ligand Exchange Process

It has been reported that it is possible the surface ligand modification of QDs by exchange reactions. In the case of TOPO ligand, it could be replaced by free carboxylic (-COOH), amine (-NH<sub>2</sub>) or thiol (-SH) groups under mild conditions such as sonication or reflux by interaction of the surface core Cd<sup>2+</sup> with the oxygen, nitrogen or sulfur, respectively.<sup>[8]</sup> In our case, we could use the polymer PS-MA-BEE because it has a free carboxylic group. Moreover, as the polymer has an anhydride block, offers the possibility to open the maleic anhydride ring by hydrolysis to form carboxylic acid groups that provides functionality to the particles enabling the immobilization of other molecules such as proteins on the QDs film surface.<sup>[70]</sup>

To replace the TOPO surface ligand on the QDs by the polymer PS-MA-BEE we use the method proposed by Xu and collaborators.<sup>[139]</sup> The method consists in exposing the QDs stabilized by TOPO to a large excess of the competing capping group. Thus, the TOPO-capped QDs powder was dissolved in a PS-MA-BEE ( $17 \text{ mg mL}^{-1}$ ) solution by using  $\text{CHCl}_3/\text{CH}_3\text{OH}$  (5:1, v/v) as solvent and then were sonicated for 30 min, Figure V.15.

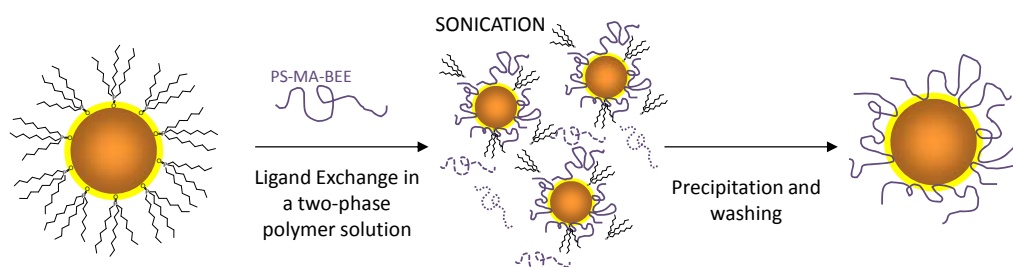


**Figure V.15.** Scheme of the different stages in the QDs surface ligand exchange process.

To remove the excess of ligands, TOPO and PS-MA-BEE, the solution was precipitated with large amount of cold methanol followed by washing with methanol and dried in vacuum. A scheme of this process is presented in Figure V.16.

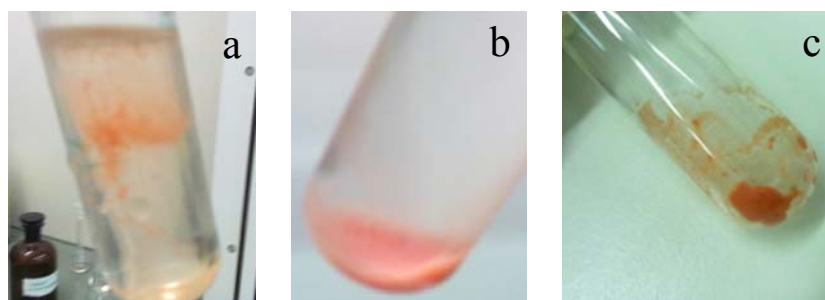


**Figure V.16.** Pictures of the precipitation stage in the QDs surface ligand exchange process: (a) Beginning of the PS-MA-BEE capped-QDs precipitation with cold methanol; (b) Precipitation after several washing steps with cold methanol; (c) QDs collected after remove the last methanol washing by a slight centrifugation step at 1000 rpm.

In order to achieve a good removing of the free ligand excess, the PS-MA-BEE excess and the TOPO ligands detached, we follow the washing steps by UV-

vis technique. We carry out the UV-vis spectrum of aliquots extracted of each washing steps and continuous washing steps until the value of the absorbance spectrum recorded is smaller enough ( $< 0.1$  at 350 nm). Thus, more washing steps do not allow us to remove more ligands and a stable situation is reached. This corresponds to five or six washing steps. Finally, the PS-MA-BEE-capped QDs,  $QD_p$ , were dissolved in  $CHCl_3/CH_3OH$  (5:1, v/v) to prepare the spreading solution.

FTIR was used as a probe of the efficiency of the ligand exchange process. For the sake of comparison, Figure V.17 shows the FTIR spectra of pure TOPO and PS-MA-BEE and PS-MA-BEE-capped nanocrystals,  $QD_p$ . The FTIR spectrum of TOPO presents a peak at  $1144\text{ cm}^{-1}$  corresponding to the P=O stretch. It was demonstrated that this peak is shifted to  $1114\text{ cm}^{-1}$  upon complexation with CdSe.<sup>[279]</sup> Therefore, the peak centred at  $1124\text{ cm}^{-1}$  that appears on the FTIR spectrum of  $QD_p$  can be ascribed to the not exchanged TOPO molecules upon the ligand exchange, bound to the nanoparticle surface. However, the low intensity of this band indicates that a small amount of TOPO remains in the  $QD_p$  capping after the exchange process.

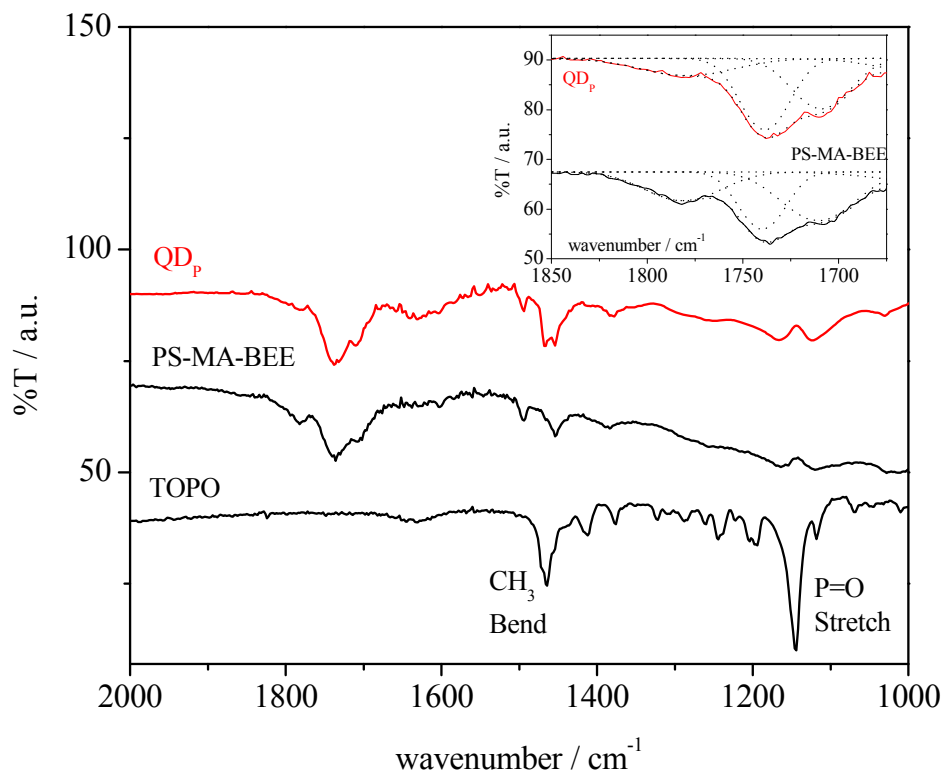


**Figure V.17.** FTIR spectra of TOPO, PS-MA-BEE and PS-MA-BEE-capped QDs ( $QD_p$ ) dispersed in KBr. The inset shows the decomposition of the carbonyl band in Gaussian functions for pure the polymer PS-MA-BEE and for PS-MA-BEE-capped QDs. For clarity, the %T-scale is shifted.

In addition, the appearance of the carbonyl-stretching band in the FTIR spectrum of  $QD_p$  unambiguously supports the presence of a polymer layer on the QDs surface. For comparison we have analyzed the carbonyl band of free polymer and polymer-capped quantum dots. The band was fitted to a sum of three Gaussian functions centred at  $1710\text{ cm}^{-1}$ ,  $1740\text{ cm}^{-1}$  and  $1782\text{ cm}^{-1}$ . The bands centred at  $1710\text{ cm}^{-1}$  and  $1740\text{ cm}^{-1}$  are assigned to the carbonyl stretching of the carboxylic and ester groups, respectively and the band centred at  $1782\text{ cm}^{-1}$  is assigned to the poly(maleic anhydride).<sup>[302]</sup> As can be seen in the inset of Figure V.17 the position and the relative intensity of these bands are similar in both, the free polymer and the PS-MA-BEE-capped QDs. All results may indicate that

TOPO molecules adsorbed at the QDs surface have been efficiently replaced by the polymer PS-MA-BEE.

The nanoparticle size was calculated from the position of the maximum of the first excitonic peak of the UV-Vis absorption spectrum, Figure V.18. The UV-Vis spectrum of  $QD_p$  in solution is blue-shifted 35 nm respect to the one corresponding to QDs stabilized by TOPO. This fact indicates that the replacement of TOPO by PS-MA-BEE decreases the QDs size. The diameter of the  $QD_p$  nanoparticles found was  $(2.8 \pm 0.3)$  nm that corresponds to a wavelength position of  $(542 \pm 5)$  nm for the first excitonic absorption peak <sup>[204]</sup> slightly influenced by the presence of methanol in the solution <sup>[303]</sup>. However this size was confirmed by TEM measurements.

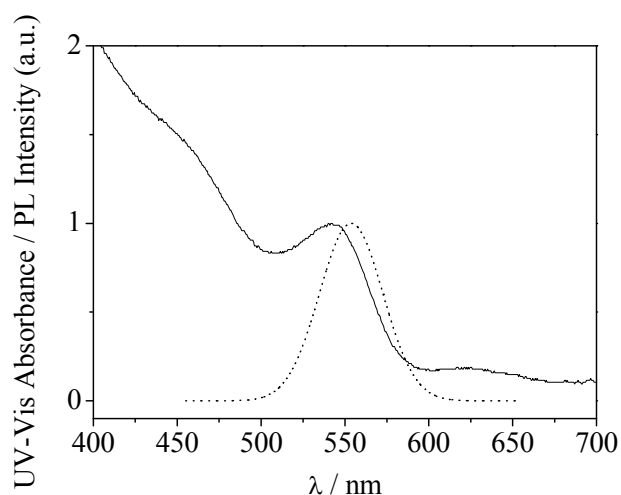


**Figure V.18.** Absorption and emission spectra normalized of a PSMABEE-capped CdSe QDs solution in  $CHCl_3/CH_3OH$  (5:1, v/v). Photoluminescence (PL) excitation at 405 nm.

### V.2.3.2. Langmuir and Langmuir-Blodgett Films of PS-MA-BEE-capped QDs

We use these modified  $QD_p$  to construct the Langmuir films precursors of the LB films. Therefore, we characterize the Langmuir monolayers by recording

the surface pressure isotherms of pure  $\text{QD}_p$  and mixtures of  $\text{QD}_p$  with PS-MA-BEE. Figure V.19a collects the isotherms obtained for different compositions and pure  $\text{QD}_p$  as inset. As can be seen in the figure the isotherms become more condensed when the polymer concentration increases. The isotherms present a plateau when the surface pressure reaches the value of  $30 \text{ mN m}^{-1}$ . This behaviour is similar to that observed for mixed monolayers containing PS-MA-BEE and QDs stabilized with TOPO. Likewise, the equilibrium elasticity isotherms are independent of the  $\text{QD}_p$  concentration and similar to the polymer one presenting a maximum at the surface pressure of  $14 \text{ mN m}^{-1}$  and a minimum at  $30 \text{ mN m}^{-1}$ , Figure V.19b. This fact indicates that the elasticity behaviour of these mixtures is governed by the polymer. This behaviour was previously explained, in section V.2.1, according to the existence of the polymer regimes: stripes and brush conformation, respectively.

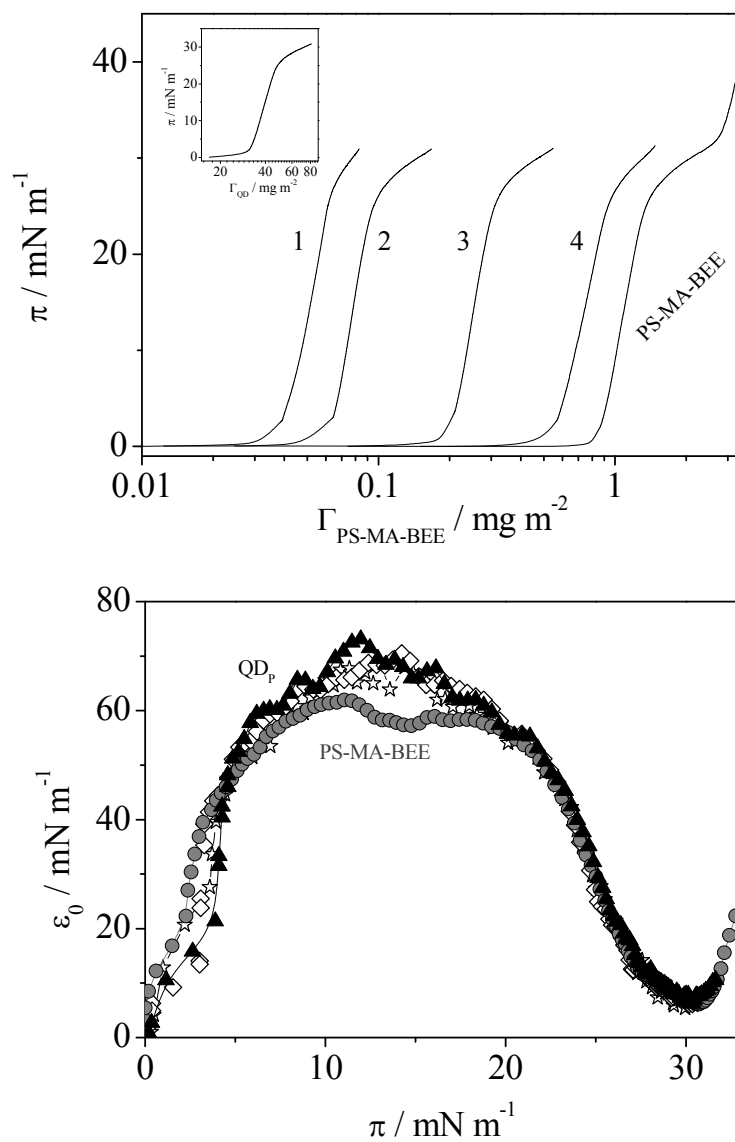


**Figure V.19.** (a) Surface pressure isotherms of mixed monolayers of PSMABEE-capped CdSe QDs with PS-MA-BEE with different polymer molar fraction: (0.50) (line 1), (0.96) (line 2), (0.98) (line 3) and (0.99) (line 4). For comparison the isotherm of pure PS-MA-BEE and QD<sub>P</sub> (inset) are represented in the figure. (b) Equilibrium surface elasticity vs. surface pressure for several mixed Langmuir monolayers of QD<sub>P</sub> and PS-MA-BEE at different polymer mole fraction: QD<sub>P</sub> (triangles); 0.96 (diamonds); 0.99 (stars) and PS-MA-BEE (circles). The isotherms were recorded at 23 °C by barrier symmetric compression at a speed of 5 mm min<sup>-1</sup>.



The BAM images of several mixtures were taken to analyze the effect of the polymer concentration on the morphology of the Langmuir films, Figure V.20. As was observed for QD/PS-MA-BEE mixed monolayers, when the polymer concentration at the air-water interface increases the QDs domains become smaller. As in the case of TOPO-capped QDs the agglomeration is promoted by the preferential QD-QD attractive interactions through the ligand, PS, in contrast to the weak interaction with water subphase,<sup>[143, 153]</sup> Figure V.20a. However, the polymer addition favours the nanoparticles spreading at the air-water interface by its hydrophilic blocks<sup>[67, 70, 147]</sup>, Figure V.20b-c.

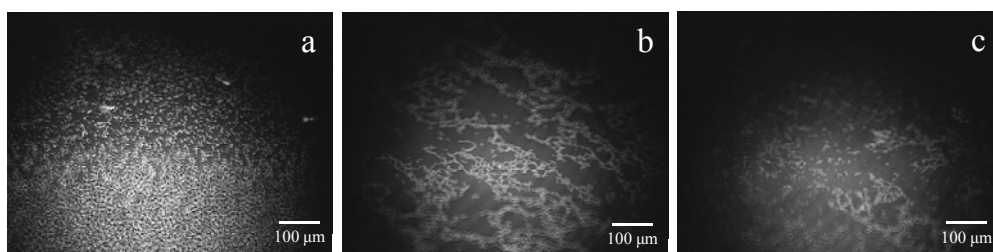


**Figure V.20.** BAM images (image size 800x600  $\mu\text{m}$ ) of pure QD<sub>p</sub> (a) and mixed monolayers (b, c) of the polymer PS-MA-BEE and QD<sub>p</sub> at the surface pressure of 14  $\text{mN m}^{-1}$ . The different polymer mole fraction are: (b) 0.96 and (c) 0.99.

The next step was to transfer the Langmuir monolayers from the air-water interface onto mica by LB technique. The surface pressure value of the monolayer selected was 14  $\text{mN m}^{-1}$ , corresponding to the maximum elasticity states. Thus, the results can be compared with those of mixed films of TOPO-capped QDs and PS-MA-BEE deposited at 14  $\text{mN m}^{-1}$ . Figure V.21 presents AFM and TEM images of LB films of pure QD<sub>p</sub> and mixed QD<sub>p</sub>/PS-MA-BEE. These images show that the QD<sub>p</sub> LB films are formed by material around holes, Figure V.21a. The height profile average value determined by AFM was 3 nm, which is consistent with the QD<sub>p</sub> diameter *ca.* 2.8 nm. This fact indicates that nanoparticles are mainly placed on the rims of holes.

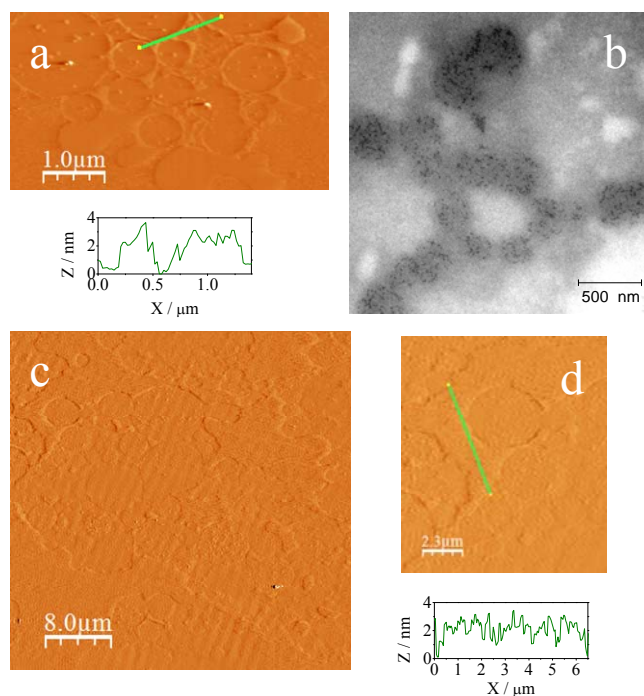


**Figure V.21.** AFM (a, c, d) and TEM (b) images of  $\text{QD}_p$  and mixed  $\text{QD}_p/\text{PS-MA-BEE}$  films deposited at the surface pressure of  $14 \text{ mN m}^{-1}$ . The film composition expressed as polymer mole fraction is:  $\text{QD}_p$  (a, b) and 0.50 (c, d).

AFM and TEM images of mixed  $\text{QD}_p/\text{PS-MA-BEE}$  LB films in Figures V.21c-d and 22, show that the network is maintained when the polymer is added. However, the network morphology depends on the polymer concentration. Thus, when the polymer concentration increases the hole and rim sizes go through a maximum at polymer mole fraction 0.5. When the polymer concentration is further increased until  $X_p > 0.97$ , AFM and TEM images show the smallest network dimensions. TEM images magnification, Figures. V.22c and d, seem indicate that the polymer molecules are preferentially located on rims, while the nanoparticles are in different regions of the both rims and holes. To illustrate this behaviour the statistical analysis of the network dimension is collected in Table V.2. These results allow us to analyze changes on the morphology produced by the polymer addition. Thus, when the polymer concentration increases the hole size and the rim width decrease. In contrast, the rim height is independent of the

polymer concentration with an average value of *ca.* 3 nm, similar to the  $QD_p$  diameter. Therefore, no 3D aggregation of nanoparticles occurs.

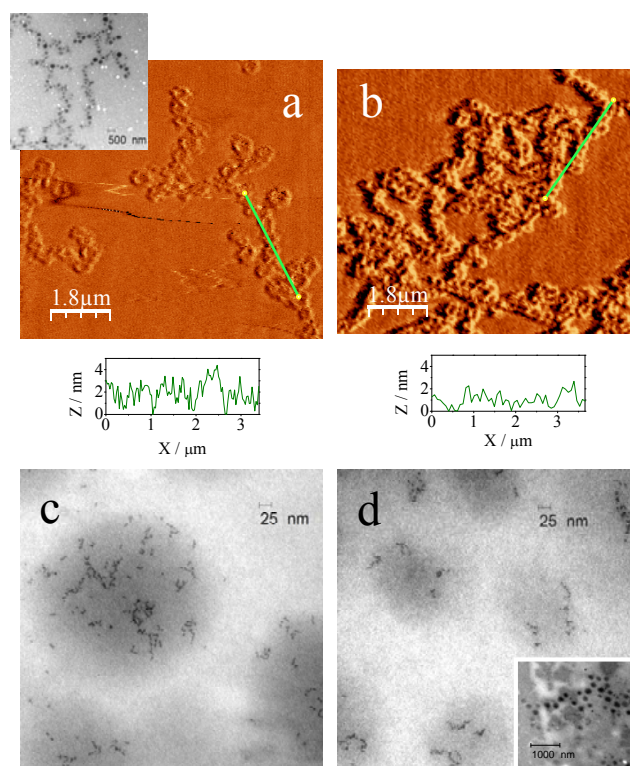


**Figure V.22.** AFM (a, b) and TEM (c, d) images of mixed  $QD_p$ /PS-MA-BEE LB films deposited at the surface pressure of  $14 \text{ mN m}^{-1}$ . The film composition expressed as polymer mole fraction is: 0.98 (a, c) and 0.99 (b, d).

As it is well established, the network formation is due to nucleation and growth of holes dewetting mechanism.<sup>[44]</sup> This mechanism was observed in  $QD_{\text{TOPO}}$ /PS-MA-BEE films obtained by transferring mixed Langmuir films in which the polymer is in brush state corresponding to low elasticity values. Accordingly, the behaviour observed for  $QD_p$  films could be unexpected. However, to interpret this picture, it is necessary to consider the different molecular weight values of the two nanoparticles stabilizers, TOPO and PS-MA-BEE. Thus, the molecular weight of PS-MA-BEE is seven times higher than the TOPO one. Therefore, one can expect that the dewetting effect driven by

gravitational effects, the growth of holes mechanism, prevailed over capillary waves in nanoparticles with higher mass as  $QD_p$ .

**Table V.2.** Average values of the feature dimensions of  $QD_p$ /PS-MA-BEE mixed LB films deposited at a surface pressure of  $14 \text{ mN m}^{-1}$  obtained from AFM measurements.

$X_p$	Hole size	Rim size
	Diameter / $\mu\text{m}$	Width / $\mu\text{m}$
$QD_p$	$0.84 \pm 0.34$	$0.13 \pm 0.13$
0.50	$3.61 \pm 2.00$	$1.21 \pm 0.75$
0.98	$0.12 \pm 0.03$	$0.15 \pm 0.04$
0.99	$0.11 \pm 0.04$	$0.08 \pm 0.02$

Reported values are averages and error represents the standard deviation determined from at least 20 surface features.

Finally, we have prepared a bilayer with  $QD_p$  and PS-MA-BEE. The methodology used is the same that in the case of nanoparticles stabilized with TOPO. Firstly we prepared the polymer LB film transferring the PS-MA-BEE monolayer at the surface pressure of  $14 \text{ mN m}^{-1}$  on mica. Then, the  $QD_p$  monolayer at the surface pressure of  $14 \text{ mN m}^{-1}$ , was transferred onto this polymer LB film. Figure V.23 presents the TEM and AFM images of this bilayer system. As can be seen, the morphology of this film is different to both, the  $QD_p$  LB film, Figure V.21a, and the bilayer system prepared with TOPO-capped QDs, Figure V.13a. By comparing with the  $QD_p$  LB film, it can be concluded that the polymer film used as coating avoids the dewetting processes observed in Figure V.21a. On the other hand, conversely to the bilayer prepared with TOPO-capped QDs, the PS-MA-BEE// $QD_p$  system presents a better QDs spreading leading to a more homogeneous distribution and smaller domains. This makes sense if we take into account that the polymer film used as template exposes the polystyrene group and the possible distribution of the polymer capping around the nanoparticle metal core. The polymer is bound to the surface of the CdSe crystal by the carboxylic group, leaving the polystyrene group exposed. Consequently, the affinity to the polymer coating is greater for the  $QD_p$  than for the  $QD_{TOPO}$ . In this situation,  $\gamma_{\text{polymer/air}} \sim \gamma_{\text{QD/air}} \sim \gamma_{\text{PS/air}}$  and  $\gamma_{\text{QD/polymer}} \sim 0$ . Therefore, the spreading

coefficient calculated from:  $S = \gamma_{polymer/air} - (\gamma_{QD/polymer} + \gamma_{QD/air})$  [44] is close to zero, indicating that cohesive and adhesion forces are balanced. This renders to a good spreading for these nanoparticles on the polymer film.

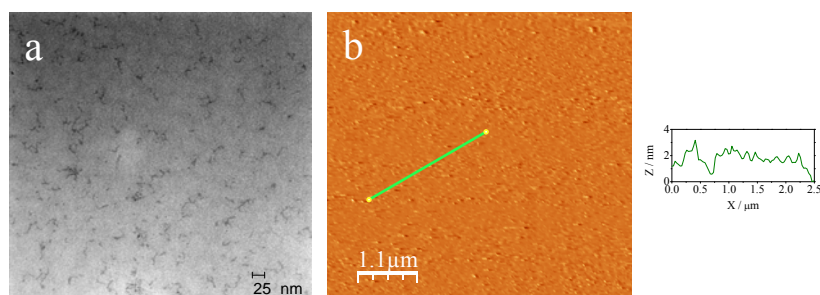


**Figure V.23.** TEM (a) and AFM (b) images of QD<sub>p</sub> transferred from a Langmuir film at the surface pressure of 14 mN m<sup>-1</sup> directly onto a LB film of PS-MA-BEE. The PS-MA-BEE film was constructed by transferring a polymer monolayer at the surface pressure of 14 mN m<sup>-1</sup>.

### V.3. Dynamic Properties of QD/PS-MA-BEE Mixed Systems

In previous sections we have presented results concerning to the fabrication of films prepared by transferring mixed Langmuir monolayers of CdSe QDs and the polymer PS-MA-BEE onto solids by the Langmuir-Blodgett methodology. Results highlighted the role of the composition in both, the monolayer state and the dewetting mechanisms produced in the transfer process. However, an important issue that must be also taking into account is the methodology used to prepare the Langmuir monolayer precursor of the LB film. In our experiments, the different states of Langmuir monolayers were obtained by continuous compression of the mixture initially deposited at the air-water interface. Thus, the surface pressure isotherms obtained relate the surface pressure to the area or surface concentration that the molecules occupy at the equilibrium. However, in several systems such as inorganic filler-polymer monolayers these curves are idealized because, even for infinitely slow compression, films often develop space-filling defects such as domain boundaries, vacancies, etc.<sup>[1, 87, 111, 304]</sup> In the case of filler-polymer films, when the filler is in the

order of the matrix molecular size, filler-polymer association can take place by chains overlapping between the fillers stabilizer and polymer. Similar associations were previously observed in polymers or nanoparticles (NPs). This kind of association slow down the dynamics in spaces between components rendering transient metastable states that finally relax towards the minimum energy configuration of the domain.<sup>[1, 87, 111, 304]</sup> A common strategy to achieve the stable state is to apply successive compression-expansion cycles and then to stop the barriers. After barriers stop, the system relaxes until it reaches a new stable state in which the surface pressure value remains constant with time. Using this approach more homogeneous and ordered nanoparticle (NP) monolayers can be obtained.<sup>[18]</sup>

Accordingly, we study the surface dynamic properties in QDs and polymer mixed films in order to improve the understanding of the hybrid system response to mechanical stress related to the film composition and morphology. It has been also proposed the employment of Langmuir monolayers as a platform to analyze the dynamic properties of ultrathin films. Recent studies about NPs dynamic behaviour have focused the investigations on the elastic and granular character of floating pliolite particle rafts,<sup>[19]</sup> the silica NPs viscoelastic properties<sup>[154]</sup> or as was mentioned, the induced organization of Au NPs with shearing<sup>[18]</sup>. Moreover, mixed Langmuir monolayers were proposed to study the modification of pulmonary surfactant interfacial properties due to the presence of silica or carbon black NPs.<sup>[21, 155]</sup> In these studies, the authors demonstrated the potential application of this technique to carry out nanocomposite dynamic studies, and to best of our knowledge, showed a lack of studies for mixtures of QDs and polymers.

In this section we analyze the effect of compression cycles on the properties of mixed monolayers of QDs and the polymer PS-MA-BEE. The next step was to transfer the different monolayers onto mica by LB technique to study the morphology of the LB films after the compression cycles. On the other hand,

the analysis of the relaxation curves obtained after the barriers stop allows us to obtain information about the dynamic processes at the interface.

### **V.3.1. Effect of Shearing on Film Morphology and Monolayer Reorganization**

Previous to apply successive compression-expansion cycles it was necessary to select the proper surface concentration. The selection criterion was that after compression cycles the monolayers for QDs and mixtures were far from the film collapse or far from the brush regime in the case of monolayers with polymer concentration above  $X_p > 0.95$ . Thus, the monolayers are in the same state, concretely liquid expanded. Besides, the surface concentration should be in the range where collective motions exist without film collapse, allowing the study of interconnected films at high strains.<sup>[18]</sup> Using this criterion the surface concentrations selected correspond to surface pressures values of 2.5 and 5 mN m<sup>-1</sup>. We also analyze the effect of the surface composition on the elastic properties of mixed monolayers before compression-expansion cycles at the surface pressures selected, 2.5 and 5 mN m<sup>-1</sup>. The corresponding elasticity values of polymer monolayers are higher than those of the QDs monolayers as was shown in Figure V.4c. Taking into account that the equilibrium elasticity is related to the system ability to store elastic energy, the behaviour observed indicates that in the polymer monolayer the molecules are more packed and the mobility is more limited than in the QDs monolayer. From this fact it is possible to conclude that cohesive polymer-polymer interactions are stronger than the QD-QD ones. Moreover, the elasticity values of mixed films are between the values corresponding to the pure components, QDs and polymer monolayers, indicating no synergistic effects in the mechanic properties of mixed monolayers.

Prior to the oscillatory barriers experiments, the stability of monolayers after cycling was checked by recording the surface pressure in successive compression-expansion cycles followed by a waiting step. An illustrative example

is shown in Figure V.24. Results in this figure correspond to the QDs monolayer but a similar trend was observed for the other monolayers. In the experiment represented in the figure, the barriers stop after the last expansion step. As can be seen, in spite of the decrease of the surface pressure during the cycling period, after the waiting step the system relaxes and reaches a constant surface pressure value. On the other hand, results presented in Figure V.24 also show that the amplitude of response decreases during the cycling period. This behaviour is observed for high strains,  $U_0 > 0.15$ , while for strain values below 0.15 the amplitude of the response remains constant. Although, the value depends on the mixture composition and the initial surface concentration. As example the strain values for three different systems are collected in Table V.3.

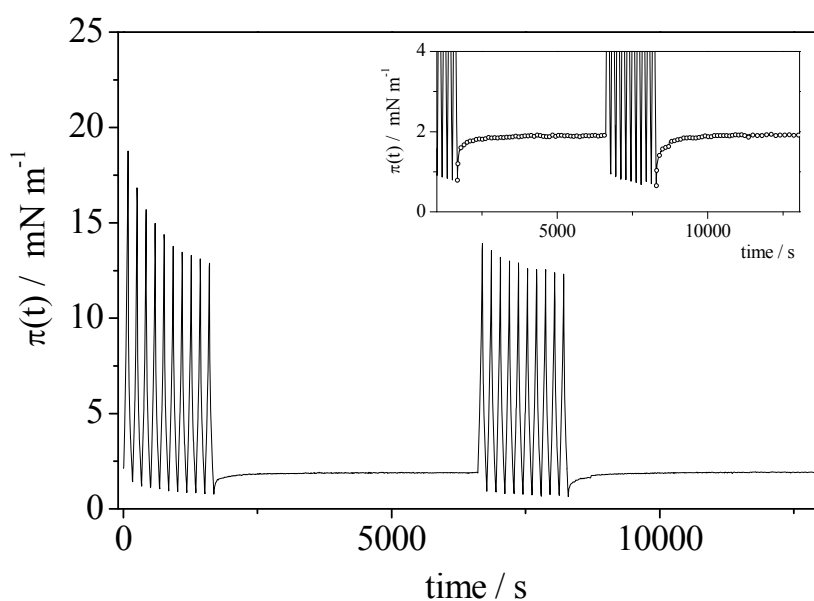


**Figure V.24.** Oscillatory experiment results for a QDs monolayer combining successive compression-expansion cycles with waiting steps. The experiment was carried out at a surface pressure of  $2.5 \text{ mN m}^{-1}$ , a strain amplitude of 0.35 and a frequency of 0.006 Hz. The inset shows a zoom of the waiting stages.



**Table V.3.** Strain values below which the amplitude of the system response remains constant at the different mixture compositions and initial surface pressures.

$X_P$	Strain ( $U_0$ )	
	$\Pi = 2.5 \text{ mN m}^{-1}$	$\Pi = 5 \text{ mN m}^{-1}$
<b>QDs</b>	0.16	0.16
<b>0.50</b>	0.25	0.21
<b>0.98</b>	0.18	0.15

The decrease of the surface pressure, observed during shearing, does not occur since a certain number of cycles. Thus, the monolayer reaches a state where the surface-pressure does not fall during the successive compression-expansion cycles ranging from the cycle 40<sup>th</sup> to 49<sup>th</sup>, depending on the strain, monolayer composition and surface concentration. In this way, when the strain and surface concentration increase the total number of cycles necessary to reach a stable situation of the surface-pressure decreases. Therefore, to reach this stable situation, we established 50 cycles to perform the oscillatory experiments

The decrease of the surface pressure observed can be due to association processes induced by shearing<sup>[18, 130, 305]</sup> or to monolayer dissolution in the subphase. To settle this issue, several experiments in which 50 compression-expansions followed by the barrier stop at the last expansion step at different strains above 0.15 were carried out. If the cycling process induces monolayer dissolution in the subphase, one expects that after the barriers stop the monolayer relaxes until it reaches the new equilibrium state. These states must be different for the distinct strains responsible for the dissolution process. Consequently, the surface pressure after the relaxation must be different for the distinct strains applied. Thus, the surface pressure values after the relaxation, referred as  $\pi_{end}$ , for monolayers of different composition were plotted against strains. For the sake of clarity some results are represented in Figure V.25.

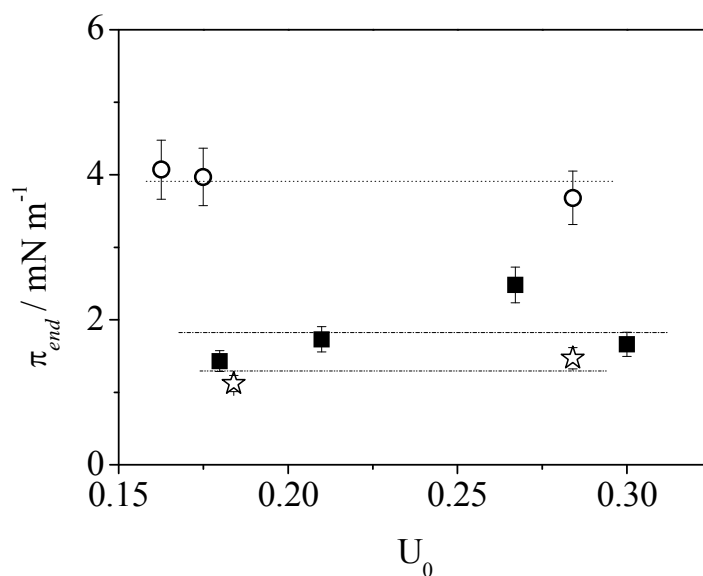


**Figure V.25.** Variation of the surface pressure values reached after a waiting stage for several monolayers at different polymer mole fraction: QDs (circles), 0.50 (squares) and 0.98 (stars), with the strain applied in the previous oscillatory experiment. The oscillatory experiments (50 cycles) were carried out at a frequency of 0.006 Hz and an initial surface pressure of 5 mN m<sup>-1</sup>.

As can be seen in the figure, the surface pressure value is independent of the strain for each monolayer studied. This trend was observed for the rest of monolayers. Accordingly, the surface pressure decrease after cycling cannot be associated to monolayer dissolution, because even at the highest strain the monolayer reaches a similar state to those reached with low strains. This fact can be interpreted considering that the monolayer shearing induces aggregation between the materials at the air-water interface, and after cycling stop, the aggregates reach a new state. The nature of this new state seems to depend on the film composition as revealed by the different surface pressure values achieved for monolayers of the distinct composition.

All these experimental results point to complex dynamic processes at the interface. Therefore, to gain insight into the dynamics of monolayers, the

relaxation curves obtained after compression-expansion cycles were analyzed. To select the proper oscillating frequency value several sinusoidal deformation experiments at different oscillating frequency, ranging from 0.003 to 0.030 Hz, were carried out. The surface pressure decrease expressed as:  $\Delta\pi = \frac{\pi_1 - \pi_s}{\pi_1}$ , where  $\pi_1$  and  $\pi_s$  represent the initial surface pressure and the final surface pressure after 50 cycles, respectively, is plotted against oscillatory frequency at different strains in Figure V.26 for two representative compositions. As can be seen,  $\Delta\pi$  is almost independent of the frequency while increases as the strain increases. The response amplitude does not significantly vary with the frequency in the range 0.003-0.012 Hz. A similar behaviour was observed for the rest of the monolayers studied. Therefore, we selected a low frequency value, 0.006 Hz, to carry out the dynamic study.

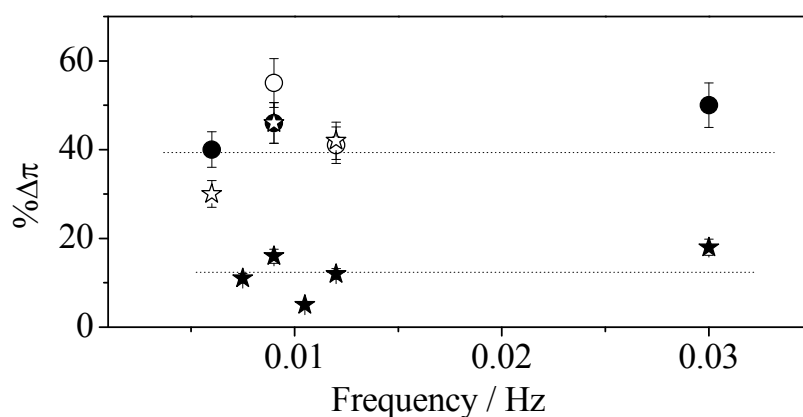


**Figure V.26.** Decrease in the surface pressure with respect to the initial state (value) after 50 cycles with the oscillation frequency for several monolayers at different polymer mole fraction: QDs (circles) and 0.98 (stars) and the strain applied: 0.04 (closed symbols) and 0.15 (open symbols).

The dynamic study was carried out by performing two different experiments. In the first one, 50 cycles of compression-expansion were applied

and the barriers were stopped at the end of the last compression. In the second experiment, after 50 cycles the barriers were stopped at the end of the last expansion. Then, the surface pressure was recorded with time until it reaches a constant value. We establish that the new equilibrium state is reached when the surface pressure is constant along the time. Figure V.27 presents representative relaxation curves for the different monolayers. The curves do not follow the exponential law and can be interpreted as a sum of three exponential functions for all systems except for polymer relaxation. In the later, the curves are interpreted by a sum of two exponential functions. Lines in the examples shown in Figure V.27 are calculated with the sum of three exponentials and the relaxation time values obtained in the fit procedure. Results in Figure V.27 represent an illustrative example of two experiments stopped at the end of the last compression for a QD/PS-MA-BEE mixed monolayer ( $X_p = 0.98$ ), Figure V.27a and the last expansion for a QD monolayer, Figure V.27b. For clarity to observe the continuous cycles in Figure V. 27, the horizontal axes of the insets are in logarithmic scale and begin at 1000 s. Similar trends were observed for the rest of experiments.

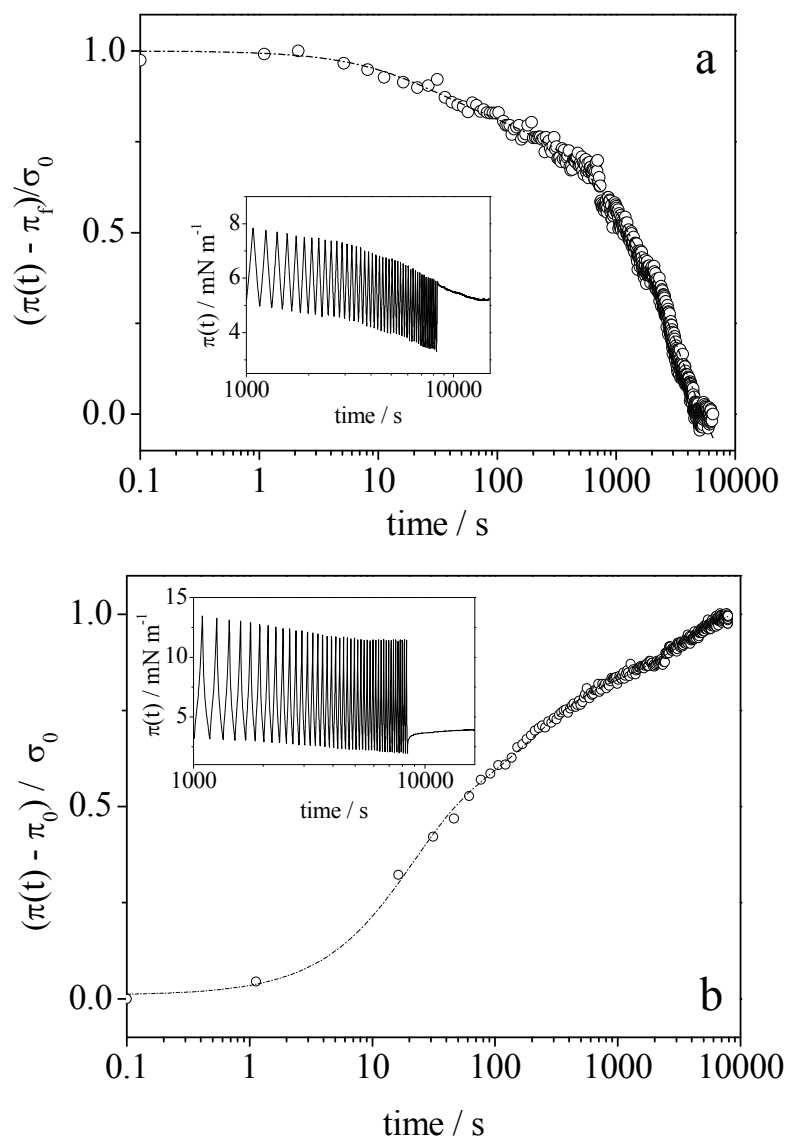


**Figure V.27.** A multi-exponential fit example of a QD/PS-MA-BEE mixed monolayer ( $X_p = 0.98$ ) relaxation after 50 cycles at the end of the last compression position at a strain of 0.06 (a). A multi-exponential fit example of a QDs relaxation after 50 cycles at the end of the last expansion position (strain 0.18) (b). Both, monolayers were prepared at a surface pressure of  $5 \text{ mN m}^{-1}$  and oscillation experiments were carried out a frequency of 0.006 Hz.

The results fitting suggests at least three mechanisms that dominate the relaxation process for QDs and QD/polymer monolayers and two relaxation mechanisms for the polymer monolayer. The first process corresponds to damping of surface fluctuation originated for the inertia of barriers sudden-stop and has been observed by other authors in silica nanoparticle films<sup>[305]</sup>. This time is the same for all systems at the different strains,  $U_0$ , and has a value (time-scale) of  $20 \pm 2$  s. The second relaxation time,  $\tau_2$ , is represented in Figure V.28 against the strain for several systems prepared at different polymer mole fractions,  $X_p$ , and the values ranged from 200 to 400 s. This relaxation process was observed in monolayers containing QDs and was not found in polymer monolayers. This relaxation time can be related to rafts movements whose time-scale is about several hundred seconds.<sup>[305, 306]</sup> The rafts formation can be promoted by compression and could be responsible for the decrease of the surface pressure observed after compression. Finally, the slowest process presents relaxation times of several thousands of seconds and can be related to particle/polymer movements inside the rafts.<sup>[305]</sup> The same behaviour was observed for relaxation curves obtained when the cycling is stopped at the last expansion step, see Figure V.28.

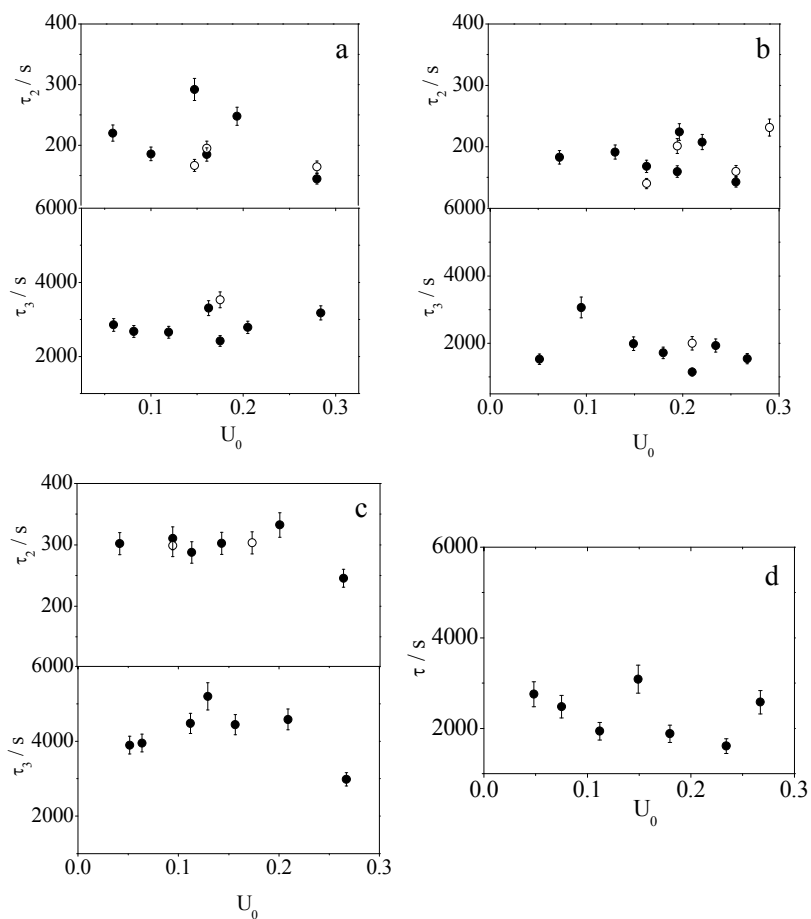


**Figure V.28.** Relaxation times values vs. strain obtained from the multi-exponential fit of the relaxation curves obtained for QDs and mixed QD/PS-MA-BEE monolayers, prepared at an initial surface pressure of  $5 \text{ mN m}^{-1}$ , after shearing 50 cycles at a frequency of  $0.006 \text{ Hz}$  stopping the barriers at the end of the last compression (closed symbols) and expansion (open symbols) stages. The composition of the monolayers expressed as polymer mole fraction is: QDs (a); 0.50 (b); 0.98 (c) and PS-MA-BEE (d).

It is interesting to notice that the relaxation time values are independent of the strain, within experimental uncertainty, while depend on the monolayer composition. In order to observe this dependence, we have calculated the average relaxation time for each relaxation process,  $\overline{\tau}_i$ , as the average of the relaxation

times calculated from curves obtained using different strains in each system. The calculated values are plotted against the polymer mole fraction,  $X_p$ , in Figure V.29. For comparative purposes the relaxation times values obtained when the cycles are stopped at the end of the expansion step are also included in the figure. As can be seen in Figure V.29, the relaxation time found when cycles are stopped at the end of the last compression and expansion steps agree with each others. This fact indicates that the same processes are observed in the two experiments. The relaxation time values ascribed to rafts movements,  $\tau_2$ , indicate that the raft movement becomes slightly slower when the polymer concentration increases. A more significant dependence on composition is observed for the relaxation times,  $\tau_3$ , corresponding to movements inside rafts and that can be related to impediments due to the polymeric matrix. These motion impediments have been proposed by theoretical models in nanoparticle/polymer mixtures, which are based on the reduction of polymer mobility close to the nanoparticle surface that promotes a local reorganization more structured. This behaviour is more marked when the nanoparticle size is similar to the polymer chains since an enormous interfacial area is involved.<sup>[22, 23, 307, 308]</sup> This could be in agreement with the increase in the relaxation time observed for mixed films of the highest polymer composition,  $X_p=0.98$ , comparing to polymer monolayer, Figure V.29.

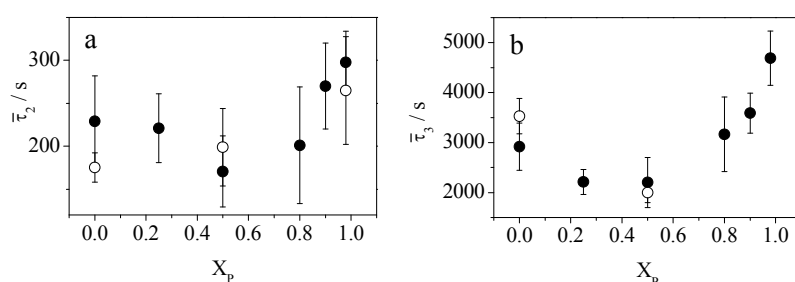


**Figure V.29.** Average relaxation times values vs. monolayer composition expressed as polymer mole fraction,  $X_p$ , obtained from the statistical treatment of the relaxation times obtained for QDs and mixed QD/PS-MA-BEE monolayers, prepared at an initial surface pressure of  $5 \text{ mN m}^{-1}$ ,



after shearing 50 cycles at a frequency of 0.006 Hz stopping the barriers at the end of the last compression (closed symbols) and expansion (open symbols) stages.

According to the scenario proposed, a schematic model showing the two processes involved in the nanoparticles monolayers is presented in Figure V.30.

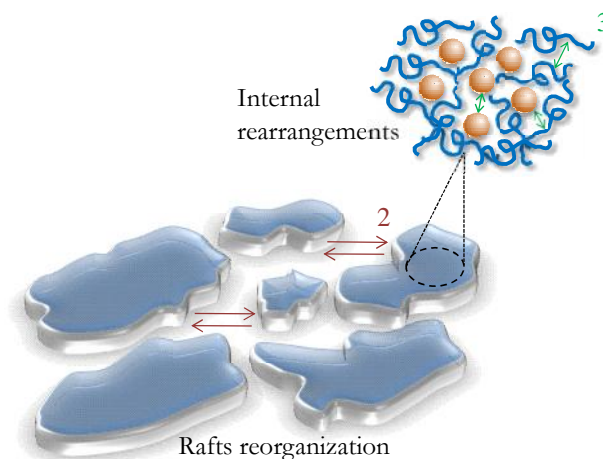


**Figure V.30.** The cartoon model represents the movements that dominate the relaxation of the monolayers that contains nanoparticles.

In an attempt to visualize the rafts movements, BAM images of the monolayers before and after cycling were taken. Illustrative images corresponding to the Langmuir monolayer prepared with QDs, and mixtures of QDs with PS-MA-BEE at polymer mole fraction values of  $X_p = 0.5$  and  $0.98$ , are collected in Figure V.31.

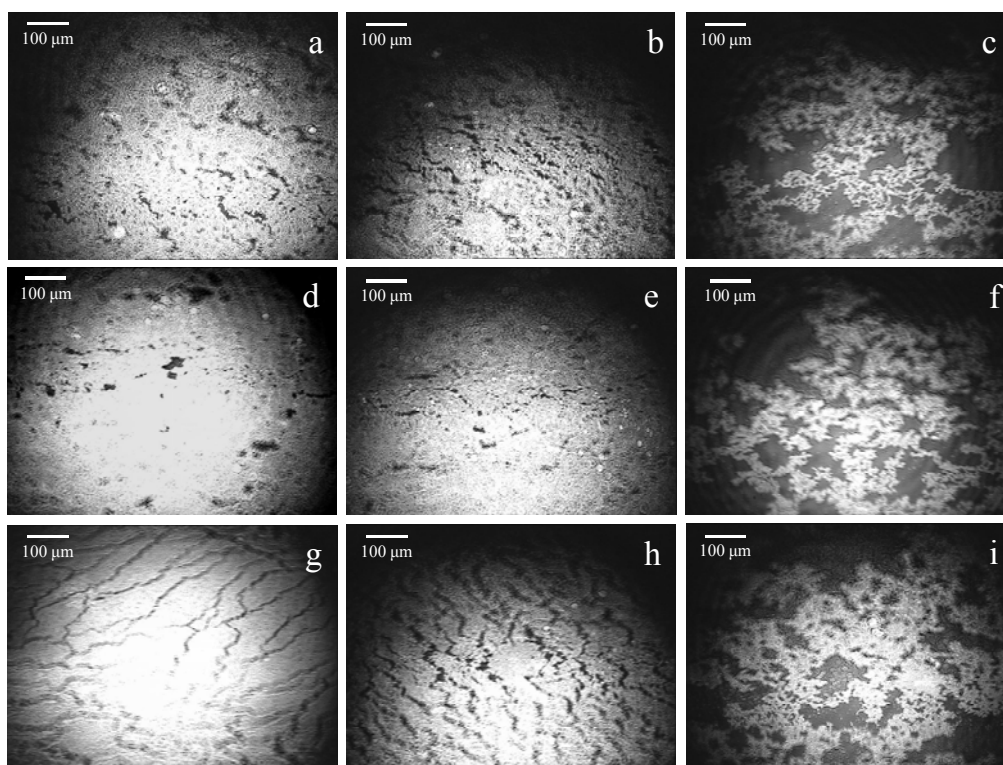


**Figure V.31.** BAM images ( $800 \times 600 \mu\text{m}$ ) at the initial state of the monolayer,  $\pi = 2.5 \text{ mN m}^{-1}$ , (a, b, c) and after shearing 50 cycles at high strains ( $U_0 > 0.20$ ) at the compression (d, e, f) and expansion (g, h, i) stages for different QD/PS-MA-BEE monolayers with a polymer mole fraction: QDs (a, d, g); 0.50 (b, e, h) and 0.98 (c, f, i).

BAM images of the pure polymer film show no contrast enough to observe the monolayer morphology; consequently, we do not show images of this film. The BAM images show that for films prepared with QDs, Figures V.31d and g, and mixtures of polymer composition  $X_p = 0.50$ , Figures V.31e and h, the compression induces compact domains and after expansion step the film presents cracks that propagate in the perpendicular direction to the applied stress. Mixed films of polymer mole fraction 0.98 present domains less compacted and consequently, the cracks produced after the expansions are greater than those observed for other compositions.

To confirm the raft movements, BAM images of monolayers after and before compression are presented in Figure V.32. Arrows in the figure point to a given raft to better visualize the raft movements. As can be clearly seen, in the compression step the monolayers become more compact and some cracks disappear. Conversely, the expansion step regenerates some cracks and the monolayer becomes more expanded. The BAM images allow us to confirm rafts movements during the shearing process. These movements present relaxation times in the order of several hundred seconds determined from the relaxation curves obtained after the cycling period.

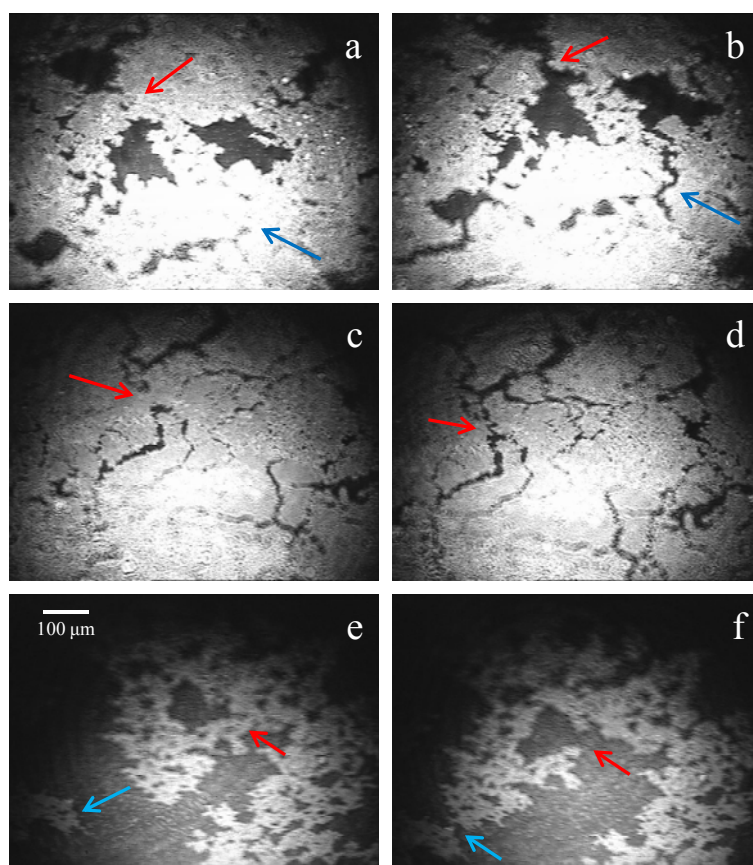


**Figure V.32.** BAM images ( $800 \times 600 \mu\text{m}$ ) showing several rafts movements promoted in the expansion stage (b, d, f) for different QD/PS-MA-BEE monolayers with a polymer mole fraction: QDs (a, b); 0.50 (c, d) and 0.98 (e, f).

We are interested in analyzing the effect of compression cycles on the morphology of the LB films by transferring the films after shearing 50 cycles at low ( $U_0=0.05$ ) and high ( $U_0=0.25$ ) strain values at the end of the last compression step. Figure V.33 shows the AFM images of different films. It is interesting to notice that even the LB films containing small concentration of QDs ( $X_p=0.98$ ), Figures V.33e and f, present a film morphology quite different to that of the polymer film, Figures V.33g and h. This fact indicates that QDs modify the interactions between polymer molecules resulting in films with different morphologies as a function of the QDs composition.<sup>[308]</sup> The AFM images also confirm that the LB film becomes more close-packed after shearing. This fact is more marked at high strains. For comparison, results in Table V.4 shows a statistic study of the domain dimensions for the QD/PS-MA-BEE film at  $X_p = 0.98$  at low (0.05) and high (0.25) strains.

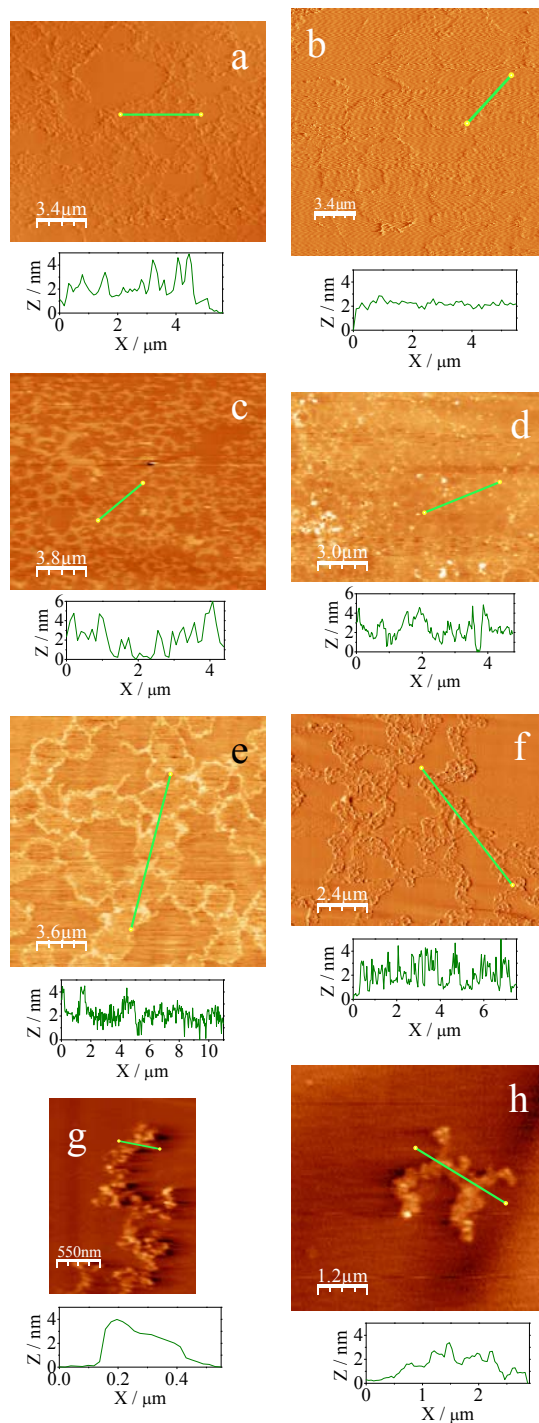


**Figure V.33.** AFM images of QD/PS-MA-BEE LB films deposited after shearing 50 cycles at low (0.05) (a, c, e, g) and high strains (0.25) (b, d, f, h) for monolayers prepared at different polymer mole fraction,  $X_p$ : QDs (a, b); 0.50 (c, d); 0.98 (e, f) and PS-MA-BEE (g, h). The initial surface

pressure of the monolayers was  $2.5 \text{ mN m}^{-1}$ , except for PS-MA-BEE monolayers that was  $3.5 \text{ mN m}^{-1}$ .

**Table V.4.** Mean features dimensions of QD/PS-MA-BEE mixed LB film prepared at  $X_p = 0.98$  based on AFM measurements.

Strain ( $U_0$ )	X-direction / $\mu\text{m}$	Y-direction / $\mu\text{m}$
0.05	$2.53 \pm 0.56$	$2.17 \pm 0.27$
0.25	$0.45 \pm 0.12$	$0.38 \pm 0.13$

\*Reported values are averages and error represents the standard deviation determined from at least 20 surface features.

The morphology of these films was analyzed by TEM. This technique complements the AFM images because QDs can be observed in the TEM images. Representative TEM images of films prepared by transferring Langmuir monolayers after 50 compression-expansion cycles are collected in Figure V.34. TEM images of QDs, Figs. V.34a and b, correspond to aggregates obtained by using different strains. The images show that the domain size decreases when the strain increases. This behaviour agrees with the information obtained from the AFM images of these films. This picture is also consistent with a directional-stress order in the film induced by X-deformation. This behaviour was previously observed in monolayers containing  $\text{BaCrO}_4$  nanorods.<sup>[309]</sup> TEM images for the mixed QD/polymer films indicate that, as expected, the QDs domain size also decreases when the QDs concentration decreases. Figures V.34c and d show that the LB films of  $X_p = 0.50$  presents the closest domains. The images also demonstrate that in this film when the strain increases the domains merge in big domains, Figure V.34d. When the polymer mole fraction is further increased until 0.98 the polymer molecules predominate and the QDs domains become smaller than the ones observed for film with high QDs concentration, Figure V.34e and f.

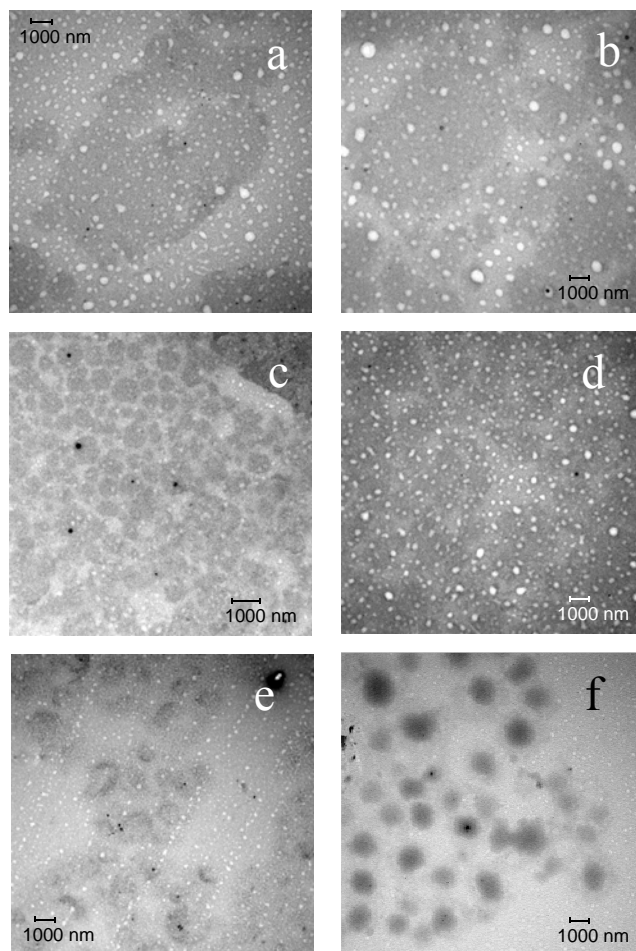


**Figure V.34.** TEM images of QD/PS-MA-BEE LB films deposited after shearing 50 cycles at low (0.05) (a, c, e) and high (0.25) (b, d, f) strain for monolayers prepared at a polymer mole fraction: (a, b) QDs; (c, d) 0.50 and (e, f) 0.98. The initial surface pressure of the monolayers was  $2.5 \text{ mN m}^{-1}$ .

In summary, the results are in excellent agreement with those observed by other authors who observed that the inorganic filler monolayers develop metastable filler aggregates probably due to chains overlapping of the fillers stabilizer.<sup>[18, 304]</sup> In the current work, we apply successive compression-expansion cycles<sup>[18]</sup> to prepare ordered QDs monolayers. The methodology used allows us to obtain information of the different relaxation processes produced after the compression-expansion cycles. Thus, two relaxation processes were observed for

QDs and mixed QD/polymer films. The fastest one was ascribed to rafts movements, while the slowest was related to movements inside rafts. Moreover, the time-scales of these processes are related to the film composition. Thus, slower relaxations correspond to systems with high polymer mole fraction.

#### **V.4. Photoluminescence of QDs in Langmuir-Blodgett Films**

In previous sections we presented different methodologies to construct CdSe QDs films: co-spreading and bilayer approaches. Our results showed that the morphology of these films depends on the methodology employed to prepare them. In this section the aim is to study the effect of the film morphology on the photoluminescence properties since the understanding of the optical properties of assembled QDs is important for their applications. This is an important issue for the construction of optoelectronic devices, such as LEDs, photodetectors, solar cells and nanosensors,<sup>[9, 310, 311]</sup> where highly-ordered structures with homogeneous and known photophysical properties<sup>[7]</sup> are necessary. In this sense, it is important to study the influence of the QDs' density, environment (capping and mixed systems), inter-dot distance and excitation energy in the photophysical properties of QDs films. Within the different spectroscopic techniques, time-resolved photoluminescence has the advantage of being a technique highly sensitive to surface and environmental changes, but this information is often concealed by the intrinsically complex excited-state dynamics of QDs.<sup>[25]</sup> Therefore, the photoluminescence dynamics of QD/PS-MA-BEE films were measured by confocal fluorescence lifetime microscopy by analyzing the decay curves and fluorescence images. This technique is not available at the Universidad de Salamanca, therefore this part of the work was performed during a short stay in the Molecular Photochemistry Group (IST, Lisbon). The results show the influence of the different self-assembly strategies with the polymer on the fluorescence dynamics of QDs.



Some optoelectronic applications take advantage of QDs properties incorporating them into a polymeric matrix building nanocomposites. In these cases, it is necessary to develop a controlled way to achieve good-quality polymer-QDs hybrid films.<sup>[8, 311]</sup> In order to optimize these hybrid systems, several authors have focused their attention on the effect of film matrix properties on the energy transfer processes<sup>[312, 313]</sup> or the QDs photoluminescence intermittency (blinking statistics)<sup>[314, 315]</sup>.

On the other hand, it is also essential to understand and modulate the energy transfer in a QD film. Some reports indicate that in monodispersed QD layers there is an energy transfer (ET) not only between neighbour QDs but QDs at longer distances also contribute.<sup>[316-318]</sup> This energy transfer is due to an overlap of the first absorption peak with the PL emission of the QDs and is faster in non-shell QDs capped with relatively short ligand molecules, (because of the  $r^{-6}$  distance dependence of the energy transfer). Two non-radiative mechanisms for energy transfer between QDs have been proposed, the Dexter exchange mechanism and the Förster resonant energy transfer (FRET) mechanism. However, previous theoretical and experimental studies show that energy transfer between nanocrystal QDs can be appropriately described by FRET theory in two dimensions proposed to biological membranes.<sup>[317]</sup>

The photoluminescence (PL) decay dynamics of colloidal QD ensembles present long lifetimes (tens of nanoseconds at room temperature to microseconds at low temperature) and complex behaviour reflected on multi-exponential fluorescence decays. Several explanations have been proposed to interpret the multi-exponential behaviour<sup>[319]</sup> in the QD ensemble PL decay dynamics: (i) each member of the ensemble has its own unique single-exponential (single-rate) lifetime, (ii) the PL decay is an inherently complex process for each individual QD, making the decay dynamics multi-exponential for each member of the ensemble, or (iii) the PL decay of each member is single exponential at any given

moment but it fluctuates in time, so that the time-averaged PL decay of an individual QD is multi-exponential. Alternative explanations invoke the role of surface defects of the nanocrystal as charge trapping sites that give rise to charge-trapped states that lie within the band gap. Usually these charged states are non-emissive or emit in the infrared, which further complicates the emission dynamics. Thus, fluctuations in the local electrostatic environment surrounding the QD can play an important role. This behaviour was studied in QD clusters by Van Orden and co-workers<sup>[320]</sup> that have shown that QDs clusters exhibit a behaviour not observed in isolated QDs. The QDs clusters present an enhanced blinking and a biexponential decay characterized by a prominent fast component and a slow component characteristic of isolated QDs. Moreover, in solid films, the PL complexity is further increased by the possibility of excitation energy transfer between QDs, due to the short interparticle distances in close-packed films.

#### **V.4.1. Experimental Details**

The samples were prepared by the Langmuir-Blodgett technique transferring QDs Langmuir monolayers at different surface pressures. Atomic Force Microscopy and Transmission Electron Microscopy were used to analyze the morphology of the films deposited onto quartz discs and Formvar<sup>®</sup>-carbon coated copper grids, respectively. This study was necessary because we had to change the mica substrate by quartz discs due to mica presents an important fluorescence emission that interferes with the QDs photoluminescence. In this sense, prior to the PL measurements, we check the quartz substrate cleaning and the PS-MA-BEE contributions by FLIM measurements. The visualization in both cases of images with only dark counts indicates that the RCA clean method used for the quartz substrates is good for FLIM characterization and the polymer purity meets the FLIM requirements, not interfering in the measurements at the excitation wavelength selected, 482 nm.

The photoluminescence properties of QDs are strongly dependent on the presence of surface defects due to the large relation surface area-volume. Thus, in order to avoid spurious effects from QD handling that could induce different surface conditions of QDs,<sup>[321-324]</sup> we have established a protocol of preparation of QDs solutions and films. One single batch of synthesized QDs was used for all the experiments. All the QD powder necessary to prepare the spreading solutions was extracted in a single purification. The QD concentration in the spreading solutions was the same for all samples, *ca.*  $10^{-6}$ M (0.968  $\mu$ M). The solutions were freshly prepared just before the monolayer deposition. The LB films were dried during 12 h and stored under vacuum. To ensure no aging effects, the waiting time between LB films preparation and FLIM measurements was the same for all samples.

The steady-state spectroscopy was carried out in a Perkin-Elmer Lambda 35 UV-vis spectrophotometer and in a Horiba Jobin Yvon IBH FluoroLog-3 spectrofluorimeter using front-face detection with an angle of 22.5°. The emission spectra are the average of at least ten measurements. The light dispersed by the films deposited onto quartz substrates was corrected by subtracting the corresponding reference sample in the absorption spectra. For fluorescence steady-state measurements the corrected spectra were obtained using the correction file provided with the instrument. All the spectra were recorded at room-temperature.

For the photoluminescence studies we employed the Fluorescence Lifetime Imaging technique using a MicroTime200 time-resolved confocal fluorescence microscope system from PicoQuant GmbH (Berlin, Germany). Point and area measurements ( $80 \times 80 \mu\text{m}^2$ ,  $400 \times 400$  pixels, integration time of 1ms per pixel) were carried out by using 482 nm excitation wavelength (2.5 MHz repetition rate, 152 ps/channel resolution, objective x60 N.A. 1.2 of water immersion) with a band-pass 550-690 nm filter to select emission. A pinhole of

30  $\mu\text{m}$  was used to reject out-of-focus light. The emitted light is detected with a single-photon counting avalanche photodiode (Perkin-Elmer) and digitized by TimeHarp 200 TD-SPC PC board (PicoQuant GmbH). To preserve LB films from water, we used a glass coverslip between the water drop and the sample. The measurements in solution were carried out with a quartz cuvette sample holder and an objective x40 N.A. 0.65 in air.

#### **V.4.2. Selection of the Experimental Conditions by Steady-state Measurements**

We carried out a series of preliminary experiments to select adequate work conditions. The wavelength laser excitation conditions were selected taking into account the steady-state fluorescence results of QDs in chloroform solution and on quartz substrates. To avoid the polymer excitation, the wavelength selected was 482 nm. At this wavelength only the QDs are excited, not the polymer keeping away from further complications in emission behaviour <sup>[325]</sup>. When mixed QD/PS-MA-BEE films are excited at short wavelengths, e.g. 350 nm, it is possible to observe the bands associated to each compound, Figure V.35. The first band centred at  $\sim 425$  nm corresponds to the polymer excimer emission <sup>[326]</sup> characteristic of polystyrene copolymers thin films <sup>[327]</sup>. The second one corresponds to the QDs emission. Although the QD concentration varies, the individual position of the peaks and the intensity of the polymer peak are kept indicating that no energy transfer is expected between the QD and polymer.

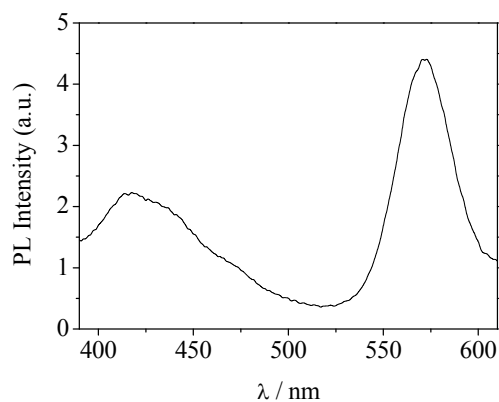


**Figure V.35.** PL spectrum of a QD/PS-MA-BEE mixed LB film deposited at  $30 \text{ mN m}^{-1}$  and prepared with a polymer mole fraction of 0.50. The excitation wavelength was 350 nm.

For the sake of comparison, the absorption and fluorescence spectra of QD in solution and LB deposited onto quartz were recorded in Figure V.36. A slight shift in the fluorescence spectra can be observed. This fact could be attributed to dipole-dipole interactions between nearest neighbour QDs, i.e., an energy transfer.<sup>[328]</sup>

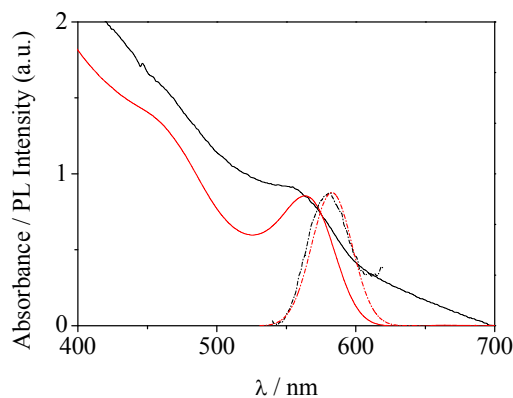


**Figure V.36.** Absorption and PL spectra for QD in chloroform solution (red line) and a QD LB film deposited at  $30 \text{ mN m}^{-1}$  (black line).

Due to we study mixed films of QDs and PS-MA-BEE, we analyze the effect of the presence of the polymer on the QDs fluorescence emission. Figure V.37 shows the photoluminescence (PL) spectra of different QD/polymer

solutions by varying the polymer mole fraction,  $X_p$ . Results show a possible quenching from the polymer due to aromatic rings could be effective quenchers of CdSe QDs emission, i.e., be capable of directly intercepting one of the charge carriers disrupting the radiative recombination process,<sup>[329]</sup> as shown in Figure V.37. However, this effect is only observed at high polymer concentrations, above  $X_p > 0.80$ .

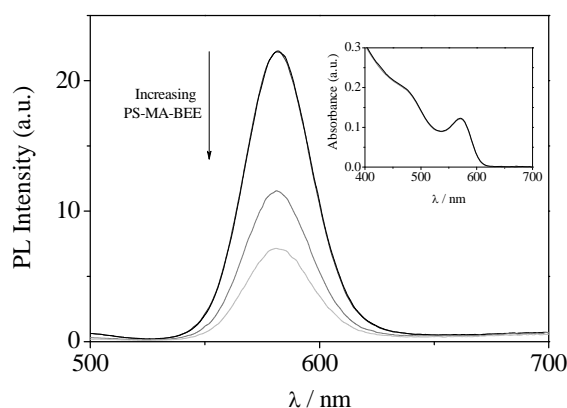


**Figure V.37.** Absorption and PL spectra of mixed QD/PS-MA-BEE chloroform solutions at different polymer molar ratios: QDs (black); (0.50) (dark gray); (0.96) (gray) and (0.98) (light gray). The QDs concentration is the same for all solution as indicate the absorption spectra (inset) and is *ca.*  $10^{-6}$  M.

In summary, the steady-state measurements allow us to determine several work conditions: the excitation wavelength, 482 nm, and the polymer mole fraction,  $X_p < 0.90$  in order to avoid the polymer influence on the QDs photoluminescence dynamics study.

#### V.4.3. Photoluminescence Dynamics of QDs

As was previously commented the PL dynamics of QDs are complex and can be affected by several experimental conditions. In the dynamic studies of QDs, we can observe the effect of the QDs' density, environment (polymer), power excitation energy and exposure time on the fluorescence average lifetime values for the different samples obtained from multi-exponential decay fit. The

average lifetime values allow us to compare our results with the literature. Therefore, a preliminary analysis of these variables on the PL dynamics becomes necessary to establish adequate work conditions to a PL dynamic study in deep of QDs LB films.

#### V.4.3.1. Photoluminescence Dynamics of QDs in Solution

Since the QD-polymer hybrid films are a complex system, we began to study the mixtures in chloroform solution. However, differences between the distinct systems are not visible in solution, the fluorescence lifetimes are similar and around  $35 \pm 2$  ns, close to the value for individual QDs, see Figure V.38 and Table V.5. Besides, the average lifetime values are not dependent on power excitation:  $35 \pm 2$  ns ( $67 \text{ W cm}^{-2}$ );  $35 \pm 2$  ns ( $134 \text{ W cm}^{-2}$ ) and  $35 \pm 1$  ns ( $244 \text{ W cm}^{-2}$ ). Thus, as the polymer addition has not a dramatic effect on the average lifetimes and the first excitonic peak (absorption spectrum Figure V.37) of QDs, the quenching observed in the PL spectra could be attributed to an excited-state charge-transfer mechanism.<sup>[325, 330]</sup> In this type of mechanism a high polymer concentration,  $X_p > 0.80$ , causes a decrease in the PL emission intensity, as in Figure V.37, but the lifetimes are not strongly influenced, Table V.5. Furthermore, the PL decay curves below this polymer mole fraction agree with the QDs one, Figure V.38. The proximity of polymer molecules to QDs allows that the polymer acts as hole acceptor to several hole trapping emitting sites of the QDs surface, eliminating fluorescence sites.<sup>[331, 332]</sup>

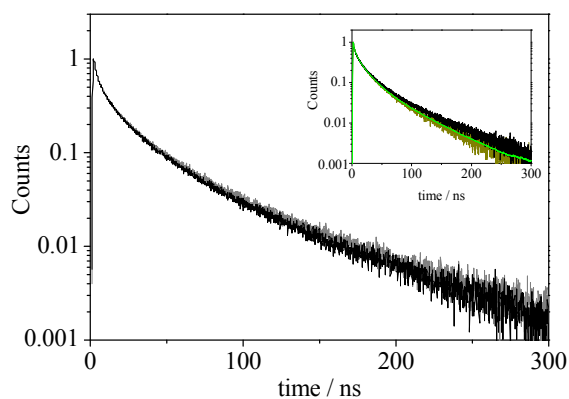


**Figure V.38.** Normalized PL decay curves for QDs (black line) and QD/PS-MA-BEE ( $X_p = 0.80$ ) mixture (gray line) in chloroform solution. The inset shows the tendency of PL decay curves for QDs when the chloroform solution is diluted from black to dark yellow lines. The solid line in green colour shows a representative fitting example of multi-exponential decay analysis.

**Table V.5.** Results from multi-exponential decay analysis for point measurement over QDs chloroform solutions at  $67 \text{ W cm}^{-2}$ . The reduced chi-square values,  $\chi^2$ , all close to 1, and the corresponding weighted residuals indicated a good fit to each data set.

	Chloroform solutions [QDs] $\sim 0.5 \mu\text{M}$				
	QDs	$X_p=0.50$	$X_p=0.96$	$X_p=0.98$	$X_p=0.99$
$\tau_1 / \text{ns}$	$1.4 \pm 0.1$	$1.8 \pm 0.2$	$1.5 \pm 0.2$	$1.7 \pm 0.2$	$1.7 \pm 0.2$
$f_1 (\%)$	$2.5 \pm 0.3$	$2.8 \pm 0.3$	$3.3 \pm 0.3$	$4.8 \pm 0.5$	$4.4 \pm 0.4$
$\tau_2 / \text{ns}$	$5.5 \pm 0.6$	$5.5 \pm 0.6$	$5.4 \pm 0.5$	$6.4 \pm 0.6$	$6.2 \pm 0.6$
$f_2 (\%)$	$10 \pm 1$	$9.1 \pm 0.9$	$13 \pm 1$	$16 \pm 2$	$15 \pm 2$
$\tau_3 / \text{ns}$	$19 \pm 2$	$18 \pm 2$	$19 \pm 2$	$21 \pm 2$	$21 \pm 2$
$f_3 (\%)$	$46 \pm 5$	$42 \pm 4$	$41 \pm 4$	$42 \pm 4$	$43 \pm 4$
$\tau_4 / \text{ns}$	$58 \pm 6$	$56 \pm 6$	$61 \pm 6$	$70 \pm 7$	$73 \pm 7$
$f_4 (\%)$	$41 \pm 4$	$46 \pm 5$	$43 \pm 4$	$37 \pm 4$	$38 \pm 4$
$\tau_{AV} / \text{ns}$	$33 \pm 3$	$34 \pm 3$	$35 \pm 4$	$36 \pm 4$	$37 \pm 4$
Counts/ms	$5.4 \pm 0.5$	$4.8 \pm 0.5$	$2.2 \pm 0.2$	$1.7 \pm 0.2$	$1.5 \pm 0.2$

Results show that the decay curves exhibit a multi-exponential dynamics. Previous studies<sup>[319, 333]</sup> indicated that the fastest decay components reflect the emission from radiative relaxation of the excited electrons to the ground state,  $\tau_r$ , and can be attributed to the initially populated core-state recombination. However, the conduction-band electrons can be localized in shallow trap states. These electrons in shallow trap states may repopulate the conduction band or



thermalize into deeper trap states, contributing to non-radiative relaxation pathways. The longest lifetime components in the decay curve are attributed to radiative recombination of carriers because they account for more and more of the total luminescence when the quantum yield of the QDs is increased.<sup>[334]</sup> Moreover, a distribution in decay times is expected as a result of the variation in the non-radiative decay rates for different QDs due to a variation in type and number of the quenching centres. A combination of all of these processes, along with differences in shape and size between the individual nanocrystals in a population, gives rise to multi-exponential emission dynamics.

If we compare the decay curves and components in solution vs. a LB film of QDs, noteworthy differences are visible, see Figure V.39. The initial part of the decay appears longer in solution where is less likely that energy transfer occurs because of the low concentration ( $\sim 10^{-6}$  M) and due to it is a system more fluid than the film. On the other hand, the enhanced close-packed and rigid LB films allow for the interactions between neighbour QDs as it is reflected in a faster initial decay and also a longer decay tail.<sup>[316]</sup>

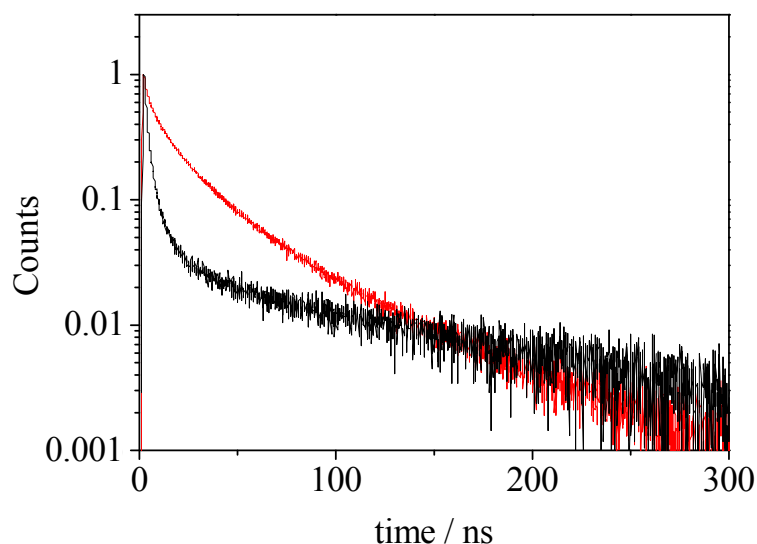


**Figure V.39.** Normalized PL decay curves for QDs in chloroform solution at  $10^{-6}$  M (red line) and a QDs LB film at high concentration ( $\pi = 30$  mN  $m^{-1}$ ) onto quartz substrate (black line).

Moreover, the sharp decay at the initial ns for QD in solution could be ascribed to surface defects promoted by a detachment of some ligand molecules when the solution is diluted,<sup>[335]</sup> as shown inset Figure V.38. Besides the dielectric environment has an influence on the radiative recombination lifetime,  $\tau_r$ .<sup>[7]</sup> The  $\tau_r$  is related to the dielectric constant of the medium,  $\epsilon_1$ , and for spherical QD longer by the factor  $[3\epsilon_1/(\epsilon_2 + 2\epsilon_1)]^{-2}$ , where  $\epsilon_2$  is the semiconductor optical dielectric constant.<sup>[336]</sup> Thus, the factor increases from  $\sim 2.6$  for chloroform ( $\epsilon_1 \sim 2.1$ ;  $\epsilon_2 \sim 6$ ) to  $\sim 7$  for the film (air) ( $\epsilon_1 \sim 1$ ;  $\epsilon_2 \sim 6$ ), which is reflected in an increase of the  $\tau_r$  from 10 ns to 30 ns.

#### V.4.3.2. Effect of the Excitation Energy on QDs LB films

Focusing the attention on the QD LB films, we check the influence of the excitation energy on the average lifetime and the integrated QDs intensity (counts). Results in Figure V.40 show a non-linear dependence of the lifetime and the integration QDs intensity (counts) with the excitation energy. Moreover, the fast component is more prominent as the power excitation increases. These facts can be attributed to multi-excitonic emission processes.

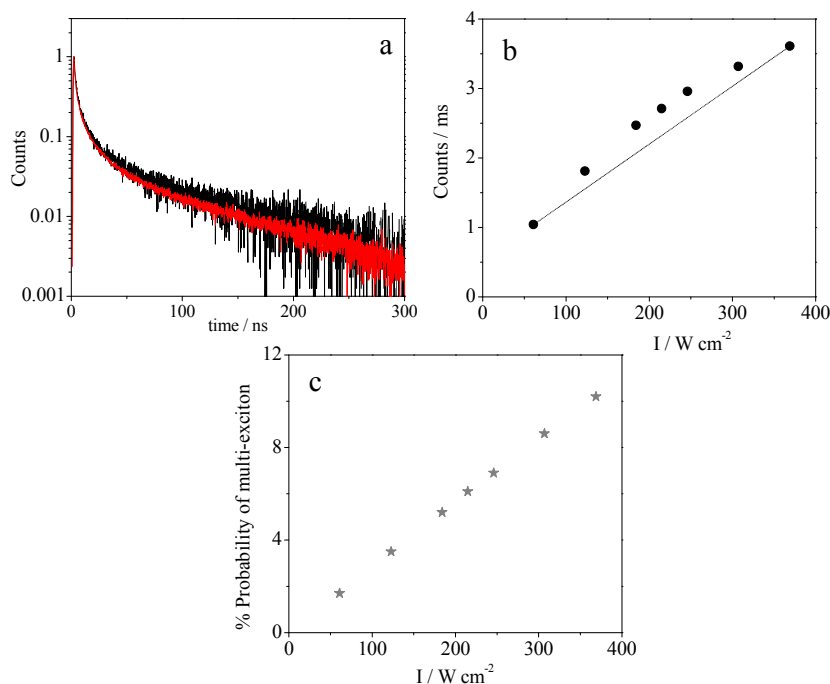


**Figure V.40.** (a) Normalized PL decays collected in the same area ( $80 \times 80 \mu\text{m}^2$ ) for a QD LB film at high and low power excitation:  $31 \text{ W cm}^{-2}$  (black line) and  $369 \text{ W cm}^{-2}$  (red line). (b) Dependence of the intensity counts with the power excitation. (c) The multi-excitonic probability vs. power excitation calculated from (Fisher, 2004<sup>[319]</sup>).

To confirm this assumption we analyze the dependence of average lifetime on power excitation. Some illustrative results are collected in Figures V.41 and 42 for point and area measurements, respectively. As can be seen in these figures, the average lifetime decreases when the excitation energy increases.<sup>[337]</sup> This fact was checked in different systems: QDs, bilayer and co-spreading, Figure V.42, and at different QD densities: high and low, Figure V.43. This behaviour is consistent with the multi-exciton generation. We have calculated the probability of multi-excitonic processes at different power excitations values assuming a Poisson function for the excitation probability.<sup>[338, 339]</sup> Results are plotted in Figure V.40c.

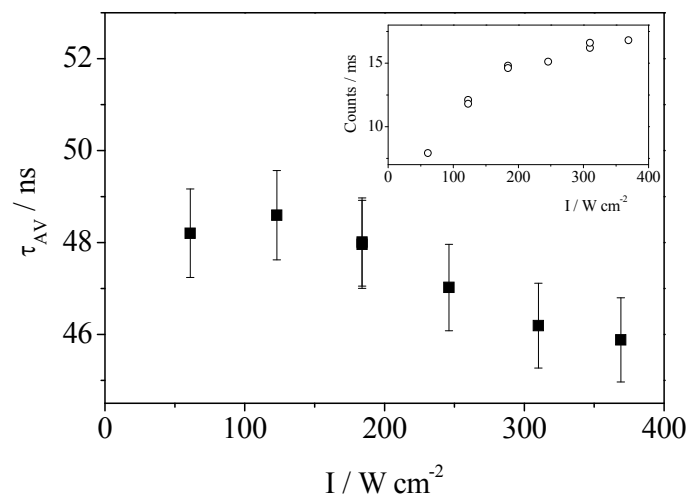


**Figure V.41.** Average lifetime and counts dependence with power excitation for a point measurement (60 s) over a QD LB film deposited at  $30 \text{ mN m}^{-1}$ .

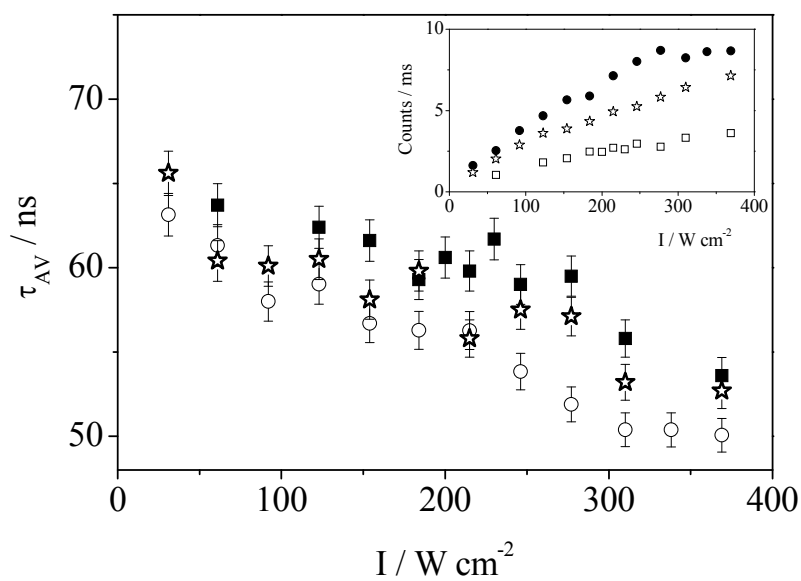


**Figure V.42.** Variation of the average lifetime and counts with the power excitation for measurements carried out over the same area in each system where the QDs are deposited at  $30 \text{ mN m}^{-1}$ : QDs (squares), bilayer (circles) and co-spreading ( $X_p = 0.50$ ) (stars).

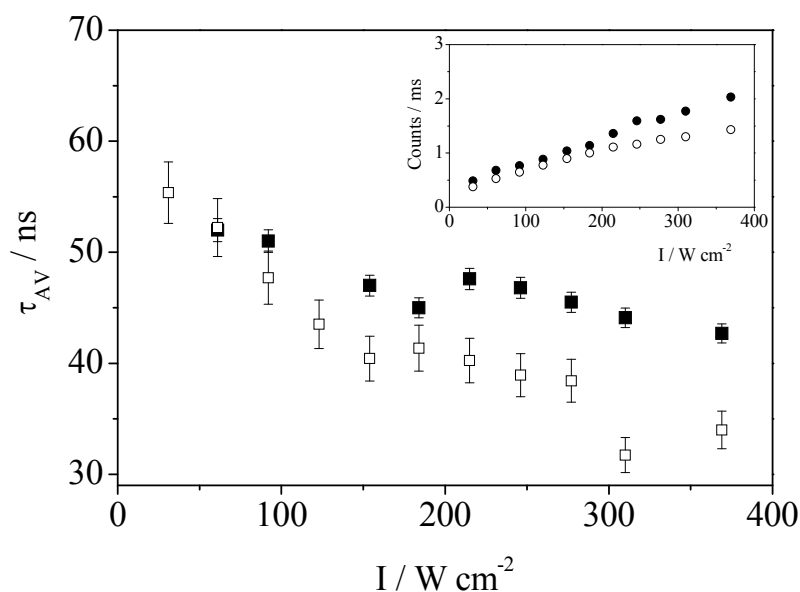


**Figure V.43.** Variation of the average lifetime and counts with the power excitation (energy ramp) for measurements carried out over the same area in co-spread ( $X_P = 0.65$ ) systems where the QDs are deposited at 14 (open symbols) and 30 (closed symbols)  $\text{mN m}^{-1}$ .

In summary, these experiments have allowed us to analyze the effect of excitation energy on LB films. The average lifetime value decreases when the power laser is increased due to a multi-exciton formation. In order to avoid multi-excitonic relaxation processes that interfere in the analysis of the QDs PL dynamics, we decided to measure at a low power excitation,  $108 \text{ W cm}^{-2}$ , which at the same time allows us to collect a PL decay with sufficient intensity counts to minimize experimental uncertainty. In the case of the power energy selected, we estimated that the formation of multi-excitonic states is low, *ca.* 3.1% (Figure V.42c).

#### V.4.3.3. Effect of the Exposure Time on QDs LB films

In order to analyze the effect of the exposure time on the PL decay we carried out several experiments by modifying this time. We performed two different sets of measurements over points and areas. The point measurements in different samples show that the PL decays vary during the exposure time,

resulting in longer lifetimes when increasing the measurement time, Figure V.44. After the exposure, if we repeat the measure in the same zone we obtain a lifetime value longer than in the beginning, i.e., the laser irradiation induces a process, which is more pronounced in close-packed zones. To check this possible enhanced PL, we analyzed the number of counts with the time. For comparison in Figure V.44 are also presented the variation of the intensity (number of counts) with the exposure time. Results demonstrate that the number counts increases as the exposure time of the sample increases.<sup>[340, 341]</sup> This behaviour, referred as photoenhancement of luminescence, could be ascribed to several process: (i) fluctuations of non-radiative decays<sup>[342]</sup>, (ii) heating effect over the capping molecules leading to the enhancement of the non-radiative recombination,<sup>[340]</sup> and (iii) water molecules adsorption on the QD surface that photo-passivates surface traps forming selenium-oxygen complexes<sup>[303, 331, 343]</sup>.

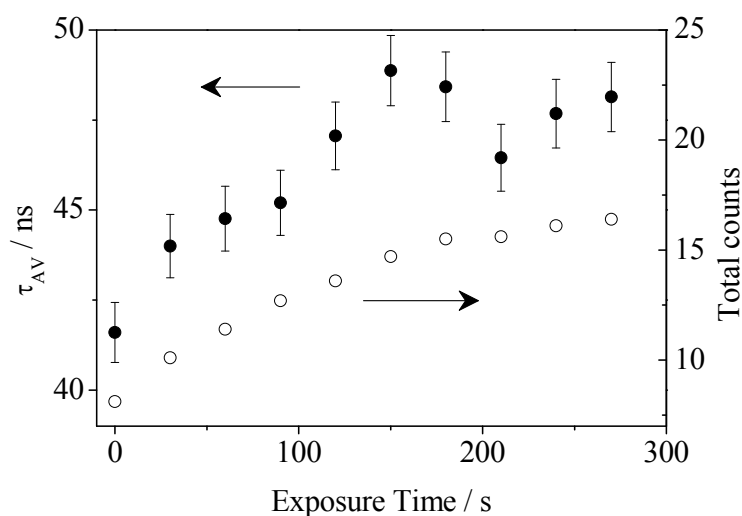


**Figure V.44.** Average lifetime and counts evolution with the laser exposure time obtained during a point measurement at  $108 \text{ W cm}^{-2}$  over a QD LB film deposited at  $30 \text{ mN m}^{-1}$ .

Furthermore, this process is quasi-reversible. To prove this, we carried out the following experiment collecting measurements in several points of the LB samples with the sequence: exposure/waiting in darkness/exposure. The exposure was

performed at different power excitations and therefore, the exposure time was increased when a lower power excitation is used to achieve a similar effect. The experimental procedure was the following: first, we take a FLIM image of the zone (A) and then record the point measurement ( $\tau^I$ , 1<sup>st</sup> exposure); immediately after, we take other FLIM image of the zone (B) and left the sample at darkness (shutter closed) during 30 min; just after, we take the third image (C) and make other point measurement ( $\tau^{II}$ , 2<sup>nd</sup> exposure) followed by the last FLIM image capture (D). Thus, in these measurements we recorded the images of the zone at the beginning and end of every period of laser irradiation and darkness waiting period steps (30 min). As an example of the point laser exposure effect on the samples, images of two different samples are shown in Figure V.45. After the laser exposure the affected zone change in the colour scale (lifetime) from green to red indicating an increasing in the lifetime. After waiting 30 min, we checked again the zone, and the observed colour highlights a partial recover to the initial state, less coloured red zone. The waiting time in darkness was established after several proofs of successive 5 min waits and image captures. The effect in the image becomes noticeable after 30 min, thus it is enough time to observe the behaviour ensuring that the scanner position is kept stable.

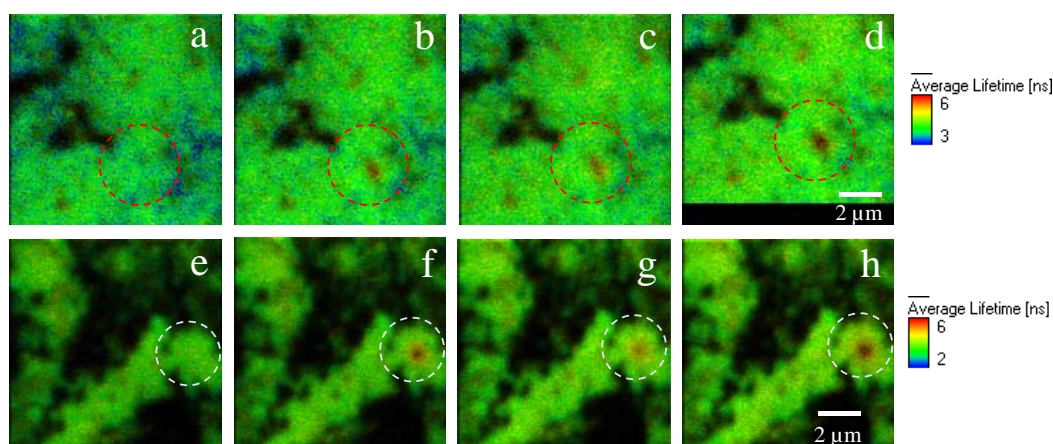


**Figure V.45.** FLIM images showing the evolution of the exposed zone to laser irradiation (a, e) zone selected; (b, f) after 5 min exposed (first laser irradiation); (c, g) after waiting 30 min; (d, h) after 5 min exposed (second laser irradiation). The experimental conditions were:  $430 \text{ W cm}^{-2}$  applied over a selected point. The images correspond to: bilayer (a-d) and co-spreading ( $X_P = 0.50$ ) (e-h) prepared at the surface pressure of  $30 \text{ mN m}^{-1}$ .

The photo-induced process is quasi-reversible. To confirm this qualitative observation, we analyze the average lifetime,  $\tau_i^j$  at the different stages of the experiment, where  $i$ , indicates the time range of laser illumination evaluated in the decay curve and  $j$  the number of exposure. We evaluated the average lifetime acquired at regular intervals during each illumination period to have an idea of the sample point state at each moment. Our results show that  $\tau_{\text{beginning}}^I < \tau_{\text{end}}^I$  highlighting the photoenhancement behaviour previously mentioned. Other fact observed is that  $\tau_{\text{end}}^I > \tau_{\text{beginning}}^{II} > \tau_{\text{beginning}}^I$ , consistent with a quasi-reversible process: the average lifetime for the initial state after waiting (2<sup>nd</sup> exposure) is lower than the corresponding to the final state after the 1<sup>st</sup> exposure. In summary, the average lifetime values and images (Table V.6, Figure V.45), both, agree with the idea that the laser illumination induces a quasi-reversible process. After the waiting in darkness, the average lifetime is decreased but it does not recover to the initial value (sample state). In the case of the images, the colour of the zone around the point exposed changes but never gets back to the initial state. This



indicates that the relaxation process implied is very slow or some irreversible changes occurs in the QD surface.<sup>[303]</sup> The most plausible mechanism could be a QD surface photo-passivation that stabilizes the surface trap states and therefore, increases the lifetime of these non-radiative trap states.<sup>[303, 343]</sup>

**Table V.6.** Representative average lifetime values of bilayer sample at  $\pi = 30 \text{ mN m}^{-1}$  obtained from measurements of three different points at distinct power excitation. The waiting time between laser exposures was 30 min. The values marked with a gray shadow compare the end state after the first exposure with the beginning state after the waiting step.

Intensity / $\text{W cm}^{-2}$	Laser Exposure	$\tau_{0-30\text{s}}$ / ns	$\tau_{270-300\text{s}}$ / ns	$\tau_{570-600\text{s}}$ / ns	$\tau_{1170-1200\text{s}}$ / ns
430	$\tau^I$	32 ± 3	47 ± 3	-	-
	$\tau^{II}$	43 ± 3	65 ± 4	-	-
215	$\tau^I$	39 ± 3	53 ± 3	56 ± 3	-
	$\tau^{II}$	47 ± 3	51 ± 3	58 ± 2	-
108	$\tau^I$	29 ± 2	34 ± 3	42 ± 3	52 ± 3
	$\tau^{II}$	43 ± 3	50 ± 2	59 ± 3	63 ± 3

In this way, these experiments have allowed us to observed a partially photoactivated PL enhancement. Thus, lengthening of the average lifetime is produced when the sample is illuminated and shortening when it is kept in the darkness due to a quasi-reversible photo-passivation of the particle surface. According to these experiments, we decided to change the laser exposure procedure and to measure over areas not points. By reducing the exposure time on the surface to 1 ms per pixel, we have avoided variations in the average lifetimes after several measurements on the same area. This fact was checked in the different samples showing an average standard deviation of  $\sim 2$  ns for at least six measurements in each area. Thus, the lifetime value obtained from areas ( $80 \times 80 \mu\text{m}^2$ ) is more representative of the sample than from points. Besides for each sample a total of 25 areas were measured in order to achieve a representative sampling according to the homogeneity of the films.

#### V.4.4. Photoluminescence Dynamics of QD/PS-MA-BEE LB Films

For comparative purposes, we studied the influence of the film preparation methodology (bilayer and co-spreading) and the QDs density in the film by changing the surface pressure selected for the LB deposition. The preliminary analysis based on average lifetimes and intensity for high density QD systems, namely, QD film, bilayer and a polymer-QD mixed film indicate that the concentration and packing of QDs affect to the lifetime, obtaining different values for each system: QD film ( $63 \pm 3$  ns;  $2.1 \pm 0.5$  counts/ms), bilayer ( $51 \pm 2$  ns;  $4.1 \pm 1.1$  counts/ms) and QD-polymer ( $X_p = 0.50$ ) mixed film ( $59 \pm 4$  ns;  $2.6 \pm 0.3$  counts/ms). These differences are also reflected in the decay curves, see Figure V.46, mainly in the short components.

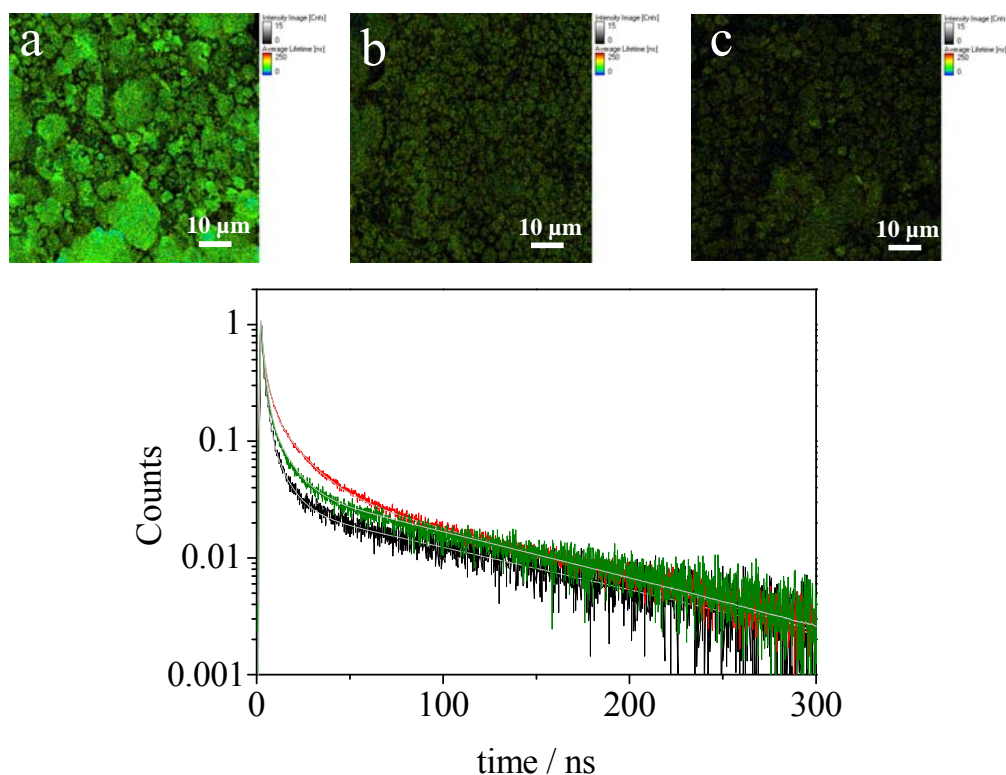


**Figure V.46.** FLIM images and normalized PL decay curves for three different QDs systems: QD film onto polymer LB film (bilayer system) (a, red line); QD/polymer mixed ( $X_p = 0.50$ ) LB film (b, green line) and QDs LB film (c, black line). The QDs films were deposited at a surface pressure

of  $30 \text{ mN m}^{-1}$ . Solid lines in grey colour show the fitting results with a multi-exponential decay analysis.

To confirm that the decay curves obtained from different regions within each sample agree with each other, we analyzed several PL decays in distinct areas. An illustrative example is shown in Figure V.47, where three different regions of the same sample are presented. The respective curves agree with each other. Therefore the average lifetime values obtained are representative of each system.

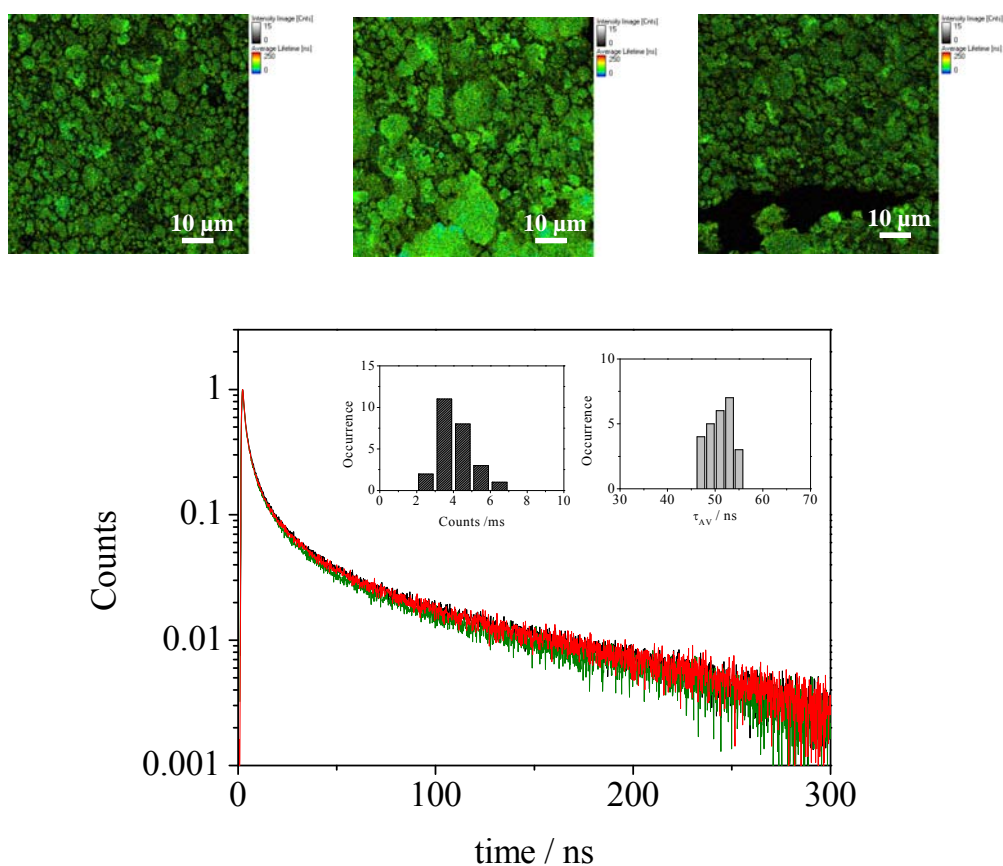


**Figure V.47.** Comparative FLIM images and normalized PL decay curves for the bilayer system over three different areas for each side of the lifetime values distribution: low (green line), medium (black line) and high (red line) respectively. The histograms show the lifetime and counts distribution in this sample.

On the other hand, the dark zones observed in the FLIM images corresponding to regions not covered were checked, and no emission was observed.

We also analyze the effect of the surface composition on the emission properties. Thus, LB films of QD/PS-MA-BEE were prepared at different polymer mole fractions,  $X_p = 0.35, 0.50$  and  $0.65$  at the surface pressure of  $30 \text{ mN m}^{-1}$ . By comparing the decays of the different co-spreading films shown in Figure V.48, we observe that the main differences are in the slowest component. This behaviour suggests that a different arrangement of QDs is obtained by varying the polymer concentration. The average lifetime and intensity counts values of each system highlight this behaviour: ( $X_p = 0.50$ ) ( $59 \pm 4 \text{ ns}$ ;  $2.6 \pm 0.3 \text{ counts/ms}$ ); ( $X_p = 0.65$ ) ( $48 \pm 3 \text{ ns}$ ;  $1.0 \pm 0.1 \text{ counts/ms}$ ) and ( $X_p = 0.35$ ) ( $44 \pm 6 \text{ ns}$ ;  $1.3 \pm 0.3 \text{ counts/ms}$ ).

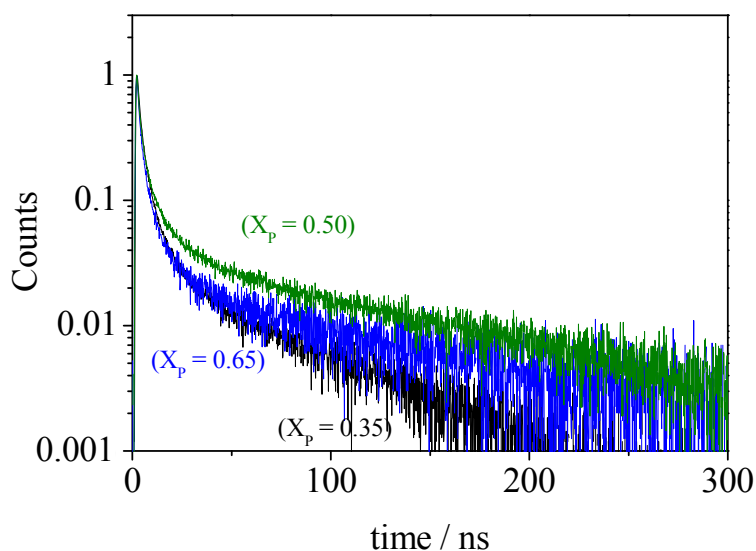


**Figure V.48.** Comparative normalized PL decay curves for three different QD-polymer mixed LB film at high surface pressure ( $30 \text{ mN m}^{-1}$ ) with a polymer mole fraction: ( $0.35$ ) (black line); ( $0.50$ ) (green line) and ( $0.65$ ) (blue line).

The effect of the surface pressure in the PL decays was also studied. As is shown in Figure V.49 at low surface pressure the film PL decays point to a lower contribution in the slow components corroborated by the lifetime average values: ( $\bar{X}_p = 0.65$ ) ( $48 \pm 4$  ns;  $0.8 \pm 0.1$  counts/ms) and ( $\bar{X}_p = 0.35$ ) ( $31 \pm 6$  ns;  $0.9 \pm 0.1$  counts/ms).

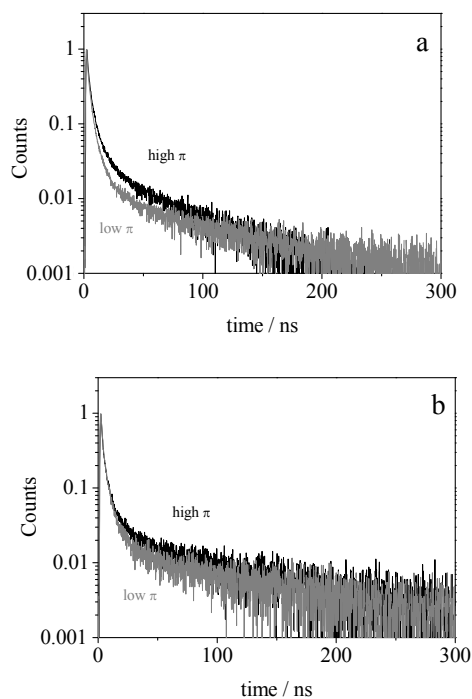


**Figure V.49.** Comparative normalized PL decay curves for two different QD-polymer LB systems at low (gray line) and high (black line) surface pressure ( $14$  and  $30$   $\text{mN m}^{-1}$ ) with a molar ratio: ( $\bar{X}_p = 0.35$ ) (a) and ( $\bar{X}_p = 0.65$ ) (b).

As was mentioned the PL decays were analyzed by a multi-exponential function that requires four exponential components to be properly fitted. Results are collected in Table V.7.

**Table V.7.** Results from multi-exponential decay analysis for area measurement over LB films at 108 W cm<sup>-2</sup>. The reduced chi-square values,  $\chi^2$ , all close to 1, and the weighted residuals indicate a good fit to each data set. Data obtained from measurements over at least 25 areas for each sample.

	<b>High <math>\pi</math></b>				
	<b>QDs</b>	<b>Bilayer</b>	<b>Co-spr</b> ( $X_p = 0.50$ )	<b>Co-spr</b> ( $X_p = 0.65$ )	<b>Co-spr</b> ( $X_p = 0.35$ )
$\tau_1 / \text{ns}$	$0.12 \pm 0.04$	$0.15 \pm 0.02$	$0.15 \pm 0.02$	$0.14 \pm 0.02$	$0.19 \pm 0.05$
$f_1 (\%)$	$19 \pm 4$	$10 \pm 1$	$12 \pm 1$	$16 \pm 2$	$16 \pm 5$
$\tau_2 / \text{ns}$	$2.0 \pm 0.1$	$2.60 \pm 0.08$	$2.15 \pm 0.07$	$2.0 \pm 0.1$	$2.4 \pm 0.2$
$f_2 (\%)$	$17 \pm 2$	$16.6 \pm 0.6$	$20 \pm 1$	$22 \pm 2$	$29 \pm 3$
$\tau_3 / \text{ns}$	$9 \pm 1$	$14.2 \pm 0.5$	$10.3 \pm 0.6$	$9 \pm 1$	$11 \pm 1$
$f_3 (\%)$	$15 \pm 2$	$27 \pm 1$	$17.5 \pm 0.6$	$20 \pm 1$	$21 \pm 2$
$\tau_4 / \text{ns}$	$123 \pm 5$	$102 \pm 3$	$118 \pm 4$	$114 \pm 7$	$116 \pm 6$
$f_4 (\%)$	$48 \pm 3$	$46 \pm 2$	$50 \pm 2$	$42 \pm 3$	$35 \pm 3$
$\tau_{\text{AV}} / \text{ns}$	$63 \pm 3$	$51 \pm 2$	$59 \pm 4$	$48 \pm 3$	$44 \pm 6$
<b>Counts/ms</b>	$2.1 \pm 0.5$	$4.1 \pm 1.1$	$2.6 \pm 0.3$	$1.0 \pm 0.1$	$1.3 \pm 0.3$

	<b>Low <math>\pi</math></b>	
	<b>Co-spr</b> ( $X_p = 0.65$ )	<b>Co-spr</b> ( $X_p = 0.35$ )
$\tau_1 / \text{ns}$	$0.13 \pm 0.04$	$0.16 \pm 0.07$
$f_1 (\%)$	$18 \pm 3$	$26 \pm 4$
$\tau_2 / \text{ns}$	$1.9 \pm 0.2$	$2.0 \pm 0.2$
$f_2 (\%)$	$26 \pm 3$	$31 \pm 3$
$\tau_3 / \text{ns}$	$6.9 \pm 0.8$	$7.0 \pm 0.9$
$f_3 (\%)$	$22 \pm 2$	$21 \pm 2$
$\tau_4 / \text{ns}$	$119 \pm 10$	$124 \pm 10$
$f_4 (\%)$	$34 \pm 4$	$21 \pm 3$
$\tau_{\text{AV}} / \text{ns}$	$48 \pm 4$	$31 \pm 6$
<b>Counts/ms</b>	$0.8 \pm 0.1$	$0.9 \pm 0.1$

In the time range analyzed, the decays exhibit a pronounced curvature that is clearly distinct for films prepared by bilayer and co-spreading deposition, see Figure V.46. The results from the multi-exponential analysis of film decays indicate that the results obtained for the bilayer film stand out, because the averaged short decay times are clearly longer than for co-spreading films, while the long decay time is quite similar for all samples prepared by the two deposition methods. Later, we will relate the former observation to differences in film morphology.

On the other hand, the relative brightness (counts) of the PL images also reflects the difference between bilayer and co-spreading films. Under the same excitation conditions, the bilayer films have a significantly higher intensity of emission compared to co-spreading films, i.e. a larger number of counts per image. This observation could be simply due to a higher surface concentration of QDs in the bilayer films. To disregard this point, the emission intensity is plotted against the particle density calculated from surface concentration, in Figure V.50. The surface concentration was calculated from the  $\pi$ - $\Gamma$  isotherms at the surface pressure of LB deposition and expressed in number of QDs per area. Results in Figure V.50 show that the PL intensity of the co-spreading films is proportional to particle density, while the PL intensity of the bilayer film stands out, indicating that it is much more emissive than the co-spreading film with the same particle density.

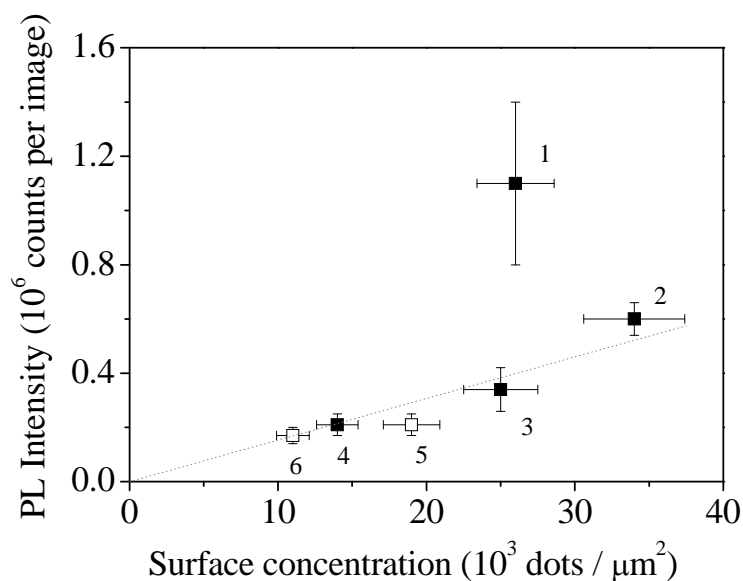


**Figure V.50.** Emission intensity from PL images vs. surface concentration of QDs calculated from the corresponding  $\pi$ - $\Gamma$  isotherms for the bilayer (1) and co-spreadings ( $X_P = 0.50$ ) (2); ( $X_P = 0.65$ ) (3, 5) and ( $X_P = 0.35$ ) (4, 6). Closed and open symbols represent data from films deposited at high and low surface pressures, 30 and 14  $\text{mN m}^{-1}$ , respectively.

#### V.4.4.1. Interpretation of the QDs Photoluminescence Dynamics

As was previously mentioned, the PL dynamics of QDs in the ns– $\mu$ s timescale are intrinsically complex due to the role of surface defect and charge trapped states in excited-state relaxation.<sup>[319, 344-347]</sup> In the solid films, the complexity is further increased by the possibility of excitation energy transfer between QDs, because of the short interparticle distances in the closely-packed film regions. Accordingly, several processes are involved in QD photoexcitation dynamics that are depicted in a schematic diagram in Figure V.51. In addition to radiative recombination process, there are other competing processes from the excited state such as the carrier trapping at QD surface defects,  $k_{ed}$ ; charge transfer into ligand-based orbitals,  $k_{el}$ , and relaxation to the ground state,  $k_{dg}$  and  $k_{bg}$ . The QD surface defect states strongly quench emission from band-edge exciton recombination,  $k_{eb}$  promoting faster excited-state decay. The surface defects can be arisen from native defect such as metal vacancies or dangling ligand bonds<sup>[348]</sup> and can be also related to detachment of ligand molecules as occurs in diluted QD solutions<sup>[335]</sup>. Other non-radiative recombination processes such as hot carrier relaxation and multi-excitonic processes can also contribute to ultrafast excited-state decay. Furthermore, in QD films the complexity is increased by the possibility of energy migration and trapping between QDs due to a compact particle arrangement in densely covered regions. Besides, the formation of small QD clusters, which act as energy traps together with QD surface defects, and the compact particle arrangement also promotes luminescence quenching due to stabilization of non-emissive charged states by Coulomb interactions between clustered QDs<sup>[320, 349-351]</sup> [349] [320, 350]. The Coulombic stabilization of charged states only induces quenching if it favours charge recombination to ground state,  $k_{bc}$ , relative to excited state. Finally, the delayed luminescence from charge transfer and trapping in the surrounding environment of the QD ( $k_{el}$  and  $k_{be}$ ) occurs and is the main contribution from isolated QDs or compact regions without traps, which do not suffer emission quenching. This emission explains the exponential



behaviour observed in the PL decays from about a hundred ns onward and is associated to a slow decay rate.

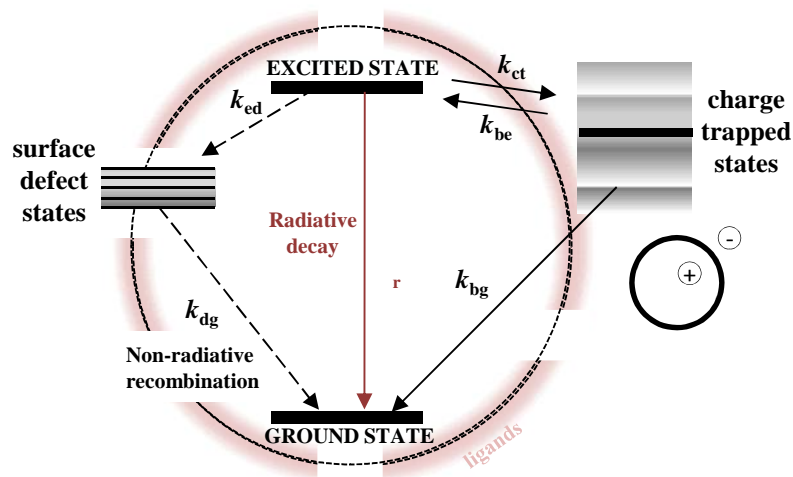


**Figure V.51.** A simplified schematic diagram of several processes involved in QD photoexcitation dynamics adapted from (Jones, 2010<sup>[25]</sup>).

Prior to the decay analysis, we describe our qualitative interpretation of the film decays, which is based on this model and the broad literature about PL dynamics of QDs and their solid films. We attribute the sharp decrease in the initial nanoseconds to QDs with extensive surface defects that strongly quench emission from band-edge exciton recombination ( $k_{ed}$  in Figure V.51).<sup>[334, 335]</sup> Within an ensemble of QDs, the surface conditions vary among the particles, and more likely there is a statistical distribution of the number of surface defects per particle. We hypothesize that a small fraction of QDs with extensive surface defects can act as excitation energy traps in our ensemble of deposited QDs in the films, as it is further discussed below.

Because the emission from surface defect states is usually observed at lower energies relatively to core exciton recombination ( $k_{dg}$  in Figure V.51), we perform PL spectral measurements. Taking into account that the QD emission from core and trap states are spectrally separable, these experiments allow us to select the emission wavelength range. The collection of both spectral features in

the same time-trace makes the PL decay analysis more difficult.<sup>[346]</sup> In order to obtain evidences, we record the PL emission at different wavelength ranges, at the blue and red sides of the PL QDs spectrum maximum. The wavelength selection is carried out using several band-pass filters placed in front of avalanche photodiodes.

The emission spectra of the QDs dissolved in chloroform and in LB film were recorded. As Figure V.52 shows, the QDs PL spectra consist of two emission bands: a sharp band-edge at  $\sim 580$  nm and a broad non-structured band at longer wavelength. The band-edge emission is due to core recombination of the exciton in the mostly delocalized states in QDs, while the broad band is ascribed to the trap-state emission and due to surface defects on the interface between the nanoparticle and the surrounding medium.<sup>[343, 344, 352]</sup> In the case of QDs in solution, Figure V.52a shows the core recombination emission band, centred at  $\sim 580$  nm, and the broad non-structured band centred at wavelengths longer than  $\sim 700$  nm. It is interesting to note that the intensity corresponding to surface defect states band is much lower than the one corresponding to the core recombination band. This fact could indicate that no significant interference occurs from the surface defects' emission on the decay curves. In the case of QDs LB films, Figure V.52b, the core exciton recombination band is also centred at  $\sim 580$  nm, but the main difference occurs in the surface defect emission band centred at  $\sim 620$  nm, which is more pronounced in the films than in solution. This predominance of surface defect emission band in the spectra of QDs films has been observed by other authors.<sup>[340]</sup>

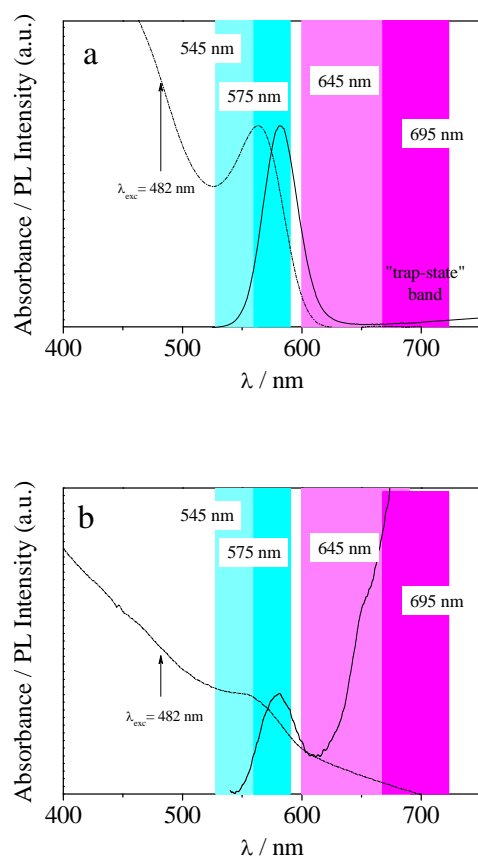


**Figure V.52.** Schematic graph to show the wavelength position of the excitation and emission collected with the different band-pass filters:  $545 \pm 17.5$  nm (light blue);  $575 \pm 15$  nm (blue);  $645 \pm 45$  nm (light magenta) and  $695 \pm 27.5$  nm (magenta) for QD in solution (a) and in LB film (b). The absorption (dotted line) and PL (solid line) spectra of QD are also show as reference.

In order to evaluate the effect of the surface defects emission on the PL decay curves, we carried out measurements over areas of the QDs LB films at  $108 \text{ W cm}^{-2}$  with the following band-pass filters available:  $545 \pm 17.5$  nm (F1),  $575 \pm 15$  nm (F2),  $645 \pm 45$  nm (F3) and  $695 \pm 27.5$  nm (F4) depicted in Figure V.52. The filters F1 and F2 select emission from core exciton recombination, whereas filter F3 is already overlapping with surface defect emission.

First, we record the decay curves for the different systems to confirm that the behaviour observed in the decay curves is independent of the QDs emission

wavelength collected. As can be seen in Figure V.53, the tendency observed in the decay curves between the different methodologies of preparation, QDs, bilayer and co-spreading, is kept in both sides of the QDs spectrum.

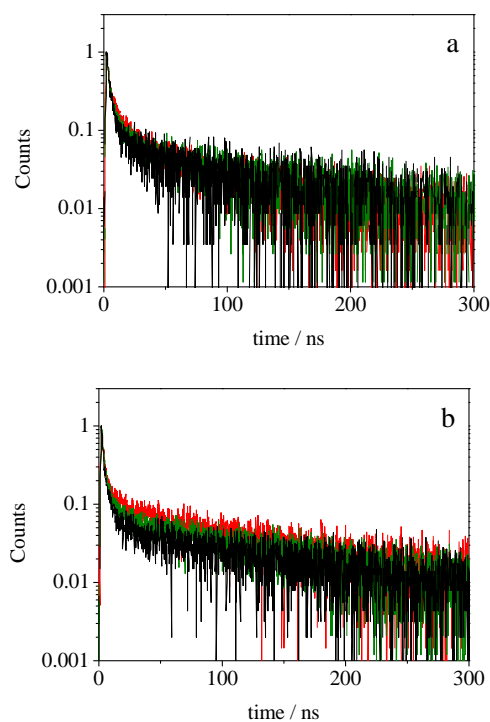


**Figure V.53.** Comparative normalized PL decay curves collected with a band-pass filter of 560-590 nm (a) and 600-690 nm (b) for three different high QDs density systems: QD film onto polymer LB film (bilayer system) (red line); QD/PS-MA-BEE mixed LB film ( $X_P = 0.50$ ) (green line) and QDs LB film (black line).

Focusing the attention within each system, see Figure V.54, the results show that the PL decays practically do not change in the emission range monitored with the filters F1, F2 and F3, i.e. 528-690 nm, except for some minor changes that may be attributed to sample heterogeneity. Thus, we select a transmission filter in the range of 550-690nm to study the samples. This filter allows us to collect the core recombination emission without almost interference from trap-state emission that could complicate the PL decay interpretation.<sup>[346]</sup> On the other hand, the quenching effect of surface defect states is observed in the

initial part of the decay curves, as a fast decay component previously referred. This fast quenching process is out of the main scope of this work and, therefore, in the data analysis the initial part of the decay curves,  $t < 10$  ns, was neglected and the analysis was focused to the longest components also attributed to emission from core exciton recombination.

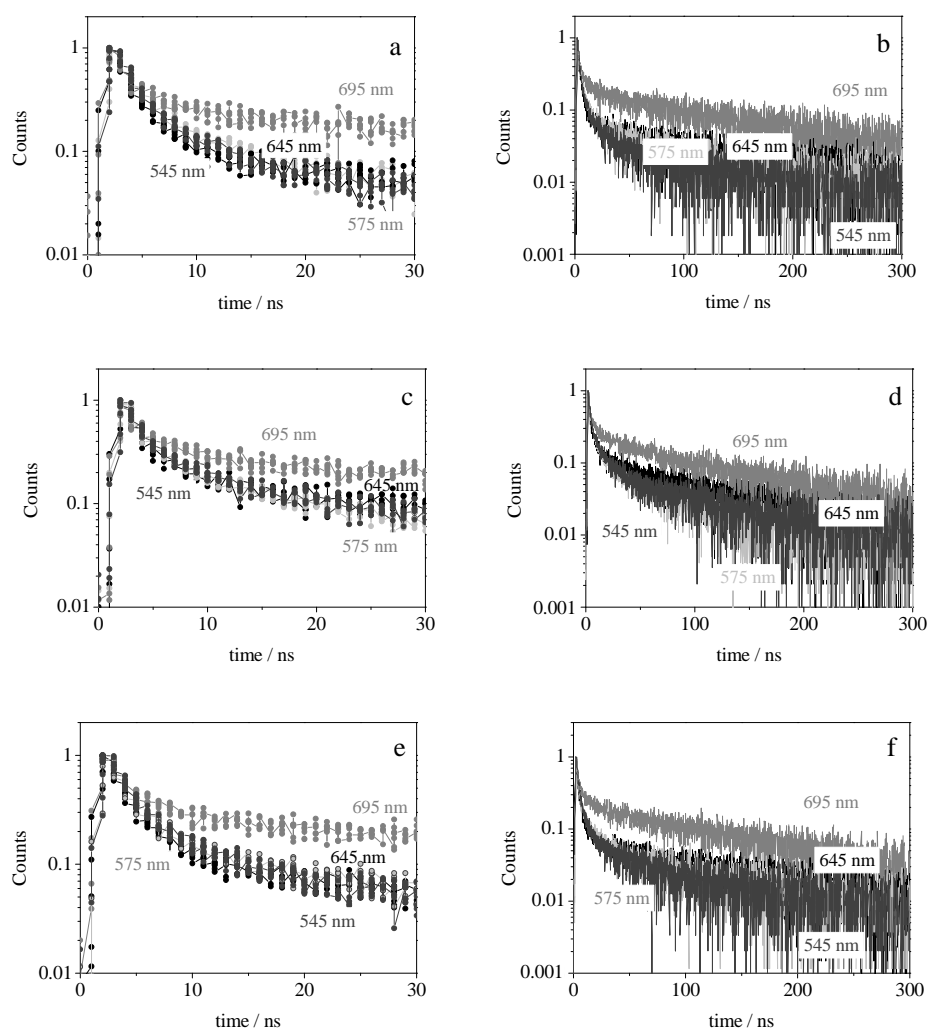


**Figure V.54.** Comparative normalized PL decay curves collected with different band-pass filters of 528-563 nm (dark gray line); 560-590 nm (light gray line); 600-690 nm (black line) and 668-723 nm (gray line) at  $108 \text{ W cm}^{-2}$  for a QDs (a, b); bilayer (c, d) and co-spread ( $X_P = 0.50$ ) (e, f) LB films where the QDs are deposited at  $30 \text{ mN m}^{-1}$ .

Finally, when we collect the emission decay in the range of surface defect emission<sup>[343, 344, 352, 353]</sup> with the filter F4 that has a transmission window between 668-723 nm, slower components appear either in solution, Figure V.55, and LB films. This behaviour is characteristic of the surface-defect emission.<sup>[352, 353]</sup>

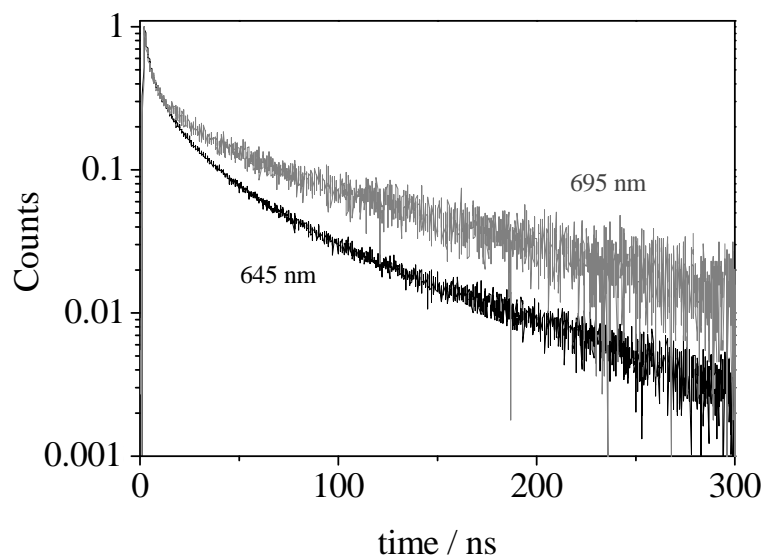


**Figure V.55.** Comparative normalized PL decay curves collected with different band-pass filters of 600-690 nm (black line) and 668-723 nm (gray line) at  $67 \text{ W cm}^{-2}$  for a QDs chloroform solution.

In summary, the photoluminescence spectral measurements collected in different zones of the QD spectrum allowed us to discard significant interference from the surface defects emission on the decay curves in the wavelength range selected. In this sense, the behaviour observed at long spectral wavelengths highlighted the surface-defects emission and allows us to ensure that the conditions selected to work are not almost influenced for this emission and collect the core-recombination emission.

Going back to the study of the effect of the films morphology on the photoluminescence properties, in an attempt to interpret the differences between the emission properties of co-spreading and bilayer films, the TEM images of

these films were analyzed. Representative TEM images are shown in Figure V.56. The TEM images show regions densely covered along with other regions more sparsely covered. Overall, the bilayer film shows a more regular particle distribution than co-spreading films. It is also noticeable the presence of small densely packed clusters of QDs, which could act as excitation energy traps. This idea is supported by previous results that reported the existence of luminescence quenching and enhanced blinking occurs in small QD clusters.<sup>[320]</sup> The stabilization of non-emissive charged states by Coulomb interactions between clustered QDs seems to be responsible for this behaviour.<sup>[320, 349-351]</sup>

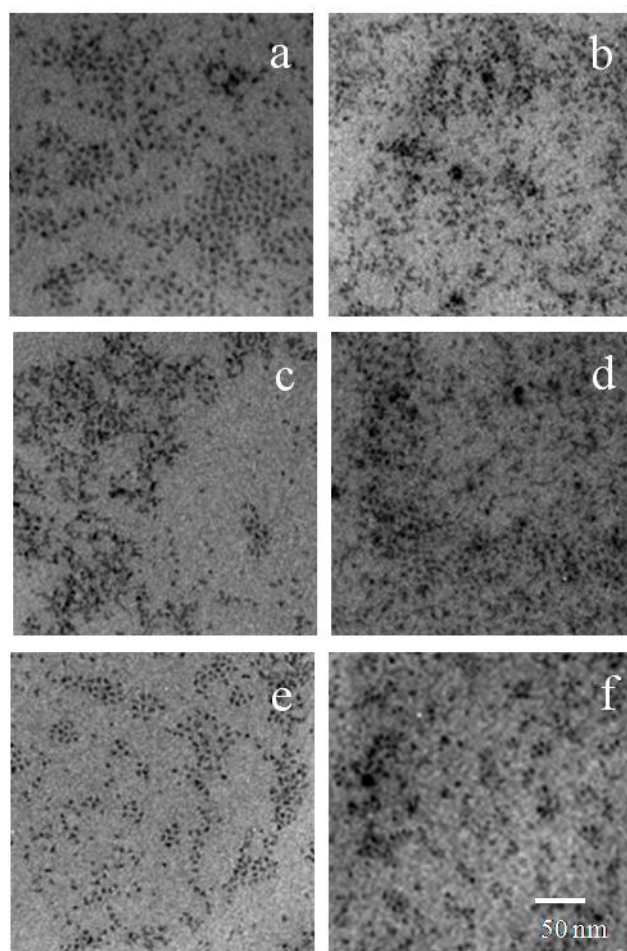


**Figure V.56.** Examples of TEM images obtained for bilayer (a) and co-spreading deposition with a QD-polymer molar ratio of  $X_p = 0.50$  (b)  $X_p = 0.65$  (c) and  $X_p = 0.35$  (d) at high pressure,  $\pi = 30 \text{ mN m}^{-1}$ ; and co-spreading with ratios of  $X_p = 0.65$  (e) and  $X_p = 0.35$  (f) at low pressure,  $\pi = 14$

$\text{mN m}^{-1}$ . The area shown in TEM images corresponds approximately to about 1 pixel in the FLIM images.

The PL dynamics of the films are affected by the surface distribution of particles, because in the regions densely covered the interparticle distances are only a few nm and dot-dot excitation energy transfer is likely to occur within the ensemble of closely packed particles. The migration of excitation energy affects the observed decay because of sample heterogeneity and, in particular, due to excitation energy traps that are commonly present in solid films. We attribute the role of energy traps in our films to QDs with extensive surface defects and to small aggregated QDs clusters, as mentioned above.

From about a hundred ns onward, the decays show an almost exponential behaviour that is attributed to isolated QDs or to closely-packed regions without energy traps, which do not suffer emission quenching. The PL of the QDs decays very slowly with lifetime components longer than hundred ns, and even reaching  $\mu\text{s}$  in chloroform solution. The long decay tail observed in the PL of QDs has been attributed in the literature to a process of delayed luminescence from charge transfer and trapping in the surrounding environment of the quantum dot.<sup>[345, 346]</sup> Furthermore, it has also been associated with the power-law statistics of emission intermittency of single-dots observed in the timescale of ms to s.<sup>[345, 354, 355]</sup> We assume that delayed luminescence from charge transfer and trapping in the surrounding environment is also responsible for the long decay tail observed in the emission of our QDs ( $k_{\text{ct}}$  and  $k_{\text{bc}}$  in Figure V.51).

Alternatively to the multi-exponential analysis of QDs film decays, we have adopted an approximate model to describe the PL dynamics in QD/polymer films, in particular, the excitation energy migration and trapping processes in the densely covered regions. The model considers two separate contributions from sparse and compact regions of immobilized QDs in the films. This picture is supported by the TEM images that show regions compactly covered with QDs



along with other regions more sparsely covered. Therefore, the decay function assumes two terms,  $S(t)$  and  $C(t)$ , that account separately for sparse and compact regions of QDs,

$$D(t) = \sigma S(t) + (1 - \sigma) C(t) \quad [\text{V.1}]$$

The  $S(t)$  term describes the intrinsic photophysics of QDs, which can be very complex because core exciton states often interact with surface localized states and the surrounding environment. In organically coated QDs, this type of interaction can result in charge trapping on surface defect sites, or on ligand-based orbitals, with the formation of an ionized core state that is usually non-emissive. Therefore, charge transfer and trapping in the surrounding environment have an important role in excited-state relaxation of QDs.<sup>[345, 346]</sup> On the other hand, the term  $C(t)$  further accounts for interparticle energy migration and trapping processes, because it describes the contribution from compact film regions. An overview on the models selected for  $S(t)$  and  $C(t)$ , and their respective parameters, is explained below. The term  $S(t)$  was assumed to be described by the Tachiya-Mozumder model.<sup>[355, 356]</sup> This model considers a mechanism of charge trapping by electron tunneling toward an uniform distribution of traps. The decay function is calculated by numerical Laplace inversion of,

$$\hat{S}(s) = \frac{1}{s + 1/\tau_r + k_{ct} (\tau_0 s)^\mu} \quad [\text{V.2}]$$

with three adjustable parameters, the radiative recombination rate  $\tau_r^{-1}$ , the charge transfer rate term  $\tau_0^\mu k_{ct}$ , and a power-law exponent  $1 + \mu$ . A value of 30 ns was taken as initial guess for  $\tau_r$  in the fittings. This value was estimated from the  $\tau_r$  fitted for decays of QDs dissolved in chloroform solution and corrected for the dielectric screening in the films. The charge transfer rate term  $\tau_0^\mu k_{ct}$  was varied to fit the long time behaviour of the film decays. The initial guess for the power-law exponent  $1 + \mu \sim 2$  was also based on our results of luminescence decays of QDs

in chloroform. Using  $1 + \mu \sim 2$ , or equivalently  $\mu \sim 1$ , then by Laplace inversion of Equation V.2,

$$S(t) \approx \exp[-t/\tau_r(1 + k_{ct}\tau_0)] \quad [\text{V. 3}]$$

Here, we notice that Equation V.3 predicts a decay law exponential, in agreement with results observed at long times in the decays of Figure V.46.

For the  $\mathcal{C}(t)$  term in Equation V.1 we have adopted results from the theoretical method of diagrammatic expansion of the Green's function developed by Fayer and co-workers.<sup>[357, 358]</sup> In the case of a two-dimensional random distribution of donors and traps that interact through a dipolar transfer rate, the Green's function  $G^s(\mathbf{r} - \mathbf{r}', t)$  for the probability that excitation is on the initially excited site at time  $t$  is given by the following self-consistent equation in Laplace domain,

$$\hat{G}^s(\epsilon) + (2^{1/3}\pi/3^{3/2}\tau_D^{1/3}\epsilon)(C_D + 2^{2/3}C_T)[\hat{G}^s(\epsilon)]^{1/3} - 1/\epsilon = 0 \quad [\text{V. 4}]$$

with  $\tau_D$ , the donor lifetime,  $C_D$  and  $C_T$ , the donor and trap reduced concentrations, as described below. From Equation 4 the probability  $P_D(t)$  that an excitation is in the donor ensemble at time  $t$  is obtained from inverse transform of,

$$\hat{G}^D(0, \epsilon) = \hat{G}^s(\epsilon) / \left\{ 1 - (2^{1/3}\pi C_D/3^{3/2}\tau_D^{1/3})[\hat{G}^s(\epsilon)]^{1/3} \right\} \quad [\text{V. 5}]$$

The corresponding decay law is obtained multiplying  $P_D(t)$  by a decaying exponential with the donor lifetime,

$$\mathcal{C}(t) = \exp(-t/\tau_D) \times P_D(t) \quad [\text{V. 6}]$$

When fitting the decays, we have assumed the approximation in Equation 3 for the individual QD decay in the timescale of hundreds of ns, which implies that the donor lifetime is  $\tau_D \sim \tau_r(1 + k_{ct}\tau_0)$ . The reduced concentrations  $C_D$  and  $C_T$  are defined by,

$$C_D = \pi(R^{DD})^2 \rho_D \quad , \quad C_T = \pi(R^{DT})^2 \rho_T \quad [\text{V. 7}]$$

with  $R^{\text{DD}}$  and  $R^{\text{DT}}$ , the Förster radius for donor-donor and donor-trap energy transfer,  $\rho_{\text{D}}$  and  $\rho_{\text{T}}$ , the number densities of donors and traps, respectively. Although the interparticle distance is comparable with the QD size, it has been shown that the dipolar approximation in Förster theory describes reasonably well the excitation energy transfer between QDs or even between QD and fluorescent molecules.<sup>[359, 360]</sup> Using the theory, we estimate a Förster radius  $R^{\text{DD}}$  of 4.1 nm for donor-donor energy transfer and assume a similar  $R^{\text{DT}}$  value for donor-trap energy transfer. However, when fitting the decays no assumption was made about  $R^{\text{DD}}$  and  $R^{\text{DT}}$  values by treating  $C_{\text{D}}$  and  $C_{\text{T}}$  as the adjustable parameters.

The decays of our QDs films are only approximately described by Equation V.1 mainly because of two reasons: i) at very short times (below ten ns), the surface defect states contribute predominantly to fast excited-state decay; and ii) the model considered for the compact regions,  $C(t)$ , does not account for boundary effects due to finite domain size. In spite of these limitations, the approximate description of Equation V.1 allows to rationalize the photoluminescence dynamics of the QDs films using only a few adjustable parameters that afford physical insight about the systems studied.

The parameters obtained from fittings with Equation V.1 to the decays of bilayer and co-spreading films are collected in Table V.8. For instance, the bilayer film exhibits a decay curvature in the time range up to a hundred ns that is less pronounced than those of co-spreading films. Accordingly, the concentration of traps  $C_{\text{T}}$  for the bilayer film is about half of that from co-spreading films. Moreover, the concentration of donors  $C_{\text{D}}$  is approximately the same for both systems and it is close to the value of 3.3 particles within the area of a Förster radius. This corresponds to a dense arrangement of QDs in the compact domains as observed in TEM images. Indeed, considering the estimated Förster radius of 4.1 nm and the QD average size of 3.5 nm, then a hexagonal compact arrangement would be achieved for a interparticle surface-to-surface distance of

about 0.7 nm, which compares well with the length of the TOPO coating molecules. The TEM images of the bilayer film show compact regions with an approximately geometrical arrangement of particles. To clarify this issue we have calculated the radial distribution function (RDF) from the distribution of interparticle centre distances in TEM images. This function provides information about the short-range order inside the QDs domains. The RDF of the TEM images from the bilayer film shows a profile with two peaks positioned at  $5.1 \pm 0.7$  and  $9.8 \pm 0.7$  nm. These features compare roughly with the peak positions for the first two shells of an hexagonal compact arrangement with the particle size and separation referred to above.<sup>[316]</sup> By contrast, the RDF of co-spreading films shows a single peak at  $6.2 \pm 0.7$  nm followed by a plateau. The differences in the radial distribution function give support to a more regular structure in the bilayer film, as previously inferred from a visual inspection of the TEM images, and further reinforce the role of film morphology on the photoluminescence properties of QD films.

**Table V.8.** Parameters fitted with the model proposed (Equation 1) to photoluminescence decays of QDs in PS-MA-BEE mixed films for several deposition conditions.

	High $\pi$			Low $\pi$		
	Bilayer	Co-spr ( $X_p = 0.50$ )	Co-spr ( $X_p = 0.65$ )	Co-spr ( $X_p = 0.35$ )	Co-spr ( $X_p = 0.65$ )	Co-spr ( $X_p = 0.35$ )
$\tau_r$ (ns)	30.0	30.0	30.1	30.0	30.0	30.0
$\tau_0^\mu k_{ct}$	1.99	1.92	1.99	1.97	2.00	2.01
$1 + \mu$	1.98	1.92	1.96	1.96	1.92	1.97
$\sigma$	0.345	0.172	0.195	0.197	0.136	0.074
$C_D$	3.30	3.34	3.34	3.28	3.34	3.29
$C_T$	0.281	0.670	0.536	0.443	0.566	0.640

The decays from both bilayer and co-spreading films are approximately exponential at long times with the same slope (Figure V.46). Thus, the model parameters  $\tau_r^{-1}$ ,  $\tau_0^\mu k_{ct}$ , and  $1 + \mu$  describing the decay of isolated QDs or domains without energy traps,  $S(t)$ , are similar for bilayer and co-spreading films. Only the relative contribution to the decay,  $\sigma$ , is different with the bilayer film having a larger contribution of 34.5 % compared to 17.2 % in the QD-polymer co-spreading film with  $X_p = 0.50$ . We relate the larger contribution of  $S(t)$  in bilayer deposition to a film structure that contains a lower number of small aggregated QDs clusters that act as energy traps. The cluster formation has been previously studied and was attributed to dewetting processes. The current work further supports that nanoparticle clustering acts as energy traps thereby reducing the PL emission, as it was proposed elsewhere.<sup>[320]</sup>

To evaluate the effect of the polymer concentration on the luminescence properties, the photoluminescence decays of films with different polymer mole fraction were analyzed according to the Equation V.1. The QD/polymer compositions selected were  $X_p = 0.35, 0.50$  and  $0.65$ . The parameter values obtained from the decay fits show no significant differences, except for a small increase of the  $S(t)$  contribution when the polymer mole fraction increases. More significant is the emission brightness observed in these films that is related to the distinct surface density of QDs as was previously noticed in the Figure V.50.

The effect of surface pressure in co-spreading deposition was also evaluated. The fitted parameters obtained for decays curves of films prepared by co-spreading method and surface pressure of  $14 \text{ mN m}^{-1}$  are collected in Table V.8. From the parameter values it is possible to conclude that at low pressure the film decays have a lower contribution from the long time exponential component (Figure V.49), while the rest of fitted parameters are almost independent of the polymer mole fraction. The decrease of the emission intensity found in these films

is also consistent with the decrease of the QDs surface concentration (Figure V.50).

#### **V.4.4.2. Effect of Capping Exchange on the QDs Photoluminescence Dynamics: PSMABEE-capped QDs LB Films**

The nature of the surfactant capping and passivation process is not yet understood and affects the QD efficiency of radiative vs. non-radiative exciton decay.<sup>[303]</sup> Therefore, in an attempt to analyze the capping ligand and the surface passivation effect on the photophysical properties of QDs<sup>[329, 333]</sup> we proposed to measure a new kind of system, polymer capped-QDs, QD<sub>p</sub> hereafter, in solution and on LB films. Besides, QDs surface treatments have been shown to lead new optical responses.<sup>[361]</sup> As was previously mentioned, the polymer causes QDs PL quenching, however, QDs with hole accepting ligands have been proposed to build photoelectric devices looking for an efficient hole transfer and charge transport. Furthermore, the hole transfer is desirable to achieve a high power conversion in photovoltaic cells but not for applications such as LEDs and biosensing.<sup>[362]</sup> The hole accepting ligands not only enhances the QD PL quenching but also their photoelectric properties generated under monochromatic illumination.<sup>[329, 330]</sup>

First, the PL steady-state measurements allow us to observe the presence of the polymer band and that the emission peak of the QDs is kept and excited at 482 nm, see Figure V.57. In this sense, the measurement conditions previously established for QD<sub>TOPO</sub> LB film can be also used for this system.

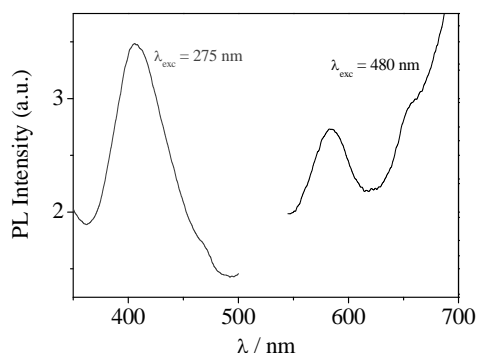


**Figure V.57.** PL spectra of a QD<sub>p</sub> LB film deposited at 14 mN m<sup>-1</sup> at different excitation wavelengths: 275 nm (dark gray) and 480 nm (black).

For comparative purposes, we also studied the QD<sub>p</sub> LB film at different power excitation analyzing the decay curves obtained over areas by a multi-exponential fit. The preliminary results: 108 W cm<sup>-2</sup> (15 ± 8 ns; 0.41 ± 0.06 counts/ms) and 369 W cm<sup>-2</sup> (11 ± 4 ns; 0.85 ± 0.10 counts/ms), show the same effect than for QD<sub>TOPO</sub>, the average lifetime decreases with the laser intensity as a consequence of multi-excitonic processes.<sup>[337]</sup> However, the most significant effect observed is the reduction in the average lifetime and counts from (63 ± 3 ns; 2.1 ± 0.5 counts/ms) for QD<sub>TOPO</sub> to (15 ± 8 ns; 0.41 ± 0.06 counts/ms) for QD<sub>p</sub>. This behaviour is observed either in solution or onto quartz substrates PL decay curves, Figure V.58.

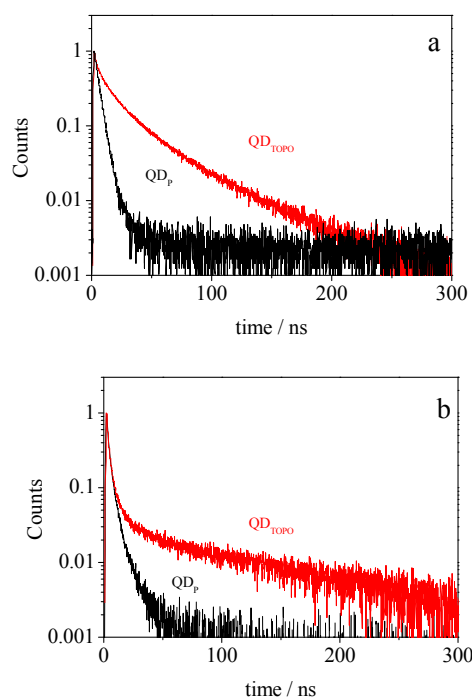


**Figure V.58.** Normalized PL decay curves for different capped-QDs in solution at  $10^{-6}$  M (a) and QDs LB film onto quartz substrate (b). The QDs ligands are: TOPO (red line) and PS-MA-BEE (black line). The LB films were transferred at  $\pi = 30$  ( $QD_{TOPO}$ ) and 14 ( $QD_p$ )  $mN\ m^{-1}$ .

This highlights that the nanoparticle size, capping and surface defects affect the average lifetime. First, the capping exchange promotes a slight reduction in the QD size due to a significant reconstruction of the nanocrystal surface (lattice) ascribed to bond distortion. However, at the laboratory conditions, above 250K, the exciton lifetime is independent of the particle size and strongly dependent on the surfactant stabilizer.<sup>[363]</sup> Moreover, taking into account that the polymer capping is carried out exchanging the TOPO molecules and that this process leaves residual TOPO molecules in the capping as shown by the  $QD_p$  IR spectrum, Figure V.17, it is expected that the  $QD_p$  surface presents a high number of defects. Besides, the PS-MA-BEE is bound to the  $Cd^{2+}$  atoms of the nanocrystal by the C=O group that presents a weaker binding energy than P=O group. The QD-PSMABEE binding energy is also reduced due to steric interactions between neighbouring polymer molecules that are larger than TOPO molecules.<sup>[364]</sup> Finally,



the styrene group interaction with QDs results in charge transfer quenching decreasing the average lifetime and PL intensity (counts/ms).<sup>[329]</sup>

In this sense, the sharper decrease of the QD<sub>p</sub> decay ( $\tau_{\text{short}} = 2.9 \pm 0.2$  ns) vs. QD<sub>TOPO</sub> one ( $\tau_{\text{short}} = 3.4 \pm 0.1$  ns) in the first nanoseconds reinforces the previous idea to ascribe this behaviour with the existence of QDs with surface defects that quench emission from band-edge exciton recombination. Where  $\tau_{\text{short}}$  is the average lifetime of the first three components of the multi-exponential fit. As the QD-polymer binding energy is lower than QD-TOPO, the loss of one ligand in solution is favoured leading to the appearance of trap states inside of the QDs band.<sup>[361]</sup> Likewise as at 482 nm the polymer is not excited, the shortening of the average lifetime could be also due to a QD-polymer hole transfer.<sup>[330]</sup> On the other hand the long component ( $\tau_4$ ) is lengthened from ( $123 \pm 5$  ns) for QD<sub>TOPO</sub> to ( $149 \pm 30$  ns) for QD<sub>p</sub>, Table V.9. Taking into account that this slow component is attributed to surface charge states and trapping in the surrounding environment of the QD, the lengthening is in agreement with a charge-transfer/hole-transfer process between particle surface and polymer.<sup>[330, 332]</sup>

**Table V.9.** Results from multi-exponential decay analysis for area measurement over LB films at 108 W cm<sup>-2</sup>. The reduced chi-square values,  $\chi^2$ , are all close to 1, indicating a good fit to each data set. Data obtained from measurements over at least 25 areas for each sample.

	QD <sub>TOPO</sub>	QD <sub>p</sub>
$\tau_1$ / ns	$0.12 \pm 0.04$	$0.22 \pm 0.13$
$f_1$ (%)	$19 \pm 4$	$23 \pm 5$
$\tau_2$ / ns	$1.9 \pm 0.1$	$2.2 \pm 0.3$
$f_2$ (%)	$17 \pm 2$	$42 \pm 6$
$\tau_3$ / ns	$9 \pm 1$	$7 \pm 1$
$f_3$ (%)	$15 \pm 2$	$29 \pm 4$
$\tau_4$ / ns	$123 \pm 5$	$149 \pm 30$
$f_4$ (%)	$48 \pm 3$	$6 \pm 2$
$\tau_{\text{AV}}$ / ns	$63 \pm 3$	$15 \pm 8$
Counts/ms	$2.1 \pm 0.5$	$0.41 \pm 0.06$

Finally, when we compare the  $\text{QD}_p$  decay in solution vs. deposited onto quartz, Figure V.59, the decrease in the first nanoseconds is slightly less sharp in solution due to a polarity medium effect. The solvent used is a mixture of chloroform and methanol (5:1), where the polar nature of the methanol diminishes the ligand-loss effects by stabilizing the surface charge states. Thus, surface traps and ligand-localized states are slightly minimized.<sup>[303, 364]</sup>

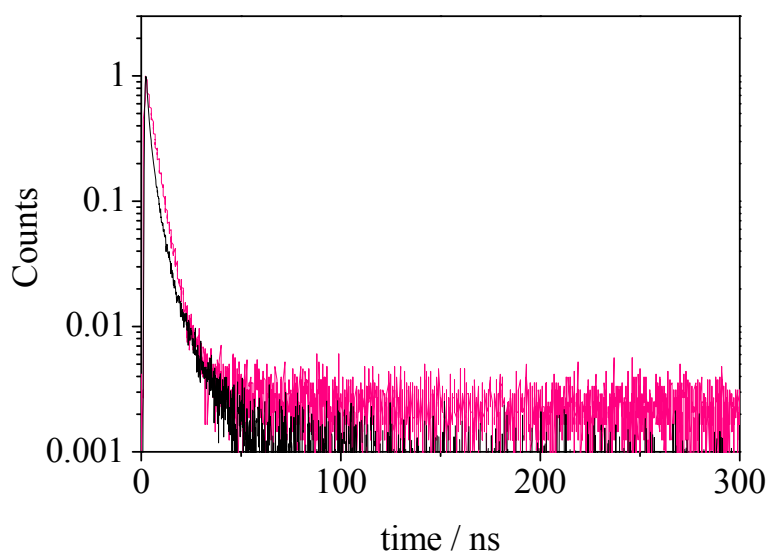


**Figure V.59.** Normalized PL decay curves for QDs in (chloroform : MeOH) solution at  $10^{-6}$  M (pink line) and a QDs LB film at low concentration ( $\pi = 14 \text{ mN m}^{-1}$ ) onto quartz substrate (black line).

In summary, the polymer capped-QDs allowed us to observe the effect of an inefficient surface passivation (defects) and the ligand nature on the QDs photoluminescence properties.

#### V.4.5. Imaging Characterization of mixed QD/PS-MA-BEE LB Films

The FLIM technique also offers the possibility of the observation of the fluorescence material deposited by FLIM images, i.e., it can be used to determine the distribution of surface luminescence at submicrometer resolution ( $\sim 0.2 \mu\text{m}$ ) fixed by the diffraction limit of the excitation light. These images show the

lifetime and intensity distributions. Thus, a colour-scale is assigned to decay times and the brightness to the amplitudes.<sup>[365]</sup>

It is important to note that the films were deposited onto quartz. Therefore, apart from the study of the material distribution, the preparation of the same films in different substrates: mica (hydrophilic) and quartz (more hydrophobic) allows us to compare the structures formed and the dewetting mechanism that occurs on the substrate after the LB deposition.

The experimental conditions used to take the FLIM images are briefly explained below. Areas measurements ( $80 \times 80 \mu\text{m}^2$ ,  $150 \times 150$  pixels, integration time of 1 ms per pixel) were carried out by using 482 nm excitation wavelength ( $5531 \text{ W/cm}^2$  power excitation, 40 MHz repetition rate, 38 ps/channel resolution, objective x60 N.A. 1.2 with water immersion) with the band-pass 550-690 nm emission filter placed in front of avalanche photodiodes.

#### **V.4.5.1. QD<sub>TOPO</sub>/PS-MA-BEE Langmuir-Blodgett Films**

We analyze the polymer structure onto quartz. At the excitation wavelength selected the polymer is not excited. Thus, the corresponding FLIM image only shows dark counts, see Figure V.60a. However, as can be seen in the AFM image of the polymer LB film shown in Figure V.60b. the morphology of the film is different that on mica or silicon but the height profile is similar, around 10 nm vs 8 nm, respectively. On quartz the polymer forms vast areas while on mica or silicon forms stripes. This fact could be attributed to the different nature of substrates: mica/silicon (hydrophilic) and cleaned quartz (more hydrophobic), and therefore, a dewetting effect of polymer blocks.<sup>[41]</sup> It is necessary to note that the surface of the quartz substrate has a greater roughness than mica, due to the fact that it is a polished surface. Therefore, there is more error in the AFM height profile measurements on this substrate.

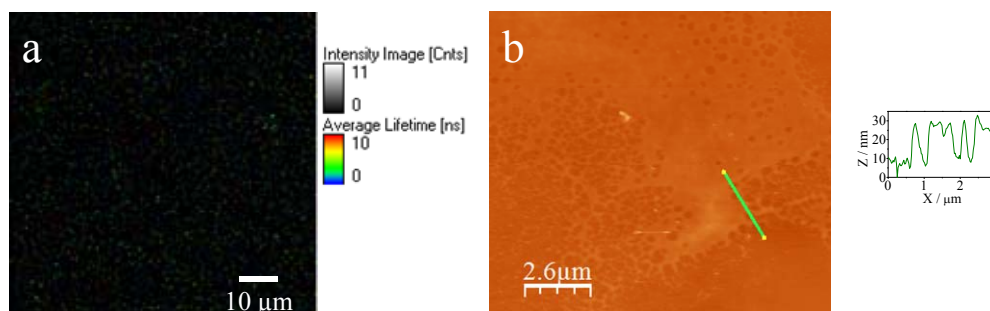


**Figure V.60.** FLIM (a) and AFM (b) images of the PS-MA-BEE LB film deposited at a surface pressure of  $14 \text{ mN m}^{-1}$  onto quartz.

As was mentioned, taking into account that the stripes formation occurs in both mica and silicon hydrophilic substrates, the different pattern observed for the polymer LB film onto the quartz slide can be attributed to the substrate surface properties. In fact, dewetting of thin polymer film on a heterogeneous substrate shows a much different manner and final structure from that on a homogenous substrate.<sup>[366, 367, 368]</sup> In our case, the quartz slides are polished and present a more hydrophobic surface than mica or silicon. Therefore, the physical small-scale surface heterogeneities, non-uniform roughness and less wettable regions, can act as nuclei lowering the excess free energy per unit area. Thus, this heterogeneity can induce the rupture of the film and therefore, promote the formation of random holes by heterogeneous nucleation dewetting in the spinodal regime.<sup>[366, 368]</sup>

If we turn to the FLIM images, we can observe that the adhesion of QDs directly onto quartz (Figure V.61a) is better than on mica. In spite of the different spatial resolution of the FLIM and TEM techniques a close-packed morphology is observed (Figure V.61b). These different techniques allow us to obtain distinct information about the QDs organization in the films at different scales. In the case of bilayers formed by the LB deposition of QDs on a polymer LB film, the homogeneity indicated by FLIM images (Figures V.61c and e) at long-scale is analogous to that of TEM images at low-scale (Figures V.61d and f), showing a

more compact film when the surface pressure increases (Figures V.61e vs f). Moreover, comparing the intensity of the FLIM images for QDs (Figure V.61a) and bilayer (Figure V.61e) at the same surface pressure of QDs, the bilayer would show a similar coverage than QDs directly onto quartz but more emission intensity. This picture could indicate that the polymer could improve the QDs adhesion. However, the previous detailed study showed that the enhance emission in the bilayer system is due to a more regular QDs arrangement with lower amount of QD clustering.

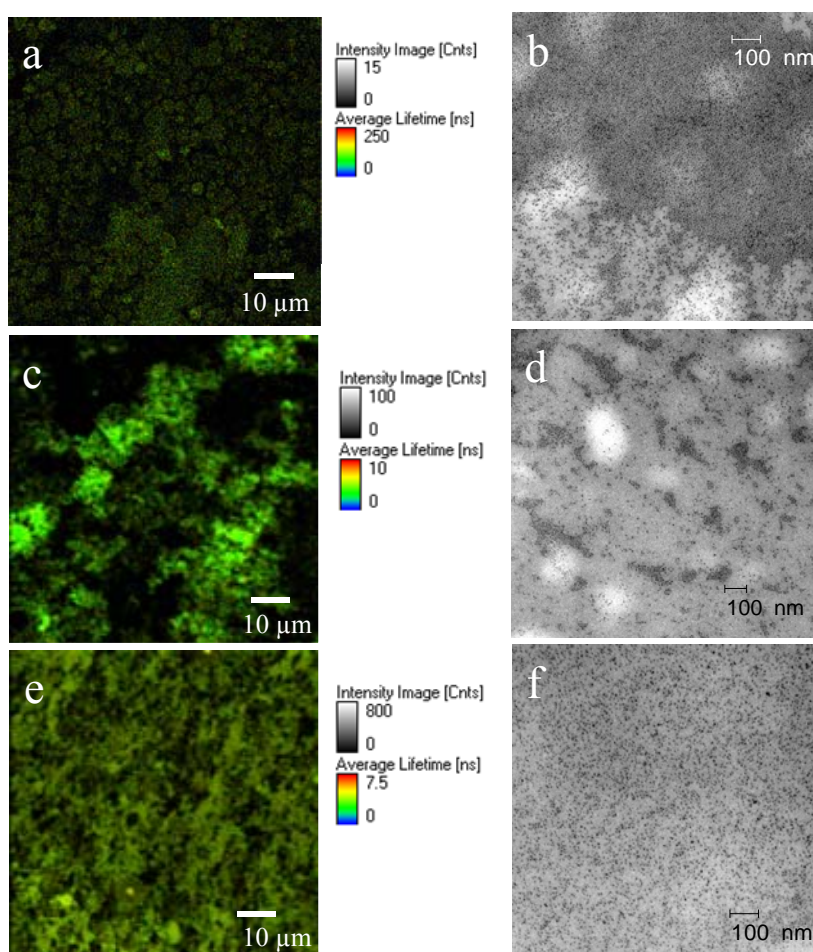


**Figure V.61.** FLIM (a) and TEM (b) images of a QDs LB film deposited at  $30 \text{ mN m}^{-1}$ . FLIM and TEM images of a QDs LB film deposited at  $9 \text{ mN m}^{-1}$  (c, d) and  $30 \text{ mN m}^{-1}$  (e, f) onto a PS-MA-BEE LB film.

When we deposit the mixed QD/PS-MA-BEE films, the morphology of the aggregates observed changes. The AFM images (Figures V.62e, h and j) show the formation of circular-shape aggregates, whose diameter size decreases when the polymer mole fraction increases. As in the case of polymer film, the AFM image in Figure V.62e shows that at  $X_p = 0.50$  the quartz physical heterogeneities can promote the continuous breakup of the film into holes.<sup>[368]</sup> While the circular domain formation, observed by AFM for samples above  $X_p > 0.50$ , is consistent with the spinodal dewetting mechanism proposed in the case of mica substrate, see Figures V.62h and j. However, the aggregates formed onto quartz present a different size, although the AFM roughness (Figures V.62e, h and j) is similar and close to 3-4 nm, approximately the QDs diameter. A possible explanation for the formation of circular aggregates with smaller size, Table V.10, could be that as the quartz is more hydrophobic than mica, cohesive interactions between the film and the substrate predominate.<sup>[369]</sup>

**Table V.10.** Average values of the domains (dots) of QD/PS-MA-BEE mixed LB films deposited at  $\pi = 14 \text{ mN m}^{-1}$  onto mica and quartz substrates obtained from AFM measurements.

Mica		Quartz	
$X_p$	size / $\mu\text{m}$	$X_p$	size / $\mu\text{m}$
0.96	$1.10 \pm 0.35$	0.98	$0.07 \pm 0.05$
0.99	$0.52 \pm 0.23$	0.99	$0.18 \pm 0.17$

\*Reported values are averages and error represents the standard deviation determined from at least 25 surface features.

Moreover, the FLIM intensity (counts) indicates that when the polymer concentration increases the intensity decreases, due to the fact that there are less quantity of fluorescence material, QDs; and also maybe, the high polymer mole fraction could affect the QDs luminescence. In fact, the photoluminescence measurements in solution showed a possible quenching from the polymer due to aromatic rings,<sup>[329]</sup> Figure V.37.

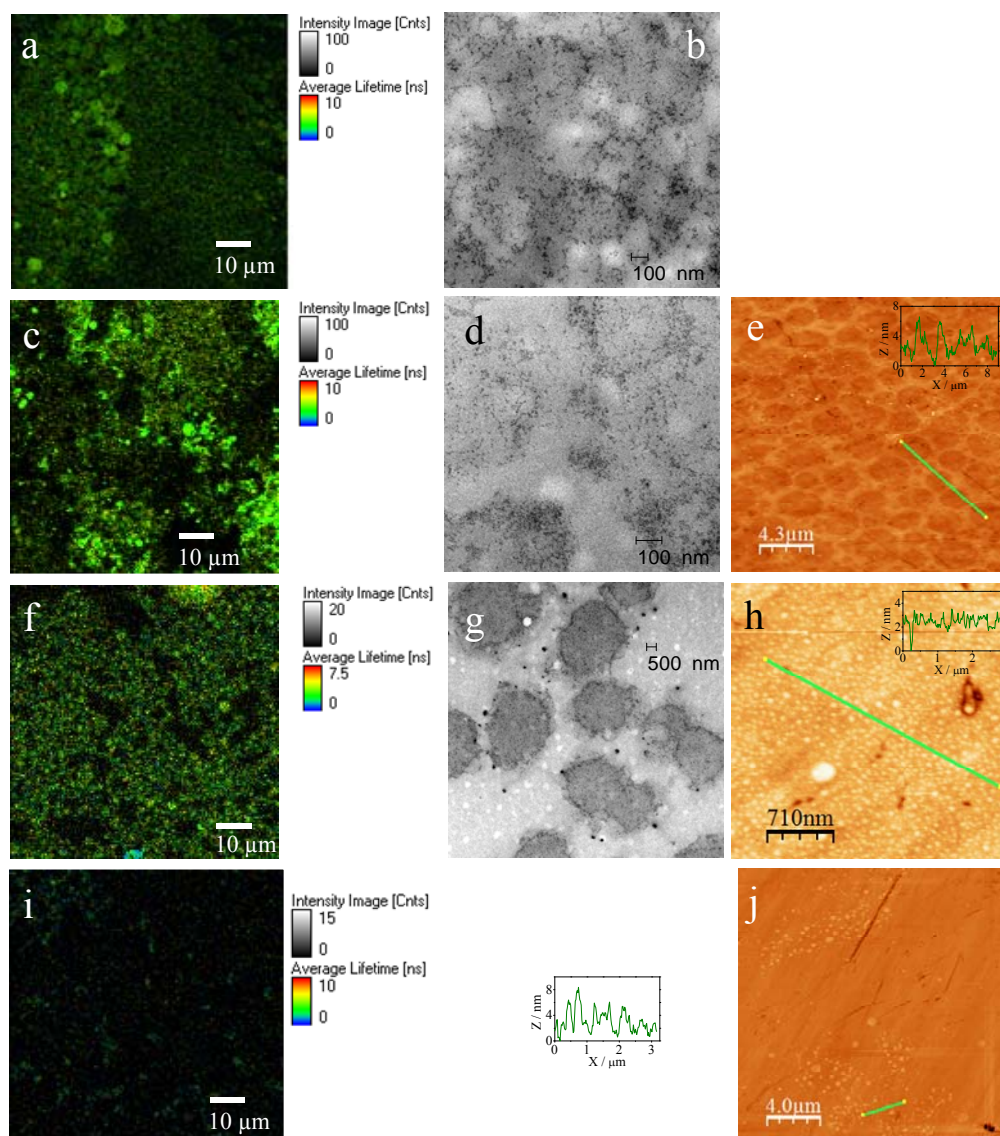


**Figure V.62.** FLIM, TEM and AFM images of mixed QD/PS-MA-BEE LB films deposited at a surface pressure of  $14 \text{ mN m}^{-1}$  for different polymer mole fractions: 0.35 (a, b); 0.5 (c, d, e); 0.98 (f, g, h); and 0.99 (i, j). The substrate for FLIM and AFM images was polished quartz wafers.

When the surface pressure is increased until  $30 \text{ mN m}^{-1}$ . The FLIM and TEM images presented in Figure V.63 show more dense films. It is important to note that in contrast with low surface coverage,  $14 \text{ mN m}^{-1}$  (Figure V.62), at high surface pressure,  $30 \text{ mN m}^{-1}$ , the FLIM images brightness is similar when polymer

mole fraction increases until exceed 0.65, from Figures V.63a, c and e to Figure V.63g with  $X_p=0.96$ .

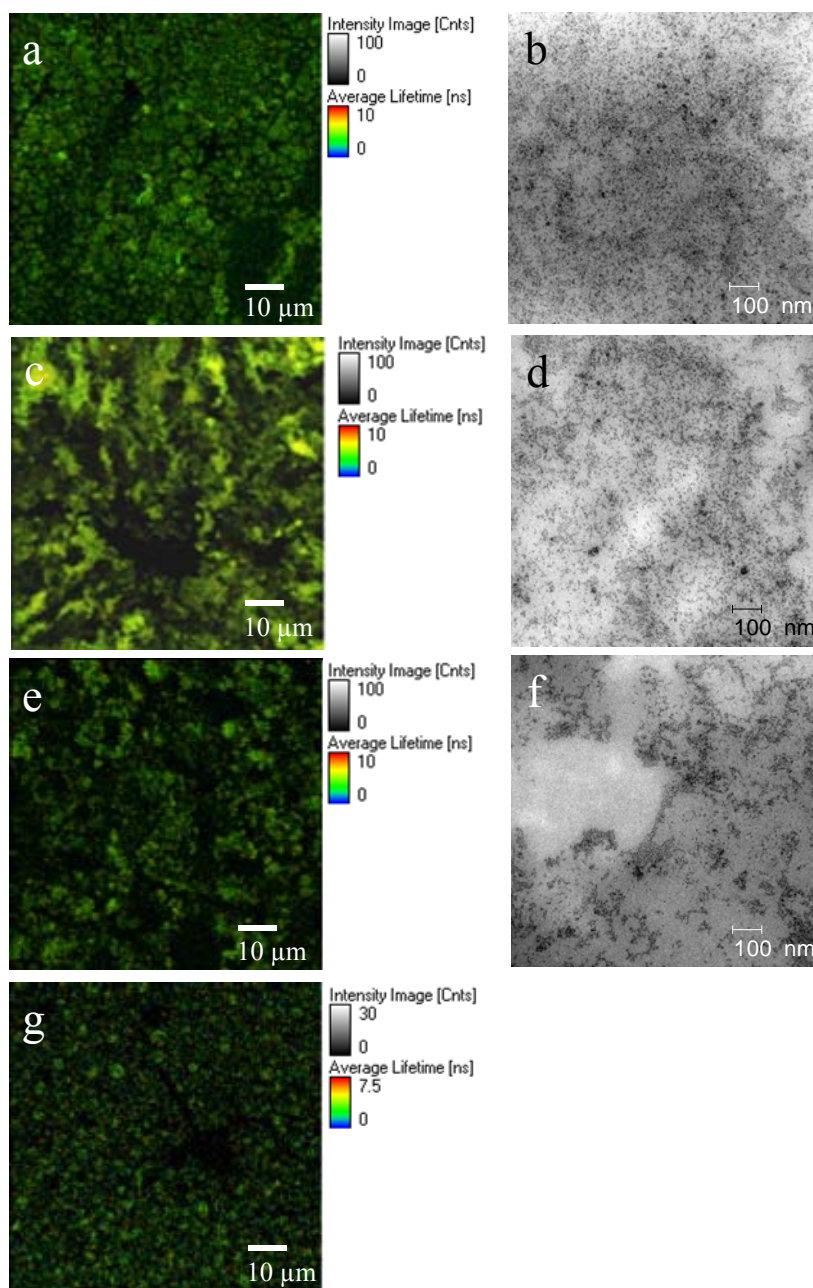


**Figure V.63.** FLIM and TEM images of mixed QD/PS-MA-BEE LB films deposited at a surface pressure of  $30 \text{ mN m}^{-1}$  for different polymer mole fractions: 0.35 (a, b); 0.5 (c, d); 0.65 (e, f); and 0.96 (g). The substrate for FLIM images was polished quartz wafers.



Finally, in reference to the lifetime scales showed in the FLIM images, built in fast FLIM mode, they only indicate that the lifetimes are in the same range order. For a detailed study, it is necessary to modify the measurement conditions, mainly, laser intensity, repetition rate and channel resolution as was done in the PL dynamics analysis.

#### **V.4.5.2. QD<sub>p</sub>/PS-MA-BEE Langmuir-Blodgett Films**

In the case of LB films built with the PS-MA-BEE-capped QDs, the morphologies observed by FLIM are different than in TOPO-capped QDs. On the one hand, the pure QD<sub>p</sub> and mixed QD<sub>p</sub>/PS-MA-BEE ( $X_p = 0.50$ ) LB films show a structure of rafts or blocks, see Figures V.64a and c. However, when the polymer mole fraction increases in the mixture (Figures V.64d and e) the shape of aggregates is better defined. As it was previously observed on mica (Figure V.22), domains are formed (Figure V.64d) by nucleation and growth of holes dewetting mechanism.<sup>[44]</sup> These FLIM and TEM images correspond to a mixed film with a polymer molar fraction of 0.99.

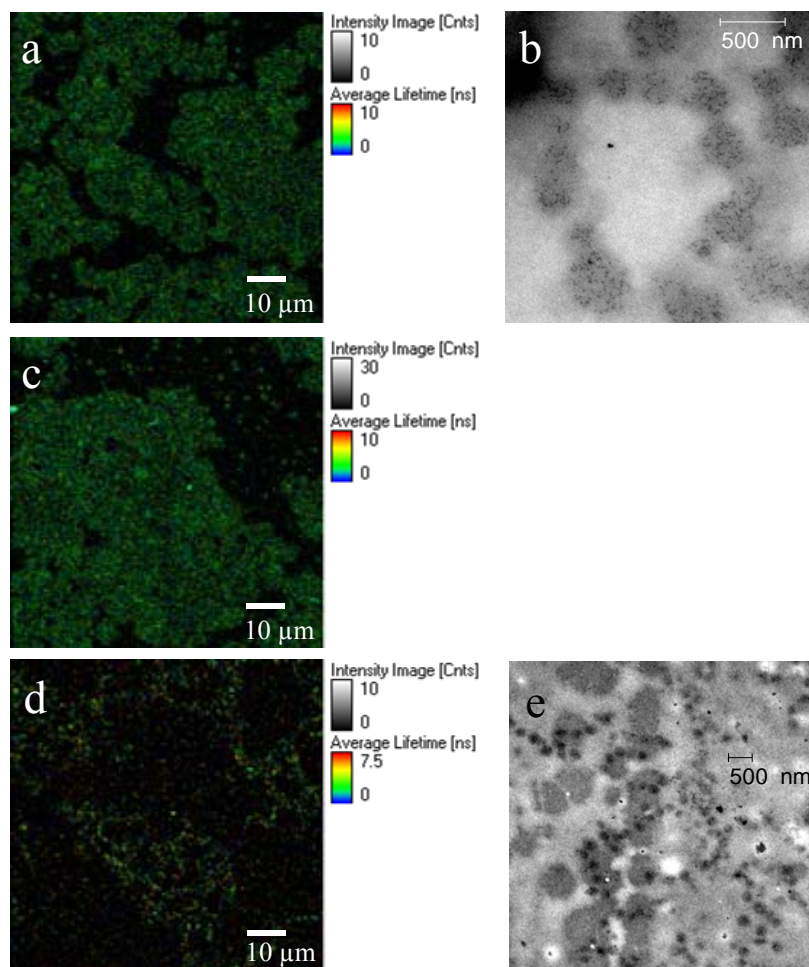
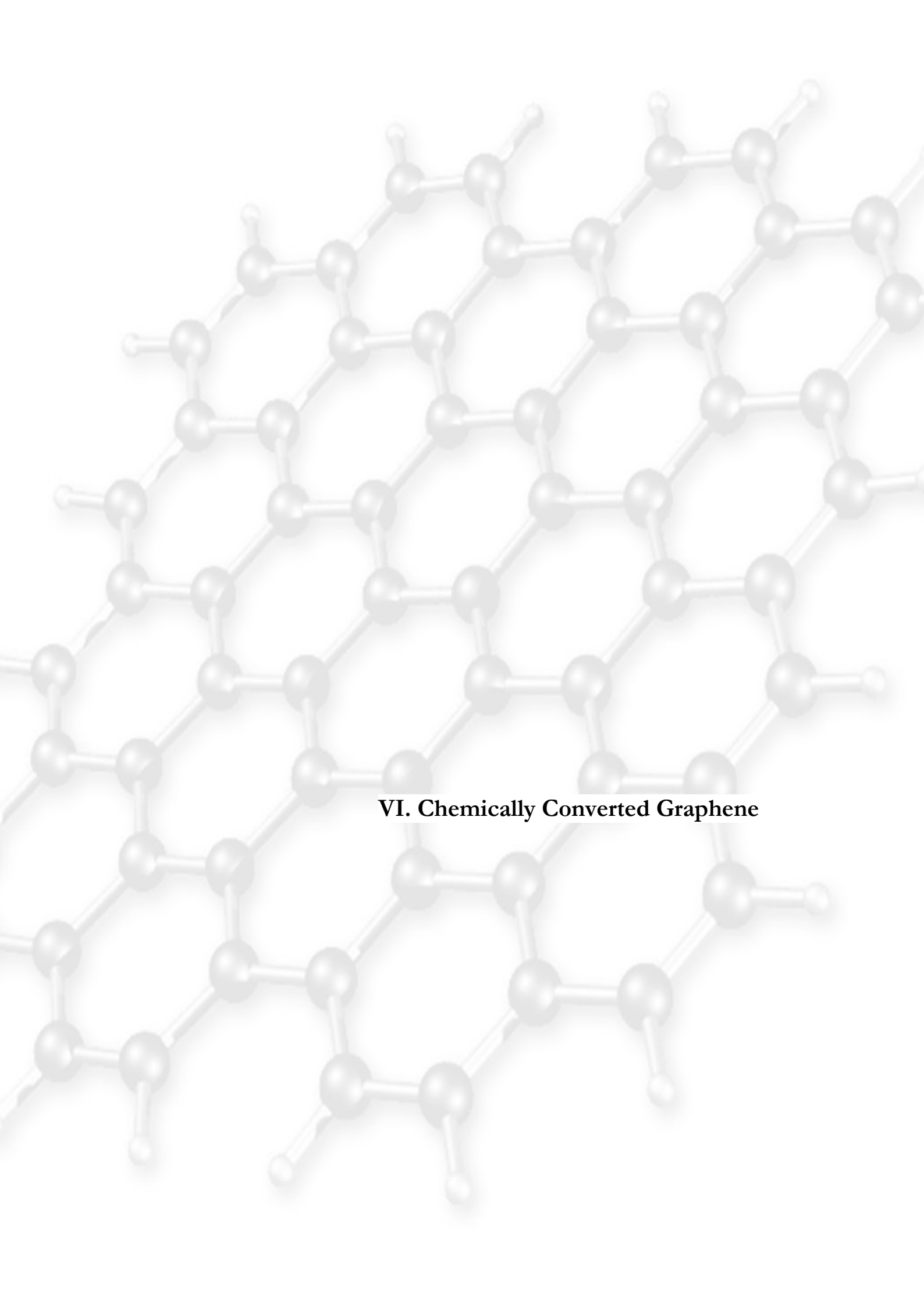


**Figure V.64.** FLIM and TEM images of pure QD<sub>p</sub> (a, b) and mixed QD<sub>p</sub>/PS-MA-BEE LB films deposited at a surface pressure of 14 mN m<sup>-1</sup>. For the mixed systems the polymer mole fractions were: 0.5 (c); and 0.99 (d, e). The substrates for FLIM images were polished quartz wafers.

It is relevant to note that the intensity (counts) observed in the samples with QD<sub>p</sub> (Figure V.64) is lower than for QD<sub>TOPO</sub> (Figure V.62). This observation could be attributed to a loss in the luminescence properties with the ligand exchange<sup>[8]</sup> due to a possible loss in the surface passivation (creating traps) and the effect of polymer aromatic rings as quenchers of CdSe QDs emission<sup>[329]</sup>.

Finally, the use of another substrate for the LB deposition has allowed us to highlight the influence of the physical surface heterogeneities of the substrate on the film dewetting mechanism.



## **VI. Chemically Converted Graphene**



## VI. Chemically converted Graphene

In recent years, graphene has received enormous interest due to its unique properties, such as high thermal conductivity, great Young modulus and high intrinsic carrier mobility. More than other materials, graphene exhibits important fundamental physical phenomena like the anomalous integer quantum Hall effect at room temperature and the fractional one at low temperatures. Due to its remarkable properties,<sup>[28, 156, 157, 370-372]</sup> graphene and its derivatives are promising candidates for the fabrication of electronic devices,<sup>[373]</sup> or reinforced filler in composites and in medicine<sup>[27]</sup>. However, these unique properties are associated with monolayer sheets. Therefore, the challenge is to obtain good quality monolayers of graphene in large quantities.

In this sense, similar to other materials, the success of graphene in technological applications is related to the availability of production methods for the synthesis of large quantities of material at low cost. The main challenge in the production of graphene is the reduction of the aggregation by  $\pi$ - $\pi$  stacking. Currently, there are three main routes to produce high-quality graphene flakes: micromechanical exfoliation,<sup>[374]</sup> chemical vapour deposition (CVD) of hydrocarbons on metal substrates,<sup>[375]</sup> and thermal reduction of silicon carbide<sup>[376]</sup>. Micromechanical exfoliation gives samples with the highest charge carrier mobility<sup>[377]</sup> although the process is time consuming. The other routes require very high temperatures and/or ultrahigh vacuum, thus that the production of graphene monolayers at sufficient scale and low cost remains a challenge. The alternative at these physical methods are the different chemical routes based on the synthesis of the material. One of them is the longitudinal "unzipping" of carbon nanotubes route by treatment with  $\text{KMnO}_4$ <sup>[378, 379]</sup> that could afford bulk quantities of graphene nanoribbons whose width depends on carbon nanotubes diameter and its scalability has yet to be demonstrated<sup>[158]</sup>. Another alternative and exciting method is the "total organic synthesis" that proposes the graphene building with

benzene-based macromolecules. The major advance in this way is the synthesis of nanoribbon-like polyacyclic hydrocarbons (PAHs) up to 12 nm in length.<sup>[380]</sup> The challenges in this approach are focused on the achievement of dispersibility and planar morphology for large PAHs and its electronic characterization, thus this technique could offer a ground-up synthesis of graphene.<sup>[29, 156]</sup>

Other approach proposed by several authors<sup>[29, 381-383]</sup> is the graphite liquid-phase exfoliation in organic solvents (e.g. N,N-dimethylformamide, tetrahydrofuran, N-methyl-2-pyrrolidone, ethylene glycol) or water but although the graphene obtained has good quality, its concentration and the percentage of graphene monolayer in the solution are too low<sup>[384]</sup>. This process can be assisted by the addition of surfactants<sup>[385, 386]</sup> or metal ions such as potassium<sup>[387]</sup> that act as intercalation compounds.

Finally, the preparation of graphene based on the chemical oxidation of graphite followed by a reduction process, is considered one of the most attractive routes to obtain graphene, because it is a low-cost, versatile for processing and chemical functionalization and scalable method.<sup>[157]</sup> However, chemical oxidation disrupts the electronic structure of graphene by introducing carbonyl, epoxy and hydroxyl groups in the network.<sup>[388]</sup> The reduction cannot remove the structural defects introduced by the oxidation process, and these defects disrupt the band structure and degrade the electronic properties of graphene. However, it can be used to prepare conductive and mechanical resistant composite materials,<sup>[389]</sup> flexible coatings,<sup>[161]</sup> gas molecular sensors<sup>[390]</sup> or even TEM transparent supports<sup>[391]</sup>.

Furthermore the reduced graphite oxide tends to agglomerate making further processing difficult. The reduction with the assistance of different stabilizers<sup>[28, 392-394]</sup> is an alternative route to obtain good quality graphene sheets. When the stabilizer is a surfactant such as dodecylbenzene sulphonate,<sup>[393]</sup> the surfactant molecule not only plays an important role in controlling the exfoliation

of graphite oxide but also functionalizes the graphene sheets. The functionalized sheets can be used in several applications such as solar energy storage<sup>[29]</sup> or Li-ion batteries<sup>[395]</sup>. Moreover, non-covalent functionalization of graphene is an alternative approach to modify the material properties allowing a better processing and interactions with other compounds without altering the chemical structure of graphene.<sup>[396]</sup>

On the other hand, the graphene oxide (GO) or its derivatives are presented as a promising route with significant economic advantages in the large scale production of polymer nanocomposites. The polymer/graphene composites are based on the use of graphene derivatives as nanofillers to improve the mechanical, electrical, thermal and optic properties.<sup>[389, 397]</sup> Depending on polymer type and reducer agent the GO reduction can be carried out *in situ* or previously, in order to avoid the polymer reduction. Moreover, if the chemically converted graphene has functional groups that are reactive with the polymer, interfacial interactions between polymer and RGO sheet surface can occur obtaining water-dispersible graphene.<sup>[398]</sup> The adhesion between graphene and polymers is also an important factor to be considered in designing composite materials. Thus, if thin layers of electrically conductive graphene can be deposited on polymer surfaces, flexible displays, thin-film transistors and photovoltaic devices will be made possible.<sup>[389]</sup>

In this chapter, we present the results corresponding to the study of the effect of the zwitterionic surfactant dodecyl dimethyl ammonium propane sulphonate (DDPS) on the quality of the reduced graphite oxide (RGO). The advantage of this approach is that the zwitterionic surfactants exhibit greater adsorption onto hydrophobic surfaces such as graphite than the ionic surfactants,<sup>[399, 400]</sup> therefore, we expect that the functionalization of RGO with DDPS provides better quality of the RGO sheets than that obtained with ionic surfactants. On the other hand, the charged groups of DDPS molecules attached



on RGO can bind metal cations<sup>[29]</sup> and different kind of polymers<sup>[282, 401-402]</sup> producing nanocomposites with potential applications in the construction of photovoltaic devices<sup>[29]</sup> and sensors,<sup>[30]</sup> respectively. Moreover, the zwitterionic surfactants present higher tolerance to extreme pH, strong electrolytes, and oxidizing and reducing agents than the ionic ones,<sup>[399]</sup> therefore they have utility in the fabrication of devices subjected to extreme conditions.

To evaluate the quality of the reduced sheets we use the criteria proposed by Luo *et al.*<sup>[403]</sup> These criteria consist in analyzing simultaneously the reduction degree, the defect repair degree and the electric conductivity of the obtained graphitic material by using AFM, X-Ray photoelectron spectroscopy (XPS), UV-vis absorption spectroscopy, Micro-Raman spectroscopy and electric conductivity measurements. We are also interested in exploring the effect of the reducer agent on the quality of the reduced graphite oxide flakes and on the functionalization process of the RGO. With this objective in mind we have selected two reducer agents, hydrazine and Vitamin C. Hydrazine is one of the most widely used reducer agents of GO and renders good quality RGO sheets<sup>[403]</sup> while Vitamin C has been proposed as substitute for hydrazine as non-toxic reagent. Previous results have demonstrated that Vitamin C is a good reducer agent of GO and renders flakes with less structural defects than hydrazine,<sup>[404-408]</sup> but a simultaneous analysis of the reduction and defect repair degrees and electric conductivity has not yet been done. Therefore, we analyze the quality of the RGO obtained by reduction with Vitamin C using the Luo's criteria<sup>[403]</sup> not only the  $sp^2$  character of the RGO. In addition, we have analyzed the effect of the reducer agents on the functionalization of the RGO samples by the surfactant DDPS. To the best of our knowledge, it is the first time that the effect of the reducer agent on the functionalization of RGO sheets has been studied.

On the other hand, the implementation of graphene obtained by chemical reduction of GO into device fabrication processes requires an uniform and

reproducible deposition methodology. Several techniques such as drop-casting<sup>[162]</sup> or spin-coating<sup>[162, 163]</sup> have been used to obtain graphene films onto solid wafers. However, these methodologies often result in non-uniform film thickness on solid substrates.<sup>[156]</sup> An effective method to obtain well defined sheets deposited onto solid wafer can be the Langmuir-Blodgett (LB) technique. This methodology has been successfully used to transfer water-insoluble molecules<sup>[3, 111]</sup> or nanomaterials<sup>[304, 409]</sup> from the air-water interface onto solids and presents several advantages since it allows a great control of the interparticle distance and, consequently, of the interparticle interactions. Recently this technique has been used for deposition of graphene oxide<sup>[76]</sup> and multilayered films of graphene sheets<sup>[75]</sup>. Therefore, we use the LB methodology to deposit no collapsed sheets of the different RGO samples. The morphology and quality of the LB deposited sheets were studied by means of atomic force microscopy (AFM), field emission scanning electron microscopy (FE-SEM) and Micro-Raman spectroscopy.

## **VI.1. Oxidation and Reduction Procedures of Graphitic Material**

In order to set the approaches selected, a run-through of the main existent methodologies for graphene oxide production and its reduction are presented.

### **VI.1.1. Graphite Oxide Production**

The first approach for the graphite oxide (GO) obtaining was developed by B.C. Brodie in 1859. The reaction performed was based on the addition of potassium chlorate ( $\text{KClO}_3$ ) to a slurry of graphite flakes in fuming nitric acid ( $\text{HNO}_3$ ).<sup>[410]</sup> Nearly 40 years after, L. Staudenmaier improved Brodie's  $\text{KClO}_3$ -fuming  $\text{HNO}_3$  preparation by adding the chlorate in multiple aliquots over the course of the reaction and also, with the addition of concentrated sulfuric acid, to increase the acidity of the mixture, rather than in a single addition as in the Brodie's method. This slight change in the procedure resulted in an overall extent of oxidation similar to Brodie's multiple oxidation approach, but performed more practically in a single reaction vessel.<sup>[411]</sup> In this procedure, nitric acid reacts

strongly with aromatic carbon surfaces resulting in the formation of various oxide-containing species including carboxyls, lactones and ketones with the liberation of gaseous  $\text{NO}_2$  and/or  $\text{N}_2\text{O}_4$  and  $\text{ClO}_2$ . Likewise, potassium chlorate is a strong oxidizing agent and an *in situ* source of oxygen, which acts as the reactive species.<sup>[412]</sup>

Later, in 1958, Hummers and Offeman developed an alternative oxidation method by reacting graphite with a mixture of potassium permanganate ( $\text{KMnO}_4$ ), sodium nitrate ( $\text{NaNO}_3$ ) and concentrated sulfuric acid ( $\text{H}_2\text{SO}_4$ ), achieving similar levels of oxidation.<sup>[413]</sup> In this case, although permanganate is an oxidant, the active species is, in fact, diamanganese heptoxide formed from the reaction of potassium permanganate with sulfuric acid. The bimetallic heptoxide is far more reactive than its monometallic tetraoxide counterpart, and is known to detonate when heated to temperatures greater than 55 °C or when placed in contact with organic compounds, therefore, the mixture is carried out over an ice-bath.<sup>[414-415]</sup>

Though others have developed slightly modified versions in the last decade, these three methods comprise the primary routes for obtaining GO, and little about them has changed. Importantly, it has since been demonstrated that the products of these reactions show strong variance, depending not only on the particular oxidants used, but also on the graphite source and reaction conditions. In fact, the slight modifications proposed are based on the change of the reactive quantities or ratios, reaction times and the sum of pre-oxidation stages (e.g. a graphite treatment with  $\text{H}_2\text{SO}_4/\text{K}_2\text{S}_2\text{O}_8/\text{P}_2\text{O}_5$ )<sup>[416]</sup> in order to obtain a carbon material more oxidized. Several efforts have been carried out in this line in these recent years. One of these modifications is the use of  $\text{KMnO}_4$  and a 9:1 mixture of concentrated  $\text{H}_2\text{SO}_4/\text{H}_3\text{PO}_4$  avoiding the  $\text{NaNO}_3$  addition, whose advantages are that the protocol for running the reaction does not involve a large exothermal step, produces no toxic gas ( $\text{NO}_2$  and/or  $\text{N}_2\text{O}_4$ ) and yields a higher fraction of well-oxidized hydrophilic carbon material.<sup>[417]</sup>

Generally, the main graphite source used in this reaction is flake graphite since it contains numerous defects in its structure that can serve as seed points for the oxidation process.<sup>[418]</sup>

**Synthesis and purification of Graphite Oxide.** The GO was prepared by using a slight modification of the Hummers' oxidation method<sup>[413]</sup> from natural graphite flakes. The modification has as objective to achieve GO samples with a greater oxidation degree than that obtained by the Hummers' method. In a typical procedure, 1 g of graphite, 0.5 g of NaNO<sub>3</sub> and 23 mL of H<sub>2</sub>SO<sub>4</sub> (98%w) were mixed in an ice-bath. While agitation, 3 g of KMnO<sub>4</sub> were slowly added controlling that the temperature not exceed of 20°C. Then, the solution was warmed to 35°C with a water-bath and maintained at that temperature overnight. In contrast to Hummers' which spend 30 min in this oxidation process, in our procedure, to achieve a more oxidized material (GO), the reactive solution (NaNO<sub>3</sub>/ H<sub>2</sub>SO<sub>4</sub>/ KMnO<sub>4</sub>/graphite) was stirred at 35°C overnight until form a thick paste (Figure VI.1). Next, 46 mL of water was slowly added and the temperature of the suspension reached to 98°C. The temperature and agitation were maintained during 30 minutes. After this time, the suspension was diluted with warm water (100°C) to 140 mL and treated with 20 mL of H<sub>2</sub>O<sub>2</sub> (30%w), turning the colour of the suspension from dark brown to yellow (Figure VI.1). Finally, the suspension was filtered, when was still warm to avoid the precipitation of the soluble salt of mellitic acid, and washed with warm water. The filter cake was dispersed in water.

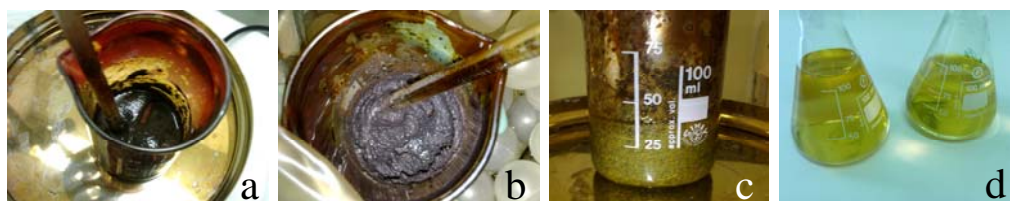


**Figure VI.1.** Photographs of different stages of the graphite oxidation process: (a) Stirring the reactive solution (NaNO<sub>3</sub>/ H<sub>2</sub>SO<sub>4</sub>/ KMnO<sub>4</sub>/graphite) (brown colour); (b) the brownish grey thick

paste oxidized after overnight; (c) addition of  $\text{H}_2\text{O}_2$  turning the solution to yellow; and (d) the GO obtained after the purification step.

In order to obtain high quality GO we use a centrifugation-based purification procedure published elsewhere.<sup>[76]</sup> Thus, the GO filter cake was dispersed in water by mechanical agitation, and centrifuged at 1000 rpm (90g) for 3-5 times, allowing to remove the biggest (visible) particles. The supernatant was treated with high-speed centrifugation at 5000 rpm (3750g) for 15 min, in order to eliminate the small GO particles and the water-soluble products of the oxidation process. Finally, the supernatant was centrifuged at 10000 rpm (8163g) for 15 min to separate the GO sediment, which was then dried at 40 °C over phosphorus pentoxide in vacuum.<sup>[413]</sup>

The GO samples were characterized by X-ray photoelectron spectroscopy (XPS) and the results are reported in Table VI.1. The  $\text{C}_{1s}$  core-level spectrum of GO was fitted by three components centred at 284.8, 286.3 and 288.6 eV, being the first two more intense than the third one (Figure VI.2a, Table VI.1). These peaks are assigned to C-C bonds in aromatic networks, to C-O bonds in alcohols or epoxy groups and to  $\text{COO}^-$  structures, respectively. In addition, the  $\text{O}_{1s}$  core-level spectrum shows two peaks at 531.4 and 533.6 eV (Figure VI.2b). The first one is assigned to oxygen in C=O groups while the later comes from C-O bonds and it is more intense than the first one. This observation indicates that the epoxy and hydroxyl groups are the major components, in agreement with results previously obtained.<sup>[419]</sup>

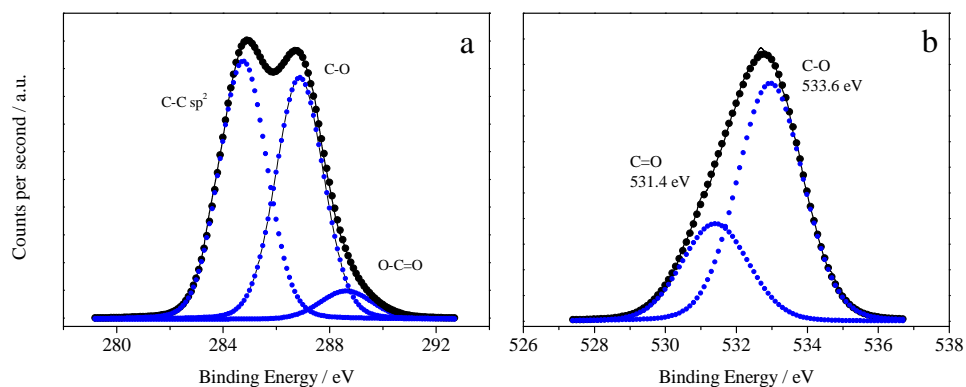


**Figure VI.2.** The C<sub>1s</sub> (a) and O<sub>1s</sub> (b) core-level spectra of graphite oxide (GO).

The O/C ratio value calculated from XPS was 0.62. This value is higher than the values found in the literature comprised between 0.37 and 0.53.<sup>[165, 392, 405-407]</sup> This fact confirms that the method used in this work allows us to obtain a more oxidized material (GO) than those reported by other oxidation procedures.

**Table VI.1.** Binding energies (eV) and O/C, N/C and S/C surface atomic ratios of graphitic samples.

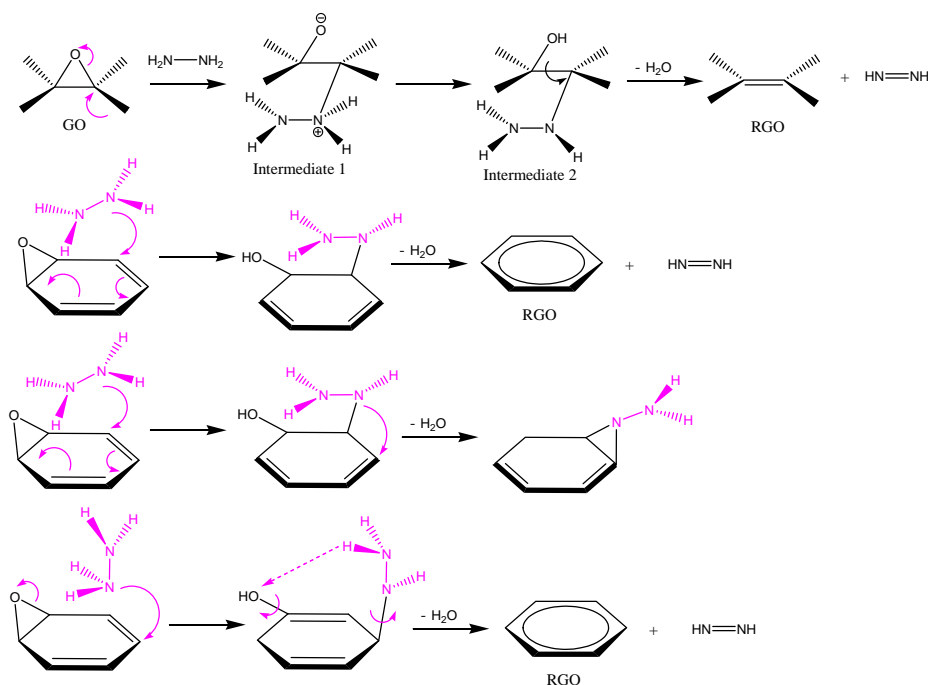
Sample	C <sub>1s</sub>	S <sub>2p</sub>	N <sub>1s</sub>	O/C	N/C	S/C
GO	284.8 (49 ± 2)					
	286.9 (45 ± 2)	-	-	0.618	-	-
	288.6 (6 ± 0.5)					
RGO Hydrazine	284.8 (63 ± 2)					
	286.3 (22 ± 2)					
	287.7 (8 ± 1)	-	400.0	0.119	0.039	-
	289.3 (7 ± 0.5)					
RGO Hydrazine (DDPS)	284.8 (82 ± 1)		399.8 (60 ± 1)			
	286.3 (16 ± 0.5)	167.8	401.9 (40 ± 1)	0.190	0.004	0.002
	289.0 (2 ± 0.5)					
RGO Vitamin C	284.8 (67 ± 1)					
	286.4(29 ± 0.4)	-	-	0.339	-	-
	288.9 (4 ± 0.2)					
RGO Vitamin C (DDPS)	284.8 (77 ± 6)					
	286.2 (20 ± 3)	168.6	402.2	0.209	0.006	0.006
	289.0 (3 ± 0.5)					
DDPS	284.8 (82)					
	286.2 (18)	167.5	402.3	0.183	0.056	0.056

### VI.1.2. Reduction of Graphite Oxide

As it was mentioned, the GO is an electrically insulating material due to its disrupted  $sp^2$  bonding network, thus, the next step is its reduction to partially restore the network and therefore its electrical conductivity. The reduction can be achieved through chemical, thermal or electrochemical reduction pathways. In our case, the reduction was carried out by chemical reaction of GO with hydrazine and Vitamin C.

**Chemical Reduction.** There are several reducer agents proposed to carry out the chemical reduction of GO. However, the most common used is the hydrazine

monohydrate ( $\text{N}_2\text{H}_4$ ).<sup>[165]</sup> While most strong reducers have slight to very strong reactivity with water, hydrazine monohydrate does not, making it an attractive option for reducing aqueous dispersions of GO. Although the mechanism of this reaction remains unclear, several mechanistic routes have been proposed. In all these routes, the hydrazine mainly attacks the epoxide groups forming diazene and in some points introducing residual nitrogen functionality on the carbon network.<sup>[165, 420]</sup> The de-epoxidation occurs in three steps: in the first, hydrazine ( $\text{N}_2\text{H}_4$ ) attacks the carbon of epoxide from the back side of the epoxide ring opening the ring. Second, the C-C bond of the intermediate 1 rotates to bring the hydrazine group ( $-\text{H}_2\text{NNH}_2$ ) attached to the opposite side of the oxygen close to the oxygen. Then one H-atom transfers from the hydrazine group to the oxygen of epoxide, forming a hydrazino alcohol intermediate 2. Third, another H of intermediate 2 transfers from the hydrazino group ( $-\text{HNNH}_2$ ) to the hydroxyl group ( $-\text{OH}$ ). This gives a water molecule ( $\text{H}_2\text{O}$ ), a *cis*-diazene (*cis*- $\text{N}_2\text{H}_2$ ), and the deoxygenated product.



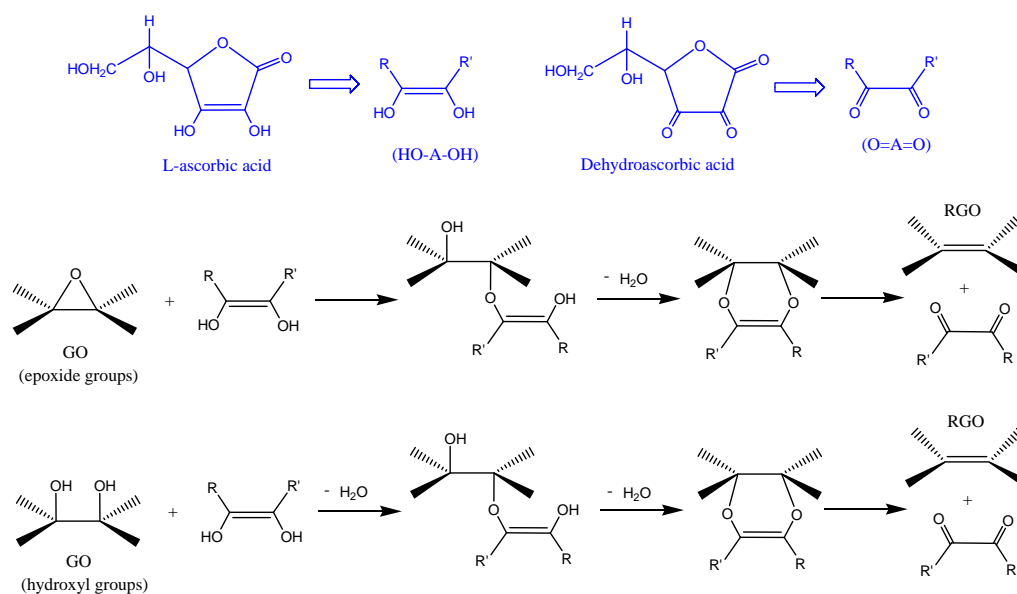
**Scheme VI.1.** Proposed reduction mechanism of GO by hydrazine (Adapted from Gao, 2009<sup>[420]</sup>).



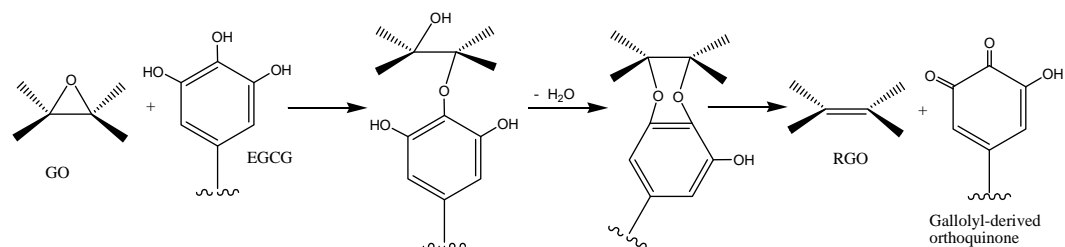
Alternative reagents to hydrazine have been proposed, although the reduction degree achieved does not exceed the hydrazine results. An example is the use of borohydride,  $\text{NaBH}_4$ , that is most effective at reducing  $\text{C}=\text{O}$  species, but has lower to moderate efficacy in the reduction of epoxides and carboxylic acids. Additional alcohols are the principal impurities that are generated during this reduction process as a result of the hydrolysis of the boronic ester.<sup>[421]</sup> Other reducers have been used for the chemical formation of graphene including hydroquinone,<sup>[421, 422]</sup> gaseous hydrogen (after thermal expansion),<sup>[423]</sup> sulfur-containing compounds,<sup>[424]</sup> aluminum powder<sup>[425]</sup> and strongly alkaline solutions ( $\text{NaOH}$ ,  $\text{KOH}$  or  $\text{NH}_3$ )<sup>[426, 427]</sup>. Reduction by hydrogen proved to be effective, while hydroquinone and alkaline solutions tend to be inferior to stronger reducers, such as hydrazine and sodium borohydride, based on published results. Reduction in organic solvents have been also proposed as the reduction with trioctylphosphine (TOP) acting as a reducing agent and an aggregation-prevention surfactant, but achieving a reduction efficiency similar to hydrazine.<sup>[428]</sup>

An alternative route for an environmental friendly chemical reduction of GO, is the use of "green" reducing agents such as Vitamin C; reducing sugars such as glucose, fructose or sucrose,<sup>[429]</sup> hydrolyzable tannins;<sup>[430]</sup> tea polyphenols<sup>[431]</sup> or L-glutathione<sup>[432]</sup>. Among them, Vitamin C (L-ascorbic acid) has demonstrated reproducible results and a reduction efficiency equal to hydrazine. Mechanism proposed<sup>[433]</sup> for the chemical reduction of GO is speculated as two-step  $\text{SN}_2$  nucleophilic reactions followed by one step of thermal elimination. The electron withdrawing five-member ring of L-ascorbic acid makes the hydroxyls more acidic, so L-ascorbic acid is ready to dissociate two protons, functioning as a nucleophile where the endiol structure ( $\text{HO-A-OH}$ ) evolves to diketone ( $\text{O=A=O}$ ) in the oxidize form. The GO contains mainly two types of reactive species, including epoxide and hydroxyl groups. In the case of epoxide, it could be opened by the oxygen anion of L-ascorbic acid ( $\text{HOAO}^-$ ) with a  $\text{SN}_2$  nucleophilic attack. The reduction may be followed by a back-side  $\text{SN}_2$  nucleophilic attack

with release of  $\text{H}_2\text{O}$ , resulting in the formation of an intermediate. Finally, the intermediate may undergo a thermal elimination, leading to formation of RGO. The ascorbic acid is oxidized into dehydroascorbic acid ( $\text{O}=\text{A}=\text{O}$ ). The reduction of hydroxyls is similar to the case of epoxide. The hydroxyls could be displaced by the oxygen anions of L-ascorbic acid ( $-\text{OAO}-$ ) with a back-side  $\text{S}_{\text{N}}2$  nucleophilic attack twice, which are subsequently reduced further by thermal elimination. A similar mechanism is also applied in the polyphenol reducing agents, as an example the proposed mechanism for epigallocatechin gallate (EGCG) is shown,<sup>[431]</sup> in which gallolyl-derived orthoquinone is formed as byproduct.



**Scheme VI.2.** Proposed reduction mechanism of GO by L-ascorbic acid (*Adapted from Gao, 2010<sup>[433]</sup>*).



**Scheme VI.3.** Proposed reduction mechanism of GO by EGCG (*Adapted from Liao, 2011<sup>[431]</sup>*).

Alternative approaches to chemical reduction are the thermal and the electrochemical reduction. The thermally-mediated reduction employs an annealing step where the oxide functionality from the surface is stripped by directly heating GO in a furnace at temperatures between 150-1100 °C. This step can be performed with other reduction approaches as a last stage in order to improve the reduction efficiency and the quality of the RGO structure.<sup>[427]</sup> Several approaches combine high temperatures with an atmosphere of Ar/H<sub>2</sub><sup>[420]</sup> or even with an acetylene-assisted reduction, using this compound as a supplemental carbon source to repair substantial defects within GO sheets<sup>[434]</sup>. The last method for the reduction of GO relies on the electrochemical removal of the oxygen functionalities. Firstly thin films of GO are deposited onto a substrate. After deposition on a variety of substrates such as glass, plastic, ITO, etc., electrodes were placed at opposite ends of the film and linear sweep voltammetry was run in a sodium phosphate buffer. Reduction began at -0.60 V and reached a maximum at -0.87 V. Rapid reduction was observed during the first 300 s, followed by a reduced rate of reduction up to 2000 s, and finally a decrease to background current levels up to 5000 s. A priori this method could avoid the use of dangerous reducers (e.g. hydrazine) and the need to dispose of the by-products.<sup>[435]</sup>

Focusing on the chemical reduction of the GO obtained, we perform two different routes: a chemical route and a chemical-colloidal route (Figure VI.3). In the first one, we use the following reducer agents: hydrazine and Vitamin C in aqueous solution. On the other, we add a surfactant, DDPS, in the GO reaction medium before the reduction step in order to improve the exfoliation stage. The reduction was carried out with the same reducer agents.

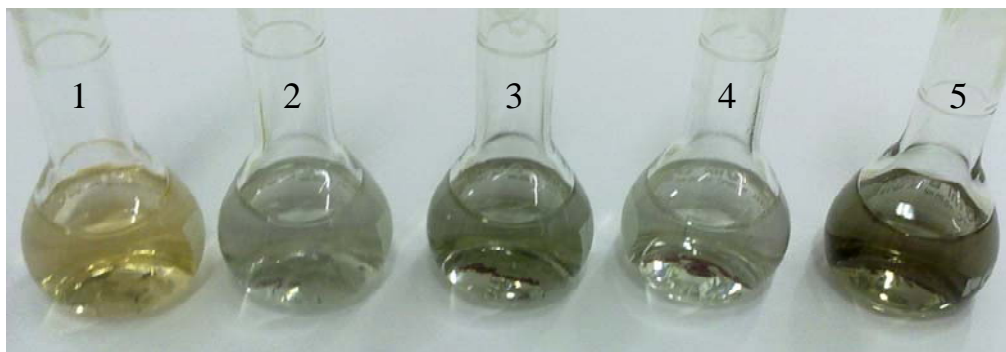


**Figure VI.3.** Photographs of aqueous dispersions of the starting material, GO, (1) and RGO obtained by reduction with: hydrazine (2); hydrazine with DDPS surfactant (3); Vitamin C (4) and Vitamin C with DDPS surfactant (5).

#### VI.1.2.1. Chemical Reduction of GO with Hydrazine

The GO ( $1 \text{ mg mL}^{-1}$ , sonication 1 h) was reduced with hydrazine in water by the Stankovich's method.<sup>[165]</sup> The hydrazine ratio was 0.02 mL per 1 mg GO and the reaction was maintained at  $100^\circ\text{C}$  during 24 h. The reduced product was filtered and washed with water and methanol. It is important to note that the reduced dispersion is only stable a few weeks, after which, the RGO sheets precipitated.

For comparative purposes, the GO reduction was also carried out by exposure of GO LB deposited sheets to hydrazine vapour (0.1 mL) during 18 h at room temperature<sup>[76]</sup> in a closed homemade container. To deposit the GO sheets by LB method, we prepared the GO Langmuir monolayer by spreading the GO dispersion in MeOH:H<sub>2</sub>O (5:1 v/v, sonication 30 min) on the air-water interface.<sup>[76]</sup> The GO sheets were transferred by symmetric barrier compression ( $50 \text{ mm min}^{-1}$ ) with the substrate into the trough by vertically dipping it up at  $2 \text{ mm min}^{-1}$  and then it was reduced by hydrazine vapour and later rinsed with water and dried in an oven for 1 h ( $80^\circ\text{C}$ ).

### VI.1.2.2. Chemical Reduction of GO with Vitamin C

To reduce the GO with Vitamin C, the pH of the GO aqueous dispersions ( $0.1 \text{ mg mL}^{-1}$ , sonication time 1 h) was adjusted to 9-10 with an ammonia solution of 25% and then, the reducer agent, Vitamin C (2 mM) was added. The reactive solution was heated at  $95^\circ\text{C}$  during 15 min.<sup>[405]</sup> The reduced dispersion was processed by filtration with a PVDF membrane ( $0.2 \mu\text{m}$  pore size) supplied by Filter-lab.

In this case, the reduction aqueous dispersion formed by the RGO samples obtained from GO reduced by Vitamin C was stable during several months.

### VI.1.2.3. Chemical Reduction of GO assisted by the Surfactant DDPS

The chemical reduction was carried out in the presence of the DDPS surfactant by using GO dispersed in surfactant solutions and the reduction procedures previously described. Thus, the concentration of the reducers, hydrazine and Vitamin C, and their respective reaction conditions (temperature and time) were kept.

To form the GO/surfactant dispersion, first we prepared a stable water dispersion of GO ( $0.5 \text{ mg mL}^{-1}$ ) by ultrasonic treatment (1 h) exfoliating the GO. Next, the surfactant was added and the dispersion was mechanically stirred during 2 h and finally again sonicated (1 h). In order to optimize the reduction of GO, the DDPS concentration was modified above and below the CMC ( $1.1 \text{ mg mL}^{-1}$ )<sup>[174]</sup>. Surfactant concentrations below the CMC did not give stable dispersions, in contrast surfactant solutions with concentrations above  $2 \text{ mg mL}^{-1}$  gave rise to small precipitates after a few days. Therefore, we keep the surfactant concentration in  $1.7 \text{ mg mL}^{-1}$  which is twice the CMC of DDPS and form stable and clear GO dispersions during a few weeks. This result indicates that the optimum surfactant concentration value required to stabilize the GO dispersion is

close to the CMC, in good agreement with results observed for ionic surfactants.<sup>[385]</sup>

After reduction, the RGO sample was filtered and then, washed with water and methanol, to remove free molecules of surfactant. Thus, the sample was washed until the disappearance of foam in the washing solvent. Finally the RGO was dried and stored in vacuum.

It is important to note for the storage and processability of RGO aqueous dispersions, that these surfactant-RGO dispersions are stable during one year. A comparison of the different RGO-dispersions, stored after one year, are shown in Figure VI.4, where one can observe a clear RGO agglomeration in the case of hydrazine reduction and an initial destabilization for the Vitamin C. This fact indicates that the surfactant could be adsorbed onto the sheets, stabilizing them by both steric and electrical repulsions.

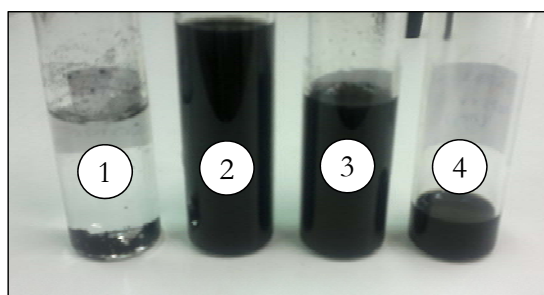


**Figure VI.4.** Photographs of aqueous dispersions taken after one year of the RGO reactive media obtained by reduction with: hydrazine (1); hydrazine with DDPS surfactant (2); Vitamin C (3) and Vitamin C with DDPS surfactant (4).

## VI.2. RGO samples: Characterization and Langmuir-Blodgett Deposition

### VI.2.1. Characterization of RGO samples

In this section, we present the characterization of the different samples obtained by chemical reduction. Therefore, we analyze the quality of the RGO

flakes by means of UV-vis and XPS measurements previous to the RGO deposition.

We evaluate the efficiency of the reducer agents by analyzing the position of the maximum of the UV-vis absorption spectra of the different samples (Figure VI.5). The maximum position values of the UV-vis spectra are reported in Table VI.2. For GO, one can see that the position of the maximum is centred at 230 nm, in agreement with the literature values.<sup>[75]</sup> After reduction, the absorption peak red shifts to 264 nm and 265 nm for reduction with hydrazine and Vitamin C, respectively. It is known that the GO reduction causes a red shift in the absorption maximum,<sup>[75]</sup> so that our observations indicate that both the Vitamin C and hydrazine are good reducer agents of GO and that reduction achieved is similar for the two reducer agents.

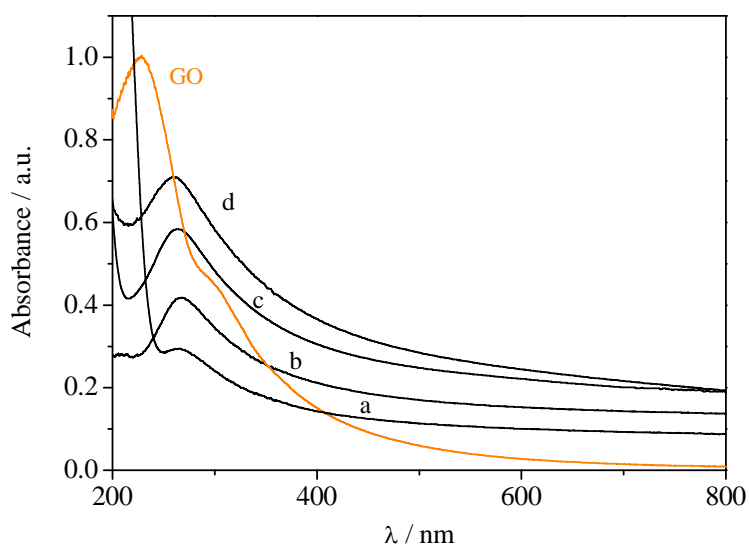


**Figure VI.5.** UV-vis absorption spectra of aqueous dispersions of the starting material, GO, and RGO obtained by reduction with: hydrazine (a); hydrazine with DDPS surfactant (b); Vitamin C (c) and Vitamin C with DDPS surfactant (d).

As the position of the maximum of the UV-vis spectra is a qualitative indicator, the X-Ray photoelectron spectroscopy (XPS) was employed to analyze the reduction degree of the RGO samples in a quantitative way.

**Table VI.2.** UV-vis absorption peak position for aqueous GO solutions and different RGO samples dissolved in chloroform. The concentration was kept constant in 0.1 mg mL<sup>-1</sup>. Percentage of C (sp<sup>2</sup>) and the Raman intensity ratio values found for different graphitic samples. Electric conductivity values of the different RGO paper-like films.

Sample	$\lambda_{\max} / \text{nm}$	% C (sp <sup>2</sup> )	I <sub>D</sub> /I <sub>G</sub>	Conductivity / S m <sup>-1</sup>
<b>Graphite Oxide</b>	230 ± 2	49 ± 1	1.42	insulator
<b>RGO Hydrazine</b>	264 ± 2	63 ± 2	---	241 ± 29
<b>RGO Hydrazine vapour</b>	---	---	1.99	---
<b>RGO Hydrazine (DDPS)</b>	268 ± 2	82 ± 1	1.45	484 ± 58
<b>RGO Vitamin C</b>	265 ± 2	67 ± 1	0.67	37 ± 4
<b>RGO Vitamin C (DDPS)</b>	266 ± 2	77 ± 6	0.92	580 ± 70

Figure VI.6a displays the C<sub>1s</sub> core-level spectra of different samples. The asymmetric peak of the C<sub>1s</sub> was fitted to three or four components centred at 284.8 eV (aromatic sp<sup>2</sup>), 286.9 eV (C-O), 287.7 eV (C=O) and 290 eV (O-C=O), respectively.<sup>[392]</sup> Results obtained for the different samples are summarized in Table VI.1. Each reported value is the average over at least three spectra, and the standard deviation of these measurements was considered the experimental error. From data reported in Table VI.1 and Figure VI.6a, it can be seen that the most significant change after the GO reduction is the increase of the sp<sup>2</sup> component, indicating an increase of the proportion of reduced carbons upon the reduction. The value of the sp<sup>2</sup> component found for RGO reduced by hydrazine is in good agreement with those obtained by other authors.<sup>[403, 433, 436]</sup> Our results also show similar sp<sup>2</sup> component for samples reduced by hydrazine and Vitamin C, in good agreement with results in the literature.<sup>[405]</sup> Moreover, results in Table VI.2 indicate



that the O/C atomic ratio of RGO sample reduced by Vitamin C is higher than for the sample reduced by hydrazine, Table VI.1. The increase of the O/C ratio can be due to the formation of hydrogen bonds between the oxidized product of Vitamin C and the residual oxygen on the RGO.<sup>[406]</sup>

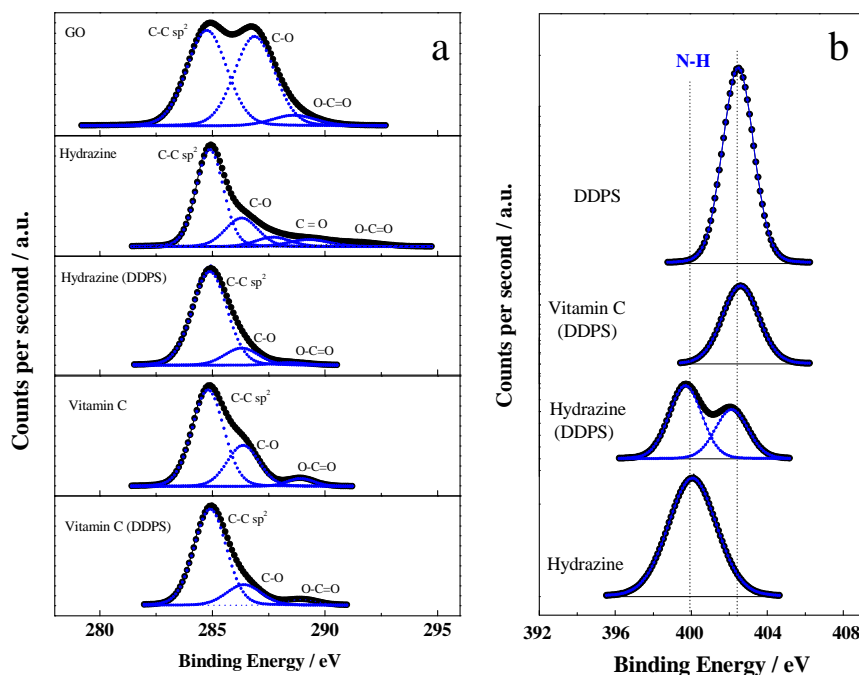
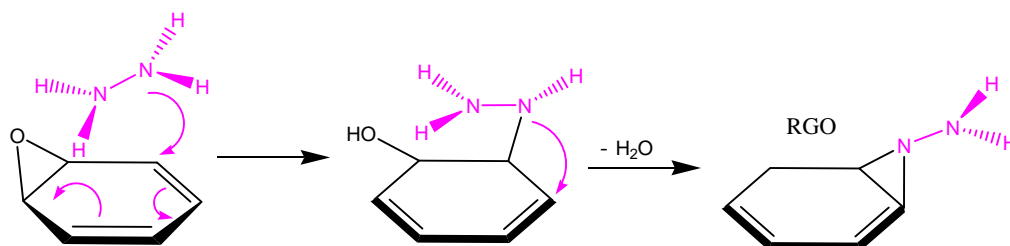


**Figure VI.6.** (a) The C<sub>1s</sub> core-level spectra of graphite oxide (GO), and RGO samples reduced with: hydrazine; hydrazine dissolved in DDPS; Vitamin C and Vitamin C dissolved in DDPS solutions. (b) The N<sub>1s</sub> core-level spectra of dodecyl dimethyl ammonium propane sulphonate (DDPS) and RGO samples reduced with: Vitamin C dissolved in DDPS solutions, hydrazine dissolved in DDPS solutions and hydrazine.

We also recorded the N<sub>1s</sub> core-level spectra of different chemically reduced graphite samples. Figure VI.6b shows the spectra of these samples. It is interesting to note that the N<sub>1s</sub> for RGO reduced with hydrazine presents one peak centred at 400 eV while no N<sub>1s</sub> peak was detected for the RGO reduced by Vitamin C. It is well documented that the reduction of the epoxy groups at the edges of the GO network using hydrazine is blocked by the formation of the hydrazino alcohol,<sup>[433]</sup> so that the XPS peak at 400 eV can be ascribed to the

nitrogen atoms ( $R_2N^-$ , amine nitrogen) attached to the RGO sheets,<sup>[437]</sup> as shown scheme VI.4.



**Scheme VI.4.** One of the possible steps in the reduction mechanism of GO with hydrazine that results in the attachment of nitrogen atoms to the RGO sheets.

On the other hand, we also analyzed the efficiency of the reduction process for the two reducer agents dissolved in surfactant solutions by analyzing both, the UV-absorption spectrum and the  $C_{1s}$  core-level spectra, Table VI.2 and Figure VI.6a, respectively. As can be seen, using these reducer agents the peak positions of the UV-vis absorption spectra are also red shifted respect to the spectrum of GO (Table VI.2) indicating that a good reduction is achieved in the presence of the surfactant. Moreover, by comparing with the spectra of RGO samples obtained without surfactant, the red shift is greater, indicating that the surfactant seems to improve the reduction efficiency. To confirm this picture the XPS spectra of these samples were recorded. The  $C_{1s}$  core-level spectra, Figure VI.6a, are decomposed into three peaks centred at 284.8 eV (aromatic  $sp^2$ ), 286.9 eV (C-O), and 290 eV (O-C=O), respectively.<sup>[392]</sup> When we compare the percentage of  $C_{sp^2}$  for RGO samples reduced in the absence of surfactant with those obtained in the presence of surfactant molecules (Tables VI.1 and 2) we can conclude that the surfactant improves the reduction of the GO. This fact can be due to the exfoliation effect carried out by the surfactant molecules attached to the GO network.

To corroborate the functionalization of the RGO flakes by the surfactant DDPS we recorded the XPS spectra of the different samples. Figure VI.6b presents the  $N_{1s}$  core-level spectra of the samples. As can be seen in the Figure VI.6b the RGO samples prepared in surfactant solutions present two peaks centred at 402 eV and 168 eV. In order to assign these peaks we compare these spectra with the XPS spectrum of the surfactant DDPS. For comparison Figure VI.6b presents the surfactant DDPS spectrum among the RGO spectra. The  $N_{1s}$  core-level spectrum of the DDPS surfactant shows a symmetric peak centred at a binding energy of 402.3 eV which is similar to that recorded for RGO samples reduced in the presence of DDPS surfactant (see Figure VI.6b and Table VI.1). The XPS spectrum of the surfactant also presents the  $S_{2p}$  core-level spectrum of the sulphonate group at the binding energy of 167.5 eV.<sup>[392]</sup> The small shift in the binding energy of  $S_{2p}$  peak in RGO samples with respect to the surfactant one reflects the zwitterionic nature of the surfactant. From these results we can conclude that the synthesis proposed in this work allows obtaining RGO flakes with surfactant molecules attached to the graphitic network, i.e., functionalized RGO.

It is also interesting to note that when the reduction is carried out with hydrazine assisted by the surfactant DDPS, the  $N_{1s}$  core-level spectrum consists of an asymmetric band that can be decomposed into two peaks centred at 399.8 eV and 402.0 eV, respectively. As commented above, the peak centred at 402 eV was ascribed to the nitrogen atoms of the surfactant attached to the RGO sheets,<sup>[437]</sup> while the peak at 399.8 eV is due to the nitrogen atoms attached to the RGO reduced with hydrazine, and it appears in the spectrum of RGO samples reduced with hydrazine as was mentioned. From our results we can conclude that the surfactant cannot completely inhibit the defects introduced by nitrogen groups attached to the network, however, improves the quality of the RGO flakes decreasing the N/C atomic ratio from 0.039 for hydrazine to 0.004 for hydrazine dissolved in DDPS.

## VI.2.2. Langmuir-Blodgett Films of Graphite Oxide

We carried out the study of the GO at the air-water interface. Thus, we prepared the GO Langmuir monolayer by spreading a GO dispersion ( $\sim 0.5 \text{ mg mL}^{-1}$ ) in MeOH:H<sub>2</sub>O (5:1 v/v, sonication 30 min) on the air-water interface. The surface pressure-area isotherm recorded by symmetric barrier compression (4 mm min<sup>-1</sup>) at 20°C and Brewster angle microscopy images of GO at the air-water interface are shown in Figure VI.7. The morphology of the isotherm is similar to other authors.<sup>[76]</sup> By BAM, only the biggest GO sheets are visible due to the resolution of the objective is 2  $\mu\text{m}$  and besides, it is not possible to discern if they are sheet aggregated or not.

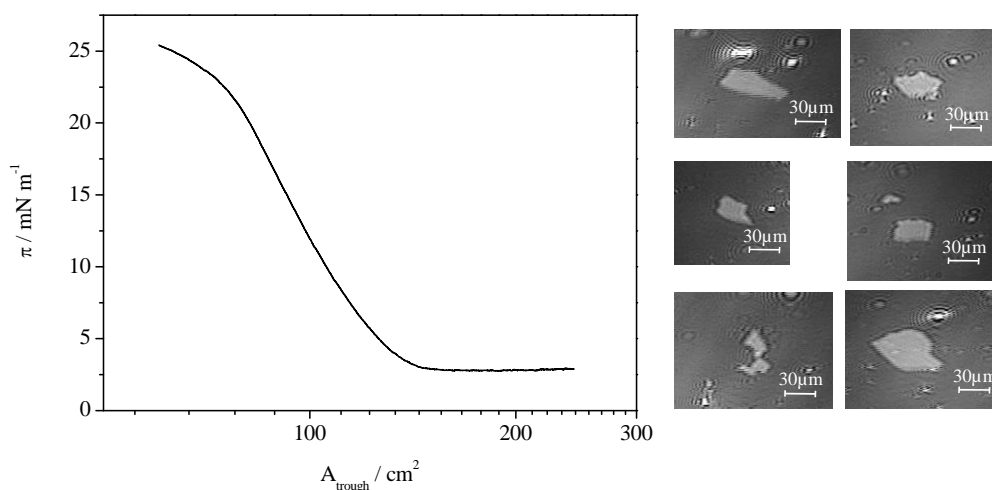


**Figure VI.7.** Surface pressure-area isotherm of GO at the air-water interface by symmetric barrier compression (4 mm min<sup>-1</sup>) at 20°C. BAM images of several GO sheets at a surface pressure of 3 mN m<sup>-1</sup>.

The next step was to transfer the GO sheets by the Langmuir-Blodgett technique onto silicon. Thus, the GO sheets were transferred by symmetric barrier compression (50 mm min<sup>-1</sup>) with the substrate into the trough by vertically dipping it up at 2 mm min<sup>-1</sup>. As the GO is soluble in water, we use a high speed for the compression to minimize the dissolution of the floating GO sheets during

the deposition process. In fact, during the formation of the monolayer, it is possible to observe how the water subphase slightly changes its colour to yellowish brown. Really, the monolayer situation is between a Langmuir (floating sheets) and a Gibbs (soluble sheets) film. Besides, we selected the surface pressure of  $3 \text{ mN m}^{-1}$  in order to obtain no overlapped sheets to a better individual later characterization of sheets by FE-SEM, AFM and Raman. Figure VI.8a shows the FE-SEM image of the GO sheets deposited on silicon. The AFM profiles of GO sheets show a height of  $\sim 1.7 \text{ nm}$  compatible with a bilayer of graphite oxide (Figure VI.8b).

The Raman spectrum (Figure VI.8c) show the D and G bands at  $1316$  and  $1586 \text{ cm}^{-1}$ . The graphite oxidation leads to a carbon network with higher disorder than in graphite, i.e., the GO Raman spectrum shows a broader G band, as well as a broad D band of higher relative intensity compared to that of the G band. The D band position,  $1316 \text{ cm}^{-1}$ , is due to the presence of epoxide and hydroxyl groups that yield a series of bands around  $1300 \text{ cm}^{-1}$ . Besides, these groups also affect to the width and a red-shift of the G band with respect to pure graphite. Thus, when the GO to RGO transformation occurs several defects and residual oxidation remains but a blue shifts the D and G bands to graphite may be observed joined to an increase of the  $I_D/I_G$  ratio due to the increase of the number of  $\text{Csp}^2$  domains.<sup>[201]</sup>

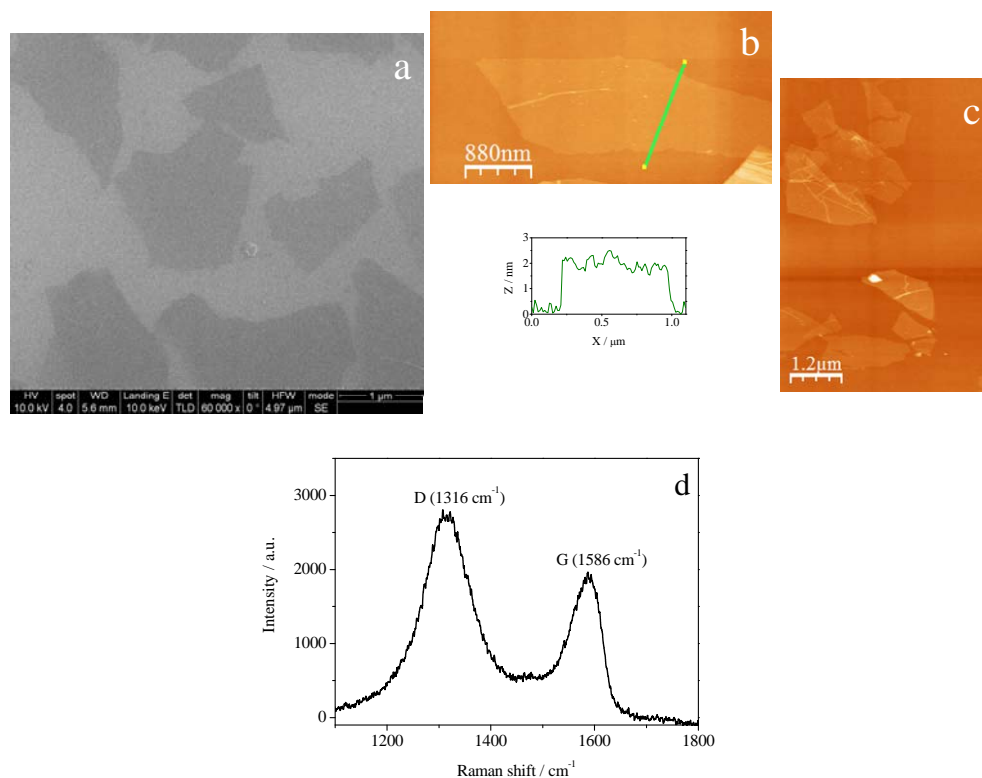


**Figure VI.8.** FE-SEM (a) and AFM (b, c) images of a Langmuir monolayer of graphite oxide at  $3\text{mN m}^{-1}$  transferred onto silicon by the Langmuir-Blodgett methodology. The corresponding cross section profile is also shown. The Micro-Raman spectrum (d) of the GO is also shown.

### VI.2.3. Langmuir-Blodgett Films of RGO Samples

After RGO characterization, the different samples were deposited onto silicon by using the LB methodology. Previously, the surface properties of the Langmuir monolayers precursors were studied. To this aim we studied the stability of the spreading solutions employed to prepare the Langmuir monolayers and the different states of the RGO Langmuir monolayers by recording the surface-pressure isotherms, Figure VI.9a. Then, we transfer Langmuir monolayers corresponding to different surface states onto silicon by LB by symmetric barrier compression at  $50\text{ mm min}^{-1}$  and dipping up at  $5\text{ mm min}^{-1}$ . Our results show that the LB films built with the densest Langmuir monolayers ( $\pi \geq 4\text{ mN m}^{-1}$ ) consist of flakes overlapped each other leading to multilayers with high AFM height

profile. An illustrative example is presented in Figure VI.9b for a LB film of RGO reduced with Vitamin C at the surface pressure of  $4 \text{ mN m}^{-1}$ . Similar behaviour was observed for the rest of samples. Therefore, we prepared the LB films by transferring dilute RGO Langmuir monolayers ( $\pi \leq 4 \text{ mN m}^{-1}$ ) since we were interested in obtaining no overlapped sheets.

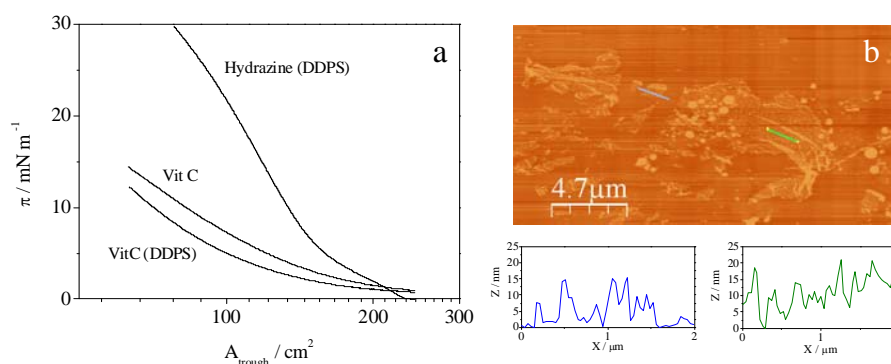


**Figure VI.9.** (a) Surface pressure isotherms at  $20^\circ\text{C}$  for monolayers of RGO reduced with: hydrazine dissolved in DDPS solutions, Vitamin C and Vitamin C dissolved in DDPS. (b) AFM image of the Langmuir-Blodgett film of RGO reduced with Vitamin C obtained by transferring a RGO Langmuir monolayer of surface pressure of  $4 \text{ mN m}^{-1}$  from the air-water interface onto silicon. Below the AFM image are two profiles obtained from AFM.

The RGO Langmuir monolayers were prepared by spreading a solution of  $\sim 0.1 \text{ mg mL}^{-1}$  of RGO dispersed in chloroform. Since it is well established that sonication of RGO prevents the re-stacking of the graphene flakes, we prepared the spreading solutions by using this method with sonication times between 75 and 150 min. The most stable solutions were achieved using sonication times ranging from 90 to 150 min, obtaining clear spreading solutions stable for a few weeks. The BAM pictures of the Langmuir monolayers do not show images of the RGO nanoplatelets. Because the graphene monolayers are almost optically transparent ( $\text{pa } 2.3\%$ ),<sup>[438]</sup> this fact suggests that the procedure used in this work provides good-quality RGO flakes.

The LB method was used for all samples except for the RGO obtained by reduction with hydrazine. In this case, it was not possible to prepare its Langmuir monolayers because the spreading solution became unstable and small amounts of precipitates were observed after 12 h (Figure VI.10a). In fact, we prepare a LB film using a fresh and transparent spreading solution, i.e., before the RGO precipitation occurs. Then, we spread this solution on the water subphase and visible aggregates are observed by BAM, Figure VI.10b. The aggregates were transferred onto silicon by the LB methodology and its morphology analyzed by AFM, Figure VI.10c. The film profiles obtained from AFM show aggregates of high height ( $>100$  nm). This fact indicates that the LB technique is not a good procedure for deposition of RGO reduced by hydrazine.

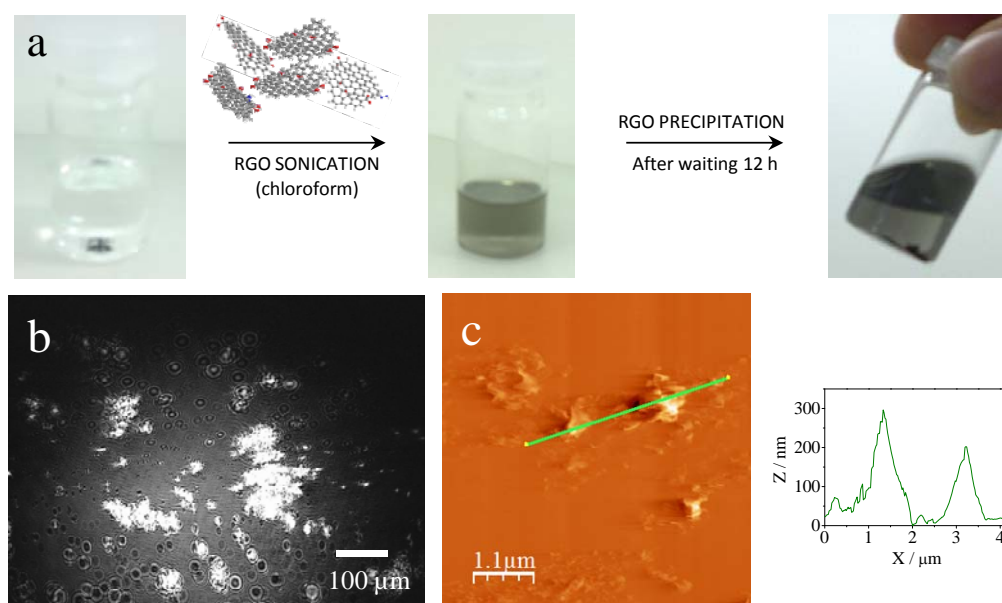


**Figure VI.10.** (a) Photographs showing the steps for the sonication-mediated dispersion of RGO reduced with hydrazine in chloroform. The last image shows how the spreading solution becomes unstable after several hours: a RGO deposit appears. (b) BAM image ( $600 \times 800 \mu\text{m}$ ) of the aggregates formed by RGO sheets reduced with hydrazine at the air-water interface. (c) AFM image of the LB film of RGO reduced with hydrazine obtained by transferring the RGO Langmuir monolayer at the surface pressure of  $1 \text{ mN m}^{-1}$  from the air-water interface onto silicon. The corresponding profile obtained from AFM is also shown.



Therefore, to solve this problem we opted to reduce *in situ* the GO deposited by the LB method on silicon by exposure to hydrazine vapour.<sup>[76]</sup> Figures VI.11a and c show a higher magnification AFM and FE-SEM images of a representative flake corresponding to the RGO obtained by *in situ* reduction of GO with hydrazine vapour. The height profile of the flake determined by AFM was  $\sim 1.5$  nm (Figure VI.11b) compatible with a 1-3 graphene layers.<sup>[439]</sup> No good quality AFM images were recorded due to the hydrazine vapour reacted with the silicon oxide layer increasing its roughness and forming several holes.

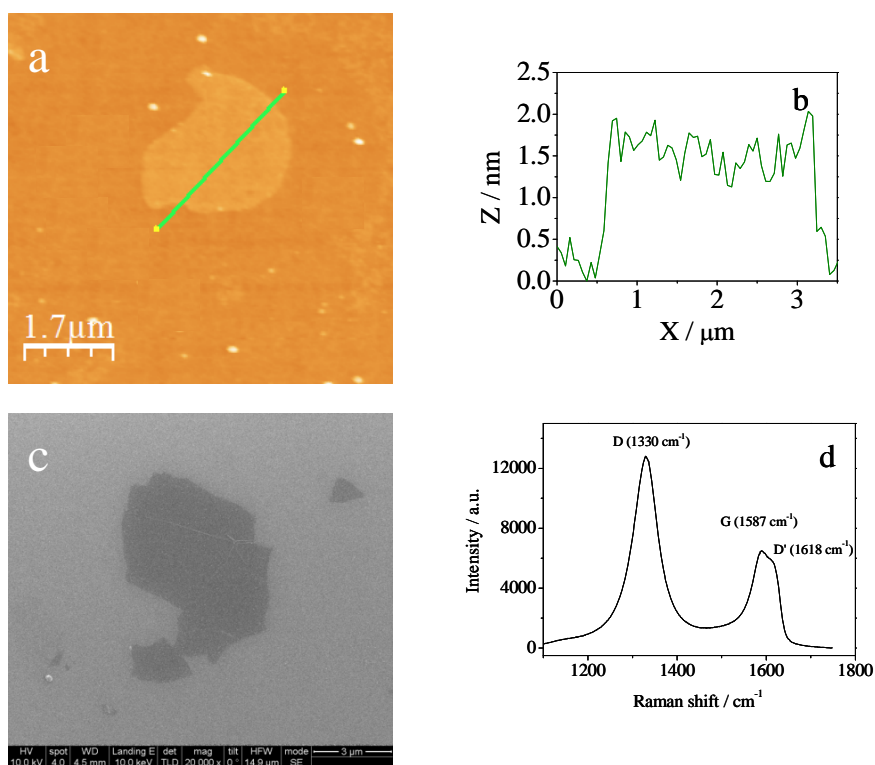


**Figure VI.11.** AFM (a) and FE-SEM (c) images of the Langmuir-Blodgett film of RGO reduced *in situ* with hydrazine. (b) Profile obtained from AFM (d) Micro-Raman spectrum of the RGO reduced *in situ* by hydrazine.

To analyze the degree of defect repair after the reduction of GO by hydrazine we have recorded the Micro-Raman spectra of RGO sheets deposited on silicon by the LB methodology. Figure VI.11d shows the Raman spectrum of a

RGO flake obtained by reduction with hydrazine vapour. The spectrum presents three bands centred at  $1587\text{ cm}^{-1}$  (G band),  $1330\text{ cm}^{-1}$  (D band) and  $1618\text{ cm}^{-1}$  (D' band), respectively. The D and D' bands are identified as disorder bands and are originated from different mechanisms, intervalley (D) and intravalley (D') resonant Raman scattering.<sup>[440, 441]</sup>

The intensity of the D band depends on the degree and nature of the basal plane disorder because this band requires defects for its activation,<sup>[442, 443]</sup> while its position depends on the incident laser energy<sup>[443]</sup>. The D band is observed in chemical derived flakes because oxidation and reduction processes seriously alter the basal plane of graphene. The  $I_D/I_G$  ratio is a measure of the defects on the  $sp^2$  bonding character. In Table VI.2 are the  $I_D/I_G$  values found for the different samples. We can note that the  $I_D/I_G$  ratio value for the RGO sample reduced in situ with hydrazine vapour is high indicating that the presence of non-reduced groups or disorder introduced by the functionalization of the graphene sheets with the nitrogen compounds due to the reduction process.

In the case of RGO reduced by Vitamin C, Figures VI.12a and c show the FE-SEM and AFM images of different LB deposited sheets obtained by transferring onto silicon the Langmuir monolayers at the surface pressure of  $1\text{ mN m}^{-1}$ . The images show that the LB films contain an elevated number of RGO nanoplatelets with a height profile of  $\sim 2\text{ nm}$ . The height profile value is similar to that obtained for RGO reduced with hydrazine. Figure VI.12b shows the magnification FE-SEM image of a RGO flake. Comparison between the size of flakes obtained by reduction with hydrazine and Vitamin C clearly indicates that Vitamin C provides larger flakes than hydrazine whereas the height is quite similar. This could be due to differences between the mechanisms involved in the reduction processes. Thus, cracking of the carbon network in the reduction process promoted by hydrazine may be rationalized taking into account the thermal instability of aziridines<sup>[165]</sup> leading to carbon nitrogen 1,3-dipoles<sup>[444]</sup>

which may be hydrolyzed under reaction conditions giving rise to complex mixtures of substituted hydrazine and carbonyl compounds [445, 446].

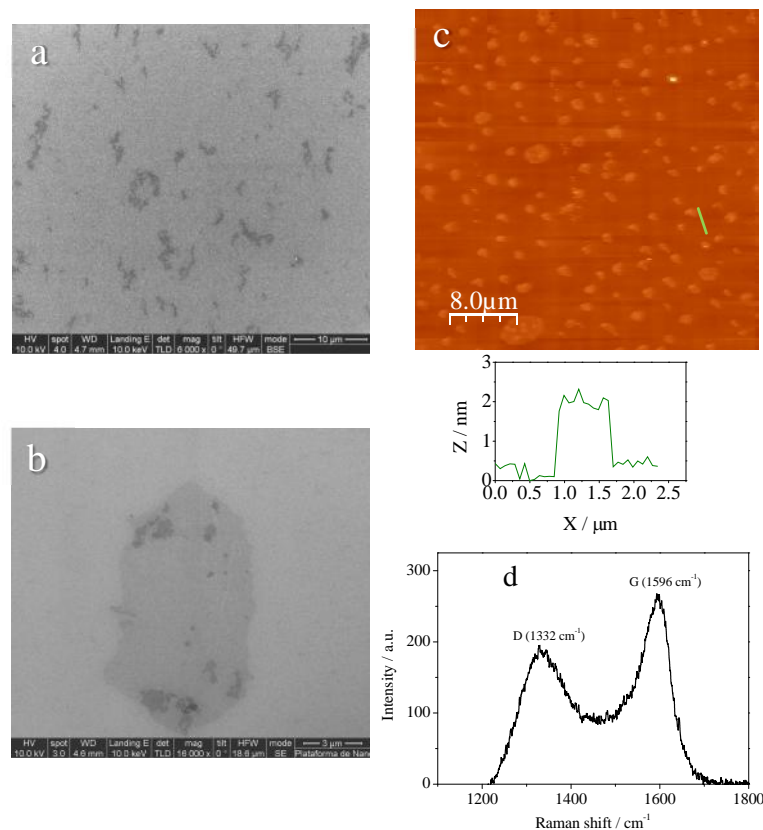


**Figure VI.12.** FE-SEM (a, b) and AFM (c) images of the Langmuir-Blodgett film of RGO reduced with Vitamin C. Below the AFM image is the profile obtained from AFM. (d) Micro-Raman spectrum of a representative RGO flake. (d) Micro-Raman spectrum of a representative RGO flake.

The Raman spectrum of flakes reduced with Vitamin C also displays the G and D bands (Figure VI.12d). However, the  $I_D/I_G$  ratio is smaller than the value found for the RGO samples obtained by reduction with hydrazine, see Table VI.2. This fact suggests an increase of the size of the  $C_{sp^2}$  domains in the RGO samples reduced with Vitamin C. This can be an unexpected result if one takes into account that the XPS spectra show a similar number of  $C_{sp^2}$  domains for both samples. This behaviour can be interpreted by considering that even though

the number of  $Csp^2$  domains is similar, the reduction with Vitamin C provides larger  $Csp^2$  domains than the reduction with hydrazine increasing the  $I_D/I_G$  ratio value.<sup>[447, 448]</sup> The  $I_D/I_G$  ratio for RGO reduced by Vitamin C is smaller (0.67) than the value found previously in the literature for RGO samples reduced by Vitamin C ( $\sim 1$ ).<sup>[406, 407]</sup> This means that the size of the  $sp^2$  domains is larger in our sample. If one takes into account that our GO samples have higher oxidation degree than the samples used by other authors,<sup>[406, 407]</sup> the Raman results seem to indicate that a higher oxidation degree of starting GO renders larger  $sp^2$  domains when the reduction is carried out by Vitamin C, while no significant changes are observed when hydrazine is employed as reducer agent.

#### **VI.2.4. Langmuir-Blodgett deposited Sheets of RGO functionalized with the Surfactant DDPS**

Figures VI.13a and b show the AFM and FE-SEM images of DDPS-functionalized RGO sheets obtained by reduction of GO with hydrazine dissolved in surfactant solutions. The surface pressure of the Langmuir monolayer precursor of the LB film was  $1 \text{ mN m}^{-1}$ . The images show significant differences between the morphology of sheets of RGO reduced with hydrazine vapour, Figure VI.11, and with hydrazine dissolved in surfactant solution. Thus, in the latter, chained nanoplatelets can be observed. The cross-sectional view of the AFM images indicates that the height profile values of sheets are of 4 nm. This height is 2.5 nm higher than the RGO sheets fabricated from hydrazine vapour. However, it is reasonable to assume that the surfactant attached on the network resulted in a thicker film.<sup>[449]</sup> Moreover, molecular simulations of the amphiphilic molecules self-assembly on graphene have shown that due to the graphene sheets finite dimension effect, these molecules can form different morphological hemimicelles on nanoscale graphene surfaces with an adsorption mechanism similar than on graphite. The aggregate morphology is dependent on the surfactant concentration and the size of graphene nanosheets.<sup>[450]</sup> In the case of

the DDPS, this surfactant forms spherical micelles on hydrophilic surfaces (solids) and hemimicelles on hydrophobic graphite at the water-graphite interface, Figure VI.14. Besides, the aggregate morphology does not depend on the surfactant concentration above the CMC.<sup>[451]</sup> Thus, taking into account that we work with a surfactant concentration above the CMC, the DDPS can be aggregate on the RGO sheets. Moreover, the hydrodynamic radius of the DDPS micelles in solution is  $\sim 1.7$  nm.<sup>[174]</sup> Accordingly, the difference between the height profile determined by AFM and the radius of the DDPS micelle is  $\sim 2.3$  nm, consistent with the height determined for non-functionalized RGO flakes, Figure VI.11b. This can be an additional argument to reinforce the idea of the formation of hemimicelles onto the RGO flakes, Figure VI.14. On the other hand, the formation of the chained sheets suggests attractive interactions between flakes, likely induced by the surfactant molecules attached to the RGO sheets.

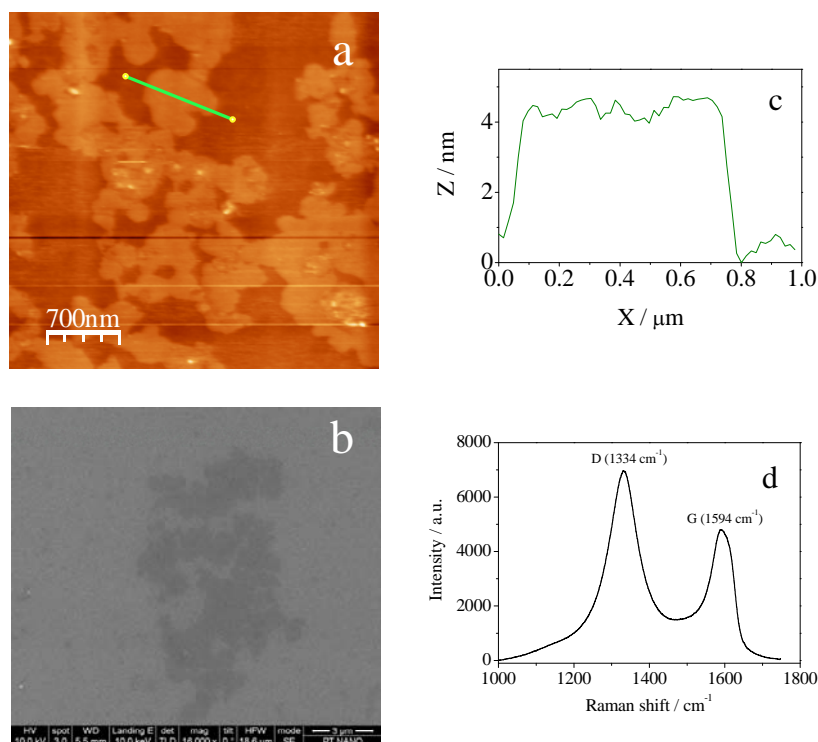


**Figure VI.13.** AFM (a) and FE-SEM (b) images of the Langmuir-Blodgett film of RGO reduced by hydrazine dissolved in DDPS surfactant solution. (c) Profile obtained from AFM and (d) Micro-Raman spectrum of a representative RGO flake.

We analyze the effect of the surfactant DDPS on the degree of defect repair after reduction by means of Micro-Raman spectroscopy. The Raman spectra of RGO functionalized with DDPS and reduced by hydrazine also presents the D and G bands, Figure VI.13d. When we compare this spectrum with that of RGO reduced with hydrazine vapour (Figure VI.11d) it is possible to see that the  $I_D/I_G$  ratio (Table VI.2) is smaller in the former. This fact, along with the higher percentage of  $C_{sp^2}$  detected by XPS for samples functionalized with the surfactant, indicate that the surfactant DDPS improves not only the reduction efficiency but also the degree of defect repair. This fact is consistent with results obtained by other authors with ionic surfactants.<sup>[385, 392, 452]</sup>

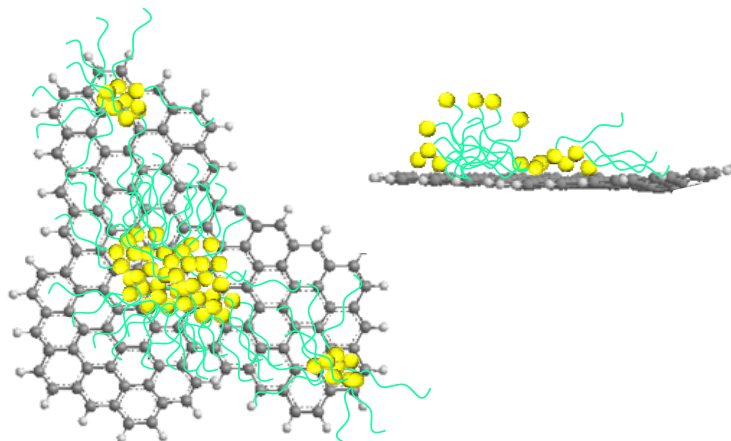


**Figure VI.14.** Scheme of surfactant molecules adsorbed on the graphene surfaces from bulk solution (*Adapted from Wu, 2012*<sup>[450]</sup>).

Figure VI.15a and b show the AFM and FE-SEM images of LB films of RGO reduced with Vitamin C functionalized with the surfactant DDPS. As it was observed for samples of functionalized RGO reduced by hydrazine, chained nanoplatelets can be observed. The height profile values of these flakes estimated from AFM are between 3 and 4 nm (Figure VI.15c). This height is similar to the value found for the DDPS-functionalized RGO flakes reduced with hydrazine and consistent with the presence of surfactant molecules attached to the carbon network.<sup>[449]</sup>

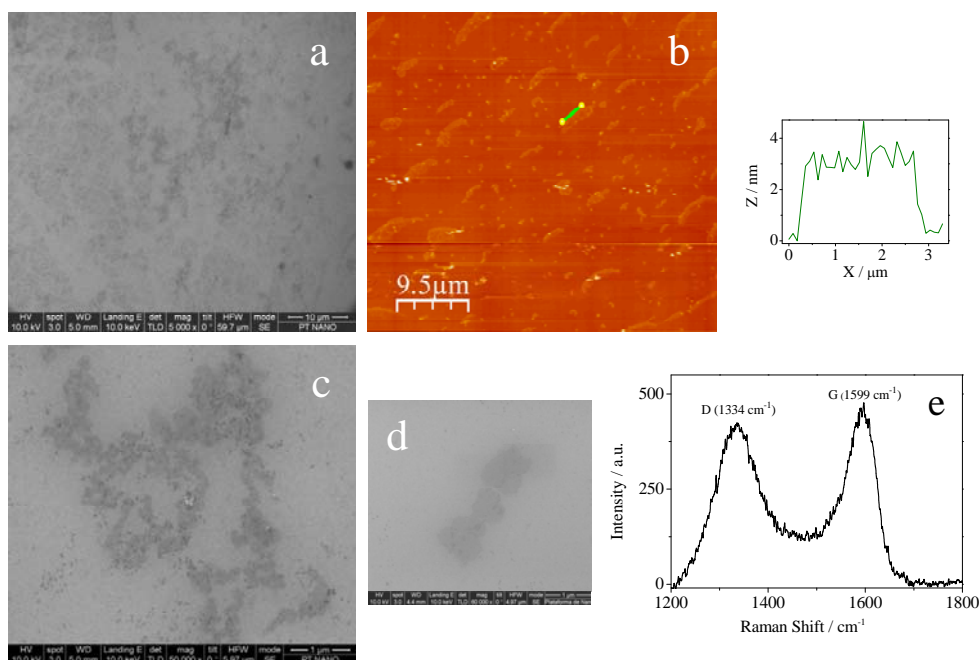


**Figure VI.15.** FE-SEM (a, c, d) and AFM (b) images of the Langmuir-Blodgett film of RGO reduced by Vitamin C dissolved in DDPS surfactant solution. Profile obtained from AFM and (e) Micro-Raman spectrum of a representative RGO flake.

Figure VI.15d shows a representative Raman spectrum of the DDPS-functionalized RGO reduced by Vitamin C and in the Table VI.2 is collected the  $I_D/I_G$  ratio found for this sample. As can be seen the spectrum also presents the D and G bands and the  $I_D/I_G$  ratio is slightly higher than that obtained by reducing GO with Vitamin C in the absence of surfactant. Our results indicate that the surfactant DDPS assists the reduction of GO by Vitamin C increasing the percentage of  $Csp^2$ , while the size of the  $sp^2$  domains is smaller than those produced by reduction with Vitamin C in the absence of surfactant.

### VI.2.5. Electric Conductivity Measurements

The criterion that reflects both the reduction and the defect repair degrees more directly is the electric conductivity. However, experimental conditions, such as layer preparation or the magnitude of the selected area modify this value even for samples with the same reduction degree. In this work, we measured the

electric conductivity by a four-point probe setup with electrodes over RGO paper-like films. This method was proposed by other authors and has been successfully used to carry out the comparative analysis of the quality of graphene samples.<sup>[209]</sup> The RGO paper-like films were fabricated by filtration using a PVDF membrane filter (0.2  $\mu\text{m}$  pore size, Filter-lab), and washing with MilliQ<sup>®</sup> water and methanol in order to remove the excess of reducer agents and free-surfactant.<sup>[209, 210]</sup> Three measurements were carried out for each sample to obtain an average value for the electric conductivity value performing by means of a Keithley 4200 SCS Semiconductor Parameter Analyzer. The film thickness was measured in a workstation combining Scanning Electron Microscopy (SEM) and Focused Ion Beam (FIB) technique sample preparation.<sup>[211]</sup> The conductivity error was estimated from the error value of the film thickness measured by SEM.

To determine the film thickness, some cross-sections of the samples in different regions of interest were made using a FEI Helios 450 dual beam FIB/SEM. To protect the sample surface two Pt layers were deposited on the graphene layer.<sup>[211]</sup> The first one is on direct contact with the RGO films and was deposited with electrons and the second, on the top of the sample, is a thicker Pt layer deposited with ions. Figure VI.16a and b illustrate the methodology employed and the results for a film of graphene reduced by Vitamin C, respectively. The film thickness of the samples is around 1  $\mu\text{m}$ .

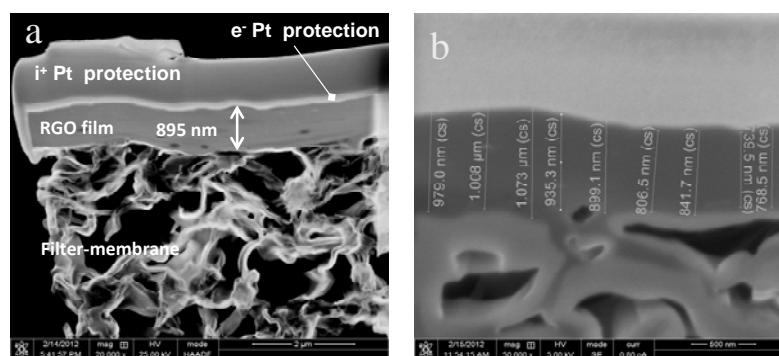


**Figure VI.16.** (a) Cross-sectional SEM images of a RGO paper-like film. The RGO was obtained by reduction of GO with Vitamin C. (b) The thickness values of this film are also indicated.



The electric conductivity values of the different samples are collected in Table VI.2. The conductivity value of RGO sheets reduced by hydrazine agrees with values obtained previously by other authors.<sup>[165, 403]</sup> We cannot compare our values for sheets reduced by Vitamin C with values in the literature, because the values found correspond to samples reduced by Vitamin C with a subsequent thermal annealing step. This annealing step can remove the oxidized form of the Vitamin C attached to the network increasing the conductivity of sheets.<sup>[165]</sup> The conductivity values in Table VI.2 show that the RGO sample reduced by Vitamin C is less conductive than the one reduced by hydrazine. This is an unexpected result if one considers that the  $C_{sp^2}$  percentages are similar in both samples while the  $I_D/I_G$  ratio is smaller for the RGO reduced by Vitamin C. This picture can be explained if one considers that the residual O-containing groups in the case of samples reduced by Vitamin C, detected by the increase of the O/C ratio, destroy the graphene structure and promote a loss of conductivity.<sup>[403]</sup>

From our results it is noteworthy that the functionalization with the zwitterionic surfactant DDPS increases the conductivity for samples reduced by both, hydrazine and Vitamin C. This is consistent with the high values of the percentage of  $C_{sp^2}$  of functionalized RGO samples, see Table VI.2, and with the decrease of the N/C (hydrazine) and O/C (Vitamin C) ratios, Table VI.1 for the functionalized RGO samples. The surfactant adsorption on the GO sheets can be responsible for this behaviour. Thus, when the GO flakes are dispersed in the surfactant aqueous solution by sonication, the adsorbed surfactants molecules avoid the restacking by steric repulsion, favouring the reduction process.<sup>[453]</sup> Additionally, the surfactant adsorbed on the sheets also avoids the restacking of the RGO sheets obtained during the reduction process.

Finally, the high electric conductivity values of the functionalized sheets can be explained if one considers that the functionalization by DDPS via

hydrophobic interactions with the graphitic networks provides interconnected network of RGO with demonstrated high conductivity.<sup>[454]</sup>

Moreover, the conductivity of our functionalized RGO samples is generally higher than values found in the literature for paper-like films of RGO functionalized with ionic surfactants.<sup>[385, 433, 455]</sup> This behaviour can be interpreted if one takes into account that the zwitterionic surfactants present higher adsorption on the hydrophobic surfaces than the ionic ones,<sup>[399, 400]</sup> providing better stabilization against the restacking process than that obtained by the ionic surfactants. Besides, the DDPS surfactant improves the conductivity value of RGO paper-like films functionalized with the zwitterionic surfactant CHAPS.<sup>[455]</sup> Structural differences between these surfactants can be responsible for this behaviour. Thus, our results suggest stronger interactions between the hydrophobic moiety of DDPS and RGO than between the hydrophobic part of CHAPS and the RGO carbon network. This fact can be due to the more hydrophilic character of the surfactant CHAPS.<sup>[402]</sup>

#### **VI.2.6. Electron Beam Lithography: RGO sheets Au-contacted**

In order to carry out an electrical characterization of the RGO sheets, we decided to contact the LB deposited sheets with Ti/Au electrodes on silicon wafers by electron beam lithography (EBL) technique. The electrodes were designed with a 300-1000 nm separation in Van der Pauw and Hall-bar geometry, that allows performing electrical measurements at different geometries.

Thus, we selected three sheets as representative sampling of each kind of RGO samples: reduction with hydrazine functionalized with DDPS, Vitamin C and Vitamin C functionalized with DDPS (Figure VI.17). We did not select the RGO reduced in situ with hydrazine, because the silicon oxide layer is damaged during the reduction process, and it may generate problems with the metal

adhesion on the wafer and does not guarantee the complete isolation with the silicon for the electrical measurements.

To design the electrodes, the main limitation was the size of the flakes. We used an optical microscope to take the measurements for the "flake" outline over which we design the electrodes geometry. As the microscope has a resolution of micrometers, we can only select the flakes greater than 5  $\mu\text{m}$ . All the samples prepared have several flakes with this size condition.

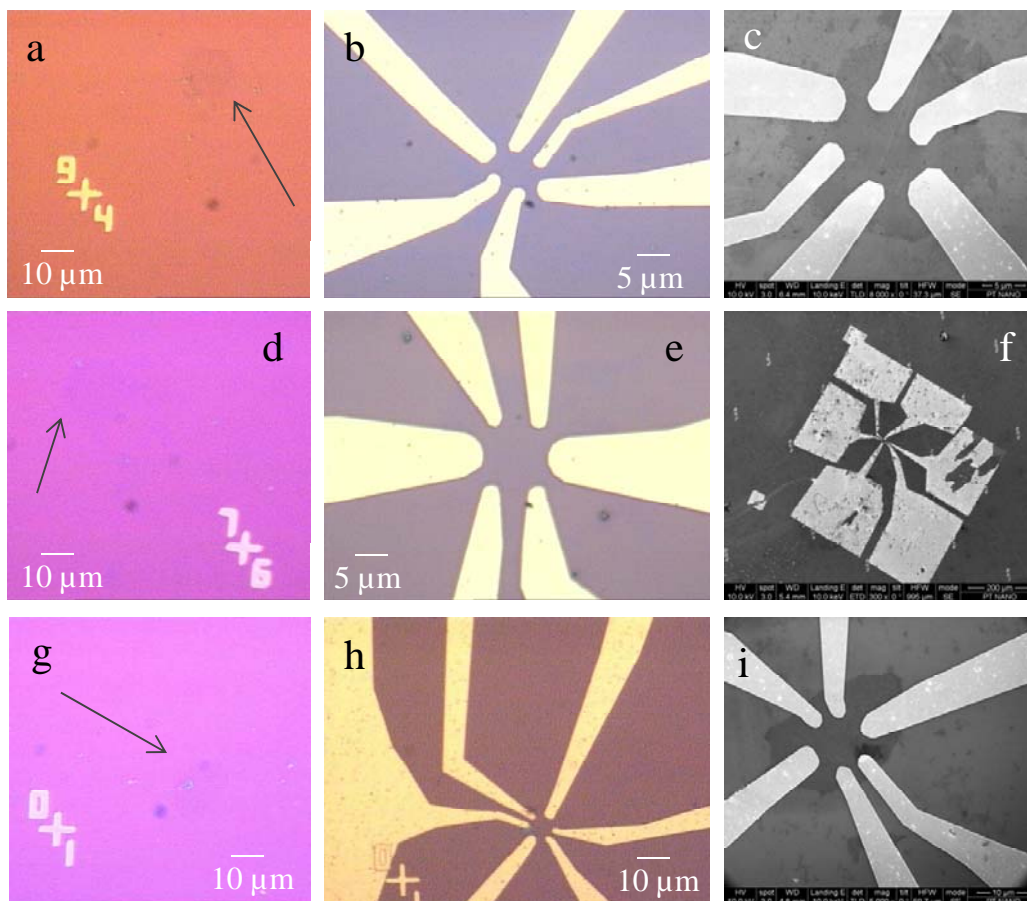


**Figure VI.17.** Optic microscope and SEM images of different RGO sheets before and after the Au/Ti electrodes deposition: reduced with hydrazine in the presence of DDPS (a, b, c); Vitamin C (d, e, f) and Vitamin C in the presence of DDPS (g, h, i). The arrows are a visual guide to localize the RGO sheets due to the optical contrast of the images is not sufficient.

The electrical measurements were carried out in a four probe station by the Van der Pauw method. However, we obtained high resistivity values out of the equipment range for the different samples not allowing the material characterization. This fact can be due to a bad contact between the Ti/Au electrodes and the RGO samples. Although, this contact has been successfully used for pristine graphene samples obtained by micromechanical exfoliation.<sup>[456, 457]</sup> However, our samples present oxygen, nitrogen or sulphur groups functionalizing the hexagonal network, therefore the contact is not good enough. In a future, it is necessary to investigate other metal contacts to improve the electrical measurements.<sup>[458]</sup>



## **VII. Conclusions**



## VII. Conclusions

In this chapter we summarized the main conclusions achieved from the experimental results of the following systems studied in this work: monolayers of anhydride maleic polymer derivatives, films of CdSe QDs and chemically derived graphene deposited onto solids by the Langmuir-Blodgett methodology.

In the case of the **polymers**, Chapter IV, the study was focused on the self-assembly at the air-water interface and onto solids. In order to prepare films supported with potential applications in the construction of electronic devices, we were interested in studying the effect of electrolytes on the equilibrium and dynamic properties of Langmuir and Langmuir-Blodgett films of the polymer poly (styrene-co-maleic anhydride) partial 2 butoxy ethyl ester cumene terminated, PS-MA-BEE. Results show that the Langmuir films deposited on saline solutions are more expanded and stable than the monolayer without salt in the subphase. These facts can be attributed to the formation of a complex between the divalent cation,  $Mg^{2+}$ , and the carboxylic groups of the polymer molecule. Our results demonstrate that the polymer- $Mg^{2+}$  complexes increase the viscoelastic behaviour of the monolayer.

Results also demonstrate surface self-assembly processes for dense polymer monolayers. The aggregates transferred from the air-liquid interface onto silicon wafers present different morphologies depending on the methodology employed to build the LB film and the subphase composition. The thickness of the LB films obtained by ellipsometry agrees with the film height determined by AFM measurements.

Moreover, in order to reinforce the complex formation between  $Mg^{2+}$  and polymer acid groups, we studied surface properties of other anhydride maleic derivative polymer without carboxylic acid groups. The copolymer chosen was poly (styrene-co-maleic anhydride) cumene terminated, PS-b-MA. Results show



the characteristic effect of electrolytes on the water-insoluble monolayers, i.e. the isotherms is shifted to smaller areas when the salt concentration in the subphase increases. This is a signature of no complexation. On the other hand, the morphology of the LB films depends on the polymer nature, stripes for PS-MA-BEE and circular domains for PS-*b*-MA molecules.

In addition, the polymer PS-*b*-MA allows us to carry out the study of the 2D glass transition temperature ( $T_g$ ) by means of equilibrium and dynamics properties. The surface potential measurements indicate that the presence of electrolytes in the aqueous subphase does not strongly modify the 2D  $T_g$ . Finally, the phase transition in PS-*b*-MA monolayers was highlighted by dynamic measurements. Results show that the glass state presents higher elasticity modulus and viscosity values than the fluid state.

In the study of the **QDs films**, presented in Chapter V, our aim was to develop different approaches to prepare QDs films by means of the Langmuir-Blodgett technique and to study the influence of the film morphology on the film photoluminescence properties. To assist the QDs self-assembly the polymer PS-MA-BEE was used. Three different approaches were employed.

In the first one, referred to as co-spreading methodology, we study the assembly ability of QD/PS-MA-BEE mixed monolayers onto solids by AFM and TEM images. Results obtained demonstrate that the surface state of the block copolymer PS-MA-BEE plays a decisive role on the morphology of the QDs assemblies. Thus, when the Langmuir monolayer precursor of the LB films presents the smallest elasticity value, corresponding to the polymer brush conformation at the surface, the films are composed by hexagonal networks with QDs adsorbed on the rims. Conversely, monolayers with the highest elasticity values give LB films with QD/polymer domains. The different architectures were interpreted in terms of distinct dewetting processes, nucleation and growth of holes for the formation of hexagonal networks and spinodal dewetting, for

QD/polymer domains. Our results demonstrate that it is possible to modulate the morphology of the QDs LB films by modifying both, the surface composition and the elastic properties of the Langmuir monolayer precursors of the LB films. This strategy could be presented as a non-template reproducible technique for patterning at the nanoscale.

In the second approach, the polymer LB film is used to modify the surface properties of the substrate. Results demonstrate that the LB film of the polymer PS-MA-BEE plays a decisive role in the increase of the surface density of QDs adsorbed on mica. Cohesive interactions between the polymer chains and the hydrocarbon moieties of the QDs stabilizer, TOPO, can be the origin of this fact. In all cases island-like QDs 2D aggregates were observed and the nanoparticle 3D agglomeration is avoided.

Finally, we proposed to study the influence of the QDs ligand nature on the nanoparticles assembly by exchanging the QDs' ligand by the polymer, PS-MA-BEE. In this way, QD/PS-MA-BEE mixed films and bilayers PS-MA-BEE//QDs were prepared. Results show that the replacement of the QDs stabilizer TOPO by the polymer PS-MA-BEE affects the morphology of the nanoparticles self-assemblies. In the case of mixed films, the high molecular weight of the film formed by QD<sub>p</sub> nanoparticles, favours the gravitational effects against the capillary wave effects. Therefore, the morphology of the self-assemblies is driven by dewetting mechanism of nucleation and growth of holes. According to the results, it is possible to modulate the morphology of the QDs LB films by combining the modification of both the nanoparticle capping ligand and the surface composition of the Langmuir monolayer precursors of the LB films. In the case of bilayers, as the QDs' ligand and the coating film exposed the same group, PS, favourable interactions lead to a better spreading of the QDs on polymer film.

Our results suggest that the monolayer compression develops transient metastable states that finally relax towards the minimum energy configuration of the domain. Therefore, to achieve the stable state we applied successive compression-expansion cycles and then the barriers were stopped. Using this approach more ordered nanoparticles monolayers were obtained. Moreover, this methodology allows us to obtain information of the different relaxation processes produced after the compression-expansion cycles. Results show two relaxation processes for QDs and mixed QD/polymer films. The fastest one was ascribed to rafts movement, while the slowest one was related to movements inside rafts. Moreover, the time-scales of these processes are related to the film composition. Thus, slower relaxations correspond to systems with high polymer mole fraction. Finally, we suggest *shearing* as a driving force to direct the assembly of nanocomposite films according to the stress-direction orientation of the QD/polymer films observed. Moreover, in this work we have proposed the combination of two direction-controlling methods: a polymer matrix and a shearing external force to assemble the nanocomposite.

Our results demonstrate that it is possible to modulate the QDs assembly by choosing the proper methodology.

Finally, we analyzed the effect of the QDs domains morphology on the film photoluminescence properties by means of FLIM. The photoluminescence time-resolved study of the films has allowed us to highlight several QD photodynamic phenomena in the LB films.

To interpret the results obtained for the different LB films we previously studied the dynamic photoluminescence emission of QDs dissolved in chloroform. Results demonstrate that the particles average lifetime in solution is independent of polymer concentration, thus, a static quenching process by charge-transfer has been proposed. On the other hand, the PL decay curves for QDs are different in solution vs. in LB films. As it is expected, the solution offers a more

fluid environment minimizing the QDs interaction, while the LB films present a different dielectric environment that increases the radiative lifetime and a compact particle arrangement that allows for QD-QD dipole interaction. On the other hand, studies carried out by analyzing the effect of the excitation energy, the time exposure and the spectral emission region collected on the PL dynamics highlighted the existence of multi-excitonic processes, a quasi-reversible photo-passivation of the particle surface and the surface-defects emission, respectively.

The photoluminescence of QD/polymer mixed films was characterized for different conditions of film deposition: bilayer or co-spreading; QD-to-polymer composition; and surface pressure at deposition. Results show that the photoluminescence dynamics of QD films are affected by energy transport and trapping processes occurring in the compact arrangement of QDs deposited. The efficiency of these processes essentially depends on inter-dot distance and on surface density of energy traps, which can be QDs with extensive surface defects or small aggregated clusters. Among the several conditions studied, the bilayer deposition yielded the surfaces with more emission intensity, i.e. more brightness. The simultaneous analysis of PL decays and TEM images allowed us to relate this behaviour to a lower amount of QD clustering in the bilayer film. The model used for decay analysis considers energy transport and trapping in the films and, although it is only an approximate model, it also allowed us to relate the photoluminescence dynamics to film morphology. Indeed, the concentration of traps retrieved from decay analysis for the bilayer film is about half of those in co-spreading films. Finally, from our results it is possible to conclude that in order to improve the photoluminescence properties of QD films, it is paramount to obtain films with regular and compact morphology and to minimize QD clustering.

The last system studied was **chemically derived graphene**, Chapter VI. The aims were to develop a new synthetic route by using the zwitterionic surfactant dodecyl dimethyl ammonium propane sulphonate, DDPS, and to

deposit the material prepared in a controlled way in order to achieve good quality and few-layer RGO sheets. Therefore, we simultaneously analyzed the reduction degree, the defect repair degree and the electric conductivity of the RGO sheets obtained by reduction of GO by hydrazine and Vitamin C and functionalized by the surfactant DDPS. Our results demonstrate that the functionalization with the zwitterionic surfactant DDPS improves the reduction efficiency of hydrazine and Vitamin C measured by the percentage of  $C_{sp^2}$ ; reduces the residual groups attached to the carbon network introduced by the reducer agents in both cases; and increases the conductivity of the RGO. Moreover, the electrical conductivity observed in our functionalized samples is generally higher than other surfactant-functionalized RGO paper-like films. Accordingly, we propose the DDPS functionalization of RGO as a good non-covalent functionalization, which increases the electrical conductivity without altering the carbon network. Furthermore, the functionalization with a zwitterionic surfactant offers a residual charge that can bind the RGO sheets with other materials in order to prepare nanocomposites with multiple applications. In addition, results also show that the Langmuir-Blodgett technique allowed us to deposit a few-layer thick RGO flakes onto silicon wafers.

## VIII. References



## VIII. References

1. Petty, M. C., *Langmuir-Blodgett Films: An Introduction*. Cambridge University Press: 1996.
2. Bardosova, M.; Pemble, M. E.; Povey, I. M.; Tredgold, R. H., The Langmuir-Blodgett Approach to Making Colloidal Photonic Crystals from Silica Spheres. *Adv. Mater.* **2010**, *22* (29), 3104-3124.
3. Park, J. Y.; Advincula, R. C., Nanostructuring Polymers, Colloids, and Nanomaterials at the Air-Water Interface through Langmuir and Langmuir-Blodgett Techniques. *Soft Matter* **2011**, *7* (21), 9829-9843.
4. Reiter, G., Probing Properties of Polymers in Thin Films. *Adv. Polym. Sci.* **2013**, *252*, 29-64.
5. Jones, R.; Winter, C. S.; Tredgold, R. H.; Hodge, P.; Hoorfar, A., Electron-beam Resists from Langmuir-Blodgett films of Poly(styrene/maleic anhydride) Derivatives. *Polymer* **1987**, *28* (10), 1619-1626.
6. Collins, S. J.; Mary, N. L.; Radhakrishnan, G.; Dhathathreyan, A., Studies of Spread Monolayers of Derivative of Styrene-Maleic Anhydride Copolymers. *J. Chem. Soc. Faraday Trans.* **1997**, *93* (22), 4021-4023.
7. Rogach, A. L., *Semiconductor Nanocrystal Quantum Dots: Synthesis, Assembly, Spectroscopy and Applications*. Springer:Wien: New York, 2008.
8. Tomczak, N.; Jaczewski, D.; Han, M.; Vancso, G. J., Designer Polymer-Quantum Dot Architectures. *Prog. Polym. Sci.* **2009**, *34* (5), 393-430.
9. Talapin, D. V.; Lee, J.-S.; Kovalenko, M. V.; Shevchenko, E. V., Prospects of Colloidal Nanocrystals for Electronic and Optoelectronic Applications. *Chem. Rev.* **2010**, *110* (1), 389-458.
10. Kim, T.-H.; Cho, K.-S.; Lee, E. K.; Lee, S. J.; Chae, J.; Kim, J. W.; Kim, D. H.; Kwon, J.-Y.; Amaratunga, G.; Lee, S. Y.; Choi, B. L.; Kuk, Y.; Kim, J. M.; Kim, K., Full-colour Quantum Dot Displays fabricated by Transfer Printing. *Nat. Photon.* **2011**, *5* (3), 176-182.



11. Selinsky, R. S.; Ding, Q.; Faber, M. S.; Wright, J. C.; Jin, S., Quantum Dot Nanoscale Heterostructures for Solar Energy Conversion. *Chem. Soc. Rev.* **2013**, *42* (7), 2963-2985.
12. Balazs, A. C., Interactions of Nanoscopic Particles with Phase-separating Polymeric Mixtures. *Curr. Opin. Colloid Interface Sci.* **1999**, *4* (6), 443-448.
13. Lin, Y.; Böker, A.; He, J.; Sill, K.; Xiang, H.; Abetz, C.; Li, X.; Wang, J.; Emrick, T.; Long, S.; Wang, Q.; Balazs, A.; Russell, T. P., Self-directed Self-assembly of Nanoparticle/Copolymer Mixtures. *Nature* **2005**, *434* (7029), 55-59.
14. Cheyne, R. B.; Moffitt, M. G., Hierarchical Nanoparticle/Block Copolymer Surface Features via Synergistic Self-Assembly at the Air-Water Interface. *Langmuir* **2005**, *21* (23), 10297-10300.
15. Li, H.; Sachsenhofer, R.; Binder, W. H.; Henze, T.; Thurn-Albrecht, T.; Busse, K.; Kressler, J., Hierarchical Organization of Poly(ethylene oxide)-block-poly(isobutylene) and Hydrophobically Modified Fe<sub>2</sub>O<sub>3</sub> Nanoparticles at the Air/Water Interface and on Solid Supports. *Langmuir* **2009**, *25* (14), 8320-8329.
16. Murray, C. B.; Kagan, C. R.; Bawendi, M. G., Synthesis and Characterization of Monodisperse Nanocrystals and Close-packed Nanocrystal Assemblies. *Annu. Rev. Mater. Sci.* **2000**, *30* (1), 545-610.
17. Worfolk, B. J.; Rider, D. A.; Elias, A. L.; Thomas, M.; Harris, K. D.; Buriak, J. M., Bulk Heterojunction Organic Photovoltaics Based on Carboxylated Polythiophenes and PCBM on Glass and Plastic Substrates. *Adv. Funct. Mater.* **2011**, *21* (10), 1816-1826.
18. Kim, J. Y.; Raja, S.; Stellacci, F., Evolution of Langmuir Film of Nanoparticles Through Successive Compression Cycles. *Small* **2011**, *7* (17), 2526-2532.
19. Cicutta, P.; Vella, D., Granular Character of Particle Rafts. *Phys. Rev. Lett.* **2009**, *102* (13), 138302.
20. Zang, D.; Langevin, D.; Binks, B. P.; Wei, B., Shearing Particle Monolayers: Strain-rate Frequency Superposition. *Phys. Rev. E* **2010**, *81* (1), 011604.

21. Guzmán, E.; Liggieri, L.; Santini, E.; Ferrari, M.; Ravera, F., Effect of Hydrophilic and Hydrophobic Nanoparticles on the Surface Pressure Response of DPPC Monolayers. *J. Phys. Chem. C* **2011**, *115* (44), 21715-21722.
22. Nodoro, T. V. M.; Böhm, M. C.; Müller-Plathe, F., Interface and Interphase Dynamics of Polystyrene Chains near Grafted and Ungrafted Silica Nanoparticles. *Macromolecules* **2012**, *45* (1), 171-179.
23. Toepperwein, G. N.; Riggleman, R. A.; de Pablo, J. J., Dynamics and Deformation Response of Rod-Containing Nanocomposites. *Macromolecules* **2012**, *45* (1), 543-554.
24. Osman, A. F.; Edwards, G. A.; Schiller, T. L.; Andriani, Y.; Jack, K. S.; Morrow, I. C.; Halley, P. J.; Martin, D. J., Structure-Property Relationships in Biomedical Thermoplastic Polyurethane Nanocomposites. *Macromolecules* **2012**, *45* (1), 198-210.
25. Jones, M.; Scholes, G. D., On the Use of Time-Resolved Photoluminescence as a Probe of Nanocrystal Photoexcitation Dynamics. *J. Mater. Chem.* **2010**, *20* (18), 3533-3538.
26. Chen, D.; Feng, H.; Li, J., Graphene Oxide: Preparation, Functionalization, and Electrochemical Applications. *Chem. Rev.* **2012**, *112* (11), 6027-6053.
27. Hu, W.; Peng, C.; Luo, W.; Lv, M.; Li, X.; Li, D.; Huang, Q.; Fan, C., Graphene-Based Antibacterial Paper. *ACS Nano* **2010**, *4* (7), 4317-4323.
28. Cui, X.; Zhang, C.; Hao, R.; Hou, Y., Liquid-phase Exfoliation, Functionalization and Applications of Graphene. *Nanoscale* **2011**, *3* (5), 2118-2126.
29. Singh, V.; Joung, D.; Zhai, L.; Das, S.; Khondaker, S. I.; Seal, S., Graphene based Materials: Past, Present and Future. *Prog. Mater. Sci.* **2011**, *56* (8), 1178-1271.
30. Shao, Y.; Wang, J.; Wu, H.; Liu, J.; Aksay, I. A.; Lin, Y., Graphene Based Electrochemical Sensors and Biosensors: A Review. *Electroanalysis* **2010**, *22* (10), 1027-1036.

31. Rao, C. N. R.; Cheetham, A. K., Materials Science at the Nanoscale. In *Nanomaterials Handbook*, Gogotsi, Y., Ed. Taylor & Francis Group: New York, 2006.
32. Dutta, J.; Hofmann, H., Self-organization of Colloidal Nanoparticles. In *Encyclopedia of Nanoscience and Nanotechnology*, Nalwa, H. S., Ed. American Scientific Publishers: New York, 2011; Vol. X, pp 1-23.
33. Bloch, J. M.; Yun, W., Condensation of Monovalent and Divalent Metal Ions on a Langmuir Monolayer. *Phys. Rev. A* **1990**, *41* (2), 844-862.
34. Knipping, E. M.; Lakin, M. J.; Foster, K. L.; Jungwirth, P.; Tobias, D. J.; Gerber, R. B.; Dabdub, D.; Finlayson-Pitts, B. J., Experiments and Simulations of Ion-Enhanced Interfacial Chemistry on Aqueous NaCl Aerosols. *Science* **2000**, *288* (5464), 301-306.
35. Laskin, A.; Gaspar, D. J.; Wang, W.; Hunt, S. W.; Cowin, J. P.; Colson, S. D.; Finlayson-Pitts, B. J., Reactions at Interfaces As a Source of Sulfate Formation in Sea-Salt Particles. *Science* **2003**, *301* (5631), 340-344.
36. Hamley, I. W., Nanotechnology with Soft Materials. *Angew. Chem. Int. Ed.* **2003**, *42* (15), 1692-1712.
37. Grzelczak, M.; Vermant, J.; Furst, E. M.; Liz-Marzán, L. M., Directed Self-Assembly of Nanoparticles. *ACS Nano* **2010**, *4* (7), 3591-3605.
38. Whitesides, G. M., Self-assembling Materials. *Sci. Am.* **1995**, *273*, 146-149.
39. Whitesides, G. M.; Boncheva, M., Beyond Molecules: Self-assembly of Mesoscopic and Macroscopic Components. *Proc. Natl. Acad. Sci. USA* **2002**, *99* (8), 4769-4774.
40. Yin, J. S.; Wang, Z. L., *Handbook of Nanophase and Nanostructured Materials*. Kluwer Academic/Plenum Publishers, Tsinghua University Press,; New York, 2003; Vol. 4.
41. Cheyne, R. B.; Moffitt, M. G., Novel Two-Dimensional “Ring and Chain” Morphologies in Langmuir–Blodgett Monolayers of PS-b-PEO Block

Copolymers: Effect of Spreading Solution Concentration on Self-Assembly at the Air–Water Interface. *Langmuir* **2005**, *21* (12), 5453-5460.

42. Rabani, E.; Reichman, D. R.; Geissler, P. L.; Brus, L. E., Drying-mediated Self-assembly of Nanoparticles. *Nature* **2003**, *426* (6964), 271-274.

43. Martin, C. P.; Blunt, M. O.; Moriarty, P., Nanoparticle Networks on Silicon: Self-Organized or Disorganized? *Nano Lett.* **2004**, *4* (12), 2389-2392.

44. Gentili, D.; Foschi, G.; Valle, F.; Cavallini, M.; Biscarini, F., Applications of Dewetting in Micro and Nanotechnology. *Chem. Soc. Rev.* **2012**, *41* (12), 4430-4443.

45. Xue, L.; Han, Y., Inhibition of Dewetting of Thin Polymer Films. *Prog. Materials Sci.* **2012**, *57* (6), 947-979.

46. Böker, A.; He, J.; Emrick, T.; Russell, T. P., Self-assembly of Nanoparticles at Interfaces. *Soft Matter* **2007**, *3* (10), 1231-1248.

47. Stine, K. J.; Moore, B. G., Langmuir Monolayers: Fundamentals and Relevance to Nanotechnology. In *Nano-Surface Chemistry*, Rosoff, M., Ed. Marcel Dekker: New York, 2002.

48. Xiao, L.; Zhou, R.; He, Y.; Li, Y.; Yeung, E. S., Direct Observation of Nanoparticle Self-Assembly Dynamics at the Water–Air Interface Using Differential Interference Contrast Microscopy. *J. Phys. Chem. C* **2009**, *113* (4), 1209-1216.

49. Clemente-León, M.; Ito, T.; Yashiro, H.; Yamase, T.; Coronado, E., Langmuir–Blodgett Films of a Mo-Blue Nanoring  $[\text{Mo}_{142}\text{O}_{429}\text{H}_{10}(\text{H}_2\text{O})_{49}(\text{CH}_3\text{CO}_2)_5(\text{CH}_3\text{CH}_2\text{CO}_2)]_{30} - (\text{Mo}_{142})$  by the Semiamphiphilic Method. *Langmuir* **2007**, *23* (7), 4042-4047.

50. Rybak, B. M.; Ornatska, M.; Bergman, K. N.; Genson, K. L.; Tsukruk, V. V., Formation of Silver Nanoparticles at the Air–Water Interface Mediated by a Monolayer of Functionalized Hyperbranched Molecules. *Langmuir* **2006**, *22* (3), 1027-1037.

51. Kinge, S.; Crego-Calama, M.; Reinhoudt, D. N., Self-Assembling Nanoparticles at Surfaces and Interfaces. *ChemPhysChem* **2008**, *9* (1), 20-42.
52. Yang, P.; Kim, F., Langmuir–Blodgett Assembly of One-Dimensional Nanostructures. *ChemPhysChem* **2002**, *3* (6), 503-506.
53. Kim, H.-C.; Park, S.-M.; Hinsberg, W. D., Block Copolymer Based Nanostructures: Materials, Processes, and Applications to Electronics. *Chem. Rev.* **2010**, *110* (1), 146-177.
54. Gonçalves da Silva, A. M.; Filipe, E. J. M.; d'Oliveira, J. M. R.; Martinho, J. M. G., Interfacial Behavior of Poly(styrene)–Poly(ethylene oxide) Diblock Copolymer Monolayers at the Air–Water Interface. Hydrophilic Block Chain Length and Temperature Influence. *Langmuir* **1996**, *12* (26), 6547-6553.
55. Cox, J. K.; Yu, K.; Constantine, B.; Eisenberg, A.; Lennox, R. B., Polystyrene–Poly(ethylene oxide) Diblock Copolymers Form Well-Defined Surface Aggregates at the Air/Water Interface. *Langmuir* **1999**, *15* (22), 7714-7718.
56. Devereaux, C. A.; Baker, S. M., Surface Features in Langmuir–Blodgett Monolayers of Predominantly Hydrophobic Poly(styrene)–Poly(ethylene oxide) Diblock Copolymer. *Macromolecules* **2002**, *35* (5), 1921-1927.
57. Cheyne, R. B.; Moffitt, M. G., Self-Assembly of Polystyrene-block-Poly(Ethylene Oxide) Copolymers at the Air–Water Interface: Is Dewetting the Genesis of Surface Aggregate Formation? *Langmuir* **2006**, *22* (20), 8387-8396.
58. Discher, D. E.; Eisenberg, A., Polymer Vesicles. *Science* **2002**, *297* (5583), 967-973.
59. Zhao, L.; Byun, M.; Rzyayev, J.; Lin, Z., Polystyrene–Polylactide Bottlebrush Block Copolymer at the Air/Water Interface. *Macromolecules* **2009**, *42* (22), 9027-9033.
60. Seo, Y.; Paeng, K.; Park, S., Molecular Weight Effect on the Behaviors of Polystyrene-block-poly(methyl methacrylate) Diblock Copolymers at Air/Water Interface. *Macromolecules* **2001**, *34* (25), 8735-8744.

61. Chung, B.; Choi, M.; Ree, M.; Jung, J. C.; Zin, W. C.; Chang, T., Subphase pH Effect on Surface Micelle of Polystyrene-b-poly(2-vinylpyridine) Diblock Copolymers at the Air–Water Interface. *Macromolecules* **2006**, *39* (2), 684-689.
62. Liu, G.; Yang, S.; Zhang, G., Conformational Changes of Poly(N-isopropylacrylamide) Chains at Air/Water Interface: Effects of Temperature, Compression Rate, and Packing Density. *J. Phys. Chem. B* **2007**, *111* (14), 3633-3639.
63. Zhao, L.; Lin, Z., Self-assembly of Non-linear Polymers at the Air/Water Interface: The Effect of Molecular Architecture. *Soft Matter* **2011**, *7* (22), 10520-10535.
64. Rosi, N. L.; Mirkin, C. A., Nanostructures in Biodiagnostics. *Chem. Rev.* **2005**, *105* (4), 1547-1562.
65. Tang, Z.; Kotov, N. A., One-Dimensional Assemblies of Nanoparticles: Preparation, Properties, and Promise. *Adv. Mater.* **2005**, *17* (8), 951-962.
66. Zhang, L.; Gaponik, N.; Müller, J.; Plate, U.; Weller, H.; Erker, G.; Fuchs, H.; Rogach, A. L.; Chi, L., Branched Wires of CdTe Nanocrystals Using Amphiphilic Molecules as Templates. *Small* **2005**, *1* (5), 524-527.
67. Gattás-Asfura, K. M.; Constantine, C. A.; Lynn, M. J.; Thimann, D. A.; Ji, X.; Leblanc, R. M., Characterization and 2D Self-Assembly of CdSe Quantum Dots at the Air–Water Interface. *J. Am. Chem. Soc.* **2005**, *127* (42), 14640-14646.
68. Ji, X.; Wang, C.; Xu, J.; Zheng, J.; Gattás-Asfura, K. M.; Leblanc, R. M., Surface Chemistry Studies of (CdSe)ZnS Quantum Dots at the Air–Water Interface. *Langmuir* **2005**, *21* (12), 5377-5382.
69. Lambert, K.; Čapek, R. K.; Bodnarchuk, M. I.; Kovalenko, M. V.; Van Thourhout, D.; Heiss, W.; Hens, Z., Langmuir–Schaefer Deposition of Quantum Dot Multilayers. *Langmuir* **2010**, *26* (11), 7732-7736.
70. Gole, A.; Jana, N. R.; Selvan, S. T.; Ying, J. Y., Langmuir–Blodgett Thin Films of Quantum Dots: Synthesis, Surface Modification, and Fluorescence Resonance Energy Transfer (FRET) Studies. *Langmuir* **2008**, *24* (15), 8181-8186.

71. Deshmukh, R. D.; Buxton, G. A.; Clarke, N.; Composto, R. J., Nanoscale Block Copolymer Templates Decorated by Nanoparticle Arrays. *Macromolecules* **2007**, *40* (17), 6316-6324.
72. Hernández, M.-P.; Monroy, F.; Ortega, F.; Rubio, R. G.; Martín-Domenech, Á.; Priego, E. M.; Sánchez, L.; Martín, N., An Experimental Study of the Stability and Dynamics of Langmuir Films of Fullerene Derivatives and Their Mixtures with Pentadecanoic Acid. *Langmuir* **2001**, *17* (11), 3317-3328.
73. Nierengarten, J.-F., Chemical Modification of C<sub>60</sub> for Materials Science Applications. *New J. Chem.* **2004**, *28* (10), 1177-1191.
74. Kim, Y.; Minami, N.; Zhu, W.; Kazaoui, S.; Azumi, R.; Matsumoto, M., Langmuir-Blodgett Films of Single-wall carbon Nanotubes: Layer-by-Layer Deposition and in-plane Orientation of Tubes. *Jpn. J. Appl. Phys.* **2003**, *42*, 7629-7634.
75. Li, X.; Zhang, G.; Bai, X.; Sun, X.; Wang, X.; Wang, E.; Dai, H., Highly Conducting Graphene Sheets and Langmuir-Blodgett Films. *Nat. Nanotechnol.* **2008**, *3* (9), 538-542.
76. Cote, L. J.; Kim, F.; Huang, J., Langmuir-Blodgett Assembly of Graphite Oxide Single Layers. *J. Am. Chem. Soc.* **2009**, *131* (3), 1043-1049.
77. Tabor, D., Babylonian Lecanomancy: An Ancient Text on the Spreading of Oil on Water. *J. Colloid Interface Sci.* **1980**, *75* (1), 240-245.
78. Chambers, A., *The Japanese Art of Marbling*. Thames & Hudson: 1993.
79. Dynarowicz-Latka, P.; Dhanabalan, A.; Oliveira Jr, O. N., Modern Physicochemical Research on Langmuir Monolayers. *Adv. Colloid Interface Sci.* **2001**, *91* (2), 221-293.
80. Franklin, B.; Brownrigg, W.; Farish, M., Of the Stilling of Waves by means of Oil. Extracted from Sundry Letters between Benjamin Franklin, LL. D. F. R. S. William Brownrigg, M. D. F. R. S. and the Reverend Mr. Farish. *Phil. Trans. Res. Soc. (London)* **1774**, *64*, 445-460.
81. Rayleigh, L., On the Superficial Viscosity of Water. *Proc. R. Soc. Ser. A* **1890**, *48*, 127-140.

82. Pockels, A., Surface Tension. *Nature* **1891**, *43*, 437-439.
83. Rayleigh, L., XXXVI. Investigations in Capillarity:—The Size of Drops.—The Liberation of Gas from Supersaturated Solutions.—Colliding Jets.—The Tension of Contaminated Water-Surfaces. *Phil. Mag. Series 5* **1899**, *48* (293), 321-337.
84. Langmuir, I., The Constitution and Fundamental Properties of Solids and Liquids. II. Liquids. *J. Am. Chem. Soc.* **1917**, *39* (9), 1848-1906.
85. Langmuir, I., The Mechanism of the Surface Phenomena of Flotation. *Trans. Faraday Soc.* **1920**, *15* (June), 62-74.
86. Blodgett, K. B., Films Built by Depositing Successive Monomolecular Layers on a Solid Surface. *J. Am. Chem. Soc.* **1935**, *57* (6), 1007-1022.
87. Gaines, G. L., *Insoluble Monolayers at the Air-Water Interface*. Interscience Publishers: 1966.
88. Jones, R. A. L.; Richards, R. W., *Polymers at Surfaces and Interfaces*. Cambridge University Press: United Kingdom, 1999.
89. Stenhagen, E., *Determination of Organic Structures by Physical Methods*. Academic Press: New York, 1955.
90. Nutting, G. C.; Harkins, W. D., Pressure-Area Relations of Fatty Acid and Alcohol Monolayers. *J. Am. Chem. Soc.* **1939**, *61* (5), 1180-1187.
91. Marsden, J.; Rideal, E. K., On Monolayers of Isomeric Unsaturated Compounds. *J. Chem. Soc.* **1938**, 1163-1171.
92. Dynarowicz-Łątka, P.; Dhanabalan, A.; Oliveira, O. N., A Study on Two-Dimensional Phase Transitions in Langmuir Monolayers of a Carboxylic Acid with a Symmetrical Triphenylbenzene Ring System. *J. Phys. Chem. B* **1999**, *103* (29), 5992-6000.
93. Laxhuber, L. A.; Moehwald, H., Thermodesorption Spectroscopy of Langmuir-Blodgett Films. *Langmuir* **1987**, *3* (5), 837-845.



94. Schwartz, D. K.; Viswanathan, R.; Zasadzinski, J. A. N., Commensurate Defect Superstructures in a Langmuir-Blodgett Film. *Phys. Rev. Lett.* **1993**, *70* (9), 1267-1270.
95. Marčelja, S., Chain Ordering in Liquid Crystals: II. Structure of Bilayer Membranes. *Biochim. Biophys. Acta* **1974**, *367* (2), 165-176.
96. De Keyser, P.; Joos, P., Desorption at Constant Surface Pressure from Slightly Soluble Monolayers. *J. Colloid Interface Sci.* **1983**, *91* (1), 131-137.
97. Barros, A. M.; Dhanabalan, A.; Constantino, C. J. L.; Balogh, D. T.; Oliveira Jr, O. N., Langmuir Monolayers of Lignins obtained with different Isolation Methods. *Thin Solid Films* **1999**, *354* (1-2), 215-221.
98. Wan Kim, T.; Park, J.-S.; Choi, J.-S.; Kang, D.-Y.,  $\pi$ -A Isotherms and Electrical Properties of Polyamic Acid Alkylamine salts (PAAS) Langmuir-Blodgett Films. *Thin Solid Films* **1996**, *284-285*, 500-504.
99. Haç-Wydro, K.; Wydro, P.; Dynarowicz-Łątka, P., A Study of the Interaction between Dialkyldimethylammonium bromides and Tri-*n*-octylphosphine oxide (topo) in Mixed Monolayers at the Air/Water Interface. *J. Colloid Interface Sci.* **2004**, *278* (1), 206-214.
100. Whitten, D. G., Photochemical Reactions in Organized Monolayer Assemblies. I. Cis-trans Isomerization of Thioindigo Dyes. *J. Am. Chem. Soc.* **1974**, *96* (2), 594-596.
101. Polymeropoulos, E. E.; Möbius, D.; Kuhn, H., Photoconduction in Monolayer Assemblies with Functional Units of Sensitizing and Conducting Molecular Components. *J. Chem. Phys.* **1978**, *68* (8), 3918-3931.
102. Shembekar, V. R.; Dhanabalan, A.; Talwar, S. S.; Contractor, A. Q., Study of Mixed System in Monolayers and Multilayers transferred by Langmuir-Blodgett Technique. *Thin Solid Films* **1999**, *342* (1-2), 270-276.
103. Kuhn, H., Present Status and Future Prospects of Langmuir-Blodgett Film Research. *Thin Solid Films* **1989**, *178* (1-2), 1-16.

104. Era, M.; Tsutsui, T.; Saito, S., Control of Chromophore Orientation in Langmuir-Blodgett Films: Molecular Mixing of two Homologous Amphiphiles. *Langmuir* **1989**, *5* (6), 1410-1411.
105. Puggelli, M.; Gabrielli, G., Behavior of Vinyl Polymers in Mixed Monolayers. *J. Colloid Interface Sci.* **1977**, *61* (3), 420-427.
106. Chifu, E.; Zsakó, J.; Tomoaia-Cotișel, M., Xanthophyll Films: I. Single-component Monolayers at the Air/Water Interface. *J. Colloid Interface Sci.* **1983**, *95* (2), 346-354.
107. Chattoraj, D. K.; Birdi, K. S., *Adsorption and the Gibbs Surface Excess*, Plenum Press: New York, 1984; pp 219-223.
108. Costin, I. S.; Barnes, G. T., Two-component Monolayers. II. Surface Pressure-Area relations for the Octadecanol-docosyl Sulphate System. *J. Colloid Interface Sci.* **1975**, *51* (1), 106-121.
109. Gálvez Ruiz, M. J.; Cabrerizo Vilchez, M. A., A Study of the Miscibility of Bile Components in Mixed Monolayers at the Air-Liquid Interface I. Cholesterol, Lecithin, and Lithocholic Acid. *Colloid Polym. Sci.* **1991**, *269* (1), 77-84.
110. Kuhn, H.; Möbius, D., Monolayer Assemblies. In *Investigations of Surfaces and Interfaces*, Rossiter, B. W.; Baetzold, R. C., Eds. John Wiley & Sons: New York, 1993; Vol. IX.
111. Roberts, G., *Langmuir-Blodgett Films*. Plenum Press New York: 1990.
112. Langmuir, I.; Schaefer, V. J., Activities of Urease and Pepsin Monolayers. *J. Am. Chem. Soc.* **1938**, *60* (6), 1351-1360.
113. Kossi, C. N.; Leblanc, R. M., Rhodopsin in a New Model Bilayer Membrane. *J. Colloid Interface Sci.* **1981**, *80* (2), 426-436.
114. Bondarenko, M. P.; Kovalchuk, V. I.; Zholkovskiy, E. K.; Vollhardt, D., Concentration Polarization at Langmuir Monolayer Deposition: The Role of Indifferent Electrolytes. *J. Phys. Chem. B* **2007**, *111* (7), 1684-1692.

115. Kovalchuk, V. I.; Bondarenko, M. P.; Zholkovskiy, E. K.; Vollhardt, D., Influence of Ion Transfer Kinetics on the Composition of Langmuir–Blodgett Films. *J. Phys. Chem. B* **2008**, *112* (36), 11333-11340.
116. Honig, E. P., Molecular Constitution of X- and Y-type Langmuir-Blodgett Films. *J. Colloid Interface Sci.* **1973**, *43* (1), 66-72.
117. Ulman, A., *An Introduction to Ultrathin Organic Films From Langmuir-Blodgett to Self-Assembly*. Academic Press, Inc.: San Diego, 1991.
118. Jones, M. N.; Chapman, D., *Micelles, Monolayers and Biological Membranes*. John Willey & Sons: New York, 1995.
119. De Gennes, P. G., *Scaling Concepts in Polymer Physics*. Cornell University Press, Ithaca: New York, 1979.
120. Flory, P. J., The Configuration of Real Polymer Chains. *J. Chem. Phys.* **1949**, *17* (3), 303-310.
121. Thirumalai, D., Two Landmarks in Polymer Physics: the Edwards Model and de Gennes' Observation. *Theor. Chem. Acc.* **2000**, *103* (3-4), 292-293.
122. Buzza, D. M. A., General Theory for Capillary Waves and Surface Light Scattering. *Langmuir* **2002**, *18* (22), 8418-8435.
123. Davies, J. T.; Rideal, E. K., *Interfacial Phenomena*. Academic Press: New York, 1963.
124. Gonçalves da Silva, A. M.; Romão, R. S.; Lucero Caro, A.; Rodríguez Patino, J. M., Memory Effects on the Interfacial Characteristics of Dioctadecyldimethylammonium bromide Monolayers at the Air–Water Interface. *J. Colloid Interface Sci.* **2004**, *270* (2), 417-425.
125. Cicuta, P.; Hopkinson, I., Scaling of Dynamics in 2d Semi-dilute Polymer Solutions. *Europhys. Lett.* **2004**, *68* (1), 65-71.
126. Sukhishvili, S. A.; Chen, Y.; Müller, J. D.; Gratton, E.; Schweizer, K. S.; Granick, S., Surface Diffusion of Poly(ethylene glycol). *Macromolecules* **2002**, *35* (5), 1776-1784.
127. Wang, X.; Foltz, V. J., Chain Conformation in Two-Dimensional Dense State. *J. Chem. Phys.* **2004**, *121* (16), 8158-8162.

- 
128. Miranda, B.; Hilles, H. M.; Rubio, R. n. G.; Ritacco, H.; Radic, D.; Gargallo, L.; Sferrazza, M.; Ortega, F., Equilibrium and Surface Rheology of Monolayers of Insoluble Polycations with Side Chains. *Langmuir* **2009**, *25* (21), 12561-12568.
129. Vilanove, R.; Rondelez, F., Scaling Description of Two-Dimensional Chain Conformations in Polymer Monolayers. *Phys. Rev. Lett.* **1980**, *45* (18), 1502-1505.
130. Hilles, H.; Monroy, F.; Bonales, L. J.; Ortega, F.; Rubio, R. G., Fourier-Transform Rheology of Polymer Langmuir Monolayers: Analysis of the Non-linear and Plastic Behaviors. *Adv. Colloid Interface Sci.* **2006**, *122* (1-3), 67-77.
131. Langevin, D.; Monroy, F., Interfacial Rheology of Polyelectrolytes and Polymer Monolayers at the Air–Water Interface. *Curr. Opin. Colloid Interface Sci.* **2010**, *15* (4), 283-293.
132. Doi, M.; Edwards, S. F., *The Theory of Polymer Dynamics*. Oxford University Press: Oxford, 1986.
133. Monroy, F.; Hilles, H. M.; Ortega, F.; Rubio, R. G., Relaxation Dynamics of Langmuir Polymer Films: A Power-Law Analysis. *Phys. Rev. Lett.* **2003**, *91* (26), 268302.
134. Tolnai, G.; Csempesz, F.; Kabai-Faix, M.; Kálmán, E.; Keresztes, Z.; Kovács, A. L.; Ramsden, J. J.; Hórvölgyi, Z., Preparation and Characterization of Surface-Modified Silica-Nanoparticles. *Langmuir* **2001**, *17* (9), 2683-2687.
135. Horozov, T. S.; Aveyard, R.; Clint, J. H.; Binks, B. P., Order–Disorder Transition in Monolayers of Modified Monodisperse Silica Particles at the Octane–Water Interface. *Langmuir* **2003**, *19* (7), 2822-2829.
136. Reculosa, S.; Massé, P.; Ravaine, S., Three-dimensional Colloidal Crystals with a Well-defined Architecture. *J. Colloid Interface Sci.* **2004**, *279* (2), 471-478.
137. van Duffel, B.; Ras, R. H. A.; De Schryver, F. C.; Schoonheydt, R. A., Langmuir-Blodgett Deposition and Optical Diffraction of Two-Dimensional Opal. *J. Mater. Chem.* **2001**, *11* (12), 3333-3336.

138. Szekeres, M.; Kamalin, O.; Schoonheydt, R. A.; Wostyn, K.; Clays, K.; Persoons, A.; Dekany, I., Ordering and Optical Properties of Monolayers and Multilayers of Silica Spheres deposited by the Langmuir-Blodgett Method. *J. Mater. Chem.* **2002**, *12* (11), 3268-3274.
139. Xu, J.; Ji, X.; Gattás-Asfura, K. M.; Wang, C.; Leblanc, R. M., Langmuir and Langmuir-Blodgett Films of Quantum Dots. *Colloids Surf. A* **2006**, *284-285*, 35-42.
140. Dabbousi, B. O.; Murray, C. B.; Rubner, M. F.; Bawendi, M. G., Langmuir-Blodgett Manipulation of Size-Selected CdSe Nanocrystallites. *Chem. Mater.* **1994**, *6* (2), 216-219.
141. Kotov, N. A.; Meldrum, F. C.; Wu, C.; Fendler, J. H., Monoparticulate Layer and Langmuir-Blodgett-Type Multiparticulate Layers of Size-Quantized Cadmium Sulfide Clusters: A Colloid-Chemical Approach to Superlattice Construction. *J. Phys. Chem.* **1994**, *98* (11), 2735-2738.
142. Santhanam, V.; Liu, J.; Agarwal, R.; Andres, R. P., Self-Assembly of Uniform Monolayer Arrays of Nanoparticles. *Langmuir* **2003**, *19* (19), 7881-7887.
143. Lee, Y.-L.; Du, Z.-C.; Lin, W.-X.; Yang, Y.-M., Monolayer Behavior of Silica Particles at Air/Water Interface: A Comparison between Chemical and Physical Modifications of Surface. *J. Colloid Interface Sci.* **2006**, *296* (1), 233-241.
144. Perez, H.; Lisboa de Sousa, R. M.; Pradeau, J. P.; Albouy, P. A., Elaboration and Electrical Characterization of Langmuir-Blodgett Films of 4-Mercaptoaniline Functionalized Platinum Nanoparticles. *Chem. Mater.* **2001**, *13* (5), 1512-1517.
145. Shen, Y.-J.; Lee, Y.-L.; Yang, Y.-M., Monolayer Behavior and Langmuir-Blodgett Manipulation of CdS Quantum Dots. *J. Phys. Chem. B* **2006**, *110* (19), 9556-9564.
146. Lee, D. K.; Kim, Y. H.; Kim, C. W.; Cha, H. G.; Kang, Y. S., Vast Magnetic Monolayer Film with Surfactant-Stabilized Fe<sub>3</sub>O<sub>4</sub> Nanoparticles Using Langmuir-Blodgett Technique. *J. Phys. Chem. B* **2007**, *111* (31), 9288-9293.

147. Gupta, S.; Singh, N.; Sastry, M.; Kakkar, R.; Pasricha, R., Controlling the Assembly of Hydrophobized Gold Nanoparticles at the Air–Water Interface by varying the Interfacial Tension. *Thin Solid Films* **2010**, *519* (3), 1072-1077.
148. Pohjalainen, E.; Pohjakallio, M.; Johans, C.; Kontturi, K. s.; Timonen, J. V. I.; Ikkala, O.; Ras, R. H. A.; Viitala, T.; Heino, M. T.; Seppälä, E. T., Cobalt Nanoparticle Langmuir–Schaefer Films on Ethylene Glycol Subphase. *Langmuir* **2010**, *26* (17), 13937-13943.
149. Lau, C. Y.; Duan, H.; Wang, F.; He, C. B.; Low, H. Y.; Yang, J. K. W., Enhanced Ordering in Gold Nanoparticles Self-Assembly through Excess Free Ligands. *Langmuir* **2011**, *27* (7), 3355-3360.
150. Cheyne, R. B.; Moffitt, M. G., Controllable Organization of Quantum Dots into Mesoscale Wires and Cables via Interfacial Block Copolymer Self-Assembly. *Macromolecules* **2007**, *40* (6), 2046-2057.
151. Mogilevsky, A.; Jelinek, R., Gold Nanoparticle Self-Assembly in Two-Component Lipid Langmuir Monolayers. *Langmuir* **2010**, *27* (4), 1260-1268.
152. Binks, B. P., Colloidal Particles at Liquid Interfaces. *Phys. Chem. Chem. Phys.* **2007**, *9* (48), 6298-6299.
153. Sear, R. P.; Chung, S.-W.; Markovich, G.; Gelbart, W. M.; Heath, J. R., Spontaneous Patterning of Quantum Dots at the Air-Water Interface. *Phys. Rev. E* **1999**, *59* (6), R6255-R6258.
154. Zang, D. Y.; Rio, E.; Langevin, D.; Wei, B.; Binks, B. P., Viscoelastic Properties of Silica Nanoparticle Monolayers at the Air-Water Interface. *Eur. Phys. J. E* **2010**, *31* (2), 125-134.
155. Guzmán, E.; Liggieri, L.; Santini, E.; Ferrari, M.; Ravera, F., DPPC–DOPC Langmuir Monolayers modified by Hydrophilic Silica Nanoparticles: Phase Behaviour, Structure and Rheology. *Colloids Surf. A* **2012**, *413*, 174-183.
156. Allen, M. J.; Tung, V. C.; Kaner, R. B., Honeycomb Carbon: A Review of Graphene. *Chem. Rev.* **2010**, *110* (1), 132-145.

157. Park, S.; Ruoff, R. S., Chemical Methods for the Production of Graphenes. *Nat. Nanotechnol.* **2009**, *4* (4), 217-224.
158. Compton, O. C.; Nguyen, S. T., Graphene Oxide, Highly Reduced Graphene Oxide, and Graphene: Versatile Building Blocks for Carbon-Based Materials. *Small* **2010**, *6* (6), 711-723.
159. Gengler, R. Y. N.; Veligura, A.; Enotiadis, A.; Diamanti, E. K.; Gournis, D.; Józsa, C.; van Wees, B. J.; Rudolf, P., Large-Yield Preparation of High-Electronic-Quality Graphene by a Langmuir–Schaefer Approach. *Small* **2010**, *6* (1), 35-39.
160. Cote, L. J.; Kim, J.; Tung, V. C.; Luo, J.; Kim, F.; Huang, J., Graphene Oxide as Surfactant Sheets. *Pure Appl. Chem.* **2011**, *83*, 95-110.
161. Eda, G.; Ball, J.; Mattevi, C.; Acik, M.; Artiglia, L.; Granozzi, G.; Chabal, Y.; Anthopoulos, T. D.; Chhowalla, M., Partially Oxidized Graphene as a Precursor to Graphene. *J. Mater. Chem.* **2011**, *21* (30), 11217-11223.
162. Becerril, H. A.; Mao, J.; Liu, Z.; Stoltenberg, R. M.; Bao, Z.; Chen, Y., Evaluation of Solution-Processed Reduced Graphene Oxide Films as Transparent Conductors. *ACS Nano* **2008**, *2* (3), 463-470.
163. Schniepp, H. C.; Li, J.-L.; McAllister, M. J.; Sai, H.; Herrera-Alonso, M.; Adamson, D. H.; Prud'homme, R. K.; Car, R.; Saville, D. A.; Aksay, I. A., Functionalized Single Graphene Sheets Derived from Splitting Graphite Oxide. *J. Phys. Chem. B* **2006**, *110* (17), 8535-8539.
164. Dobelle, W. H.; Beer, M., Chemically Cleaved Graphite Support Films for Electron Microscopy. *J. Cell. Biol.* **1968**, *39* (3), 733-735.
165. Stankovich, S.; Dikin, D. A.; Piner, R. D.; Kohlhaas, K. A.; Kleinhammes, A.; Jia, Y.; Wu, Y.; Nguyen, S. T.; Ruoff, R. S., Synthesis of Graphene-based Nanosheets via Chemical Reduction of Exfoliated Graphite Oxide. *Carbon* **2007**, *45* (7), 1558-1565.
166. Croft, R. C., Lamellar Compounds of Graphite. *Q. Rev. Chem. Soc.* **1960**, *14* (1), 1-45.

167. Cote, L. J.; Cruz-Silva, R.; Huang, J., Flash Reduction and Patterning of Graphite Oxide and Its Polymer Composite. *J. Am. Chem. Soc.* **2009**, *131* (31), 11027-11032.
168. Gilje, S.; Dubin, S.; Badakhshan, A.; Farrar, J.; Danczyk, S. A.; Kaner, R. B., Photothermal Deoxygenation of Graphene Oxide for Patterning and Distributed Ignition Applications. *Adv. Mater.* **2010**, *22* (3), 419-423.
169. Williams, G.; Seger, B.; Kamat, P. V., TiO<sub>2</sub>-Graphene Nanocomposites. UV-Assisted Photocatalytic Reduction of Graphene Oxide. *ACS Nano* **2008**, *2* (7), 1487-1491.
170. Gilje, S.; Han, S.; Wang, M.; Wang, K. L.; Kaner, R. B., A Chemical Route to Graphene for Device Applications. *Nano Lett.* **2007**, *7* (11), 3394-3398.
171. Kim, J.; Cote, L. J.; Kim, F.; Yuan, W.; Shull, K. R.; Huang, J., Graphene Oxide Sheets at Interfaces. *J. Am. Chem. Soc.* **2010**, *132* (23), 8180-8186.
172. López-Díaz, D.; Velázquez, M. M., Evidence of Glass Transition in Thin Films of Maleic Anhydride Derivatives: Effect of the Surfactant Coadsorption. *Eur. Phys. J. E.* **2008**, *26* (4), 417-425.
173. Zajac, J.; Chorro, C.; Lindheimer, M.; Partyka, S., Thermodynamics of Micellization and Adsorption of Zwitterionic Surfactants in Aqueous Media. *Langmuir* **1997**, *13* (6), 1486-1495.
174. López-Díaz, D.; García-Mateos, I.; Velázquez, M. M., Surface Properties of Mixed Monolayers of Sulfobetaines and Ionic Surfactants. *J. Colloid Interface Sci.* **2006**, *299* (2), 858-866.
175. Blake, P.; Hill, E. W.; Neto, A. H. C.; Novoselov, K. S.; Jiang, D.; Yang, R.; Booth, T. J.; Geim, A. K., Making Graphene Visible. *Appl. Phys. Lett.* **2007**, *91* (6), 063124-3.
176. Kern, W., *Handbook of Semiconductor Wafer Cleaning Technology*. Noyes Publications: New Jersey, 1993.
177. Tschoegl, N. W., *The Phenomenological Theory of Linear Viscoelastic Behaviour*. Springer-Verlag: Berlin, 1989.



178. Helmholtz, H., *Abhandlungen zur Thermodynamik Chemischer Vorgänge*. Herausgegeben von Dr. MaxPlanck: Leipzig, 1902.
179. Davies, J. T.; Rideal, S. E., Interfacial Potentials. *Can. J. Chem.* **1955**, *33*, 947-960.
180. Vogel, V.; Möbius, D., Local Surface Potentials and Electric Dipole Moments of Lipid Monolayers: Contributions of the Water/Lipid and the Lipid/Air Interfaces. *J. Colloid Interface Sci.* **1988**, *126* (2), 408-420.
181. Demchak, R. J.; Fort Jr, T., Surface Dipole Moments of Close-packed Un-ionized Monolayers at the Air-Water Interface. *J. Colloid Interface Sci.* **1974**, *46* (2), 191-202.
182. Taylor, D. M.; Oliveira Jr, O. N.; Morgan, H., The Effect of Water Quality on the Electrical Characteristics of Langmuir Monolayers. *Thin Solid Films* **1989**, *173* (2), L141-L147.
183. Adamson, A. W.; Gast, A. P., *Physical Chemistry of Surfaces*. 6th ed.; Wiley & Sons, Inc.: New York, 1997.
184. Henon, S.; Meunier, J., Microscope at the Brewster Angle: Direct Observation of First-order Phase Transitions in Monolayers. *Rev. Sci. Instr.* **1991**, *62* (4), 936-939.
185. Hoenig, D.; Moebius, D., Direct Visualization of Monolayers at the Air-Water Interface by Brewster Angle Microscopy. *J. Phys. Chem.* **1991**, *95* (12), 4590-4592.
186. Loschek, R.; Möbius, D., Metallation of Porphyrins in Lipid Monolayers at the Air/Water Interface. *Chem. Phys. Lett.* **1988**, *151* (1-2), 176-182.
187. Chechel, O. V.; Nikolaev, E. N., Devices for Production of Langmuir-Blodgett Films. *Instruments and Experimental Techniques* **1991**, *34*, 750-762.
188. Horcas, I.; Fernández, R.; Gómez-Rodríguez, J. M.; Colchero, J.; Gómez-Herrero, J.; Baro, A. M., WSXM: A Software for Scanning Probe Microscopy and a Tool for Nanotechnology. *Rev. Sci. Instrum.* **2007**, *78* (1), 013705-8.

189. Butt, H.-J.; Cappella, B.; Kappl, M., Force Measurements with the Atomic Force Microscope: Technique, Interpretation and Applications. *Surf. Sci. Rep.* **2005**, *59* (1–6), 1-152.
190. Eaton, P.; West, P., *Atomic Force Microscopy*, Oxford University Press: Oxford, 2010.
191. Chen, S.-d.; Tsai, C.-y.; Lee, S.-c., Growth of InGaAs-capped InAs Quantum Dots characterized by Atomic Force Microscope and Scanning Electron Microscope. *J. Nanopart. Res.* **2004**, *6* (4), 407-410.
192. González, R.; Pareja, R.; Ballesteros, C., *Microscopía Electrónica*. EUEDEMA: Madrid, 1991.
193. Heavens, O. S., *Optical Properties of Thin Solid Films*. Dover Publications: New York, 1965.
194. R.M.A., A.; Bashara, N. M., *Ellipsometry and Polarized Light*. North-Holland Publishing: Amsterdam, 1977.
195. Tompkins, H. G., *A User's Guide to Ellipsometry*. Academic Press Inc.: London, 1993.
196. Bertsekas, D. P., *Nonlinear Programming*. Athenas Scientific: Belmont, 1999.
197. Fakhraai, Z.; Valadkhan, S.; Forrest, J. A., Qualitative Discrepancy between Different Measures of Dynamics in Thin Polymer Films. *Eur. Phys. J. E* **2005**, *18* (2), 143-148.
198. Drude, P., *The Theory of Optics*. Longmans, Green, and Co.: New York, 1901.
199. Caridad, J. M.; Rossella, F.; Bellani, V.; Maicas, M.; Patrini, M.; Diez, E., Effects of Particle Contamination and Substrate Interaction on the Raman Response of unintentionally Doped Graphene. *J. Appl. Phys.* **2010**, *108* (8), 084321-6.
200. Ferrari, A. C.; Robertson, J., Raman Spectroscopy of Amorphous, Nanostructured, Diamond-like Carbon, and Nanodiamond. *Phil. Trans. R. Soc. A* **2004**, *362* (1824), 2477-2512.

201. Kudin, K. N.; Ozbas, B.; Schniepp, H. C.; Prud'homme, R. K.; Aksay, I. A.; Car, R., Raman Spectra of Graphite Oxide and Functionalized Graphene Sheets. *Nano Lett.* **2007**, *8* (1), 36-41.
202. Ferrari, A. C.; Meyer, J. C.; Scardaci, V.; Casiraghi, C.; Lazzeri, M.; Mauri, F.; Piscanec, S.; Jiang, D.; Novoselov, K. S.; Roth, S.; Geim, A. K., Raman Spectrum of Graphene and Graphene Layers. *Phys. Rev. Lett.* **2006**, *97* (18), 187401.
203. Harris, D. C., *Quantitative Chemical Analysis*. Freeman & Co Eds.: New York, 2002.
204. Jasieniak, J.; Smith, L.; Embden, J. v.; Mulvaney, P.; Califano, M., Re-examination of the Size-Dependent Absorption Properties of CdSe Quantum Dots. *J. Phys. Chem. C* **2009**, *113* (45), 19468-19474.
205. Pasto, D. J.; Johnson, C. R., *Organic Structure Determination*. Prentice Hall Inc.: New Jersey, 1969.
206. Rubio, N.; Fabbro, C.; Herrero, M. A.; de la Hoz, A.; Meneghetti, M.; Fierro, J. L. G.; Prato, M.; Vázquez, E., Ball-Milling Modification of Single-Walled Carbon Nanotubes: Purification, Cutting, and Functionalization. *Small* **2011**, *7* (5), 665-674.
207. Watts, J. F.; Wolstenholme, J., *An Introduction to Surface Analysis by XPS and AES*. John Wiley & Sons: Chichester, 2003.
208. Morais, V.; Encinar, M.; Prolongo, M. G.; Rubio, R. G., Dynamical Mechanical Behavior of Copolymers made of Styrene and Methyl Methacrylate: Random, Alternate and Diblock Copolymers. *Polymer* **2006**, *47* (7), 2349-2356.
209. Gao, W.; Alemany, L. B.; Ci, L.; Ajayan, P. M., New Insights into the Structure and Reduction of Graphite Oxide. *Nat Chem* **2009**, *1* (5), 403-408.
210. Dikin, D. A.; Stankovich, S.; Zimney, E. J.; Piner, R. D.; Dommett, G. H. B.; Evmenenko, G.; Nguyen, S. T.; Ruoff, R. S., Preparation and Characterization of Graphene Oxide Paper. *Nature* **2007**, *448* (7152), 457-460.
211. Angelomé, P. C.; Pastoriza-Santos, I.; Pérez-Juste, J.; Rodríguez-González, B.; Zelcer, A.; Soler-Illia, G. J. A. A.; Liz-Marzán, L. M., Growth and Branching

- of Gold Nanoparticles through Mesoporous Silica Thin Films. *Nanoscale* **2012**, *4* (3), 931-939.
212. Giannuzzi, L. A.; Stevie, F. A., *Introduction to FIBs: Instrumentation, Theory, Techniques and Practice*. Springer: New York, 2005.
213. Wahl, M., *Technical Note on Time-Correlated Single Photon Counting*. PicoQuant GmbH: 2009.
214. Wahl, M., *Technical Note on Time-Tagged Time-Resolved*. PicoQuant GmbH: 2004.
215. *FluoFit: User's Manual and Technical Data*. PicoQuant GmbH: 2004.
216. Lakowicz, J. R., *Principles of Fluorescence Spectroscopy*. Springer: New York, 2006.
217. Tseng, A. A.; Chen, K.; Chen, C. D.; Ma, K. J., Electron Beam Lithography in Nanoscale Fabrication: Recent Development. *IEEE Trans. on Electronics Packaging Manufacturing* **2003**, *26* (2), 141-149.
218. Bernstein, G. H.; Hill, D. A.; Liu, W., New high-contrast Developers for Poly(methyl methacrylate Resist. *J. Appl. Phys.* **1992**, *71* (8), 4066-4075.
219. Gómez-Navarro, C.; Weitz, R. T.; Bittner, A. M.; Scolari, M.; Mews, A.; Burghard, M.; Kern, K., Electronic Transport Properties of Individual Chemically Reduced Graphene Oxide Sheets. *Nano Lett.* **2007**, *7* (11), 3499-3503.
220. Stamm, M., *Polymer Surfaces and Interfaces: Characterization, Modification and Applications*. Springer-Verlag: Berlin, 2008.
221. Regismond, S. T. A.; Winnik, F. M.; Goddard, E. D., Surface Viscoelasticity in Mixed Polycation Anionic Surfactant Systems studied by a Simple Test. *Colloids Surf. A* **1996**, *119* (2-3), 221-228.
222. Hilles, H. M.; Ortega, F.; Rubio, R. G.; Monroy, F., Long-Time Relaxation Dynamics of Langmuir Films of a Glass-Forming Polymer: Evidence of Glasslike Dynamics in Two Dimensions. *Phys. Rev. Lett.* **2004**, *92* (25), 255503.
223. Hilles, H.; Maestro, A.; Monroy, F.; Ortega, F.; Rubio, R. G.; Velarde, M. G., Polymer Monolayers with a Small Viscoelastic Linear Regime: Equilibrium

- and Rheology of Poly(octadecyl acrylate) and Poly(vinyl stearate). *J. Chem. Phys.* **2007**, *126* (12), 124904-10.
224. Hilles, H. M.; Ritacco, H.; Monroy, F.; Ortega, F.; Rubio, R. G., Temperature and Concentration Effects on the Equilibrium and Dynamic Behavior of a Langmuir Monolayer: From Fluid to Gel-like Behavior. *Langmuir* **2009**, *25* (19), 11528-11532.
225. Hilles, H. M.; Sferrazza, M.; Monroy, F.; Ortega, F.; Rubio, R. G., Equilibrium and Dynamics of Langmuir Monolayers when the Interface is a Selective Solvent: Polystyrene-b-poly(t-butyl acrylate) block Copolymers. *J. Chem. Phys.* **2006**, *125* (7), 074706-8.
226. Petkov, J. T.; Gurkov, T. D.; Campbell, B. E.; Borwankar, R. P., Dilatational and Shear Elasticity of Gel-like Protein Layers on Air/Water Interface. *Langmuir* **2000**, *16* (8), 3703-3711.
227. Luinge, J. W.; Nijboer, G. W.; Hagting, J. G.; Vorenkamp, E. J.; Fuller, G. G.; Schouten, A. J., Rheological Behavior of Precursor PPV Monolayers. *Langmuir* **2004**, *20* (26), 11517-11522.
228. Chen, X.; Lenhert, S.; Hirtz, M.; Lu, N.; Fuchs, H.; Chi, L., Langmuir-Blodgett Patterning: A Bottom-Up Way To Build Mesostuctures over Large Areas. *Acc. Chem. Res.* **2007**, *40* (6), 393-401.
229. Schwartz, D. K., Langmuir-Blodgett Film Structure. *Surf. Sci. Rep.* **1997**, *27* (7-8), 245-334.
230. Ghaskadvi, R. S.; Carr, S.; Dennin, M., Effect of Subphase  $\text{Ca}^{2+}$  Ions on the Viscoelastic Properties of Langmuir Monolayers. *J. Chem. Phys.* **1999**, *111* (8), 3675-3678.
231. Mann, S., Molecular Tectonics in Biomineralization and Biomimetic Materials Chemistry. *Nature* **1993**, *365* (6446), 499-505.
232. Maestro, A.; Ortega, F.; Rubio, R. G.; Rubio, M. A.; Kragel, J.; Miller, R., Rheology of Poly(methyl methacrylate) Langmuir Monolayers: Percolation Transition to a Soft Glasslike System. *J. Chem. Phys.* **2011**, *134* (10), 104704-12.

233. Keddie, J. L.; Jones, R. A. L.; Cory, R. A., Size-dependent Depression of the Glass Transition Temperature in Polymer Films. *Europhys. Lett.* **1996**, *27*, 59-64.
234. Forrest, J. A.; Dalnoki-Veress, K., The Glass Transition in Thin Polymer Films. *Adv. Colloid Interface Sci.* **2001**, *94* (1-3), 167-195.
235. Bordi, F.; Cametti, C.; Sennato, S., Polyions act as an Electrostatic Glue for Mesoscopic Particle Aggregates. *Chem. Phys. Lett.* **2005**, *409* (1-3), 134-138.
236. Li, S.; Clarke, C. J.; Eisenberg, A.; Lennox, R. B., Langmuir Films of Polystyrene-b-Poly(alkyl acrylate) Diblock Copolymers. *Thin Solid Films* **1999**, *354* (1-2), 136-141.
237. Hosoi, A. E.; Kogan, D.; Devereaux, C. E.; Bernoff, A. J.; Baker, S. M., Two-Dimensional Self-Assembly in Diblock Copolymers. *Phys. Rev. Lett.* **2005**, *95* (3), 037801.
238. Jayathilake, H. D.; Driscoll, J. A.; Bordenyuk, A. N.; Wu, L.; da Rocha, S. R. P.; Verani, C. N.; Benderskii, A. V., Molecular Order in Langmuir-Blodgett Monolayers of Metal-Ligand Surfactants Probed by Sum Frequency Generation. *Langmuir* **2009**, *25* (12), 6880-6886.
239. Durbin, M. K.; Malik, A.; Richter, A. G.; Huang, K. G.; Dutta, P., In-Situ X-ray Diffraction Study of Langmuir-Blodgett Deposition. *Langmuir* **1997**, *13* (24), 6547-6549.
240. Meine, K.; Vollhardt, D.; Weidemann, G., Atomic Force Microscopy Study of the Texture of Condensed Phase Domains in 1-Monostearoylglycerol Monolayers. *Langmuir* **1998**, *14* (7), 1815-1821.
241. Liao, Q.; Carrillo, J.-M. Y.; Dobrynin, A. V.; Rubinstein, M., Rouse Dynamics of Polyelectrolyte Solutions: Molecular Dynamics Study. *Macromolecules* **2007**, *40* (21), 7671-7679.
242. Palik, E. D., *Handbook of Optical Constant of Solid*. Academic Press Inc.: San Diego, 1993.

243. Suematsu, N. J.; Ogawa, Y.; Yamamoto, Y.; Yamaguchi, T., Dewetting Self-assembly of Nanoparticles into Hexagonal Array of Nanorings. *J. Colloid Interface Sci.* **2007**, *310* (2), 648-652.
244. Yabu, H.; Shimomura, M., Preparation of Self-Organized Mesoscale Polymer Patterns on a Solid Substrate: Continuous Pattern Formation from a Receding Meniscus. *Adv. Funct. Mater.* **2005**, *15* (4), 575-581.
245. Karthaus, O.; Mikami, S.; Hashimoto, Y., Control of Droplet Size and Spacing in Micrometer-sized Polymeric Dewetting Patterns. *J. Colloid Interface Sci.* **2006**, *301* (2), 703-705.
246. Zhu, J.; Eisenberg, A.; Lennox, R. B., Interfacial Behavior of Block Polyelectrolytes. 1. Evidence for Novel Surface Micelle Formation. *J. Am. Chem. Soc.* **1991**, *113* (15), 5583-5588.
247. Zhu, J.; Eisenberg, A.; Lennox, R. B., Interfacial Behavior of Block Polyelectrolytes. 5. Effect of varying block Lengths on the Properties of Surface Micelles. *Macromolecules* **1992**, *25* (24), 6547-6555.
248. Perepichka, I. I.; Borozenko, K.; Badia, A.; Bazuin, C. G., Pressure-Induced Order Transition in Nanodot-Forming Diblock Copolymers at the Air/Water Interface. *J. Am. Chem. Soc.* **2011**, *133* (49), 19702-19705.
249. Jiang, R.; Li, B.; Wang, Z.; Yin, Y.; Shi, A.-C., Self-Assembled Morphologies of Diblock Copolymer Brushes in Poor Solvents. *Macromolecules* **2012**, *45* (11), 4920-4931.
250. Velázquez, M. M.; Ortega, F.; Monroy, F.; Rubio, R. G.; Pegiadou, S.; Pérez, L.; Infante, M. R., Langmuir Monolayers of the Zwitterionic Surfactant Hexadecyl 1-N-l-tryptophan glycerol ether. *J. Colloid Interface Sci.* **2005**, *283* (1), 144-152.
251. Schneider, H. A., Flexibility and Phase Transitions of Polymers. *J. Appl. Polym. Sci.* **2003**, *88* (6), 1590-1599.
252. Ngai, K. L.; Rizos, A. K.; Plazek, D. J., Reduction of the Glass Temperature of Thin freely standing Polymer Films caused by the Decrease of the

- Coupling Parameter in the Coupling Model. *J. Non-Cryst. Solids* **1998**, 235–237, 435-443.
253. Yang, Z.; Fujii, Y.; Lee, F. K.; Lam, C.-H.; Tsui, O. K. C., Glass Transition Dynamics and Surface Layer Mobility in Unentangled Polystyrene Films. *Science* **2010**, 328 (5986), 1676-1679.
254. Kamat, P. V., Quantum Dot Solar Cells. Semiconductor Nanocrystals as Light Harvesters. *J. Phys. Chem. C* **2008**, 112 (48), 18737-18753.
255. Goodman, M. D.; Xu, J.; Wang, J.; Lin, Z., Semiconductor Conjugated Polymer–Quantum Dot Nanocomposites at the Air/Water Interface and Their Photovoltaic Performance. *Chem. Mater.* **2009**, 21 (5), 934-938.
256. Steckel, J. S.; Snee, P.; Coe-Sullivan, S.; Zimmer, J. P.; Halpert, J. E.; Anikeeva, P.; Kim, L.-A.; Bulovic, V.; Bawendi, M. G., Color-Saturated Green-Emitting QD-LEDs. *Angew. Chem. Int. Ed.* **2006**, 45 (35), 5796-5799.
257. Neeleshwar, S.; Chen, C. L.; Tsai, C. B.; Chen, Y. Y.; Chen, C. C.; Shyu, S. G.; Seehra, M. S., Size-dependent Properties of CdSe Quantum Dots. *Phys. Rev. B* **2005**, 71 (20), 201307.
258. Li, H.; Wang, X., Single Quantum Dot-Micelles coated with Gemini Surfactant for Selective Recognition of a Cation and an Anion in Aqueous Solutions. *Sensors and Actuators B* **2008**, 134 (1), 238-244.
259. Yu, W. W.; Chang, E.; Drezek, R.; Colvin, V. L., Water-soluble Quantum Dots for Biomedical Applications. *Biochem. Biophys. Res. Comm.* **2006**, 348 (3), 781-786.
260. Tang, Z.; Wang, Y.; Podsiadlo, P.; Kotov, N. A., Biomedical Applications of Layer-by-Layer Assembly: From Biomimetics to Tissue Engineering. *Adv. Mater.* **2006**, 18 (24), 3203-3224.
261. Ganesan, V., Some Issues in Polymer Nanocomposites: Theoretical and Modeling Opportunities for Polymer Physics. *J. Polym. Sci. B* **2008**, 46 (24), 2666-2671.
262. Bockstaller, M. R.; Thomas, E. L., Optical Properties of Polymer-Based Photonic Nanocomposite Materials. *J. Phys. Chem. B* **2003**, 107 (37), 10017-10024.



263. Zhao, L.; Goodman, M. D.; Bowden, N. B.; Lin, Z., Self-assembly of an Ultra-high-molecular-weight comb Block Copolymer at the Air-Water Interface. *Soft Matter* **2009**, *5* (23), 4698-4703.
264. Zou, S.; Hong, R.; Emrick, T.; Walker, G. C., Ordered CdSe Nanoparticles within Self-Assembled Block Copolymer Domains on Surfaces. *Langmuir* **2007**, *23* (4), 1612-1614.
265. Rahedi, A. J.; Douglas, J. F.; Starr, F. W., Model for Reversible Nanoparticle Assembly in a Polymer Matrix. *J. Chem. Phys.* **2008**, *128* (2), 024902-9.
266. Voudouris, P.; Choi, J.; Gomopoulos, N.; Sainidou, R.; Dong, H.; Matyjaszewski, K.; Bockstaller, M. R.; Fytas, G., Anisotropic Elasticity of Quasi-One-Component Polymer Nanocomposites. *ACS Nano* **2011**, *5* (7), 5746-5754.
267. Chiu, J. J.; Kim, B. J.; Kramer, E. J.; Pine, D. J., Control of Nanoparticle Location in Block Copolymers. *J. Am. Chem. Soc.* **2005**, *127* (14), 5036-5037.
268. Listak, J.; Hakem, I. F.; Ryu, H. J.; Rangou, S.; Politakos, N.; Misichronis, K.; Avgeropoulos, A.; Bockstaller, M. R., Effect of Chain Architecture on the Compatibility of Block Copolymer/Nanoparticle Blends. *Macromolecules* **2009**, *42* (15), 5766-5773.
269. Gaponik, N.; Talapin, D. V.; Rogach, A. L.; Hoppe, K.; Shevchenko, E. V.; Kornowski, A.; Eychmüller, A.; Weller, H., Thiol-Capping of CdTe Nanocrystals: An Alternative to Organometallic Synthetic Routes. *J. Phys. Chem. B* **2002**, *106* (29), 7177-7185.
270. Hines, M. A.; Guyot-Sionnest, P., Bright UV-Blue Luminescent Colloidal ZnSe Nanocrystals. *J. Phys. Chem. B* **1998**, *102* (19), 3655-3657.
271. Schabas, G.; Yusuf, H.; Moffitt, M. G.; Sinton, D., Controlled Self-Assembly of Quantum Dots and Block Copolymers in a Microfluidic Device. *Langmuir* **2008**, *24* (3), 637-643.

272. Harirchian-Saei, S.; Wang, M. C. P.; Gates, B. D.; Moffitt, M. G., Patterning Block Copolymer Aggregates via Langmuir–Blodgett Transfer to Microcontact-Printed Substrates. *Langmuir* **2010**, *26* (8), 5998-6008.
273. Martín-García, B.; Velázquez, M. M.; Pérez-Hernández, J. A.; Hernández-Toro, J., Langmuir and Langmuir–Blodgett Films of a Maleic Anhydride Derivative: Effect of Subphase Divalent Cations. *Langmuir* **2010**, *26* (18), 14556-14562.
274. Flodström, K.; Alfredsson, V., Influence of the Block Length of Triblock Copolymers on the Formation of Mesoporous Silica. *Microporous Mesoporous Mater.* **2003**, *59* (2–3), 167-176.
275. Flodström, K.; Alfredsson, V.; Källrot, N., Formation of a New Ia $\overline{3}d$  Cubic Meso-Structured Silica via Triblock Copolymer-Assisted Synthesis. *J. Am. Chem. Soc.* **2003**, *125* (15), 4402-4403.
276. Flodström, K.; Wennerström, H.; Alfredsson, V., Mechanism of Mesoporous Silica Formation. A Time-Resolved NMR and TEM Study of Silica–Block Copolymer Aggregation. *Langmuir* **2004**, *20* (3), 680-688.
277. Kipkemboi, P.; Fogden, A.; Alfredsson, V.; Flodström, K., Triblock Copolymers as Templates in Mesoporous Silica Formation: Structural Dependence on Polymer Chain Length and Synthesis Temperature. *Langmuir* **2001**, *17* (17), 5398-5402.
278. Yu, W. W.; Peng, X., Formation of High-Quality CdS and Other II–VI Semiconductor Nanocrystals in Noncoordinating Solvents: Tunable Reactivity of Monomers. *Angew. Chem. Int. Ed. Engl.* **2002**, *41* (13), 2368-2371.
279. Cotton, F. A.; Barnes, R. D.; Bannister, E., The Effect of Complex-formation by Phosphine Oxides on their P-O Stretching Frequencies. *J. Chem. Soc.* **1960**, 2199-2203.
280. Katari, J. E. B.; Colvin, V. L.; Alivisatos, A. P., X-ray Photoelectron Spectroscopy of CdSe Nanocrystals with Applications to Studies of the Nanocrystal Surface. *J. Phys. Chem.* **1994**, *98* (15), 4109-4117.

281. Kopping, J. T.; Patten, T. E., Identification of Acidic Phosphorus-Containing Ligands Involved in the Surface Chemistry of CdSe Nanoparticles Prepared in Tri-N-octylphosphine Oxide Solvents. *J. Am. Chem. Soc.* **2008**, *130* (17), 5689-5698.
282. Delgado, C.; Merchán, M. D.; Velázquez, M. M., Effect of the Addition of Polyelectrolytes on Monolayers of Carboxybetaines. *J. Phys. Chem. B* **2008**, *112* (3), 687-693.
283. Gonçalves da Silva, A. M.; Viseu, M. I.; Campos, C. S.; Rechená, T., Effect of the Spreading Procedure on the Formation of Cationic–Anionic Mixed Monolayers. *Thin Solid Films* **1998**, *320* (2), 236-240.
284. Alejo, T.; Merchán, M. D.; Velázquez, M. M.; Pérez-Hernández, J. A., Polymer/Surfactant assisted Self-assembly of Nanoparticles into Langmuir–Blodgett Films. *Mat. Chem. Phys.* **2013**, *138* (1), 286-294.
285. Noskov, B. A.; Lin, S. Y.; Loglio, G.; Rubio, R. G.; Miller, R., Dilational Viscoelasticity of PEO-PPO-PEO Triblock Copolymer Films at the Air-Water Interface in the Range of High Surface Pressures. *Langmuir* **2006**, *22* (6), 2647-2652.
286. Glagola, C. P.; Miceli, L. M.; Milchak, M. A.; Halle, E. H.; Logan, J. L., Polystyrene–Poly(ethylene oxide) Diblock Copolymer: The Effect of Polystyrene and Spreading Concentration at the Air/Water Interface. *Langmuir* **2012**, *28* (11), 5048-5058.
287. Díez-Pascual, A. M.; Monroy, F.; Ortega, F.; Rubio, R. G.; Miller, R.; Noskov, B. A., Adsorption of Water-Soluble Polymers with Surfactant Character. Dilational Viscoelasticity. *Langmuir* **2007**, *23* (7), 3802-3808.
288. Lucassen, J., Longitudinal Capillary Waves. Part 1.-Theory. *Trans. Faraday Soc.* **1968**, *64*, 2221-2229.
289. Sides, S. W.; Kim, B. J.; Kramer, E. J.; Fredrickson, G. H., Hybrid Particle-Field Simulations of Polymer Nanocomposites. *Phys. Rev. Lett.* **2006**, *96* (25), 250601.

- 
290. Langner, K. M.; Sevink, G. J. A., Mesoscale Modeling of Block Copolymer Nanocomposites. *Soft Matter* **2012**, *8* (19), 5102-5118.
291. Reis, F. D. A. A. o., Modeling Self-Assembly of Diblock Copolymer-Nanoparticle Composites. *Macromolecules* **2008**, *41* (22), 8932-8937.
292. Vogel, V.; Moebius, D., Resonance of Transverse Capillary and Longitudinal Waves as a Tool for Monolayer Investigations at the Air-Water Interface. *Langmuir* **1989**, *5* (1), 129-133.
293. Shafrin, E. G.; Zisman, W. A., Constitutive Relations in the Wetting of low Energy Surfaces and the Theory of the Refraction Method of preparing Monolayers. *J. Phys. Chem.* **1960**, *64* (5), 519-524.
294. Krishnan, R. S.; Mackay, M. E.; Duxbury, P. M.; Pastor, A.; Hawker, C. J.; Van Horn, B.; Asokan, S.; Wong, M. S., Self-Assembled Multilayers of Nanocomponents. *Nano Lett.* **2007**, *7* (2), 484-489.
295. Maury, P.; Escalante, M.; Reinhoudt, D. N.; Huskens, J., Directed Assembly of Nanoparticles onto Polymer-Imprinted or Chemically Patterned Templates Fabricated by Nanoimprint Lithography. *Adv. Mater.* **2005**, *17* (22), 2718-2723.
296. Baumgart, T.; Offenhäusser, A., Polysaccharide-Supported Planar Bilayer Lipid Model Membranes. *Langmuir* **2002**, *19* (5), 1730-1737.
297. Kundu, S.; Bal, J. K., Reorganization of Au Nanoparticle Langmuir-Blodgett Films on Wet Chemically Passivated Si(001) Surfaces. *J. Appl. Phys.* **2011**, *110* (11), 114302-8.
298. Bunk, J. K. G.; Pospiech, D. U.; Eichhorn, K.-J.; Müller, M.; Werner, C.; Bellmann, C.; Simon, F.; Pleul, D.; Grundke, K., Studying the Influence of Chemical Structure on the Surface Properties of Polymer Films. *Colloids Surf. A* **2010**, *362* (1-3), 47-57.
299. Mark, J. E., *Polymer Data Handbook*. Oxford University Press, Inc.: New York, 1999.

300. Zehner, R. W.; Lopes, W. A.; Morkved, T. L.; Jaeger, H.; Sita, L. R., Selective Decoration of a Phase-Separated Diblock Copolymer with Thiol-Passivated Gold Nanocrystals. *Langmuir* **1998**, *14* (2), 241-244.
301. Chou, T.-H.; Chu, I. M., Behavior of DSPC/DSPE-PEG2000 Mixed Monolayers at the Air/Water Interface. *Colloids Surf. A* **2002**, *211* (2-3), 267-274.
302. De Roover, B.; Sclavons, M.; Carlier, V.; Devaux, J.; Legras, R.; Momtaz, A., Molecular Characterization of Maleic Anhydride-functionalized Polypropylene. *J. Polym. Sci. A* **1995**, *33* (5), 829-842.
303. Jones, M.; Nedeljkovic, J.; Ellingson, R. J.; Nozik, A. J.; Rumbles, G., Photoenhancement of Luminescence in Colloidal CdSe Quantum Dot Solutions. *J. Phys. Chem. B* **2003**, *107* (41), 11346-11352.
304. Tao, A. R.; Huang, J.; Yang, P., Langmuir-Blodgett of Nanocrystals and Nanowires. *Acc. Chem. Res.* **2008**, *41* (12), 1662-1673.
305. Zang, D.-Y.; Zhang, Y.-J.; Langevin, D., Rheological Study of Silica Nanoparticle Monolayers via two Orthogonal Wilhelmy Plates. *Acta Phys. Sin.* **2011**, *60* (7), 76801-076801.
306. Lucassen, J., Dynamic Dilational Properties of Composite Surfaces. *Colloids and Surfaces* **1992**, *65* ( ), 139-149.
307. Vacatello, M., Monte Carlo Simulations of Polymer Melts Filled with Solid Nanoparticles. *Macromolecules* **2001**, *34* (6), 1946-1952.
308. Ghanbari, A.; Nodoro, T. V. M.; Leroy, F.; Rahimi, M.; Böhm, M. C.; Müller-Plathe, F., Interphase Structure in Silica-Polystyrene Nanocomposites: A Coarse-Grained Molecular Dynamics Study. *Macromolecules* **2012**, *45* (1), 572-584.
309. Kim, F.; Kwan, S.; Akana, J.; Yang, P., Langmuir-Blodgett Nanorod Assembly. *J. Am. Chem. Soc.* **2001**, *123* (18), 4360-4361.
310. Coe, S.; Woo, W.-K.; Bawendi, M.; Bulovic, V., Electroluminescence from Single Monolayers of Nanocrystals in Molecular Organic Devices. *Nature* **2002**, *420* (6917), 800-803.
311. Saunders, B. R., Hybrid Polymer/Nanoparticle Solar Cells: Preparation, Principles and Challenges. *J. Colloid Interface Sci.* **2012**, *369* (1), 1-15.

312. Kaufmann, S.; Stoferle, T.; Moll, N.; Mahrt, R. F.; Scherf, U.; Tsami, A.; Talapin, D. V.; Murray, C. B., Resonant Energy Transfer within a Colloidal Nanocrystal Polymer Host System. *Appl. Phys. Lett.* **2007**, *90* (7), 071108-3.
313. Chen, C. W.; Wang, C. H.; Chen, Y. F.; Lai, C. W.; Chou, P. T., Tunable Energy Transfer Efficiency based on the Composite of mixed CdSe Quantum Dots and Elastomeric Film. *Appl. Phys. Lett.* **2008**, *92* (5), 051906-3.
314. Issac, A.; von Borczyskowski, C.; Cichos, F., Correlation between Photoluminescence Intermittency of CdSe Quantum Dots and Self-trapped States in Dielectric Media. *Phys. Rev. B* **2005**, *71* (16), 161302.
315. Issac, A.; Krasselt, C.; Cichos, F.; von Borczyskowski, C., Influence of the Dielectric Environment on the Photoluminescence Intermittency of CdSe Quantum Dots. *ChemPhysChem* **2012**, *13* (13), 3223-3230.
316. Achermann, M.; Petruska, M. A.; Crooker, S. A.; Klimov, V. I., Picosecond Energy Transfer in Quantum Dot Langmuir–Blodgett Nanoassemblies. *J. Phys. Chem. B* **2003**, *107* (50), 13782-13787.
317. Lunz, M.; Bradley, A. L.; Chen, W.-Y.; Gun'ko, Y. K., Two-Dimensional Förster Resonant Energy Transfer in a Mixed Quantum Dot Monolayer: Experiment and Theory. *J. Phys. Chem. C* **2009**, *113* (8), 3084-3088.
318. Lunz, M.; Bradley, A. L.; Chen, W.-Y.; Gerard, V. A.; Byrne, S. J.; Gun'ko, Y. K.; Lesnyak, V.; Gaponik, N., Influence of Quantum Dot Concentration on Förster Resonant Energy Transfer in Monodispersed Nanocrystal Quantum Dot Monolayers. *Phys. Rev. B* **2010**, *81* (20), 205316.
319. Fisher, B. R.; Eisler, H.-J.; Stott, N. E.; Bawendi, M. G., Emission Intensity Dependence and Single-Exponential Behavior In Single Colloidal Quantum Dot Fluorescence Lifetimes. *J. Phys. Chem. B* **2004**, *108* (1), 143-148.
320. Shepherd, D. P.; Whitcomb, K. J.; Milligan, K. K.; Goodwin, P. M.; Gelfand, M. P.; Van Orden, A., Fluorescence Intermittency and Energy Transfer in Small Clusters of Semiconductor Quantum Dots. *J. Phys. Chem. C* **2010**, *114* (35), 14831-14837.

321. Kalyuzhny, G.; Murray, R. W., Ligand Effects on Optical Properties of CdSe Nanocrystals. *J. Phys. Chem. B* **2005**, *109* (15), 7012-7021.
322. Bullen, C.; Mulvaney, P., The Effects of Chemisorption on the Luminescence of CdSe Quantum Dots. *Langmuir* **2006**, *22* (7), 3007-3013.
323. Munro, A. M.; Jen-La Plante, I.; Ng, M. S.; Ginger, D. S., Quantitative Study of the Effects of Surface Ligand Concentration on CdSe Nanocrystal Photoluminescence. *J. Phys. Chem. C* **2007**, *111* (17), 6220-6227.
324. Morris-Cohen, A. J.; Donakowski, M. D.; Knowles, K. E.; Weiss, E. A., The Effect of a Common Purification Procedure on the Chemical Composition of the Surfaces of CdSe Quantum Dots Synthesized with Trioctylphosphine Oxide. *J. Phys. Chem. C* **2010**, *114* (2), 897-906.
325. Selmarten, D.; Jones, M.; Rumbles, G.; Yu, P.; Nedeljkovic, J.; Shaheen, S., Quenching of Semiconductor Quantum Dot Photoluminescence by a  $\pi$ -Conjugated Polymer. *J. Phys. Chem. B* **2005**, *109* (33), 15927-15932.
326. Gupta, M. C.; Gupta, A.; Horwitz, J.; Kliger, D., Time-Resolved Fluorescence and Emission Depolarization Studies on Polystyrene: Photochemical Processes in Polymeric Systems. *Macromolecules* **1982**, *15* (5), 1372-1376.
327. O'Connor, D. B.; Scott, G. W.; Coulter, D. R.; Yavrouian, A., Emission Spectra and Kinetics of Copolymer Films of Styrene and 2,3,4,5,6-Pentafluorostyrene. *Macromolecules* **1991**, *24* (9), 2355-2360.
328. Kimura, J.; Uematsu, T.; Maenosono, S.; Yamaguchi, Y., Photoinduced Fluorescence Enhancement in CdSe/ZnS Quantum Dot Submonolayers Sandwiched between Insulating Layers: Influence of Dot Proximity. *J. Phys. Chem. B* **2004**, *108* (35), 13258-13264.
329. Liu, I. S.; Lo, H.-H.; Chien, C.-T.; Lin, Y.-Y.; Chen, C.-W.; Chen, Y.-F.; Su, W.-F.; Liou, S.-C., Enhancing Photoluminescence Quenching and Photoelectric Properties of CdSe Quantum Dots with Hole Accepting Ligands. *J. Mater. Chem.* **2008**, *18* (6), 675-682.

330. Bhattacharyya, S.; Paramanik, B.; Kundu, S.; Patra, A., Energy/Hole Transfer Phenomena in Hybrid  $\alpha$ -Sexithiophene ( $\alpha$ -STH) Nanoparticle–CdTe Quantum-Dot Nanocomposites. *ChemPhysChem* **2012**, *13* (18), 4155-4162.
331. Landes, C.; Burda, C.; Braun, M.; El-Sayed, M. A., Photoluminescence of CdSe Nanoparticles in the Presence of a Hole Acceptor: n-Butylamine. *J. Phys. Chem. B* **2001**, *105* (15), 2981-2986.
332. Zhang, Y.; Jing, P.; Zeng, Q.; Sun, Y.; Su, H.; Wang, Y. A.; Kong, X.; Zhao, J.; Zhang, H., Photoluminescence Quenching of CdSe Core/Shell Quantum Dots by Hole Transporting Materials. *J. Phys. Chem. C* **2009**, *113* (5), 1886-1890.
333. Ruedas-Rama, M. J.; Orte, A.; Hall, E. A. H.; Álvarez-Pez, J. M.; Talavera, E. M., Effect of Surface Modification on Semiconductor Nanocrystal Fluorescence Lifetime. *ChemPhysChem* **2011**, *12* (5), 919-929.
334. Wang, X.; Qu, L.; Zhang, J.; Peng, X.; Xiao, M., Surface-Related Emission in Highly Luminescent CdSe Quantum Dots. *Nano Lett.* **2003**, *3* (8), 1103-1106.
335. Hartmann, L.; Kumar, A.; Welker, M.; Fiore, A.; Julien-Rabant, C.; Gromova, M.; Bardet, M.; Reiss, P.; Baxter, P. N. W.; Chandezon, F.; Pansu, R. B., Quenching Dynamics in CdSe Nanoparticles: Surface-Induced Defects upon Dilution. *ACS Nano* **2012**, *6* (10), 9033-9041.
336. Wehrenberg, B. L.; Wang, C.; Guyot-Sionnest, P., Interband and Intraband Optical Studies of PbSe Colloidal Quantum Dots. *J. Phys. Chem. B* **2002**, *106* (41), 10634-10640.
337. Yeh, Y.-C.; Yuan, C.-T.; Kang, C.-C.; Chou, P.-T.; Tang, J., Influences of Light Intensity on Fluorescence Lifetime of Nanorods and Quantum Dots. *Appl. Phys. Lett.* **2008**, *93* (22), 223110-3.
338. Fisher, B.; Caruge, J.-M.; Chan, Y.-T.; Halpert, J.; Bawendi, M. G., Multiexciton Fluorescence from Semiconductor Nanocrystals. *Chem. Phys.* **2005**, *318* (1–2), 71-81.



339. Fisher, B.; Caruge, J. M.; Zehnder, D.; Bawendi, M., Room-Temperature Ordered Photon Emission from Multiexciton States in Single CdSe Core-Shell Nanocrystals. *Phys. Rev. Lett.* **2005**, *94* (8), 087403.
340. Simurda, M.; Nemeč, P.; Trojáněk, F.; Malý, P., Substantial Enhancement of Photoluminescence in CdSe Nanocrystals by Femtosecond Pulse Illumination. *Thin Solid Films* **2004**, *453-454* (0), 300-303.
341. Pechstedt, K.; Whittle, T.; Baumberg, J.; Melvin, T., Photoluminescence of Colloidal CdSe/ZnS Quantum Dots: The Critical Effect of Water Molecules. *J. Phys. Chem. C* **2010**, *114* (28), 12069-12077.
342. Schlegel, G.; Bohnenberger, J.; Potapova, I.; Mews, A., Fluorescence Decay Time of Single Semiconductor Nanocrystals. *Phys. Rev. Lett.* **2002**, *88* (13), 137401.
343. Cordero, S. R.; Carson, P. J.; Estabrook, R. A.; Strouse, G. F.; Buratto, S. K., Photo-Activated Luminescence of CdSe Quantum Dot Monolayers. *J. Phys. Chem. B* **2000**, *104* (51), 12137-12142.
344. Bawendi, M. G.; Carroll, P. J.; Wilson, W. L.; Brus, L. E., Luminescence Properties of CdSe Quantum Crystallites: Resonance between Interior and Surface localized States. *J. Chem. Phys.* **1992**, *96* (2), 946-954.
345. Sher, P. H.; Smith, J. M.; Dalgarno, P. A.; Warburton, R. J.; Chen, X.; Dobson, P. J.; Daniels, S. M.; Pickett, N. L.; O'Brien, P., Power Law Carrier Dynamics in Semiconductor Nanocrystals at Nanosecond Timescales. *Appl. Phys. Lett.* **2008**, *92* (10), 101111-3.
346. Jones, M.; Lo, S. S.; Scholes, G. D., Signatures of Exciton Dynamics and Carrier Trapping in the Time-Resolved Photoluminescence of Colloidal CdSe Nanocrystals. *J. Phys. Chem. C* **2009**, *113* (43), 18632-18642.
347. Nadeau, J. L.; Carlini, L.; Suffern, D.; Ivanova, O.; Bradforth, S. E., Effects of  $\beta$ -Mercaptoethanol on Quantum Dot Emission Evaluated from Photoluminescence Decays. *J. Phys. Chem. C* **2012**, *116* (4), 2728-2739.

348. Kim, D.; Miyamoto, M.; Mishima, T.; Nakayama, M., Strong Enhancement of Band-edge Photoluminescence in CdS Quantum Dots prepared by a Reverse-micelle Method. *J. Appl. Phys.* **2005**, *98* (8), 083514-4.
349. Koole, R.; Liljeroth, P.; de Mello Donegá, C.; Vanmaekelbergh, D.; Meijerink, A., Electronic Coupling and Exciton Energy Transfer in CdTe Quantum-Dot Molecules. *J. Am. Chem. Soc.* **2006**, *128* (32), 10436-10441.
350. Yu, M.; Van Orden, A., Enhanced Fluorescence Intermittency of CdSe-ZnS Quantum-Dot Clusters. *Phys. Rev. Lett.* **2006**, *97* (23), 237402.
351. Lee, J. D.; Maenosono, S., Intensified Blinking, Continuous Memory Loss, and Fluorescence Enhancement of Interacting Light-Emission Quantum Dots. *Phys. Rev. B* **2009**, *80* (20), 205327.
352. Kapitonov, A. M.; Stupak, A. P.; Gaponenko, S. V.; Petrov, E. P.; Rogach, A. L.; Eychmüller, A., Luminescence Properties of Thiol-Stabilized CdTe Nanocrystals. *J. Phys. Chem. B* **1999**, *103* (46), 10109-10113.
353. Petrov, E. P.; Cichos, F.; von Borczyskowski, C., Intrinsic Photophysics of Semiconductor Nanocrystals in Dielectric Media: Formation of Surface States. *J. Lum.* **2006**, *119–120* (0), 412-417.
354. Cichos, F.; von Borczyskowski, C.; Orrit, M., Power-law Intermittency of Single Emitters. *Curr. Opin. Colloid Interface Sci.* **2007**, *12* (6), 272-284.
355. Tachiya, M.; Seki, K., Unified Explanation of the Fluorescence Decay and Blinking Characteristics of Semiconductor Nanocrystals. *Appl. Phys. Lett.* **2009**, *94* (8), 081104-3.
356. Tachiya, M.; Mozumder, A., Kinetics of Geminate-ion Recombination by Electron Tunnelling. *Chem. Phys. Lett.* **1975**, *34* (1), 77-79.
357. Gochanour, C. R.; Andersen, H. C.; Fayer, M. D., Electronic Excited State Transport in Solution. *J. Chem. Phys.* **1979**, *70* (9), 4254-4271.
358. Loring, R. F.; Fayer, M. D., Electronic Excited State Transport and Trapping in One-and Two-Dimensional Disordered Systems. *Chem. Phys.* **1982**, *70* (1-2), 139-147.

359. Crooker, S. A.; Hollingsworth, J. A.; Tretiak, S.; Klimov, V. I., Spectrally Resolved Dynamics of Energy Transfer in Quantum-Dot Assemblies: Towards Engineered Energy Flows in Artificial Materials. *Phys. Rev. Lett.* **2002**, *89* (18), 186802.
360. Curutchet, C.; Franceschetti, A.; Zunger, A.; Scholes, G. D., Examining Förster Energy Transfer for Semiconductor Nanocrystalline Quantum Dot Donors and Acceptors. *J. Phys. Chem. C* **2008**, *112* (35), 13336-13341.
361. Kilina, S.; Ivanov, S.; Tretiak, S., Effect of Surface Ligands on Optical and Electronic Spectra of Semiconductor Nanoclusters. *J. Am. Chem. Soc.* **2009**, *131* (22), 7717-7726.
362. Xu, Z.; Hine, C. R.; Maye, M. M.; Meng, Q.; Cotlet, M., Shell Thickness Dependent Photoinduced Hole Transfer in Hybrid Conjugated Polymer/Quantum Dot Nanocomposites: From Ensemble to Single Hybrid Level. *ACS Nano* **2012**, *6* (6), 4984-4992.
363. de Mello Donegá, C.; Bode, M.; Meijerink, A., Size- and Temperature-dependence of Exciton Lifetimes in CdSe Quantum Dots. *Phys. Rev. B* **2006**, *74* (8), 085320.
364. Fischer, S. A.; Crotty, A. M.; Kilina, S. V.; Ivanov, S. A.; Tretiak, S., Passivating Ligand and Solvent Contributions to the Electronic Properties of Semiconductor Nanocrystals. *Nanoscale* **2012**, *4* (3), 904-914.
365. Togashi, D. M.; Costa, S. M. B.; Sobral, A. J. F. N., Lipophilic Porphyrin Microparticles induced by AOT Reverse Micelles: A Fluorescence Lifetime Imaging Study. *Biophysical Chemistry* **2006**, *119* (2), 121-126.
366. Thiele, U.; Velarde, M. G.; Neuffer, K., Dewetting: Film Rupture by Nucleation in the Spinodal Regime. *Phys. Rev. Lett.* **2001**, *87* (1), 016104.
367. Kargupta, K.; Sharma, A., Creation of Ordered Patterns by Dewetting of Thin Films on Homogeneous and Heterogeneous Substrates. *J. Colloid Interface Sci.* **2002**, *245* (1), 99-115.

368. Xue, L.; Han, Y., Pattern Formation by Dewetting of Polymer Thin Film. *Progress in Polymer Sci.* **2011**, *36* (2), 269-293.
369. Bollinne, C.; Cuenot, S.; Nysten, B.; Jonas, A. M., Spinodal-like Dewetting of Thermodynamically-stable Thin Polymer Films. *Eur. Phys. J. E* **2003**, *12* (3), 389-396.
370. Geim, A. K.; Novoselov, K. S., The Rise of Graphene. *Nat Mater* **2007**, *6* (3), 183-191.
371. Geim, A. K., Graphene: Status and Prospects. *Science* **2009**, *324* (5934), 1530-1534.
372. Rao, C. N. R.; Sood, A. K.; Subrahmanyam, K. S.; Govindaraj, A., Graphene: The New Two-Dimensional Nanomaterial. *Angew. Chem. Int. Ed.* **2009**, *48* (42), 7752-7777.
373. Liscio, A.; Veronese, G. P.; Treossi, E.; Suriano, F.; Rossella, F.; Bellani, V.; Rizzoli, R.; Samori, P.; Palermo, V., Charge Transport in Graphene-Polythiophene Blends as studied by Kelvin Probe Force Microscopy and Transistor Characterization. *J. Mater. Chem.* **2011**, *21* (9), 2924-2931.
374. Novoselov, K. S.; Geim, A. K.; Morozov, S. V.; Jiang, D.; Zhang, Y.; Dubonos, S. V.; Grigorieva, I. V.; Firsov, A. A., Electric Field Effect in Atomically Thin Carbon Films. *Science* **2004**, *306* (5696), 666-669.
375. Land, T. A.; Michely, T.; Behm, R. J.; Hemminger, J. C.; Comsa, G., STM Investigation of Single Layer Graphite Structures produced on Pt(111) by Hydrocarbon Decomposition. *Surf. Sci.* **1992**, *264* (3), 261-270.
376. Berger, C.; Song, Z.; Li, X.; Wu, X.; Brown, N.; Naud, C.; Mayou, D.; Li, T.; Hass, J.; Marchenkov, A. N.; Conrad, E. H.; First, P. N.; de Heer, W. A., Electronic Confinement and Coherence in Patterned Epitaxial Graphene. *Science* **2006**, *312* (5777), 1191-1196.
377. Du, X.; Skachko, I.; Barker, A.; Andrei, E. Y., Approaching Ballistic Transport in Suspended Graphene. *Nat Nanotechnol.* **2008**, *3* (8), 491-495.
378. Jiao, L.; Zhang, L.; Wang, X.; Diankov, G.; Dai, H., Narrow Graphene Nanoribbons from Carbon Nanotubes. *Nature* **2009**, *458* (7240), 877-880.

379. Kosynkin, D. V.; Higginbotham, A. L.; Sinitskii, A.; Lomeda, J. R.; Dimiev, A.; Price, B. K.; Tour, J. M., Longitudinal Unzipping of Carbon Nanotubes to form Graphene Nanoribbons. *Nature* **2009**, *458* (7240), 872-876.
380. Yang, X.; Dou, X.; Rouhanipour, A.; Zhi, L.; Räder, H. J.; Müllen, K., Two-Dimensional Graphene Nanoribbons. *J. Am. Chem. Soc.* **2008**, *130* (13), 4216-4217.
381. Hernandez, Y.; Nicolosi, V.; Lotya, M.; Blighe, F. M.; Sun, Z.; De, S.; McGovern, I. T.; Holland, B.; Byrne, M.; Gun'Ko, Y. K.; Boland, J. J.; Niraj, P.; Duesberg, G.; Krishnamurthy, S.; Goodhue, R.; Hutchison, J.; Scardaci, V.; Ferrari, A. C.; Coleman, J. N., High-yield Production of Graphene by Liquid-phase Exfoliation of Graphite. *Nat Nano* **2008**, *3* (9), 563-568.
382. Bourlinos, A. B.; Georgakilas, V.; Zboril, R.; Steriotis, T. A.; Stubos, A. K., Liquid-Phase Exfoliation of Graphite Towards Solubilized Graphenes. *Small* **2009**, *5* (16), 1841-1845.
383. De, S.; King, P. J.; Lotya, M.; O'Neill, A.; Doherty, E. M.; Hernandez, Y.; Duesberg, G. S.; Coleman, J. N., Flexible, Transparent, Conducting Films of Randomly Stacked Graphene from Surfactant-Stabilized, Oxide-Free Graphene Dispersions. *Small* **2010**, *6* (3), 458-464.
384. Coleman, J. N., Liquid-Phase Exfoliation of Nanotubes and Graphene. *Adv. Funct. Mater.* **2009**, *19* (23), 3680-3695.
385. Lotya, M.; Hernandez, Y.; King, P. J.; Smith, R. J.; Nicolosi, V.; Karlsson, L. S.; Blighe, F. M.; De, S.; Wang, Z.; McGovern, I. T.; Duesberg, G. S.; Coleman, J. N., Liquid Phase Production of Graphene by Exfoliation of Graphite in Surfactant/Water Solutions. *J. Am. Chem. Soc.* **2009**, *131* (10), 3611-3620.
386. Sun, Z.; Hasan, T.; Torrisi, F.; Popa, D.; Privitera, G.; Wang, F.; Bonaccorso, F.; Basko, D. M.; Ferrari, A. C., Graphene Mode-Locked Ultrafast Laser. *ACS Nano* **2010**, *4* (2), 803-810.
387. Catheline, A.; Valles, C.; Drummond, C.; Ortolani, L.; Morandi, V.; Marcaccio, M.; Iurlo, M.; Paolucci, F.; Penicaud, A., Graphene Solutions. *Chem. Comm.* **2011**, *47* (19), 5470-5472.

388. He, H.; Klinowski, J.; Forster, M.; Lerf, A., A New Structural Model for Graphite Oxide. *Chem. Phys. Lett.* **1998**, *287* (1–2), 53-56.
389. Kim, H.; Abdala, A. A.; Macosko, C. W., Graphene/Polymer Nanocomposites. *Macromolecules* **2010**, *43* (16), 6515-6530.
390. Robinson, J. T.; Perkins, F. K.; Snow, E. S.; Wei, Z.; Sheehan, P. E., Reduced Graphene Oxide Molecular Sensors. *Nano Lett.* **2008**, *8* (10), 3137-3140.
391. Wilson, N. R.; Pandey, P. A.; Beanland, R.; Young, R. J.; Kinloch, I. A.; Gong, L.; Liu, Z.; Suenaga, K.; Rourke, J. P.; York, S. J.; Sloan, J., Graphene Oxide: Structural Analysis and Application as a Highly Transparent Support for Electron Microscopy. *ACS Nano* **2009**, *3* (9), 2547-2556.
392. Stankovich, S.; Piner, R. D.; Chen, X.; Wu, N.; Nguyen, S. T.; Ruoff, R. S., Stable Aqueous Dispersions of Graphitic Nanoplatelets via the Reduction of Exfoliated Graphite Oxide in the Presence of Poly(sodium 4-styrenesulfonate). *J. Mater. Chem.* **2006**, *16* (2), 155-158.
393. Lomeda, J. R.; Doyle, C. D.; Kosynkin, D. V.; Hwang, W.-F.; Tour, J. M., Diazonium Functionalization of Surfactant-Wrapped Chemically Converted Graphene Sheets. *J. Am. Chem. Soc.* **2008**, *130* (48), 16201-16206.
394. Zheng, J.; Di, C.-a.; Liu, Y.; Liu, H.; Guo, Y.; Du, C.; Wu, T.; Yu, G.; Zhu, D., High Quality Graphene with Large Flakes exfoliated by Oleyl amine. *Chem. Commun.* **2010**, *46* (31), 5728-5730.
395. Xiao, J.; Mei, D.; Li, X.; Xu, W.; Wang, D.; Graff, G. L.; Bennett, W. D.; Nie, Z.; Saraf, L. V.; Aksay, I. A.; Liu, J.; Zhang, J.-G., Hierarchically Porous Graphene as a Lithium–Air Battery Electrode. *Nano Lett.* **2011**, *11* (11), 5071-5078.
396. Qi, X.; Pu, K.-Y.; Li, H.; Zhou, X.; Wu, S.; Fan, Q.-L.; Liu, B.; Boey, F.; Huang, W.; Zhang, H., Amphiphilic Graphene Composites. *Angew. Chem. Int. Ed.* **2010**, *49* (49), 9426-9429.
397. Ramanathan T; Abdala, A. A.; Stankovich S; Dikin, D. A.; Herrera Alonso, M.; Piner, R. D.; Adamson, D. H.; Schniepp, H. C.; Chen X; Ruoff, R. S.; Nguyen,

- S. T.; Aksay, I. A.; Prud'Homme, R. K.; Brinson, L. C., Functionalized Graphene Sheets for Polymer Nanocomposites. *Nat Nanotechnol.* **2008**, *3* (6), 327-331.
398. Xu, Y.; Shi, G., Assembly of Chemically Modified Graphene: Methods and Applications. *J. Mater. Chem.* **2011**, *21* (10), 3311-3323.
399. Ducker, W. A.; Grant, L. M., Effect of Substrate Hydrophobicity on Surfactant Surface-Aggregate Geometry. *J. Phys. Chem.* **1996**, *100* (28), 11507-11511.
400. Tiberg, F.; Brinck, J.; Grant, L., Adsorption and Surface-induced Self-assembly of Surfactants at the Solid-Aqueous Interface. *Curr. Opin. Colloid Interface Sci.* **1999**, *4* (6), 411-419.
401. Ribera, R.; Velázquez, M. M., Effect of Water-Soluble Polymers on the Surface Properties of 3-(Dimethyldodecylammonio)Propanesulfonate in Aqueous Solutions. *Langmuir* **1999**, *15* (20), 6686-6691.
402. Merchán, M. D.; Velázquez, M. M., Properties of CHAPS Micelles Modulated by Different Polyelectrolytes. *Colloids Surf. A* **2010**, *366* (1-3), 12-17.
403. Luo, D.; Zhang, G.; Liu, J.; Sun, X., Evaluation Criteria for Reduced Graphene Oxide. *J. Phys. Chem. C* **2011**, *115* (23), 11327-11335.
404. Dua, V.; Surwade, S. P.; Ammu, S.; Agnihotra, S. R.; Jain, S.; Roberts, K. E.; Park, S.; Ruoff, R. S.; Manohar, S. K., All-Organic Vapor Sensor Using Inkjet-Printed Reduced Graphene Oxide. *Angew. Chem. Int. Ed.* **2010**, *49* (12), 2154-2157.
405. Fernández-Merino, M. J.; Guardia, L.; Paredes, J. I.; Villar-Rodil, S.; Solís-Fernández, P.; Martínez-Alonso, A.; Tascón, J. M. D., Vitamin C is an Ideal Substitute for Hydrazine in the Reduction of Graphene Oxide Suspensions. *J. Phys. Chem. C* **2010**, *114* (14), 6426-6432.
406. Zhang, J.; Yang, H.; Shen, G.; Cheng, P.; Zhang, J.; Guo, S., Reduction of Graphene Oxide via L-ascorbic acid. *Chem. Commun.* **2010**, *46* (7), 1112-1114.
407. Zhou, X.; Zhang, J.; Wu, H.; Yang, H.; Zhang, J.; Guo, S., Reducing Graphene Oxide via Hydroxylamine: A Simple and Efficient Route to Graphene. *J. Phys. Chem. C* **2011**, *115* (24), 11957-11961.

408. Paredes, J. I.; Villar-Rodil, S.; Fernández-Merino, M. J.; Guardia, L.; Martínez-Alonso, A.; Tascón, J. M. D., Environmentally Friendly Approaches toward the Mass Production of Processable Graphene from Graphite Oxide. *J. Mater. Chem.* **2011**, *21* (2), 298-306.
409. Collier, C. P.; Saykally, R. J.; Shiang, J. J.; Henrichs, S. E.; Heath, J. R., Reversible Tuning of Silver Quantum Dot Monolayers Through the Metal-Insulator Transition. *Science* **1997**, *277* (5334), 1978-1981.
410. Brodie, B. C., On the Atomic Weight of Graphite *Philos. Trans. R. Soc. London* **1859**, *149*, 249-259.
411. Staudenmaier, L., Verfahren zur Darstellung der Graphitsäure. *Ber. Dtsch. Chem. Ges.* **1898**, *31* (2), 1481-1487.
412. Cotton, F. A.; Wilkinson, G.; Murillo, C. A.; Bochmann, M., *Advanced Inorganic Chemistry*. Wiley India: Singapore, 2004.
413. Hummers, W. S.; Offeman, R. E., Preparation of Graphitic Oxide. *J. Am. Chem. Soc.* **1958**, *80* (6), 1339-1339.
414. Koch, K. R., Oxidation by  $Mn_2O_7$ : An Impressive Demonstration of the Powerful Oxidizing Property of Dimanganeseheptoxide. *J. Chem. Educ.* **1982**, *59* (11), 973.
415. Simon, A.; Dronskowski, R.; Krebs, B.; Hettich, B., The Crystal Structure of  $Mn_2O_7$ . *Angew. Chem. Int. Ed.* **1987**, *26* (2), 139-140.
416. Kovtyukhova, N. I.; Ollivier, P. J.; Martin, B. R.; Mallouk, T. E.; Chizhik, S. A.; Buzaneva, E. V.; Gorchinskiy, A. D., Layer-by-Layer Assembly of Ultrathin Composite Films from Micron-Sized Graphite Oxide Sheets and Polycations. *Chem Mater.* **1999**, *11* (3), 771-778.
417. Marcano, D. C.; Kosynkin, D. V.; Berlin, J. M.; Sinitskii, A.; Sun, Z.; Slesarev, A.; Alemany, L. B.; Lu, W.; Tour, J. M., Improved Synthesis of Graphene Oxide. *ACS Nano* **2010**, *4* (8), 4806-4814.
418. Dreyer, D. R.; Park, S.; Bielawski, C. W.; Ruoff, R. S., The Chemistry of Graphene Oxide. *Chem. Soc. Rev.* **2010**, *39* (1), 228-240.



419. Hontoria-Lucas, C.; López-Peinado, A. J.; López-González, J. D.; Rojas-Cervantes, M. L.; Martín-Aranda, R. M., Study of Oxygen-containing Groups in a Series of Graphite Oxides: Physical and Chemical Characterization. *Carbon* **1995**, *33* (11), 1585-1592.
420. Gao, X.; Jang, J.; Nagase, S., Hydrazine and Thermal Reduction of Graphene Oxide: Reaction Mechanisms, Product Structures, and Reaction Design. *J. Phys. Chem. C* **2009**, *114* (2), 832-842.
421. Bourlinos, A. B.; Gournis, D.; Petridis, D.; Szabó, T.; Szeri, A.; Dékány, I., Graphite Oxide: Chemical Reduction to Graphite and Surface Modification with Primary Aliphatic Amines and Amino Acids. *Langmuir* **2003**, *19* (15), 6050-6055.
422. Wang, G.; Yang, J.; Park, J.; Gou, X.; Wang, B.; Liu, H.; Yao, J., Facile Synthesis and Characterization of Graphene Nanosheets. *J. Phys. Chem. C* **2008**, *112* (22), 8192-8195.
423. Wu, Z.-S.; Ren, W.; Gao, L.; Liu, B.; Jiang, C.; Cheng, H.-M., Synthesis of High-quality Graphene with a Pre-determined Number of Layers. *Carbon* **2009**, *47* (2), 493-499.
424. Chen, W.; Yan, L.; Bangal, P. R., Chemical Reduction of Graphene Oxide to Graphene by Sulfur-Containing Compounds. *J. Phys. Chem. C* **2010**, *114* (47), 19885-19890.
425. Fan, Z.; Wang, K.; Wei, T.; Yan, J.; Song, L.; Shao, B., An Environmentally Friendly and Efficient Route for the Reduction of Graphene Oxide by Aluminum Powder. *Carbon* **2010**, *48* (5), 1686-1689.
426. Fan, X.; Peng, W.; Li, Y.; Li, X.; Wang, S.; Zhang, G.; Zhang, F., Deoxygenation of Exfoliated Graphite Oxide under Alkaline Conditions: A Green Route to Graphene Preparation. *Adv. Mater.* **2008**, *20* (23), 4490-4493.
427. Boehm, H. P.; Clauss, A.; Fischer, G. O.; Hofmann, U., Das Adsorptionsverhalten sehr dünner Kohlenstoff-Folien. *Anorg. Allg. Chem.* **1962**, *316* (3-4), 119-127.

428. Liu, J.; Jeong, H.; Liu, J.; Lee, K.; Park, J.-Y.; Ahn, Y. H.; Lee, S., Reduction of Functionalized Graphite Oxides by Trioctylphosphine in Non-polar Organic Solvents. *Carbon* **2010**, *48* (8), 2282-2289.
429. Zhu, C.; Guo, S.; Fang, Y.; Dong, S., Reducing Sugar: New Functional Molecules for the Green Synthesis of Graphene Nanosheets. *ACS Nano* **2010**, *4* (4), 2429-2437.
430. Lei, Y.; Tang, Z.; Liao, R.; Guo, B., Hydrolysable Tannin as Environmentally Friendly Reducer and Stabilizer for Graphene Oxide. *Green Chem.* **2011**, *13* (7), 1655-1658.
431. Liao, R.; Tang, Z.; Lei, Y.; Guo, B., Polyphenol-Reduced Graphene Oxide: Mechanism and Derivatization. *J. Phys. Chem. C* **2011**, *115* (42), 20740-20746.
432. Pham, T. A.; Kim, J. S.; Kim, J. S.; Jeong, Y. T., One-step Reduction of Graphene Oxide with L-glutathione. *Colloids Surf. A* **2011**, *384* (1-3), 543-548.
433. Gao, J.; Liu, F.; Liu, Y.; Ma, N.; Wang, Z.; Zhang, X., Environment-Friendly Method to Produce Graphene that Employs Vitamin C and Amino Acid. *Chem. Mater.* **2010**, *22* (7), 2213-2218.
434. Yanyu, L.; Johannes, F.; Linjie, Z.; Hassan, N.-A.; Xinliang, F.; Jürgen, P. R.; Norbert, K.; Klaus, M., Transparent, Highly Conductive Graphene Electrodes from Acetylene-assisted Thermolysis of Graphite Oxide Sheets and Nanographene Molecules. *Nanotechnology* **2009**, *20* (43), 434007.
435. Zhou, M.; Wang, Y.; Zhai, Y.; Zhai, J.; Ren, W.; Wang, F.; Dong, S., Controlled Synthesis of Large-Area and Patterned Electrochemically Reduced Graphene Oxide Films. *Chem. Eur. J.* **2009**, *15* (25), 6116-6120.
436. Paredes, J. I.; Villar-Rodil, S.; Solís-Fernández, P.; Martínez-Alonso, A.; Tascón, J. M. D., Atomic Force and Scanning Tunneling Microscopy Imaging of Graphene Nanosheets Derived from Graphite Oxide. *Langmuir* **2009**, *25* (10), 5957-5968.
437. Panchakarla, L. S.; Subrahmanyam, K. S.; Saha, S. K.; Govindaraj, A.; Krishnamurthy, H. R.; Waghmare, U. V.; Rao, C. N. R., Synthesis, Structure, and

- Properties of Boron- and Nitrogen-Doped Graphene. *Adv. Mater.* **2009**, *21* (46), 4726-4730.
438. Nair, R. R.; Blake, P.; Grigorenko, A. N.; Novoselov, K. S.; Booth, T. J.; Stauber, T.; Peres, N. M. R.; Geim, A. K., Fine Structure Constant Defines Visual Transparency of Graphene. *Science* **2008**, *320* (5881), 1308.
439. Vadukumpully, S.; Paul, J.; Valiyaveetil, S., Cationic Surfactant mediated Exfoliation of Graphite into Graphene Flakes. *Carbon* **2009**, *47* (14), 3288-3294.
440. Pimenta, M. A.; Dresselhaus, G.; Dresselhaus, M. S.; Cancado, L. G.; Jorio, A.; Saito, R., Studying Disorder in Graphite-based Systems by Raman Spectroscopy. *Phys. Chem. Chem. Phys.* **2007**, *9* (11), 1276-1290.
441. Nourbakhsh, A.; Cantoro, M.; Vosch, T.; Pourtois, G.; Clemente, F.; van der Veen, M. H.; Hofkens, J.; Heyns, M. M.; de Gendt, S.; Sels, B. F., Bandgap Opening in Oxygen Plasma-treated Graphene *Nanotechnology* **2010**, *21*, 435203.
442. Tuinstra, F.; Koenig, J. L., Raman Spectrum of Graphite. *J. Chem. Phys.* **1970**, *53* (3), 1126-1130.
443. Vidano, R. P.; Fischbach, D. B.; Willis, L. J.; Loehr, T. M., Observation of Raman Band shifting with Excitation Wavelength for Carbons and Graphites. *Solid State Commun.* **1981**, *39* (2), 341-344.
444. Huisgen, R.; Maeder, H., Azomethine ylide from Dimethyl 1-(p-methoxyphenyl)aziridine-2,3(cis)-dicarboxylate. *J. Am. Chem. Soc.* **1971**, *93* (7), 1777-1779.
445. Heine, H. W.; Peavy, R.; Durbetaki, A. J., Aziridines. XIII. Reactions of 1,2,3-Triarylaziridines with Activated Alkenes and Alkynes. *J. Org. Chem.* **1966**, *31* (12), 3924-3927.
446. Woller, P. B.; Cromwell, N. H., 1,3-Dipolar Cycloaddition Reactions of the Geometrical Isomers of some Methyl 1-alkyl-2-(p-biphenyl)-3-aziridinecarboxylates. *J. Org. Chem.* **1970**, *35* (4), 888-898.
447. Ferrari, A. C.; Robertson, J., Interpretation of Raman Spectra of Disordered and Amorphous Carbon. *Phys. Rev. B* **2000**, *61* (20), 14095-14107.

448. Ferrari, A. C.; Robertson, J., Resonant Raman Spectroscopy of Disordered, Amorphous, and Diamondlike Carbon. *Phys. Rev. B* **2001**, *64* (7), 075414.
449. Wang, D.; Kou, R.; Choi, D.; Yang, Z.; Nie, Z.; Li, J.; Saraf, L. V.; Hu, D.; Zhang, J.; Graff, G. L.; Liu, J.; Pope, M. A.; Aksay, I. A., Ternary Self-Assembly of Ordered Metal Oxide-Graphene Nanocomposites for Electrochemical Energy Storage. *ACS Nano* **2010**, *4* (3), 1587-1595.
450. Wu, D.; Yang, X., Coarse-Grained Molecular Simulation of Self-Assembly for Nonionic Surfactants on Graphene Nanostructures. *J. Phys. Chem. B* **2012**, *116* (39), 12048-12056.
451. Grant, L. M.; Ducker, W. A., Effect of Substrate Hydrophobicity on Surface-Aggregate Geometry: Zwitterionic and Nonionic Surfactants. *J. Phys. Chem. B* **1997**, *101* (27), 5337-5345.
452. Lotya, M.; King, P. J.; Khan, U.; De, S.; Coleman, J. N., High-Concentration, Surfactant-Stabilized Graphene Dispersions. *ACS Nano* **2010**, *4* (6), 3155-3162.
453. Huang, L.; Wu, B.; Yu, G.; Liu, Y., Graphene: Learning from Carbon Nanotubes. *J. Mater. Chem.* **2011**, *21* (4), 919-929.
454. Choi, B. G.; Park, H.; Park, T. J.; Yang, M. H.; Kim, J. S.; Jang, S.-Y.; Heo, N. S.; Lee, S. Y.; Kong, J.; Hong, W. H., Solution Chemistry of Self-Assembled Graphene Nanohybrids for High-Performance Flexible Biosensors. *ACS Nano* **2010**, *4* (5), 2910-2918.
455. Fernández-Merino, M. J.; Paredes, J. I.; Villar-Rodil, S.; Guardia, L.; Solís-Fernández, P.; Salinas-Torres, D.; Cazorla-Amorós, D.; Morallón, E.; Martínez-Alonso, A.; Tascón, J. M. D., Investigating the Influence of Surfactants on the Stabilization of Aqueous Reduced Graphene Oxide Dispersions and the Characteristics of their Composite Films. *Carbon* **2012**, *50* (9), 3184-3194.

- 
456. Amado, M.; Diez, E.; López-Romero, D.; Rossella, F.; Caridad, J. M.; Dionigi, F.; Bellani, V.; Maude, D. K., Plateau–insulator Transition in Graphene. *New Journal of Physics* **2010**, *12* (5), 053004.
457. Cobaleda, C.; Rossella, F.; Pezzini, S.; Diez, E.; Bellani, V.; Maude, D.; Blake, P., Quantum Hall Effect in Inhomogeneous Trilayer Graphene. *Physica E* **2011**, *44* (2), 530-533.
458. Robinson, J. A.; LaBella, M.; Zhu, M.; Hollander, M.; Kasarda, R.; Hughes, Z.; Trumbull, K.; Cavalero, R.; Snyder, D., Contacting Graphene. *Appl. Phys. Lett.* **2011**, *98* (5), 053103-3.

**Articles / Manuscripts**



## Articles/Manuscripts

This appendix includes the two articles which has been already published, a just-accepted manuscript and another one submitted and currently under revision.

### **Chapter IV. Polymer Monolayers**

Martín-García, B.; Velázquez, M. M.; Pérez-Hernández, J. A.; Hernández-Toro, J., Langmuir and Langmuir–Blodgett Films of a Maleic Anhydride Derivative: Effect of Subphase Divalent Cations. *Langmuir* **2010**, *26* (18), 14556-14562.

### **Chapter V. Preparation and Properties of QDs Films**

Martín-García, B.; Velázquez, M.M., Block Copolymer assisted Self-assembly of Nanoparticles into Langmuir-Blodgett Films: Effect of Polymer Concentration. *Mat. Chem. Phys.* **2013** (just accepted)

Martín-García, B.; Paulo, P.M.R.; Costa, S.M.B.; Velázquez, M.M., Photoluminescence Dynamics of CdSe QD/Polymer Langmuir-Blodgett Thin Films: Morphology Effects. *J. Phys. Chem. C* (submitted)

### **Chapter VI. Chemically converted Graphene**

Martín-García, B.; Velázquez, M. M.; Rossella, F.; Bellani, V.; Diez, E.; García Fierro, J. L.; Pérez-Hernández, J. A.; Hernández-Toro, J.; Claramunt, S.; Cirera, A., Functionalization of Reduced Graphite Oxide Sheets with a Zwitterionic Surfactant. *ChemPhysChem* **2012**, *13* (16), 3682-3690.





## Appendix



## **Nomenclature**



## Nomenclature

<b>2D</b>	<i>Two-dimensional</i>
<b>3D</b>	<i>Three-dimensional</i>
<b>A</b>	<i>Surface area</i>
<i>a</i>	<i>Capilar length of the top part of the meniscus formed by the Wilhelmy plate</i>
<b>A<sub>12</sub></b>	<i>Mean area per molecule</i>
<b>A<sup>exc</sup></b>	<i>Excess area of mixing</i>
<b>AFM</b>	<i>Atomic Force Microscopy</i>
<i>a<sub>i</sub></i>	<i>Pre-exponential factor in fluorescence lifetimes</i>
<b>A<sub>i</sub></b>	<i>Molecular area of component i</i>
<b>A<sub>i</sub></b>	<i>Amplitude of the i<sup>th</sup> decay component</i>
<b>ASF</b>	<i>Atomic Sensitivity Factors method in XPS</i>
<b>BAM</b>	<i>Brewster Angle Microscopy</i>
<b>BEI</b>	<i>Backscattered Electron Image in FE-SEM</i>
<b>Bkgr<sub>Dec</sub></b>	<i>Decay background</i>
<b>Bkgr<sub>IRF</sub></b>	<i>IRF background</i>
<b>c</b>	<i>Concentration</i>
<b>c*</b>	<i>Overlap concentration</i>
<b>[C]</b>	<i>Concentration of the component C</i>
<i>ca.</i>	<i>Circa</i>
<b>CCD</b>	<i>Charge-Coupled Device</i>
<b>C<sub>D</sub></b>	<i>Donor reduced concentration in QDs</i>
<b>CHAPS</b>	<i>3-[(3-Cholamidopropyl) dimethylammonio]-1-propanesulfonate</i>
<b>CMC</b>	<i>Critical Micelle Concentration</i>
<b>Co-spr</b>	<i>Co-spreading</i>
<b>C<sub>p</sub></b>	<i>Heat capacity</i>
<b>C<sub>s</sub></b>	<i>Isothermal compressibility</i>
<b>C<sub>T</sub></b>	<i>Trap reduced concentration in QDs</i>

---

<b>C(t)</b>	<i>Contribution from compact regions of immobilized QDs to the PL decay</i>
<b>CVD</b>	<i>Chemical Vapour Deposition</i>
<b>d</b>	<i>Spatial dimensionality</i>
<b>d</b>	<i>Distance between plates in the Kelvin Probe</i>
<b>d</b>	<i>Distance between probes in conductivity measurements</i>
<b>D(t)</b>	<i>Decay function</i>
<b>DDPS</b>	<i>Dodecyl dimethyl ammonium propane sulphonate</i>
<b>DNA</b>	<i>Deoxyribonucleic acid</i>
<b>DSC</b>	<i>Differential Scanning Calorimetry</i>
<b>E<sub>B</sub></b>	<i>Binding energy</i>
<b>EBL</b>	<i>Electron Beam Lithography</i>
<b>EGCG</b>	<i>Epigallocatechin gallate</i>
<b>E<sub>k</sub></b>	<i>Kinetic energy</i>
<b>ET</b>	<i>Energy Transfer</i>
<b>F1, F2, F3, F4</b>	<i>Band-pass filters corresponding to 545±17.5 nm (F1), 575±15 nm (F2), 645±45 nm (F3) and 695±27.5 nm (F4)</i>
<b>FE-SEM</b>	<i>Field Emission Scanning Electron Microscopy</i>
<b>f<sub>i</sub></b>	<i>Intensity fraction of the i<sup>th</sup> decay component</i>
<b>FIB</b>	<i>Focused Ion Beam</i>
<b>FLIM</b>	<i>Fluorescence Lifetime Imaging Microscopy</i>
<b>FRET</b>	<i>Förster Resonant Energy Transfer</i>
<b>FTIR</b>	<i>Fourier Transform Infra-Red Spectroscopy</i>
<b>FWHM</b>	<i>Full Width at Half Maximum</i>
<b>G</b>	<i>Gas phase</i>
<b>GFIS</b>	<i>Gas Field Ionization Sources</i>
<b>GO</b>	<i>Graphene Oxide / Graphite Oxide</i>
<b>h</b>	<i>Height of the top part of the meniscus formed by the Wilhelmy plate</i>
<b>HO-A-OH</b>	<i>Ascorbic acid or Vitamin C</i>
<b>h<sub>op</sub></b>	<i>Film thickness in ellipsometry</i>

---

<b>HV</b>	<i>High Vacuum</i>
<b>h<math>\nu</math></b>	<i>Photon energy</i>
<b>I</b>	<i>Intensity</i>
<b>I</b>	<i>Current</i>
<b>I<sub>D</sub></b>	<i>Intensity of the D band in the Raman spectrum</i>
<b>I<sub>G</sub></b>	<i>Intensity of the G band in the Raman spectrum</i>
<b>IPA</b>	<i>Isopropyl alcohol</i>
<b>IR</b>	<i>Infra-Red</i>
<b>IRF</b>	<i>Instrument Response Function</i>
<b>ITO</b>	<i>Indium Tin Oxide</i>
<b><math>k_{be}</math></b>	<i>Kinetic coefficient related to the charge recombination to the excited state from charge trapped states in QDs</i>
<b><math>k_{bg}</math></b>	<i>Kinetic coefficient related to the relaxation to the ground state from charge trapped states in QDs</i>
<b><math>k_{ct}</math></b>	<i>Kinetic coefficient related to the charge transfer into ligand-based orbitals in QDs</i>
<b><math>k_{dg}</math></b>	<i>Kinetic coefficient related to the relaxation to the ground state from surface defect states in QDs</i>
<b><math>k_{ed}</math></b>	<i>Kinetic coefficient related to the carrier trapping at QD surface defects</i>
<b>L<sub>a</sub></b>	<i>In-plane correlation length (Raman microscopy)</i>
<b>LB</b>	<i>Langmuir-Blodgett</i>
<b>LC</b>	<i>Liquid-Condensed phase</i>
<b>LE</b>	<i>Liquid-Expanded phase</i>
<b>LED</b>	<i>Light Emitting Device</i>
<b>LMIS</b>	<i>Liquid Metal Ion Sources</i>
<b>LS</b>	<i>Langmuir-Schaefer</i>
<b>MA</b>	<i>Methacrylate</i>
<b>MCS</b>	<i>Intensity time trace analysis (Multi-Channel-Scalers)</i>
<b>MIBK</b>	<i>Methyl isobutyl ketone</i>
<b>MM2</b>	<i>Molecular Mechanics</i>



---

<b><math>M_n</math></b>	<i>Number average molecular weight</i>
<b>N</b>	<i>Number of monomers in a polymer chain</i>
<b>n</b>	<i>Refractive index</i>
<b>N.A.</b>	<i>Numerical Aperture</i>
<b><math>n_i</math></b>	<i>Refractive index of the "i" medium</i>
<b>NIPAM</b>	<i>Poly (N-isopropylacrylamide)</i>
<b>NP</b>	<i>Nanoparticle</i>
<b>O=A=O</b>	<i>Dehydroascorbic acid</i>
<b>P</b>	<i>Pressure</i>
<b>p</b>	<i>Perimeter of the Wilhelmy plate</i>
<b>pa</b>	<i>Percentage of absorption (opacity)</i>
<b>PAHs</b>	<i>Polyacyclic hydrocarbons</i>
<b>PEO</b>	<i>Poly(ethylene oxide)</i>
<b>PL</b>	<i>Photoluminescence</i>
<b>PLA</b>	<i>Poly lactide</i>
<b>PMAO</b>	<i>Poly(maleic anhydride-alt-1-octadecene)</i>
<b>PMMA</b>	<i>Poly methyl methacrylate</i>
<b>PS</b>	<i>Polystyrene</i>
<b>PS-b-MA</b>	<i>Poly (styrene-co-maleic anhydride) cumene terminated</i>
<b>PS-MA-BEE</b>	<i>Poly (styrene-co-maleic anhydride) partial 2-butboxy ethyl ester cumene terminated</i>
<b>PVDF</b>	<i>Polyvinylidene difluoride</i>
<b>PVP</b>	<i>Polyvinyl pyridine</i>
<b>Q</b>	<i>Energy in the DSC thermogram</i>
<b>QD</b>	<i>Quantum dot</i>
<b>QD<sub>p</sub></b>	<i>PS-MA-BEE capped QDs</i>
<b>QD<sub>TOPO</sub></b>	<i>TOPO capped QDs</i>
<b>QWP</b>	<i>Quarter-Wave Plate</i>
<b>R</b>	<i>Ideal gas constant</i>

---

<b>r</b>	<i>Fresnel's reflection coefficient</i>
<b>R</b>	<i>Total reflection coefficient</i>
<b>R(t<sub>i</sub>)</b>	<i>Weighted residuals</i>
<b>RCA</b>	<i>Radio Corporation of America</i>
<b>R<sup>DD</sup></b>	<i>Förster radius for donor-donor energy transfer</i>
<b>RDF</b>	<i>Radial Distribution Function</i>
<b>R<sup>DT</sup></b>	<i>Förster radius for donor-trap energy transfer</i>
<b>R<sub>g</sub></b>	<i>Radius of gyration / Flory's radius</i>
<b>RGO</b>	<i>Reduced Graphene Oxide</i>
<b>RNA</b>	<i>Ribonucleic acid</i>
<b>rpm</b>	<i>Revolutions per minute</i>
<b>S</b>	<i>Solid phase</i>
<b>S</b>	<i>Spreading coefficient</i>
<b>S(t)</b>	<i>Contribution from sparse regions of immobilized QDs to the PL decay</i>
<b>SEI</b>	<i>Secondary Electron Image in FE-SEM</i>
<b>SEM</b>	<i>Scanning Electronic Microscopy</i>
<b>Shift<sub>IRF</sub></b>	<i>Time shift between IRF and decay</i>
<b>S<sub>i</sub></b>	<i>Sensitivity atomic factor of the component i</i>
<b>SMU</b>	<i>Source Measure Unit in conductivity measurements</i>
<b>SWNT</b>	<i>Single-Wall Carbon Nanotube</i>
<b>T</b>	<i>Temperature</i>
<b>T</b>	<i>Transmittance</i>
<b>t</b>	<i>Film thickness in conductivity measurements</i>
<b>t</b>	<i>Time</i>
<b>TCSPC</b>	<i>Time-Correlated Single Photon Counting</i>
<b>TEM</b>	<i>Transmission Electronic Microscopy</i>
<b>T<sub>g</sub></b>	<i>Glass transition temperature</i>
<b>TOP</b>	<i>Triethylphosphine</i>
<b>TOPO</b>	<i>Triethylphosphine oxide</i>

---

<b>TOPSe</b>	<i>Trioctylphosphine selenide</i>
<b>TTTR</b>	<i>Time-Tagged Time-Resolved mode</i>
<b>U</b>	<i>Deformation amplitude (strain)</i>
<b>UV</b>	<i>Ultraviolet</i>
<b>UV-vis</b>	<i>Ultraviolet-Visible</i>
<b>V</b>	<i>Surface potential</i>
<b>V</b>	<i>Voltage difference between the inner probes</i>
<b>V(z)</b>	<i>Potential energy</i>
<b>W</b>	<i>Weight</i>
<b>w</b>	<i>Film width in conductivity measurements</i>
<b>X<sub>i</sub></b>	<i>Mole fraction of component i</i>
<b>XPS</b>	<i>X-Ray Photoelectron Spectroscopy</i>
<b>Z</b>	<i>Atomic number</i>
<b>z</b>	<i>Distance between probe and sample in AFM measurements</i>
<b>β</b>	<i>Phase thickness of the film</i>
<b>Γ</b>	<i>Surface concentration</i>
<b>Γ*</b>	<i>Overlap surface concentration</i>
<b>γ</b>	<i>Surface tension</i>
<b>γ<sub>0</sub></b>	<i>Surface tension of the liquid subphase</i>
<b>γ<sub>i/j</sub></b>	<i>Interfacial tension between the components i and j</i>
<b>Δ</b>	<i>Relative phase change</i>
<b>δ</b>	<i>Change of phase between the parallel and perpendicular components</i>
<b>Δℓ</b>	<i>Film thickness</i>
<b>ΔQ</b>	<i>Derivate of energy in the DSC thermogram</i>
<b>ΔV<sub>F</sub></b>	<i>Surface potential final</i>
<b>Δπ</b>	<i>Surface pressure decrease during shearing</i>
<b>Δσ<sub>k</sub></b>	<i>Amplitude of the k-order harmonics / Fourier coefficients</i>
<b>ε</b>	<i>Dynamic elasticity</i>
<b>ε</b>	<i>Electric permittivity of the medium</i>

---

$ \varepsilon $	<i>Dilatational modulus</i>
$\varepsilon_0$	<i>Equilibrium surface elasticity</i>
$\varepsilon_0$	<i>Electric permittivity of air</i>
$\varepsilon_i$	<i>Electric permittivity of the medium "i"</i>
$\theta$	<i>Contact angle between the subphase and the Wilhelmy plate</i>
$\theta_B$	<i>Brewster angle</i>
$\theta_i$	<i>Incident angle</i>
$\theta_r$	<i>Refracted angle</i>
$\kappa$	<i>Conductivity</i>
$\kappa$	<i>Dilatational viscosity</i>
$\lambda$	<i>Wavelength</i>
$\mu$	<i>Blinking coefficient in QDs</i>
$\mu_i$	<i>Dipolar moment (component i)</i>
$\mu_n$	<i>Normal component of the dipole moment per adsorbed molecule (Kelvin Probe)</i>
$\mu^\alpha$	<i>Dipole moment contribution in the air/film interface</i>
$\mu^\beta$	<i>Dipole moment contribution in the film/water interface</i>
$\nu$	<i>Flory's scaling exponent</i>
$\xi$	<i>Correlation length</i>
$\Pi$	<i>Osmotic pressure</i>
$\pi$	<i>Surface pressure</i>
$\pi_1$	<i>Initial surface pressure in an oscillatory experiment</i>
$\pi_{\text{end}}$	<i>Final surface pressure reached by monolayer relaxation after a shearing experiment</i>
$\pi_f$	<i>Final surface pressure reached by monolayer relaxation after a step-compression experiment</i>
$\pi_s$	<i>Final surface pressure in an oscillatory experiment</i>
$\pi_\perp$	<i>Surface pressure measured perpendicular to the trough barriers</i>
$\pi_{//}$	<i>Surface pressure measured parallel to the trough barriers</i>

---

$\rho_D$	<i>Number density of donors</i>
$\rho_T$	<i>Number density of traps</i>
$\sigma$	<i>Relative contribution to the PL decay</i>
$\sigma$	<i>Standard deviation</i>
$\sigma$	<i>Surface density of charge in the Kelvin Probe</i>
$\sigma_0$	<i>Amplitude of the stress response in oscillatory experiment</i>
$\sigma_0$	<i>Relaxation amplitude</i>
$\tau$	<i>Relaxation time</i>
$\tau_0$	<i>Time resolution of the TCSPC</i>
$\tau_{AV}$	<i>Average lifetime</i>
$\tau_D$	<i>Donor lifetime in QDs</i>
$\tau_i$	<i>Lifetime of the <math>i^{\text{th}}</math> decay component</i>
$\overline{\tau_i}$	<i>Average of the relaxation times corresponding to the process "i"</i>
$\tau^I, \tau^{II}, \dots$	<i>Average lifetime after the first exposure (I), the second (II),...</i>
$\tau_i^j$	<i>Average lifetime where <math>i</math> is the time range evaluated and <math>j</math> is the number of exposure</i>
$\tau_r$	<i>Radiative relaxation (recombination) lifetime</i>
$\phi$	<i>Material work function</i>
$\phi_i$	<i>Angles of incidence and refraction in Fresnel equation</i>
$\varphi$	<i>Phase lag angle</i>
$\chi^2$	<i>Reduced chi-squared function</i>
$\Psi$	<i>Relative amplitude change</i>
$\Psi_0$	<i>Surface potential contribution of the double-layer electric formed below the interface</i>
$\omega$	<i>Angular velocity / frequency</i>
$\mathfrak{R}$	<i>Reflectance</i>

**Resumen**



## Índice

<b>I. Introducción</b>	<b>III</b>
<b>II. Objetivos</b>	<b>IV</b>
<b>III. Métodos y Técnicas Experimentales</b>	<b>IX</b>
III.1. Materiales y Reactivos	X
III.2. Técnicas Experimentales	XI
<b>IV. Monocapas de Polímeros</b>	<b>XVI</b>
IV.1. Monocapas del Polímero PS-MA-BEE	XVII
IV.2. Monocapas del Polímero PS-b-MA	XVII
<b>V. Preparación y Propiedades de Películas de Puntos Cuánticos de CdSe</b>	<b>XVIII</b>
V.1. Preparación de las Películas de Langmuir-Blodgett de QD/PS-MA-BEE	XIX
V.2. Propiedades Dinámicas de las Monocapas mixtas QD/PS-MA-BEE	XXIII
V.3. Propiedades Fotoluminiscentes de las Películas LB de QD/PS-MA-BEE	XXIV
<b>VI. Grafeno obtenido químicamente</b>	<b>XXVI</b>
VI.1. Obtención y Deposición de RGO	XXVII
<b>VII. Conclusiones</b>	<b>XXX</b>
<b>VIII. Bibliografía</b>	<b>XXXVII</b>





## I. Introducción

En los últimos años, el desarrollo y el estudio de los nanomateriales ha centrado la atención de los científicos para utilizarlos a modo de piezas que conforman un material en busca de nuevas propiedades para aplicaciones tecnológicas y biológicas. El reducido tamaño de los materiales conduce a propiedades únicas que permiten la construcción de pequeños dispositivos que van desde nanómetros a unos pocos micrómetros (miniaturización). Dentro de este campo uno de los temas más importante es el control del tamaño y la forma de estas estructuras con el fin de poder utilizarlos. En este sentido, dos de los retos en estos momentos son el conocimiento y la comprensión de la formación de estructuras para modular la arquitectura del sistema formado por nanomateriales en busca de la modulación de sus propiedades.

En algunas aplicaciones, como la construcción de dispositivos optoelectrónicos tales como sensores, dispositivos emisores de luz (LEDs) o células fotovoltaicas, los nanomateriales se depositan sobre sólidos. En estos casos es necesario el desarrollo de una metodología adecuada para lograr un buen recubrimiento, evitar la aglomeración en 3D del material y permitir la variación de la densidad, separación y disposición de los nanomateriales. Un método eficaz y ventajoso para diseñar sobre una superficie a escala nm- $\mu$ m sin el uso de procesos litográficos, es el auto-ensamblaje. Se trata de una técnica de bajo coste, escalable a grandes áreas, que permite el procesamiento en disolución y no requiere de equipos sofisticados. En el auto-ensamblaje, el comportamiento del nanomaterial en la interfase, en la que se dispone, juega un papel importante. Así, para obtener una buena calidad o para optimizar la formación del ensamblado, es importante entender el mecanismo o fuerzas implicadas en el proceso de auto-ensamblado. Por lo tanto, el estudio del comportamiento de los nanomateriales en las interfases, mediante las propiedades de equilibrio y dinámicas, es el punto de partida para lograr la modulación del ensamblado. En este sentido, el objetivo

general de esta tesis es estudiar el proceso de auto-ensamblaje de tres nanomateriales diferentes en la interfase aire-agua y sobre sólidos. Los sistemas propuestos son polímeros, puntos cuánticos (QDs) de CdSe y grafeno obtenido químicamente. El aspecto común entre ellos es el uso de las técnicas Langmuir y Langmuir-Blodgett (LB) para evaluar el efecto de las propiedades de equilibrio y dinámicas en su proceso de auto-ensamblaje. Estas técnicas permiten llevar a cabo el proceso de auto-ensamblaje de los diferentes nanomateriales en la interfase aire-agua bajo condiciones controladas y reproducibles. La técnica de LB fue elegida debido a que ha demostrado ser un método versátil e interesante para obtener películas delgadas permitiendo un control sobre la concentración superficial que puede ser fácilmente modificada mediante la compresión o expansión de la película utilizando las barreras. Además, algunos procesos de secado que se han observado en la preparación de las películas LB podrían ser utilizados para diseñar estructuras en la nanoescala.<sup>[1-3]</sup>

## II. Objetivos

La primera parte del trabajo se enfocó en el estudio de películas delgadas de polímeros. La investigación sobre películas delgadas de polímero ha revelado que varias propiedades físicas como inestabilidades inesperadas, conformaciones de cadena, procesos de secado o variaciones en la temperatura de transición vítrea, presentan características muy diferentes del comportamiento en 3D, con implicaciones importantes para la mayoría de aplicaciones tecnológicas basadas en películas de tamaño nanométrico.<sup>[4]</sup> A pesar del extenso trabajo de investigación existente, todavía no se ha alcanzado una comprensión clara de las propiedades de las películas delgadas de polímeros. Es por ello que, con el fin de preparar películas de buena calidad para que puedan utilizarse en la construcción de dispositivos, es necesario estudiar las propiedades de equilibrio y dinámicas de las monocapas precursoras de las películas LB. Así, el objetivo fue estudiar películas de polímeros derivados del estireno-anhídrido maleico ya que estos polímeros han

demostrado potenciales aplicaciones en la fabricación de guías ópticas de onda, películas resistentes a haces de electrones y fotodiodos.<sup>[5, 6]</sup> Los polímeros seleccionados fueron dos copolímeros de bloque estireno-b-anhídrido maleico-b-ácido 4-etoxi-4-oxo-2-butenoico-cumeno, PS-MA-BEE, y estireno-b-anhídrido maleico-cumeno, PS-b-MA, que podrían utilizarse para la fabricación de dispositivos electrónicos moleculares. Además, debido a que las películas de polímero están expuestas a perturbaciones externas el estudio de la reología interfacial es importante. Las propiedades de estabilidad de las películas son relevantes en aplicaciones tales como los procesos de revestimiento o adhesión.

En este sentido, el objetivo fue estudiar el efecto de la adición de electrolitos inertes en la subfase acuosa, sobre las que se depositan las monocapas de polímero, y la temperatura sobre las propiedades de equilibrio y dinámicas de las monocapas de Langmuir de los dos polímeros seleccionados. Además, con el propósito de analizar la influencia de diferentes factores como la composición de la subfase, la temperatura y la naturaleza del polímero en la formación de la película se han caracterizado por diferentes técnicas películas LB preparadas a partir de monocapas de polímero sobre diferentes sustratos.

Las películas de puntos cuánticos hidrófobos de CdSe fue el siguiente sistema estudiado. Estas nanopartículas presentan atractivas aplicaciones ópticas en la fabricación de células solares o LEDs debido a su modulable banda prohibida de energía. Los QDs presentan propiedades opto-electrónicas dependientes del tamaño que permiten modular el solapamiento de la absorción con el espectro solar en dispositivos fotovoltaicos o mejorar el rendimiento de emisión produciendo luz blanca (o de color) en LEDs. Las ventajas ópticas más importantes son un espectro de absorción amplio y continuo (UV-IR lejano), un estrecho espectro de emisión cuya posición máxima depende del tamaño del QD, propiedades físico-químicas afectadas por la naturaleza del ligando y alta estabilidad a la luz. Sin embargo, las aplicaciones de dispositivos opto-electrónicos

basados en QDs a menudo requieren la deposición de un gran número de partículas en un ensamblado de arquitectura controlable para evitar el deterioro del rendimiento cuántico de la película formada. Es por ello que el control del espesor y la uniformidad en el procesamiento de las películas de QDs ensamblados son factores determinantes para las propiedades de emisión de las películas.<sup>[7-10]</sup> Algunos estudios teóricos sugieren que las interacciones entre las partículas y un material auto-ensamblado pueden producir estructuras ordenadas.<sup>[11]</sup> Por otro lado, se ha observado que los copolímeros de bloque auto-ensamblan espontáneamente formando estructuras del orden de decenas nanómetros de longitud, y que estas estructuras pueden ser transferidas a sustratos mediante métodos como LB o recubrimiento por inmersión en disolución.<sup>[12]</sup> Algunas investigaciones revelaron que la organización de las nanopartículas está dirigida por las interacciones moleculares entre los copolímeros de bloque y las nanopartículas que constituyen las monocapas mixtas en la interfase aire-agua.<sup>[13,14]</sup> A pesar de algunos resultados exitosos, es necesario dedicar más esfuerzos que permitan desarrollar estructuras nanométricas que puedan proporcionar nuevas propiedades asociadas con la reducción del tamaño de los materiales.<sup>[15]</sup> Así, el objetivo de este trabajo fue utilizar la capacidad de los copolímeros de auto-ensamblar en la interfase aire-agua para modular la organización de QDs formando sistemas híbridos mediante la técnica de LB. Así, este trabajo se centra en el proceso de auto-ensamblaje de QDs de CdSe sobre sustratos sólidos asistido por el polímero PS-MA-BEE. Se exploraron diferentes estrategias que utilizan la metodología LB como técnica de deposición y el polímero PS-MA-BEE para asistir el auto-ensamblaje de los QDs sobre el sólido. Por un lado, la película LB de polímero fue empleada para modificar las propiedades superficiales del sustrato y por otro, el polímero asiste la formación de la monocapa de Langmuir de los QDs. En esta última estrategia, el polímero se mezcló con las nanopartículas fabricando monocapas mixtas de Langmuir con diferentes composiciones. Para comprender la morfología de las películas se estudiaron las propiedades de equilibrio y dinámicas de estas monocapas mixtas de Langmuir de QD/polímero. De esta

manera, también se analizó la influencia de la concentración de polímero y la naturaleza del ligando de las nanopartículas en la morfología de las películas. El papel del ligando de los QDs se estudió mediante el intercambio del ligando procedente de la síntesis orgánica de los QDs, óxido de trioctilfosfina (TOPO), por el polímero PS-MA-BEE.

El estudio de las propiedades dinámicas es importante para asegurar un buen procesado y la fiabilidad de las películas mixtas QD/polímero para la construcción y el funcionamiento de dispositivos.<sup>[16]</sup> Además, en monocapas de nanopartículas preparadas por compresión llevan generalmente a la formación de estados metaestables. Una manera de evitar estos estados y promover la formación de películas más ordenadas y homogéneas es la aplicación de sucesivos ciclos de compresión y expansión.<sup>[17]</sup> En este sentido, la interface aire-agua (balanza de Langmuir) se ha propuesto como una buena plataforma para llevar a cabo el estudio de las propiedades dinámicas de películas delgadas. En este campo, aún quedan aspectos por estudiar con monocapas de nanopartículas, debido a la complejidad de la recogida e interpretación de los datos experimentales. Los estudios disponibles se centran principalmente en el estudio de las nanopartículas.<sup>[17-19]</sup> Por otra parte, hasta donde alcanza nuestro conocimiento, en sistemas mixtos sólo existen estudios experimentales realizados con tensioactivos y nanopartículas.<sup>[20]</sup> En el caso de sistemas de nanopartículas con polímeros existen algunos trabajos teóricos sobre la reorganización y la dinámica de estos sistemas.<sup>[21-23]</sup> En este sentido, nuestro objetivo es estudiar la influencia de la cizalla sobre la morfología de la película de QD/PS-MA-BEE y los procesos dinámicos implicados en la reorganización de estas monocapas que se produce después del cizallamiento.

Por otra parte, como las propiedades ópticas de los QDs son relevantes para su aplicación, se analizaron las propiedades fotofísicas de las películas LB de QD/polímero sobre sólidos por medio de la técnica de fluorescencia resuelta en

el tiempo (FLIM). El objetivo de este estudio fue evaluar el efecto de la disposición de los QDs en las películas y el papel del ligando en sus propiedades de fotoluminiscencia. La técnica FLIM fue seleccionada porque presenta una alta sensibilidad a cambios superficiales y ambientales.<sup>[24]</sup>

En último sistema objeto de estudio fue grafeno obtenido químicamente. El grafeno ha recibido una gran atención debido a sus extraordinarias propiedades mecánicas y eléctricas.<sup>[25]</sup> Estas propiedades notables hacen al grafeno y sus derivados candidatos prometedores para la fabricación de dispositivos electrónicos y como partículas de refuerzo en materiales compuestos con aplicaciones en medicina.<sup>[26]</sup> El éxito del grafeno en aplicaciones tecnológicas está condicionado por la disponibilidad de métodos de producción que permitan obtener grandes cantidades de material sintético a bajo coste. Se han propuesto varios métodos con un elevado coste, crecimiento epitaxial, exfoliación micromecánica, deposición química de vapor, que consiguen las mejores propiedades del material, pero hoy en día la expectativa se centra en el procesado químico en disolución que proporciona material a bajo coste. Este método está basado en la exfoliación del grafito mediante su oxidación química y posterior reducción para recuperar la estructura  $Csp^2$  del grafito. Además es necesaria la deposición sobre sólidos del material obtenido. Es por ello que los esfuerzos se están centrando en el desarrollo de procesos químicos y de deposición para conseguir láminas de buena calidad (grado de reducción alto y pocos defectos estructurales) y una adhesión controlable sobre sólidos. Sin embargo, la oxidación química altera la estructura electrónica del grafeno mediante la introducción de grupos que contienen oxígeno en la red, que no pueden ser completamente eliminados por reducción química. Además, la tendencia del óxido de grafito reducido (RGO) a aglomerarse hace su procesamiento más complicado. Con el fin de evitar esto, se ha propuesto la funcionalización del óxido de grafito con diferentes estabilizadores, tales como los tensioactivos iónicos.<sup>[27]</sup> Asimismo, debido a que las propiedades más importantes están asociadas al grafeno con

pocas capas ( $\leq 5$  capas), es importante un control en el espesor de la película. En este escenario, el objetivo que se propone es desarrollar una ruta químico-coloidal donde la reducción química es asistida por un tensioactivo zwitteriónico, 11,3-(dimetil-dodecilamonio)-propanosulfonato (DDPS), con el fin de mejorar el grado de reducción y la reparación de defectos alcanzado por los agentes reductores y, además, funcionalizar el RGO obtenido. Esta opción se basa en la mayor adsorción que presentan estos tensioactivos en las superficies de grafito frente a los iónicos. Además, esta funcionalización puede permitir unir cationes metálicos o polímeros para la construcción de nanocompuestos con posibles aplicaciones.<sup>[28,</sup>  
<sup>29]</sup> Por otro lado, el tensioactivo también puede modular el auto-ensamblaje de las láminas en la interfase aire-agua propuesta como una buena plataforma para estudiar los derivados de grafeno ya que presentan una alta superficie específica. Así, los objetivos de este trabajo son desarrollar y comprobar la nueva ruta sintética y el análisis de la calidad del material obtenido. Por medio de diferentes técnicas, tales como espectroscopia fotoelectrónica de rayos X, espectroscopia Raman, y medidas de conductividad se evaluó el efecto del tensioactivo sobre el grado de reducción y reparación de defectos para dos agentes de reducción diferentes: hidracina y vitamina C. Además, como la transferencia del material sobre sólidos de manera controlable también es importante para la caracterización del material y su aplicación, en este trabajo se ha propuesto la técnica de LB para llevar a cabo la deposición de este material sobre silicio multicristalino. De este modo, se estudió la influencia de las propiedades del material en el ensamblaje de las láminas depositadas sobre silicio mediante la técnica de LB.

### III. Métodos y Técnicas Experimentales

En esta sección se exponen las características de los reactivos empleados, junto con la metodología, las condiciones experimentales y la instrumentación principal que han sido necesarias para el desarrollo del presente trabajo.



### III.1. Materiales y Reactivos

Los polímeros empleados son el copolímero de bloque estireno -b- anhídrido maleico -b- ácido 4-etoxi-4-oxo-2-butenoico- cumeno ( $M_r = 2.5$  kDa; relación grupos ácido y éster 1:1), PS-MA-BEE, y el copolímero de bloque estireno-b-anhídrido maleico ( $M = 1.9$  kDa, 75%w estireno), PS-b-MA, ambos suministrados por Sigma Aldrich<sup>®</sup>.

Los puntos cuánticos (QDs) de CdSe fueron sintetizados partiendo de CdO (99.99%) y Se (99.99%) en polvo utilizando como estabilizante óxido de trioctilfosfina y octadeceno como disolvente de acuerdo a la síntesis propuesta por otros autores.<sup>[30]</sup> En el estudio de las monocapas de estas nanopartículas también fue utilizado el óxido de trioctilfosfina (TOPO, > 99%). Los reactivos fueron suministrados por Sigma Aldrich<sup>®</sup>.

El óxido de grafito (GO) fue preparado a partir de láminas de grafito (Qingdao super grafito, LTD. 99.02C) siguiendo el método de Hummers empleando como oxidantes  $H_2SO_4$ ,  $KMnO_4$  y  $H_2O_2$ ,<sup>[31]</sup> pero empleando un tiempo de oxidación mayor, aproximadamente 12 h. Para su extracción y purificación se llevó a cabo un proceso de centrifugación.<sup>[32]</sup> Otros compuestos empleados en la reducción química del GO fueron, la vitamina C (L-ácido ascórbico, purísimo), hidracina (80%w) y el tensioactivo zwitteriónico 11,3-(dimetil-dodecilamonio)-propanosulfonato, DDPS, ( $M_m = 335.55$ ) suministrados por Sigma Aldrich<sup>®</sup>. El tensioactivo fue purificado previo a su utilización por sucesivas recristalizaciones en propanol.<sup>[33]</sup>

El cloroformo, empleado como disolvente para la preparación de las disoluciones, es de calidad PAI, filtrado y suministrado por la casa comercial Sigma Aldrich<sup>®</sup>. El agua utilizada como subfase en las monocapas, calidad reactiva, está desionizada a través del sistema Rios de Millipore<sup>®</sup> y posteriormente tratada con un sistema Milli-Q de la misma casa comercial y presenta una resistividad inferior a  $18.2 \mu\Omega \text{ cm}^{-1}$ . En el caso de las subfase iónica fue empleado nitrato de magnesio hexahidratado ( $Mg(NO_3)_2 \cdot 6 H_2O$ , 99%, Sigma Aldrich<sup>®</sup>).

Los sustratos utilizados fueron escogidos atendiendo a la aplicación posterior, concretamente la técnica de medida: AFM, elipsometría, Raman, FLIM o TEM. De este modo se emplearon como sustratos para la deposición de Langmuir-Blodgett: mica (grado V1, TedPella<sup>®</sup>), obleas de silicio (100) (SiO<sub>2</sub> nativo, Siltronix), obleas de silicio (SiO<sub>2</sub> 300nm térmicamente crecido y As-dopado, Graphene Industries), discos de cuarzo (TedPella<sup>®</sup>) y rejillas de cobre recubiertas con Formvar<sup>®</sup>-carbón (Servicio de Microscopía).

### III.2. Técnicas Experimentales

A continuación se exponen brevemente las principales técnicas utilizadas en la investigación, centrándonos en los equipos, el tipo de medidas realizadas y las condiciones de trabajo.

**Balanzas de Langmuir y Langmuir-Blodgett.** Los equipos empleados para la realización de las isothermas presión superficial-concentración, los estudios dinámicos y la deposiciones sobre sólidos, fueron dos balanzas de teflón modelos Mini y Standard (KSV, Finlandia) colocadas sobre una mesa antivibraciones. Las disoluciones de los diferentes compuestos fueron depositadas sobre la subfase empleando una jeringa Hamilton (precisión  $\pm 1 \mu\text{L}$ ). El modo de preparación de las monocapas fue por adición y por compresión. En el primer caso, la modificación de la concentración superficial se realiza mediante la deposición de cantidades sucesivas del compuesto (área constante de balanza). La segunda consiste en cambiar el área disponible con el movimiento de las barreras tras la deposición de una cantidad de material determinada. Para la medida de la presión superficial se utiliza una placa Pt-Wilhelmy, colocada en la interfase aire-líquido, conectada a una electrobalanza. La regulación de la temperatura de la subfase se controla a través de una sonda, regulándose mediante un encamisado situado en la parte inferior conectado a un criostato Lauda Ecoline RE-106. Las deposiciones Langmuir-Blodgett fueron llevadas a cabo en la balanza Standard. La monocapa fue transferida por compresión, con el sustrato previamente sumergido en la

subfase, levantando el substrato a una velocidad de  $1-5 \text{ mm min}^{-1}$ . La velocidad de compresión oscila entre  $5-50 \text{ mm min}^{-1}$ , dependiendo del tipo de material depositado.

En los estudios dinámicos de monocapas insolubles se perturba el sistema en equilibrio. Una opción para perturbar la monocapa son los experimentos de relajación, que consisten en aplicar una deformación al sistema y analizar la respuesta de éste mediante el estudio de la relajación de las tensiones que actúan sobre el mismo registrando la variación de la presión superficial con el tiempo. Según el tipo de deformación aplicada se distinguen dos tipos de experimentos: los de deformación súbita y los de deformación sinusoidal (barreras oscilantes).<sup>[34]</sup> En los experimentos de deformación súbita las barreras se desplazan con un movimiento rápido de las barreras (tiempo  $< 2 \text{ s}$ ) modificando el área disponible en la monocapa hasta alcanzar una deformación de área determinada. Durante la compresión el sistema pierde la situación de equilibrio y se produce un aumento en la presión superficial. Una vez cesa la compresión comienza la relajación de tensiones en la monocapa disminuyendo la presión superficial hasta que se alcanza un valor constante. La curva de relajación es válida si el valor de presión superficial alcanzado en la relajación se corresponde con el valor de presión en equilibrio para el área final. Por otro lado, los experimentos de deformación sinusoidal consisten en la deformación sinusoidal en función del tiempo del área disponible en la monocapa. Para llevarlos a cabo se programan movimientos oscilatorios de las barreras, manteniendo la frecuencia constante. De modo que, mediante el análisis de la respuesta de la presión superficial a distintos cambios de área, puede determinarse además de las propiedades viscoelásticas de la monocapa, el margen de área en el cual la respuesta del sistema es lineal.

**Potencial superficial.** Se trata de una magnitud que da información no solo de la estructura de la doble capa eléctrica, si la hubiera, del material adsorbido en la interfase sino también de la orientación de las moléculas en la interfase. El

método empleado en este trabajo para medir el potencial superficial es la sonda Kelvin (SPOT 1, KSV). Su funcionamiento está basado en la variación de la capacidad del condensador formado entre un electrodo metálico colocado a unos 2 mm de la superficie y otro de referencia sumergido en la subfase. El potencial superficial de las monocapas es determinado en relación al potencial superficial de la subfase. El equipo empleado permite obtener valores de potencial superficial con una precisión de 20 mV.

**Microscopia de ángulo Brewster (BAM).** Las monocapas de Langmuir fueron visualizadas con un microscopio de ángulo Brewster Optrel BAM 3000 (KSV) equipado con un laser de He-Ne de 10 mW de potencia (632.8 nm) que incide sobre la interfase aire-agua con el ángulo Brewster del agua, 53.15°. El principio de funcionamiento se basa en el cambio en el índice de refracción, y por tanto, en el cambio en el ángulo Brewster que se origina cuando una sustancia se deposita en la interfase aire-agua para formar la monocapa y que produce la reflexión de la luz. El microscopio está equipado con una cámara digital (Kam Pro-02, (768 X 494 pixels), EHD). Las imágenes fueron tomadas con un objetivo 5x (tamaño de imagen 800x600  $\mu\text{m}$ ) de la casa comercial Mitutoyo (Japón).

**Microscopia de fuerza atómica (AFM).** Las imágenes de las películas Langmuir-Blodgett depositadas sobre sustratos de mica o silicio fueron obtenidas en el modo de fuerza repulsiva constante. El equipo cuenta con una punta de silicio piramidal (radio  $< 20$  nm) y un soporte rectangular de nitruro de silicio (constante de elasticidad  $0.73 \text{ N m}^{-1}$ , Olympus OMCL-RC800PSA) de altura 100  $\mu\text{m}$ . El rango de frecuencias de escaneo utilizado fue 0.5-2.0 Hz por línea. Las medidas fueron llevadas a cabo en condiciones ambientales. Las imágenes fueron obtenidas con el programa WSXM 5.0.<sup>[35]</sup>

**Microscopia electrónica de transmisión (TEM) y de barrido (SEM).** Las imágenes de microscopia electrónica de transmisión (TEM) de las películas LB fueron tomadas con un microscopio ZEISS EM 902 utilizando un voltaje de 80

kV y rejillas de cobre como sustrato. También se llevaron a cabo medidas de microscopía electrónica de barrido de emisión de campo (FE-SEM) con un microscopio Nova NanoSEM 230-FEI utilizando el detector de alta resolución en alto vacío con un voltaje de aceleración de 10 kV.

**Elipsometría.** Esta técnica fue empleada para la determinación del índice de refracción y espesor de películas LB depositadas sobre obleas de silicio mediante medidas realizadas a distintos ángulos de incidencia. El equipo utilizado fue un elipsómetro de tipo anulación modelo EP<sup>3</sup> (Nanofilm, Alemania). Para llevar a cabo las medidas, los sustratos son colocados en el plato provisto de goniómetro, se hace incidir el haz laser de Nd-YAG ( $\lambda = 532$  nm) sobre las películas LB y que posteriormente pasa por un analizador y un detector. A través de la técnica se determinan los valores de los ángulos elipsométricos  $\Delta$  y  $\Psi$  que en un posterior análisis de datos se ajustan a un modelo de interfase concreto. En nuestro caso la interfase se interpreta con un modelo de tres capas (silicio, óxido de silicio y monocapa).<sup>[36]</sup> La precisión en la medida de los ángulos elipsométricos es *ca.* 0.0006.

**Microscopía Raman.** Las medidas de dispersión Raman sobre películas LB depositadas en obleas de silicio fueron llevadas a cabo en condiciones ambientales con un espectrómetro micro-Raman (Horiba Jobin-Yvon Labram RH) empleando un objetivo 100x (foco laser  $\sim 1\mu\text{m}^2$ ), una resolución espectral  $\sim 2$   $\text{cm}^{-1}$  y una longitud de onda de excitación del laser de 632.81 nm. La calibración del equipo se realizó comprobando la banda Rayleigh y la banda del silicio a 0 y 520.7  $\text{cm}^{-1}$ , respectivamente. La muestra fue escaneada con una resolución espacial de aproximadamente 0.5  $\mu\text{m}$ , con un tiempo de adquisición de unos pocos minutos en cada punto así como una energía de excitación por debajo de 1 mW para evitar el calentamiento de la zona.

**Espectroscopia fotoelectrónica de rayos X (XPS).** El espectro de fotoelectrónico de rayos X de muestras en polvo fueron obtenidos en un

espectrómetro VG Escalab 200 R (Fisons Instruments) trabajando a una energía de paso en analizador de 20 eV. Este equipo cuenta con una fuente de  $MgK\alpha$  ( $h\nu = 1253.6$  eV) y un analizador hemisférico de electrones. La presión residual en la cámara de análisis fue mantenida por debajo de  $2 \cdot 10^{-7}$  Pa durante la recogida de datos.

**Medidas de conductividad: Estación de puntas y Haz de iones focalizado (FIB)/ microscopia electrónica de barrido (SEM).** Para realizar las medidas de conductividad de los óxidos reducidos de grafeno se prepararon películas finas sobre filtros de PVDF (0.2  $\mu\text{m}$  tamaño de poro, Filter-lab) por filtración y posterior lavado con agua y metanol para eliminar el restos de agentes reductores y/o tensioactivo. Para realizar las medidas cuatro electrodos de oro fueron colocados sobre la superficie de la muestra y conectados en una mesa de puntas (Keithley 4200 SCS).<sup>[37]</sup> Para complementar las medidas de conductividad fue necesario determinar el espesor de las películas combinando FIB y SEM para cortar transversalmente la muestra y tomar una imagen de la misma.<sup>[38]</sup>

**Microscopia confocal de tiempos de vida de fluorescencia (FLIM).** Medidas de fotoluminiscencia superficial fueron llevadas a cabo con un microscopio de fluorescencia resuelta en el tiempo (MicroTime 200, PicoQuant GmbH).<sup>[39]</sup> La fuente de excitación empleada fue un laser de diodo pulsado emitiendo a 482 nm con una frecuencia de repetición de 2.5 MHz. La iluminación y recogida de luz se realiza a través de un objetivo de inmersión de agua 60x y apertura numérica 1.2 (UPLSAPO 60XW, Olympus). Las muestras son escaneadas con una estación piezométrica xy. La emisión de fluorescencia es limpiada espectralmente a través de un espejo dicróico y un filtro de paso de banda con transmisión en el intervalo 550-690 nm. Para rechazar la luz fuera de foco se utiliza un *pinhole* (estenopo) de 30  $\mu\text{m}$ . La luz emitida es detectada por un detector contador de fotones con diodo de avalancha (Perkin-Elmer) y digitalizada por un panel de control, TimeHarp 200 TC-SPC, conectado al

ordenador. La función de respuesta del instrumento tiene su máximo entorno a 1 ns, y el intervalo de tiempo de muestreo es 150 ps/canal.

Las medidas principalmente se han realizado sobre áreas ( $80 \times 80 \mu\text{m}^2$ ) compuestas por  $(256 \times 256)$  pixels. El tiempo de integración por pixel seleccionado fue de 1 ms y la energía de excitación,  $108 \text{ W cm}^{-2}$ , para minimizar efectos derivados de la exposición de la muestra en la emisión.<sup>[40, 41]</sup> El decaimiento de luminiscencia integrado sobre el área muestreada se obtiene a partir del histograma de tiempo de llegada de todos los fotones detectados. El número total de fotones detectados por imagen supera el millón de cuentas asegurando curvas de decaimiento fiables. El análisis de los datos con una función multi-exponencial fue llevado a cabo con el programa SymPhoTime. La calidad de los ajustes fue evaluada con el parámetro  $\chi^2$  y el peso de los residuales.

**Litografía por haz de electrones.** En un intento de medir la conductividad de láminas aisladas de grafeno químicamente reducido depositado sobre obleas de silicio (300 nm de  $\text{SiO}_2$ ) se llevó a cabo un procesado de la muestra. En este procesado se diseña la geometría en barra Hall de los contactos de Ti/Au (50/500 Å) mediante litografía por haz de electrones sobre una película de PMMA. Tras el revelado de la misma con disolventes (metil isobutil cetona : isopropanol) se realiza en una cámara la deposición por evaporación con un haz de electrones de los contactos metálicos. Finalmente mediante un proceso de *lift-off* con acetona se eliminan los residuos metálicos de la deposición.

#### IV. Monocapas de Polímeros

El trabajo con monocapas de polímeros se centró en el estudio del efecto de la adición de electrolitos en la subfase en las propiedades de equilibrio y dinámicas en la interfase aire-agua y en la morfología de los agregados formados en sólidos cuando las monocapas son depositadas por la técnica de Langmuir-Blodgett. Los polímeros seleccionados fueron dos copolímeros de bloque del anhídrido maleico, PS-MA-BEE y PS-b-MA, poseyendo el primero un bloque

hidrófilo adicional con un grupo ácido, permitiendo observar la influencia de la estructura del polímero en las diferentes propiedades estudiadas.

El electrolito seleccionado para el estudio fue nitrato de magnesio, debido a que los iones divalentes interactúan más fuertemente que los monovalentes con los grupos ácidos<sup>[42]</sup> y concretamente el magnesio es de interés para aplicaciones biológicas<sup>[43]</sup>.

#### **IV.1. Monocapas del Polímero PS-MA-BEE**

Se llevó a cabo el estudio de las propiedades de equilibrio mediante las isotermas de presión superficial, potencial superficial y elasticidad de equilibrio. Los resultados demostraron que las monocapas del polímero se vuelven más expandidas cuando la concentración de electrolito en la subfase aumenta y la formación de un complejo entre el catión  $Mg^{2+}$  y el grupo ácido de las moléculas de polímero. Asimismo, las propiedades dinámicas indicaron una mayor estabilidad de la monocapa con la presencia de electrolitos en la subfase.

Por otro lado, las monocapas preparadas por dos diferentes metodologías: adición y compresión, se transfirieron de la interfase aire-líquido a sustratos mediante la técnica de LB. La morfología de las películas fue analizada por AFM. Los resultados mostraron que las distintas metodologías llevan a la formación de distintas estructuras, siendo las más reproducibles aquellas obtenidas por compresión. Además, la morfología de las películas se modifica con la adición de electrolitos en la subfase. Así, en el caso de la preparación por compresión, se observaron bandas de  $\sim 8$  nm de espesor cuando la subfase es agua, y agregados circulares de  $\sim 5$  nm de espesor para el caso de la presencia del  $Mg^{2+}$ . Estos espesores fueron corroborados con medidas de elipsometría.

#### **IV.2. Monocapas del Polímero PS-b-MA**

Las propiedades de equilibrio de las monocapas de este polímero en



subfase con nitrato de magnesio, mostraron que la monocapa se vuelve más comprimida con la adición de electrolitos. La observación de un comportamiento contrario al polímero PS-MA-BEE refuerza la idea de la formación del complejo entre  $Mg^{2+}$  y el grupo ácido de dicho polímero, ya que la estructura del PS-b-MA es análoga a éste a excepción del bloque que contiene el grupo ácido.<sup>[44]</sup>

Por otro lado, se llevó a cabo la preparación de películas LB del polímero PS-b-MA con monocapas en subfase acuosa y en presencia de electrolitos. Las imágenes de AFM mostraron la formación de agregados circulares de 3-4 nm de espesor en ambos casos. Por tanto, la morfología de las películas no se modifica con la presencia de electrolitos, indicando la no interacción con el  $Mg^{2+}$  de este polímero. Sin embargo, la morfología observada es diferente que en el caso del PS-MA-BEE comparando las películas preparadas empleando agua como subfase.

El estudio de la variación del potencial superficial con la temperatura, indicó que la presencia de electrolitos en la subfase no modifica significativamente la temperatura de transición vítrea en 2D,  $\sim 295K$ . Además, las propiedades dinámicas estudiadas por encima y por debajo de dicha temperatura, mostraron un aumento en el módulo de elasticidad y la viscosidad de la monocapa en el estado vítreo.<sup>[45, 46]</sup>

## **V. Preparación y Propiedades de Películas de Puntos Cuánticos de CdSe**

Los objetivos que se pretenden en el trabajo con puntos cuánticos de CdSe son: la preparación mediante tres metodologías diferentes basadas en la capacidad de ensamblaje del polímero PS-MA-BEE de películas mixtas depositadas por la técnica de LB de los QDs y el polímero; evaluar la influencia de la aplicación de una fuerza externa como el cizallado en la interfase aire-agua en la morfología de las películas; y el estudio del efecto de la morfología de las películas en las propiedades fotoluminiscentes de los QDs.

La morfología de las películas fue analizada por AFM y TEM, mientras que el estudio de fotoluminiscencia fue llevado a cabo con la técnica de fluorescencia resuelta en el tiempo.

### V.1. Preparación de las Películas Langmuir-Blodgett de QD/PS-MA-BEE

Las metodologías desarrolladas en este trabajo son: (i) la preparación de monocapas mixtas QD/polímero mediante la co-deposición en la interfase aire-agua de una disolución en la que están mezclados ambos componentes; (ii) la preparación de bicapas, donde una película LB de polímero recubre el sólido modificando sus propiedades superficiales para mejorar el proceso de adhesión de la película LB de QDs; y (iii) se sustituye el estabilizante de los QDs, TOPO, por el polímero.

En el caso de la **co-deposición QD/PS-MA-BEE** el estudio se centró en la influencia de la composición y el estado superficial de las monocapas mixtas en la morfología de las películas. De este modo, se varió la fracción molar de polímero en la disolución de deposición,  $X_p$ , y la presión superficial de deposición de las monocapas preparadas.

Para la elección de la presión superficial para la deposición LB, se realizó un estudio previo de las isothermas de presión superficial y elasticidad de equilibrio, donde se observó que para  $X_p \geq 0.95$  las isothermas de  $\pi$  presentan un *plateau* a  $\sim 30 \text{ mN m}^{-1}$  que se corresponde con un mínimo en las isothermas de elasticidad. Este comportamiento también se observa en la monocapa del polímero por lo que se atribuye a la conformación en cepillo de las moléculas del polímero.<sup>[47]</sup> Las presiones superficiales fueron seleccionadas de acuerdo a los datos de elasticidad de equilibrio a diferentes composiciones, de modo que se pudieran analizar dos estados diferentes de la monocapa. Las presiones superficiales escogidas fueron 14 y 30  $\text{mN m}^{-1}$ , correspondientes al estado de máxima elasticidad del sistema y de

mínima elasticidad donde el polímero se encuentra en conformación de cepillo en monocapas  $X_p \geq 0.95$ .

Previamente al estudio de las películas LB mixtas QD/PS-MA-BEE, se depositaron sobre el sustrato, mica, las monocapas de los componentes puros. El análisis de las imágenes de AFM de las películas de QDs, mostró la formación de agregados e incluso de aglomerados en el caso de  $\pi = 30 \text{ mN m}^{-1}$ , indicando poca afinidad por el sustrato empleado y una gran interacción entre las partículas. Por otro lado, en el caso del polímero, dos tipos de estructuras fueron observadas: bandas de  $\sim 8\text{-}10 \text{ nm}$  de espesor ( $\pi = 14 \text{ mN m}^{-1}$ ) y una película con algunos huecos de espesor  $\sim 2 \text{ nm}$  ( $\pi = 30 \text{ mN m}^{-1}$ ). Las estructuras formadas fueron interpretadas acorde a dos procesos de secado en la interfase aire-sólido: el mecanismo espinodal, donde predominan las ondas capilares, y la nucleación y ruptura con formación de agujeros en la película, donde predominan los efectos gravitatorios.<sup>[48]</sup> Así, para el caso de la formación de bandas, son los efectos de las ondas capilares los que dominan el proceso de secado en el sólido, ya que el coeficiente de amortiguación es máximo cuando la elasticidad es mínima y viceversa, disminuye cuando aumenta la elasticidad de la película.<sup>[49]</sup> Mientras que los efectos gravitatorios promueven el crecimiento de agujeros en la película depositada a  $\pi = 30 \text{ mN m}^{-1}$ .

En el caso de las monocapas mixtas QD/PS-MA-BEE, las imágenes de AFM mostraron que la adición del polímero incluso en pequeñas cantidades mejora la adhesión de los QDs en mica. Este comportamiento puede ser debido a la interacción entre el estabilizante y el poliestireno del polímero, de modo que el grupo hidrófilo del polímero favorece la adsorción en la mica.<sup>[50]</sup>

Analizando el efecto de la composición de la película en la morfología para cada una de las presiones superficiales seleccionadas dos tendencias fueron observadas. En el caso de las películas depositadas a  $\pi = 14 \text{ mN m}^{-1}$ , para una composición  $X_p < 0.50$ , grandes dominios formando una película casi homogénea

son observados. Sin embargo, cuando la cantidad de polímero aumenta,  $X_p \geq 0.50$ , se produce una ruptura de la película formándose dominios circulares cuyo tamaño disminuye al aumentar la concentración de polímero donde las nanopartículas se sitúan en el interior de los mismos, acorde con las imágenes de TEM. Por otro lado, para las películas depositadas a  $\pi = 30 \text{ mN m}^{-1}$ , el cambio en la morfología es observado a mayores concentraciones de polímero. Así, para  $X_p < 0.95$  la estructura de las películas es análoga a las anteriores a bajas concentraciones de polímero, con grandes dominios unidos formando la película. Por contra cuando  $X_p \geq 0.95$ , las monocapas presentan un mínimo en la elasticidad correspondiente a la conformación de cepillo del polímero. En este estado superficial, las imágenes de AFM de las películas LB mostraron la formación de redes hexagonales donde el material se acumula en los bordes formando huecos en el interior. En todos los casos los perfiles de AFM indicaron espesores de 3-4 nm compatibles con el tamaño de las partículas y por tanto, de la inhibición de aglomerados en 3D.

Asimismo, cabe destacar que para ambas presiones superficiales y altas concentraciones de polímero  $X_p > 0.95$ , la morfología de las películas es completamente diferente a la correspondiente del polímero, indicando que incluso una pequeña cantidad de QDs modifica las interacciones entre las moléculas de polímero.<sup>[51-53]</sup>

Teniendo en cuenta que el estado de la monocapa es de máxima elasticidad cuando ( $\pi = 14 \text{ mN m}^{-1}$ ) y ( $\pi = 30 \text{ mN m}^{-1}$  y  $X_p < 0.95$ ), la formación de estructuras observadas está promovida por el mecanismo espinodal. Por contra cuando  $\pi = 30 \text{ mN m}^{-1}$  y  $X_p \geq 0.95$ , las monocapas están en el mínimo de elasticidad donde las ondas capilares están amortiguadas y por tanto son los efectos gravitatorios los que predominan en el proceso de secado.

La siguiente metodología empleada fue la modificación de las propiedades superficiales de la mica mediante la deposición LB de una película de polímero a

presión superficial de  $14 \text{ mN m}^{-1}$ , donde forma bandas que se extienden a lo largo del sustrato. Posteriormente, sobre la película LB de polímero se deposita la película de QDs, formándose así una **bicapa**. Para comprobar el efecto de la concentración de QDs se seleccionaron dos presiones superficiales de deposición, 9 y  $30 \text{ mN m}^{-1}$ , correspondiendo la primera al máximo en la isoterma de elasticidad. Las morfologías observadas mediante AFM y TEM, indicaron que las nanopartículas depositadas sobre el polímero forman agregados aislados e irregulares en tamaño en ambos casos, cuya población aumenta con la presión superficial de deposición. Además, al igual que ocurría en la co-deposición, se evita la formación de aglomerados en 3D de QDs sobre mica. Para interpretar estos resultados es necesario evaluar las fuerzas implicadas en el proceso de formación de la película de QDs sobre el polímero. El recubrimiento del sólido produce un aumento de su energía superficial minimizando los procesos de secado,<sup>[54, 55]</sup> de modo que el proceso de ensamblado de los QDs se relaciona con las interacciones entre las capas en contacto<sup>[56]</sup> y por tanto, la capacidad de mojado de la película que recubre el sustrato. Es por ello, que decidimos analizar el proceso mediante la determinación aproximada del coeficiente de mojado (S). Este coeficiente ha sido empleado por otros autores para evaluar la estabilidad<sup>[57]</sup> y la formación de nanoestructuras<sup>[58]</sup> en películas LB. El valor del coeficiente S determinado para el sistema PS-MA-BEE//QD es negativo, indicando interacciones débiles entre la parte hidrófoba del polímero expuesta a las partículas, PS, y el estabilizante de las mismas, TOPO, respecto a las interacciones QD-QD, de ahí, la formación de agregados.

La tercera metodología de preparación se basa en el **intercambio del estabilizante** de los QDs, TOPO, por el polímero, PS-MA-BEE, aprovechando la presencia del grupo -COOH en el polímero y la interacción de éste con la superficie metálica de la partícula, concretamente con  $\text{Cd}^{2+}$ , durante el proceso de intercambio.<sup>[8]</sup> Una vez obtenidos los QDs recubiertos con el polímero,  $\text{QD}_p$ , la sistemática de trabajo fue análoga a las anteriores, estudiando la morfología de las

películas preparadas por co-deposición con el polímero y como bicapas. En el primer caso, y a modo comparativo se prepararon películas LB de monocapas mixtas de QD<sub>p</sub> y PS-MA-BEE variando la composición de las mismas y a la presión superficial de 14 mN m<sup>-1</sup>, correspondiente al máximo de elasticidad. La morfología de las películas observada por AFM y TEM, mostró la formación de redes hexagonales y un espesor de 2-3 nm, compatible con la formación de monocapas. En este caso, dado que el polímero posee una masa molecular casi siete veces mayor que el TOPO, los efectos gravitatorios son más importantes. Por tanto, pese a encontrarse en un estado de máxima elasticidad, el mecanismo que predomina es la nucleación y crecimiento de huecos en las películas promovido por efectos gravitatorios.

Por otro lado, el estudio de las bicapas formadas por PS-MA-BEE// QD<sub>p</sub> mostró que el esparcimiento logrado es mucho mayor que en el anterior caso, ya que esta favorecido por la interacción PS//PS y por tanto tiene asociado un coeficiente de mojado próximo a cero.

## **V.2. Propiedades Dinámicas de las Monocapas mixtas QD/PS-MA-BEE**

En las metodologías planteadas, la deposición se realizó por compresión de la monocapa tras la adición del material en la interfase aire-agua. Sin embargo, este modo de preparación lleva a la deposición de sistemas metaestables.<sup>[1, 42, 59]</sup> Algunos autores han sugerido el empleo de sucesivos ciclos de compresión y expansión para inducir orden a largo y corto alcance en la reorganización de nanopartículas.<sup>[17]</sup> Así, siguiendo esta línea de investigación decidimos estudiar la morfología de las películas depositadas después de realizar 50 ciclos de cizalla con las barreras de la balanza de Langmuir. Los resultados de las imágenes de AFM y TEM indicaron que el aumento de la deformación del área durante la cizalla reduce el tamaño de los dominios formados y produce un mayor

empaquetamiento.

Por otro lado, se llevó a cabo el estudio de los procesos de reorganización involucrados en la relajación de la monocapa después de cizallarla con 50 ciclos de compresión-expansión. El análisis multi-exponencial de las curvas de relajación mostró que se trata de una dinámica compleja en la que están involucrados tres tiempos de relajación: la inercia de las barreras al parar ( $\tau_1$ ); el movimiento de los bloques formados por los QDs o los QDs y el polímero ( $\tau_2$ ); y la reorganización en el interior de estos bloques de sus componentes ( $\tau_3$ ). En el caso de las monocapas de polímero solo existen dos procesos: la inercia de las barreras ( $\tau_1$ ) y la reorganización de las moléculas de polímero ( $\tau$ ). Los datos obtenidos para los tiempos  $\tau_2$  y  $\tau_3$  con la variación de la composición de las monocapas, indicaron que para altas concentraciones de polímero,  $X_p > 0.80$ , los procesos de relajación se vuelven más lentos, siendo el efecto más acusado en el caso de la reorganización interna dentro de los bloques ( $\tau_3$ ). Este comportamiento puede estar relacionado con impedimentos debido a la presencia de la matriz polimérica. Estos impedimentos están basados en la reducción de la movilidad del polímero cuando está próximo a la nanopartícula que promueve una reorganización más estructurada de los componentes y que está acentuado cuando el tamaño de los componentes es similar.<sup>[21, 22, 60, 61]</sup> Este comportamiento también se reflejaría en el aumento del tiempo de relajación ( $\tau_3$ ) en las monocapas mixtas con alta concentración de polímero, respecto del tiempo de relajación de la monocapa de polímero.

### **V.3. Propiedades Fotoluminiscentes de las Películas LB de QD/PS-MA-BEE**

Finalmente, tras la preparación de las películas LB con las nanopartículas, se llevo a cabo su caracterización mediante el estudio de las propiedades fotoluminiscentes. El estudio se centró principalmente sobre las películas

preparadas con QDs estabilizados con TOPO y en la evaluación del efecto de la metodología de preparación, bicapas y co-deposición; la composición de las películas y la concentración de QDs en las propiedades fotoluminiscentes de las mismas mediante la técnica de fluorescencia resuelta en el tiempo (FLIM).

Las condiciones de trabajo, longitud de onda y energía de excitación y rango de longitudes de onda de recogida de la emisión, se seleccionaron, a partir de estudios preliminares, de modo que únicamente las nanopartículas fueran excitadas, se minimizaran los procesos multi-excitónicos y de exposición y se recogiera la emisión procedente de la recombinación en el interior del QD. Una vez establecidas, el estudio se enfocó en el análisis de las imágenes y las curvas de decaimiento obtenidas por FLIM para las diferentes muestras. Para interpretar las curvas de decaimiento se propuso un modelo aproximado de ajuste construido en base al análisis de las imágenes de TEM. De este modo la función de decaimiento,  $D(t)$ , está compuesta por dos términos,  $S(t)$  y  $C(t)$ , correspondientes a regiones dispersas y compactas (clústeres) de nanopartículas, respectivamente,

$$D(t) = \sigma S(t) + (1 - \sigma)C(t) \quad [\text{VIII.1}]$$

El término  $S(t)$  fue interpretado con el modelo propuesto por Tachiya-Mozumder<sup>[62, 63]</sup> mientras que el término  $C(t)$  fue adaptado del método teórico de la expansión diagramática de la función de Green desarrollada por Fayer *et al.*<sup>[64, 65]</sup>

A partir de los resultados del ajuste de las curvas de decaimiento con este modelo, concretamente de los valores de los parámetros  $\sigma$  y la concentración reducida de trampas superficiales,  $C_T$ , y el análisis de las imágenes de TEM y FLIM, se pone de manifiesto que el sistema en bicapa proporciona una mayor intensidad de emisión, una estructura más regular y con menos clústeres de QDs y una menor concentración de trampas superficiales que las películas preparadas por co-deposición.



## VI. Grafeno obtenido químicamente

En esta parte del trabajo uno de los objetivos planteados era desarrollar una nueva ruta de síntesis de óxido de grafeno reducido (RGO) partiendo de óxido de grafeno (GO) empleando tensioactivos que permitan mejorar la calidad del material obtenido e incluso funcionalizarlo. De este modo, desarrollamos una síntesis químico-coloidal empleando un tensioactivo zwitteriónico, concretamente el DDPS. La ventaja que ofrece esta estrategia es aprovechar la mayor adsorción en superficies hidrófobas como el grafito que presentan los tensioactivos zwitteriónicos frente a los iónicos,<sup>[66, 67]</sup> por lo que en principio deberían proveer una mejor funcionalización de las láminas de RGO. Además este tipo de tensioactivos presentan una mayor tolerancia a pH extremos, electrolitos fuertes y agentes oxidantes y reductores que los tensioactivos iónicos,<sup>[66]</sup> permitiendo trabajar en condiciones extremas. Por otro lado, las moléculas de DDPS unidas a las láminas de RGO pueden interactuar con cationes metálicos<sup>[28]</sup> o polímeros<sup>[68]</sup> permitiendo la formación de nanocompuestos con potenciales aplicaciones en dispositivos fotovoltaicos<sup>[28]</sup> o sensores<sup>[29]</sup>.

Para evaluar la calidad del material obtenido, RGO, utilizamos el criterio propuesto por Luo *et al.*<sup>[69]</sup> Este criterio se basa en el análisis del grado de reducción, el grado de reparación de defectos tras el proceso de reducción y la conductividad eléctrica del material gráfitico obtenido mediante las técnicas de AFM, XPS, espectroscopia UV-vis, espectroscopia Raman y medidas de conductividad eléctrica.

Para estudiar el efecto de la presencia del tensioactivo en la reducción del GO, seleccionamos dos agentes reductores con demostrada capacidad de reducción de GO: hidracina y vitamina C.<sup>[69-72]</sup> En el caso de la hidracina se trata de un reductor muy utilizado en la reducción de GO y con buenos resultados,<sup>[70-74]</sup> mientras que la vitamina C se presenta como una alternativa ecológica que además permite obtener láminas con menos defectos estructurales que con hidracina<sup>[73, 74]</sup>.

Por otro lado, otro de los objetivos planteados era la deposición controlada y reproducible del RGO evitando el apilamiento de las láminas observado con otras técnicas como el *spin-coating*<sup>[75]</sup> o el *drop-casting*<sup>[76]</sup>. Para ello, utilizamos la técnica de Langmuir-Blodgett que recientemente ha mostrado un gran control para la deposición de GO<sup>[32]</sup> y multicapas de RGO<sup>[77]</sup>. La morfología y la calidad de las láminas depositadas por LB en obleas de silicio fueron estudiadas con las técnicas de AFM, FE-SEM y espectroscopia micro-Raman.

## VI.1. Obtención y Deposición de RGO

En primer lugar, la investigación se centró en la síntesis del RGO. Para ello el material de partida empleado fue GO obtenido por oxidación de láminas de grafito llevando a cabo una pequeña modificación en el método propuesto por Hummers<sup>[31]</sup>. Con esta modificación se pretendía obtener un material más oxidado ya que, tal y como confirmaron nuestros resultados, una mayor oxidación produce también una mayor exfoliación del material. A partir del GO, el siguiente paso fue reducir el GO empleando únicamente los agentes reductores: hidracina y vitamina C de acuerdo al procedimiento descrito por otros autores.<sup>[70, 78]</sup> Antes de llevar a cabo la reducción del GO en presencia de tensioactivo, fue necesario establecer la concentración de tensioactivo adecuada. De este modo, las dispersiones de GO preparadas con una concentración de DDPS inferior a la CMC ( $1.1 \text{ mg mL}^{-1}$ )<sup>[67]</sup> no eran estables, mientras que aquellas con concentraciones de DDPS superiores a  $2 \text{ mg mL}^{-1}$  daban lugar en unos días a la aparición de precipitados. Finalmente se seleccionó una concentración de tensioactivo de  $1.7 \text{ mg mL}^{-1}$ , próxima a la CMC y que producía dispersiones claras y estables de GO durante semanas. Este resultado indica que la concentración de tensioactivo necesaria está próxima a la CMC y concuerda con resultados previos obtenidos con tensioactivos iónicos.<sup>[79]</sup>

Con el material obtenido de las síntesis, GO y RGO, se lleva a cabo un análisis del grado de reducción alcanzado mediante las diversas rutas planteadas utilizando espectroscopia UV-vis y XPS. En el caso de los espectros de absorción,

comparando los espectros para el GO y los RGOs, se observa un desplazamiento a longitudes de onda mayores de la banda de 230 nm correspondiente al GO cuando se produce su reducción con cualquiera de las metodologías propuestas. Sin embargo, el desplazamiento de la banda es mayor cuando la reducción se lleva a cabo en presencia de tensioactivo, de 264-265 nm hasta 266-268 nm, indicando que se ha alcanzado un mayor grado de reducción. Estos datos fueron corroborados con los resultados de XPS, donde los espectros  $C_{1s}$  mostraron que el porcentaje de  $C_{sp^2}$  obtenido en presencia de tensioactivo es mayor. Además el análisis de los espectros  $N_{1s}$  y  $S_{2p}$  permitió obtener más información del material obtenido. En el caso de los RGO reducidos con hidracina la presencia de una banda a  $\sim 400$  eV en el espectro  $N_{1s}$  indicó la existencia de grupos funcionales  $R-NH_2$  en las láminas de RGO.<sup>[80]</sup> Mientras que en el caso de los RGO reducidos en presencia de DDPS, los espectros  $N_{1s}$  y  $S_{2p}$  presentaban bandas adicionales en  $\sim 402$  y  $\sim 168$  eV. Comparando estas posiciones con los espectros  $N_{1s}$  y  $S_{2p}$  del tensioactivo esas energías corresponden a los grupos  $R-NH_4^+$  y  $SO_3^{2-}$ , por lo que la presencia de estas bandas demuestra que la metodología empleada en esta investigación produce la funcionalización del RGO con el DDPS. Por otro lado el análisis de los ratios O/C y N/C permitió observar que las muestras reducidas con vitamina C presentan una relación O/C mayor que las muestras reducidas con hidracina; por otra parte, la presencia del tensioactivo en la síntesis con hidracina reduce la relación N/C observada respecto a las muestras reducidas con hidracina sin el tensioactivo DDPS. Estos resultados sugieren la formación de enlaces de hidrógeno entre el producto oxidado de la vitamina C y el oxígeno residual en el RGO,<sup>[71]</sup> y por otro lado, que la presencia del tensioactivo en la síntesis con hidracina disminuye los defectos introducidos reduciendo la presencia de grupos nitrogenados producidos durante la reducción del GO con la hidracina<sup>[80]</sup>.

El siguiente paso fue la deposición mediante la técnica de Langmuir-Blodgett de láminas de RGO sobre obleas de silicio. Las dispersiones utilizadas para depositar el material sobre la interfase aire-agua se prepararon por sonicación

de RGO en cloroformo. Los mejores resultados en estabilidad y dispersión se obtuvieron utilizando tiempos de sonicación entre 90-150 min. Además, las películas depositadas a presiones superficiales superiores a  $4 \text{ mN m}^{-1}$  demostraron la formación de multicapas de láminas. Es por ello que para tener un control en el espesor, se seleccionó una presión superficial inferior para trabajar, concretamente  $1 \text{ mN m}^{-1}$ . Por otro lado, cabe destacar que para el caso del RGO obtenido con hidracina (sin DDPS) se forman agregados en la dispersión a los pocos minutos y aunque se intentó realizar la deposición, las medidas de BAM y de AFM mostraron la formación de agregados tanto en la interfase aire-agua como en el sustrato. La alternativa fue depositar GO sobre la oblea de silicio y posteriormente reducir con vapor de hidracina.<sup>[32]</sup> De este modo fue posible realizar medidas de AFM, FE-SEM y espectroscopia de micro-Raman.

La altura de los perfiles de las plaquetas determinada mediante AFM mostró que el espesor de las láminas obtenidas para el caso de la reducción con hidracina y vitamina C, eran muy similares y se encontraban entre 1.5-2 nm. Estos valores son compatibles con plaquetas formadas por 1 a 3 capas de grafeno. Sin embargo, en el caso de las láminas funcionalizadas con DDPS el espesor aumentó hasta unos 4 nm, es decir, 2.5 nm más que cuando la reducción se lleva a cabo únicamente con los agentes reductores. Esto puede ser debido a la presencia del tensioactivo unido a las láminas.<sup>[81]</sup> Por otro lado, las imágenes de AFM y FE-SEM muestran láminas encadenadas de RGO para el caso de la reducción hidracina/DDPS, que indicarían interacciones atractivas entre las láminas probablemente promovidas por la presencia del tensioactivo.

Respecto a los datos de espectroscopia Raman, el estudio se centró en la evaluación del cociente de intensidades,  $I_D/I_G$ , de las bandas D y G del espectro que se relaciona con el grado de defectos que presenta la estructura.<sup>[82]</sup> Así, un elevado valor  $I_D/I_G$  indica la presencia de grupos no reducidos o desorden en la estructura  $\text{Csp}^2$ . Comparando entre los agentes reductores, la hidracina presenta

un valor de 1.99, lo que indica un elevado número de defectos, que son probablemente debidos a la funcionalización con los grupos nitrogenados, mientras que la vitamina C con un valor de 0.67 presenta una estructura con mayores dominios  $C_{sp}^2$ . Incluso el valor obtenido para la muestra reducida con vitamina C es inferior a los datos de la bibliografía,  $I_D/I_G = 1$ ,<sup>[71, 72]</sup> indicando que partir de un GO más oxidado se alcanza un mayor tamaño de dominios  $C_{sp}^2$ . Por otro lado, la incorporación del tensioactivo en el proceso de reducción permite disminuir esta relación, y por tanto los defectos en la estructura, para el caso de la hidracina hasta un valor  $I_D/I_G = 1.45$ , mientras que se eleva a 0.92 para el caso de la reducción con vitamina C.

Por último, se realizaron medidas de conductividad eléctrica sobre películas preparadas por filtración,<sup>[37]</sup> debido a que las medidas con los nanocontactos preparados por litografía no ofrecieron resultados fiables al encontrarse fuera del rango del equipo de medida. Estas medidas permiten observar de una forma más directa el grado de reducción y de defectos del material obtenido. Así, acorde con los resultados obtenidos mediante las técnicas de XPS y micro-Raman, que indicaban el porcentaje de  $C_{sp}^2$  y el grado de defectos, respectivamente, las muestran que presentaron mayor valor de conductividad fueron las funcionalizadas con tensioactivo. Mientras que la de menor conductividad fue la obtenida por reducción con vitamina C (sin DDPS), debido probablemente a la presencia de la forma oxidada de la vitamina C unida a las láminas.<sup>[71]</sup>

## VII. Conclusiones

En este capítulo se resumen las principales conclusiones obtenidas a partir de los resultados experimentales de los diferentes sistemas estudiados en este trabajo: monocapas de polímeros derivados del anhídrido maleico, películas de puntos cuánticos de CdSe y grafeno obtenido químicamente depositados sobre sólidos mediante la metodología de Langmuir-Blodgett.

En el caso de los **polímeros**, Capítulo IV, el trabajo se enfocó en el estudio del auto-ensamblaje en la interfase aire-agua y en los sólidos. Con el fin de preparar películas compatibles con aplicaciones potenciales en la construcción de dispositivos electrónicos, nuestro interés se centró en estudiar el efecto de los electrolitos en las propiedades de equilibrio y dinámicas de las películas de Langmuir y Langmuir-Blodgett del copolímero de bloque estireno-b-anhídrido maleico-b-ácido 4-etoxi-4-oxo-2-butenoico-cumeno, PS-MA-BEE. Los resultados muestran que las monocapas de Langmuir depositadas sobre subfases salinas son más expandidas y estables que las monocapas preparadas sobre subfase acuosa sin electrolitos. Estos hechos pueden ser atribuidos a la formación de un complejo entre el catión divalente,  $Mg^{2+}$ , y los grupos carboxílicos de la molécula de polímero. Nuestros resultados demuestran que los complejos de polímero- $Mg^{2+}$  aumentan el comportamiento viscoelástico de la monocapa.

Los resultados también mostraron procesos de auto-ensamblaje superficial en las monocapas de polímero más densas. Los agregados transferidos desde la interfase aire-líquido a obleas de silicio presentan morfologías diferentes dependiendo de la metodología empleada para construir la película LB y de la composición de la subfase. El espesor de las películas LB obtenido por elipsometría concuerda con la altura de la película determinada con medidas de AFM.

Además, con el fin de reforzar la formación de complejos entre el catión  $Mg^{2+}$  y los grupos ácido del polímero, estudiamos las propiedades superficiales de otro polímero derivado del anhídrido maleico que no posee grupos de ácido carboxílico. El copolímero elegido fue poli-(estireno-co-anhídrido maleico)-cumeno, PS-b-MA. Los resultados mostraron el efecto característico de electrolitos en las monocapas insolubles en agua, es decir, las isoterms se desplazan a menores áreas cuando la concentración de sal en la subfase aumenta. Este comportamiento es indicativo de la ausencia de formación de complejos. Por

otro lado, la morfología de las películas LB depende de la naturaleza del polímero, observándose agregados en forma de bandas para PS-MA-BEE y dominios circulares para PS-b-MA.

Además, el polímero PS-b-MA nos permite llevar a cabo el estudio de la temperatura de transición vítrea en 2D por medio de las propiedades de equilibrio y dinámicas. Las medidas de potencial superficial indicaron que la presencia de electrolitos en la subfase acuosa no modifica significativamente la  $T_g$  en 2D. Por último, la transición de fase en monocapas de PS-b-MA se puso de manifiesto mediante medidas dinámicas. Los resultados muestran que el estado vítreo presenta mayores módulos de elasticidad y viscosidad que el estado fluido.

En el estudio de las películas de **puntos cuánticos (QDs) de CdSe**, presentados en el Capítulo V, nuestro objetivo era desarrollar metodologías diferentes para preparar películas de QDs mediante la técnica de Langmuir-Blodgett y estudiar la influencia de la morfología de la película en sus propiedades fotoluminiscentes. Para modular el auto-ensamblaje de los QDs se utilizó el polímero PS-MA-BEE proponiéndose tres sistemáticas diferentes.

En la primera de ellas, referida como co-deposición, estudiamos la capacidad de ensamblaje de monocapas mixtas de QD/PS-MA-BEE en sólidos mediante imágenes de AFM y TEM. Los resultados obtenidos demostraron que el estado superficial del copolímero de bloques PS-MA-BEE juega un papel decisivo en la morfología de los ensamblados de nanopartículas. Por lo tanto, cuando la monocapa de Langmuir precursora de las películas LB presenta el valor más bajo de elasticidad, que corresponde a la conformación cepillo del polímero en la superficie, las películas están compuestas por redes hexagonales donde los QDs están adsorbidos en los bordes. Por el contrario, las monocapas con los valores más altos de elasticidad dan lugar a películas LB con dominios de QD/polímero. Las diferentes estructuras fueron interpretadas en términos de distintos procesos de secado, nucleación y crecimiento de agujeros en la formación de redes

hexagonales y mecanismo espinodal, en el caso de los dominios de QD/polímero. Nuestros resultados demostraron que es posible modular la morfología de las películas LB de QDs modificando tanto, la composición superficial como las propiedades elásticas de las monocapas de Langmuir precursoras de las películas LB. Esta estrategia podría ser presentada como una técnica reproducible alternativa a la litografía para diseñar en la nanoescala.

En la segunda metodología, la película LB de polímero se utiliza para modificar las propiedades superficiales del sustrato. Los resultados demuestran que la película LB del polímero PS-MA-BEE juega un papel importante en el aumento de la densidad superficial de QDs adsorbidos sobre mica. Interacciones cohesivas entre las cadenas de polímero y las cadenas hidrocarbonadas del estabilizador de los QDs, TOPO, puede ser el origen de este hecho. En todos los casos se observaron agregados en 2D en forma de islas y se evita la aglomeración en 3D de las nanopartículas.

Por último, se propuso estudiar la influencia de la naturaleza del ligando en el ensamblaje de las nanopartículas mediante el intercambio del ligando de los QDs por el polímero, PS-MA-BEE. En este sentido, se prepararon películas mixtas de QD/PS-MA-BEE y bicapas de PS-MA-BEE//QDs. Los resultados muestran que la sustitución del estabilizador TOPO de los QDs por el polímero PS-MA-BEE afecta a la morfología de los ensamblados de nanopartículas. En el caso de películas mixtas, el elevado peso molecular de la película formada por nanopartículas QD<sub>p</sub>, favorece los efectos gravitatorios frente a los efectos de las ondas capilares. Por lo tanto, la morfología de los auto-ensamblados es promovida por el mecanismo de secado de nucleación y crecimiento de agujeros. Según los resultados, es posible modular la morfología de las películas LB de QDs mediante la combinación de la modificación del ligando de las nanopartículas y la composición superficial de las monocapas de Langmuir precursoras de las películas LB. En el caso de las bicapas, como el ligando de los QDs y la película



que recubre el sustrato exponen el mismo grupo, PS, las interacciones favorables conducen a una mejor distribución de los QDs sobre la película de polímero.

Nuestros resultados sugirieron que la compresión de la monocapa desarrolla estados metaestables transitorios que finalmente relajan hacia la configuración de mínima energía del dominio. Por lo tanto, para alcanzar el estado estable, se aplican sucesivos ciclos de compresión-expansión y posteriormente se detienen las barreras. Esta estrategia conduce a la obtención de monocapas de nanopartículas más ordenadas. Por otra parte, esta metodología nos permite obtener información de los diferentes procesos de relajación que se producen después de aplicar los ciclos de compresión-expansión. Los resultados mostraron la existencia de dos procesos de relajación en películas de QDs y QD/polímero. El proceso más rápido fue atribuido al movimiento de los bloques, mientras que el más lento se relacionó con movimientos dentro de los bloques. Además, el valor de los tiempos de estos procesos depende de la composición de la película. Así, las relajaciones más lentas corresponden a sistemas con alta concentración de polímero. Finalmente, se sugiere la cizalla como una fuerza externa para dirigir el ensamblaje de las películas de nanocompuestos ya que se observó una orientación en la dirección de los esfuerzos aplicados de las películas QD/polímero. Además, en este trabajo se ha propuesto la combinación de dos métodos para controlar el ensamblaje del nanocompuesto: una matriz de polímero y una fuerza de externa de cizalla. Nuestros resultados demuestran que escogiendo una metodología apropiada es posible modular el ensamblaje de los QDs.

Finalmente, analizamos el efecto de la morfología de los dominios de QDs en las propiedades de fotoluminiscencia de la película utilizando la técnica de FLIM. El estudio de fotoluminiscencia resuelta en el tiempo de las películas nos ha permitido poner de manifiesto varios fenómenos de la fotodinámica de los QDs en las películas LB.

Para interpretar los resultados obtenidos para las diferentes películas LB previamente estudiamos la emisión de fotoluminiscencia dinámica de los QDs disueltos en cloroformo. Los resultados demostraron que la vida media de las partículas en disolución es independiente de la concentración de polímero, sugiriendo la existencia de un proceso de *quenching* estático por transferencia de carga entre los QDs y el polímero. Por otra parte, las curvas de decaimiento de fotoluminiscencia para los QDs son diferentes en disolución y en películas LB. En principio, la disolución ofrece un entorno más fluido minimizando la interacción entre los QDs, mientras que las películas LB presentan un entorno dieléctrico diferente que aumenta el tiempo de vida medio radiativo y proporciona una disposición compacta de partículas que permite interacciones dipolares QD-QD. Por otra parte, los estudios llevados a cabo analizando el efecto de la energía de excitación, el tiempo de exposición y el margen de longitudes de onda de emisión del espectro recogido en la dinámica de fotoluminiscencia puso de manifiesto la existencia de procesos multi-excitónicos, una foto-pasivación cuasi-reversible de la superficie de la partícula y la emisión de los estados correspondiente a los defectos de superficie, respectivamente.

La fotoluminiscencia de las películas mixtas de QD/polímero se caracterizó para distintas condiciones de deposición de la película: bicapa o co-deposición; composición de la mezcla, y la presión superficial de deposición. Los resultados muestran que la dinámica de fotoluminiscencia de las películas de QDs está afectada por el transporte de energía y los procesos de captura que se producen en las zonas compactas de QDs depositados. La eficacia de estos procesos depende esencialmente de la distancia entre partículas y la densidad superficial de trampas de energía, que pueden ser QDs con muchos defectos superficiales o agrupaciones de clústeres. Entre las diferentes condiciones estudiadas, la deposición en bicapa mostró las superficies con mayor intensidad de emisión, es decir, más brillo en las imágenes. El análisis simultáneo de los decaimientos de fotoluminiscencia y las imágenes de TEM nos permitió relacionar

este comportamiento a una menor cantidad de agregación en clústeres de los QDs en la disposición en bicapa. El modelo utilizado para el análisis de las curvas de decaimiento considera el transporte de energía y procesos de captura en las películas y, aunque es sólo un modelo aproximado, nos ha permitido relacionar la dinámica de fotoluminiscencia con la morfología de la película. De hecho, la concentración de trampas obtenida a partir del análisis de las curvas de decaimiento de la bicapa es aproximadamente la mitad de la que se observa en las películas preparadas por co-deposición. Finalmente, a partir de los resultados, es posible concluir que con el fin de mejorar las propiedades de fotoluminiscencia de películas de QDs, es importante obtener películas con una morfología regular y compacta para reducir al mínimo la agregación en clústeres de los QDs.

El último sistema estudiado fue grafeno obtenido químicamente, Capítulo VI. Los objetivos fueron desarrollar una nueva ruta sintética mediante el uso del tensioactivo zwitteriónico 11,3-(dimetil-dodecilamonio)-propanosulfonato, DDPS, y la deposición controlada del material preparado con el fin de conseguir una buena calidad y láminas de RGO de bajo espesor. De este modo, analizamos el grado de reducción, el grado de reparación de defectos y la conductividad eléctrica de las láminas de RGO obtenidos por reducción de GO con hidracina y la vitamina C y funcionalizado mediante el tensioactivo DDPS. Los resultados demuestran que la funcionalización con el tensioactivo zwitteriónico DDPS mejora la eficiencia en la reducción de la hidracina y de la vitamina C, medida por el porcentaje de  $C_{sp^2}$ ; reduce los grupos residuales unidos a la red de carbono introducidos por los agentes reductores en ambos casos, y aumenta la conductividad del RGO. Además, la conductividad eléctrica observada en nuestras muestras funcionalizadas es generalmente mayor que la mostrada por películas soportadas sobre papel de RGO funcionalizados con otros tensioactivos. En consecuencia, se propone la funcionalización de RGO con DDPS como una buena funcionalización no covalente, que aumenta la conductividad eléctrica sin alterar la red de carbono. Además, la funcionalización con un tensioactivo

zwitteriónico ofrece una carga residual que puede unir las láminas de RGO con otros materiales con el fin de preparar nanocompuestos con múltiples aplicaciones. Los resultados también mostraron que la técnica de Langmuir-Blodgett permitió depositar láminas finas de RGO en obleas de silicio para poder llevar a cabo la caracterización del material.

### VIII. Bibliografía

1. Petty, M. C., *Langmuir-Blodgett Films: An Introduction*. Cambridge University Press: 1996.
2. Bardosova, M.; Pemble, M. E.; Povey, I. M.; Tredgold, R. H., The Langmuir-Blodgett Approach to Making Colloidal Photonic Crystals from Silica Spheres. *Adv. Mater.* **2010**, *22* (29), 3104-3124.
3. Park, J. Y.; Advincula, R. C., Nanostructuring Polymers, Colloids, and Nanomaterials at the Air-Water Interface through Langmuir and Langmuir-Blodgett Techniques. *Soft Matter* **2011**, *7* (21), 9829-9843.
4. Reiter, G., Probing Properties of Polymers in Thin Films. *Adv. Polym. Sci.* **2013**, *252*, 29-64.
5. Jones, R.; Winter, C. S.; Tredgold, R. H.; Hodge, P.; Hoorfar, A., Electron-beam Resists from Langmuir-Blodgett films of Poly(styrene/maleic anhydride) Derivatives. *Polymer* **1987**, *28* (10), 1619-1626.
6. Collins, S. J.; Mary, N. L.; Radhakrishnan, G.; Dhathathreyan, A., Studies of Spread Monolayers of Derivative of Styrene-Maleic Anhydride Copolymers. *J. Chem. Soc. Faraday Trans.* **1997**, *93* (22), 4021-4023.
7. Rogach, A. L., *Semiconductor Nanocrystal Quantum Dots: Synthesis, Assembly, Spectroscopy and Applications*. Springer:Wien: New York, 2008.
8. Tomczak, N.; Jaczewski, D.; Han, M.; Vancso, G. J., Designer Polymer-Quantum Dot Architectures. *Prog. Polym. Sci.* **2009**, *34* (5), 393-430.

9. Talapin, D. V.; Lee, J.-S.; Kovalenko, M. V.; Shevchenko, E. V., Prospects of Colloidal Nanocrystals for Electronic and Optoelectronic Applications. *Chem. Rev.* **2010**, *110* (1), 389-458.
10. Selinsky, R. S.; Ding, Q.; Faber, M. S.; Wright, J. C.; Jin, S., Quantum Dot Nanoscale Heterostructures for Solar Energy Conversion. *Chem. Soc. Rev.* **2013**, *42* (7), 2963-2985.
11. Lee, J. Y.; Shou, Z.; Balazs, A. C., Predicting the Morphologies of Confined Copolymer/Nanoparticle Mixtures. *Macromolecules* **2003**, *36* (20), 7730-7739.
12. Lin, Y.; Böker, A.; He, J.; Sill, K.; Xiang, H.; Abetz, C.; Li, X.; Wang, J.; Emrick, T.; Long, S.; Wang, Q.; Balazs, A.; Russell, T. P., Self-directed Self-assembly of Nanoparticle/Copolymer Mixtures. *Nature* **2005**, *434* (7029), 55-59.
13. Cheyne, R. B.; Moffitt, M. G., Hierarchical Nanoparticle/Block Copolymer Surface Features via Synergistic Self-Assembly at the Air-Water Interface. *Langmuir* **2005**, *21* (23), 10297-10300.
14. Li, H.; Sachsenhofer, R.; Binder, W. H.; Henze, T.; Thurn-Albrecht, T.; Busse, K.; Kressler, J., Hierarchical Organization of Poly(ethylene oxide)-block-poly(isobutylene) and Hydrophobically Modified Fe<sub>2</sub>O<sub>3</sub> Nanoparticles at the Air/Water Interface and on Solid Supports. *Langmuir* **2009**, *25* (14), 8320-8329.
15. Murray, C. B.; Kagan, C. R.; Bawendi, M. G., Synthesis and Characterization of Monodisperse Nanocrystals and Close-packed Nanocrystal Assemblies. *Annu. Rev. Mater. Sci.* **2000**, *30* (1), 545-610.
16. Worfolk, B. J.; Rider, D. A.; Elias, A. L.; Thomas, M.; Harris, K. D.; Buriak, J. M., Bulk Heterojunction Organic Photovoltaics Based on Carboxylated Polythiophenes and PCBM on Glass and Plastic Substrates. *Adv. Funct. Mater.* **2011**, *21* (10), 1816-1826.
17. Kim, J. Y.; Raja, S.; Stellacci, F., Evolution of Langmuir Film of Nanoparticles Through Successive Compression Cycles. *Small* **2011**, *7* (17), 2526-2532.

18. Cicuta, P.; Vella, D., Granular Character of Particle Rafts. *Phys. Rev. Lett.* **2009**, *102* (13), 138302.
19. Zang, D.; Langevin, D.; Binks, B. P.; Wei, B., Shearing Particle Monolayers: Strain-rate Frequency Superposition. *Phys. Rev. E* **2010**, *81* (1), 011604.
20. Guzmán, E.; Liggieri, L.; Santini, E.; Ferrari, M.; Ravera, F., Effect of Hydrophilic and Hydrophobic Nanoparticles on the Surface Pressure Response of DPPC Monolayers. *J. Phys. Chem. C* **2011**, *115* (44), 21715-21722.
21. Nodoro, T. V. M.; Böhm, M. C.; Müller-Plathe, F., Interface and Interphase Dynamics of Polystyrene Chains near Grafted and Ungrafted Silica Nanoparticles. *Macromolecules* **2012**, *45* (1), 171-179.
22. Toepperwein, G. N.; Riggleman, R. A.; de Pablo, J. J., Dynamics and Deformation Response of Rod-Containing Nanocomposites. *Macromolecules* **2012**, *45* (1), 543-554.
23. Osman, A. F.; Edwards, G. A.; Schiller, T. L.; Andriani, Y.; Jack, K. S.; Morrow, I. C.; Halley, P. J.; Martin, D. J., Structure-Property Relationships in Biomedical Thermoplastic Polyurethane Nanocomposites. *Macromolecules* **2012**, *45* (1), 198-210.
24. Jones, M.; Scholes, G. D., On the Use of Time-Resolved Photoluminescence as a Probe of Nanocrystal Photoexcitation Dynamics. *J. Mater. Chem.* **2010**, *20* (18), 3533-3538.
25. Chen, D.; Feng, H.; Li, J., Graphene Oxide: Preparation, Functionalization, and Electrochemical Applications. *Chem. Rev.* **2012**, *112* (11), 6027-6053.
26. Hu, W.; Peng, C.; Luo, W.; Lv, M.; Li, X.; Li, D.; Huang, Q.; Fan, C., Graphene-Based Antibacterial Paper. *ACS Nano* **2010**, *4* (7), 4317-4323.
27. Cui, X.; Zhang, C.; Hao, R.; Hou, Y., Liquid-phase Exfoliation, Functionalization and Applications of Graphene. *Nanoscale* **2011**, *3* (5), 2118-2126.
28. Singh, V.; Joung, D.; Zhai, L.; Das, S.; Khondaker, S. I.; Seal, S., Graphene based Materials: Past, Present and Future. *Prog. Mater. Sci.* **2011**, *56* (8), 1178-1271.

29. Shao, Y.; Wang, J.; Wu, H.; Liu, J.; Aksay, I. A.; Lin, Y., Graphene Based Electrochemical Sensors and Biosensors: A Review. *Electroanalysis* **2010**, *22* (10), 1027-1036.
30. Yu, W. W.; Peng, X., Formation of High-Quality CdS and Other II–VI Semiconductor Nanocrystals in Noncoordinating Solvents: Tunable Reactivity of Monomers. *Angew. Chem. Int. Ed. Engl.* **2002**, *41* (13), 2368-2371.
31. Hummers, W. S.; Offeman, R. E., Preparation of Graphitic Oxide. *J. Am. Chem. Soc.* **1958**, *80* (6), 1339-1339.
32. Cote, L. J.; Kim, F.; Huang, J., Langmuir-Blodgett Assembly of Graphite Oxide Single Layers. *J. Am. Chem. Soc.* **2009**, *131* (3), 1043-1049.
33. Zajac, J.; Chorro, C.; Lindheimer, M.; Partyka, S., Thermodynamics of Micellization and Adsorption of Zwitterionic Surfactants in Aqueous Media. *Langmuir* **1997**, *13* (6), 1486-1495.
34. Hilles, H.; Monroy, F.; Bonales, L. J.; Ortega, F.; Rubio, R. G., Fourier-Transform Rheology of Polymer Langmuir Monolayers: Analysis of the Non-linear and Plastic Behaviors. *Adv. Colloid Interface Sci.* **2006**, *122* (1-3), 67-77.
35. Horcas, I.; Fernández, R.; Gómez-Rodríguez, J. M.; Colchero, J.; Gómez-Herrero, J.; Baro, A. M., WSXM: A Software for Scanning Probe Microscopy and a Tool for Nanotechnology. *Rev. Sci. Instrum.* **2007**, *78* (1), 013705.
36. Tompkins, H. G., *A User's Guide to Ellipsometry*. Academic Press Inc.: London, 1993.
37. Gao, W.; Alemany, L. B.; Ci, L.; Ajayan, P. M., New Insights into the Structure and Reduction of Graphite Oxide. *Nat Chem* **2009**, *1* (5), 403-408.
38. Angelomé, P. C.; Pastoriza-Santos, I.; Pérez-Juste, J.; Rodríguez-González, B.; Zelcer, A.; Soler-Illia, G. J. A. A.; Liz-Marzán, L. M., Growth and Branching of Gold Nanoparticles through Mesoporous Silica Thin Films. *Nanoscale* **2012**, *4* (3), 931-939.
39. Paulo, P. M. R.; Costa, S. M. B., Single-Molecule Fluorescence of a Phthalocyanine in PAMAM Dendrimers Reveals Intensity-Lifetime Fluctuations from Quenching Dynamics. *J. Phys. Chem. C* **2010**, *114* (44), 19035-19043.

40. Simurda, M.; Nemeč, P.; Trojánek, F.; Malý, P., Substantial Enhancement of Photoluminescence in CdSe Nanocrystals by Femtosecond Pulse Illumination. *Thin Solid Films* **2004**, *453-454* (0), 300-303.
41. Pechstedt, K.; Whittle, T.; Baumberg, J.; Melvin, T., Photoluminescence of Colloidal CdSe/ZnS Quantum Dots: The Critical Effect of Water Molecules. *J. Phys. Chem. C* **2010**, *114* (28), 12069-12077.
42. Roberts, G., *Langmuir-Blodgett Films*. Plenum Press New York: 1990.
43. Bordi, F.; Cametti, C.; Sennato, S., Polyions act as an Electrostatic Glue for Mesoscopic Particle Aggregates. *Chem. Phys. Lett.* **2005**, *409* (1&€“3), 134-138.
44. Dynarowicz-Latka, P.; Dhanabalan, A.; Oliveira Jr, O. N., Modern Physicochemical Research on Langmuir Monolayers. *Adv. Colloid Interface Sci.* **2001**, *91* (2), 221-293.
45. Yang, Z.; Fujii, Y.; Lee, F. K.; Lam, C.-H.; Tsui, O. K. C., Glass Transition Dynamics and Surface Layer Mobility in Unentangled Polystyrene Films. *Science* **2010**, *328* (5986), 1676-1679.
46. Maestro, A.; Ortega, F.; Rubio, R. G.; Rubio, M. A.; Kragel, J.; Miller, R., Rheology of Poly(methyl methacrylate) Langmuir Monolayers: Percolation Transition to a Soft Glasslike System. *J. Chem. Phys.* **2011**, *134* (10), 104704-12.
47. Noskov, B. A.; Lin, S. Y.; Loglio, G.; Rubio, R. G.; Miller, R., Dilational Viscoelasticity of PEO-PPO-PEO Triblock Copolymer Films at the Air-Water Interface in the Range of High Surface Pressures. *Langmuir* **2006**, *22* (6), 2647-2652.
48. Gentili, D.; Foschi, G.; Valle, F.; Cavallini, M.; Biscarini, F., Applications of Dewetting in Micro and Nanotechnology. *Chem. Soc. Rev.* **2012**, *41* (12), 4430-4443.
49. Lucassen, J., Longitudinal Capillary Waves. Part 1.-Theory. *Trans. Faraday Soc.* **1968**, *64*, 2221-2229.
50. Zou, S.; Hong, R.; Emrick, T.; Walker, G. C., Ordered CdSe Nanoparticles within Self-Assembled Block Copolymer Domains on Surfaces. *Langmuir* **2007**, *23* (4), 1612-1614.



51. Sides, S. W.; Kim, B. J.; Kramer, E. J.; Fredrickson, G. H., Hybrid Particle-Field Simulations of Polymer Nanocomposites. *Phys. Rev. Lett.* **2006**, *96* (25), 250601.
52. Reis, F. D. A. A. o., Modeling Self-Assembly of Diblock Copolymer-Nanoparticle Composites. *Macromolecules* **2008**, *41* (22), 8932-8937.
53. Langner, K. M.; Sevink, G. J. A., Mesoscale Modeling of Block Copolymer Nanocomposites. *Soft Matter* **2012**, *8* (19), 5102-5118.
54. Krishnan, R. S.; Mackay, M. E.; Duxbury, P. M.; Pastor, A.; Hawker, C. J.; Van Horn, B.; Asokan, S.; Wong, M. S., Self-Assembled Multilayers of Nanocomponents. *Nano Lett.* **2007**, *7* (2), 484-489.
55. Shafrin, E. G.; Zisman, W. A., Constitutive Relations in the Wetting of low Energy Surfaces and the Theory of the Refraction Method of preparing Monolayers. *J. Phys. Chem.* **1960**, *64* (5), 519-524.
56. Maury, P.; Escalante, M.; Reinhoudt, D. N.; Huskens, J., Directed Assembly of Nanoparticles onto Polymer-Imprinted or Chemically Patterned Templates Fabricated by Nanoimprint Lithography. *Adv. Mater.* **2005**, *17* (22), 2718-2723.
57. Baumgart, T.; Offenhäusser, A., Polysaccharide-Supported Planar Bilayer Lipid Model Membranes. *Langmuir* **2002**, *19* (5), 1730-1737.
58. Kundu, S.; Bal, J. K., Reorganization of Au Nanoparticle Langmuir-Blodgett Films on Wet Chemically Passivated Si(001) Surfaces. *J. Appl. Phys.* **2011**, *110* (11), 114302-8.
59. Tao, A. R.; Huang, J.; Yang, P., Langmuir-Blodgettry of Nanocrystals and Nanowires. *Acc. Chem. Res.* **2008**, *41* (12), 1662-1673.
60. Vacatello, M., Monte Carlo Simulations of Polymer Melts Filled with Solid Nanoparticles. *Macromolecules* **2001**, *34* (6), 1946-1952.
61. Ghanbari, A.; Nodoro, T. V. M.; Leroy, F.; Rahimi, M.; Böhm, M. C.; Müller-Plathe, F., Interphase Structure in Silica-Polystyrene Nanocomposites: A Coarse-Grained Molecular Dynamics Study. *Macromolecules* **2012**, *45* (1), 572-584.

- 
62. Tachiya, M.; Mozumder, A., Kinetics of Geminate-ion Recombination by Electron Tunnelling. *Chem. Phys. Lett.* **1975**, *34* (1), 77-79.
63. Tachiya, M.; Seki, K., Unified Explanation of the Fluorescence Decay and Blinking Characteristics of Semiconductor Nanocrystals. *Appl. Phys. Lett.* **2009**, *94* (8), 081104-3.
64. Gochanour, C. R.; Andersen, H. C.; Fayer, M. D., Electronic Excited State Transport in Solution. *J. Chem. Phys.* **1979**, *70* (9), 4254-4271.
65. Loring, R. F.; Fayer, M. D., Electronic Excited State Transport and Trapping in One-and Two-Dimensional Disordered Systems. *Chem. Phys.* **1982**, *70* (1-2), 139-147.
66. Ducker, W. A.; Grant, L. M., Effect of Substrate Hydrophobicity on Surfactant Surface-Aggregate Geometry. *J. Phys. Chem.* **1996**, *100* (28), 11507-11511.
67. Tiberg, F.; Brinck, J.; Grant, L., Adsorption and Surface-induced Self-assembly of Surfactants at the Solid-Aqueous Interface. *Curr. Opin. Colloid Interface Sci.* **1999**, *4* (6), 411-419.
68. Delgado, C.; Merchán, M. D.; Velázquez, M. M., Effect of the Addition of Polyelectrolytes on Monolayers of Carboxybetaines. *J. Phys. Chem. B* **2008**, *112* (3), 687-693.
69. Luo, D.; Zhang, G.; Liu, J.; Sun, X., Evaluation Criteria for Reduced Graphene Oxide. *J. Phys. Chem. C* **2011**, *115* (23), 11327-11335.
70. Fernández-Merino, M. J.; Guardia, L.; Paredes, J. I.; Villar-Rodil, S.; Solís-Fernández, P.; Martínez-Alonso, A.; Tascón, J. M. D., Vitamin C is an Ideal Substitute for Hydrazine in the Reduction of Graphene Oxide Suspensions. *J. Phys. Chem. C* **2010**, *114* (14), 6426-6432.
71. Zhang, J.; Yang, H.; Shen, G.; Cheng, P.; Zhang, J.; Guo, S., Reduction of Graphene Oxide via L-ascorbic acid. *Chem. Commun.* **2010**, *46* (7), 1112-1114.
72. Zhou, X.; Zhang, J.; Wu, H.; Yang, H.; Zhang, J.; Guo, S., Reducing Graphene Oxide via Hydroxylamine: A Simple and Efficient Route to Graphene. *J. Phys. Chem. C* **2011**, *115* (24), 11957-11961.

73. Paredes, J. I.; Villar-Rodil, S.; Fernández-Merino, M. J.; Guardia, L.; Martínez-Alonso, A.; Tascón, J. M. D., Environmentally Friendly Approaches toward the Mass Production of Processable Graphene from Graphite Oxide. *J. Mater. Chem.* **2011**, *21* (2), 298-306.
74. Dua, V.; Surwade, S. P.; Ammu, S.; Agnihotra, S. R.; Jain, S.; Roberts, K. E.; Park, S.; Ruoff, R. S.; Manohar, S. K., All-Organic Vapor Sensor Using Inkjet-Printed Reduced Graphene Oxide. *Angew. Chem. Int. Ed.* **2010**, *49* (12), 2154-2157.
75. Becerril, H. A.; Mao, J.; Liu, Z.; Stoltenberg, R. M.; Bao, Z.; Chen, Y., Evaluation of Solution-Processed Reduced Graphene Oxide Films as Transparent Conductors. *ACS Nano* **2008**, *2* (3), 463-470.
76. Schniepp, H. C.; Li, J.-L.; McAllister, M. J.; Sai, H.; Herrera-Alonso, M.; Adamson, D. H.; Prud'homme, R. K.; Car, R.; Saville, D. A.; Aksay, I. A., Functionalized Single Graphene Sheets Derived from Splitting Graphite Oxide. *J. Phys. Chem. B* **2006**, *110* (17), 8535-8539.
77. Li, X.; Zhang, G.; Bai, X.; Sun, X.; Wang, X.; Wang, E.; Dai, H., Highly Conducting Graphene Sheets and Langmuir-Blodgett Films. *Nat. Nanotechnol.* **2008**, *3* (9), 538-542.
78. Stankovich, S.; Dikin, D. A.; Piner, R. D.; Kohlhaas, K. A.; Kleinhammes, A.; Jia, Y.; Wu, Y.; Nguyen, S. T.; Ruoff, R. S., Synthesis of Graphene-based Nanosheets via Chemical Reduction of Exfoliated Graphite Oxide. *Carbon* **2007**, *45* (7), 1558-1565.
79. Lotya, M.; Hernandez, Y.; King, P. J.; Smith, R. J.; Nicolosi, V.; Karlsson, L. S.; Blighe, F. M.; De, S.; Wang, Z.; McGovern, I. T.; Duesberg, G. S.; Coleman, J. N., Liquid Phase Production of Graphene by Exfoliation of Graphite in Surfactant/Water Solutions. *J. Am. Chem. Soc.* **2009**, *131* (10), 3611-3620.
80. Panchakarla, L. S.; Subrahmanyam, K. S.; Saha, S. K.; Govindaraj, A.; Krishnamurthy, H. R.; Waghmare, U. V.; Rao, C. N. R., Synthesis, Structure, and Properties of Boron- and Nitrogen-Doped Graphene. *Adv. Mater.* **2009**, *21* (46), 4726-4730.

- 
81. Wang, D.; Kou, R.; Choi, D.; Yang, Z.; Nie, Z.; Li, J.; Saraf, L. V.; Hu, D.; Zhang, J.; Graff, G. L.; Liu, J.; Pope, M. A.; Aksay, I. A., Ternary Self-Assembly of Ordered Metal Oxide-Graphene Nanocomposites for Electrochemical Energy Storage. *ACS Nano* **2010**, *4* (3), 1587-1595.
82. Tuinstra, F.; Koenig, J. L., Raman Spectrum of Graphite. *J. Chem. Phys.* **1970**, *53* (3), 1126-1130.





VNiVERSiDAD  
D SALAMANCA

CAMPUS DE EXCELENCIA INTERNACIONAL